UNIVERSIDADE DE SÃO PAULO
INSTITUTO DE GEOCIÊNCIAS

Geologia e petrologia de kimberlitos da região Oeste de Minas Gerais: Charneca, Grota do Cedro, Régis e Indaiá

CASSANDRA TERRA BARBOSA

Orientador: Prof. Dr. Excelso Ruberti

Tese de Doutorado

Nº 585

COMISSÃO JULGADORA

Dr. Excelso Ruberti

Dr. Darcy Pedro Svizzero

Dr. Valdecir de Assis Janasi

Dr. Elson Paiva de Oliveira

Dra. Maria Zélia Aguiar de Sousa

SÃO PAULO
2018

Serviço de Biblioteca e Documentação do IGc/USP
Ficha catalográfica gerada automaticamente com dados fornecidos pelo(a) autor(a) via programa desenvolvido pela Seção Técnica de Informática do ICMC/USP

Bibliotecários responsáveis pela estrutura de catalogação da publicação:
Sonia Regina Yole Guerra - CRB-8/4208 | Anderson de Santana - CRB-8/6658

Terra Barbosa, Cassandra
Geologia e petrologia de kimberlitos da região Oeste de Minas Gerais: Charneca, Grota do Cedro, Régis e Indaiá / Cassandra Terra Barbosa; orientador Excelso Ruberti. -- São Paulo, 2018.
389 p.

Tese (Doutorado - Programa de Pós-Graduação em Mineralogia e Petrologia) -- Instituto de Geociências, Universidade de São Paulo, 2018.

1. Kimberlito. 2. Rocha Alcalina. 3. Petrologia Ígnea. 4. Província Ígnea do Alto Paranaíba. 5. Diamante. I. Ruberti, Excelso, orient. II. Título.

Dedico este trabalho aos meus Irmãos,
aos meus companheiros desta Jornada de hoje,
de ontem e de muitas que virão.

Agradecimentos

Agradeço primeiramente ao meu grande Amigo Dr. Celso Charuri, por me indicar a direção, o norte para me manter paciente, e por permitir a escolha de caminharmos juntos nesta jornada. Esteja onde estiver, o meu muito Obrigada. Aos meus pais Jerônimo e Nicole que me apoiaram todos esses anos e me possibilitaram a oportunidade de estar aqui. Agradeço aos meus irmãos Sarah, Rafael e Ricardo pelas risadas e o aconchego de sempre. À sobrinha preferida Ágatha que sempre esteve no coração. Agradeço a todos os familiares que mesmo longe estavam pertos em pensamento. Em especial agradeço também ao Anderson Brasil pelo suporte nesta finalização de uma etapa tão importante e que foi um Grande Homem fundamental neste caminho.

Agradeço ao professor Excelso pela assistência no trabalho, paciência e amizade, e por me mostrar um novo caminho de conhecimento. Ao professor Rogério Azzone pelo auxílio nos trabalhos de campo. Ao professor Daniel Atencio pela confiança e disposição em ajudar nos mais variados temas. Agradeço ao professor Rainer Aloys Schultz Guttler pelo apoio durante tantos anos e pelo incentivo em continuar a trabalhar pelo que acreditamos. Agradeço também aos professores Adriana Alves, Patrício Muñoz, Silvio Vlach, Fábio Ramos e Danielle Giordano que colaboraram de diferentes formas para a conclusão deste trabalho.

Aos amigos de “corredor” Maria Isabel, Astrid Velandia, Caio vulgo Fofona, Pedro Rosa, Giovanna, Melina, John que sempre estiveram presentes com sorrisos nos rostos e disposição para ajudar. Obrigada à querida Serena pelo companheirismo e apoio nos mais diversos temas. Ao Gabriel que com muita disposição e paciência ajudou na em etapas importantíssimas deste trabalho. Aos funcionários do Instituto de Geociências, especialmente ao Marcos Mansueto, Leandro Moraes, Vasco Loios, Vinícius Martins, Sandra Andrade, Samuca e Paulinho que contribuíram imensamente para o desenvolvimento da tese.

À CAPES pelo apoio financeiro referente à bolsa de doutorado, à FAPESP - Fundação de Amparo à Pesquisa do Estado de São Paulo (Proc. 2012/06082-6) pelo suporte financeiro que viabilizou todo este trabalho, e ao Instituto de Geociências pelo apoio e auxílio durante todos esses anos. Agradeço a todos que contribuíram diretamente ou não, mas que foram importantes para cada passo nesta caminhada.

RESUMO

O estudo da mineralogia, ascensão e dinâmica de erupção das rochas kimberlíticas é um desafio, devido à mistura de diferentes fases cristalizadas do líquido magmático e de xenocristais de diversas origens, frequentemente mascarados por intensa alteração. Essa complexidade permite importantes investigações acerca da composição e dinâmica do manto da Terra, além da compreensão sobre a formação e preservação dos diamantes. Este trabalho apresenta o estudo de quatro kimberlitos conhecidos por Charneca, Grota do Cedro, Régis e Indaiá I. Esses corpos estão inseridos na Província Ígnea do Alto Paranaíba (PIAP) no estado de Minas Gerais, a qual representa uma das maiores ocorrências em volume de rochas máficas potássicas no mundo. O estudo consistiu em três linhas de pesquisa. A primeira refere-se à petrografia das feições texturais dessas rochas, com foco principal na discriminação e classificação de clastos juvenis. Os kimberlitos Charneca e Indaiá I apresentam textura uniforme, poucos clastos kimberlíticos e estruturas peletais, baixa ocorrência de xenólitos crustais e uma mineralogia típica de fácies hipoabissal. De acordo com essas características, somadas às suas respectivas peculiaridades, permitem classificar essas rochas em uma variedade de fácies hipoabissal e fácies de transição, respectivamente. Em contrapartida, os kimberlitos Grota do Cedro e Régis exibem textura inequigranular, alta porcentagem de clastos juvenis compostos por diferentes composições de material kimberlítico com maior viscosidade, frequentes xenólitos crustais e características tipicamente de fácies mais rasas, e.g. calcita secundária e texturas de segregação. As múltiplas fases de formação dessas ocorrências possibilitam classifica-las como pertencentes à fácies vulcanoclástica e diatrema, respectivamente. A segunda foi dirigida para a geoquímica mineral, com análises químicas inéditas de elementos maiores, menores e traços realizadas *in-situ* e em concentrados de minerais pesados, esta última técnica permitiu a obtenção de dados químicos com alto grau de confiabilidade principalmente em grãos com capa de alteração. Foram estudados granada, olivina, piroxênio, flogopita, espinélio, ilmenita e perovskita, provenientes principalmente de uma fonte peridotítica. O caráter magnesiano, pobre em Cr_2O_3, Al_2O_3, e CaO do manto é registrado particularmente nos cristais de granada peridotítica-lherzolíticas analisados, os quais exibem diferentes graus de enriquecimento metassomático da fonte mantélica. Os kimberlitos Grota do Cedro e Régis exibem granada com maiores teores de Cr_2O_3 e CaO, enquanto àquelas provenientes do

kimberlito Charneca exibem maior depleção nesses elementos e em lantanídeos leves, além de um enriquecimento em Al_2O_3, TiO_2 e lantanídeos pesados. As baixas razões $(Sm/Er)_N$ combinadas às poucas variações de Ti/Eu dos cristais de granada e clinopiroxênio dos kimberlitos Charneca e Régis, apontam para um fluido de composição essencialmente silicática. Já os cristais de clinopiroxênio do Grota do Cedro, através da pequena e ampla variação das razões Ti/Eu e $(Sm/Er)_N$, respectivamente, indicam composições intermediárias entre fluidos carbonatíticos e silicáticos. Outras fontes mantélicas, como piroxenitos e suíte MARID, também contribuíram principalmente para a assembleia mineralógica dos kimberlitos Grota do Cedro e Régis, respectivamente. Flogopita com altos teores de TiO_2 e grupos de piroxênio com baixos valores de Mg# e altos teores de Cr_2O_3 e TiO_2, têm respectivamente como prováveis fontes a suíte MARID e piroxenítica. Uma ampla variedade do grupo dos óxidos também foi registrada, espinélio com variáveis teores de Cr_2O_3 são predominantes no trend kimberlítico Fe-Ti. Os grãos de ilmenita apresentam distintas variações composicionais de MnO e Al_2O_3 entre os diferentes tamanhos analisados. Cristais de perovskita pouco evoluída ocorrem nos kimberlitos Indaiá I, Régis e Charneca, enquanto o Grota do Cedro apresenta uma fase incomum de Nb-perovskita com altos teores de Nb_2O_5. A terceira linha de pesquisa consistiu na obtenção das razões isotópicas $^{87}Sr/^{86}Sr$ em cristais de perovskita através de LA-ICPMS. Todos os kimberlitos aqui estudados demonstram em diferentes graus alguma contaminação crustal, o kimberlito Régis é o que apresenta maior similaridade com as rochas da PIAP, enquanto maiores variações são exibidas pelo kimberlito Charneca, o qual apresenta valores muito acima das rochas dessa região.

Palavras-chave: kimberlito, rocha alcalina, petrografia, petrologia ígnea, Província ígnea do Alto Paranaíba, diamante

ABSTRACT

The mineralogical study, magmatic ascension and eruption dynamics of kimberlite rocks is a challenge, due to the different crystallized phase's mixture of magma xenocrystals with different origins, often masked by intense alteration. Fortunately, this complexity allows important investigations into the composition and dynamics of the Earth's mantle, besides to comprehend the formation and preservation of diamonds. This work is based on the study of four kimberlites known by the Charneca, Grota do Cedro, Régis and Indaiá I. These rock bodies are located in the Alto Paranaiba Igneous Province (APIP) in the state of Minas Gerais, which represents one of the largest occurrences of potassic mafic rocks in the world. The set of alkaline rocks, such as kimberlites, lamproites, kamafugites and carbonatites, occur predominantly aligned with the Azimuth 125 ° lineament (AZ 125 °), which consists of a set of faults oriented in the NW-SE direction that served as a conduit for magma ascent. This study consisted of three phases. Firstly, a petrographic study of the texture features was carried out, with a main focus on the discrimination and classification of juvenile clasts. Charneca and Indaiá I kimberlites exhibit coherent texture, few kimberlitic clasts and pelletal structures, low incidence of crustal xenoliths and typical hypabyssal mineralogy facies. According to these characteristics, in addition to their peculiarities, it is possible to classify these rocks in a hypabyssal-facies variety and transition-facies, respectively. In comparison, the Grota do Cedro and Régis kimberlites exhibit inequigranular texture, high frequency of juvenile clasts composed of different kimberlitic materials with higher viscosity, frequent crustal xenoliths and typical characteristics of shallower facies, e.g. secondary calcite and segregation textures. The multiple phases of formation of these occurrences make it possible to classify them as belonging to the volcaniclastic-facies and diatreme-facies, respectively. In the second part of this study, unpublished chemical analyzes of major- minor and trace elements were carried out in-situ and in heavy mineral concentrates, this last technique allowed to obtain reliable chemical data mainly in grains covered by alteration. The analyzed minerals were garnet, olivine, pyroxene, phlogopite, spinel, ilmenite and perovskite, and the peridotite rocks are the main sources of the silicates studied. The Magnesian character, poor in Cr_2O_3, Al_2O_3, and CaO of the mantle is recorded mainly by the analyzed peridotite-lherzolite garnet crystals, which exhibit different metasomatic enrichment degrees of the mantle source. Grota do Cedro and Régis kimberlites exhibit higher amounts of Cr_2O_3

and CaO than Charneca, which exhibit depletion of light rare-earth elements and enrichment of Al_2O_3, TiO_2 and heavy rare-earth elements. The low $(Sm/Er)_N$ ratios combined with the few Ti/Eu variations of the garnet and clinopyroxene crystals from Charneca and Régis kimberlites point to silicate composition melt. While clinopyroxene crystals from the Grota do Cedro, through the small and wide variation of the Ti/Eu and $(Sm/Er)_N$ ratios, respectively, indicate intermediate compositions between carbonatite and silicate melts. Other mantle sources, such as pyroxenites and the MARID suite, also contributed mainly to the mineralogical assembly of the Grota do Cedro and Régis kimberlites, respectively. Phlogopite with high levels of TiO_2 and pyroxene groups with low Mg# values and high levels of Cr_2O_3 and TiO_2, have as their probable sources the MARID suite and pyroxenite rocks, respectively. A wide variety of the oxide minerals was also recorded, spinel with varying amounts of Cr_2O_3 are predominant in the Fe-Ti kimberlitic trend. The ilmenite grains present a distinct compositional variation of MnO and Al_2O_3 among the different analyzed sizes. Little evolved perovskite crystals occur in the Indaiá I, Régis and Charneca kimberlites, while the Grota do Cedro presents unusual Nb-perovskites with high levels of Nb_2O_5. The third part of this thesis consisted of $^{87}Sr/^{86}Sr$ isotopic analyses of perovskite determined by LA-ICPMS. All the kimberlites studied demonstrate differently degrees of crustal contamination, the Régis kimberlite is the one that presents greater similarity with the APIP rocks, whereas greater variations are exhibited by the Charneca kimberlite, which presents values much above than the rocks from this region.

Key words: kimberlite, alkaline rock, petrography, igneous petrology, Alto Paranaíba Igneous Province, diamonds

Sumário

Lista de Figuras

Lista de Tabelas

CAPÍTULO 1

1. INTRODUÇÃO

1.1 Organização da tese

Inicialmente uma breve introdução sobre os kimberlitos é apresentada, seguindo-se com uma contextualização geológica da região dos campos kimberlíticos onde os corpos estudados ocorrem e a tese se desenvolve, bem como dos fundamentos petrológicos que envolvem estudos evolutivos da Província Ígnea do Alto do Paranaíba (PIAP), tendo como foco principal as rochas kimberlíticas. Neste capítulo ainda constam os objetivos que justificaram a realização deste estudo bem como a localização e principais acessos a essas ocorrências.

No capítulo 2 são apresentados os materiais e métodos utilizados, com detalhamento dos trabalhos de campo, técnicas de separação mineral e métodos analíticos utilizados para cumprir os propósitos deste trabalho.

Foram quatro ocorrências kimberlíticas da PIAP estudadas: Charneca, Grota do Cedro, Régis e Indaiá I. Os resultados são apresentados na língua inglesa na forma de artigos independentes para a submissão em periódicos internacionais após apreciação da comissão julgadora. O capítulo 3 compreende os títulos preliminares e, de acordo com as normas do Instituto de Geociências (Programa Mineralogia e Petrologia) para alunos do curso de Doutorado matriculados até 28/11/2014, esses artigos encontram-se ao final da tese na seção Apêndice.

As feições texturais do magma kimberlítico, as quais refletem os processos de colocação desses corpos, foram pela primeira vez descritas neste trabalho de uma forma sistemática. Os dados geoquímicos gerados, particularmente os elementos traço e as razões isotópicas $^{87}Sr/^{86}Sr$, em sua maioria inéditos (à exceção de traços para Indaiá), resultaram de análises *in situ* direto em grãos de concentrado mineral, os quais foram obtidos a partir da desagregação das rochas kimberlíticas, um método eficaz principalmente para análise de minerais parcialmente alterados.

O último capítulo busca comparar a petrologia e a geoquímica mineral das quatro ocorrências entre si, tendo em vista o potencial diamantífero de duas delas

(Charneca e Régis), além da evolução destes corpos no contexto da PIAP e a possível natureza das fontes mantélicas onde foram gerados esses magmas. Finalmente, as conclusões abrangem os resultados e discussões obtidos.

1.2 Kimberlitos

Kimberlitos são rochas ígneas potássicas e ultrabásicas de pequeno volume, ricas em voláteis e que ocorrem em todos os continentes na forma de pequenos pipes vulcânicos, diques e sills (Clement et al., 1984; Jelsma et al., 2009). Possuem textura inequigranular representada por megacristais/macrocristais imersos em uma matriz fina e frequentemente contêm inclusões de rochas ultramáficas provenientes de regiões do manto, além de quantidades variáveis de xenocristais e xenólitos crustais (Dawson and Stephens, 1975; Mitchel, 1986; Skinner and Clement, 1979). As erupções dos kimberlitos envolvem uma rápida ascensão do magma desde a base da litosfera continental, cerca de 150 a 200 Km de profundidade (Mitchell, 2008a; Sparks et al., 2006).

Além da mistura de diversas fases cristalinas (xenocristais) e fragmentos de origem diversa, a compreensão deste tipo de rocha torna-se mais complexa devido à susceptibilidade a alterações intensas, resultando no mascaramento de muitos componentes e texturas originais pela alteração, dificultando a interpretação de texturas preservadas relacionadas à erupção e processos de ascensão do magma (Cas et al., 2008). Não somente os kimberlitos, mas todas as associações alcalinas potássicas/ultrapotássicas, representadas por lamproítos, kimberlitos e kamafugitos, e xenólitos associados, são importantes fontes de informações sobre a evolução de províncias magmáticas alcalinas e as regiões mantélicas onde os magmas foram gerados, bem como sobre as potencialidades metalogenéticas das rochas derivadas.

Atualmente, esquemas de classificação baseados na mineralogia e geoquímica são bem conhecidos (Becker and Le Roex, 2006; Dawson and Smith, 1975b; Mitchell, 1995; Woolley et al., 1996) e, em vista aos modelos sul-africanos, tem-se a divisão dos kimberlitos em Grupo I e II (Smith, 1983), ou kimberlito e orangeito (Mitchell, 1995).

Os kimberltios do grupo I são ricos em voláteis (dominantemente CO_2), ultrabásicos e potássicos, mineralogicamente são classificados como serpentina calcita kimberlito ou calcita kimberlito (Skinner and Clement, 1979). Cristais de olivina são comuns, em sua maioria serpentinizados ou cloritizados, e constituem uma fase abundante (10-33%) enquanto que cristais de phlogopita e ilmenita são menos frequentes (<10% e <5%, respectivamente). Minerais como Ti-piropo, diopsídio e enstatita, que têm composições relativamente pobres em cromo (<2% Cr_2O_3) são também característicos. Serpentina e calcita predominam na matriz, ocorrendo também monticellita, flogopita, perovskita, espinélio (soluções sólidas de ulvoespinélio magnesiano - Mg-cromita, ulvoespinélio e magnetita) e apatita. Minerais acessório podem também estar presentes como rutilo, zircão e diamante.

O grupo II corresponde aos orangeítos (ou kimberlitos micáceos), são rochas ultrapotássicas peralcalinas e ricas principalmente em H_2O. Ao contrário dos kimberlitos grupo I, este caracterizam-se principalmente por serem ricos em flogopita, sendo mineralogicamente classificados como flogopita kimberlito ou calcita flogopita / flogopita calcita kimberlito. Cristais de flogopitas estiradas estão presentes acima de 20% enquanto a calcita é a fase mais comum na matriz (Becker and Le Roex, 2006), além de diopsídio (comumente zonado a manteado por aegirina titanífera), espinélios (desde cromita contendo Mg e magnetita contento Ti), perovskita rica em Sr e ETR, apatita rica em Sr; fosfatos ricos em ETR, titanatos de K e Ba (grupo da hollandita), rutilo contendo Nb e picroilmenita contendo Mn. Silicatos de Zr (wadeíta, zircão, granada kinzeyitica e silicatos de Ca e Zr) são comuns como minerais tardios da matriz. Em membros evoluídos deste grupo sanidina e richterita potássica podem ocorrer.

É pertinente lembrar que o termo “macrocristal” é empregado para xenocristais >0.5mm e <10mm e que apenas a forma euedral, até então correspondente aos fenocristais, pode não ser suficiente para distinguir a sua origem. Alguns estudos sugerem outras interpretações acerca da origem dos grãos euedrais da olivina (Arndt et al., 2010; Brett et al., 2009; Kamenetsky et al., 2008), como por exemplo, terem o desenvolvimento das facetas durante a recristalização em estado sólido de dunitos antes ou durante a passagem do magma kimberlítico. Alguns autores propõem critérios adicionais além da morfologia para a distinção entre feno e xenocristais, como a composição e a deformação interna.

Em termos da morfologia do conduto vulcânico até três tipos ou classes distintas foram descritas baseadas na forma do conduto, características texturais e posição de diferentes facies dentro do pipe. A classe I, é baseado nos exemplos sul-africanos e foi dividido em fácies cratera, diatrema e hipoabissal (Clement and Skinner, 1985). As classes II e III referem-se aos modelos canadenses descritos por Field e Smith (1998), o primeiro caracterizado por zona cratera rasa resultando na forma de "taça aberta" preenchido principalmente por kimberlítico piroclástico (PK) (tipo Prairies), e o segundo estreito e pequeno preenchido principalmente por abundante material kimberlítico vulcanoclástico ressedimentado (RVK) (tipo Lac de Gras). Um dos aspectos importantes no reconhecimento destas três classes é a presença da zona diatrema apenas nos pipes classe 1 (Field and Smith, 1998).

1.2.1 Geração e ascenção do magma kimberlítico

As condições sob as quais o magma do kimberlito é gerado no manto podem ser investigadas através de estudos experimentais, geoquímicos, estudos dos xenólitos, xenocristais e suas inclusões. Algumas das dificuldades são dadas pela contaminação que o magma kimberlítico provavelmente sofre durante a sua ascensão e colocação.

O grupo I é menos radiogênicos em Sr e mais em Nd, mostrando semelhanças com os basaltos de ilhas oceânicas e foram associados a uma fonte do manto astenosférico, enquanto o grupo II é mais radiogênico em Sr e admite-se a fonte ao manto litosférico subcontinental (Smith, 1983). As suas fontes ainda são ambiguas, diversos outros trabalhos as associam às fontes essencialmente astenosférica.

Estudos experimentais de altas pressões e temperaturas ajudam a entender a petrogênese dos kimberlitos (e.g. Girnis et al., 2011; Russell et al., 2012). Russel et al. (2012) realizaram experimentos a temperaturas de 1000 a 1100°C para demonstrar os mecanismos envolvidos na fase volátil durante a subida do magma kimberlítico. Eles propõem que o magma primário seja carbonatítico e que pela assimilação do ortopiroxênio durante a sua ascensão gera os magmas kimberlíticos (Figura 1).

A dissolução do carbonato e liberação do CO_2 ocorrem ao mesmo tempo em que sílica e magnésio são adicionados ao sistema. Este modelo ajuda a explicar a

ausência de xenocristais de ortopiroxênio. De acordo com a Figura 1c, a assimilação de ortopiroxênio controla composições mais ou menos silicáticas, causando a diminuição na solubilidade do CO_2 e exsolução da fase fluida. A contínua assimilação causa contínua exsolução dessas fases, e resulta em um líquido kimberlítico saturado em olivina com cerca de 18-32 % de SiO_2.

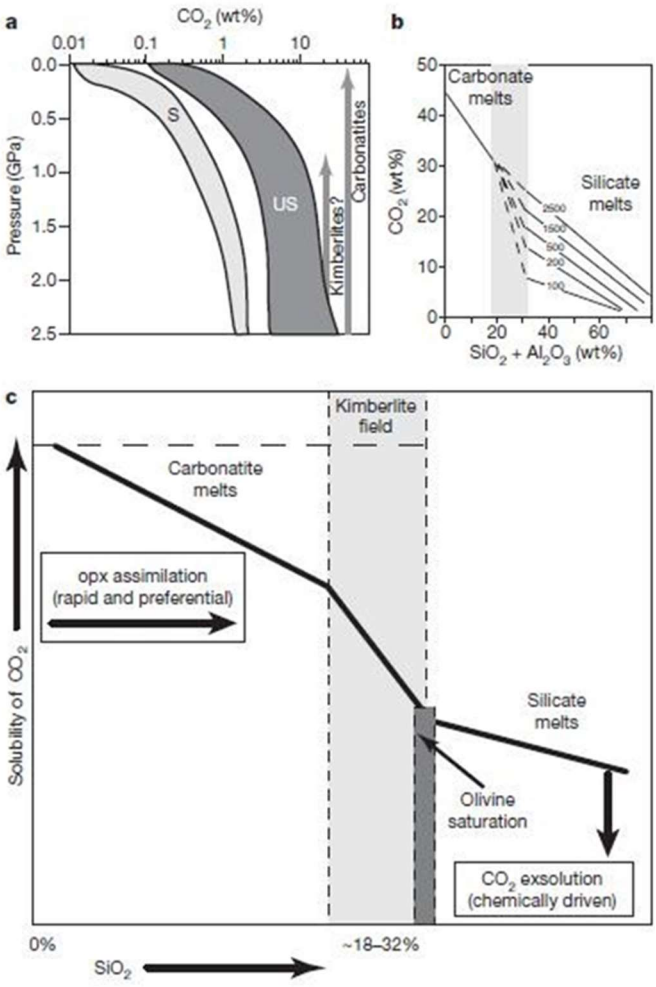

Fig. 1. Solubilidade de SiO2 para líquidos silicáticos e carbonatíticos: a – limite de solubilidade do CO2 para líquidos saturados e insaturados em sílica e solubilidades hipotética de líquidos carbonatítico e kimberlíticos; b – pressão e composição dependente da solubilidade do CO2 durante toda a transição carbonática-silicática; c – modelo esquemático da assimilação induzida pela exsolução do fluido de líquidos carbonatítico ou kimberlíticos (Russell et al. 2012).

Mesmo que xenocristais de olivina sejam normalmente encontrados em kimberlitos, assume-se que são derivados da desagregação de xenólitos do manto empobrecido (harzburgito). Ortopiroxênios mostrando texturas de dissolução estão relacionados com kimberlitos carbonatítico. Outra explicação da ausência dos

ortopiroxênios é de que xenocristais de olivina são provenientes do rompimento de xenólitos duníticos ao invés de hazburgitos (Arndt et al., 2010) e que o ortopiroxênio é instável em líquidos kimberlíticos ricos em água (Mitchell, 2008b).

As erupções dos kimberlitos envolvem uma rápida ascensão do magma desde a base da litosfera continental, cerca de 150 a 200 Km de profundidade (Mitchell, 1995; Skinner and Marsh, 2004; Walters et al., 2006). Diversos estudos acerca da ascensão do magma kimberlítico direcionam a atenção para as mudanças das propriedades do magma e o papel da exsolução de voláteis como gatilho para essa subida (Kavanagh and Sparks, 2009; Russell et al., 2012; Sparks et al., 2007; Wilson and Head III, 2007). Um dos aspectos menos compreendidos desse processo é o conjunto de mecanismo atuante no líquido parcialmente segregado que cria condições que irão ativar o "gatilho" para que a subida aconteça.

De acordo com Sparks (2013) alguns dos fatores que influenciam esse evento incluem: a taxa de fusão, o fluxo controlado pela flutuabilidade do líquido e cisalhamento tectônico, pressão, estado de stress tectônico e força do manto que está ao redor. Duas hipóteses são sugeridas para explicar qual o "gatilho" para a ascensão do líquido kimberlítico: através de pulsos magmáticos, os quais podem ser uma resposta à dinâmica do manto, como a ascensão de uma pluma mantélica, ou pela deformação de um cráton, ocasionando a geração contínua desse líquido.

Lensky et al. (2006) propuseram que a explosão de uma bolha de nucleação do líquido kimberlítico saturado em CO_2 pode gerar altas pressões que fragmentam as rochas do manto e isto poderia iniciar a subida do magma. Profundas mudanças nas condições físico-químicas e propriedades de magma são esperadas quando magmas kimberlíticos descomprimem durante a subida e são colocados próximo a superfície. Essas mudanças incluem provável arrastamento de crosta e xenólitos do manto, reabsorção da carga de xenocristais, cristalização induzida por resfriamento, desgaseificação, e mudanças de estado de oxidação.

Wilson & Head (2007) apresentaram uma visão dinâmica do papel da exsolução de voláteis em que o CO_2 é liberado na ponta do dique gerando pressões de aproximadamente 70 MPa. O gradiente de pressão em excesso ao longo do dique é calculado em dezenas de vezes maior do que em erupções basálticas, o que leva a velocidades de subida de dezenas de metros por segundo.

1.3 Contexto Geológico Regional

Expressivas manifestações de magmatismo máfico/ultramáfico alcalino no Continente Sul-Americano ocorreu durante o período cretáceo ao longo de um "trend" estrutural alinhado com o lineamento AZ 125° (Bardet, 1977), situado na borda sul do cráton Amazônico até sudeste do cráton São Francisco. Carbonatitos e principalmente kamafugitos, kimberlitos e lamproítos (Brod et al., 2000; Azzone et al., 2013) caracterizam as províncias alcalinas resultantes desse magmatismo (Ulbrich et al, 1981; Almeida, 1983; Bizzi et al., 1993, 1994). Essas ocorrências situam-se predominantemente dentro da Faixa Brasília e nas bordas da Bacia do Paraná nos estados de Minas Gerais e Goiás formando a Província Ígnea do Alto Paranaíba (APIP) e a Província Alcalina de Goiás (GAP), respectivamente (Araújo et al., 2001; Gibson et al., 1995; Junqueira-Brod et al., 2005).

Essas associações alcalinas têm a predominância na região da Faixa Brasília, devido a um soerguimento que teve seu início no Eocretáceo, com desenvolvimento em maior intensidade durante o Neocretáceo, e que separou as bacias do Paraná e São Francisco (Campos & Dardenne, 1997). Formou-se, então, a Província Ígnea do Alto Paranaíba, a qual coincide estruturalmente com este antigo cinturão Proterozóico formado durante o ciclo Brasiliano (800 - 450 Ma) (Schobbenhaus & Campos, 1984; Almeida, 1967). Este cinturão, que corresponde à Faixa Brasília, corresponderia a uma possível sutura unindo o cráton do São Francisco e um núcleo cratônico antigo hipotético, localizado abaixo da Bacia do Paraná (Leonardos & Fyfe, 1974) (Figura 2 e 3).

A colisão de dois crátons é sugerida pelo encurtamento e cavalgamento tectônico da Faixa Brasília, resultantes da colisão entre as placas Panamericana e Sanfranciscana. Estudos mostram (Dardenne; Schobbenhaus, 2001) que o limite aflorante é representado pela frente de cavalgamento que sobrepõe as rochas da faixa de Dobramentos Brasília aos sedimentos cratônicos do Grupo Bambuí. Apesar dessas rochas parecerem ser de natureza não-cratônica, estudos estruturais (Corsini, 1995; Peyve, 2010), sísmicos (Rocha, 2008; Vandecar et al., 1995), gravimétricos (Dutra et al., 2012; Pires, 1986;) e xenólitos (Leonardos et al., 2003; Carlson, 2007; Silva, 2008; Almeida, 2009; Costa, 2013; Nannini, 2016), demonstram que o cráton São Francisco se estende por baixo da Faixa Brasília, assim, grande parte dessas intrusões estariam sobre a litosfera cratônica.

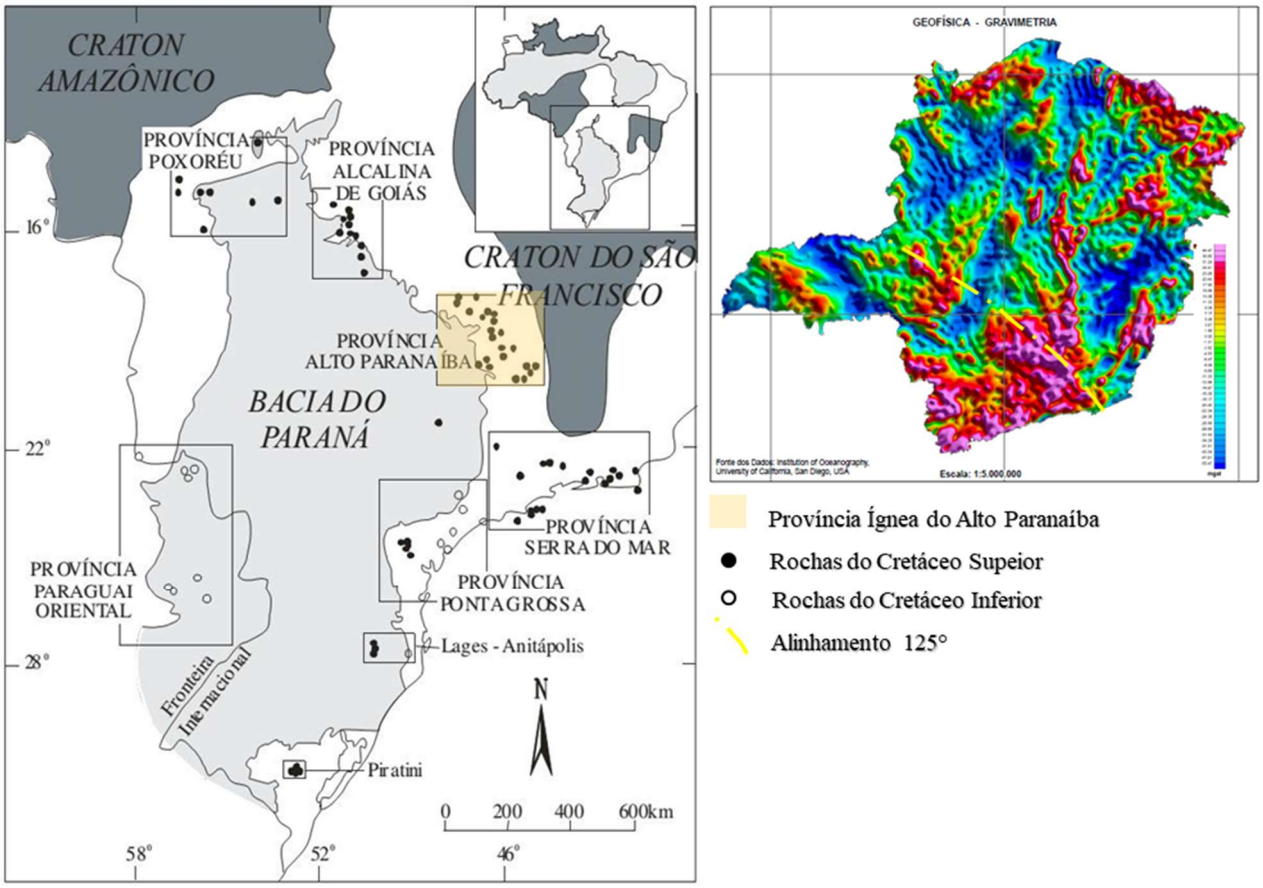

Fig. 2 Localização das Províncias Alcalinas nas margens da Bacia do Paraná com destaque em amarelo para a Província Ígnea do Alto Paranaíba (modificado de GIBSON et al., 1995). À direita, mapa de gravimetria do estado de Minas gerais (Institution of Oceanography, University of California, San Diego, USA). É possível notar que a maior parte das regiões com fortes anomalias magnéticas (rosa, vermelho, amarelo) coincidem com o lineamento AZ 125° (CPRM, 2014).

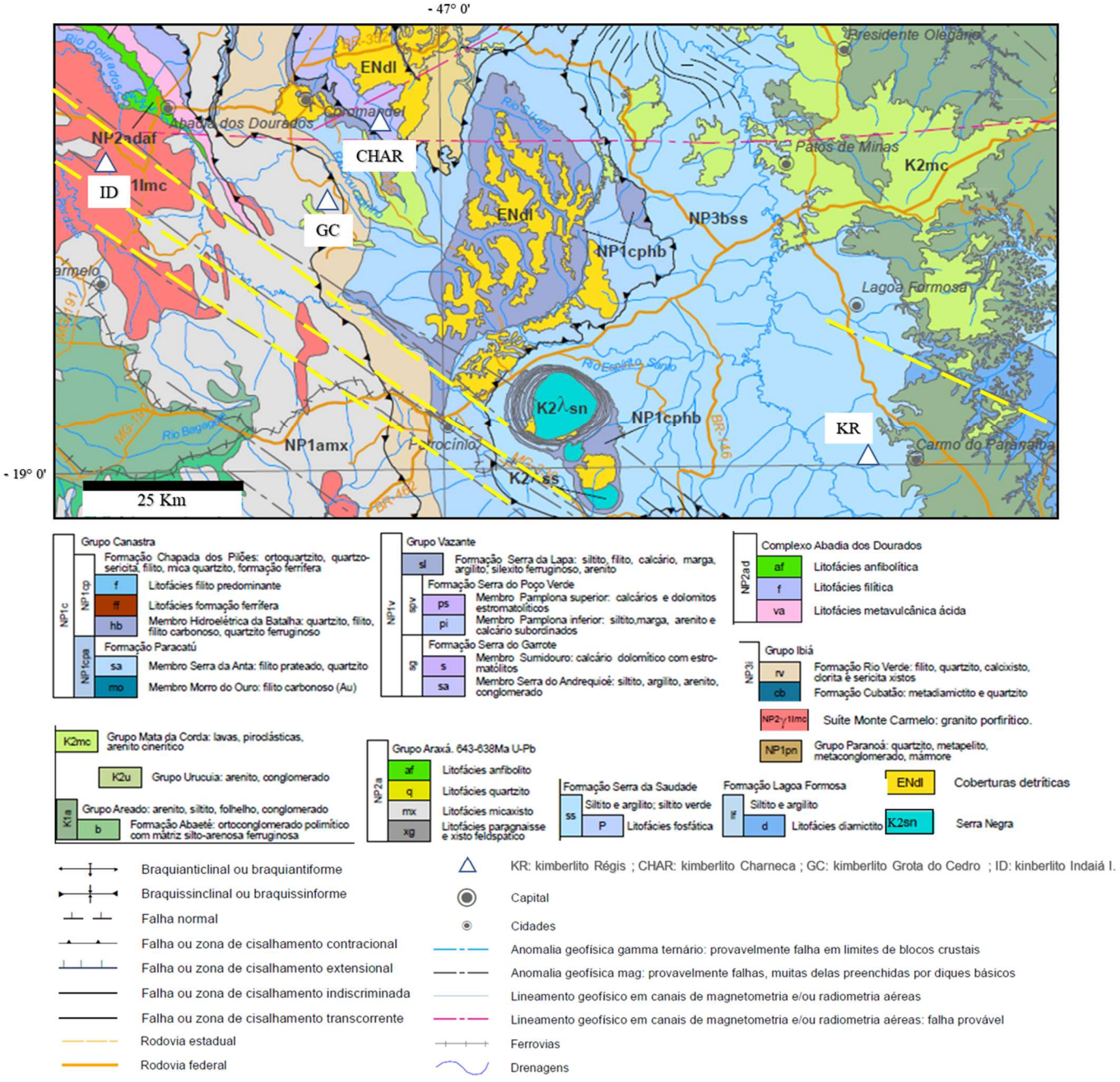

Fig. 3. Mapa geológico da região de Coromandel (MG) com a localização dos kimberlitos estudados neste trabalho (CPRM, 2014).

1.3.1 Província Ígnea do Alto Paranaíba (PIAP)

Localizada na porção ocidental do estado de Minas Gerais, representa uma das maiores ocorrências em volume de rochas máficas potássicas no mundo (>20x10^5 Km^3) (Gomes & Comin-Chiaramonti, 2005). Apresenta-se como uma estrutura alongada NW-SE com aproximadamente 400 x 150 Km dividindo as bacias do Paraná e São Franciscana, estendendo-se da área do Rio-Verde - Iporá (sudeste do estado de Goiás), a

aproximadamente 1500 km S-SE para a região do Bambuí em Minas Gerais. Kamafugitos predominam largamente em relação aos kimberlitos e complexos alcalinos (Gibson et al., 1995) (Figura 4).

Estudos de magnetometria (Moraes Rocha et al., 2014) indicam a existência de diversos lineamentos magnéticos que coincidem com o Az 125°, aonde as rochas respondem altamente ao magnetismo e muitas não estão aflorantes na superfície. Datações realizadas em muitos corpos desta província indicam uma dinâmica formação ocorrida em amplo espaço de tempo. Seguindo esse mesmo NW-SE trend, os diques máficos situados em Pará de Minas foram datados através do método U-Pb em badeleíta, resultando em idades entre 1795 Ma e 766 Ma (Cederberge et al., 2016), indicando pelo menos três gerações de diques datados do Paleo - Neoproterozoico.

Enquanto kimberlitos, lamproítos e kamafugitos desta região datam, até o momento, entre 68 e 126 Ma (Felgate, 2014; Gibson et al., 1995; Guarino et al., 2013; Pereira, 2007; Read et al., 2004), sugerindo pelo menos dois eventos principais responsáveis pela colocação dessas rochas: a fragmentação do Gondwana (aproximadamente 180 Ma) e a passagem da Pluma de Trindade (~80 Ma).

As regiões crustais mais rasas correspondem às áreas da APIP e GAP (Moraes Rocha et al., 2015), de 10km até 24 km e de 12 km até 25km de profundidade, respectivamente. Os resultados também mostraram que o Az 125° está relacionado com profundidades maiores (15,7 até 30 km) do que as regiões GAP e APIP, acreditando-se que esses corpos intrusivos tenham raízes mais rasas do que a maioria das falhas do Az 125°. Esta profundidade mais rasa pode ser reflexo das falhas lístricas desenvolvidas ao longo dos planos das falhas de empurrão (associadas à orogenia Brasiliana) e que exercem controle secundário na colocação dessas intrusões (Pereira & Fuck, 2005), contribuindo para uma maior concentração de kimberlitos e rochas relacionadas na borda sul-sudoeste do Cráton do São Francisco na PIAP.

Através da análise de minerais recuperados de diferentes manifestações vulcânicas associados ao desenvolvimento de um sistema é possível inferir a natureza do manto litosférico (O'Reilly and Griffin, 1996). Resultados de cálculos de pressão e temperatura de clinopiroxênios (Read et al., 2004) de kimberlitos (~90 a ~120 Ma), recuperados nas cabeceiras dos rios Abaeté, São Bento e Indaiá, mostram temperaturas mais baixas (700 e 950°C) do que aquelas resultantes dos clinopiroxênios provenientes

de kamafugitos (~75 a ~85 Ma) (800 e 1200°C). Estes dados revelam que em um período de aproximadamente 5 Ma ocorreu um aquecimento cerca de 250°C nessas regiões e um adelgaçamento da litosfera na área afetada pelo arco. Estes contrastes, além de permitirem um monitoramento da evolução da mesma, auxiliam no entendimento da preservação ou não do diamante, como por exemplo, o fato destes kimberlitos terem intrudido numa litosfera mais fria adequada para a preservação deste mineral.

Apesar das idades, o fato do magmatismo kimberlítico ser anterior ao magmatismo kamafugítico na região (Read et al., 2004) não pode ser generalizado para todas as ocorrências. O kimberlito Santa Rosa 04 localizado na região de Coromandel e que se insere dentro do campo de estabilidade do diamante indica idade Rb-Sr em mica de 83Ma (Skinner, 1996 apud Pereira and Rogério, 2007), ou seja, mais próximo das idades estabelecidas para os kamafugitos.

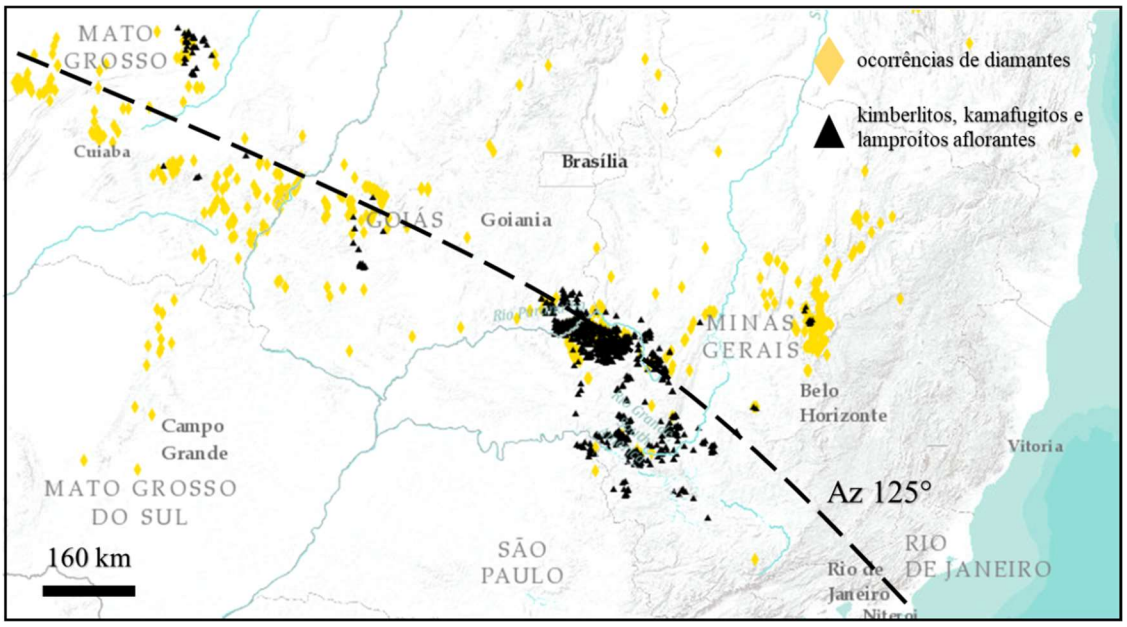

Fig. 4. Mapa com as principais áreas de ocorrências de diamantes, afloramentos de kimberlitos e rochas relacionadas dos estados de Minas Gerais, Goiás e Mato Grosso. As ocorrências e afloramentos seguem um "trend" coincidindo com o alinhamento 125° (Projeto Diamante Brasil - CPRM).

1.4 Justificativas e Objetivos

A complexidade que envolve o estudo de kimberlitos devido à mistura de materiais de diferentes origens e às complexas texturas resultantes do dinâmico

processo de ascensão e colocação dessas rochas, e mascaradas por intensas alterações, tornam o seu estudo um desafio tanto do ponto de vista químico elemental e isotópico, tectônico como textural. No entanto, as características primárias do magma kimberlítico, assim como das regiões mantélicas por onde esse líquido percorreu, permanecem impressas nessas rochas, tornando as dificuldades do seu estudo um estímulo para estudos científicos e de exploração.

A descoberta de depósitos primários de diamantes nos kimberlitos e rochas associadas gerou um esforço significativo para a caracterização sistemática da dinâmica da colocação, idades, petrografia, mineralogia, características texturais e configuração tectônica desses corpos. No Brasil, as investigações científicas sobre os kimberlitos vem contribuindo cada vez mais para o conhecimento do contexto petrológico e geodinâmico das ocorrências associadas ao magmatismo potássico-ultrapotássico brasileiro (lamprófiros, kamafugitos e kimberlitos), com vistas a uma definição mais segura da natureza desses magmas, a história evolutiva dessas associações e a natureza da região fonte, além de contribuir também para os estudos das possíveis relações entre as associações geoquímicas e ocorrências de diamantes na Província Ígnea do Alto Paranaíba (PIAP).

Dentro desse contexto, os objetivos desta tese envolvem o estudo petrológico de quatro intrusões pertencentes aos campos kimberlíticos na região de Coromandel e Carmo do Paranaíba (MG), os kimberlitos Charneca, Grota do Cedro, Régis e Indaiá I, por meio de:

- Estudo sistemático de petrografia para uma caracterização textural, mineralógica e modal pormenorizada, com a finalidade de classificar corretamente a rocha e identificar minerais indicadores de condições físico-químicas magmáticas e da natureza da região mantélica próximo à fonte onde se originou.
- Determinação da composição química *in situ* dos minerais constituintes em termos de elementos maiores e menores (microssonda eletrônica) e traço (LA-ICP-MS), de modo a investigar as assinaturas geoquímicas desses minerais e determinar parâmetros intensivos para o melhor entendimento sobre a natureza composicional dos minerais no contexto de geração e das condições físico-químicas atuantes durante a evolução destes magmas.

- Identificação das condições petrológicas durante evolução impressas nas associações minerais e sua influência na estabilidade do diamante.
- Comparação e possível correlação dos resultados entre essas quatro ocorrências e as relações petrológicas de cada uma no contexto da PIAP.

1.5 Localização e acessos

Todas as ocorrências desse estudo localizam-se no estado de Minas Gerais e ocorrem não distantes umas das outras (Charneca – Grota do Cedro ~15 km, Charneca – Indaiá ~ 35 km, Charneca – Régis ~70 km), na região que compreende os municípios de Carmo do Paranaíba, Patos de Minas, Patrocínio e Coromandel (Figura 5). O acesso é feito, com origem em São Paulo, através da rodovia BR-050 até a cidade de Uberlândia e BR-365 até o município de Patrocínio.

Para o acesso ao kimberlito Charneca, após passar o município de Patrocínio, continuar na rodovia BR-365 (em direção a Patos de Minas) e entrar na MG-188. Após cerca de 34 km acessar uma estrada vicinal de terra à direita (a qual não está registrada nos mapas das rodovias), segue por ela cerca de 5,0 km quando se chega até a ocorrência do Kimberlito Charneca. Esta estrada de terra é bastante estreita, com terreno irregular e a descida é constante e íngreme até a chegada em um vale onde a ocorrência se localiza (UTM 239685 / 7946290).

O kimberlito Grota do cedro é acessado, a partir do município de Patrocínio, pela BR-365 e depois LMG-731 (direção oeste de Patrocínio). Seguir pela MG-731 por cerca de 3,3 km e acessar uma vicinal à direita que levará até a cidade de Coromandel, passando por Santa Rosa dos Dourados. Após passar por esse município, continuar nesta rodovia por mais 15 km (em média) e nesta altura o kimberlito Grota do Cedro estará a 2 km ao leste desta vicinal. O kimberlito fica numa drenagem profunda com cerca de 5 m de profundidade (UTM 271712 / 7940386).

O acesso ao kimberlito Indaiá I foi feito pela BR-365 (à oeste de Patrocínio), seguindo por essa estrada acessar a MG-223 e depois a MG-190. Após o município de Monte Carmelo, seguir por mais cerca de 19,6 km (1,2 km m antes da entrada para a MG-741). Neste ponto (GPS: 243792/7943684) encontra-se uma estrada de terra a oeste

(esquerda da estrada), a qual leva até ao kimberlito Indaiá I e II. Prosseguir por mais 3,2 km nesta vicinal, a ocorrência Indaiá I localiza-se numa drenagem de 3 metros de profundidade, escondida numa vegetação mais densa que se destaca da paisagem ao redor (UTM 240612 / 7944871).

Para o acesso ao kimberlito Régis seguir pela BR-365 em direção a Patos de Minas e então acessar à rodovia BR-354 (em direção a Carmo do Paranaíba). Nesta rodovia seguir por cerca de 16 km e na altura de Lagoa Formosa acessar uma vicinal à direita, a qual leva à Fazenda Régis, aonde está o kimberlito de mesmo nome.

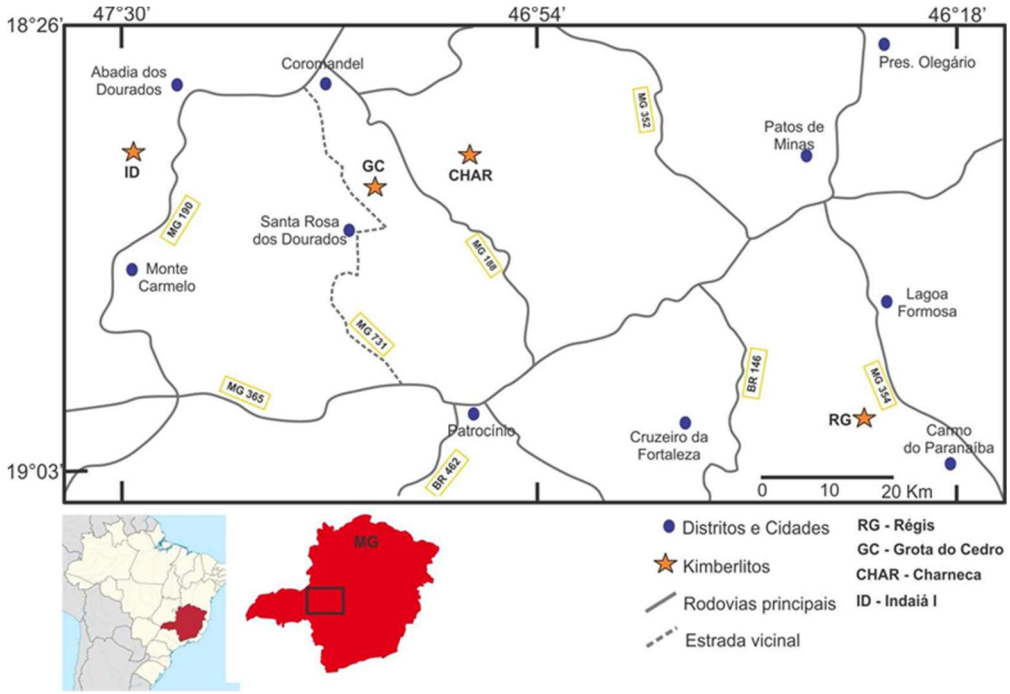

Fig. 5. Mapa de localização e acessos às ocorrências kimberlíticas Charneca, Grota do Cedro, Régis e Indaiá I (Minas Gerais).

CAPÍTULO 2

2. MATERIAIS E MÉTODOS

2.1 Trabalhos de campo

O material de estudo para esta tese foi coletado nas áreas das respectivas ocorrências pesquisadas, durante os trabalhos de campo realizados no mês de julho de 2014 na região entre os municípios de Patrocínio e Coromandel (Minas Gerais). Os trabalhos contaram com o auxílio dos professores Excelso Ruberti e Rogério Guitarrari Azzoni, um técnico e ex-funcionário da DeBeers, e a aluna de graduação Mariana Ciotta.

Com o auxílio de mapas, GPS, martelo e marretas foram feitas a amostragem superficial de três ocorrências: Charneca, Grota do Cedro e Indaiá I. Já para o Kimberlito Régis foi utilizado dois furos de sondagens que atingem 250,6 e 316,4 metros de profundidade disponibilizados pela empresa SAMSUL mineração, os quais foram estudados em trabalho de mestrado por Thomaz (2009). Esta ocorrência não foi visitada, devido ao alto grau de alteração da porção aflorante e a coleta de superfície desse material não acrescentariam dados relevantes para este trabalho.

2.1.1 Kimberlito Charneca

O acesso ao kimberlito Charneca foi feito com o auxílio de um ex-funcionário da DeBeers que conhecia o dono do local. A amostragem foi realizada em um ponto da ocorrência aflorante, nas laterais de um poço retangular (3,0x1,80) com cerca de 3 metros de profundidade. O local estava parcialmente alagado por já estar abandonado pelos garimpeiros que antes extraiam diamantes no local. No entanto, cerca de 80 metros dali, havia extração ativa e, por prudência, o reconhecimento do local foi feito de forma breve, somente o necessário para a coleta de material (Figura 6).

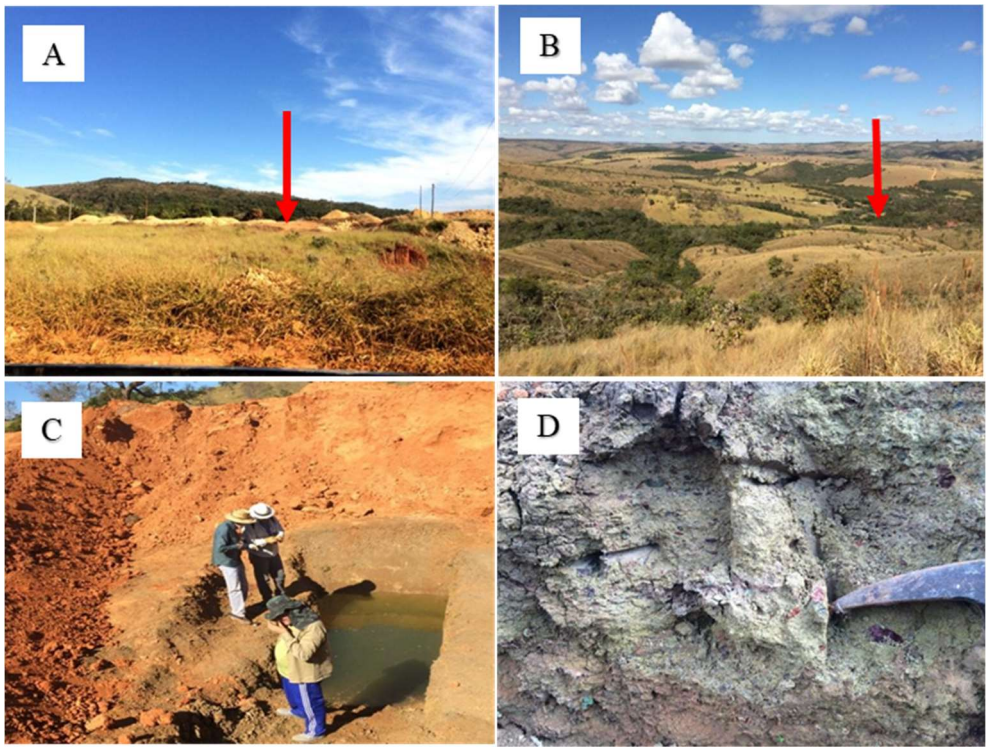

Fig. 6. Localização e afloramento do kimberlito Charneca. A) Extração de diamantes próximo ao kimberlito. B) Garimpo visto do alto do morro, onde o kimberlito se torna mais alterado e tende a predominar somente as rochas encaixantes. C) Poço do garimpo da Charneca onde as amostras de kimberlito foram coletadas; nesse local havia extração de diamante e foi abandonado por esgotamento. D) solo esverdeado do kimberlito.

2.1.2 Kimberlito Grota do Cedro

O kimberlito Grota do Cedro foi de difícil acesso, pois a estrada de terra para chegar até a ocorrência é sinuosa e com muitas bifurcações para outras estradas vicinais. Depois de um longo trecho o caminho termina no alto de um morro e o kimberlito localiza-se numa drenagem cerca de 300 metros abaixo. A drenagem é profunda e a vegetação ao redor é densa e de difícil acesso. As amostras foram coletadas ao longo da parte aflorante do córrego.

Uma parede com cerca de 5 metros de altura é encontrada numa parte do leito da drenagem. O kimberlito ali exposto encontra-se muito alterado e com muitos xenólitos crustais, às vezes com até 30cm de comprimento (Figura 7). Nas porções superiores o kimberlito apresenta coloração rósea, provavelmente devido à percolação de material do nível superior. É possível ver o contato do kimberlito com a rocha encaixante, aonde também ocorre xenólitos com até 30cm de comprimento.

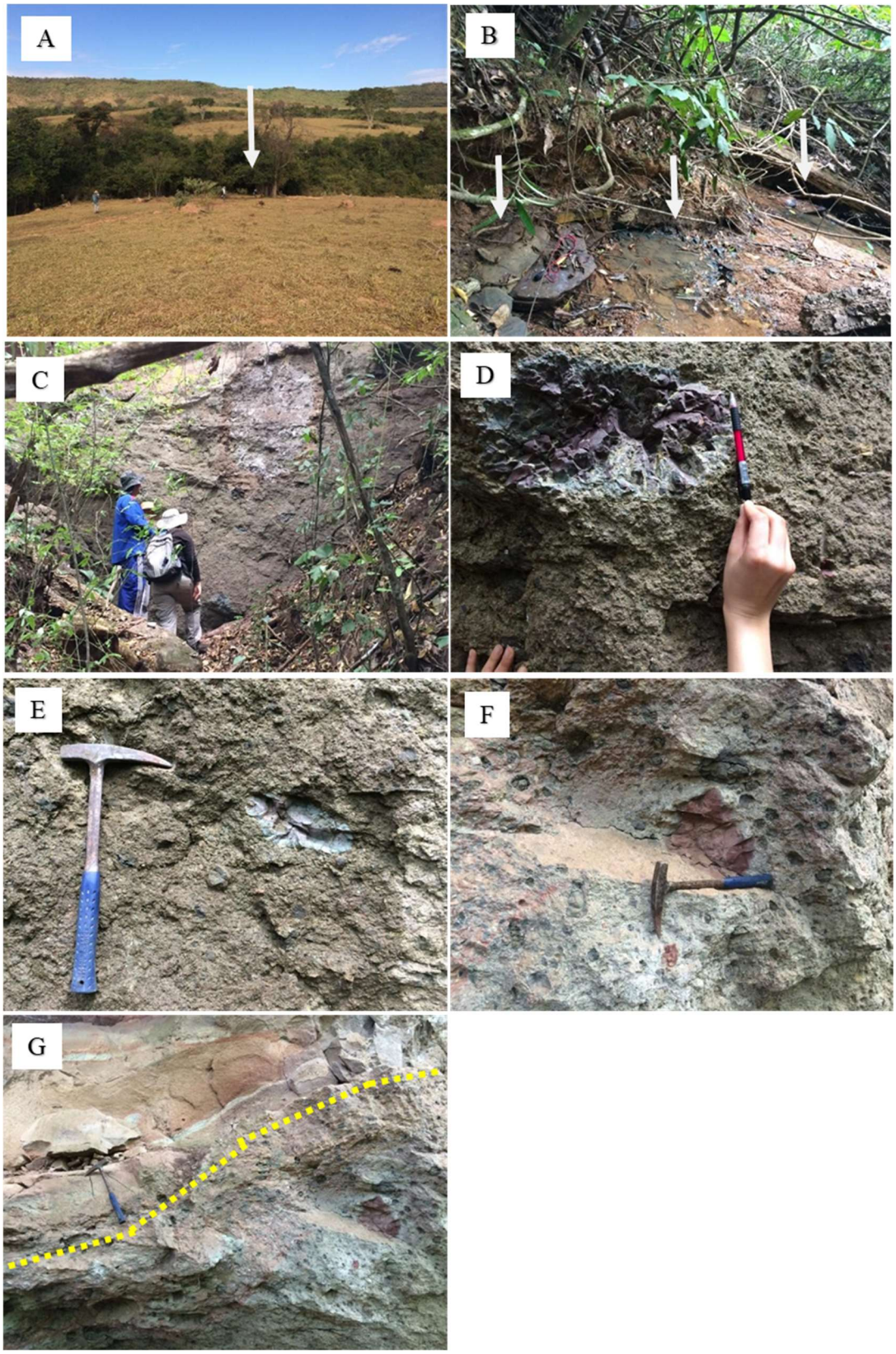

Fig. 7. Localização com a vista da área e o afloramento do kimberlito Grota do Cedro. A) localizado em drenagem profunda. B) kimberlito aflorante ao longo da drenagem. C) Porção com cerca de 5 metros do kimberlito alterado. D) Xenólitos crustais com borda de reação. E) Xenólito crustal com forma elipsoide (filito). F) Xenólito crustal arredondado e macrocristais dispersos aleatoriamente na matriz fina e serpentinizada. G) Contato da encaixante (arenito) com o kimberlito.

2.1.3 Kimberlito Indaiá I

O kimberlito Indaiá é de fácil acesso e próximo à estrada principal. Aflora em um vale localizado na porção sul, ao longo do contato com a encaixante granítica regional. O afloramento ocorre no final de uma drenagem e a coleta foi dificultada pela alta dureza da rocha. As amostras foram coletadas em quatro pontos distintos seguindo a drenagem abaixo (Figura 8).

A presença de vegetação densa na área da intrusão contrasta com a vegetação rala e retorcida do cerrado ao redor. A coloração cinza escura e azulada do kimberlito e a alta dureza caracterizam um material fresco com minerais bem preservados.

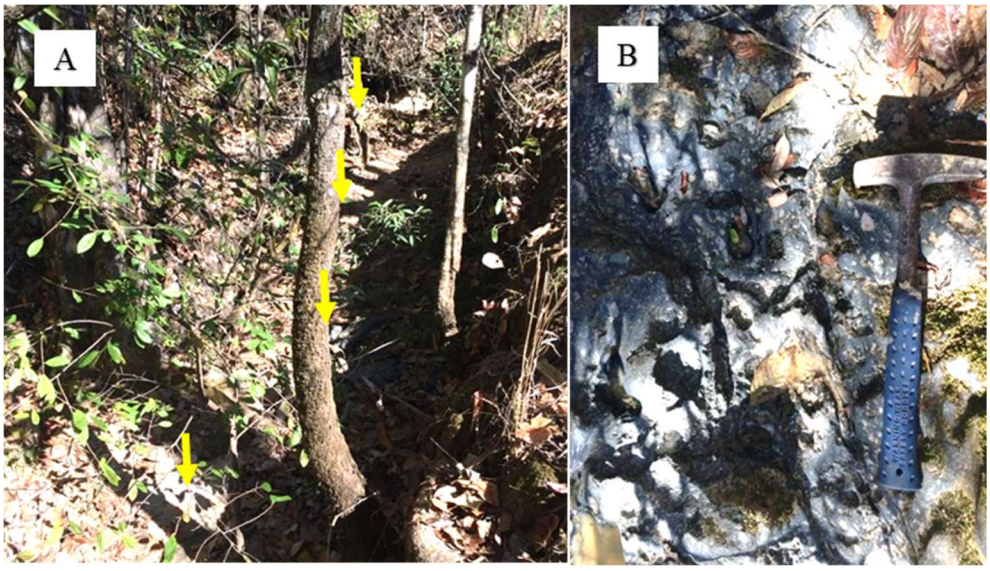

Fig. 81. Afloramento do kimberlito Indaiá I. A) Drenagem onde aflora o kimberlito e locais de coletas (setas amarelas) das amostras. B) Rocha fresca do kimberlito Indaiá I.

2.2 Microscopia óptica

Para a confecção das lâminas petrográficas foi necessário a impregnação das amostras com resina antes do processo de laminação, devido ao alto grau de alteração e fragilidade do material. Foram analisadas 70 seções delgadas ao microscópio petrográfico de luz transmitia e refletida para a caracterização dos minerais e das relações texturais dos componentes dos kimberlitos. A determinação

da porcentagem modal aproximada foi realizada através da contagem de pontos e da carta de estimação visual (BEST, 2003). Mesmo com a utilização do método de contagem de pontos, preferimos por rigor considerar as porcentagens modais realizadas neste trabalho como “estimadas”, devido à grande heterogeneidade textural e ao alto grau de alteração das ocorrências, particularmente Charneca, Grota do Cedro e Régis. Os microscópios utilizados foram das marcas Olympus BXP-50 e Zeiss Axioplan, com objetivas permitindo aumentos de 2,5, 10, 20 e 40 vezes, do Laboratório de Microscopia Petrográfica do Departamento de Mineralogia e Geotectônica do Instituto de Geociências da USP. As fotomicrografias das feições texturais, das microestruturas e dos minerais foram registradas por um microscópio Zeiss Axio Imager.A2m acoplado a uma câmera modelo AxioCamMR3 e obtidas em um programa AxioVision 4.9.1 SP1.

2.3 Química Mineral

2.3.1 Preparação das amostras

Após a caracterização petrográfica foram identificadas as principais assembleias minerais dos kimberlitos estudados (olivina, granada, ilmenita, espinélio, piroxênio, perovskita, flogopita), e destes foram eleitos, à medida do possível, os minerais ‘inalterados’ e de interesse petrológico para serem analisados *in situ* por microssonda eletrônica (EDS/WDS) e posteriormente por ICP-LA-MS. Em função do alto grau de alteração das amostras, com exceção do kimberlito Indaiá I, optou-se também pela concentração das distintas fases componentes dessas rochas, com vistas à seleção e recuperação dos minerais inalterados ou pouco alterados para conduzir análise nos grãos. Assim, além da execução de análises *in situ* diretamente nas lâminas delgadas polidas (exceto ao kimberlito Charneca), também poderia contar com um número maior de análises por meio de concentrados minerais. Nesse contexto foi realizada uma minuciosa separação dos minerais pesados e inalterados e montados em seções de grãos. Esta separação não foi realizada para o kimberlito Régis devido a impregnação já realizada nas amostras.

Este método de estudo aplicado a kimberlitos foi pela primeira vez realizado no IGc-USP, e devido à sua importância está detalhadamente descrita em etapas para a recuperação dos minerais de interesse.

Etapa 1 – separação das primeiras frações e peneiramento a úmido

As amostras mais friáveis foram desintegradas a mão (Charneca) e as mais duras com uma marreta (Indaiá I, Grota do Cedro) e as diferentes granulometrias separadas em peneiras de 4, 9, 25, 40, 60, 100 e 250 MESH, quanto maior a unidade MESH menor a abertura da peneira.

Foi realizado um peneiramento a úmido (amostras >25 e <60 MESH) com ajuda de água corrente para que o material muito fino, como as argilas, pudesse ser descartado, mas sempre com o cuidado de utilizar peneiras empilhadas, reduzindo ao máximo a perda de material. Para a retirada do material mais fino nas amostras >60 e <100 MESH, uma mistura de água e detergente foi acrescentada em parte iguais num recipiente, e utilizando um lavador ultrassônico a argila foi eficientemente separada do material mais pesado. Este processo foi repetido cerca de 4 a 5 vezes. Após essa separação prévia o material foi secado sob lâmpadas incandescentes por cerca de 24h. Neste estágio do processo já foi possível recuperar minerais com até 5mm de tamanho, porém apenas para o kimberlito Charneca.

Etapa 2 – diminuição da granulometria para amostras menos friáveis

As frações maiores que não puderam ser peneiradas nas peneiras de 4 ou 9 MESH foram moídas em um britador de mandíbula. Neste processo procurou-se gerar fragmentos com cerca de 6 mm de tamanho, e sucessivas rebritagens reduziram o material para granulometrias menores (<3mm). O material britado e ainda muito resistente (Indaiá I e Grota do Cedro) foi processado em moinho de disco, e depois lavado em peneira de 230 MESH para a remoção das frações mais finas.

Optou-se por não utilizar o mortar de ferro ou pilão para a diminuição da granulometria, tendo em vista que a intensidade de trituramento dos grãos é de

difícil controle e poderia destruir os minerais de interesse. Assim, esta etapa foi feita com cautela e de modo gradual para a maior preservação dos grãos.

Etapa 3 – mesa concentradora vibratória (Wilfley)

As amostras com granulometrias >100 e < 250 MESH foram colocadas em mesa vibratória para a concentração de minerais pesados, à medida que a concentração vai ocorrendo, aconselha-se verificar o tipo de material que está sendo separado, assim, ajustes durante o processo, como a inclinação da mesa ou intensidade da água, podem ser controlados para uma melhor separação. Após este processo, o material concentrado é secado sob lâmpadas incandescentes por 24h.

Etapa 4 – separação densimétrica

A frações > 60 e < 100, as quais não foram processadas na mesa "wilfley", foram separadas utilizando um líquido altamente denso como o bromofórmio (2,89 g/cm^3). Esta separação foi feita dentro de uma capela, devido à toxidade deste líquido, utilizando uma coluna composta por dois funis e um béquer. O bromofórmio é colocado no primeiro funil misturado ao material para separação, a fração leve flutua no líquido, enquanto a mais pesada vai sendo decantado através de um canal de borracha que regula a saída do líquido e os grãos pesados. Este material é recuperado pelo segundo funil protegido por um filtro de papel, enquanto o líquido filtrado é armazenado no béquer. Outros líquidos também podem ser utilizados, como o iodeto de metileno e o licor de Clèrici, entretanto são mais tóxicos que o bromofórmio.

Etapa 5 – separação magnética: imã de mão e Frantz

Após as etapas de separação dos minerais pesados, é necessário processar a retirada da magnetita nas frações > 60 e < 120 MESH, com um imã de mão. Aconselha-se a repetição quantas vezes necessárias desta separação para que o material esteja com a menor quantidade possível de magnetita, a fim de evitar a obstrução do próximo aparelho que será utilizado.

O material com pouquíssima magnetita pode ser agora processado no separador eletromagnético Frantz. Aqui as amostras foram separadas em frações com diferentes graus de susceptibilidade magnética, de 0,3 A até 1,0 A, com 10° de inclinação. A inclinação de 15° foi utilizada adicionalmente apenas nas frações magnéticas e não-magnéticas. Na amperagem 0,4 A foi verificado uma separação mais homogênea e com melhor concentração de granadas. O quadro da tabela 1 sintetiza os principais minerais recuperados para cada kimberlito estudado, nas diferentes amperagens.

Cada espécie possui o seu grau de magnetismo (paramagnéticos ou diamagnéticos), sendo importante lembrar que os minerais separados nas diferentes amperagens do separador magnético tende a homogeneizar o material. No entanto, o mineral pode ser ou não atraído em amperagens que não correspondem à sua, mas este fato pode acontecer por falhas durante as etapas anteriores, ou simplesmente devido às peculiares características do próprio kimberlito analisado.

Tabela 1. Predomínio dos principais minerais identificados em concentrados obtidos por diferentes amperagens e inclinações para os kimberlitos Charneca, Indaiá I e Grota do Cedro. As amperagens em cores amarela e verde indicam "magnético" e "não-magnético", respectivamente. Abreviações: ilm, ilmenita; prv, perovskita; chr, cromita; spn, espinélio; grt, granada; px, piroxênio; calc, calcita; tur, turmalina; olv, olivina; zr, zircão; ap, apatita; brt, barita.

	Charneca	Grota do Cedro	Indaiá I
0,3 A / 10°	ilm	ilm	ilm
0,4 A / 10°	prv; chr	spn; grt; prv	px; olv
0,4 A / 15°	x	-	x
0,5 A / 10°	grt; chr, px	px; tur; prv; ap	prv; px; olv
0,6 A / 10°	grt	px; chr; prv;	-
0,7 A / 10°	calc	calc	calc
0,8 A / 10°	qtz	spn	px
1,0 A / 10°	zr; qtz	zr; brt	px; rut; zr; brt
0,4 A / 15°	grt; ilm	-	-
0,5 A / 10°	px; prv	-	-
0,6 A / 10°	-	-	-
1,0 A / 10°	rut; zr	-	-

Etapa 6 – separação densimétrica adicional

Foi verificado que o material não-magnético separado a 0,7 A apresentava-se ainda com muita mistura de diferentes espécies minerais. Deste modo, optou-se por

aplicar a etapa 4 novamente, tendo verificado uma melhor homogeneidade desta fração.

A aplicação da separação mineral por líquidos densos após a separação magnética não é imprescindível e tão pouco usual. No entanto, para os kimberlitos estudados neste trabalho, esta etapa adicional se mostrou eficaz, podendo ser aplicada caso a separação magnética pelo separador Frantz não tenha sido o esperado.

Etapa 7 – separação mineral

Com auxílio de um pincel e uma lupa (até 5x) os diferentes minerais foram separados de acordo com as cores, formatos e brilho (Figura 9), características que inicialmente permitiram distinguir o conjunto de minerais presentes em cada kimberlito estudado.

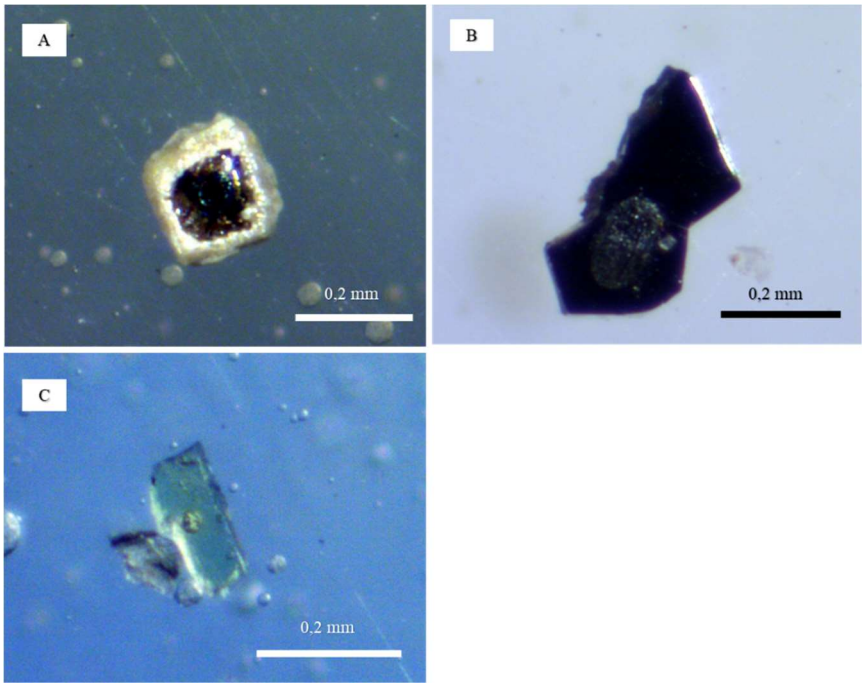

Fig. 9. Exemplo de alguns minerais separados. A) perovskita com capa de alteração (Charneca). B) ilmenita (Charneca); C) diopsídio (Indaiá I).

Depois de concluídas todas essas etapas, o material na forma de concentrados minerais foi preparado em montagens de grãos (mounts) para o programa analítico *in situ* por microssonda eletrônica e LA-ICP-MS.

2.3.2 Microssonda eletrônica (EDS/WDS)

A microssonda eletrônica é um método analítico que permite a visualização do material alvo e a análise química *in situ* em minerais, sendo uma técnica não destrutiva a qual é amplamente utilizada no campo da geologia, como apresentado por Gomes (2005). O aparelho contém um canhão eletrônico que emite um feixe de elétrons que incide sobre a superfície da amostra (resolução espacial de até 1 μm de diâmetro), que em resposta emite um espectro de raios X característicos dos elementos químicos presentes, que é detectado e analisado em espectrômetros acoplados ao conjunto.

Todas as seções delgadas polidas e as montagens de grãos foram recobertas com carbono à vácuo. As análises foram realizadas no Instituto de Geociências da Universidade de São Paulo com uma microssonda eletrônica de fabricação JEOL modelo JXA-FE 8530F, com um canhão eletrônico do tipo Field Emission (FE), composta por 5 espectrômetros. As análises em geral foram executadas com um potencial de aceleração de 15 kv (mais raramente com 20 kv) e corrente do feixe eletrônico de 20 ηA. O diâmetro do feixe utilizado para todas as rotinas analíticas utilizadas de 1 μm. As análises foram acompanhadas de imagens de elétrons retroespalhados (BEI-COMPO) para fins de controle textural. Os dados foram corrigidos pelo programa CITZAF (Armstrong, 1991) e posteriormente tratados para obtenção de suas proporções catiônicas, fórmulas estruturais e componentes moleculares finais (end members) por meio do programa Microsoft Office Excel e o programa de geoquímica PetroGraph. Esses dados estão dispostos em tabelas no corpo do texto no capítulo “Resultados”.

2.3.3 LA-Q-ICP-MS

As análises químicas de elementos traço em minerais através da técnica analítica *in situ* de ablação a laser associada com um espectrômetro de massas com plasma indutivamente acoplado (LA-ICP-MS) é um ramo da geoquímica analítica que se expande cada vez mais rápido. O princípio do método consiste em um laser a gás que arranca partículas por ablação na superfície do mineral e as transporta até o espectroscópio de massa acoplado a um plasma, e assim, a quantificação dos elementos é realizada.

A sensibilidade do método em determinar elementos incompatíveis (e.g., os elementos terra raras, Nb, Ta, Th, U, etc) é uma das inúmeras vantagens deste aparelho, somente pequenas quantidades da amostra sólida já são o suficiente para a detecção pelo espectroscópio, ao contrário de outras técnicas que envolvem a remoção de uma porção maior da amostra sólida ou a dissolução em soluções ácidas, aumentando a exposição a produtos químicos perigosos, contaminantes ou a perda de componentes. Outra vantagem é permitir a análise de possíveis zoneamentos químicos preservados no mineral, além da possível análise de grãos com pequenas dimensões utilizando um feixe de pequeno diâmetro (~15 μm) sem comprometer a qualidade das análises.

As análises realizadas foram obtidas no Laboratório de ICP do NAP Geoanalítica-USP do Instituto de Geociências por um espectrômetro quadrupolo (Q) ICP-MS Perkin-Elmer modelo ELAN-600 com amostrador a laser de 216nm. Para este trabalho os mesmos grãos analisados na microssonda eletrônica foram escolhidos para a análise por este método, utilizando feixes entre 15 e 50 μm de diâmetro e a cada 5 análises a calibração pelos padrões externos era realizada. A exatidão do método é constantemente avaliada pela análise desses materiais de referência.

As calibrações sempre foram realizadas antes, durante e após as análises, utilizando materiais de referências certificados. Os padrões NIST 610/612 (vidros artificiais produzidos pelo NIST- National Institute of Standards and Technology" – USA) e BIR-IG e BCR-2G (vidros de composição basáltica) foram utilizados como padrões externos. Para os padrões internos utilizou-se elementos químicos específicos que são importantes na composição de cada mineral e que previamente foram obtidos por microssonda eletrônica (e.g., Mg25 para espinélio, flogopita e piroxênio, Ti para ilmenita e Ca42 para perovskita). As análises na ordem de ppm (partes por milhão) estão dispostas em tabelas no corpo do texto no capítulo "Resultados".

2.4. Geoquímica isotópica

2.4.1 Método Sr/Sr em perovskita

A investigação geoquímica elemental e geoquímica isotópica de kimberlitos é dificultada devido à natureza explosiva do magma rico em voláteis e que traz consigo inúmeras porções de outras fases mineralógicas. A assimilação parcial ou total de xenólitos do manto e da crosta, além da facilidade de alteração dos minerais formadores dessas rochas, torna-se um desafio para os estudos e interpretações devido à inevitável contaminação.

A análise isotópica de Sr em perovskita é capaz de fornecer registros eficazes das composições isotópicas iniciais, uma vez que esse mineral, além de ser resistente às alterações, contém significativas quantidades de Sr e pouquíssimo Rb. Além disso, as perovskita podem ser imunes quanto à contaminação crustal, por ser um mineral de cristalização tardia. No entanto, uma das limitações para análise por LA-ICP-MS é o seu diminuto tamanho que pode variar entre os diversos kimberlitos (5 a 150 μm) (PATON et al., 2007).

Análises isotópicas de Sr foram obtidas em cristais de perovskitas por LA-MC-ICPMS no CPGeo-USP, composto por um laser 193nm Ar-F excimer acoplado a um espectrômetro de massa ThermoFinnigan NeptuneTm equipado com 9 coletores Faraday (com resistores de 10-11 Ω). Para o kimberlito Régis e Indaiá I as análises foram realizadas in situ em lâminas delgadas polidas de rocha, para os kimberlitos Charneca e Grota do Cedro foram obtidas direto nos grãos separados anteriormente pelas técnicas de separação de minerais pesados.

Foi realizado o monitoramento do fracionamento do isótopo de Sr através de um padrão de coral. Para a ablação os diâmetros dos spots e as intensidades variaram de acordo com o tamanho dos grãos (e.g., 79 μm /14 a 20Hz; 63 μm / 20Hz; 47 μm / 10 a 14Hz; 32 μm / 14 a 19Hz; 25 μm / 22Hz). As interferências isobáricas advindas do “branco” (o qual ser refere ao Kr contido no gás Ar utilizado na ablação sobre as massas 84, 86 e 87 de Sr) e de ^{87}Rb sobre ^{87}Sr eram retiradas logo após as análises que envolviam 60 ciclos de um segundo cada.

As médias e desvios padrão relativo obtidos em algumas análises representativas em cristais de perovskita são mostradas na Tabela 2. Os cálculos e procedimentos foram de acordo com Segal et al. (2003).

Tabela 2. Razões isotópicas $^{87}Sr/^{86}Sr$ obtidas em cristais de perovskita com as médias e desvios padrão para todas as análises de referência.

	$^{87}Sr/^{86}Sr$	erro 2s	$^{84}Sr/^{86}Sr$	erro 2s	$^{84}Sr/^{88}Sr$	erro 2s
Charneca	0.706472	0.000848	0.055847	0.000220	0.006668	0.000026
Charneca	0.706128	0.000721	0.056786	0.000151	0.006780	0.000018
Charneca	0.704740	0.000493	0.057367	0.000153	0.006850	0.000018
Charneca	0.706272	0.000673	0.057294	0.000266	0.006841	0.000032
Charneca	0.707388	0.000616	0.056773	0.000154	0.006779	0.000018
média	0.706200	0.000670	0.056813	0.000189	0.006784	0.000022
d.v	0.000952	0.000131	0.000607	0.000050	0.000070	0.000006
Grota	0.705486	0.000384	0.056388	0.000131	0.006733	0.000016
Grota	0.705156	0.000551	0.056454	0.000127	0.006741	0.000015
Grota	0.706447	0.000366	0.056950	0.000106	0.006800	0.000013
Grota	0.705385	0.000406	0.055816	0.000154	0.006664	0.000018
Grota	0.706147	0.000405	0.056900	0.000114	0.006794	0.000014
média	0.705724	0.000422	0.056502	0.000126	0.006746	0.000015
d.v	0.000547	0.000073	0.000459	0.000018	0.000055	0.000002
Régis	0.704724	0.000666	0.055798	0.000229	0.006662	0.000050
Régis	0.704660	0.000764	0.056082	0.000216	0.006696	0.000026
Régis	0.704927	0.000465	0.056428	0.000204	0.006738	0.000024
Régis	0.704259	0.000688	0.056224	0.000289	0.006713	0.000035
Régis	0.704238	0.000761	0.054596	0.000259	0.006519	0.000031
média	0.704562	0.000669	0.055826	0.000239	0.006666	0.000033
d.v	0.000302	0.000122	0.000725	0.000034	0.000086	0.000010
Indaiá I	0.704028	0.001085	0.055352	0.000454	0.006609	0.000054
Indaiá I	0.709303	0.000985	0.055241	0.000295	0.006596	0.000035
média	0.706665	0.001035	0.055297	0.000374	0.006602	0.000045
d.v	0.003730	0.000071	0.000078	0.000113	0.000009	0.000013

A qualidade dos dados pode ser verificada através do monitoramento das razões invariantes $^{84}Sr/^{86}Sr$ (~ 0.0565) e $^{84}Sr/^{88}Sr$ (~ 0.00675). Esses dados serão discutidos e interpretados preliminarmente para cada uma das ocorrências, mas conscientes de que mais análises deverão ser realizadas.

CAPÍTULO 3

3. RESULTADOS

Os resultados contemplam os estudos petrológicos com base na petrografia, química mineral e razões isotópicas $^{87}Sr/^{86}Sr$ de perovskita dos quatro kimberlitos aqui estudados. Para fins de publicação e de acordo com as normas do Instituto de Geociências (Programa Mineralogia e Petrologia) para alunos do curso de Doutorado matriculados até 28/11/2014, os resultados são apresentados na língua inglesa e, juntamente com os dados químicos obtidos através da microssonda eletrônica e LA-ICP-MS, estão localizados ao final da tese como Apêndices.

Os apêndices 1, 2, 3 e 4 referem-se aos resultados do kimberlito Charneca, Grota do Cedro, Régis e Indaiá I, respectivamente, enquanto o apêndice 5 apresenta a química mineral obtida para todos os kimberlitos. Lembrando que os títulos e a estrutura de cada artigo são preliminares e poderão sofrer modificações quando forem publicados.

CAPÍTULO 4

4. CONSIDERAÇÕES FINAIS

As rochas magmáticas potássicas máficas da PIAP são caracterizadas por grande variedade química (Gibson et al., 1995) evidenciado principalmente pela diversidade petrológica e pelos processos metassomáticos de diferentes graus e composições. A análise petrográfica dos principais constituintes das rochas aqui estudadas e dos diferentes tipos de texturas e mineralogia apresentada para cada uma delas, diz respeito a uma variação espacial e temporal da estrutura e composição do preenchimento do pipe.

Os clastos kimberlíticos de Charneca são muito similares na morfologia com aqueles do Indaiá, enquanto àqueles que ocorrem nos kimberlitos Régis e Grota do Cedro são mais semelhantes entre si. O alto grau de esfericidade e suavidade das bordas dos clastos de Charneca e Indaiá pode estar relacionado com a quebra de clastos já existentes ou abrasão durante o transporte e deposição. A ausência ou baixa ocorrência de vesículas associada à pouca indentação das margens desses clastos indicam um magma com pouca viscosidade.

Durante a subida deste material esses clastos podem ter sofrido reabsorção resultando em morfologias mais arredondadas e suaves. Em contraposição, os clastos dos kimberlitos Régis e Grota possuem formatos mais alongados, bordas irregulares e maiores indentações das margens, gerando clastos com formatos ameboides e em forma de “tubos”, sugerindo alto grau de plasticidade do material. Estas características morfológicas aliadas com a alta quantidade de vesículas em alguns clastos sugerem um magma de maior viscosidade.

A diferença das margens desses clastos é também marcante. Os kimberlitos Régis e Grota exibem clastos com margens mais definidas, enquanto a Charneca e Indaiá as margens são mais difusas, o que sugere diferentes processos de formação entre eles. As margens difusas do kimberlito Charneca provavelmente podem ser resultados de alteração, enquanto as margens menos marcantes dos clastos do Indaiá têm outra origem. Neste kimberlito essas estruturas se apresentam muito alteradas quando comparadas ao material fresco ao redor. Isto sugere que os clastos do Indaiá são mais

antigos do que o próprio kimberlito que os envolve, ou seja, podendo ser um material kimberlítico já existente e que foi interceptado pelo conduto vulcânico.

Em relação às estruturas peletais, são mais frequentes nos kimberlitos Grota e Régis, nos quais ocorrem com múltiplas bordas e frequentemente com minerais alinhados, sugerindo múltiplos estágios de formação. Essas estruturas são incipientes nos outros dois kimberlitos estudados, sendo possível notar que no Indaiá as estruturas peletais foram formadas por processos de menor intensidade, podendo ser reflexo direto da sua alta profundidade.

De acordo com os estudos petrográficos, observa-se que os kimberlitos Régis e Grota apresentam maior diversidade e plasticidade de material kimberlítico, sugerindo intensa dinâmica no processo eruptivo envolvendo várias fases de formação. Em oposição, os kimberlitos Charneca e Indaiá apresentam baixa variedade de material kimberlítico e pouca frequência de estruturas juvenis, indicando um processo eruptivo menos intenso para as fácies estudadas.

Os cristais de olivina dos kimberlitos estudados estão muito alterados, com exceção do Indaiá. A grande maioria desses cristais é encontrada dentro dos clastos ou como núcleo das estruturas peletais e, quando dispersos na matriz, é frequente ocorrer apenas o contorno do grão com aureolas de perovskitas. Por ser um produto primário da cristalização de magmas ricos em magnésio e pobres em sílica, a olivina pode trazer importantes informações acerca do magma parental e a certeza da sua origem é de extrema importância.

Os kimberlitos com texturas mais uniformes e coerentes, exibindo poucas estruturas peletais e clastos kimberlíticos, são algumas evidências de fácies hipoabissal, normalmente, correspondem à região mais profunda do pipe e menor contaminação de rochas de níveis crustais superiores. O kimberlito Indaiá I representa muito bem esta fácies, caracterizado por macro- e microcristais de olivina relativamente frescos imersos numa matriz mais fina riquíssima principalmente em magnetita, carbonato e perovskita. A presença de clastos juvenis são muito comuns em face diatrema, no entanto, eles podem ocasionalmente ocorrer em fácies hipoabissais, portanto, o kimberlito Indaiá I pode ser considerado uma variedade desta fácies.

O kimberlito Charneca também exibe textura hipoabissal, no entanto, o seu alto grau de alteração, possivelmente posterior à colocação da rocha, não preservou a maior

parte dos componentes. A baixa abundância de fragmentos crustais e de clastos juvenis com textura hipoabissal e ausência de vesículas, a deformação e orientação dos cristais de flogopita, apontam para uma fácies com características hipoabissais. No entanto, algumas feições são características de fácies diatrema, como micrólitos de diopsídio, cristais de olivina completamente alterados e carbonato secundário. Por ocorrer uma mistura dessas feições sugere-se que o kimberlito Charneca exibe características de fácies transicional, ou seja, localizada entre a porção final da hipoabissal e início da diatrema.

As características petrográficas da fáceis estudada do kimberlito Régis, a partir de 180,90 metros até 278,93 metros de profundidade, é típica de fácies diatrema. As evidências da mistura de diferentes tipos de magmas revelam diferentes pulsos com composições distintas. É caracterizada pela completa serpentinização da olivina, presença de texturas de segregação, riquíssima variação de clastos kimberlíticos juvenis com e sem núcleos, cristais de calcita secundária preenchendo veios e vesículas formando por vezes padrões radiais, e abundância de fragmentos crustais com formatos angulosos.

O kimberlito Grota do Cedro apresenta muita semelhança com o Régis, no entanto, o menor tamanho dos cristais de olivina de alguns clastos em relação à matriz, a abundância de calcita secundária preenchendo vesículas e substituindo totalmente clastos kimberlíticos, indicam uma origem vulcanoclástica, a qual pode estar associada tanto à fácies diatrema como à fácies cratera. Assim como o Régis, o kimberlito Grota do Cedro também registra diversos tipos de magmas com composição e plasticidade distintas, revelando também uma heterogeneidade do manto.

Assim como discutido no apêndice 4, olivina com hábito euédrico não é necessariamente diagnóstico de um fenocristal. A abordagem sobre a forma dos grãos de olivina e a sua origem é pertinente nos estudos de kimberlitos e, apesar de não ter sido o foco neste trabalho, é apropriado ressaltar a importância deste estudo em trabalhos futuros. Esta nova perspectiva acerca deste mineral tem significativas implicações na estimativa da composição do líquido kimberlítico e, juntamente com o estudo das texturas e clastos juvenis, traz informações a respeito da dinâmica de ascensão do magma e na preservação e distribuição de diamantes nos kimberlitos.

Os estudos de química mineral demostram que os peridotitos são provavelmente as principais fontes dos silicatos analisados, como por exemplo, granada, diopsídio e flogopita. Além das particularidades entre os diferentes tipos de peridotitos, como por exemplo, granada-lherzolito, flogopita peridotito e entre outros, a ocorrência de prováveis minerais provenientes de piroxenitos e da associação mineralógica MARID (mica, anfibólio, rutilo, ilmenita e diopsídio) nos kimberlitos Grota do Cedro e Régis, respectivamente, confirmam a variedade composicional do manto nesta região. Além disso, a evidência do líquido metassomático de composições distintas revela uma história evolutiva complexa desses kimberlitos.

O caráter magnesiano, pobre em Cr, Al e Ca de um manto depletado (Viljoen et al., 2014) é registrado principalmente pelos cristais de granada. É possível notar que as composições da granada do kimberlito Grota do Cedro são as mais enriquecidas em Cr e Ca quando comparados com os cristais da Charneca e Régis, os quais apresentam menores teores desses elementos. Isto está de acordo com o enriquecimento em lantanídeos pesados e anomalias negativas em Sr desses dois últimos kimberlitos.

Pelo menos dois diferentes tipos de fluidos responsáveis pelo enriquecimento metassomático no manto são registrados nos xenocristais de granada desses kimberlitos e provavelmente possuem composições carbonática e principalmente silicática, os quais são os principais agentes metassomáticos presentes no manto litosférico (Howarth et al., 2014). A primeira composição (carbonática) foi registrada apenas no kimberlito Grota do Cedro, enquanto a segunda (silicática) parece estar presente em todos os kimberlitos estudados.

Altas razões de $(La/Yb)_N$ (Howarth et al., 2014) ou $(Sm/Er)_N$ (Shchukina et al., 2017) combinadas com a razão Ti/Eu constante podem ser usadas para distinguir os dois diferentes fluidos metassomáticos. A razão $(Sm/Er)_N < 1$ e > 5 caracteriza o metassomatismo silicático e carbonático, respectivamente, enquanto $1 < (Sm/Er)_N < 5$ apresenta um caráter transicional que corresponde à mistura dos dois tipos de fluidos. A maior parte dos clinopiroxênios do Grota do Cedro demonstram valores com pouca variação da razão Ti/Eu (até 5487), exceto apenas um grão, e ampla variação da razão $(Sm/Er)_N$ (0.30 – 8.85) indicando que o líquido metassomático varia de uma mistura entre o silicático e o carbonatítico com predomínio deste último. As granadas do kimberlito Charneca apontam para um fluido de composição essencialmente silicática, devido às baixas razões $(Sm/Er)_N$ da suite megacristal e lherzolítica (0.48 – 0.81 e 0.11

– 0.25, respectivamente) combinadas às poucas variações de Ti/Eu (4388 – 10329). As granadas do kimberlito Régis também indicam uma mistura entre fluidos carbonatíticos e silicáticos, no entanto, ao contrário do Grota do Cedro, o predomínio tende à uma composição mais silicática.

O primeiro estágio de enriquecimento metassomático de uma fonte mantélica é caracterizado pela formação de granadas ricas em cromo e pobres em cálcio, e pelo padrão sinusoidal de lantanídeos (Shchukina et al., 2017) provavelmente com agente metassomático de composição carbonatítica; a granada é enriquecida em lantanídeos leves e o agente metassomático é fortemente depletado em lantanídeos pesados. Resultados de modelamento geoquímico (Kargin et al., 2016; Shchukina et al., 2017) que calcularam uma composição hipotética do fluido parental em equilíbrio com granadas de composições harzburgíticas, indicam uma composição próxima ao OIB.

Nenhum grupo de granadas estudado apresenta essas características. O contínuo enriquecimento metassomático resulta na evolução de composições harzburgíticas para lherzolíticas inicialmente ricas em cromo. As granadas do Grota do Cedro e Régis evidenciam moderado enriquecimento metassomático exibindo ainda significativas composições de Cr (~ 5.22 wt.% and ~ 3.65 wt.%, respectivamente).

O maior grau de empobrecimento das granadas analisadas é exibido por aquelas provenientes do kimberlito Charneca, as quais exibem depleção em CaO-Cr_2O_3 e lantanídeo leves, e enriquecimento em Al_2O_3, TiO_2 e lantanídeos pesados, refletindo uma típica composição lherzolítica, a qual reflete o final do estágio metassomático da região mantélica (Shchukina et al., 2017). É possível sugerir um enriquecimento metassomático hipotético inicialmente representado pelas granadas do kimberlito Grota do Cedro, as quais evoluem para composições semelhantes àquelas provenientes do kimberlito Régis e, com o contínuo processo de depleção, as composições evoluem para àquelas semelhantes às granadas do Charneca, as quais correspondem ao final da evolução do enriquecimento metassomático.

Apenas o kimberlito Régis e Grota do Cedro apresentam granadas que demonstram diferentes estágios metassomáticos, indicando que esses kimberlitos registram fontes mantélicas que sofreram múltiplos eventos de metassomatismo. Essas impressões da interação rocha/fluido nos minerais mantélicos quase sempre permanecem preservadas independente dos processos de ascensão e colocação dessas

rochas na crosta. Esta dinâmica resulta em corpos intrusivos com diferentes formatos, composições e estruturas que evidenciam as características do processo evolucionário de cada corpo kimberlítico.

Este último kimberlito citado apresenta incomuns Nb-perovskitas com altos teores de Nb_2O_5 (até 62.30 wt.%). Até o momento, não há registros de perovskitas em kimberlitos brasileiros com teores tão altos de nióbio. Esta variedade em kimberlito é uma importante descoberta que pode revelar diferentes características do magma "protokimberlítico" ainda não estudados na região da PIAP.

As Nb-perovskitas podem ser evidências de um magma parental altamente enriquecido em nióbio ou de algum processo petrogenético atuante durante a formação das perovskitas que disponibilizou grandes quantidades desse elemento. Os altos valores de nióbio resultaram em altas razões Nb/La (21.5 – 126.54) e somadas aos valores altos de Zr/Hf, além de piroxênios com altas razões de La/Yb, apontam assinaturas de fluidos com composição carbonatítica (Rudnick et al., 1993).

As razões relativamente baixas de $^{87}Sr/^{86}Sr(i)$ em rocha-total de kimberlitos do Grupo I (Becker and Le Roex, 2006; Boyd et al., 1984; Woodhead et al., 2009) em perovskitas, podem refletir uma adição de Rb durante a assimilação de material crustal (Donnelly et al., 2012). Os valores obtidos da razão $^{87}Sr/^{86}Sr(i)$ de todos os kimberlitos combinados com as evidências petrográficas de zoneamento nas perovskitas, indicam uma cristalização a partir de um magma kimberlítico em evolução submetido à condições diversas. A assimilação de material crustal pode ocorrer em qualquer nível durante a ascensão do kimberlito através da crosta e um número considerável de potenciais contaminantes são capazes de produzir heterogeneidades isotópicas no magma, como por exemplo, o manto litosférico (baixos teores de Sr) e MARID (rico em Sr) (Erlank et al. 1987; Kopylova et al., 2009).

Foi observado uma variação moderada na razão $^{87}Sr/^{86}Sr(i)$ entre os kimberlitos estudados, o Charneca demonstra os maiores valores e o Régis os menores, enquanto o Indaiá I e Grota do Cedro situam-se em valores intermediários entre os dois primeiros. O kimberlito Régis demonstra maior similaridade com as rochas da PIAP em relação ao intervalo da razão $^{87}Sr/^{86}Sr(i)$ enquanto o kimberlito Charneca possui valores muito acima. A variabilidade de composição química representada pelos elementos maiores e traços combinadas com a interação com xenólitos do manto, refletem uma fonte

peridotítica depletada que foi submetida a interações com diferentes fluidos e rochas mantélicas. A variação dos valores de razão $^{87}Sr/^{86}Sr(i)$ entre os kimberlitos estudados sugerem fonte mantélica com grande heterogeneidade, a partir da qual diferentes interações rocha/fluido, combinadas com ascensões e colocações dinâmicas, são refletidas pelas peculiaridades petrológicas e geoquímicas exibidas por essas rochas.

5. REFERÊNCIAS

Abersteiner, A., Giuliani, A., Kamenetsky, V.S., Phillips, D., 2017, Petrographic and melt-inclusion constraints on the petrogenesis of a magmaclast from the Venetia kimberlite cluster, South Africa: Chemical Geology, v. 455, p. 331–341, doi: 10.1016/j.chemgeo.2016.08.029.

Agee, J.J., Garrison, J.R., Taylor, L.A, 1982, Petrogenesis of oxide minerals in kimberlite, Elliot County Kentucky: American Mineralogist, v. 67, p. 28-42.

Almeida F.F.M., 1967, Origem e evolução da plataforma brasileira. Boletim da Divisão de Geologia e Mineralogia, DNPM, v. 241, p. 1-36.

Almeida, F.F.M., 1983, Relações tectônicas das rochas alcalinas mesozóicas da região meridional da plataforma sul-americana: Revista Brasileira de Geociências, v. 13, p. 139-158.

Almeida, V.V., 2009, Mineralogia e petrologia de xenólitos mantélicos das regiões de Ubatuba (SP) e Monte Carmelo (MG): evidências de fusão parcial e metassomatismo no manto superior do sudeste do Brasil [Dissertação de Mestrado]: São Paulo, Universidade de São Paulo, Instituto de Geociências, 153 p.

Andrade, K.W., and Chaves, M.L. de S.C., 2011, Geologia E Mineralogia Do Kimberlito Grota Do Cedro (Coromandel, MG): Geonomos, v. 19, p. 39–45.

Araújo, A.L.N., Carlson, R.W., Gaspar, J.C., Bizzi, L.A., 2001, Petrology of kamafugites and kimberlites from the Alto Paranaíba Alkaline Province, Minas Gerais, Brazil: Contributions to Mineralogy and Petrology, v. 142, p. 163–177, doi: 10.1007/s004100100280.

Arndt, N.T., Guitreau, M., Boullier, A.M., Le Roex, A., Tommasi, A., Cordier, P., and Sobolev, A., 2010, Olivine, and the origin of kimberlite: Journal of Petrology, v. 51, p. 573–602, doi: 10.1093/petrology/egp080.

Azzone, R.G., Enrich, G.E.R., Gomes, C.B.G., Ruberti, E., 2013, Trace element composition of parental magmas from mafic–ultramafic cumulates determined by in situ mineral analyses: The Juquiá mafic–ultramafic alkaline–carbonatite massif, SE Brazil: Journal of South American Earth Sciences, v. 41, p. 5-21, doi:

10.1016/j.jsames.2012.07.005

Banas, A., Stachel, T., Phillips, D., Shimizu, N., Viljoen, K.S., and Harris, J.W., 2009, Ancient metasomatism recorded by ultra-depleted garnet inclusions in diamonds from DeBeers Pool, South Africa: Lithos, v. 112, p. 736–746, doi: 10.1016/j.lithos.2009.04.043.

Bardet, M. G., 1977, Geólogie du diamante. Troisièmepartie: Gisementesde dediamants d'Asie, d'Amérique, d'Europe et d'Australasie. Mémoires du Bureau de recherches géologiques et minières, V.83, 169 p.

Barnes, S.J., and Roeder, P.L., 2001, The Range of Spinel Compositions in Terrestrial Mafic and Ultramafic Rocks: Journal of Petrology, v. 42, p. 2279–2302, doi: 10.1093/petrology/42.12.2279.

Beard, A.D., Downes, H., Hegner, E., and Sablukov, S.M., 2000, Geochemistry and mineralogy of kimberlites from the Arkhangelsk Region, NW Russia: Evidence for transitional kimberlite magma types: Lithos, v. 51, p. 47–73, doi: 10.1016/S0024-4937(99)00074-2.

Becker, M., and Le Roex, A.P., 2006, Geochemistry of South African on- and off-craton, group I and group II kimberlites: Petrogenesis and source region evolution: Journal of Petrology, v. 47, p. 673–703, doi: 10.1093/petrology/egi089.

Bhat, I.M., Ahmad, T., and Subba Rao, D. V., 2017a, Compositional variability of spinel-group minerals from the shergol serpentinized peridotites along indus suture zone, ladakh himalaya (India): constraints on tectonomagmatic history: Chemie der Erde - Geochemistry, v. 77, p. 587–595, doi: 10.1016/j.chemer.2017.10.003.

Bhat, I.M., Ahmad, T., and Subba Rao, D. V., 2017b, Geochemical Characterization of Serpentinized Peridotites from the Shergol Ophiolitic Slice along the Indus Suture Zone (ISZ), Ladakh Himalaya, India: The Journal of Geology, v. 125, p. 501–513, doi: 10.1086/692653.

Bizzi, L.A., Smith, C.B., Meyer, H.O.A., Dewit, M.J., 1993, Mesozoic kimberlites and related rocks ins southwestern Sao Francisco craton, Brazil: a case for local mantle reservoirs and their interaction: Proceedings of the Proc. Fifth Int. Kimberlite Conf., Araxá, v. 2, p.156-171.

Bizzi, L.A., Smith, C.B., Meyer, H.O.A., Armstrong, R.A., Dewit, M.J., 1994, Mesozoickimberlites and related rocks in southwestern São Francisco craton, Brazil: a case for local reservoir and their interaction. In: Meyer H.O.A., Leonardos O.H. (eds) Proc 5th Int Kimberlite Conf, Araxá. Companhia de Pesquisa de Recursos Minerais, Brasília, p. 156-171.

Boyd, F.R., Nixon, P.H., and Boctor, N.Z., 1984, Rapidly crystallized garnet pyroxenite xenoliths possibly related to discrete nodules: Contributions to Mineralogy and Petrology, v. 86, p. 119–130, doi: 10.1007/BF00381839.

Brett, R.C., Russell, J.K., and Moss, S., 2009, Origin of olivine in kimberlite: Phenocryst or impostor? Lithos, v. 112, p. 201–212, doi: 10.1016/j.lithos.2009.04.030.

Brod, A.F., Gibson, S.A., Thompson, R.N., Junqueira-Brod, T.C., Seer, H.J., Moraes, L.C., Boaventura, G.R., 2000, The kamafugite-carbonatite association in the Alto Paranaíba igneous province (APIP) Southeastern Brazil: Revista Brasileira de Geociências, v. 30, p. 404-408.

Campos, J.E.G., Dardenne, M.A., 1997, Origem e evolução tectônica da Bacia Sanfranciscana: Revista Brasileira de Geociências, v. 27, p. 283-294.

Carlson, R.W., Araújo, A.L.N., Junqueira-Brod, T.C., Gaspar, J.C., Brod, J.A., Petrinovic, I.A., Hollanda, M.H.B., 2007, Chemical and isotopic relationships between peridotite xenoliths and mafic–ultrapotassic rocks from Southern Brazil: Chemycal Geology, v. 242, p. 415–434.

Cas, R., Porritt, L., Pittari, A., and Hayman, P., 2008, A new approach to kimberlite facies terminology using a revised general approach to the nomenclature of all volcanic rocks and deposits: Descriptive to genetic: Journal of Volcanology and Geothermal Research, v. 174, p. 226–240, doi: 10.1016/j.jvolgeores.2007.12.018.

Cas, R.A.F., Hayman, P., Pittari, A., and Porritt, L., 2008, Some major problems with existing models and terminology associated with kimberlite pipes from a volcanological perspective, and some suggestions: Journal of Volcanology and Geothermal Research, v. 174, p. 209–225, doi: 10.1016/j.jvolgeores.2007.12.031.

Cas, R.A.F., Porritt, L., Pittari, A., and Hayman, P.C., 2009, A practical guide to terminology for kimberlite facies: A systematic progression from descriptive to

genetic, including a pocket guide: Lithos, v. 112, p. 183–190, doi: 10.1016/j.lithos.2009.03.051.

pocket guide: Lithos, v. 112, p. 183–190, doi: 10.1016/j.lithos.2009.03.051.

Castillo-Oliver, M., Galí, S., Melgarejo, J.C., Griffin, W.L., Belousova, E., Pearson, N.J., Watangua, M., and O'Reilly, S.Y., 2016, Trace-element geochemistry and U-Pb dating of perovskite in kimberlites of the Lunda Norte province (NE Angola): Petrogenetic and tectonic implications: Chemical Geology, v. 426, p. 118–134, doi: 10.1016/j.chemgeo.2015.12.014.

Cederberg, J., Söderlund, U., Oliveira, E.P., Ernst, R.E., and Sergei, A., 2016, U-Pb baddeleyite dating of the Proterozoic Pará de Minas dyke swarm in the São Francisco craton (Brazil) – implications for tectonic correlation with the Siberian , Congo and North China cratons:, doi: 10.1080/11035897.2015.1093543.

Chaves, M.L. de S.C., 2012, Kimberlito vargem-1 (Coromandel, MG): bulk sample confirma mineralização diamantífera: Rem: Revista Escola de Minas, v. 65, p. 509–511, doi: 10.1590/S0370-44672012000400011.

Chaves, M.L. de S.C., Andrade, K.W., Dussin, I.A., and Azzi, A. de A., 2012, Geologia, Geoquímica e Mineralogia Comparativa Entre as Intrusões Diamantíferas Canastras-1 e Abel Régis (Minas Gerais): Geociencias, v. 31, p. 516–533.

Chaves, M.L. de S.C., Andrade, K.W., Moreira, L.A., Lqwuxvlrqv, U., Nqrzq, D.U.H., Wkh, L.Q., Fkdqjhv, V., Uhodwlrq, L.Q., Wkh, W.R., Frqfhswv, D., Lpsruwdqw, P., Erg, V., Rxw, S., Wkh, W., et al., 2009, A intrusão diamantífera Abel Régis (Carmo do Paranaíba, MG): kimberlito ou lamproíto? REM: R. Esc.Minas, Ouro Preto, v. 62(4), p. 431–438.

Chaves, M.L. de S.C., Brandão, P.R.G., Girodo, A.C., Benitez, L., and Brandão, G.P.R., 2008, Kimberlito Canastra-1 (São Roque de Minas , MG): geologia , mineralogia e reservas diamantíferas: Rem: Revista Escola de Minas, v. 61, p. 357–364, doi: 10.1590/S0370-44672008000300014.

Chakhmouradian, A.R., and Mitchell, R.H., 2000, Occurrence, alteration patterns and compositional variation of perovskite in kimberlites: Canadian Mineralogist, v. 38, p. 975–994, doi: 10.2113/gscanmin.38.4.975.

Chakhmouradian, a R., and Mitchell, R.H., 2001, Three compositional varieties of perovskite from kimberlites of the Lac de Gras field (Northwest Territories , Canada): Mineralogical Magazine, v. 65, p. 133–148, doi: 10.1180/002646101550082.

Chakhmouradian, A.R., Reguir, E.P., Kamenetsky, V.S., Sharygin, V. V., and Golovin, A. V., 2013, Trace-element partitioning in perovskite: Implications for the geochemistry of kimberlites and other mantle-derived undersaturated rocks: Chemical Geology, v. 353, p. 112–131, doi: 10.1016/j.chemgeo.2013.01.007.

Chen, M.M., Tian, W., Suzuki, K., Tejada, M.L.G., Liu, F.L., Senda, R., Wei, C.J., Chen, B., and Chu, Z.Y., 2014, Peridotite and pyroxenite xenoliths from Tarim, NW China: Evidences for melt depletion and mantle refertilization in the mantle source region of the Tarim flood basalt: Lithos, v. 204, p. 97–111, doi: 10.1016/j.lithos.2014.01.005.

Clement, C.R., Skinner, E.M.W., 1985, A textural-genetic classification of kimberlites. Transactions of the Geological Society of South Africa, p. 403–409.

Costa, V.S., 2013, Mineralogia e Petrologia de xenólitos mantélicos da Província Kimberlitica de Juína, MT [Tese de Doutorado]: São Paulo, Universidade de São Paulo, Instituto de Geociências, 447 p, doi: 10.11606/T.44.2013.tde-15052014-094703.

CPRM - Companhia de Pesquisa de Recursos Minerais, 2014, Mapa geológico e gravimétrico do estado de Minas Gerais: http://geosgb.cprm.gov.br/ (acessado Agosto 2018).

Dawson, J.B., Smith, J. V., 1975a, Chemistry and origin of phlogopite megacrysts in kimberlite: Nature, v. 253, p. 336–338, doi: 10.1038/253336b0.

Dawson, J.B., Smith, J. V., 1975b, Occurrence of diamond in a mica-garnet lherzolite xenolith from kimberlite: Nature, v. 254, p. 580–581.

Dawson, J.B., Stephens, W.E., 1975c, Statistical Classification of Garnets from Kimberlite and Associated Xenoliths Author (s): J . B . Dawson and W . E . Stephens Reviewed work (s): Source : The Journal of Geology , Vol . 83 , No . 5 (Sep ., 1975), pp . 589-607 Published by : The Univ: Journal of Geology, v. 83, p. 589–607.

Dawson, J.B., Smith, J. V., 1977, The MARID (mica-amphibole-rutile-ilmenite-diopside) suite of xenoliths in kimberlite: Geochimica et Cosmochimica Acta, v. 41, doi: 10.1016/0016-7037(77)90239-3.

Dardenne, M.A., Schobbenhaus, C., 2001, Metalogênese do Brasil: Editora Universidade de Brasília, 392p.

Donnelly, C.L., Griffin, W.L., O'Reilly, S.Y., Pearson, N.J., and Shee, S.R., 2011, The Kimberlites and related rocks of the Kuruman Kimberlite Province, Kaapvaal Craton, South Africa: Contributions to Mineralogy and Petrology, v. 161, p. 351–371, doi: 10.1007/s00410-010-0536-9.

Donnelly, C.L., Griffin, W.L., Yang, J.H., O'reilly, S.Y., Li, Q.L., Pearson, N.J., Li, X.H., 2012, In situ U-PB dating and SR-ND isotopic analysis of perovskite: Constraints on the age and petrogenesis of the Kuruman Kimberlite Province, Kaapvaal Craton, South Africa: Journal of Petrology, v. 53, p. 2497–2522, doi: 10.1093/petrology/egs057.

Dutra, A.C., Marangoni, Y.R., and Junqueira-Brod, T.C., 2012, Investigation of the Goiás Alkaline Province, Central Brazil: Application of gravity and magnetic methods: Journal of South American Earth Sciences, v. 33, p. 43–55, doi: 10.1016/j.jsames.2011.06.004.

Erlank, A. J., Waters, F. G., Hawkesworth, C. J., Haggerty, S. E., Allsopp, H. L., Rickard, R. S. & Menzies, M. A., 1987, Evidence for mantle metasomatism in peridotite nodules from the Kimberley pipes, South Africa: In Menzies, M. A. & Hawkesworth, C. J. (eds) Mantle Metasomatism. London: Academic Press, p. 221-311.

Felgate, M.R., 2014, The Petrogenesis of Brazilian kimberlites and kamafugites intruded along the 125 ° lineament [Tese de Doutorado] : University of Melbourne, School of the Earth Sciences, 275 p.

Field, M., Scott Smith, B.H., 1998, Textural and Genetic Classification Schemes for Kimberlites : a New Perspective: Proceedings of the Seventh International Kimberlite Conference, Cape Town, April 1998, p. 1-4.

Field, M., Scott Smith, B.H., 1999, Contrasting geology and near-surface emplacement of kimberlite pipes in Southern Africa and Canada: Proceedings of the VIIth

International Kimberlite Conference, The J. B. Dawson Volume, v. 1, p. 214–237.

Francis, D., and Patterson, M., 2010, Reply to the Discussion by Mitchell and Tappe on "Kimberlites and aillikites as probes of the continental lithospheric mantle": Lithos, v. 115, p. 293–295, doi: 10.1016/j.lithos.2009.12.003.

Gernon, T.M., Brown, R.J., Tait, M.A., Hincks, T.K., 2012, The origin of pelletal lapilli in explosive kimberlite eruptions: Nature Communications, v. 3, p. 832–837, doi: 10.1038/ncomms1842.

Gibson, S.A., Thompson, R.N., Leonardos, O.H., Dickin, A.P., Mitchell, J.G., 1995, The late cretaceous impact of the trindade mantle plume: Evidence from large-volume, mafic, potassic magmatism in SE Brazil: Journal of Petrology, v. 36, p. 189–229, doi: 10.1093/petrology/36.1.189.

Girnis, A. V., Bulatov, V.K., and Brey, G.P., 2011, Formation of primary kimberlite melts - Constraints from experiments at 6-12GPa and variable CO_2/H_2O: Lithos, v. 127, p. 401–413, doi: 10.1016/j.lithos.2011.09.018.

Giuliani, A., Phillips, D., Kamenetsky, V.S., Goemann, K., 2016, Constraints on kimberlite ascent mechanisms revealed by phlogopite compositions in kimberlites and mantle xenoliths: Lithos, v. 240–243, p. 189–201, doi: 10.1016/j.lithos.2015.11.013.

Golubkova, A.B., Nosova, A.A., Larionova, Y.O., 2013, Mg-ilmenite megacrysts from the Arkhangelsk kimberlites, Russia: Genesis and interaction with kimberlite melt and postkimberlite fluid: Geochemistry International, v. 51, p. 353–381, doi: 10.1134/S0016702913030038.

Gomes, C.B., Comin-Chiaramonti, P., 2005, An introduction to the alkaline and alkaline-carbonatiticmagmatism in and around the Paraná·Basin, in Comin-Chiaramonti, P., Gomes, C.B., eds., Mesozoic to Cenozoic Alkaline Magmatism in the Brazilian Platform, Edusp – Editora da Universidade de São Paulo, p. 21-30.

Grégoire, M., Bell, D.R., and Le Roex, A.P., 2003, Garnet Lherzolites from the Kaapvaal Craton (South Africa): Trace Element Evidence for a Metasomatic History: Journal of Petrology , v. 44, p. 629–657, doi: 10.1093/petrology/44.4.629.

Griffin, W.L., Fisher, N.I., Friedman, J., Ryan, C.G., O'Reilly, S.Y., 1999, Cr-Pyrope

Garnets in the Lithospheric Mantle: Journal of Petrology, v. 40, p. 679–704, doi: 10.1093/petroj/40.5.679.

Griffin, W.L., Shee, S.R., Ryan, C.G., Win, T.T., Wyatt, B. A., 1999, Harzburgite to lherzolite and back again: metasomatic processes in ultramafic xenoliths from the Wesselton kimberlite, Kimberley, South Africa: Contributions to Mineralogy and Petrology, v. 134, p. 232–250, doi: 10.1007/s004100050481.

Grütter, H.S., Gurney, J.J., Menzies, A.H., and Winter, F., 2004, An updated classification scheme for mantle-derived garnet, for use by diamond explorers: Lithos, v. 77, p. 841–857, doi: 10.1016/j.lithos.2004.04.012.

Guarino, V., Wu, F.Y., Lustrino, M., Melluso, L., Brotzu, P., Gomes, C. de B., Ruberti, E., Tassinari, C.C.G., Svisero, D.P., 2013, U-Pb ages, Sr-Nd- isotope geochemistry, and petrogenesis of kimberlites, kamafugites and phlogopite-picrites of the Alto Paranaíba Igneous Province, Brazil: Chemical Geology, v. 353, p. 65–82, doi: 10.1016/j.chemgeo.2012.06.016.

Hardman, M.F., Pearson, D.G., Stachel, T., and Sweeney, R.J., 2018, Statistical approaches to the discrimination of crust- and mantle-derived low-Cr garnet – Major-element-based methods and their application in diamond exploration: Journal of Geochemical Exploration, v. 186, p. 24–35, doi: 10.1016/j.gexplo.2017.11.012.

Hetman, C.M., Scott Smith, B.H., Paul, J.L., Winter, F., 2004, Geology of the Gahcho Kué kimberlite pipes, NWT, Canada: Root to diatreme magmatic transition zones: Lithos, v. 76, p. 51–74, doi: 10.1016/j.lithos.2004.03.051.

Howarth, G.H., Barry, P.H., Pernet-Fisher, J.F., Baziotis, I.P., Pokhilenko, N.P., Pokhilenko, L.N., Bodnar, R.J., Taylor, L.A., and Agashev, A.M., 2014, Superplume metasomatism: Evidence from Siberian mantle xenoliths: Lithos, v. 184–187, p. 209–224, doi: 10.1016/j.lithos.2013.09.006.

Ionov, D.A., Chanefo, I., and Bodinier, J.L., 2005, Origin of Fe-rich lherzolites and wehrlites from Tok, SE Siberia by reactive melt percolation in refractory mantle peridotites: Contributions to Mineralogy and Petrology, v. 150, p. 335–353, doi: 10.1007/s00410-005-0026-7.

Jang, Y.D., and Naslund, H.R., 2002, Major and trace element variation in ilmenite in

the Skaergaard Intrusion: Petrologic implications: Chemical Geology, v. 193, p. 109–125, doi: 10.1016/S0009-2541(02)00224-3.

Janney, P.E., Shirey, S.B., Carlson, R.W., Pearson, D.G., Bell, D.R., Le Roex, A.P., Ishikawa, A., Nixon, P.H., and Boyd, F.R., 2010, Age, composition and thermal characteristics of South African off-craton mantle lithosphere: Evidence for a multi-stage history: Journal of Petrology, v. 51, p. 1849–1890, doi: 10.1093/petrology/egq041.

Jelsma, H., Barnett, W., Richards, S., and Lister, G., 2009, Tectonic setting of kimberlites: Lithos, v. 112, p. 155–165, doi: 10.1016/j.lithos.2009.06.030.

Junqueira-Brod T.C, B.J.., 1999, Spinning droplets - a conspicuous lapilli-size structure in Kamafugitic diatremes of Southern Goiás, Brazil: Revista Brasileira de Geociencias, v. 29, p. 437–440.

Junqueira-Brod, T.C., Gaspar, J.C., Brod, J.A., and Kafino, C.V., 2005, Kamafugitic diatremes: Their textures and field relationships with examples from the Goi??s alkaline province, Brazil: Journal of South American Earth Sciences, v. 18, p. 337–353, doi: 10.1016/j.jsames.2004.11.002.

Kamenetsky, V.S., Kamenetsky, M.B., Sobolev, A. V., Golovin, A. V., Demouchy, S., Faure, K., Sharygin, V. V., and Kuzmin, D. V., 2008, Olivine in the Udachnaya-East kimberlite (Yakutia, Russia): Types, compositions and origins: Journal of Petrology, v. 49, p. 823–839, doi: 10.1093/petrology/egm033.

Karfunkel, J., Hoover, D., Fernandes, A.F., Sgarbi, G.N.C., Kambrock, K., Oliveira, G.D., Karfunkel, J., Hoover, D., Fernandes, A.F., Sgarbi, G.N.C., Kambrock, K., and Oliveira, G.D., 2014, Diamonds from the Coromandel Area, West Minas Gerais State, Brazil: an update and new data on surface sources and origin: Brazilian Journal of Geology, v. 44, p. 325–338, doi: 10.5327/Z2317-4889201400020011.

Kargin, A. V., Sazonova, L. V., Nosova, A.A., and Tretyachenko, V. V., 2016, Composition of garnet and clinopyroxene in peridotite xenoliths from the Grib kimberlite pipe, Arkhangelsk diamond province, Russia: Evidence for mantle metasomatism associated with kimberlite melts: Lithos, v. 262, p. 442–455, doi: 10.1016/j.lithos.2016.07.015.

Kargin, A. V., Sazonova, L. V., Nosova, A.A., Lebedeva, N.M., Tretyachenko, V. V., and Abersteiner, A., 2017, Cr-rich clinopyroxene megacrysts from the Grib kimberlite, Arkhangelsk province, Russia: Relation to clinopyroxene–phlogopite xenoliths and evidence for mantle metasomatism by kimberlite melts: Lithos, v. 292–293, p. 34–48, doi: 10.1016/j.lithos.2017.08.018.

Kavanagh, J.L., and Sparks, R.S.J., 2009, Temperature changes in ascending kimberlite magma: Earth and Planetary Science Letters, v. 286, p. 404–413, doi: 10.1016/j.epsl.2009.07.011.

Kopylova, M.G., Nowell, G.M., Pearson, D.G., and Markovic, G., 2009, Crystallization of megacrysts from protokimberlitic fluids: Geochemical evidence from high-Cr megacrysts in the Jericho kimberlite: Lithos, v. 112, p. 284–295, doi: 10.1016/j.lithos.2009.06.008.

Kostrovitsky, S.I., Malkovets, V.G., Verichev, E.M., Garanin, V.K., and Suvorova, L. V., 2004, Megacrysts from the Grib kimberlite pipe (Arkhangelsk Province, Russia): Lithos, v. 77, p. 511–523, doi: 10.1016/j.lithos.2004.03.014.

la Terra, E.F., Menezes, P. de T.L., and Fontes, S.L., 2010, Metodologia exploratória para delimitação de condutos vulcânicos kimberlíticos com o uso do método CSAMT, MG, Brasil: Revista Brasileira de Geofisica, v. 28, p. 357–370, doi: 10.1590/S0102-261X2010000300004.

Lensky, N.G., Niebo, R.W., Holloway, J.R., Lyakhovsky, V., and Navon, O., 2006, Bubble nucleation as a trigger for xenolith entrapment in mantle melts: Earth and Planetary Science Letters, v. 245, p. 278–288, doi: 10.1016/j.epsl.2005.11.064.

Leonardos JR., O.H., Fyfe, W.S., 1974, Ultrametamorphism and melting of a continental margin in the Rio de Janeiro region. Contributions to Mineralogy and Petrology, v. 45, p. 201-214.

Leonardos, O.H., Meyer, H.O.A., 1991, Outline of the geology of western Minas Gerais. In: 5º Internat. Kimberlite Conference. Araxá, Proceedings, Field Guide Book, p. 17-24.

Liu, Y., Taylor, L.A., Sarbadhikari, A.B., Valley, J.W., Ushikubo, T., Spicuzza, M.J., Kita, N., Ketcham, R.A., Carlson, W., Shatsky, V., and Sobolev, N. V., 2009, Metasomatic origin of diamonds in the world's largest diamondiferous eclogite:

Lithos, v. 112, p. 1014–1024, doi: 10.1016/j.lithos.2009.06.036.

Lloyd, F.E., Stoppa, F., 2003, Pelletal Lapilli in Diatremes – Some Inspiration from the Old: v. 15, p. 65–71.

Malarkey, J., Pearson, D.G., Kjarsgaard, B.A., Davidson, J.P., Nowell, G.M., Ottley, C.J., Stammer, J., 2010, From source to crust: tracing magmatic evolution in a kimberlite and a melilitite using microsample geochemistry. Earth and Planetary Science Letters 299, 80–90.

Marangoni, Y.R., and Mantovani, M.S.M., 2013, Geophysical signatures of the alkaline intrusions bordering the Paraná Basin: Journal of South American Earth Sciences, v. 41, p. 83–98, doi: 10.1016/j.jsames.2012.08.004.

McBirney, A.R., 2002, The Skaergaard Layered Series. Part VI. Excluded trace elements: Journal of Petrology, v. 43, p. 535–556, doi: 10.1093/petrology/43.3.535.

McDonough, W.F., and Sun, S.S., 1995, the Composition of the Earth: Chemical Geology, v. 120, p. 223–253.

Melluso, L., Lustrino, M., Ruberti, E., Brotzu, P., de Barros Gomes, C., Morbidelli, L., Morra, V., Svisero, D.P., and D'Amelio, F., 2008, Major- and trace-element composition of olivine, perovskite, clinopyroxene, Cr-Fe-Ti oxides, phlogopite and host kamafugites and kimberlites, Alto Paranaíba, Brazil: Canadian Mineralogist, v. 46, p. 19–40, doi: 10.3749/canmin.46.1.19.

Meyer, O.A., Svisero, D.P., 1991, The Limeira and Indaiá Intrusion. In: Fifth Int. Kimb. Conf., Field guide Book, CPRM, Spec. Publ. 3/91, p. 49-55.

Mitchell, R.H., 1995, The role of petrography and lithogeochemistry in exploration for diamondiferous rocks: Journal of Geochemical Exploration, v. 53, p. 339–350, doi: 10.1016/0375-6742(94)00014-3.

Mitchell, R.H., 2008a, Petrology of hypabyssal kimberlites: Relevance to primary magma compositions: Journal of Volcanology and Geothermal Research, v. 174, p. 1–8, doi: 10.1016/j.jvolgeores.2007.12.024.

Mitchell, R.H., 2008b, Petrology of hypabyssal kimberlites: Relevance to primary magma compositions: Journal of Volcanology and Geothermal Research, v. 174, p.

1–8, doi: 10.1016/j.jvolgeores.2007.12.024.

Mitchell, R. H., Reed, S. J., 1988, Ion microprobe determination of rare earth elements in perovskite from kimberlites and alnoites: Mineralogical Magazine, v. 52, p. 331-339.

Moraes Rocha, L.G. de, Pires, A.C.B., Carmelo, A.C., and Araújo Filho, J.O. de, 2014, Geophysical characterization of the Azimuth 125° lineament with aeromagnetic data: Contributions to the geology of central Brazil: Precambrian Research, v. 249, p. 273–287, doi: 10.1016/j.precamres.2014.05.005.

Moraes Rocha, L.G. de, Pires, A.C.B., Carmelo, A.C., and Oksum, E., 2015, Curie surface of the alkaline provinces of Goiás (GAP) and Alto Paranaíba (APAP), central Brazil: Journal of Volcanology and Geothermal Research, v. 297, p. 28–38, doi: 10.1016/j.jvolgeores.2015.03.006.

Nannini, F., 2011, Petrografia e química mineral de xenólitos mantélicos da intrusão kimberlítica Indiá, Monte Carmelo, MG[Dissertação de Mestrado]: Universidade de São Paulo, Instituto de Geociências, 108p.

Nannini, F., 2016, Geologia e Petrologia de Xenólitos Mantélicos da Província Ígnea do Alto Paranaíba, Minas Gerais [Tese de Doutorado]: São Paulo, Instituto de Geociências,doi:10.11606/T.44.2016.tde-04052016-112733.

Nimis, P., Zanetti, A., Dencker, I., and Sobolev, N. V., 2009, Major and trace element composition of chromian diopsides from the Zagadochnaya kimberlite (Yakutia, Russia): Metasomatic processes, thermobarometry and diamond potential: Lithos, v. 112, p. 397–412, doi: 10.1016/j.lithos.2009.03.038.

O'Reilly, S.Y., and Griffin, W.L., 1996, 4-D Lithosphere Mapping: methodology and examples: Tectonophysics, v. 1, p. 3–18, doi: 10.1016/0040-1951(96)00010-8.

Paton C., Hergt J.M., Phillips D., Woodhead J.D., Shee S.R., 2007, New insights into the genesis of Indian kimberlites from the Dharwar Craton via in situ Sr isotope analysis of groundmass perovskite: Geology, v. 35, p. 1011-1014.

Pereira, R.S., Fuck, R.A., 2005, Archean Nuclei and the distribution of kimberlite and related rocks in the São Francisco Craton, Brazil: Revista Brasileira de Geociências, v 35(3), p. 93–104.

Pereira, S.R., 2007, Cráton do São Francisco, kimberlitos e diamantes [Tese de Doutorado]: Brasília, Universidade de Brasília, Instituto de Geociências, 104 p.

Pereira, R. S.; Fuck, R.A.; França, O.S.; Leite, A.A., 2017, Evidence of young, proximal and primary (YPP) diamond source occurring in alluviums in the Santo Antônio do Bonito, Santo Inácio and Douradinho rivers in Coromandel region, Minas Gerais: Brazilian Journal of Geology, v. 3, p. 383–401, doi: 10.1590/2317.

Pires, F.R.M., Gonçalves, F.T.T., Ribeiro, L.A.S., Siqueira, A.J.B., 1986, Controle das mineralizações auríferas do Grupo Cuiabá, Mato Grosso. In: Congresso Brasileiro de Geologia, Goiânia, v. 5, p. 2383-2396.

Pivin, M., Féménias, O., and Demaiffe, D., 2009, Metasomatic mantle origin for Mbuji-Mayi and Kundelungu garnet and clinopyroxene megacrysts (Democratic Republic of Congo): Lithos, v. 112, p. 951–960, doi: 10.1016/j.lithos.2009.03.050.

Porritt, L.A., Cas, R.A.F., Schaefer, B., and McKnight, S.W., 2012, Textural analysis of strongly altered kimberlite: Examples from the Ekati diamond mine, Northwest Territories, Canada: Canadian Mineralogist, v. 50, p. 625–641, doi: 10.3749/canmin.50.3.625.

Read, G., Grutter, H., Winter, S., Luckman, N., Gaunt, F., and Thomsen, F., 2004, Stratigraphic relations, kimberlite emplacement and lithospheric thermal evolution, Quiricó Basin, Minas Gerais State, Brazil: Lithos, v. 77, p. 803–818, doi: 10.1016/j.lithos.2004.04.011.

Rocha, M.P., 2008, Tomografia sísmica com ondas P e S para o estudo do manto superior no Brasil: , p. 86, doi: 10.11606/T.14.2008.tde-29092008-212459.

Roeder, P.L., and Schulze, D.J., 2008, Crystallization of groundmass spinel in kimberlite: Journal of Petrology, v. 49, p. 1473–1495, doi: 10.1093/petrology/egn034.

Rudnick, R.L., McDonough, W.F., and Chappell, B.W., 1993, Carbonatite metasomatism in the northern Tanzanian mantle: petrographic and geochemical characteristics: Earth and Planetary Science Letters, v. 114, p. 463–475, doi: 10.1016/0012-821X(93)90076-L.

Russell, J.K., Porritt, L.A., Lavallé, Y., and Dingwell, D.B., 2012, Kimberlite ascent by

assimilation-fuelled buoyancy: Nature, v. 481, p. 352–356, doi: 10.1038/nature10740.

Sarkar, C., Storey, C.D., and Hawkesworth, C.J., 2014, Using perovskite to determine the pre-shallow level contamination magma characteristics of kimberlite: Chemical Geology, v. 363, doi: 10.1016/j.chemgeo.2013.10.032.

Schobbenhaus, C., Campos, D.A., 1984, A evolução da Plataforma Sulamericana no Brasil e suas principais concentrações minerais. In: Schobbenhaus C. et al. Coords. Geologia do Brasil. Brasília, DNPM, p. 9-53.

Schobbenhaus, C., Neves, B.B.B., 2003. A geologia do Brasil no contexto da plataforma Sul-americana. Geol. tectonica e Recur. minerais do Bras. 5–54.

Schulze, D.J., 2001, Origins of chromian and aluminous spinel macrocrysts from kimberlites in Southern Africa: Canadian Mineralogist, v. 39, p. 361–376, doi: 10.2113/gscanmin.39.2.361.

Schulze, D.J., 2003, A classification scheme for mantle-derived garnets in kimberlite: a tool for investigating the mantle and exploring for diamonds: Lithos, v. 71, p. 195–213, doi: 10.1016/S0024-4937(03)00113-0.

Scott Smith, B.H., Nowicki, T.E., Russell, J.K., Webb, K.J., Hetman, C.M., Harder, M., and Mitchell, R.H., 2008, Kimberlites : Descriptive Geological Nomenclature and Classification: Journal of Volcanology and Geothermal Research, p. 1–3.

Shchukina, E. V., Agashev, A.M., Kostrovitsky, S.I., and Pokhilenko, N.P., 2015, Metasomatic processes in the lithospheric mantle beneath the V. Grib kimberlite pipe (Arkhangelsk diamondiferous province, Russia): Russian Geology and Geophysics, v. 56, p. 1701–1716, doi: 10.1016/j.rgg.2015.11.004.

Shchukina, E. V., Agashev, A.M., and Pokhilenko, N.P., 2017, Metasomatic origin of garnet xenocrysts from the V. Grib kimberlite pipe, Arkhangelsk region, NW Russia: Geoscience Frontiers, v. 8, p. 641–651, doi: 10.1016/j.gsf.2016.08.005.

Silva, S., 2008, Petrografia e química mineral das intrusões Indaiá I e Indaiá II, oeste do estado de Minas Gerais [Dissertação de Mestrado]: São Paulo, Universidade de São Paulo, Instituto de Geociências, 113 p.

Skinner, E.M.W., and Clement, C.R., 1979, Mineralogical classification of Southern

African kimberlites: Proceedings of the Second International Kimberlite Conference, v. 15, p. 129–139, doi: 10.1029/SP015p0129.

Skinner, E.M.W., and Marsh, J.S., 2004, Distinct kimberlite pipe classes with contrasting eruption processes: Lithos, v. 76, p. 183–200, doi: 10.1016/j.lithos.2004.03.044.

Skinner, E.M.W., 2008, The emplacement of class 1 kimberlites. J. Volcanol. Geotherm. Res. 174, 40–48. https://doi.org/10.1016/j.jvolgeores.2007.12.022

Smith, C.B., 1983, Pb, Sr and Nd isotopic evidence for sources of African cretaceous kimberlites: Nature, v. 304, p. 51–54.

Skinner, E.M.W., 2008, The emplacement of class 1 kimberlites: Journal of Volcanology and Geothermal Research, v. 174, p. 40–48, doi: 10.1016/j.jvolgeores.2007.12.022.

Smith, C.B., 1983, Pb, Sr and Nd isotopic evidence for sources of African cretaceous kimberlites: Nature, v. 304, p. 51–54.

Sokol, A.G., Kruk, A.N., Chebotarev, D.A., Palyanov, Y.N., 2016, Carbonatite melt-peridotite interaction at 5.5–7.0 GPa: implications for metasomatism in lithospheric mantle: Lithos, p. 248–251, doi.org/10.1016/j.lithos.2016.01.013.

Solov'eva, L. V., Lavrent'ev, Y.G., Egorov, K.N., Kostrovitskii, S.I., Korolyuk, V.N., and Suvorova, L.F., 2008, The genetic relationship of the deformed peridotites and garnet megacrysts from kimberlites with asthenospheric melts: Russian Geology and Geophysics, v. 49, p. 207–224, doi: 10.1016/j.rgg.2007.09.008.

Sparks, R.S.J., Baker, L., Brown, R.J., Field, M., Schumacher, J., Stripp, G., and Walters, A., 2006, Dynamical constraints on kimberlite volcanism: Journal of Volcanology and Geothermal Research, v. 155, p. 18–48, doi: 10.1016/j.jvolgeores.2006.02.010.

Sparks, R.S.J., Brown, R.J., Field, M., and Gilbertson, M., 2007, Kimberlite ascent and eruption: Nature, v. 450, p. 6435–6436, doi: 10.1038/nature06435.

Sparks, R.S.F., 2013, Kimberlite Volcanism: Annual Review of Earth and Planetary Sciences, v. 41, p. 497–528.

Svisero, D.P., Meyer, H.O.A., Haralyi, N.L.E., Hasui, Y., 1984, A note on the geology of some Brazilian kimberlites. J. Geol., v. 92, p. 331-338.

Svisero, D.P., Haralyi, N.L.E., 1984, O kimberlito Indaiá, Monte Carmelo, MG: Anais 33° Congresso Brasileiro de Geologia, 10: 5014 – 5026.

Svisero, D.P., 1995, Distribution and origin of diamonds in Brazil: an overview: Journal of Geodynamics, v. 20, p. 493-514.

Thomaz, L.V., 2009, Estudo petrográfico e química mineral da intrusão kimberlítica Régis, no oeste de Minas Gerais [Dissertação de Mestrado]: São Paulo, Universidade de São Paulo, Instituto de Geociências, 143 p.

Ulbrich, H. H. G. J., Gomes, C. B., 1981, Alkaline rocks from continental Brazil: Earth-Science Reviews, v. 17, p. 135-154.

VanDecar, J.C., James, D.E., and Assumpção, M., 1995, Seismic evidence for a fossil mantle plume beneath south america and implications for plate driving forces: Nature, v. 378, p. 25–31, doi: 10.1038/378025a0.

Viljoen, K.S., Harris, J.W., Ivanic, T., Richardson, S.H., and Gray, K., 2014, Trace element chemistry of peridotitic garnets in diamonds from the Premier (Cullinan) and Finsch kimberlites, South Africa: Contrasting styles of mantle metasomatism: Lithos, v. 208, p. 1–15, doi: 10.1016/j.lithos.2014.08.010.

Walters, A.L., Phillips, J.C., Brown, R.J., Field, M., Gernon, T., Stripp, G., and Sparks, R.S.J., 2006, The role of fluidisation in the formation of volcaniclastic kimberlite: Grain size observations and experimental investigation: Journal of Volcanology and Geothermal Research, v. 155, p. 119–137, doi: 10.1016/j.jvolgeores.2006.02.005.

Wanderson, K., 2016, Química de minerais indicadores de intrusões kimberlíticas com ênfase na Província Diamantífera Serra da Canastra (MG): importância na prospecção de intrusões férteis [Dissertação de Mestrado]: Belo Horizonte, Universidade Federal de Minas Gerais, 156 p.

Webb, K.J., 2006, Juvenile Clasts in Kimberlites : Standardized Comprehensive Description Towards Unravelling Emplacement Mechanisms: Proceedings of the Kimberlite Emplacement Workshop Long Abstract, p. 1-5.

Wilson, L., Head III, J.W., 2007, An integrated model of kimberlite ascent and eruption: Nature, v. 447, p. 53–57, doi: 10.1038/nature05692.

Woodhead, J., Hergt, J., Phillips, D., and Paton, C., 2009, African kimberlites revisited: In situ Sr-isotope analysis of groundmass perovskite: Lithos, v. 112, p. 311–317, doi: 10.1016/j.lithos.2009.03.031.

Woolley, A.R., Bergman, S.C., Edgar, A.D., Le Bas, M.J., Mitchell, R.H., Rock, N.M.S., and Scott Smith, B.H., 1996, Classification of lamprophyres, lamproites, kimberlites, and the kalsilitic, melilitic, and leucitic rocks: Canadian Mineralogist, v. 34, p. 175–186.

Wyatt, B.A., Baumgartner, M., Anckar, E., Grutter, H., 2004, Compositional classification of ‘‘kimberlitic’’ and ‘‘non-kimberlitic’’ ilmenite. Lithos, v. 77, p. 819–840, doi: 10.1016/j.lithos.2004.04.025.

APÊNDICE 1 – Kimberlito Charneca

Major and Trace Element Compositions of mineral constituents from the Charneca diamondiferous kimberlite, West of Minas Gerais, Brazil

Summary

1. Introduction

Preliminary studies allowed the recognition of two main subgroups of diamond-bearing rocks in southern Africa: the basaltic (mica-poor) and the lamprophyric (mica-rich) kimberlites (Wagner, 1914). Based on olivine, phlogopite and calcite content, Mitchell (1970) further classified kimberlites into three categories: kimberlites (equivalent to basaltic kimberlites), micaceous kimberlites (equivalent to "lamprophyric") and calcitic kimberlites (after calcite having been recognized as a primary mineral). According to their petrographic and geochemical differences, kimberlites have been classified into two groups, I and II (Smith, 1983; Becker and Le Roex, 2006), the latter not actually corresponding to kimberlites, hence their suggested renaming to ‘‘orangeite’’ in recognition of their distinct character (Mitchell & Bergman 1991, Mitchell 1995). Pipe intrusion shape is also a classification criterion (eg. the typical African kimberlite pipe consists of three morphological zones: crater, diatreme, and root). Important contributions are due to the discovery and study of lamproites and kimberlites in Australia and Canada, respectively.

Circa a hundred kimberlite intrusions and correlated rocks are known in Brazil, most of them along the Alto Paranaíba Igneous Province (APIP, Minas Gerais State). The intrusions resulted from mafic-alkalic magmatism events that took place along a NW-SE lineament in Late Cretaceous (Gibson et al., 1995). The Alto Paranaíba Igneous Province intrudes the Brasília Belt basement. It also intrudes and overlies basalts and sedimentary rocks from the northern border of the Paraná Basin (Araújo et al., 2001; Junqueira-Brod et al., 2005; Carlson et al., 2007). Hundreds of sterile or non-economic kimberlite intrusions were discovered in the State of Minas Gerais over the last half century, mainly near Coromandel City (Karfunkel et al., 2014). The production of diamonds in these regions is mainly from alluvial sources, and their origin is still a topic of discussion (Karfunkel et al., 2014; Pereira et al., 2017; Pereira and Rogério, 2007; Svisero, 1995).

Systematic petrographical-geochemical-geochronological studies of many kimberlite intrusions in Coromandel area were performed by Andrade and Chaves (2011), Chaves (2012), Guarino et al. (2013), Karfunkel et al. (2014), Melluso et al. (2008), Nannini (2011), Pereira et al. (2017), Silva (2008), Svisero (1995) and Tompkins and Gonzaga (1989).

This study presents the first petrographic and mineralogical geochemistry characterization of the Charneca kimberlite, a diamondiferous kimberlite intrusion located in

the homonym region. The kimberlite body is located to the SE of Coromandel city, Minas Gerais (Fig. 1). Currently, diamonds are extracted from the highly weathered rock, whose mineralogy and geochemistry are favorable for diamond preservation. This work aim is to contribute to the textural characterization, mineral chemistry and petrogenesis of Brazilian kimberlites, from the APIP context, as well as to compare their favorable characteristics for diamond preservation to nearby sterile kimberlitic occurrences.

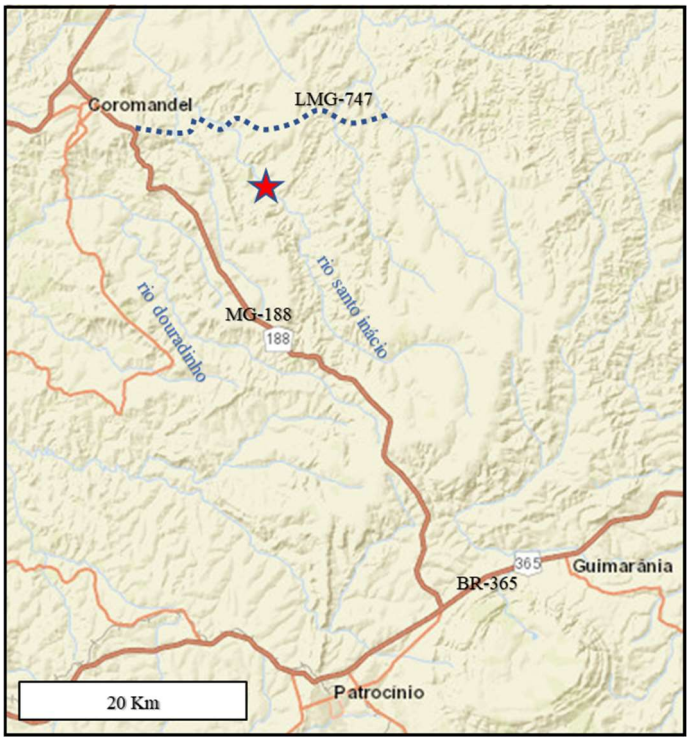

Fig. 1. Location map of the Charneca kimberlite (red star) near Coromandel and Patrocínio.

2. Geology and geological setting of the Charneca kimberlite

The Alto Paranaíba Igneous Province (APIP) encompasses several alkaline-carbonatite plutonic complexes, kamafugites, kimberlites and rare lamproites (Almeida, 1983; Almeida and Svisero, 1991; Araújo et al., 2001; Brod et al., 2004; Comin-Chiaramonti et al., 2005; Gibson et al., 1995; Guarino et al., 2013b; Hayman et al., 2008; Junqueira-Brod et al., 2005; Leonardos et al., 1991; Melluso et al., 2008). The province established along an elongated NW–SE structure called the Alto Paranaíba Arc. The alkaline magmas were emplaced into Precambrian

rocks from internal and external zones of the Brasília Fold Belt (Almeida, 1967; Araújo et al., 2001; Schobbenhaus and Neves, 2003).

The main sedimentary units of the Brasilia Fold Belt are, from base to top: the Canastra, Paranoá e Vazante groups (Meso/Neoproterozoic); felsic and mafic granulites and orthogneisses, the Araxá Group, the Ibiá Formation and the Bambuí Group (Neoproterozoic). The Canastra and Vazante groups and the Ibiá Formation constitute a complex system of nappes that thrust over the sedimentary rocks of the Bambuí Group to the east (Dardenne, 2000). The Charneca kimberlite emplaced itself into the Vazante Group, which corresponds to a narrow area with N-S direction. The contact zone with the Canastra and Bambuí groups consists of phyllites, slates, quartzites, metassiltites, rare limestones and abundant dolomites (Madalosso and Valle, 1978; Marini et al., 1984b; Pinho, 1990; Nogueira, 1993; Dardenne et al., 1997; Souza, 1997; Dardenne, 2000).

The metasedimentary rocks cover an area of approximately 250 km along a 25–30 km wide N-S-striking region (Fig. 2). These rocks were affected by a lower greenschist facies metamorphism and at least three deformation events (Monteiro et al., 2006; Dardenne, 2000; Slezak et al., 2014).

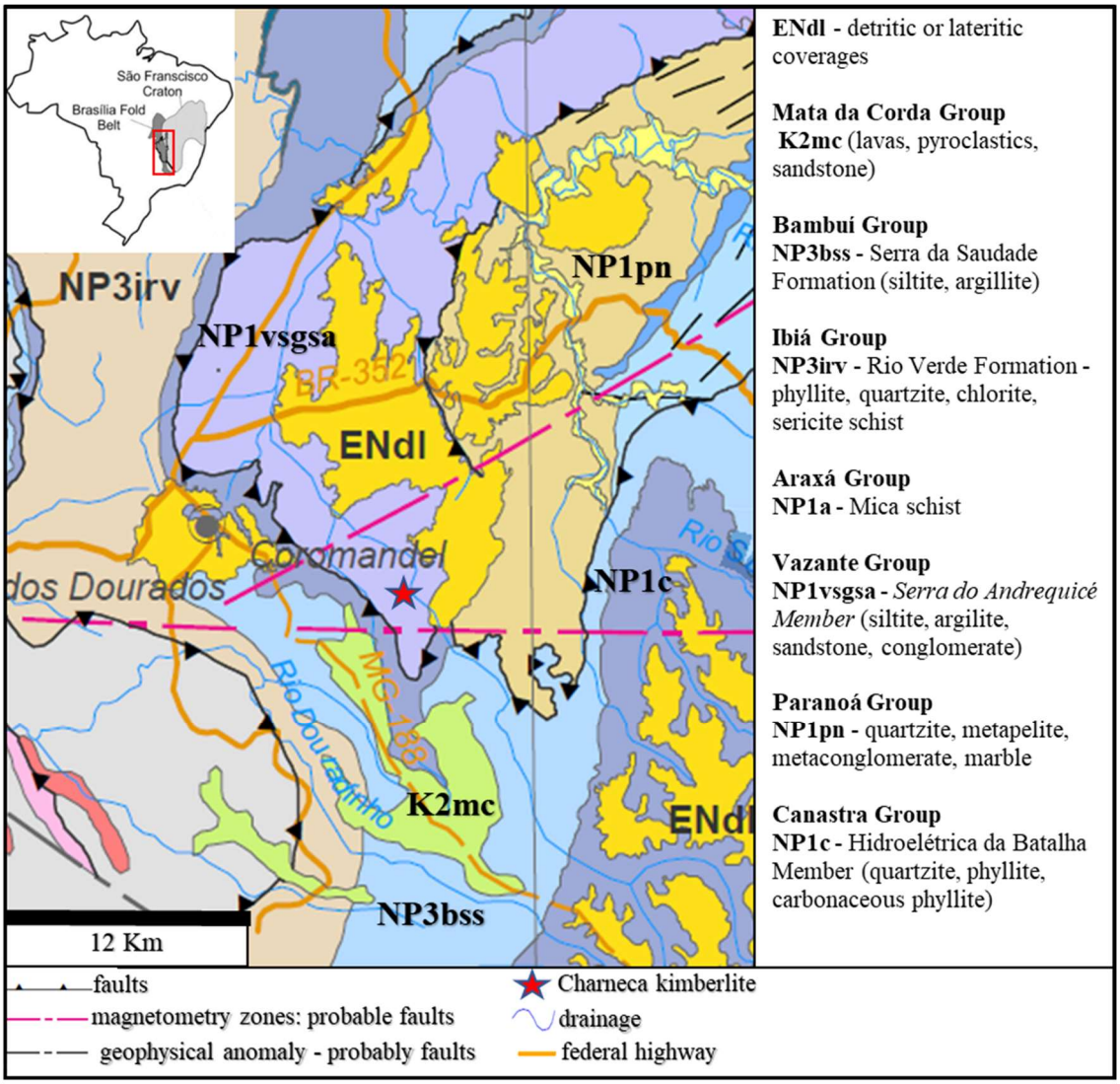

Fig. 2. Geological and geotectonic setting of the Charneca kimberlite (red star). Modified from CPRM, 2014.

3. Petrography

The Charneca kimberlite has juvenile components, which includes pseudo-olivines, juvenile clasts and rare country rocks. It shows a matrix-supported, moderately to poorly sorted inequigranular texture. Coarse ash- to medium-lapilli-sized juvenile fragments and accessory clasts of country and mantle xenoliths are set in an interstitial medium dominated by serpentine, phlogopite, carbonates and opaque minerals (Fig. 3).

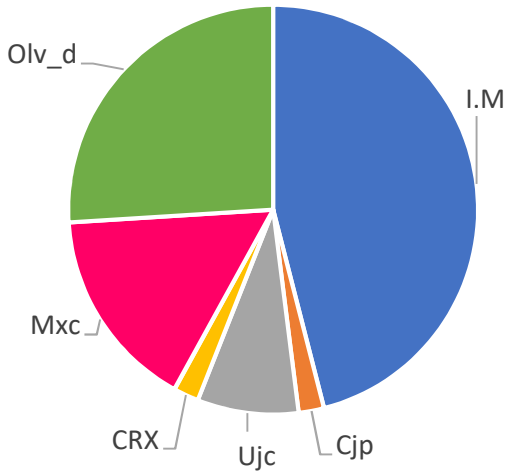

Fig. 3 – Estimated average composition of the Charneca kimberlite. Olv_d = discrete olivine macrocrysts. Cjp = cored juvenile pelletal ash-lapilli. Ujc = uncored juvenile clasts. Mxc = mantle-derived xenocrysts (eg. phlogopite and garnet). CRX = country rock xenoliths. IM = interstitial medium. All olivine crystals are pseudomorphs.

The high intensity of alteration can obscure the original sorting and texture of the Charneca kimberlite determined from thin section observation. In general, grain size ranges from ash to medium lapilli and scarcely country-rocks. Poorly sorted framework grains are dispersed in a finer-grained alteration interstitial medium dominated by serpentine, xenocrysts and optically irresolvable oriented phyllosilicates, resulting in matrix-supported texture (Fig. 4).

Juvenile clasts are rare and range from ash to lapilli size and occur in several shapes, controlled by core size and shape, with frequent mainly olivine, and by the dynamics of emplacement. Single and multiple, symmetrical and asymmetric, complete and incomplete rims are observed, ranging from ash to lapilli size, with variable shapes with angular to amoeboid margins, reflecting different deformation levels.

3.1 Texture

The Charneca kimberlite shows a very poorly sorted matrix-supported texture, with few clast-clast contacts. In thin section, medium to coarse ash-sized crystals and juvenile clasts are supported by an interstitial medium dominated by serpentine and opaque minerals (Fig. 4).

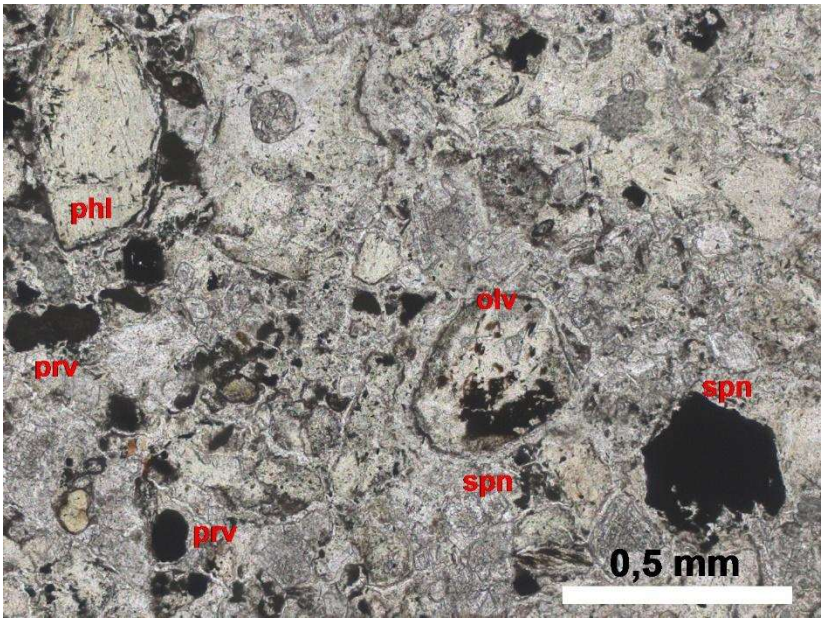

Fig. 4 – Matrix-supported texture of Charneca kimberlite. Olivine pseudomorph (olv), altered phlogopite (phl), spinel (spn) and perovskites (prv) immersed in a serpentinized interstitial medium.

3.2 Interstitial medium

The interstitial medium of the Charneca kimberlite consists of irregular patches of pale-brown clay, cryptocrystalline phyllosilicate minerals with cloudy aspect and yellowish color. Locally, acicular microlites of diopside were observed (Fig. 5). In samples, the alteration intensity is high, resulting in pale brown speckled serpentine + clay with phyllosilicates showing orientation.

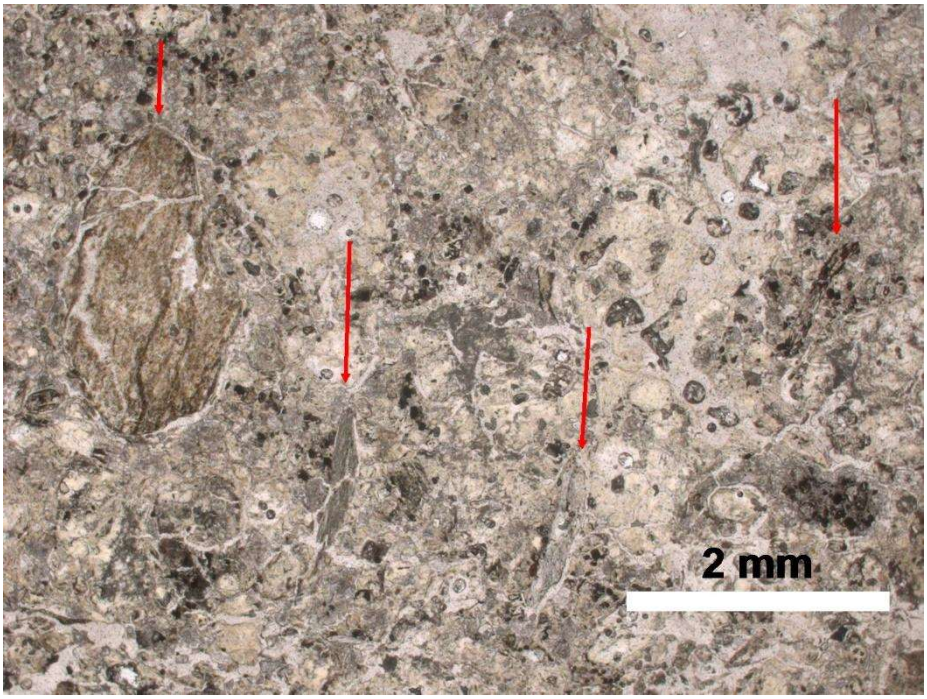

Fig. 5. Interstitial medium of the Charneca Kimberlite. Arrows indicate oriented phlogopite crystals.

3.3 Juvenile clasts

Clasts of magma form in vents during explosive eruptions. The term “juvenile” refers to solidified material, in this case a volcanic rock clast preserved in deposits (Cas et al., 2008). In volcanological nomenclature, juvenile pyroclasts are generated from disruption as a direct result of volcanic action (Schmid, 1981). However, in kimberlites the term can be either magmatic or clastic, ‘juvenile clast’ being used loosely for juvenile pyroclasts and juvenile pseudo-clasts (produced by alteration and replacement processes). The term excludes discrete (free) crystals and xenoliths (Webb, 2006). As introduced by Field and Smith (1998), juvenile magma clast is a non-genetic term that encompasses all juvenile clasts and discrete cognate crystals.

In order to discriminate among the different constituents of the Charneca kimberlite, the approach of Cas et al., (2008) was taken. For the description and characterization of juvenile clasts, the non-genetic scheme of Webb (2006) was used, as summarized in tables 1 and 2.

3.3.1 Kimberlite lithic clasts

The term kimberlite lithic clast refers to co-magmatic kimberlite that solidified deeper in the vent and was then incorporate (Cas et al., 2008). Seven types of kimberlitic clasts are present in the Charneca kimberlite that differ in modal abundance, shape and frequency (Fig. 6 and 7). Table 1 summarizes the characteristics of each type of clast.

Type A clasts have diffuse margins and are characterized by subequant shape, rounded, sub-irregular, non-vesicular outlines. They are composed of moderately abundant subhedral to anhedral pseudo-olivine phenocrysts (12%), with very low abundance of phlogopite and perovskite microcrystals (<1%) and 5 % of spinels microcrystals less than 0.02mm wide, set in a very poorly crystallized serpentine interstitial medium with octahedrons red micro-spinels and scattered altered opaque minerals.

Type B clasts have diffuse margins, sub-elongate shape, rounded or smoothly curved, non-vesicular outlines. They are characterized by the low abundance of olivine (2%) phenocrysts, spinel (5%) and perovskite (<1%) microcrystals set in a very poorly crystallized, green interstitial medium with calcite crystals and spinels microlites. Olivine pseudo-pelletal ash (0.54 mm) with red alteration rim.

Subequant, sub-angular, irregular curvilinear and non-vesicular Type C juvenile clasts have defined margins, are composed of moderately abundant olivine and spinel phenocrysts (10%) and perovskite microlites (8%) set in a very poorly crystallized interstitial medium with speckled altered orange-brown phlogopite crystals.

Type D juvenile clasts are composed of moderately abundance of sub-anhedral pseudo-olivine phenocrysts (10%) with low abundance of perovskite (<1%) and spinel (3%). Speckled phlogopite and opaque minerals are dispersed in a very poorly crystallized brown interstitial medium. Elongate and sub-irregular non-vesicular shapes are present, with irregular curvilinear outlines.

Type E clasts have defined margins, equant shapes, well-rounded, smoothly curved outlines. They are non-vesicular, composed of low perovskite microcrystals (1%) and moderate spinel (10%). Crystals set in a very poorly crystallized mass of octahedral spinel microcrysts, speckled phlogopite and serpentine interstitial medium.

Type F clasts are composed of single pseudo-olivine phenocrysts (10-15%) that varies from 0.15 to 0.63mm, low abundance of spinel (3%) and no rare this mineral occurs with perovskite edges. Crystals are set in a very poorly crystallized, red octahedrons spinels, altered opaque minerals serpentine interstitial medium.

Subequant, sub-rounded, sub-irregular outlines, non-vesicular and diffuse margins characterize Type G clasts. They are composed of moderately abundant (13%) olivine. Three single 0.03, 0.04 and 0.09 mm red spinel crystals occur, set in a very poorly crystallized spinel phlogopite brown interstitial medium.

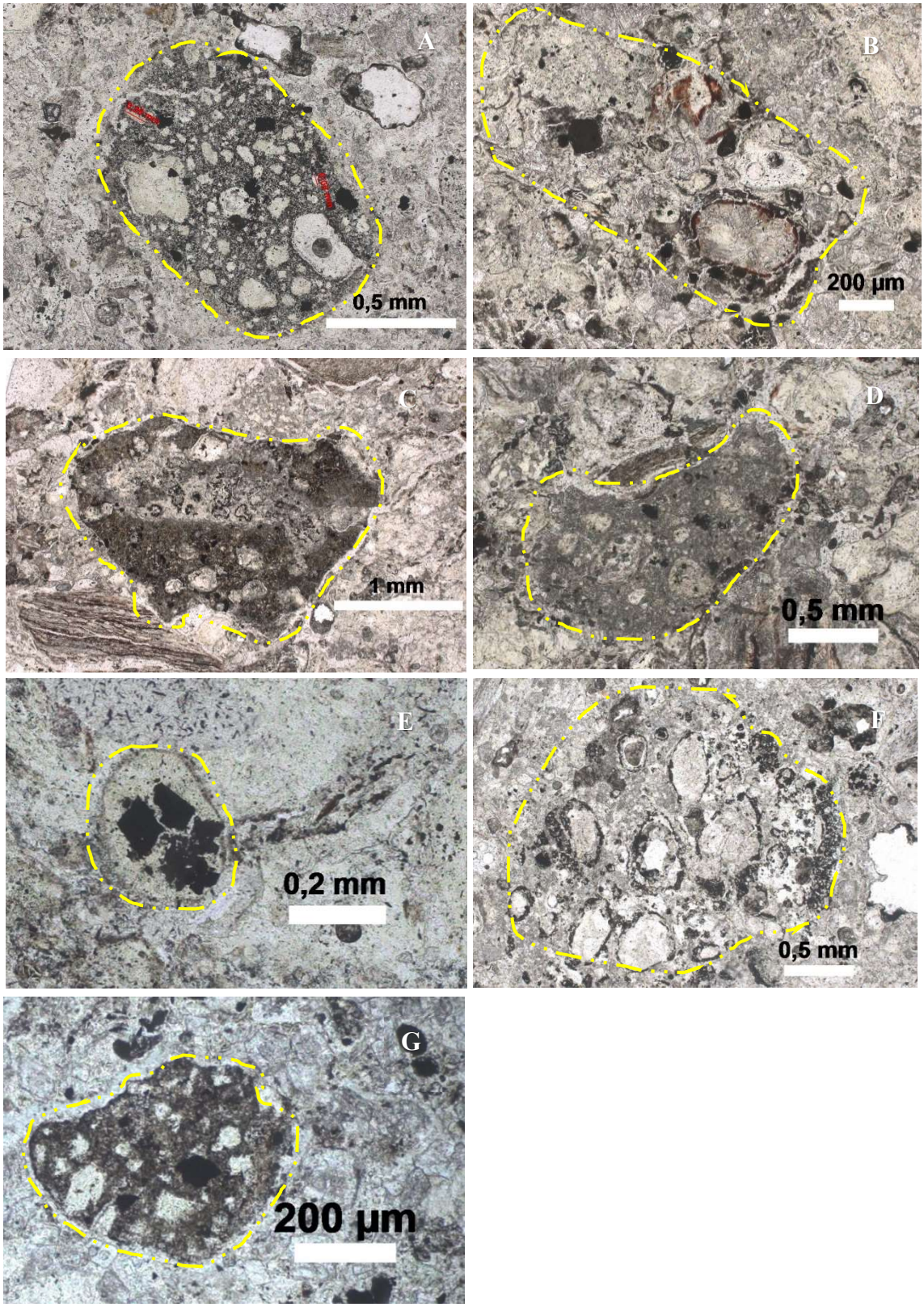

Fig. 6. Seven types of uncored juvenile clasts (A to G) of the Charneca kimberlite, distinguished based on relative modal mineral abundance and shapes. Yellow lines delimit clast edges that are diffuse due high alteration degree.

Table 1 Petrographic characteristics summary of uncored juvenile clasts of the Charneca kimberlite.

	MORPHOLOGY	VESICULARITY	CLAST-HOST RELATIONSHIP	MINERALOGY	INTERSTITIAL MEDIUM CRYSTALLINITY	SIZE RANGE
A	SbQ /R / SbI	Non-vesicular.	Diffuse margins clast set in a undefined gray interstitial medium with carbonate, serpentine and clay.	Pseudo-olivine: moderate (12%), sub-anhedral, micro to medium (0.05-0.32mm). Phlogopite: low (< 1%), subhedral, micro to fine crystals (0.05 - 0.09mm). Perovskite: low (< 1%), subhedral, fine crystals (<0.07 mm). Spinel: low (5%), sub-anhedral, microcrystals (<0.02mm).	Very poorly crystallized, red octahedrons microspinels and altered opaque minerals occurs scattered in the serpentine interstitial medium.	Ash to lapilli (1.0 - 2.0mm)
B	SbQ / R / Sc	Non-vesicular.	Diffuse margins clast set in a undefined gray interstitial medium with carbonate, serpentine and clay.	Pseudo-olivine: low(2%), subhedral, microcrystals (< 0.34mm). Perovskite: low (3%), sub-euhedral, microcrystals (0.05-0.14mm). Spinels: low (5%), sub-euedral, microcrystals (<0.06). Olivine pseudo-pelletal ash (0.54mm) with red alteration rim.	Very poorly crystallized, green interstitial medium with calcite crystals and spinels microlites.	Ash to lapilli (1.40 - 2.0mm)
C	SbQ / SbA / Ic	Non-vesicular.	Defined margins clast set in a cement.	Pseudo-olivine: moderate (10%), sub-anhedral, fine crystals (0.09 - 0.31mm). Perovskite: low (8%), sub-anhedral, microlites (<0.06mm). Spinel: moderate (10%), sub-anhedral, microlites.	Poorly crystallized interstitial medium with speckled altered orange-brown phlogopite crystals.	Lapilli (2.10 - 2.9mm)
D	El/ SbR / Ic	Non-vesicular.	Defined margins clast set in a yellow-green cement with calcite crystals.	Pseudo-olivine: moderate (10%), sub-anhedral, fine - medium (0.10-0.36mm). Perovskite: low (<1%), sub-anhedral, microcrystals. Spinel: low (3%), anhedral, micro - fine crystals (<0.12mm).	Very poorly crystallized brown interstitial medium with speckled phlogopite and opaque minerals.	Ash (1.0 - 1.5mm)
E	Eq / Wr / Sc	Non-vesicular.	Defined margins clast set in a yellow-green cement with calcite crystals.	Perovskite: low (1%), subhedral, microcrystals. Spinel: moderate (10%), euedral, micro - fine crystals (<0.10).	Very poorly crystallized, octahedrons microspinel, splecked phlogopite and serpentine interstitial medium.	Ash (0.3 - 0.6mm)
F	Eq-SbQ / Wr / Sc	Non-vesicular.	Defined margins clast set in a yellow-green cement with calcite crystals.	Pseudo-olivine: moderate (10-15%), subhedral, medium - coarse crystals (0.15 - 0.63mm). Alterated spinel with perovskite edges: low (8%), anhedral, microcrystals. (<0.06mm).Spinel: low (3%), euhedral, fine microcrystals (<0.06mm).	Very poorly crystallized, red octahedrons microspinels and altered opaque minerals occurs scattered in the serpentine interstitial medium.	Lapilli (2.0 - 2.8mm)
G	SbQ / SbR / SbI	Non-vesicular.	Diffuse margins clast set in a yellow-green cement with calcite crystals.	Pseudo-olivine: moderate (13%), sub - anhedral, fine crystals (< 0.10mm). Red spinel: low (1%), 3 single crystals, microcrystals (0.03mm, 0.04mm, 0.09mm).	Very poorly crystallized, spinels phlogopite brown interstitial medium.	Ash (0.5 - 1.8mm)

Sphericity: Elongate (El); Subelongate (SbE); Subequant (SbQ); Equant (Eq).

Roundness: Well-rounded (Wr); Rounded (R); Sub-rounded (SbR); Sub-angular (SbA); Angular (Ang).

Irregularity: Smoothly curved (Sc); Subirregular (SbI); Irregular curvilinear (Ic); Irregular ameboid (Ia).

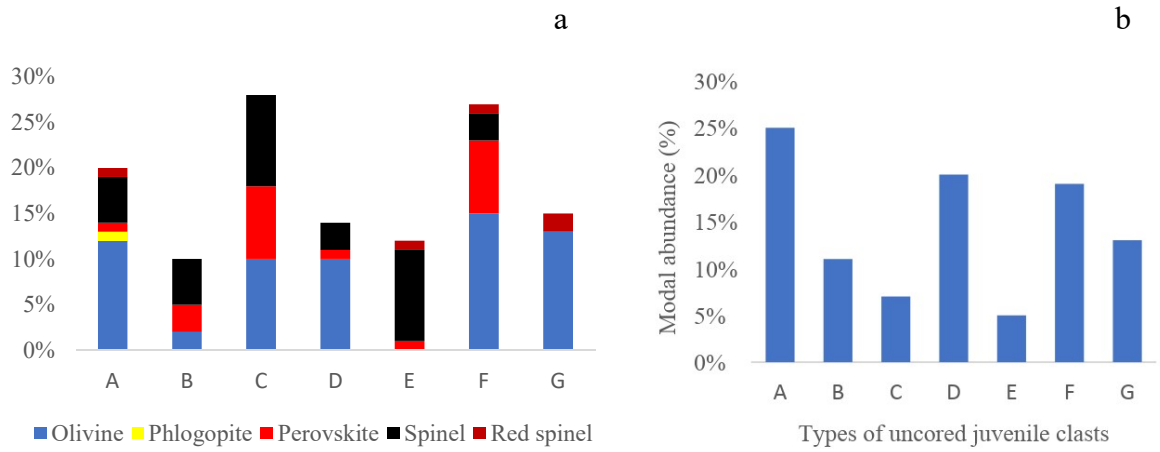

Fig. 7. Composition (a) and estimated abundance b) of uncored juvenile clasts of the Charneca kimberlite.

3.3.2 Pelletal structures

Pelletal structures encompasses all round to elliptical juvenile clasts of ash, lapilli or bomb size, composed kimberlitic material in varied degrees of crystallization, with core. Crystal shells may or not display flow orientation. When clasts or crystals have alteration rinds, they are called pseudo- pelletal lapilli (Cas et al., 2008). Pelletal or ash lapilli represent the interface between volatile components and the erupting magma (Lloyd and Stoppa, 2003).

A predominance of two types of cored juvenile pelletal ash / lapilli is observed in the Charneca kimberlite, with symmetrical and asymmetrical cores composed usually by euhedral to subhedral olivine crystals totally replaced by usually deformed serpentine and phlogopite crystals. Only a single rim was observed, maybe due to the high alteration degree (Fig. 8).

Type 1 has diffuse margins and is subequant, rounded, sub-irregular, non-vesicular and cored by deformed phlogopite. A single, asymmetrical, complete ultra-thin to very thin micro-rim is composed of oriented spinel (dark red, euhedral) crystals surrounding phlogopite crystals in a poorly-crystallized phlogopite (and / or ilmenites) interstitial medium.

Type 2 has subequant shape, rounded and smoothly curved outlines, diffuse margins and is non-vesicular. A single, symmetrical, complete, ultra-thin rim mimic the shape of the pseudo-olivine core and comprise microcrystals of perovskite (3%), olivine (4%) and spinel (5%) set in a carbonate, opaque minerals, speckled yellow-brown interstitial medium.

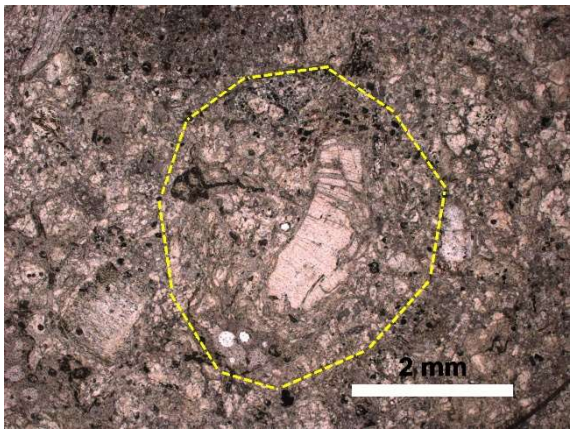

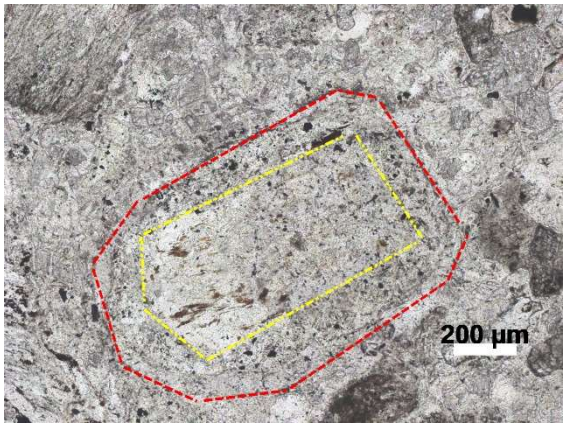

Fig. 8. Types of cored juvenile clasts of the Charneca kimberlite. Most common are deformed phlogopite cores. The shape of the pelletals follows shape of the nucleus.

3.4 Accessory lithic clast (country rocks)

In the Charneca kimberlite, rock fragments of crustal origin are mainly quartzites and dolomites (2%). These lithic fragments occur in elongate shapes, with angular to rounded outlines with ash to lapilli size.

4. Mineral Chemistry

4.1 Garnet

Pyrope-almandine is the predominant end-member (~69.82% and ~17.59%, respectively) in the Charneca kimberlite (Table 3). Peridotite-lherzolite is the main source, followed by a Cr-poor megacryst suite, as in Schulze (2003) and Grütter et al., (2004) classifications. The Charneca peridotitic garnets are characterized by low Cr_2O_3 and TiO_2 content (1.47 to 2.06 wt.% and 0.20 to 0.41 wt.%, respectively), moderate CaO and FeO content (3.95 to 4.52 wt.% and 8.53 to 9.80 wt.%, respectively) and a high amount of MgO (19.18 to 19.93 wt.%). While garnet megacrysts exhibit similar Cr_2O_3 values (0.40 to 2.82 wt.%, except for a single grain with Cr < 1%), slightly higher values of CaO and FeO (4.64 to 5.14 wt.%, 7.67 to 11.13%) and higher TiO_2 (0.98 to 1.31 wt.%) as compared to the lherzolitic source. A positive Ca-Cr correlation is observed. Because of the similar Cr_2O_3 amount in all analyzed

grains, the higher TiO_2 content (>0.5 wt.%) made it possible to distinguish between both sources.

According to the G-number nomenclature in the classification of Grütter et al., (2004), the Charneca lherzolitic and Cr-poor megacryst garnet suites correspond to G9 and G1, respectively. They are plotted in the CaO vs Cr graphic (Fig. 9B). Notice that lherzolite source garnet falls within the G5 area, this occurs due overlapping of G5 and G9 fields (separated only by Cr_2O_3 content) disregarding MGNUM limit (where MGNUM = (MgO/40.3)/(MgO/40.3 + FeO_t/ 71.85) [oxides in wt.%]). According Grütter et al., (2004), this may result in misunderstandings; therefore, we isolate these fields for correct classification and better separation of G5 and G9 garnets, thus, a MGNUM x Cr_2O_3 graphic was made demonstrating a better visualization of these fields. We recommend using the CaO vs Cr_2O_3 graph of Grütter et al., (2004) first, and after certifying that the garnets belong to one of these classifications, use the additional graphic as exemplified in this work (Fig 9B) to avoid misunderstandings.

Figures 9 (D,E) compare data on Charneca kimberlite megacryst garnet to datasets presented by Grütter et al., (2004). Cr-poor megacryst garnet shows only a small Ca/(Ca +Mg + Fe) and Mg/(Mg + Fe) range, unlike the large one exhibited by eclogite garnet (Fig. 9 D). A small overlap is observed, and a distinction between both groups is clear at 0.5 wt.% TiO_2, as illustrated in Fig. 9 C. Eclogite garnet with TiO_2 > 0.5 wt.% are recorded in Kaalvallei kimberlite (Viljoen, 1994), which would cause them to be misidentified for Cr-poor megacryst garnet. However, only 2% of the eclogites overlap garnet from the Cr-poor megacryst suite (Grütter et al., 2004).

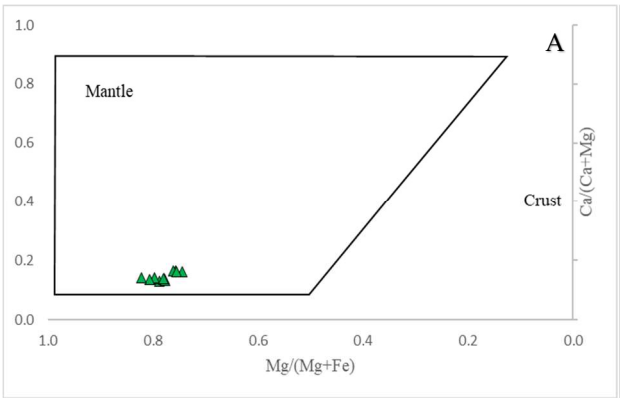

C

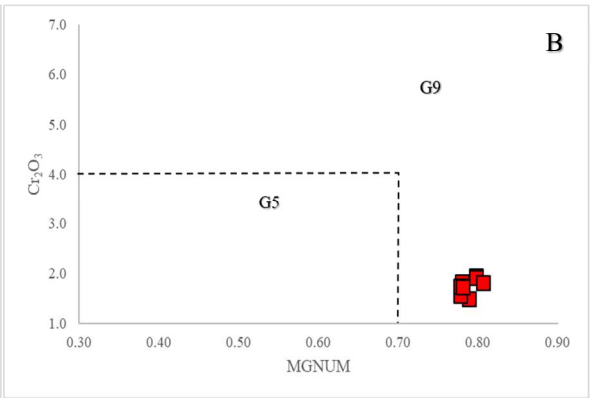

D

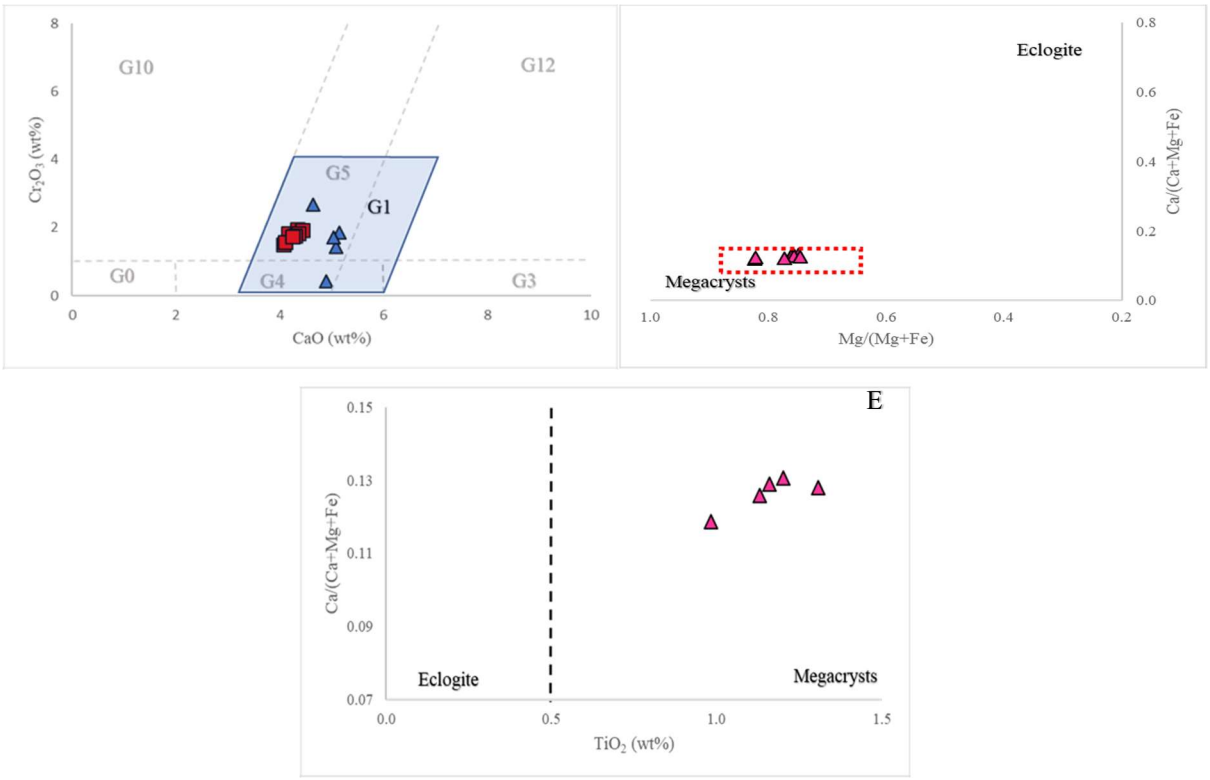

Fig. 9. Chemical characteristics of garnet crystals from the Charneca kimberlite; (a) Mantle-derived *vs.* Charneca kimberlite garnet in terms of Mg/(Mg+Fe) and Ca/(Ca+Mg), after Schulze (2003); (b) Cr_2O_3 vs. MGNUM diagram of Charneca kimberlite garnet, with overlapping G9 and G5 fields, after Grütter et al., (2004); (c) CaO vs Cr_2O_3 diagram to separat pyroxenitic (G5) from lherzolitic garnet (G9); (d) Charneca Cr-poor garnet megacrysts plot on a Mg/(Mg+ Fe) vs Ca/(Ca+Mg +Fe) Schulze (2003) diagram for discriminating between Cr-poor megacryst suite garnet and eclogitic source ones. Solid lines correspond to overlapping of eclogite garnet and Cr-poor megacrysts; dashed line corresponds to a Cr-poor megacryst dataset studied by Schulze (2003); (e) TiO_2 vs. Ca/(Ca+Mg+Fe) variation Schulze (2003) plot of Charneca kimberlite garnet.

Peridotitic-lherzolitic garnet occur as large grains (up to 1 cm) and range in Sr from 0.02 to 0.05 ppm, in Y from 13.83 to 17.78 ppm, in Zr from 9.92 to 16.6 ppm, In Ba from 0 to 0.04 ppm, in Hf from 0.20 to 0.04 ppm, in Ni from 29 to 37.81 ppm, in Zn from 14.22 to 12.72 ppm, and in Ga from 10.29 to 12.72 ppm. Cr-poor megacryst garnet occur as minor grains (~50 um) and range in Sr from 1.13 to 2.42 ppm, in Y from 19.33 to 33.93 ppm, in Zr from 70.16 to 161.35 ppm, in Ba from 0 to 7.62 ppm, in Hf from 1.78 to 4.65 ppm, in Ni from 43.43 to 141.11 ppm, in Zn from 26.43 to 38.54 ppm, and in Ga from 12.33 to 28.67 ppm (Table 4).

The Cr-poor megacryst suite exhibits a higher REE_N concentration than lherzolitic garnet (N denotes normalization to the chondrite composition of Boynton 1984) Shapes correspond to “flat” and “normal” patterns, respectively, following the terminology of Banas et al., (2009) and Viljoen et al., (2014). A “flat” pattern is characterized by positive $LREE_N$ slopes

from La to Eu (Fig. 10A). Slightly positive slopes mark a sinusoidal pattern for Gd. From $MREE_N$ to $HREE_N$, an overall flat slope is seen. The “normal” pattern is humped from La to Eu, which denotes $LREE_N$ enrichment. Flat slopes in $HREE_N$ are similar to that of Cr-poor megacryst suite one. Lherzolitic garnet grains present a lower concentration of incompatible trace elements than the Cr-poor megacryst suite. Negative slope trends are similar for Sr, Nb and Th, as are Zr, Hf, Pb and U peaks. Both groups differ in Cs and Rb, which are absent in the peridotitic material, and in in the concentration of Ba, which is lower in the Cr-poor megacryst suite (Fig. 10B).

REE_N and incompatible trace element patterns of Charneca kimberlite garnet grains are similar to lherzolitic ones that occur as inclusions in diamonds from the Premier and Finsch diamondiferous kimberlite bodies (Viljoen et al., 2014), which are characterized by flat, normal and sinuous patterns, with a Zr and Y decrease where patterns become flat. Great similarities are also observed with megacryst and lherzolitic garnet grains (Lz2) from the V. Grib kimberlite pipe deposit in the Arkhangelsk diamondiferous province (Shchukina et al., 2015).

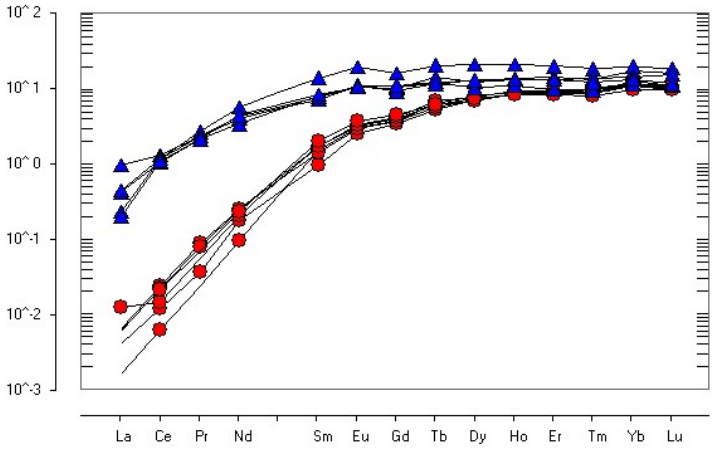

(A)

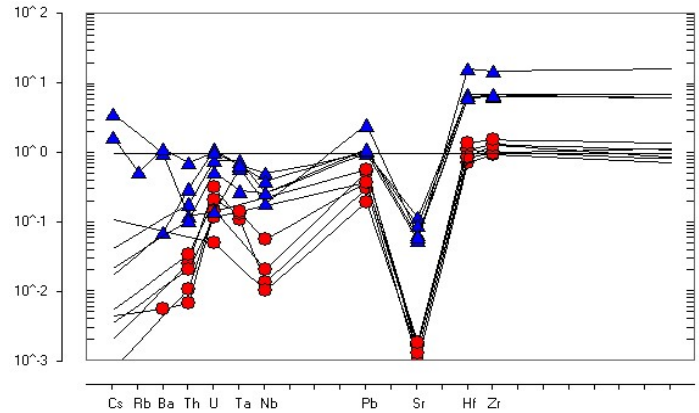

(B)

Fig. 10. A) Chondrite-normalised REE patterns (Boynton 1984), and (B) primitive mantle-normalized incompatible element pattern (McDonough & Sun, 1995) for Charneca peridotite-lherzolitic garnet (red circles) and Charneca Cr-poor megacryst garnet (blue triangles).

4.2 Spinel

Analyzed spinel-group minerals from the Charneca kimberlite are very homogenous, with very little compositional variation (Table 4). They occur in both euhedral and anhedral forms, in sizes varying from 0.10mm to 0.25mm. Euhedral crystals exhibit high Cr spinel composition cores (43.51 wt.% Al_2O_3, 25.91 wt.% Cr_2O_3, 17.74 wt.% MgO and 14.17 wt.% FeO), with magnesian chromite rims (16.01 wt.% Al_2O_3, 42.60 wt.% Cr_2O_3, 11.91 wt.% MgO and 29.60 wt.% FeO), being characterized by low Cr/(Cr+Al) and $Fe^{2+}/(Mg+Fe^{2+})$ (0.29 and 0.28, respectively).

The anhedral crystals cores consist of magnesian chromite - chromite (0.43 - 2.30 wt.% TiO_2, 41.10 - 48.10 wt.% Cr_2O_3, 12.60 - 10.73 wt.% MgO, 22.71 - 36.54 wt.% FeO and 11.27 - 17.84 wt.% Al_2O_3) and, in some cases, spinel (~31.18 wt.% Cr_2O_3, ~15.64 wt.% MgO, ~15.65 wt.% FeO and ~39.49 wt.% Al_2O_3) They are compositionally homogeneous. Magnesian chromite shows almost no compositional zoning, displaying a slight increase in TiO_2 and FeO from core to rim (0.43 to 0.70 wt. % and 22.71 to 23.37 w.%, respectively), while chromite cores exhibit magnesian chromite rims (0.70 - 0.85 wt.% TiO_2, 42.60 - 47.30 wt.% Cr_2O_3, 11.91 - 12.15 wt.% MgO, 23.73 - 29.60 wt.% FeO and 16.01 - 17.50 wt.% Al_2O_3) with TiO_2 and FeO decrease and Al_2O_3 increase from core to rim, Cr_2O_3. Magnesium remains constant.

Because of the high Al_2O_3 and low TiO_2 contents and homogeneity, the spinel macrocrysts analyzed belong to the macrocrystal trend of Mitchell (1995). They are described as Cr-rich magnesian aluminous chromites (MAC) and, according to that author, are latter spinels that occur as a primary groundmass phase. Their compositional evolution therefore, is towards Cr and Fe enrichment at the expense of Al and Mg. Figure 11B show this evolution trend. The spinel-group analyzed follows the Cr-Al and Fe-Ti trend defined by Barnes & Roeder (2001). The first ones are characterized by low Cr/(Cr+Al) (from 0.29 to 0.35) and $Fe^{2+}/(Mg+Fe^{2+})$ (from 0.28 to 0.0.35). The second ones exhibit an increase in Fe^{3+}, accompanied by a very slight increase in TiO_2. This is also evident in Fig. 11A, $Mg / Mg + Fe^{2+}$ values being practically constant while $Fe^{3+}/(Fe^{3+} + Cr + Al)$ exhibits a slight increase (indicated by the arrow), except for in one crystal.

According Barnes & Roeder (2001) "*The Al-Cr trend correspond to spinels equilibrating with olivine of constant composition at constant temperature evident in the various mantle and lower-crustal samples, it is probably the result if equilibria between Al-bearing pyroxenes and Mg-Al-rich spinels and may suggest the origin of these crystals being from mantle xenoliths. While the Fe-Ti trend may be related to evolution of spinel compositions during fractional crystallization from the host magma, which increases the Fe/Mg ratio and the Ti content of the melt*".

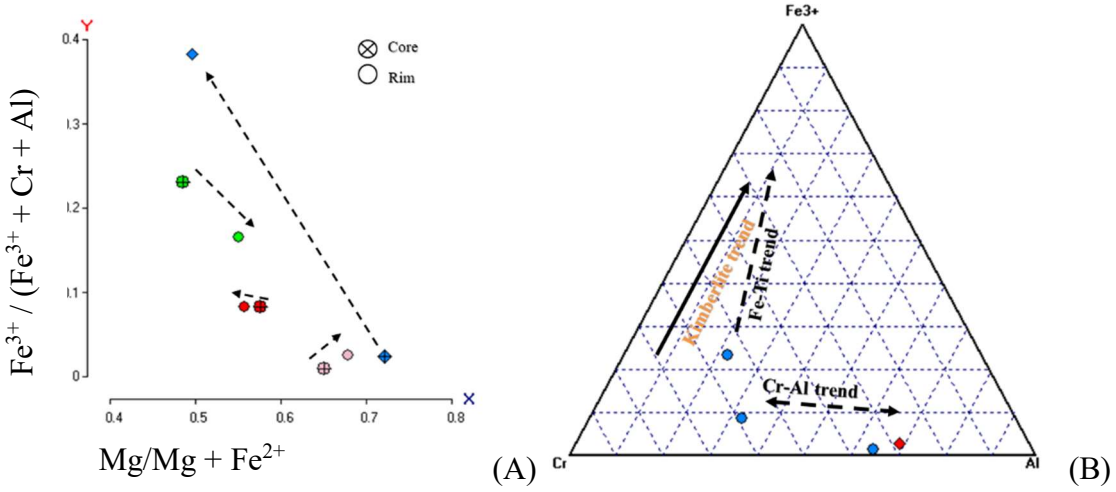

Fig. 11. A) Mg# (Mg^{2+}/ (Mg^{2+}+Fe^{2+})) *versus* Fe^{3+}# (Fe^{3+}/(Fe^{3+}+Al+Cr)) of spinel-group specimens from the Charneca kimberlite. Compositional variation of euhedral (lozenge) and anhedral (circle) spinel crystals indicating a Fe# increase from core to rim and variable Mg#, except for in one chromite core with a magnesian chromite rim (green). B) Fe^{3+} - Cr - Al diagram showing the Ti-Fe and Cr-Al trends defined by Barnes et al., (2001).

In the Charneca kimberlite, spinel-group minerals range in Co from 275.95 to 542.58 ppm, in Zr from 0.44 to 5.28 ppm, in Nb from 0.07 to 8.42 ppm, and in Sn from 0.73 to 10.52 ppm. They present similar trace element variations for both euhedral and anhedral crystals, with sinusoidal patterns (Fig. 12 A). A slight increase is observed from Rb to K, positive slopes for Pb, negative slopes for La, Ce, Sr and Y, and increased enrichment from Nd to Ti.

Although most grains present $HREE_N$ values below the detection limit, an enrichment from La to Eu ($LREE_N$) the distribution follows a normal pattern (Fig. 12 B).

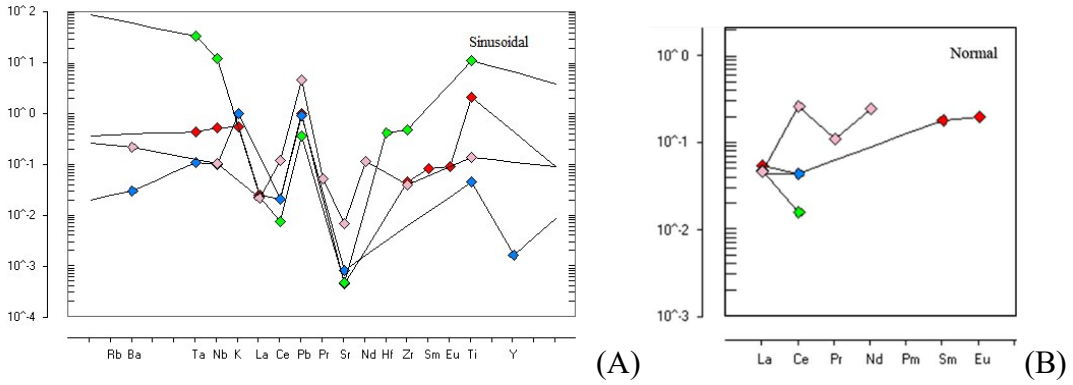

Fig.12. A) primitive mantle-normalized incompatible trace element pattern (McDonough & Sun 1995); B) Chondrite normalized REE patterns (Boynton 1984) for spinel-group minerals from the Charneca kimberlite.

4.3 Ilmenite

Two types of ilmenite from the Charneca kimberlite were analyzed: microcrysts ilmenite (0.15 to 0.33 mm) and macrocrysts ilmenite (2.50 to 3.60 mm). Both are rich in Mg, ranging from 7.44 to 12.93 wt.% and from 6.18 to 11.61, respectively. The distinction between groundmass and macrocrystic origin was initially based on size only (Mitchell 1995).

Microcrysts ilmenite cores exhibit typically high FeO_t and TiO_2 amounts (29.07 to 42.96 wt.% and 43.60 to 52.33 wt.%, respectively), Cr_2O_3 (0.08 to 2.57 wt.%), Nb_2O_3 (0.06 to 0.53 wt.%) and minor amounts of Al_2O_3 (< 0.53 wt.%) and MnO (< 0.43wt.%) (table 5). From core to rim, there is an increase in MnO and FeO_2 and a decrease in MgO and Fe_2O_3. Compositional variations, however, are subtle.

Ilmenite macrocryst cores are typically high in FeO_t and TiO_2 (33.76 to 45.01 wt.% and 44.83 to 53.91 wt.%, respectively), Cr_2O_3 (0.11 to 2.01 wt.%), Nb_2O_3 (0.04 to 0.54 wt.%) and bear minor amounts of Al_2O_3 (< 1.08 wt.%) and MnO (< 0.29wt.%). Rims present practically the same amounts in relation to cores (varying up to ~1 wt.%), which indicates homogeneity throughout the crystals.

Data grains were plotted on a MgO *versus* TiO_2 graphic (Haggerty 1975, 1976; Wyatt et al., 2004), which establishes a parabolic arc typical of many kimberlitic ilmenite populations. Reference lines of constant hematite content were added to the scatter plots, for the differentiation between kimberlitic and non-kimberlitic ilmenite. Both ilmenite populations fall within kimberlitic field, confirming the kimberlitic origin of the analyzed grains (Fig. 13).

Figure 14 shows a MnO x Al_2O_3 plot for kimberlitic ilmenite from the Charneca kimberlite. Two kimberlitic ilmenite fields become evident: a microcrysts ilmenite one, characterized by > 0.29 wt.% MnO, and a macrocryst ilmenite one characterized by < 0.29 wt.% MnO. An ilmenite grain 0.35 mm large fell within the megacryst field, possible being a ripped-off fragment from a mega- or macrocryst during the kimberlite emplacement.

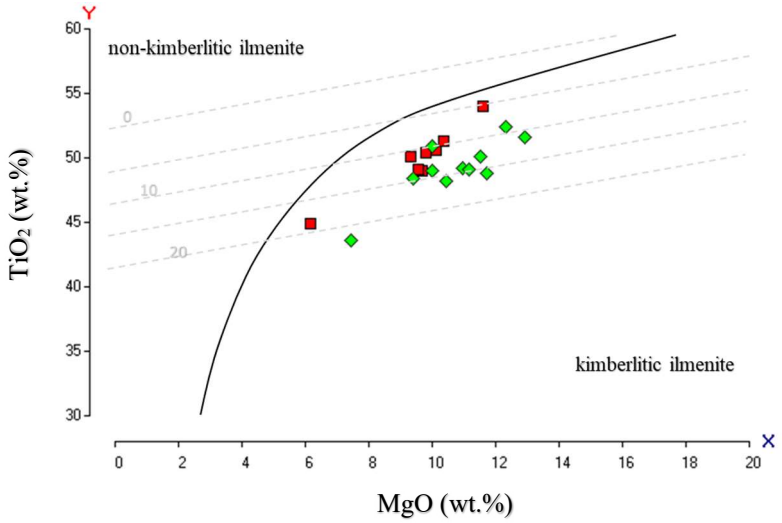

Fig.13. MgO *versus* TiO_2 for ilmenite grains from the Charneca kimberlite. Red squares and green lozenges correspond to macrocrysts (2.50 to 3.60mm) and microcrysts ilmenite (0.15 to 0.33mm), respectively. Percent Fe_2O_3 lines are shown as dashed light-grey lines. Black line represents the bounding reference line of the kimberlitic ilmenite field (after Haggerty (1975, 1976) and Wyatt et al., (2004)).

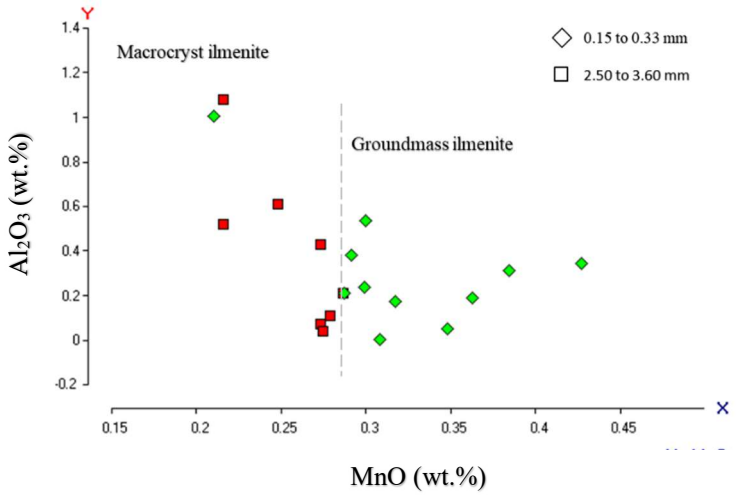

Figure 14. Plot of MnO versus Al_2O_3 for [macrocryst and microcrysts] ilmenite from the Charneca kimberlite. Two fields are defined, based on data from this study: macrocrysts (above 2.30 mm in size and <0.29 wt.% MnO) and groundmass (above 0.15 mm in size and >0.29 wt.% MnO). Notice the slight increase in Al_2O_3 in megacryst ilmenite. A grain that fell within the megacryst field might be a fragment from a mega or macrocrystal.

Macrocryst ilmenite from the Charneca kimberlite contains significate amounts of Sc, that range from 14.12 to 29.25 ppm, V (425.68 to 2011.09 ppm), Co (110.35 to 200.30), Ni (451.42 to 941.77 ppm), Zr (236.09 to 717.92), Sn (8.17 to 47.60 ppm), Hf (9.14 to 29.19 ppm), and Ta (23.22 to 422.04 ppm) (Table 5).

Groundmass ilmenite ranges in Sc from 19.37 to 36.46 ppm, in V from 1411.58 to 2131.94 ppm, in Co from 163.20 to 208.84, in Ni from 669.44 to 1845.01 ppm, in Zr from 527.57 to 1144.93, in Sn from 8.58 to 48.06 ppm, in Ba from 0.08 to 44.83 ppm, in Hf from 9.09 to 44.42 ppm, and in Ta from 18.46 to 466.32 ppm.

Normalized to the primitive mantle (McDonough and Sun, 1995), the incompatible elements from macrocryst to groundmass ilmenite exhibit enriched subparallel patterns, both with positive Ta, Nb, Hf, Zr and Ti spikes (Fig. 15 A). However, chondrite-normalized REE patterns (Boyton, 1984), are, on average, unusually depleted in $LREE_N$ with a slight enrichment towards $MREE_N$ and $HREE_N$, with the exception of three groundmass ilmenite specimens, which exhibit a slight enrichment in $LREE_N$ and depletion in $MREE_N$ and $HREE_N$ (Fig. 15 B), resulting in a flat pattern. It can be noticed that groundmass ilmenite contains incompatible trace elements and REE values slightly higher than those of macrocrysts ilmenite.

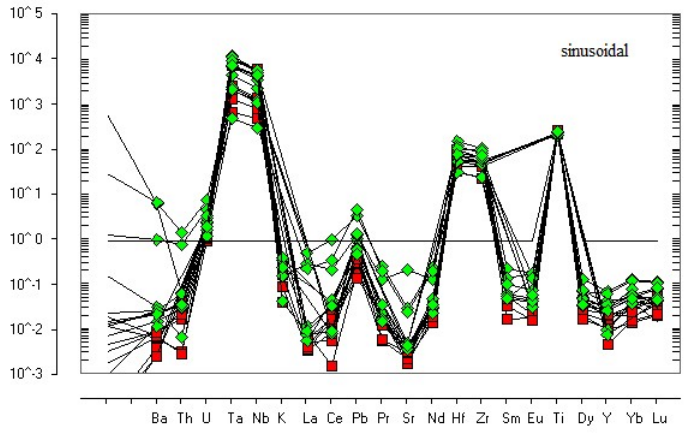

(A)

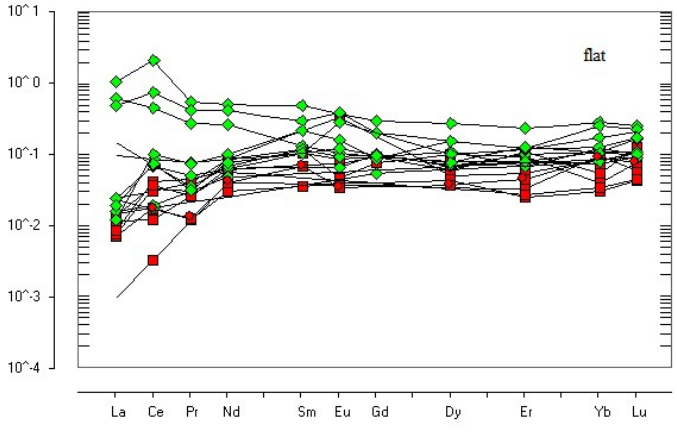

(B)

Fig. 15. A) Incompatible ilmenite elements normalized to the primordial mantle (McDonough & Sun, 1995). B) Chondrite-normalized REE distribution patterns (Boyton 1984) in ilmenite from the Charneca kimberlite. Green lozenges: microcrysts; red squares: macrocrysts ilmenite.

4.4 Perovskite

This mineral is a late-stage magmatic product and it is an important repository of trace elements and REE in kimberlitic magmas (Chakhmouradian & Mitchell, 2001; Sarkar 2011). Most perovskite analyses were not performed within ideal composition conditions ($CaTiO_3$) due to the abundant presence of trace unanalyzed elements. Castillo-Oliver et al., (2016) distinguished different perovskite types in kimberlites based on crystal perfection and zoning pattern (texture). Based on such parameters and terminology, the Charneca perovskite is recognized as Type Ia.

In the Charneca kimberlite, perovskite is a primary phase and it occurs scattered throughout a strongly altered groundmass, in anhedral to subhedral forms that range from 0.19 to 0.24 mm in size, the latter as rimmed olivine pseudomorphs.

With the exception of one crystal specimen analyzed, perovskite is partially altered to rims of TiO_2, but with most cores unaltered. The alteration results in atoll texture. A "cavernous" appearance is observed sometimes (Fig. 16). This results from cation leaching and replacement with Ti-bearing minerals. Titanium dioxide (TiO_2) is the most common product of perovskite alteration in kimberlites (Chakhmouradian & Mitchell 2000). Different polymorphs of TiO_2 can replace perovskite, e.g. rutile, anatase and brookite, so careful further investigation is necessary.

Zoning patterns are common in perovskite and they reflect complex compositional variation. The grains analyzed can or cannot present a subtle zoning pattern in back-scattered electron (BSE) images, normally with dark cores and brighter rims. However, the opposite occurs in some grains. Major and trace element data for the Charneca perovskites are listed in table 6.

Based on major-element composition and variation from core to rim, perovskite can be divided into different groups (Castillo-Oliver et al., 2016; Chakhmouradian & Mitchell, 2001). The normal pattern corresponds to a decrease in LREE and Th, with varying Na and Nb

contents. The reverse pattern exhibits enrichment in LREE and Th towards the rims, possibly Fe and Nb increase, while LREE values can remain constant or decrease slightly. The oscillatory pattern corresponds to significant variations in Nb, Na, Ce, Fe and Nd within a single grain.

Such observations were made by authors studying African and Canadian kimberlites (*e.g.* Chakhmouradian et al., 2013; Chakhmouradian & Mitchell, 2000; Donnelly et al., 2012). Due to the wide chemical compositional variety of the mineral, classification of perovskite into a "universal standard" can be complicated. However, a pattern was recognized in the Charneca kimberlite that can be broken down into different groups, exhibiting similarities with groups proposed by the afore mentioned authors. In addition, further rim LREE analyzes are necessary.

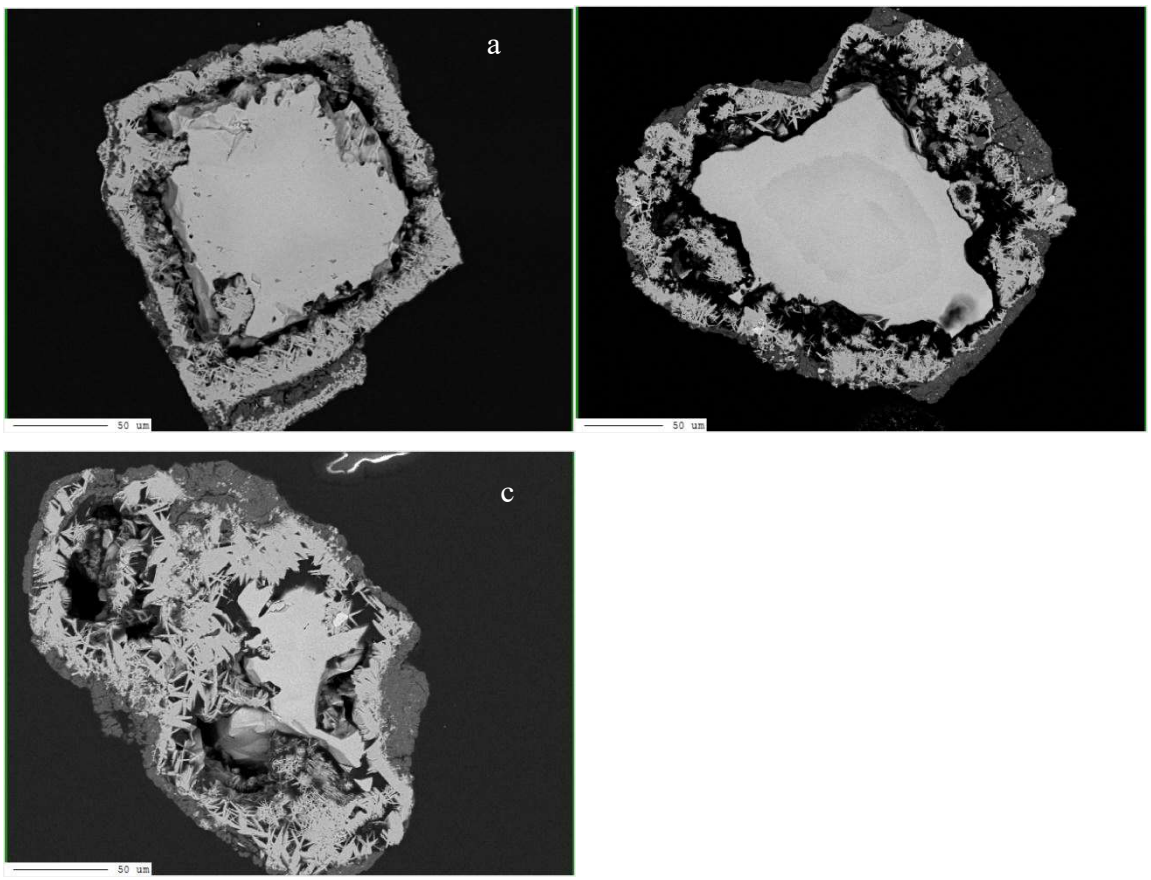

Fig. 16. Characteristic alteration patterns of perovskite from the Charneca kimberlite observed in BSE images. Scale bar is 50µm. (a,b) Atoll-textured perovskite with a rim of TiO_2 (c) "Cavernous" reaction-induced rim of TiO_2 around perovskite.

"Normal" and "reverse" zoned crystal patterns were observed. Fig. 17 illustrates these variations. The "normal" pattern observed in grains with dark cores and brighter rims is characterized by a decrease in Na, Ce, La and ΣLREE and a slight increase in Nb and Th from core to rim, while the "reverse" pattern is observed in brighter cores and dark rims, exhibiting an initial decrease in Na, Ce, La, Th and ΣLREE until the middle parts of the crystals, with an accentuated increase in Na, Ce, La and ΣLREE towards the rims, while Th contents are null on the rims and Nb is almost constant. Many variations to these standards can exist due to the presence of transitional zones within perovskite crystals.

In the Charneca kimberlite, Type Ia is in good agreement with those found in perovskite I as defined by Chakhmouradian & Mitchell (2001) for Canadian kimberlites and with the perovskite group 1 defined by Castillo-Oliver et al., (2016). It is characterized (Fig. 18) by being Al-poor (up to 0.36 wt.%) and, unlike in Lac de Gras rocks, it has low Sr and K contents (up to 0.39 wt.% and 0.14 wt.%, respectively), significative amounts of Ce (0.01 to 2.03 wt.%), moderate amounts of La (0.28 to 0.88 wt.%) and Nb (0.15 to 0.66 wt.%), and low amounts of Na and Th (up to 0.51 wt.% and 0.47 wt.%, respectively).

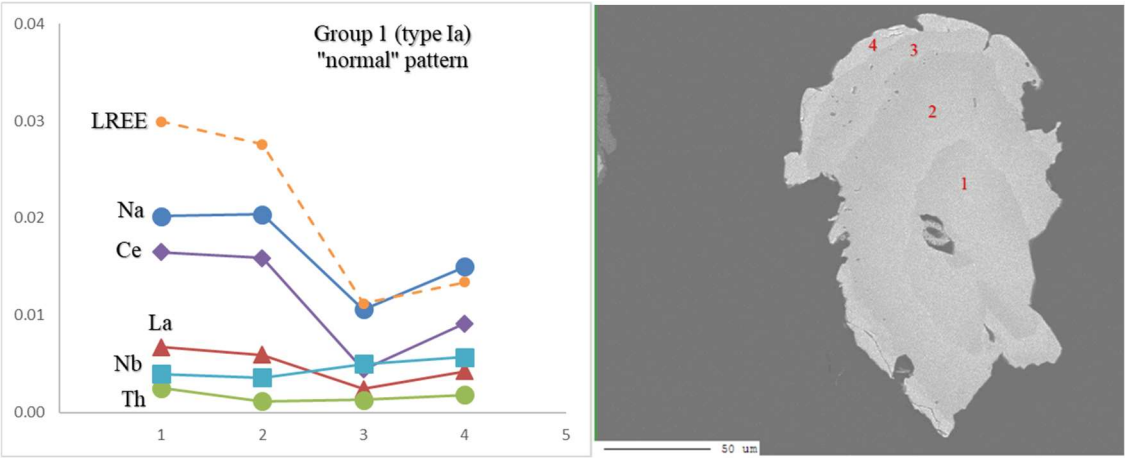

(A)

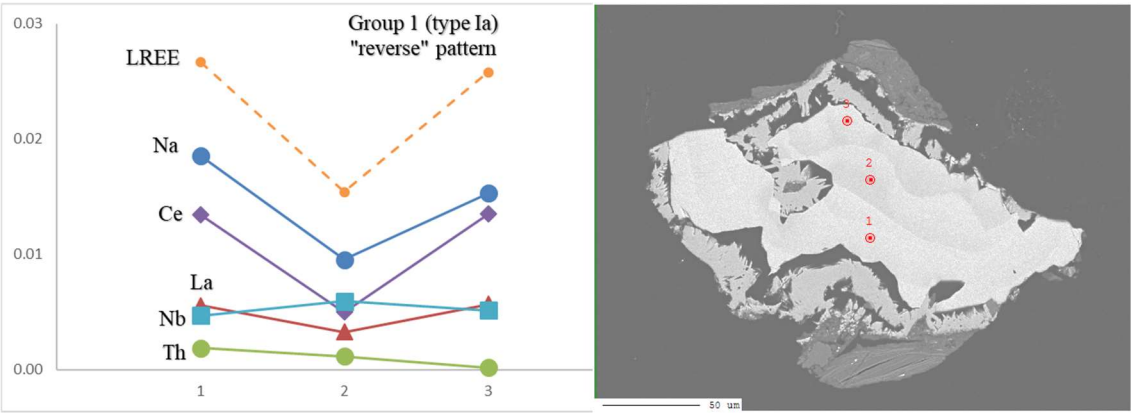

Fig. 17. Back-scattered electron (BSE) images of perovskite from the Charneca kimberlite showing zoning patterns and compositions. The grains analyzed in this study are Type Ia and can or can not to exhibit zoning patterns. Perovskite with dark core and bright rim display a “normal” pattern, while grains with bright cores and darks rims are characterized by “reverse” patterns.

Their $CaTiO_3$ content, of 96 mol% (Fig. 18), is similar to that of Bathlaros kimberlite. Low variations of Nb and Sr are observed; negative correlations of Na and Fe against Ti and REE and SrO against CaO follow the perovskite pattern of the Bathlaros kimberlite. In general, substitution of minor elements is higher in most south African kimberlites than in the Charneca intrusion, which is very similar to that of Bathlaros.

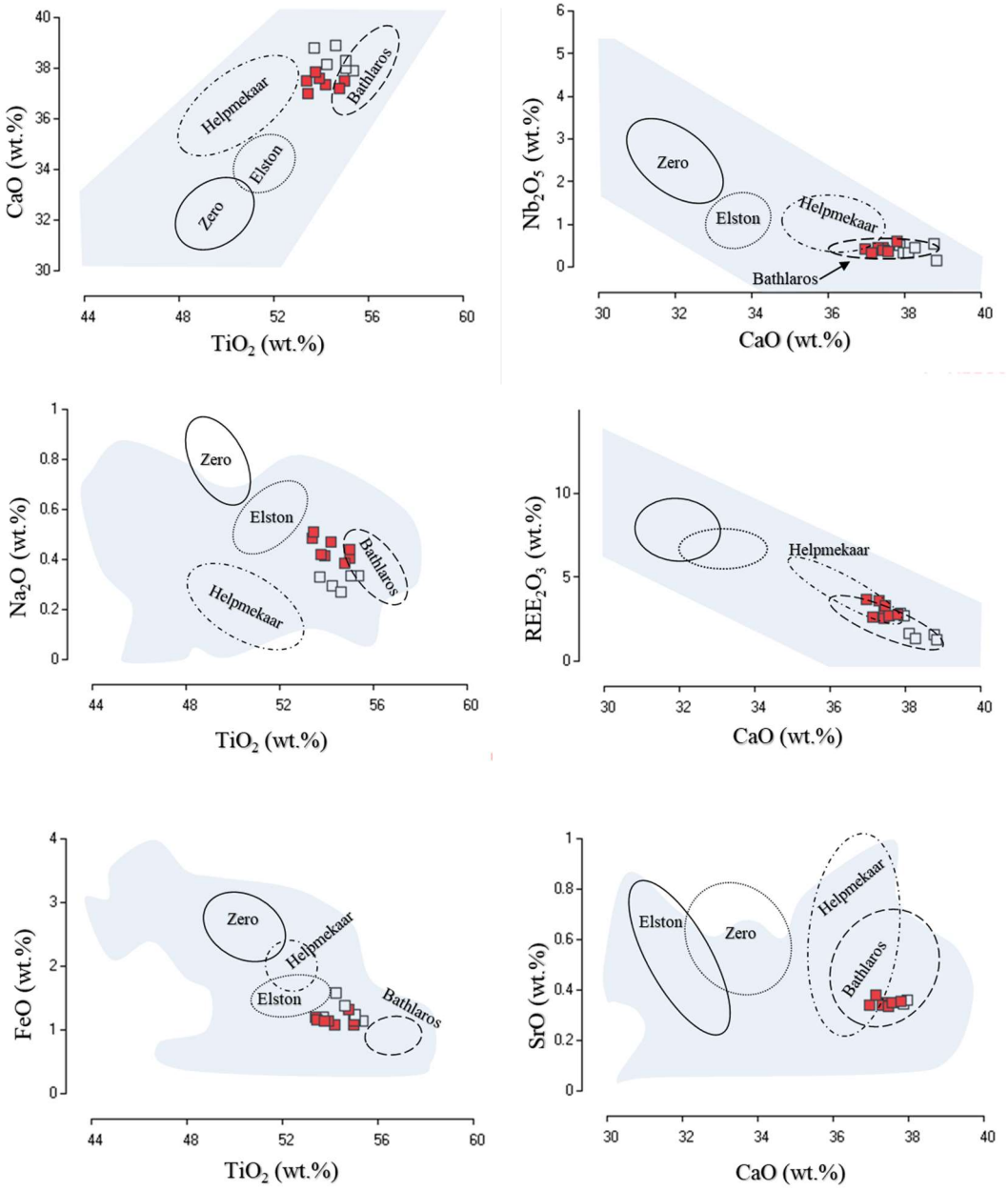

Fig. 18. Binary diagrams of major-element chemistry for perovskites (core: full; rim: empty) from the Charneca kimberlite. Delimited areas: Kuruman kimberlites; Darker shaded areas represent perovskite composition fields worldwide (data sources, Donnelly et al., 2011). REE_2O_3 includes La_2O_3, Ce_2O_3 and Nd_2O_3.

The Charneca kimberlite has variable incompatible trace element values for Zr (306.77 to 490.98 ppm), V (84.43 to 104.37 ppm), Ba (26.29 to 40.64 ppm), U (62.76 ppm), Y (140 to 182.63 ppm) and Ta (289.13 to 419.50). The multi-element normalized diagram pattern (Fig. 19A) shows negative anomalies for Ba, K, Pb, Sr and Zr. Such characteristics are in accordance with patterns exhibited by perovskites from kimberlites worldwide, e.g. Colorado, Wyoming,

Siberia and Canada (Chakhmouradian et al., 2013) and PIAP alkaline rocks (Melluso et al., 2008).

Zr/Hf values (17.6 - 20.3) suggest no major fractionation between these elements; Nb/Ta values (6.14 - 11.9) are generally lower than chondritic values, suggesting a slight preferential partitioning of Ta for perovskite (Melluso et al., 2008). Lu/ Hf values are very low (0.02 - 0.03) and show almost no variation. All these ratios are in agreement with data from PIAP alkaline rocks. However, they remain at the lower limits defined for these rocks by Melluso et al., (2008): Zr/Hf (16-37); Nb/Ta (3.8-25.3); Lu/Hf (0.007-0.12).

REE_N exhibit a humped pattern, reflecting enrichment in $LREE_N$ with respect to the $MREE_N$ and $HREE_N$ (Fig. 19B). The Charneca perovskites are characterized by a low fractionation of light over heavy REE (La/Yb ratios between 403 and 989), in agreement with Kuruman kimberlites (La/Ybn from 321 and 2180). The light over heavy rare-earth fractionation and the Eu anomalies (in the range 0.85 to 1.03) are within the range of kimberlitic perovskite from PIAP rocks (La/Ybn from ~175 to ~2000 and Eu/Eu* in the range 0.88-1.1, after Melluso et al., (2008))

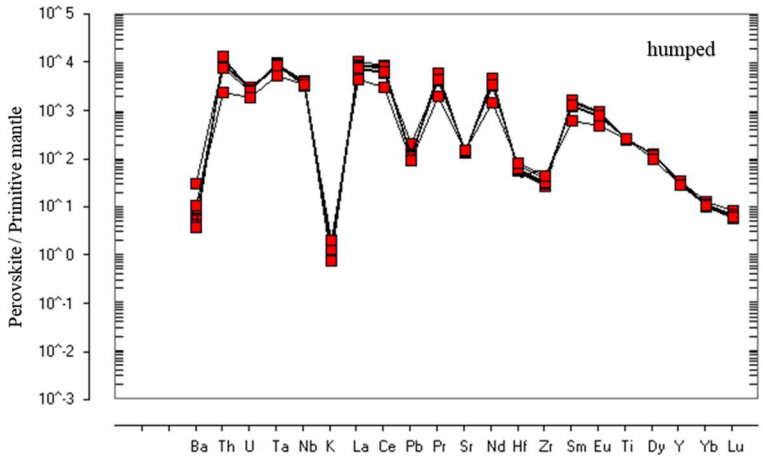

(A)

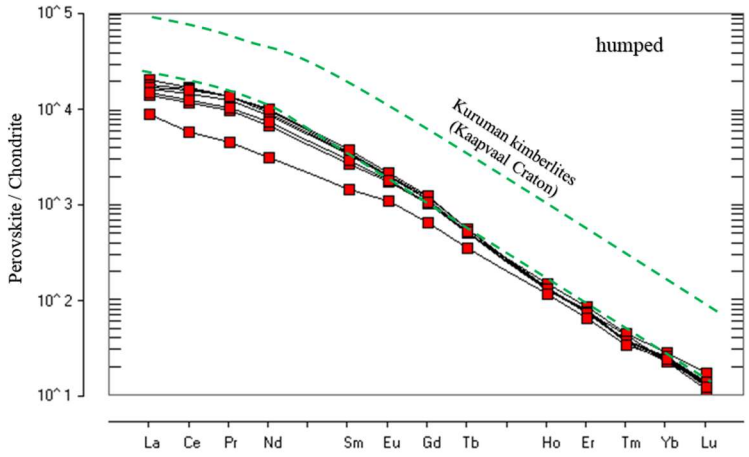

(B)

Fig. 19. A) Primitive mantle-normalized (McDonough & Sun, 1995) perovskite incompatible elements from the Charneca kimberlite. B) C1 chondrite-normalized (Boyton 1984) REE perovskite patterns for the Charneca kimberlite. Green dashed lines: averaged REE_N concentration field of perovskite from the Kuruman kimberlite Province, South Africa (Donnelly et al., 2012).

4.5 Pyroxene

According Morimoto (1990) the macrocrystals analyzed are anhedral grains with up to 1.50 mm in diameter and correspond mainly to augite and diopside end-member (table 7). The clinopyroxene are rich in Cr_2O_3 contents (1.02 to 2.58 wt%), TiO_2-poor (0.02 to 0.15 wt%) and have Mg# values ranging from 0.92 to 0.93. The Al_2O_3 (1.61 to 1.97 wt%) and Na_2O (0.0 to 0.04 wt%) contents increase with decreasing Mg#, Cr# (0.29 to 0.50) and Ca# (0.44 to 0.45) values. Based mainly in a major chemical composition, the clinopyroxene from Charneca have great similarity with garnet peridotite xenoliths from Grib kimberlite (Fig. 20).

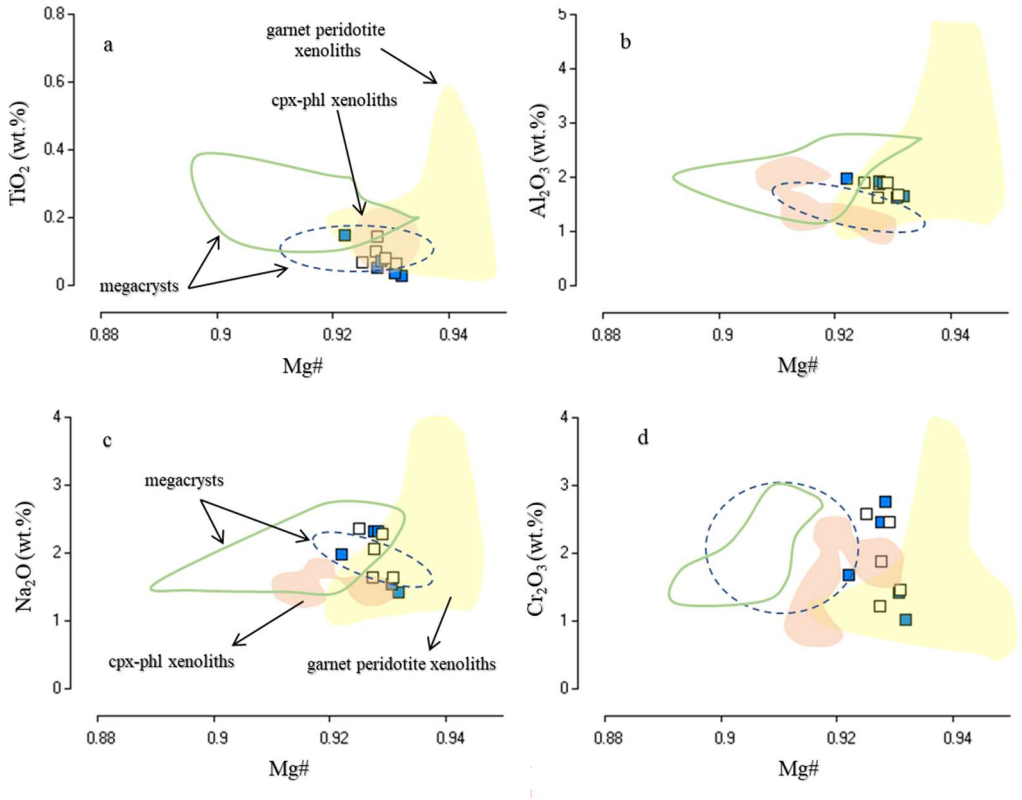

Fig. 20. Bivariate plots for the clinopyroxene cores (full squares) and rims (empty squares) from Charneca kimberlite. The yellow field shows the compositional range for clinopyroxene from garnet peridotite xenoliths in the Grib kimberlite (Kargin et al., 2016). The orange field and dashed line represent major concentration of megacryst clinopyroxene of clinopyroxene-phlogopite xenoliths and megacrysts from Grib kimberlite (Kargin et al., 2017). The green line field show the megacryst clinopyroxene dataset from Grib kimberlite (Kostrovitsky et al., 2004).

According to McDonough & Sun (1995), primitive mantle-normalized incompatible elements pattern for clinopyroxene from Charneca show strong negative slopes in U, Nb and Zr, and flat pattern from La to Nd with different intensities (Fig. 21A). In addition, these megacrysts are characterized by $(Zr/Hf)_N$ values from 15.24 to 61.72 and negative anomalies in Ba, Nb, K, Ta, Zr, Hf, and Ti. The C1 chondrite-normalized REE patterns (Boynton 1984) are shown in Fig. 21B. They are enriched in LREE–MREE, with flat patterns in the La–Nd region at 15 times chondrite, and depleted in HREE resulting in a slightly humped pattern. The fractionated values vary from 23.11 to 116.49 for $(La/Yb)_N$, 0.65 to 1.58 for $(La/Nd)_N$, 0.76 to 3.35 for $(La/Sm)_N$ and from 22.82 to 41.18 for $(Sm/Yb)_N$.

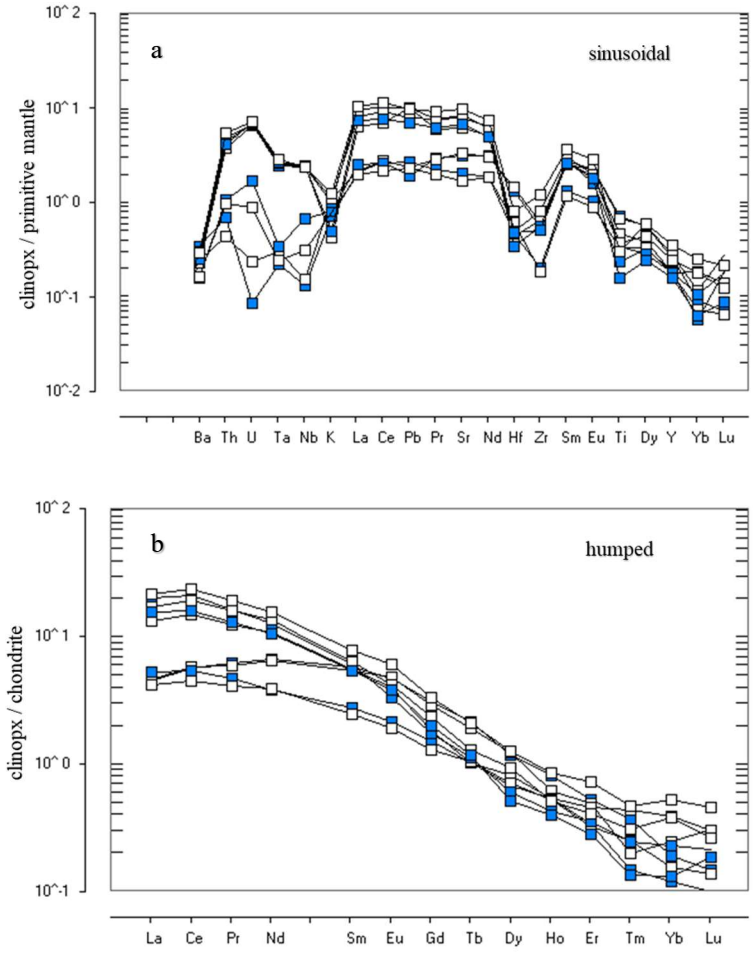

Fig. 21. (a) primitive mantle-normalized incompatible elements pattern (McDonough and Sun, 1995) and b) Chondrite normalised REE patterns (Boynton 1984) for clinopyroxenes cores (full squares) and rims (empty squares) from Charneca kimberlite.

5. Sr isotope analysis

The Sr-isotope compositions of the Charneca perovskite are summarized in table 8. Seventeen analyses of individual perovskite grains from Charneca was carried out, and due to isobaric interferences of ^{87}Rb over ^{87}Sr, only nine chemical analyses were considered $^{87}Sr/^{86}Sr$ ratio between 0.705082 and 0.707388. The isobaric ^{87}Rb contribution over ^{87}Sr was corrected by using the ^{85}Rb ion signal and the $^{87}Rb/^{85}Rb$ natural ratio (Ramos et al., 2004), however, we opted to exclude some analyzes that were interpreted to have some uncertainty degree, and for better accuracy of the data only values up to the third decimal place. Due to their very low Rb/Sr ratios (< 0.005) (Sarkar et al., 2014) and the relatively young age of the kimberlites, no age

correction was applied on the measured Sr isotope ratios. Furthermore, the data obtained were considered initial.

The isobaric interferences should be corrected for the accuracy of resultant $^{87}Sr/^{86}Sr$ ratios. Munoz et al., (2016) implemented measurements of half-masses ($^{171}Yb^{2+}$) allows the accurate assessment of lanthanide interferences, permitting the determination of Sr isotopes in important REE-rich accessory phases. The appropriate results are achieved in Sr-rich and Rb-poor phases (Rb/Sr <0.02), materials with Rb/Sr ratios > 0.02 are not suitable for the acquisition of accurate Sr isotope ratios via LA-MC-ICP-MS (Ramos et al., 2004), whereas others advocate that an efficient correction can be performed for materials with far greater Rb/Sr ratios (<0.2 Davidson et al., 2001). Due to siethe very low amounts of Rb (< ~5.7ppm; Donnelly et al., 2012) in perovskites, if interference occurs, this influence will be minimum.

Table 8. $^{87}Sr/^{86}Sr$-isotope results for perovskite analyzed in this study.

SrO (average): 3025 ppn	
Sr^{87}/Sr^{86}_i	2 sigma
0.707388	0.000616
0.706128	0.000721
0.706472	0.000848
0.705359	0.000680
0.705294	0.000496
0.705909	0.000877
0.705082	0.000594
0.706272	0.000673

6. Discussions

Many factors control the alteration degree of kimberlite rocks, eg. porosity, permeability, fluid composition, temperature, and different alteration degrees almost always are related to the differences in composition (Porritt et al., 2012). The presence mainly of clays in Charneca may indicate hydrothermal fluids and/or meteoric water actions. For longer periods

during and after an eruption, large volumes of volcanic gases flow through the vent, in many cases hydrothermal fluids may also flow through the vent system post-eruptively, in addition, after an eruption the vent is a trap for meteoric water (Cas et al., 2008).

Alteration minerals replace, overprint and mask original components, despite the effects of alteration, original textures, such as grain contacts and sorting of framework grains, can be identified in many cases (Porritt et al., 2012). The classification of kimberlitic facies should be done with caution, hypabyssal-, transitional- and diatreme- types are based in classical African and Canadian kimberlite models (Clement and Skinner, 1985; Field and Scott Smith, 1998), and according with some characteristics it is possible to suggest which Charneca kimberlite facies was studied.

These names and textural terms are applied to rocks where the origin is not necessarily well-established (Sparks et al., 2006), the classification thus provides a useful starting point. It is important to remember that the terms used for the facies description in this work have a more descriptive and non-genetic sense. In well-studied and delimited African and Canadian kimberlite pipes, these terms immediately confer a genetic significate, however, for the Brazilian kimberlites more accurate investigations are required, such as the characterization through drilling holes and magnetometry, for the correct reconstruction of the pipe and more accurate classification of the facies.

The most hypabyssal-facies kimberlites (HFK) have uniform magmatic texture and rarely segregationary, unaltered olivines can occurs and abundant primary calcite and serpentine in groundmass, primary diopside is rare (or absent) and country rock xenoliths, when present, are always highly altered. The HFKs can present rare segregationary textures (e.g. globular and pelletal segregations) consisting of earlier crystallized minerals like olivine and phlogopite set in an inter-globular matrix of late crystallizing. Initially these features were attributed only to diatreme facies (Clement 1975), but subsequent discovery of similar rocks in dykes and root zones indicates that they are a variety of HFK (Skinner & Marsh, 2004).

The diatreme-facies kimberlite (DFK) is characterized by pelletal and juvenile structures, serpentinized olivine, a groundmass with serpentine, country rock xenoliths are angular and relatively unaltered, abundant microlitic diopside and absence of primary calcite (Skinner & Marsh, 2004). The transitional-facies kimberlite (TFK) grades continuously between two main end- member varieties, the recognition of TFK, localized in the lower parts

of the pipe (towards the base of the diatreme zone and towards the top of the root zone) is a relatively new development (*e.g*. Hetman et al., 2004; Skinner & Marsh, 2004).

The Charneca kimberlite displays features of hypabyssal and diatreme facies, these are descriptive terms, because crater facies could also occur in the diatreme zone, and hypabyssal or coherent kimberlite could occur at any level of a pipe (Cas et al., 2009). The low abundance of country rocks (< 2%) with high alteration degree, the presence of small juvenile clasts (<2.8mm) with hypabyssal texture and no vesicles, the occurrence of incipient pelletal structures (~1%) with poor- or no orientation rim and the evidence of limited flow and deformation observed mainly in the phlogopite macrocrysts from interstitial medium, point to hypabissal-facies. Carbonates minerals are abundant within interstitial medium in Charneca, however, the origin is doubtful.

The most carbonate in kimberlites is secondary, showing diffusely bounded patches, and veins, but it could be primary (a segregation product) in carbonatite and kimberlite magmas (Cas et al., 2008). In the studied kimberlite, the carbonates occur mainly like euhedral crystals dispersed within interstitial medium, however, diffusely bounded patches were observed. In addition, besides high alteration, which can crystallize secondary carbonates, one of the host rocks of Charneca kimberlite is dolomite, then, the origin of carbonates can be from host rocks or deuteric process.

The presence of locally diopside microlites and the completely serpentinized olivine crystals in addition of apparently secondary carbonates, can point to diatreme-facies. Therefore, based on the mixture features described above, is coherent suggest a transitional-facies for Charneca kimberlite. However, the overprint of original textures difficult a classification mainly about the carbonate origin. In addition, microlitic diopside can occur in hypabyssal-facies patchily distributed (Skinner & Marsh, 2004), therefore, the affinity with the hypabyssal-facies kimberlite must be considerate.

The mineral chemistry has the potential to reflect the chemical character of the parent magma, however, the distinction between the minerals of different origins it is not always possible. Furthermore, metasomatic fluids are important agents for chemical exchange in the mantle (Howarth et al., 2014); e.g., metasomatism is responsible for refertilization of previously depleted mantle sources and triggering diamond growth (Liu et al., 2009).

The grain size criterion is not self-sufficient to establish the relationship between megacrysts and macrocrysts due to the fact that both can be derived from larger grains crystals (Pivin et al., 2009), including megacrysts and xenolith-derived fragments, which may have been mechanically reduced during the process of the primary kimberlite material. In this study, most mineral grains available are in fact smaller than 10 mm in diameter and do not fit the strict definition of megacrysts. Therefore, based on major and trace element compositions, the word "megacrysts" can be linked to genetic processes rather than just as a description of mineral size.

Mantle process recorded by major elements

The Cr content of garnet is a primary indicator of the degree of depletion of the host rock (Griffin et al., 1999). The low chromium (< 2.82%) of garnets analysed from Charneca and the negative correlations with Fe, Y, Ti and Ga, suggest a primary depletion process reflected by chromium removal. In addition, the highly subcalcic compositions imply in a depleted character. Similar garnets from Proton suites (2·5–1 Ga) are subcalcic exhibiting typically low-Cr, and occur at shallower depths (100-120 Km; T = 700 – 1000°C) (Griffin et al., 1999). According Grütter et al., (1999) the "normal" subcalcic garnets (CaO > 1.8 wt.%) reflect melt extraction in excess of 20% (clinopyroxene exhaustion).

The major element compositions of clinopyroxenes (Fig. 20) analyzed overlap in Mg#, TiO_2, Na_2O and Cr_2O_3 contents mainly xenoliths fields, which correspond to garnet peridotite (Kargin et al., 2016), clinopyroxene–phlogopite (Kargin et al., 2017) and phlogopite peridotites xenoliths (Nannini, 2016). The clinopyroxenes associated with low-Ti studied by Kargin et al., (2016) have similar compositions with those studied in this work (similarities in Mg#, $(La/Sm)_N$ values and trace elements patterns with deep negative Zr–Hf and shallow negative Ti and Nb–Ta anomalies) and are from coarse-grained mantle garnet peridotite xenoliths.

Even with the overlapping of Grib kimberlite high Cr-megacryst fields, the features above suggest that the clinopyroxene analyzed from Charneca represent disintegrated fragments of peridotite xenoliths (probably garnet peridotite) and in addition, the Mg#, Ca# and Cr# values are higher than worldwide megacrysts and similar to worldwide peridotites (Pivin et al., 2009). The assimilation of xenoliths, e.g. peridotite, enriched the kimberlitic melt in silicate and the formation of the low-Cr and Fe-Ti-rich megacrysts occur, in this case, the presence of Mg-ilmenites with high Al and low Mn and Cr. The strong depletion of Ti, Nb, Ta, Zr and Hf may reflect the precipitation of Ti-oxides, such as ilmenite due to preferential

fractionation (Golubkova et al., 2013), maybe the low-Ti contents in the clinopyroxene (Table 7) with high-Cr could be explained by the ilmenite formation.

Mantle process recorded by trace elements

The two suites of garnets analyzed from Charneca corresponding to lherzolitic and megacrysts trend and exhibit low and high TiO_2 concentrations (< 0.5% and > 0.5%, respectively). Low-Ti and high-Ti garnets have different REE and primitive mantle (PM)-normalized trace element patterns and are in agreement with lherzolitic and megacrysts garnets from Grib kimberlite pipe (Kargin et al., 2016). They are also depleted in the LREE and TiO_2 relative to garnet megacrysts and have similar trace element compositions (Fig. 10).

Residual garnets have increasing concentrations from La to Lu with HREE contents of about 10 chondritic units (Shchukina et al., 2015) and theses features are similar to those exhibited by garnets from Charneca, which can be interpreted as low Cr_2O_3 (< 2.82 wt.%) depleted residual garnets that survived partial melting. This REE pattern is typical for garnets from fertile (or refertilized) lherzolites (Howarth et al., 2014; Shchukina et al., 2017).

The positive correlation between Y and Zr concentrations corresponding to the “melt” metasomatic trend (Griffin, Fisher, et al., 1999) and this feature is exhibited by both garnet types analyzed, however, the megacrysts suite presents higher metasomatic enriqueciment than lherzolitic garnets. The higher values of $(Sm/Er)_N$ and $(La/Yb)_N$ ratios also indicate a major influence of metasomatic fluids in the megacrysts suite. It is common that the garnets of this type occur together with clinopyroxenes in peridotites (Howarth et al., 2014; Shchukina et al., 2015). The (Sm/Er) ratios of megacrysts (0.48 – 0.81) and lherzolite-garnets (0.11 – 0.25) are lower than 1 and plot in the field of the silicate metasomatism.

The normal fractional crystallization of magmas bodies in the deep lithosphere is proposed for low-chromium megacrysts origin (Gurney et al., 1979). These garnet types are supposed to be the product of crystallization of OIB-type asthenospheric magma at high PT conditions (Griffin et al., 1997; Nowell et al., 2004). They have been interpreted to be a reaction product of kimberlite melts with the lithospheric mantle and assimilation of rocks enriched in incompatible elements (Agashev et al., 2006). Shchukina et al., (2017) attribute the megacrysts suite garnets from Grib kimberlite as products of direct crystallization of the silicate melt with

REE composition close to mica-poor alkaline picrites, which are very similar to those of the "protokimberlite" magmas.

According to the depleted character of lherzolitic garnets from Charneca, they can be product in a final stage in a metasomatic enrichment, probably by silicate composition of the metasomatic agent with high LREE, due to enrichment in HREE displayed by these garnets analyzed. The Fig. 22 shows the lherzolite-garnets within depleted field and megacrysts garnets following the high-T metasomatism, suggesting a depleted peridotite mantle. The higher Zr, Y and Ti contents of high-T megacrysts suite can be comparable to depleted lherzolitic garnets, the rise of this elements is also accompanied by increases in Na, P and Ga (Table 3) and this fact can suggest that infiltration of melts along the foliation of the lherzolites was responsible for the high-T metasomatism (Griffin et al., 1999).

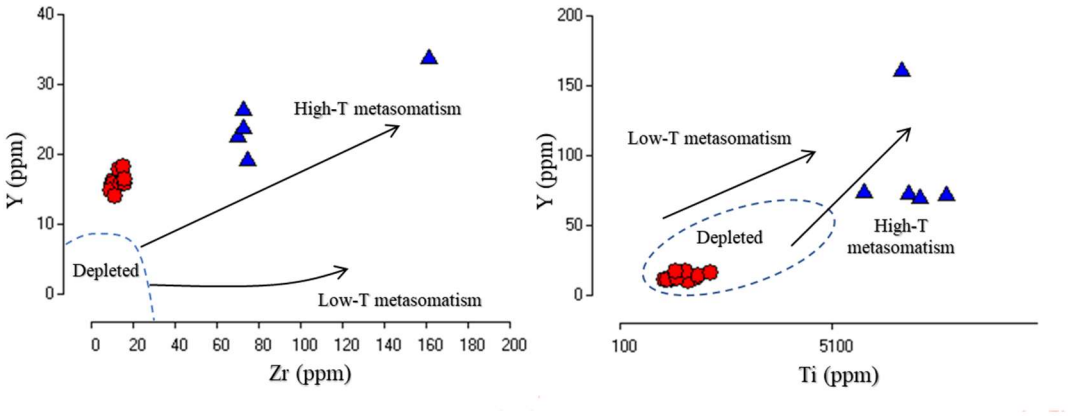

Fig. 22. Garnet trace-element variation diagrams of Charneca mantle peridotites. a) Garnet Yb vs Y *vs*. Zr and b) Zr *vs*. Ti variations suggest both low-and high-temperature metasomatism (950 – 1100°C and 1300 – 1500°C, respectively, after Griffin et al., 1999), originating from a depleted peridotite source (dashed lines field). Symbols: red circles: lherzolitic garnets; blue triangles: garnet megacrysts.

The high LREE concentrations of clinopyroxenes associated with negative Nb, Ta, Zr, Hf and Ti anomalies have been interpreted to result from metasomatism of the subcontinental lithospheric mantle (SCLM) by silicate melts/fluids (Shchukina et al., 2015), or kimberlite melts (Kargin et al., 2016). They could be the final product of a metasomatism of garnet

peridotites within the SCLM (Kargin et al., 2017), and maybe the same source that formed the lherzolitic garnets (Fig. 23).

Higher $(La/Yb)_N$ at constant Ti/Eu can be used to distinguish between carbonatite and kimberlite metasomatism. Clinopyroxenes analyzed in this study have relatively high Ti/Eu values, inconsistent with carbonatite metasomatism, indicating that the LREE enrichment is likely related to kimberlite metasomatism.

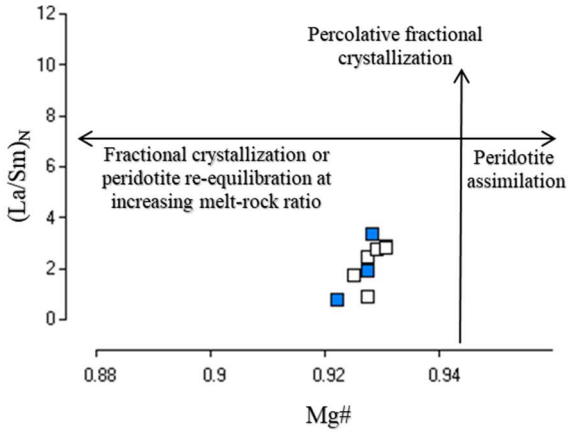

Fig. 23. Relations between Mg# values and LREE fractionation for clinopyroxene (after Kargin et al., 2016; Nimis et al., 2009).

The equilibrium with kimberlite magma is represent by ilmenites generally with higher concentrations of incompatible elements, such as Sr, Ba, LREE, Pb, Th, U, Zn, and lower abundances of HFSE (Zr, Nb, Ta, Hf) (Golubkova et al., 2013). The ilmenites from Charneca present the opposite of these features. It is notable the very strong positive anomalies in high field strength elements (HFSE), suggesting that these grains were not in equilibrium with kimberlitic magma. In addition, calculated composition melts which were in equilibrium with Mg-ilmenite megacrysts with flat patterns (Golubkova et al., 2013), resulted in an enriched LREE melt composition.

The all silicates analyzed (garnet and clinopyroxenes) have depletion in Hf, Nb, Ta, and Zr, however, ilmenites are rich in these high field strength elements (HFSE). These elements remain relatively constant during the first 80% of crystallization and then increase during the final stages (Jang and Naslund, 2002). These can be explained the higher trace elements values

displayed by microcrysts ilmenites, which can be related to latter crystallization in relation to macrocrysts ilmenites.

The Ba/Ce ratios has been suggested as a possible fingerprint for the influx of new magma during ilmenite crystallization (McBirney, 2002). The mots of microcrysts ilmenites with high-Cr (>1 wt.%) show the higher Ba/Ce ratios (11.18 to 115) and the most of microcrysts ilmenites with low-Cr show low Ba/Ce values (1.7 to 4). Initial stage of crystallization is represented by positive correlation between the Cr contents and Ba/Ce values in the ilmenites from Charneca. The high Ba/Ce ratios indicate an initial stage of crystallization, in this case, represented by high-Cr ilmenites microcrysts, and low (3-4) to very low (<3) values of this ratio indicate middle and later stages of crystallization, respectively, and the low-Cr ilmenites microcrysts can be a latter crystallization phase. This observation leads to suggest that the residual liquid became depleted in chromium, resulting in ilmenites phase with low contents of this element.

It was observed that the Ba/Ce ratios remain low (up to 4) in the macrocrystal ilmenites (high or low Cr). It would be seem to be contradictory to affirm that the macrocrystals represent a late phase of crystallization; if considering the lower (HFSE) values when compared to microcysts ilmenites analyzed. Therefore, it may be one of the evidences that the macrocrysts may have been formed by another event than the microcrystals, that is, the macrocrystal can be a late crystallization phase of another mineral assemblage.

The typical kimberlite trend (Agee et al., 1982) of early Cr- and Al-rich spinels is followed by late-stage crystallization of spinels enriched in Fe^{3+} and Ti. The spinel commonly occurs in groundmass kimberlite and can be primary or from xenoliths. Most of macrocrysts of spinel-group minerals are likely to be xenocrysts from garnet-bearing peridotite due to compositional overlap between macrocryst and xenoliths (Schulze, 2001). One grain analyzed (CHAR 1_0024) have strong Fe depletion from core to rim (Table 4) and have presents reaction rim resulted by interaction with kimberlitic magma, can evidence a primary phase.

Macrocrysts of aluminium magnesio-chromite can be phenocrysts formed in the early stages of kimberlite crystallization (Mitchell 1986). However, small euhedral spinels of identical composition occur in matrix olivine in some kimberlites, and the trends of small euhedral and macrocrysts in terms of Cr/(Cr + Al) and Fe^{2+}/(Fe^{2+} + Mg) is identical to that of spinel-group minerals from xenoliths (Schulze, 2001). The Cr# values increase with the evolution of partial melting. The Charneca spinel exhibit variable Cr# (Cr/(Cr + Al) (0.29 -– 83

0.83) and this range can indicate a garnet peridotite source (Schulze, 2001). In addition, the lower Cr/(Cr + Al) values (< 0.5) can indicate equilibrium with Mg-rich peridotite and are xenocrysts from less strongly depleted peridotite. However, the high values Cr# (>0.6 or >0.8) and low Ti (Bhat et al., 2017) are characteristics of depleted peridotite, and can indicate a "primary fertile" peridotite.

The interaction between residual peridotites with MORB composition melts (Ti-rich), become the spinels enricher in TiO_2 without increasing their Cr#. (Pearce et al., 2000). Some spinels from Charneca have low Ti contents typically < 0.09 wt.% but others have higher concentration of 0.4 – 2.3 wt.% and in addition to low and high Cr#, they reflect complex origin of the host peridotites.

Trace element characteristics, including mobile elements and $^{87}Sr/^{86}Sr$ ratios are typically used to explore crustal contamination in kimberlite magma (Sarkar et al., 2014). The more evolved and isotopically enriched upper crust would modify the magma to a greater degree, and the bulk rock compositions of kimberlites are sensitive to the effects of contamination and post-emplacement alteration. Strontium isotope compositions can also be used as supporting evidence against significant crustal contamination of the magma from which the perovskite crystallized.

The average of isotopic data are compared with perovskites $^{87}Sr/^{86}$ Sr ratios from APIP kimberlites (Guarino et al., 2013) and bulk-rock data from Group I and II kimberlites (Becker & Le Roex, 2006; Skinner et al., 1992, Woodhead et al., 2009). Fig. 24 show the perovskite $^{87}Sr/^{86}$ Sr ratios from Charneca kimberlite and occur an overlapping between APIP perovskites and bulk-rock of Group I. On average, the ratios Charneca acquired are higher than APIP rocks, no sufficiently for equal to Group II. This transitional character was previously reported (Gibson et al., 1995; Guarino et al., 2013; Melluso et al., 2008). The Charneca present variable $^{87}Sr/^{86}Sr_i$ ratios (0.705082 to 0.707388) than APIP rocks (0.70506–0.70565; data from Guarino et al., 2013) and Group I kimberlites (0.70328 to 0.70537; data from Becker & Le Roex, 2006).

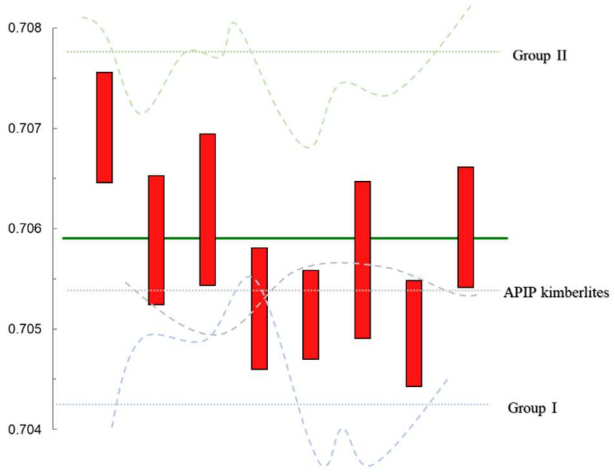

Fig. 24. $^{87}Sr/^{86}Sr$ perovskite data from Charneca compared with $^{87}Sr/^{86}Sr$ perovskite data for APIP kimberlites (Guarino et al., 2013) and bulk-rock from Group I and Group II kimberlites (Becker and Le Roex, 2006).

These suggested that the Sr isotope compositions from groundmass perovskite are more representative of the uncontaminated kimberlite magma than those from bulk rock studies, which are often contaminated (Paton et al., 2007). Therefore, the major variance between bulk rock and perovskite analyses is more marked for fragmental, massive volcaniclastic or pyroclastic kimberlites (Sarkar et al., 2014). The Charneca kimberlite does not have uniform Sr isotopic compositions, as is seen in some APIP rocks and Indian and Chinese kimberlites (Guarino et al., 2013; Woodhead et al., 2009), suggesting major upper crustal contamination.

The Charneca perovskites also are compositionally similar to other kimberlitic perovskite (e.g. Kuruman kimberlites; Donnelly et al., 2011), and show considerable enrichment in REE, Nb, Th and Na, and typically shows the highest concentrations of REE. The compositional variation between different perovskite types within Charneca kimberlite point to multiple generations of perovskite, and probably reflect different crystallization conditions (Chakhmouradian and Mitchell, 2001), as perovskite can crystallize over a wide range of pressure-temperature conditions, and under differing activities of minor elements.

A progressive assimilation of crustal material into the kimberlite magma, through melt-wall-rock interactions over the range of perovskite crystallization temperatures, can result in compositional and isotopic variations in perovskite (Malarkey et al., 2010). Another evidence that can suggest a crustal contamination are La/Yb values of the perovskites (403 and 989)

relative to the whole-rock samples are consistent with contamination after the crystallization of the perovskite Mitchell & Reed (1988).

APÊNDICE 2 – Kimberlito Grota do Cedro

Petrology and Geochemistry minerals of the Grota do Cedro kimberlite, West of Minas Gerais, Brazil

Summary

1. Introduction

The combination of materials from different origins during the ascension and emplacement of kimberlites makes for the complexity of studying such rocks. Also, being composed of minerals that are highly susceptible to alteration, kimberlites are even more difficult to understand and reconstruct in terms of primary magma characteristics. Their ultramafic, potassic and volatile-rich character and their significant amounts of compatible and incompatible trace elements suggest derivation from mantle source regions with a complex evolutionary history (Becker and Le Roex, 2006).

Potassic-ultrapotassic magmatic events gave rise to the Alto Paranaíba Igneous Province (APIP), the largest potassic–ultrapotassic occurrences in the world, which occupies approximately ~3,000 km^2 and >15000 km^3 to the northeast of the Paraná Basin and to the southwest of the São Francisco craton (Almeida, 1983; Araújo, et al., 2001; Bizzi et al., 1993, 1994; Gibson et al., 1995; Gomes & Comin-Chiaramonti, 2005; Ulbrich & Gomes, 1981). The province consists of several alkaline-carbonatite plutonic complexes, kamafugites, kimberlites and lamproites (Almeida, 1983, Almeida & Svisero 1991, Leonardos et al. 1991, Gibson et al. 1995, Brod et al. 2000, 2004, Comin-Chiaramonti et al. 2005, Carlson et al. 2007).

The significant diamondiferous kimberlites that occur within APIP have been subject of numerous studies (Andrade and Chaves, 2011; Chaves, 2012; Karfunkel et al., 2014; Pereira, et al., 2017; Svisero, 1995; Tompkins and Gonzaga, 1989). Moreover, in the context of APIP, these rocks present an opportunity to investigate partial melting processes that took place in deeper levels of the Earth's upper mantle (e.g. Araújo, et al., 2001; Carlson et al., 2007; Gibson et al., 1995; Guarino et al., 2013; Marangoni and Mantovani, 2013; Melluso et al., 2008; Natali et al., 2018; Read et al., 2004; Ruberti et al., 2005, 2002).

In this paper, we present new data on the major- and trace-element contents of main minerals phases. We present the first textural characterization of the Grota do Cedro kimberlite, also known as Douradinho-8, located to the southeast of Coromandel city, Minas Gerais, Brazil (Fig. 2.1). This work aims to contribute to the characterization of this kimberlitic intrusion, which so far has been poorly studied for petrology and chemistry, as well as to the understanding of its emplacement in the context of the Alto Paranaíba Igneous Province.

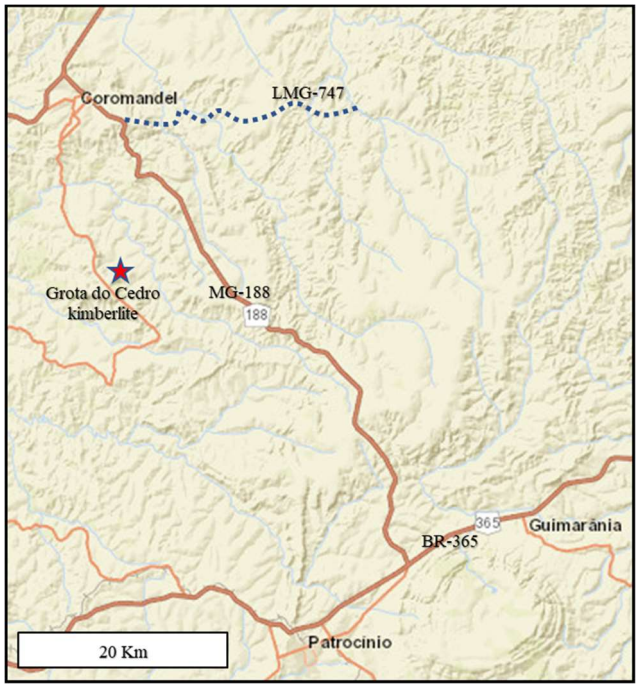

Figure 2.1. Location of the Grota do Cedro kimberlite (red star) near Coromandel and Patrocínio cities.

2. Geological Setting of Grota do Cedro kimberlite

The alkaline APIP rocks intruded into Proterozoic metamorphosed crustal sequences of the Brasilia mobile belt (Almeida et al. 2000) during the Late Cretaceous (~90–75 Ma; Gibson et al. 1995, Sgarbi et al. 2004, Gomes & Comin-Chiaramonti 2005, Carlson et al. 2007).

The Grota do Cedro kimberlite makes abrupt contact with mica schists of the Araxá Group, a Neoproterozoic sedimentary unit in the Brasilia mobile belt (Dardenne, 2000) (Fig. 2.2). This kimberlite body occupies a low-lying drainage system of the Grota do Cedro stream, a Douradinho river tributary. Radiometric outline works (Andrade and Chaves, 2011) demonstrated that the intrusion forms an elliptic body with a slightly longer E-W axis (350 m) than the axis (300 m).

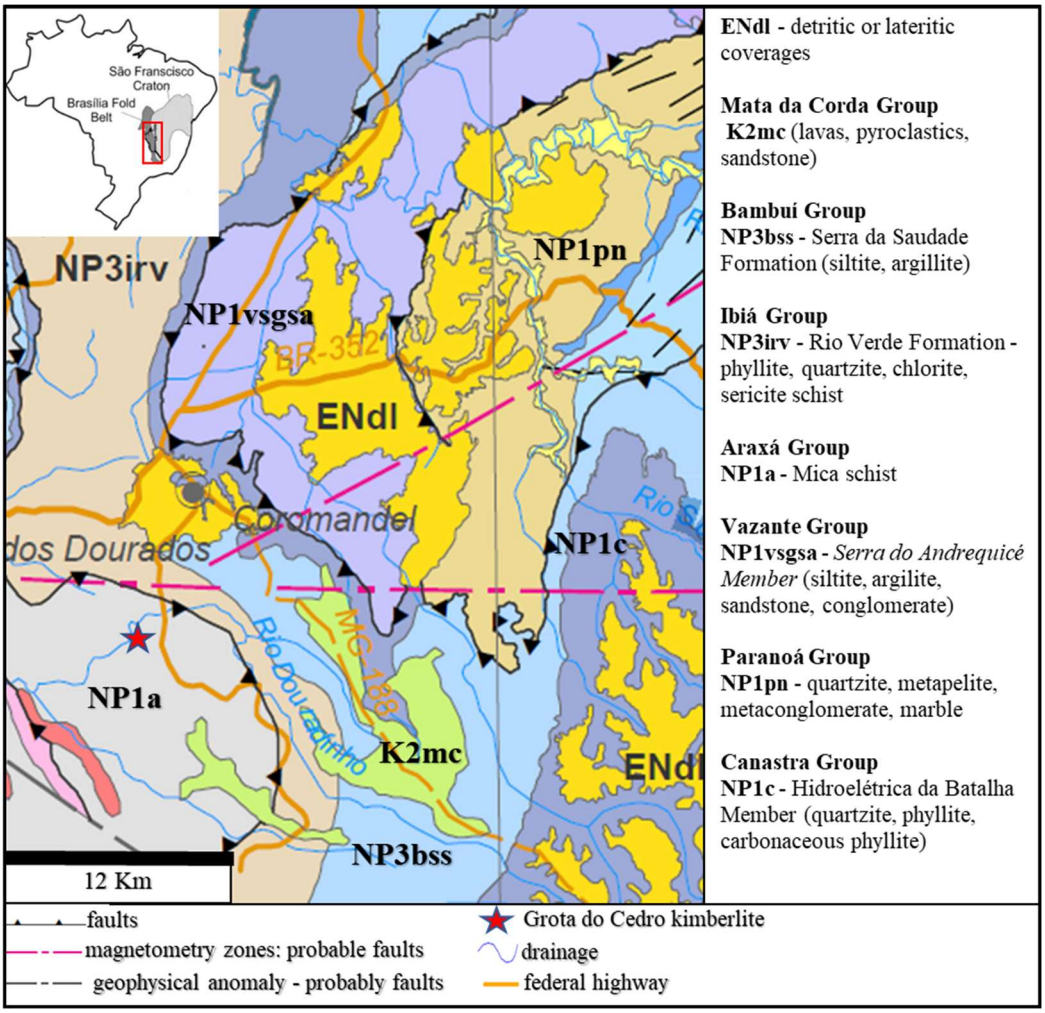

Figure 2.2. Geology and geotectonic setting of the Grota do Cedro kimberlite (red star). (Modified from CPRM, 2014).

The Grota do Cedro kimberlite was discovered in 1970. No relation between the intrusion and diamonds that are found in many streams and rivers of the region has been established so far (Chaves et al., 2006).

This occurrence was studied by Andrade and Chaves (2011) only. Besides surface delimitation of the intrusion (Andrade & Chaves, 2009), garnet crystals were found to contain significant amounts of chromium (2.18 – 8.72 wt. %), predominantly within G5 and G9 fields as proposed by Grütter et al. (2004). According to Andrade and Chaves (2011), the Grota do Cedro kimberlite bears strong textural similarities with the Vargem-1 kimberlite, an intrusion located nearby to the East.

3. Petrography

In general, the Grota do Cedro kimberlite shows inequigranular, moderately to poorly sorted matrix-supported textures. Clast-supported textures are locally present. Coarse ash- to medium-lapilli-sized juvenile fragments and accessory clasts of country and mantle xenoliths, discrete olivine pseudomorphs and phlogopite macrocrystals are common, set in an interstitial medium dominated by carbonates and serpentine (Fig 2.3).

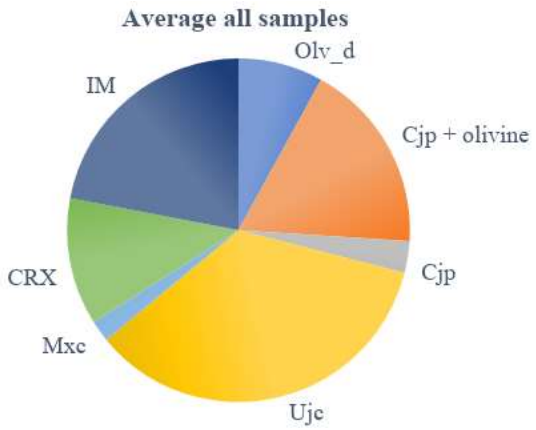

Figure 2.3 Estimated average composition of the Grota do Cedro kimberlite. Olv_d = discrete olivine macro and phenocrysts. Cjp + olivine = cored juvenile pelletal ash-lapilli with olivine core. Cjp = cored juvenile pelletal ash-lapilli (excluding constituent olivine). Ujc = uncored juvenile clasts. Mxc = mantle-derived xenocrysts (eg. phlogopite and garnet). CRX = country rock xenoliths. IM = interstitial medium. All olivine crystals are pseudomorphs.

Almost all of the kimberlitic material analyzed in this work occurs as uncored and cored juvenile clasts within a fine interstitial medium with local replacement texture and predominance of carbonate.

The cored juvenile clasts range from ash to lapilli in size and occur in several shapes, controlled by core size and shape, often consisting of phlogopite and olivine and, occasionally country rock fragments. Single and multiple symmetrical and asymmetric, complete and incomplete rims are observed. Six different types of uncored juvenile clasts are recorded, ranging from ash to lapilli in size, with varied shapes and angular to amoeboid margins that reflect different deformation levels. The juvenile clast types are detailed above.

Most crustal xenoliths of the Grota do Cedro kimberlite correspond to schists from the Araxá group. They occur in elongated, angular to sub angular shapes, reaching up to 12 mm in size. Very rare ones constitute cores of pelletal lapilli, mainly as single occurrences in the interstitial medium or encompassed by kimberlitic clasts. Less than 2% of single crystals occupy the interstitial medium (with the exception of discrete olivine crystals), mainly phlogopite and garnet macrocrystals.

3.1 Texture

The Grota do Cedro kimberlite usually shows a matrix-supported texture. Occasionally, the texture is clast-supported. Sorting is moderate to poor in both macroscopically and microscopically samples (Fig. 2.4). In most samples, clasts are predominantly supported by a finer-grained interstitial medium. Locally, flow orientation is evidenced by the alignment of macrocrystals of phlogopite.

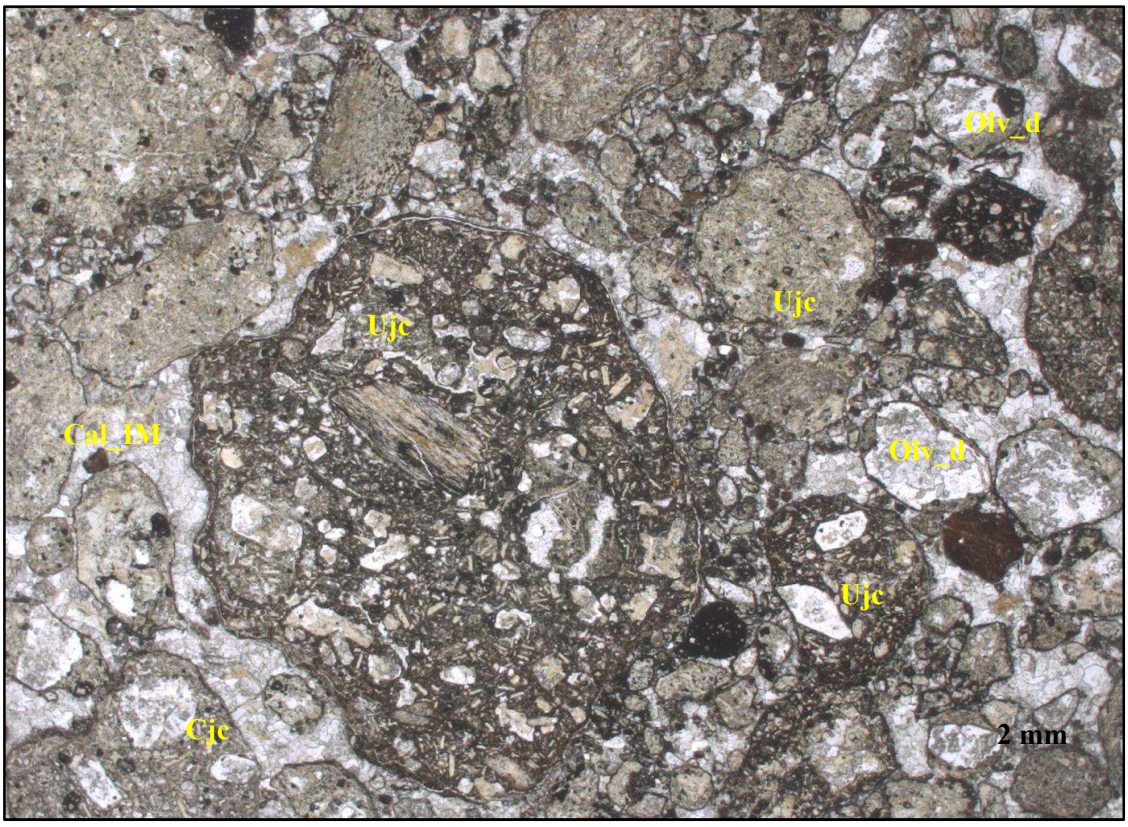

Figure 2.4 Microscopic matrix-supported texture of the Grota do Cedro kimberlite. Olv_d = discrete olivine macro and phenocrysts. Cjp + olivine = cored juvenile pelletal ash-lapilli with olivine core. Ujc = uncored juvenile clasts. Calc_IM = interstitial medium dominated by calcite.

3.2 Interstitial medium

The origin of the interstitial medium of kimberlites is generally ambiguous. Whether it is primary, secondary pore-filling cement or a replacement of original fine-grained ash matrix is contentious (Porritt et al., 2012). The most common interstitial medium observed in the Grota do Cedro kimberlite consists of a well-crystallized carbonate (mainly calcite), locally with large crystals and granoblastic texture (Fig 2.5), a mixture dominated by serpentine, clay and carbonates was also observed, resulting in a light brown yellowish interstitial medium with a cement aspect.

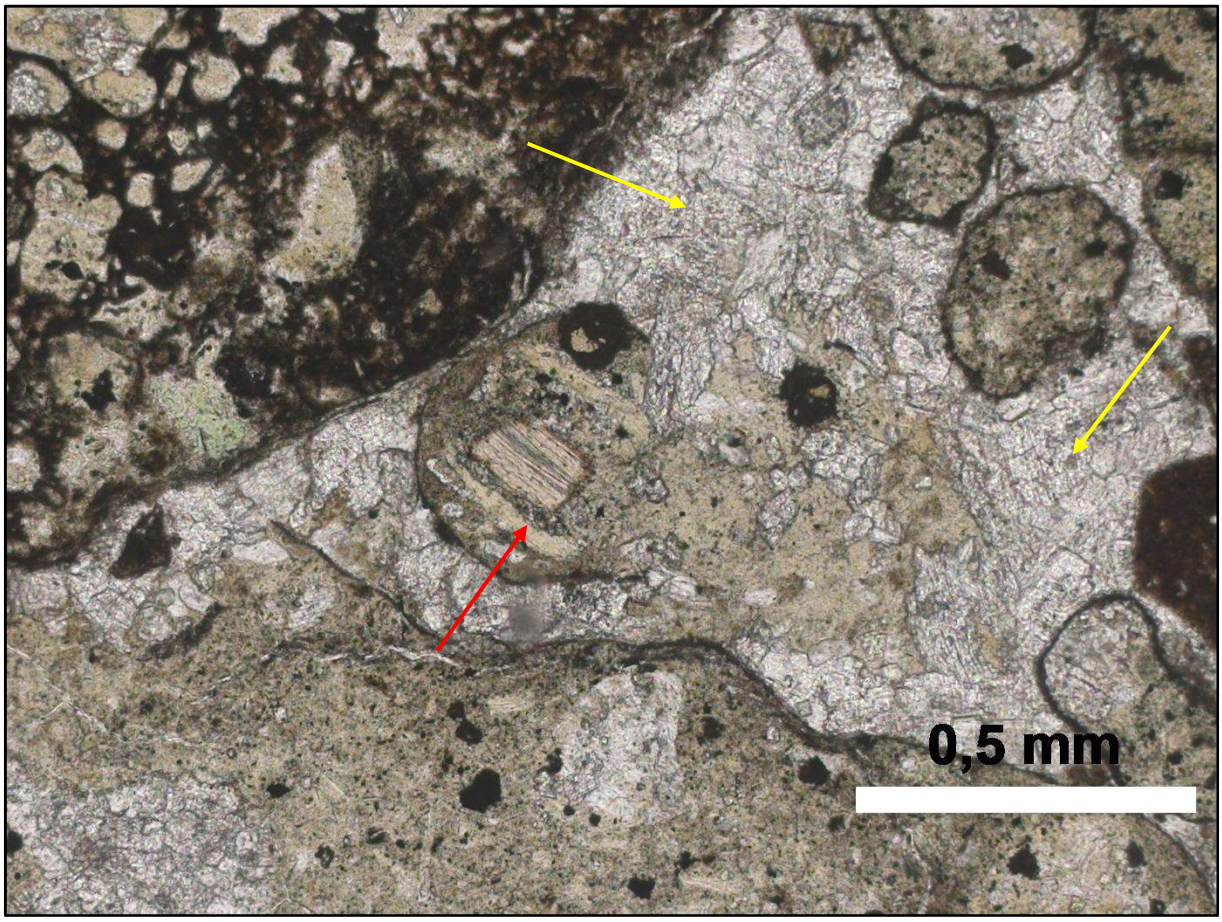

Figure 2.5 Interstitial medium in the Grota do Cedro Kimberlite. Note the well crystallized calcite that composes the interstitial medium (yellow arrows); serpentine also occurs, resulting in a light brown yellowish color. To the center, a cored juvenile ash (red arrow) partially replaced with serpentine calcite interstitial medium.

3.3 Juvenile Clasts

Magma clasts form in vents during explosive eruptions, the term “juvenile” referring to solidified material, in this case, a volcanic rock clast preserved in deposits (Cas et al., 2008). In volcanological nomenclature, juvenile pyroclasts are generated by disruption as a direct result of volcanic action (Schmid, 1981). In kimberlites, however, the term refers to either magmatic or clastic; “juvenile clast” being used loosely for juvenile pyroclasts and juvenile pseudo-clasts (produced by alteration and replacement processes), excluding discrete (free) crystals and xenoliths (Webb, 2006). Juvenile magmaclast was introduced by Field and Smith (1998), a non-genetic term that encompasses all juvenile clasts and discrete cognate crystals.

The approach of Cas et al. (2008) was taken for the discrimination of the different components of the Grota do Cedro kimberlite. For the description and characterization of juvenile clasts, the non-genetic scheme of Webb (2006) was used, as summarized in tables 2.1 and 2.2.

3.3.1 Kimberlite lithic clasts

Kimberlite lithic clast refers to a co-magmatic kimberlite that solidified deeper in the vent and was then incorporated (Cas et al., 2008). In the Grota do Cedro kimberlite, six types of kimberlitic clasts (Fig. 2.6) are observed that differ in modal abundance, shape and frequency. A descriptive approach is summarized in Table 2.1, following the terminology of Webb (2006).

Type A clasts have well-defined margins and are characterized by elongated shapes, angular, sub-irregular to irregular curvilinear outlines, and by being moderately vesicular, with unfilled, irregular and elongate shapes. This is the only type that occurs in bottle-like shapes. They are composed of moderately abundant subhedral pseudo-olivine phenocrysts (10%), highly abundant euhedral phlogopite and atoll spinel (25% and 20%, respectively) and less than 1% of perovskite (<1%), set in a very poorly crystallized, spinel oxide opaque serpentine green interstitial medium.

Type B clasts are composed of less than 1% olivine microphenocrystals, a low abundance (3%) of perovskite, and rare (<1%) orange spinel single crystals with octahedral habit, set in a very poorly-crystallized, opaque spinel phlogopite brown interstitial medium.

Clasts have distinct margins, with elongate and rounded forms, irregular curvilinear outlines and are non-vesicular.

Equant, rounded, smoothly curved and irregular sparsely vesicular juvenile clasts type C have well-defined margins and are composed of moderately abundant (12%) pseudo-olivine, highly abundant (25%) euhedral salmon phlogopite and small amounts of atoll spinels (8%). The interstitial medium is poorly-crystallized, with speckled diopside, opaque oxide, spinel and serpentine. This is the only type of clasts composed of salmon color phlogopite, and its occurrence is restricted.

Type D juvenile clasts are composed of euhedral, single and intergrown olivine phenocrystals (18%), with a moderate abundance of phlogopite and perovskite (15% and 10%, respectively), and significant amounts (30%) of spinel microlites, set in a poorly crystallized, yellowish green serpentine interstitial medium. Clasts have well-defined margins, elongate shapes, sub-angular and irregular curvilinear outlines, being sparsely to moderately vesicular, with partially filled elongate to irregular and rounded vesicles. This is the only type that occurs with tube-shaped (Fig. 2.7).

Type E clasts have well-defined margins, elongate to subequant shapes, sub-rounded, sub-irregular to irregular curvilinear outlines, are moderately to highly vesicular, with spherical and irregular vesicles filled by carbonate and serpentine. They are composed of euhedral, single and intergrown olivine crystals (25%), a high abundance (35%) of phlogopite up to 1.10mm wide, and a low abundance of spinel, atoll spinel and perovskite (5%, 8%, 5%, respectively), set in a very poorly crystallized, phlogopite spinel opaque serpentine light brown interstitial medium.

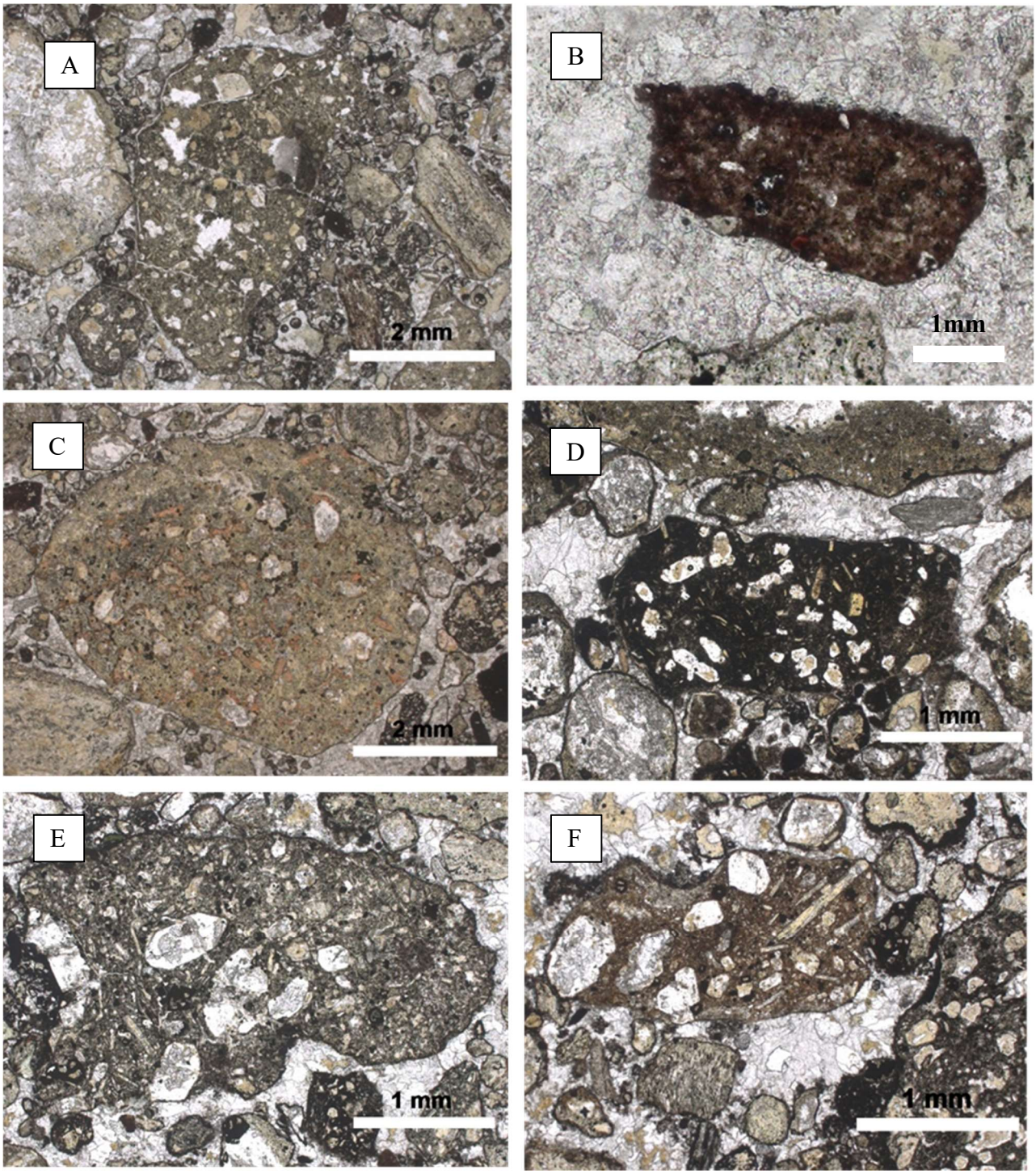

Figure 2.6 – Six types (A to F) of uncored juvenile clasts in the Grota do Cedro kimberlite, distinguished among themselves based on relative mineral abundance and shape.

Table 2.1 - Petrographic characteristics summary of uncored juvenile clasts of the Grota do Cedro kimberlite.

	MORPHOLOGY	VESICULARITY	CLAST-HOST RELATIONSHIP	MINERALOGY	INTERSTITIAL MEDIUM CRYSTALLINITY	SIZE RANGE
A	El / Ang / SbI - Ia	Moderately vesicular no filled. Irregular and sometimes with elongate form.	Well-defined margins clast set in a clay and carbonate interstitial medium.	Olivine: moderate (10%), subhedral, medium to coarse (0.28-0.82mm). Phlogopite: high (25%), euhedral, micro to fine crystals (up to 0.20mm). Spinel and atoll spinel: high (20%), sub-euedral, micro to fine crystals (<0.07). Perovskite: low (1%), sub-euhedral, microcrystals (<0.08 mm).	Very poorly crystallized, spinel oxide opaque serpentine green interstitial medium.	Lapilli (2.0 - 5.0mm)
B	El / R / Ic	Non-vesicular	Defined margins clast set in a crystallized carbonate interstitial medium.	Pseudo-olivine: low (1%), micro (<0.06mm). Perovskite: low (3%), subhedral, microcrystals. Orange spinel: Low (<1%), euhedral, microcystal (0.03mm).	Very poorly-crystallized, opaque spinel phlogopite brown interstitial medium.	Ash(<0.60 mm)
C	Eq / R / Sc	Sparsely vesicular. Irregular shape and no fill.	Well-defined to diffuse margins clast set in carbonate cement.	Pseudo-olivine: moderate (12%), sub-euhedral single crystals, medium to coarse (0.32-0.61mm). Phlogopite: high (25%), euhedral, fine to medium (0.13-0.44mm). Atoll spinel: low (8%), euhedral, fine (up to 0.10mm).	Poorly-crystallized green interstitial medium with speckled diopside, oxide opaques, spinel and serpentine.	Lapilli (2.0 - 5.0mm)
D	El/ SbA / Ic	Sparsely to moderate vesicular, with elongate to irregular and rounded shapes partially filled.	Well-defined margins clast set in a cement and carbonate interstitial medium.	Pseudo-olivine: moderate (18%), euhedral single and intergrowth crystals, fine to medium (0.06 - 0.32mm). Phlogpite: moderate (10-15%), euhedral and deformed, micro to fine crystals (< 0.14 mm). Perovskite: moderate (10%), euhedral, microcrystals. Spinel: high (30%), euedral-anhedral, microlites.	Poorly-crystallized, serpentine brown interstitial medium.	Ash to lapilli (1.6 - 2.48mm)
E	SbE/ SbR / SbI	Moderately to highly vesicular, spherical and irregular shapes filled by carbonate and serpentine.	Defined margins clast set in a cement and carbonate interstitial medium.	Pseudo-olivine: moderate (25%), euhedral and multiple intergrowths, fine to coarse (0.09-0.86mm). Phlogpite: high (35%), euhedral, micro to coarse crystals (up to 1.10mm). Spinel: low (5%), euedral, microcrystals. Perovskite: low (5%) subhedral, microcrystals. Atoll spinel: low (8%), sub-euedral, micro to medium (up to 0.10mm).	Very poorly crystallized, phlogopite spinel opaque serpentine greenish-brown interstitial medium.	Ash to lapilli (1.0 - 6.0 mm)
F	El / SbR / Ic	Sparsely vesicular; elongate shape partially filled vesicles.	Defined to defined margins set in a cement.	Pseudo-olivine: moderate (15%), euhedral single crystals and multiple intergrowths, fine to coarse crystal (0.10-o.51mm). Phlogopite: moderate (10%), euhedral, fine to coarse (0.10-0.71mm). Atoll spinels: low (3%), euedral, micro to fine crystals (0.06-0.10mm). Spinel: Low (2%), sub-euhedral, microcrystals.	Light brown very poorly-crystallized opaque minerals interstitial medium.	Lapilli (2.5 - 6.50 mm)

Sphericity: Elongate (El); Subelongate (SbE); Subequant (SbQ); Equant (Eq).

Roundness: Well-rounded (Wr); Rounded (R); Sub-rounded (SbR); Sub-angular (SbA); Angular (Ang).

Irregularity: Smoothly curved (Sc); Subirregular (SbI); Irregular curvilinear (Ic); Irregular ameboid (Ia).

Elongate, sub-rounded, irregular curvilinear outlines, defined margins with partially filled, sparsely elongate vesicles characterize Type F clasts. They are composed of a moderate abundance (15%) of euhedral, single and multiple intergrown olivine phenocrystals (up to 0.51mm wide), a moderate abundance (10%) of euhedral phlogopite (up to 0.71mm) and low amounts of spinel and atoll spinel (~2%), set in a very poorly-crystallized opaque light brown interstitial medium.

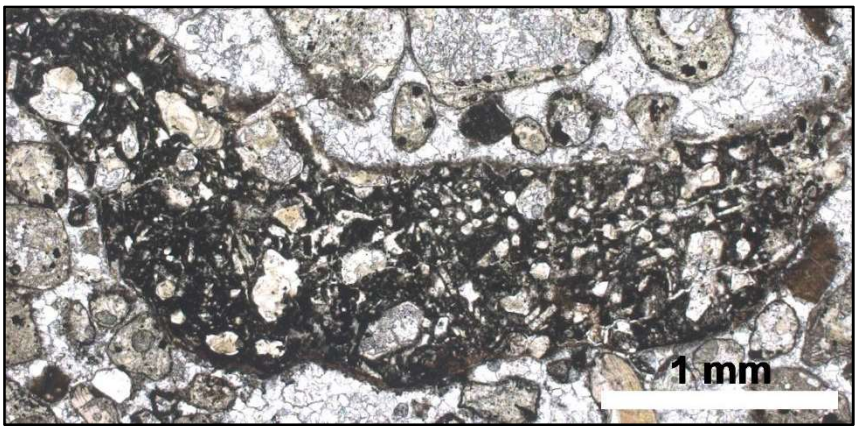

Figure 2.7 – Tube-shaped exhibited by Type D clasts, evidencing a different viscosity than other clast types.

Fig. 2.8 shows the composition and frequency of uncored juvenile clasts in the Grota do Cedro kimberlite. Phlogopite phenocrystals prevail in almost all the recorded clasts (except for B clasts). Discrete olivine grains are common, with euhedral shapes, all replaced with serpentine. Oftentimes, atoll spinel rims olivine grains (Fig. 2.9).

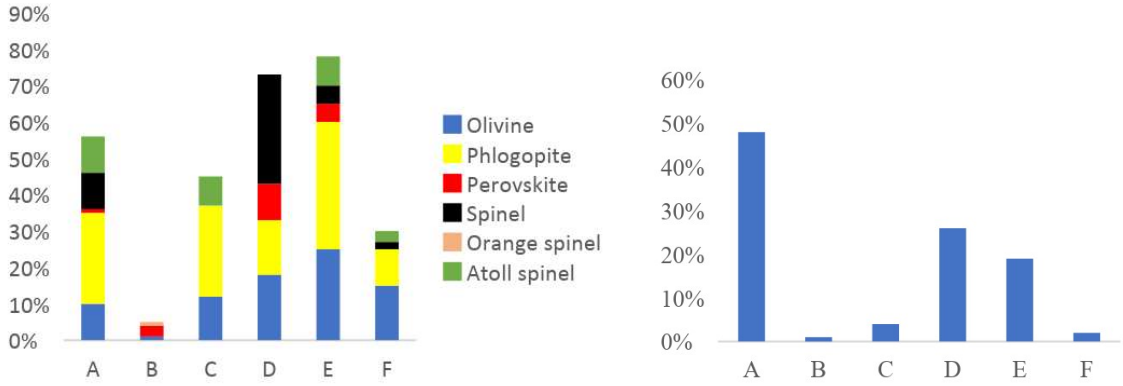

Figure 2.8 – Composition (a) and estimated abundance (b) of uncored juvenile clasts. Mineral frequency within juvenile clasts is also conditioned to the alteration degree and may not reflect the kimberlitic clast primary composition.

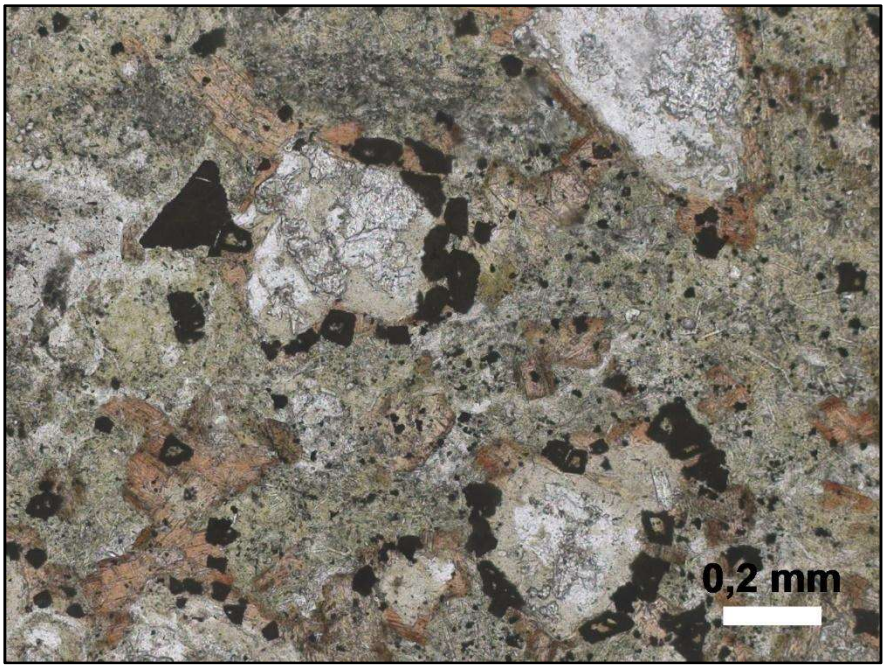

Figure 2.9– Atoll-spinel surrounding olivine pseudomorphs, totally replaced with calcite and serpentine of Type C clast interstitial medium. Salmon phlogopite is also abundant.

3.3.2 Pelletal structures

Pelletal structures encompasses all round to elliptical juvenile clasts of ash, lapilli or bomb size composed of variably crystallized kimberlitic material with core. Crystal shell arrangement can or can not reflect flow. When clasts or crystals show alteration rinds, they are called pseudo- pelletal lapilli (Cas et al., 2008). Pelletal or ash lapilli represent the interface between volatile components and the erupting magma (Lloyd and Stoppa, 2003).

Eight types of cored juvenile pelletal ash/lapilli are predominant in the Grota do Cedro kimberlite, with symmetrical and asymmetrical cores composed mainly of altered and deformed phlogopite and olivine crystals. A single rim is more commonly found, however pelletal forms occur with multiple rims in different sizes and compositions (Table 2.2, Fig. 2.10).

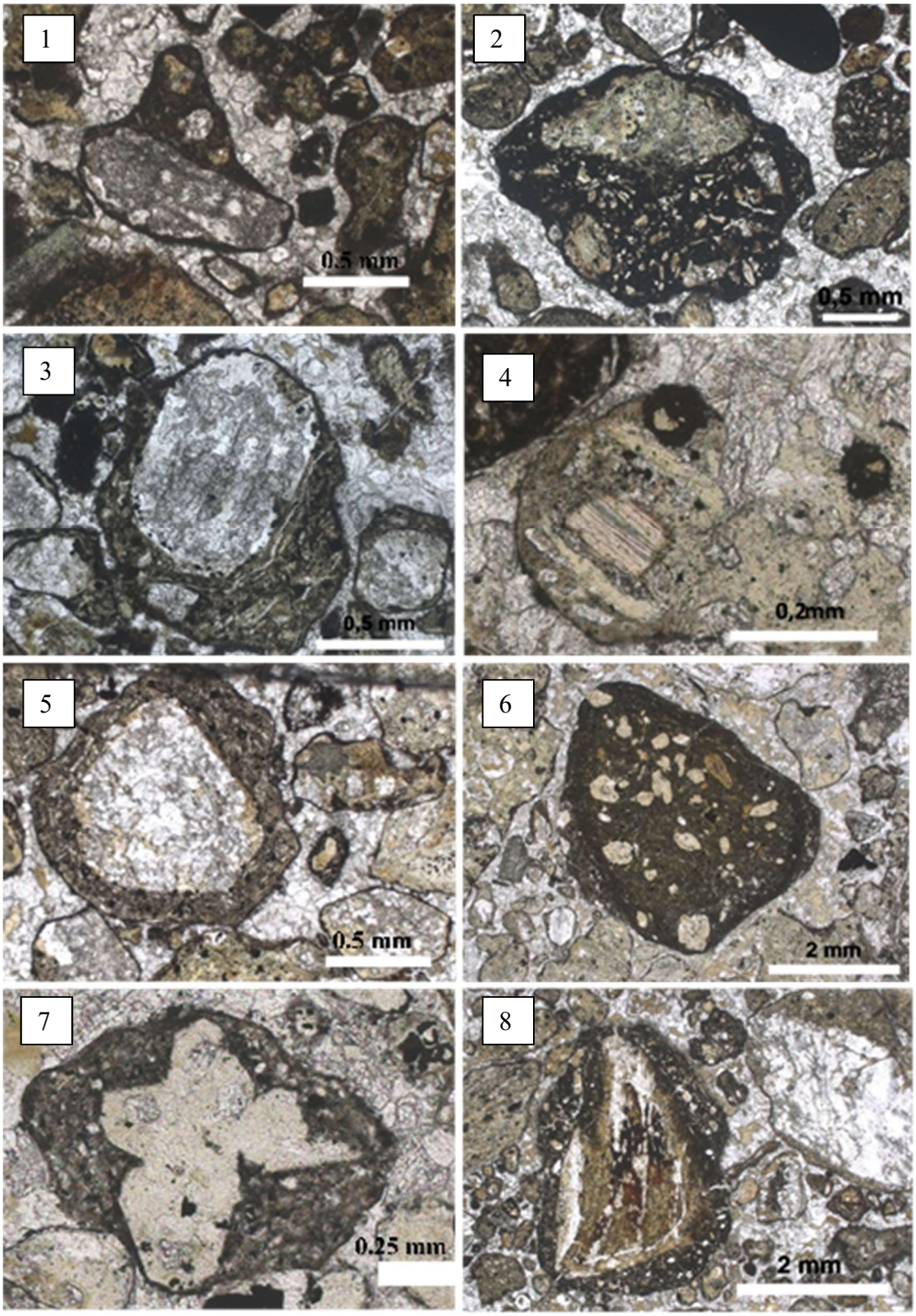

Figure 2.10 – Eight types of cored juvenile clasts of the Grota do Cedro kimberlite. The shape of the pelletal is in accordance with the shape of the nucleus. Olivine pseudomorphs are the main core constituent. Phlogopite crystals are also very common, however less frequent.

Table 2.2 Petrographic characteristics summary of core juvenile clasts of the Grota do Cedro kimberlite.

	MORPHOLOGY	INTERNAL STRUCTURE		VESICULARITY	CLAST-HOST RELATIONSHIP	MINERALOGY	INTERSTITIAL MEDIUM CRYSTALLINITY	SIZE RANGE
		Type of core	Rims					
1	Eq / R / Ic	core: olivine	Single, asymetrical, incomplete, super thin micro rim.	Non-vesicular.	Defined margins clast set in a well-crystallized carbonate interstitial medium.	Rim: phlogopite, perovskite, opaque minerals.	Rim: brown poorly-crystallized interstitial medium.	cored juvenile pelletal ash (0.65-1.0 mm)
2	Eq / Wr / Sc	core: sub-euhedral serpentinized olivine	Single, symetrical, complete, ultra thin rim.	Non-vesicular.	Defined margins clast set in a well-crystallized carbonate interstitial medium.	Rim: phlogopite, spinel, oxide opaque, serpentine (clast type C).	Rim: dark brown poorly-crystallized interstitial medium.	cored juvenile pelletal ash/lapillli (1.5 2.0 mm)
3	Eq / SbR / SbI	core: olivine	Single, asymetrical, incomplete, super thin micro rim.	Non-vesicular.	Defined margins clast set in a clay and well-crystallized carbonate interstitial medium.	Rim - oriented phlogpite, spinel and opaques (clast B) crystals.	Rim: very poorly crystallized, spinel oxide opaque serpentine green interstitial medium.	cored juvenile pelletal ash (0.5 - 1.12mm)
4	Eq / Wr / Sc	core: phlogpite	Single, symetrical, complete, ultra thin rim.	Non-vesicular.	Defined to diffuse margins set in a well-crystalized carbonate serpentine interstitial medium.	Rim: perovskite, spinel, oxide opaque and serpentine.	Rim: poorly-crystallized green interstitial medium.	cored juvenile pelletal ash (< 1.0 mm)
5	Eq / Wr / SbI	core: Olivine replaced by interstitial medium material	Single, symetrical, complete, ultra-super thin micro rim.	Non-vesicular.	Well-defined margins clast set in a well-crystallized carbonate interstitial medium.	Rim - oriented phlogpite, spinel and perovskite crystals.	Rim: very poorly crystallized, spinel oxide opaque serpentine green interstitial medium.	cored juvenile pelletal ash (<1.2 mm)
6	Eq / Wr / SbI	core: kimberlitic clast	Multiple rims, asymetrical, complete, super thin micro-rims.	Non-vesicular.	Well-defined margins clast set in a clay serpentine carbonate interstitial medium.	Core: olivine (15%, sub-euhedral, fine to coarse 0.13-0.59mm) and perovskite (5%, sub-euhedral, fine <0.21mm). Internal rim: altered oriented spinel, oxide opaques and perovskite crystals; oriented pelletal ash. External rim: rich oriented phlogopite, spinel, perovskite, oxide opaque crystals.	Core: spinel phlogopite opaque interstitial medium. Rims: greenish-brown poorly-crystallized interstitial medium.	cored juvenile pelletal lapilli (2.0 - 4.5mm)
7	SbE / R / SbI	core: intergrowth olivine crystal	Single rim, symetrical, incomplete, ultra thin rim.	Non-vesicular.	Well-defined margins clast set in a clay serpentine carbonate interstitial medium.	Rim: perovskite, spinel, oxide opaque and serpentine with high alteration degree.	Rim: very poorly-crystallized greenish-brown interstitial medium.	cored juvenile pelletal ash (<1.0mm)
8	SbE / SbR / SbI	core: altered phlogopite	Single rim, asymetrical, complete, very thin micro-rim.	Non-vesicular.	Defined margins clast set in a clay serpentine carbonate interstitial medium.	Rim: olivine (10%, euhedral, micro-medium 0.10-0.32mm).	Rim: poorly-crystallized phlogopite spinel perovskite dark brown interstitial medium.	cored juvenile pelletal lapilli (2.0 - 6.0mm)

Sphericity: Elongate (El); Subelongate (SbE); Subequant (SbQ); Equant (Eq).

Roundness: Well-rounded (Wr); Rounded (R); Sub-rounded (SbR); Sub-angular (SbA); Angular (Ang).

Irregularity: Smoothly curved (Sc); Subirregular (SbI); Irregular curvilinear (Ic); Irregular ameboid (Ia).

Type 1 has defined margins and is equant, rounded, irregular curvilinear, non-vesicular, cored manly by altered olivine. The single, asymmetrical, incomplete super-thin micro-rim is composed of phlogopite, perovskite, opaque minerals set in a brown poorly- interstitial medium.

Type 2 has equant shape, well-rounded and smoothly curved outlines, defined margins and is non-vesicular. The single, symmetrical, complete, ultra-thin rim reproduces the shape of the serpentinized olivine core and comprises microcrystals of phlogopite, spinel, oxide opaque, serpentine set in a dark brown poorly-crystallized interstitial medium.

Cored mainly by kimberlitic olivine, Type 3 juvenile pelletal ashes are typically subequant, sub-rounded, sub-irregular and non-vesicular. They consist of single, asymmetrical, incomplete, super-thin micro-rims composed of oriented phlogopite, spinel, and opaque minerals set in a very poorly crystallized, spinel oxide opaque serpentine green interstitial medium.

Type 4 clasts have defined to diffuse margins and are equant, well-rounded, smoothly curved, non-vesicular, cored by phlogopite. They are characterized by single, symmetrical, complete, ultra-thin rims. The internal rim is composed of perovskite, spinel, oxide opaque and serpentine set in a poorly-crystallized green interstitial medium.

Type 5 pelletal structures are cored by interstitial replacement of olivine with medium material, with well-defined, typically elongated margins, being well-rounded, sub-irregular, and non-vesicular. The single, symmetrical, complete, very thin micro-rim mimics the shape of the core, consisting oriented phlogopite, spinel and perovskite crystals.

Type 6 structures have well-defined margins, equant shapes, well-rounded and sub-irregular outlines, are non-vesicular, cored by kimberlitic clast, being composed of moderately abundant olivine (15%) and a low abundance of perovskite (5%) set in a spinel phlogopite opaque interstitial medium. The internal rim consists of oriented altered spinel, oxide opaque, perovskite crystals and oriented pelletal ashes. The external rim is rich in oriented phlogopite, spinel, perovskite and oxide opaque crystals, both set in a greenish-brown poorly-crystallized interstitial medium.

Type 7 occurs as a single, symmetrical, incomplete, ultra-thin rim, which reproduces the shape of the intergrown olivine core. The rim is composed of perovskite, spinel, oxide opaque and serpentine, with a high alteration degree, set in a very poorly-crystallized greenish-

brown interstitial medium. These juvenile clasts have well-defined margins, subequant shapes, rounded and sub-irregular outlines, and are non-vesicular.

Type 8 juvenile pelletal ash are cored mainly by altered phlogopite, being typically subequant, sub-rounded, sub-irregular and non-vesicular. They consist of single, asymmetrical, complete, very thin micro-rims composed of moderate olivine (10%) set in a poorly-crystallized phlogopite spinel perovskite dark brown interstitial medium.

3.4 Accessory lithic clast (country rocks)

Rock fragments of the Grota do Cedro kimberlite of crustal origin correspond mainly to mica schists, probably from Araxá Group. Such fragments are frequent (~12% and up to 12 mm) and occur with elongate shapes and smooth outlines (Fig. 2.11).

Figure 2.11 – Country rock fragments in the Grota do Cedro kimberlite, composed mainly by mica schist.

4. Mineral Chemistry

4.1 Garnet

Garnet is one of the most important mineral species in the study of mantellic processes and also an indicator in diamond exploration. Based on it is chemical composition, a distinction between garnet from different parageneses is possible (Dawson and Stephens, 1975; Hardman et al., 2018; Schulze, 2003). The crustal garnet studied here corresponds mainly to almandine (> 50%) and it is characterized by lower Mg/(Mg+Fe) (0.11 – 0.39), MgO (~ 6.33 wt%), CaO (~ 1.83 wt%) and Cr_2O_3 (~0.03 wt%) values compared to mantle garnet varieties (Mg/(Mg+Fe) = 0.77 – 0.81; 17.89 wt% MgO; ~ 6.11 wt% CaO; ~ 5.22 wt% Cr_2O_3) also studied, which correspond mainly to pyrope (> 60%), with significant amounts of uvarovite (10.36–18.01 wt%). In the classifications of Schulze (2003) and Grütter et al. (2004), the mantellic garnet varieties of Grota do Cedro (Table 5) correspond to peridotitic ones, given their Cr_2O_3 and TiO_2 values. Owing to the positive correlation between CaO and Cr_2O_3, they are identified as lherzolitic, corresponding to the G9 field (Fig. 2.12 B).

The Schulze (2003) classification scheme does not differentiate among pyroxenitic garnet terms. Dawson and Stephens (1975) classify them as G9 (lherzolitic) and G3 (eclogitic). Grütter et al. (2004), however, differentiate among them by the smaller amount of Cr_2O_3 (<4.0%) and MGNUM <0.7, (where MGNUM = (MgO/40.3)/(MgO/40.3 + FeO_t/ 71.85) [oxides in wt%]) compared to lherzolitic varieties, grouping them as G5 garnet. Meanwhile, the classic CaO x Cr_2O_3 diagram of Grütter et al. (2004) separates G5 and G9 fields only by Cr and Ca values, disregarding the limit for MGNUM, showing that field overlap may occur.

Field overlap may lead to misunderstanding as in Andrade and Chaves (2011), who identified Grota do Cedro garnet specimens as pertaining to the G5 group disregarding field overlap. We isolate fields for correct identification (Fig. 2.12. C) and better separation among G5, G9 and G12 occurrences. A MGNUM x Cr_2O_3 x CA_INT diagram is plotted from the present work and Andrade and Chaves (2011) datasets for better field separation.

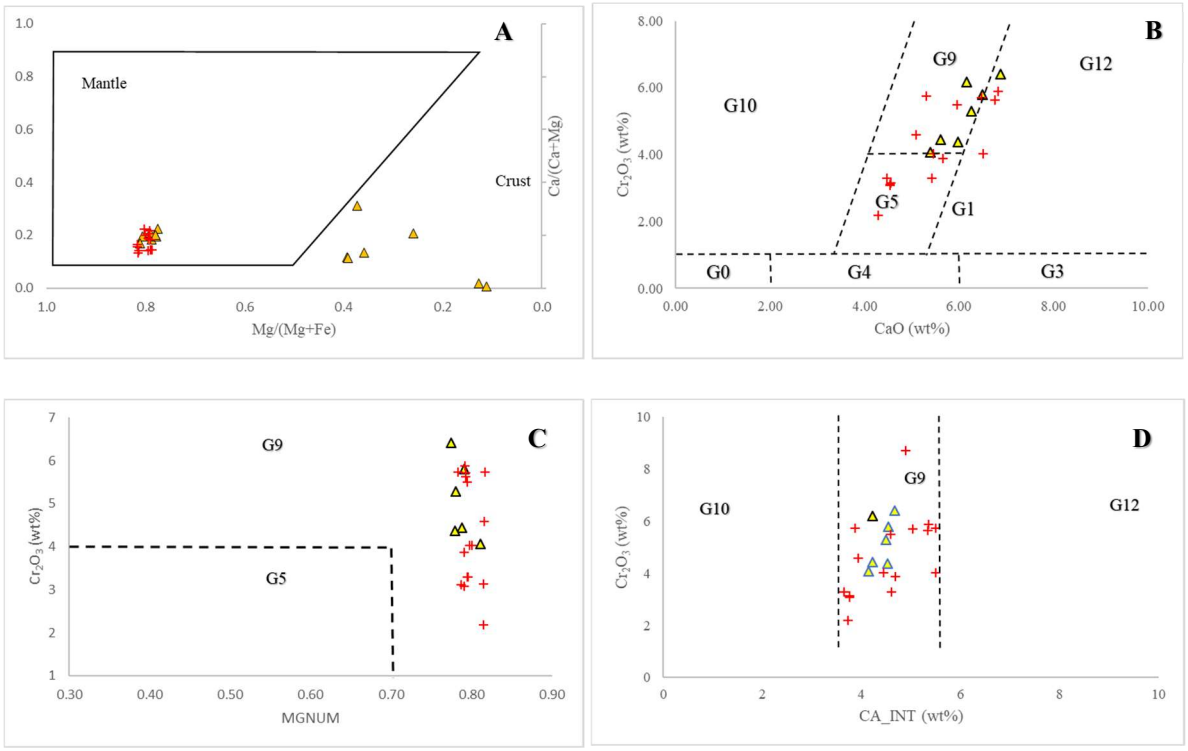

Fig.2.12. Chemical characteristics of garnets from Grota do Cedro kimberlite; the dates of this study (triangle symbol) are plotted together with dataset from Andrade and Chaves (2011) (cross symbol). (a) Distinction between mantle-derived garnets and those from crustal rocks from Grota do Cedro kimberlite, in terms of Mg/(Mg+Fe) and Ca/(Ca+Mg), after Schulze (2003). (b) Cr2O3 vs. CaO diagram of Grota do Cedro garnets, with overlap G9 and G5 field, after Grütter et al. (2004). (c) MGNUM vs Cr2O3 diagram for separation pyroxenitic (G5) from lherzolitic garnets (G9). (d) CA_INT vs Cr_2O_3 for better separation of G9 and G12 fields.

4.2 Spinel

The spinel group minerals from the Grota do Cedro kimberlite analyzed here are compositionally zoned and occur in both euhedral and anhedral forms (Table 2). The former vary from 0.02 mm to 0.15 mm in size, their cores comprising mainly titanian magnesium chromite and titanian chromite (2.50 - 15.19 wt% TiO_2, 4.64 – 56.08 wt% Cr_2O_3, 2.62 – 10.25 wt% MgO, 32.89 – 81.94 wt% FeO and 0.28 – 4.67 wt% Al_2O_3) and less frequently titanian magnesian chromite (4.39 wt% TiO_2, 47.77 wt% Cr_2O_3, 12.19 wt% MgO, 27.97 wt% FeO and 6.94 wt% Al_2O_3) and aluminous spinel (11.84 – 12.33 wt% TiO_2, 1.20 – 1.90 wt% Cr_2O_3, 5.87 – 6.05 wt% MgO, 80.26 – 80.27 wt% FeO and 1.61 – 1.64 wt% Al_2O_3). Discreetly zoned rims overgrow the mineral cores. In chromite rims, the content of Fe and Ti gradually increase, while Cr decreases and Al and Mg vary. In aluminous spinel rims, there is little variation as compared to the cores.

The anhedral spinel grains vary from 0.10 mm to 0.25 mm and correspond to aluminous magnesian chromite (08.30 – 17.10 wt% Al_2O_3, 42.35 – 53.32 wt% Cr_2O_3, 11.80 – 13.97 wt% MgO, 18.16 – 24.05 wt% FeO and 0 – 0.49 wt% TiO_2). There is no significant variation from core to rim, only a discreet decrease in Mg (12.71 – 17.71 wt%).

Figure 2.13 shows the compositional trend of spinel-group minerals from the Grota do Cedro kimberlite. Two distinct chromite groups can be noticed, with $TiO_2 < 8$ wt% and < 16 wt% following the kimberlite and Fe-Ti trends defined by Barnes and Roeder (2001). Chromite exhibits an increase in Fe^{3+} and $Fe^{2+}/(Mg + Fe^{2+})$, accompanied by increasing TiO_2. These features are also evident in Fig 2.14 A. Mg / Mg + Fe^{2+} values are inversely proportional to $Fe^{3+}/(Fe^{3+} + Cr + Al)$ values in the spinel-group varieties. An increase in Fe^{3+} together with TiO_2 (indicated by the arrow) can be observed. According to Barnes and Roeder (2001), this could be related to the evolution of spinel compositions during fractional crystallization from the host magma, which increases the Fe/Mg ratio and Ti content of the melt.

The magnesian chromite macrocrystals follow the Cr-Al trend, characterized by variable Cr/(Cr+Al) (0.62 to 0.81) and low $Fe^{2+}/(Mg+Fe^{2+})$ (0.31 to 0.41). This trend conotes equilibrium between spinel and olivine at constant composition and temperature, as evident in various mantle and lower-crustal samples (Barnes and Roeder, 2001) and it may suggest the origin of these magnesian chromites as being from mantle xenoliths. These macrocrystals are also compared by Al_2O_3 x TiO_2 and fall within the xenocryst spinel field of harzburgites and lherzolites (Fig.2.15).

There is a distinct separation between pheno- (euhedral crystals) and macrocrystals (anhedral crystals) regarding the content of Mg / Mg + Fe^{2+}, in the range of 0.10 to 0.5 and higher than 0.6, respectively (Fig. 2.14 B). Cr/(Cr+Al) contents remain constant for both populations, except for aluminum spinels, which are characterized by lower values. However, chromite Mg / Mg + Fe^{2+} values increase from core to rim, while the opposite it is observed in aluminous spinel.

In Fig 2.14 C of Mitchell (1995), it can be noticed that in Grota do Cedro the spinel-group evolved from titanian magnesian chromite and titanian chromite (TMC, TC) containing $TiO_2 < 8$ wt%, towards members of the ulvöspinel-magnetite (MUM) containing $TiO_2 < 16$ wt%. Although the points fall in the middle area of trend 1 and 2 fields, these characteristics point, for the most part, to trend 1 (in the range $0.65 < Cr/(Cr + Al) < 0.98$ and $0.56 < Fe^{2+}/(Fe^{2+} + Mg) < 0.90$.

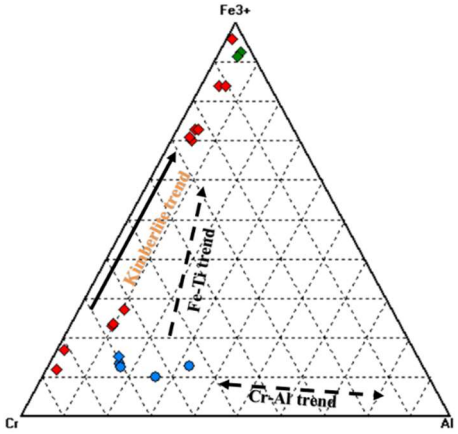

Fig.2.13. A) Fe^{3+} – Cr – Al diagram for Grota do Cedro spinel showing Ti-Fe and Cr-Al trends defined by Barnes et al. (2001). Symbols: red and green lozangle correspond to euhedral chromite and aluminous spinel, respectively; blue circle: anhedral grains.

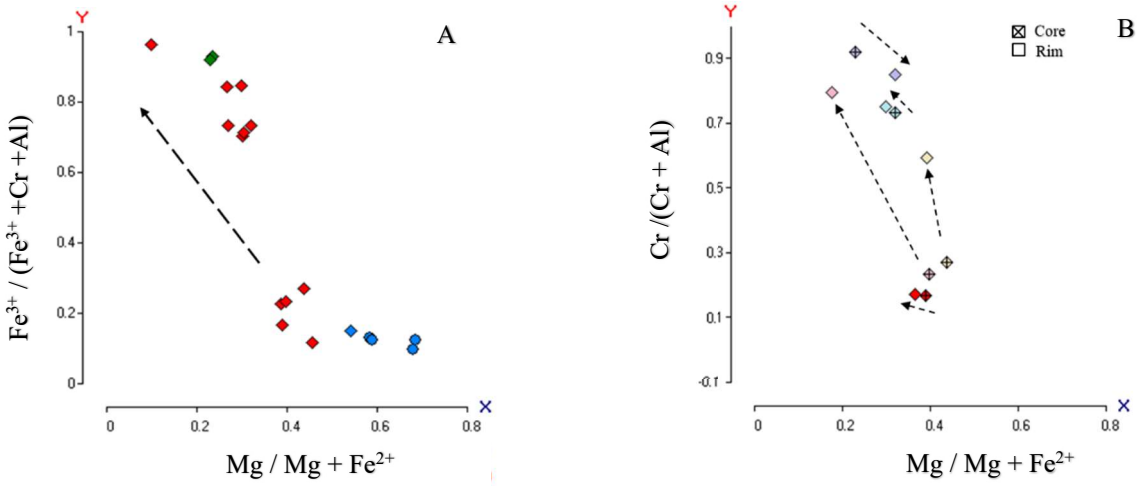

Fig.2.14. Mg# (Mg^{2+}/ (Mg^{2+}+Fe^{2+})) *versus* Fe^{3+}# (Fe^{3+}/(Fe^{3+}+Al+Cr)) for spinel-group minerals from the Grota do Cedro kimberlite. (A) TiO_2 content increase (arrow) proportional to Fe^{3+} (a). Mg# (Mg^{2+}/ (Mg^{2+}+Fe^{2+})) *versus* Cr# (Cr/(Cr+Al)) indicating a distinction between euhedral and anhedral spinel-group crystals (b). Compositional variation of euhedral chromite crystals indicating a Mg# decrease and a Fe# increase from core to rim, with exception of one grain that exhibits an aluminous spinel rim (lilac colour). Symbols: red and green lozangle correspond to euhedral chromite and aluminous spinel, respectively; blue circle: anhedral grains.

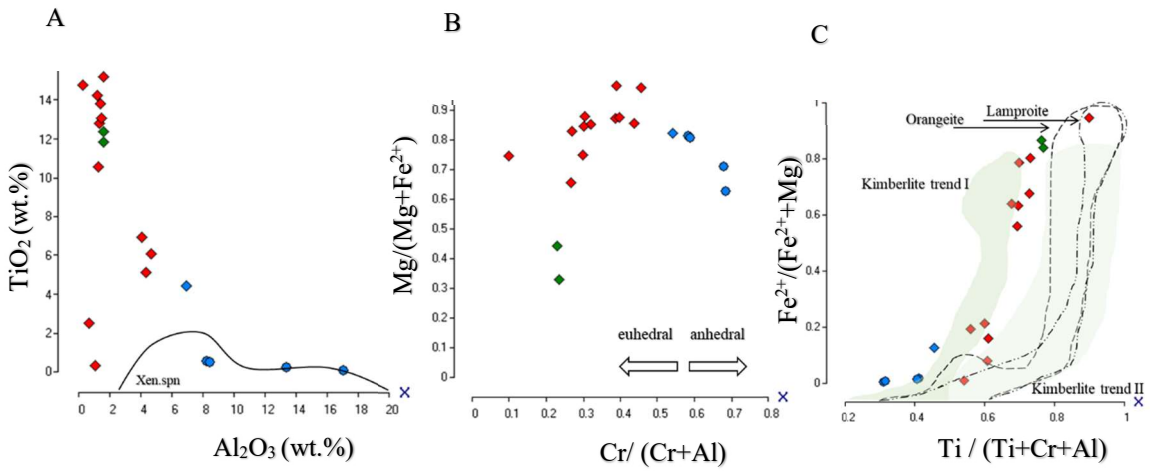

Fig.2.15. A) Al_2O_3 *versus* TiO_2 in euhedral and anhedral spinel-group minerals from the Grota do Cedro kimberlite. The line corresponds to the highest concentration field of spinel xenocrysts from harzburgites and lherzolites of Griffin et al. (1991). B) Mg# (Mg^{2+}/ (Mg^{2+}+Fe^{2+})) *versus* Cr# (Cr/(Cr+Al)) showing clear separation between euhedral and anhedral crystals. C) Ti/(Ti+Cr+Al) *versus* Fe^{2+}# (Fe^{2+}/(Fe^{2+}+Mg)) diagram showing a concentration closer to kimberlite trend I as defined by Mitchell (1995). Symbols: red and green lozangle correspond to euhedral chromite and aluminous spinel, respectively; : blue circle: anhedral grains.

In Grota do Cedro, chromite Co ranges from 134.64 to 450.70 ppm, Zr from 0.49 to 1097.05 ppm, Nb from 0.12 to 2704.91 ppm, Ba from 0.22 to 318.09 ppm and Ta from 0.23 to 215.94 ppm (Table 2). Primitive mantle-normalized trace elements display two different variation patterns for euhedral and anhedral crystals: a sinusoidal and weakly sinusoidal ones, respectively (Fig.2.15).

Despite some overlapping areas, it can be noticed that euhedral chromite shows a higher enrichment in incompatible elements, yet with more accentuated negative Ce, Sr and Y anomalies and strong positive Ta, Nb, Pb, Hf and Zr anomalies. Chromite macrocrystals present a homogeneous variation in trace elements, resulting in a weakly sinusoidal pattern with positive Th, Ta and Hf anomalies. In general, they present a slight descent when compared with the sinusoidal pattern, which is variable.

Most grains of two populations present REE_N values below the limit of detection. However, an enrichment of $LREE_N$ can be noticed, with constant depletion towards $HREE_N$, resulting in a slightly humped pattern (Fig.2.16 B), except for two positive slopes in Gd and Yb.

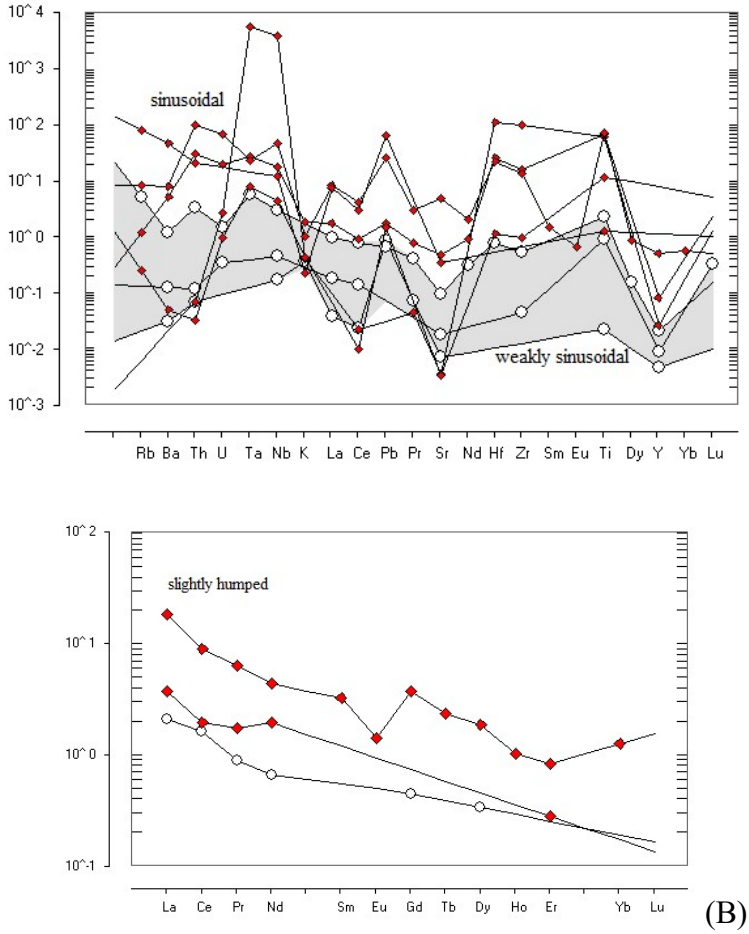

Fig. 2.16. A) Primitive mantle-normalized (McDonough and Sun, 1995) incompatible element pattern of spinels from the Grota do Cedro kimberlite; grey field corresponds to anhedral crystals. (B) Chondrite-normalised REE patterns (Boynton, 1984) of spinel from the Grota do Cedro kimberlite. Empty circles, macrocrystals; red lozenge, euhedral crystals. Concentration normalized to the primitive-mantle composition of McDonough and Sun (1995) and to the C1 chondrite of Boyton (1984), respectively.

4.3 Phlogopite

Three modes of occurrence of mica are present in the Grota do Cedro kimberlite: groundmass (0.20 – 0.32 mm), macrocryst (~1.14 mm) and inclusion in spinel and pyroxene crystals (~0.04 mm) (Table 15).

Groundmass (or microcrystals) phlogopite occurrences are characterized by low TiO_2 and Cr_2O_3 (0.19 to 0.48 wt% and 0.19 to 0.33 wt%) with exception of one grain, that exhibits high TiO_2 (3.80 wt%), FeO (4.89 to 6.21 wt%), K_2O (4.96 to 10.39 wt%), Al_2O_3 (5.13 to 12.82 wt%) and MgO (21.0 to 32.81 wt%) contents. Mg# varies from 0.87 to 0.92. Zoned groundmass phlogopite is also found, involving Al, Fe and K decrease and Mg increase in dark core parts as compared to brighter core parts. Toward the rims, a Ti, Fe, Al and K increase is noticed.

Only one macrocryst grain was analyzed, characterized by high TiO_2 and Cr_2O_3 core (4.15 wt% and 0.48 wt%, respectively), FeO (6.28 wt%), K_2O (9.93 wt%), Al_2O_3 (13.47 wt%) and MgO (22.09 wt%). Mg# is lower than in microcrysts phlogopite (0.86). There is a slightly Ti, Al increase and Mg, Fe decrease from core to rim.

In phlogopite inclusions, TiO_2 ranges from 1.52 to 3.80 wt%, FeO from 7.75 to 10.44, K_2O from 10.24 to 10.03 wt% and MgO from 18.66 to 22.44 wt%. Mg# varies from 0.76 to 0.84. It can be noticed that phlogopite included into pyroxene exhibits higher chemical values than those included in spinel, except for Mg.

High Ti-Cr core macrocryst and high-Ti/low-Cr groundmass phlogopite variations from Grota do Cedro correspond to the Ti-Fe-rich kimberlite trend defined by Beard et al. (2000) (Fig. 2.17a), while low Ti-Cr cores fall out of this field. Low Ti-Cr core groundmass falls within the phlogopite K-richterite peridotite field (PKP) defined by Early et al. (1987) (Fig. 2.17 A). Macrocryst and high-Ti/low-Cr microcrysts phlogopite exhibits a lower Mg# than low Ti-Cr core groundmass and plots close to the high Ti-Cr field, coinciding with low-Cr groundmass phlogopite from the Bultfontein kimberlite (Fig.2.17), indicating a possible kimberlitic origin instead of from xenoliths.

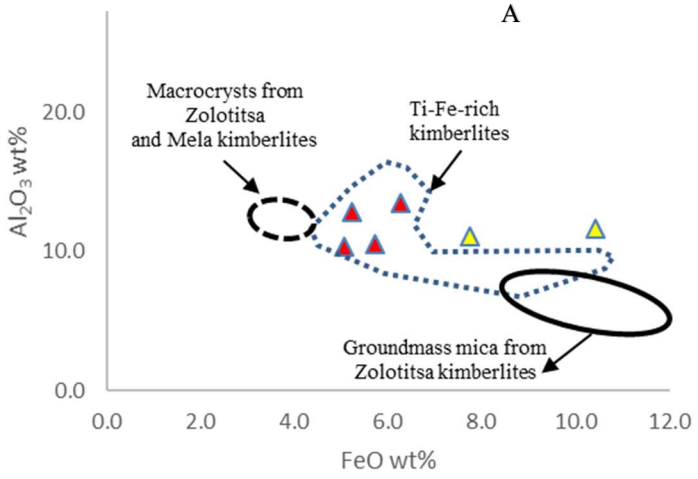

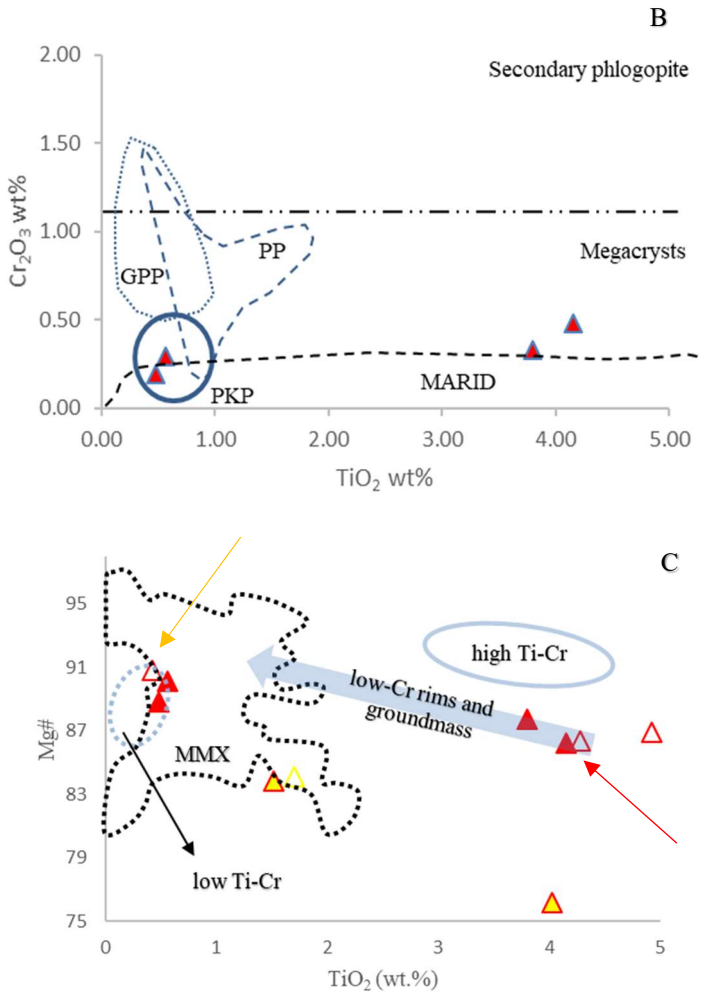

Fig.2.17. Compositional variation of macrocryst (indicated by red arrow), microcrysts (indicate by yellow arrow) and included phlogopite (yellow triangles) from Grota do Cedro. A) Al_2O_3 wt% *vs.* FeO wt% diagram (after Beard et al., 2000); B) Cr_2O_3 wt% *vs.* TiO_2 wt% diagram (after Dawson and Smith, 1975), with xenolith fields from Erlank et al. 1987; GPP: garnet phlogopite peridotite, PP: phlogopite peridotite, PKP: phlogopite K-richterite peridotite. C) TiO_2 wt% *vs.* Mg# diagram (after Giuliani et al., 2016); delimited fields are major concentrations of macrocrystal phlogopite from the Bultfontein kimberlite and metasomatized mantle xenoliths (MMX) from Kimberley (after Giulliani et al. (2016) and Grégoire et al. (2002), respectively); arrows show compositional trends towards more evolved compositions for groundmass grains and macrocryst rims (after Giulliani et al. (2016)).

The three modes of phlogopite occurrence of Grota do Cedro exhibit different incompatible trace element patterns (Fig. 2.18). On average, they present high levels of Ni (302.05 to 1329.07 ppm), Rb (530.04 to 5198.07 ppm), Ba (91.20 to 52783.13 ppm), low REE (up to 0.328 ppm La, up to 0.584 ppm Ce, up to 0.011 ppm Pr) and HREE below the detection limit (~17.92 ppm Eu) (Table 16– Annex II). Other trace elements vary considerably (V: 51.74 to 7962.01ppm, Sr: 10.92 to 1588.39 ppm, and Zr: 2.46– 82.68 ppm).

The correlation of Ti vs. Ni, Zr, Ba (ppm) is similar to that of phlogopite crystals from the Bultfontein kimberlite studied by Giulliani et al. (2016) (Fig. 2.18 A-C). Low Ti-Cr groundmass cores fall within the field of metasomatized mantle xenoliths (MMX) from Kimberley and other South African kimberlites. It seems to be likely that such cores derive from disaggregation of mantle rocks (Dawson and Stephens, 1975). It can be noticed that the phlogopite cores evolve towards an even more distinctive Ni-rich composition with respect to high-Ti/low-Cr microcrysts and high Ti-Cr macrocryst crystals (Fig. 2.18 A). The latter evolve towards to Zr, Ba, Sr and Nb- rich compositions with respect to the other types.

Abundances of incompatible elements normalized to the primitive mantle of (McDonough and Sunn 1995) are show in Fig. 2.19. The three phlogopite modes from Grota do Cedro have similar behavior from Cs to K, with strong negative Th anomalies. Groundmass crystals remain in the same pattern from La to Y, displaying slightly positive Pb and Ti anomalies and negative Ce, Nd and Y anomalies. The enrichment from Pr to Zr exhibited by high-Ti/low-Cr groundmass grains is more pronounced than the others, and negative peaks are the highest of all. The opposite is observed in high Ti-Cr macrocrystals, which present the highest values of trace elements, with strong positive Ba and Pb anomalies and depletion of Sr towards Y.

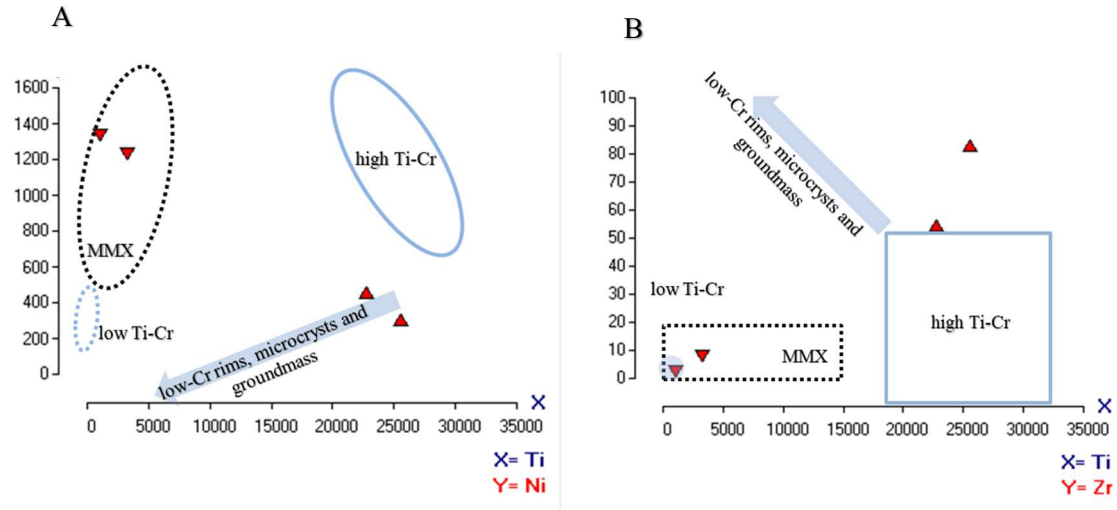

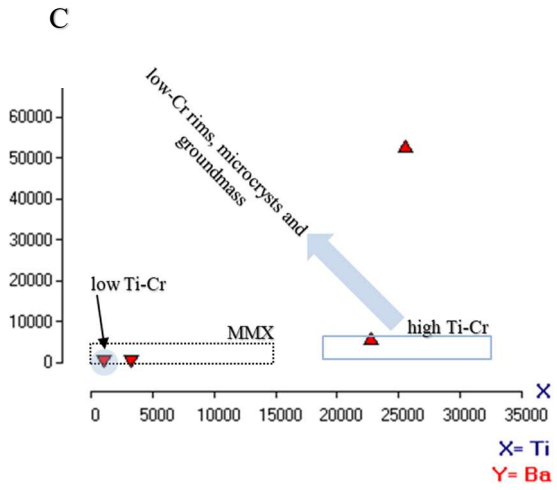

Fig.2.18. Trace element co-variation diagrams for microcrystals and macrocryst phlogopite from the Grota do Cedro kimberlite: Low Ti-Cr microcrystals phlogopite (up-pointing triangle); high-Ti/low Cr microcrysts and high Ti-Cr macrocrystal (down-pointing triangle). Notice that macrocrystal values are always higher than in other crystals. Delimited fields represent major concentration of macrocrystal phlogopite from the Bultfontein kimberlite and from metasomatized mantle xenoliths (MMX) from Kimberley (after Giulliani et al. (2016), Grégoire et al. (2002)). Arrows show compositional trends towards more evolved compositions for microcrysts grains and macrocryst rims (after Giulliani et al. (2016)).

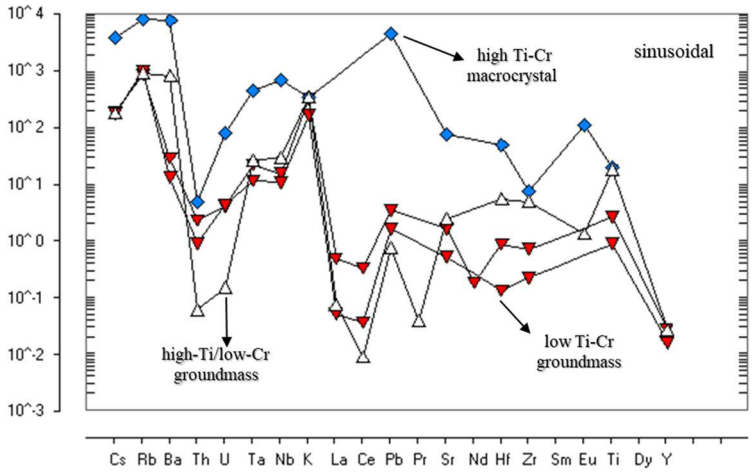

Fig.2.19. Primitive mantle-normalized incompatible elements pattern (McDonough and Sun, 1995) for macrocryst and groundmass phlogopite from the Grota do Cedro kimberlite. Notice that the high Ti-Cr macrocrystal is the most enriched and that the high-Ti/low-Cr groundmass phlogopite shows the most negative anomalies compared the other groundmass one.

4.4 Perovskite

The perovskite varieties from Grota do Cedro studied occur as anhedral or euhedral, grains scattered throughout the fine-grained interstitial medium of kimberlitic clasts. However strong zoning observed in back-scattered electron (BSE) images is a very common feature of euhedral perovskite forms, homogeneous grains were observed. Anhedral crystals also exhibit a zoning pattern, although less pronounced than that of euhedral grains. They can be interpreted as a primary phase that crystallized directly from magma, distinguished based on the crystal perfection and zoning pattern (texture) following Castillo-Oliver et al. (2016) parameters and terminology:

Type Ia perovskite

These are anhedral crystals up to 0.15 mm in size. They occur usually scattered in the interstitial medium in kimberlitic clasts or as rimmed olivine pseudomorphs. This texture is described in many perovskite occurrences in Canadian and South African kimberlites (e.g. Castillo-Oliver et al., 2016; Chakhmouradian and Mitchell, 2000; Donnelly et al., 2012). In back-scattered electron (BSE) images, their zoning patterns are usually very subtle, with rhythmic light and dark bands less pronounced than in Type Ib.

Type Ib perovskite

This type of perovskite occurs as discrete single euhedral crystals up to 0.09 mm wide, with very strong zoning patterns in BSE images and brighter cores / dark rims.

Type Ic perovskite

Type 1c perovskite appears as euhedral grains up to 0.10 mm wide. Unlike in type Ia grains, it is not possible to identify any zoning pattern in MeV images, and their composition is homogeneous. There is no correspondence between Type 1c perovskite and Castillo-Oliver et al. (2016) types.

Zoning patterns reflect compositional variations within perovskite crystals. Chakhmouradian and Mitchell (2000) defined three zoning patterns: normal (decrease in LREE and varying Th with Na and Nb contents towards the rims), reverse (enrichment in LREE, increase in Th, Fe and Nb, and constant or slightly decreasing LREE values) and oscillatory (significant Nb, Na, Ce, Fe and Nd variation within a single grain). In Grota do Cedro,

perovskite exhibits a “normal” pattern, with brighter cores and dark rims, varying Na content, and slightly increased rim content in some grains (Fig. 2.20).

Owing to their wide chemical composition range, it can be very difficult identify a perovskite occurrence as a “standard” one. In Grota do Cedro, perovskite grains exhibit high amounts of Nb (48.27 to 62.30 wt%), Nb/Ti ratio is very high, as expected from substitutions of Ti by Nb. The chemical formula of these perovskite grains could represent a substitution series between end-members: $Ca_2Nb_2O_7$ (average 48.3 mol%), lueshite – $NaNbO_3$ (average 27.8 mol%), perovskite - $CaTiO_3$ (average 13.5 mol%) and $ThNb_4O_{12}$ (average 9.89 mol%), no one of them corresponding to perovskite compositions from other APIP kimberlites or, possibly, worldwide.

Chakhmouradian and Mitchell (2001) described Type III perovskite as significantly enriched in Nb and LREE in kimberlites (up to 13.0 and 22.6 wt% oxides, respectively). However, such occurrences were found exclusively as rims around other perovskite grains with lower values of these elements (types I and II) apparently confined to hypabyssal kimberlites. Castillo-Oliver et al. (2016) reported Nb-rich (up to 10.6 wt% Nb_2O_5), LREE (1.8–4.0 wt% ΣLREE) and Na (0.8–1.6 wt% Na_2O) overgrowth on some perovskite crystals from the Mulepe 2 kimberlite. Sarkar (2011) also described perovskite-lueshite (Ca + Ti = Nb + Na) substitution (9.5-11 wt% Nb_2O_5) in South African kimberlites.

Major and trace element co-variation diagrams for perovskite grains from the Grota do Cedro kimberlite are shown in Fig. 2.21. The strong negative correlation between Ca+Ti *vs* Nb+Na in these perovskite forms indicates substitution of Ti with Nb (Table 12).

In Grota do Cedro, Type Ia perovskite is characterized by a significant enrichment in Nb_2O_5 (50.15 to 59.55 wt%), CaO (10.52 to 18.08 wt%) and $LREE_2O_3$ (3.71 to 10.67 wt%), significant amounts of SrO (0.24 to 3.44 wt%), Na_2O (0.43 to 5.28 wt%), Ce_2O_3 (1.97 to 12.04 wt%) and ThO_2 (0 to 5.01 wt%), and by low amounts of ZrO (up to 3.90 wt%), La_2O_3 (up to 1.64 wt%) and Nd_2O_3 (up to 1.37 wt%).

Type Ib perovskite is enriched in Nb_2O_5 (48.27 to 62.30 wt%), CaO (9.46 to 16.11 wt%) and $LREE_2O_3$ (3.79 to 5.36 wt%), with significative amounts of Na_2O (0.29 to 6.51 wt%), Ce_2O3(2.11 to 7.75 wt%) and ThO_2 (0 to 5.42 wt%) and low amounts of ZrO_2 (up to 3.31 wt%), La_2O_3 (up to 1.47 wt%) and Nd_20_3 (up to 0.91 wt%).

Type Ic is characterized by a high Nb_2O_5 (52.27 to 54.37 wt%), CaO (15.54 to 19.11 wt%) and $LREE_2O_3$ (4.16 to 17.49 wt%) content, with significative amounts of Na_2O (1.91 to 4.69 wt%) and Ce_2O_3 (2.9 to 13.74 w.%) and low amounts of ZrO_2 (up to 1.87 wt%), La (up to 2.16 wt%), Nd_2O_3 (up to 2.28 wt%) and ThO_2 (up to 1.43 wt%).

Nb content variation remaining of low across the three types, types Ia and Ic are more enriched in Ce and LREE, the latter being depleted in Th and Zr and enriched in Nd as compared to other types (Fig. 2.20).

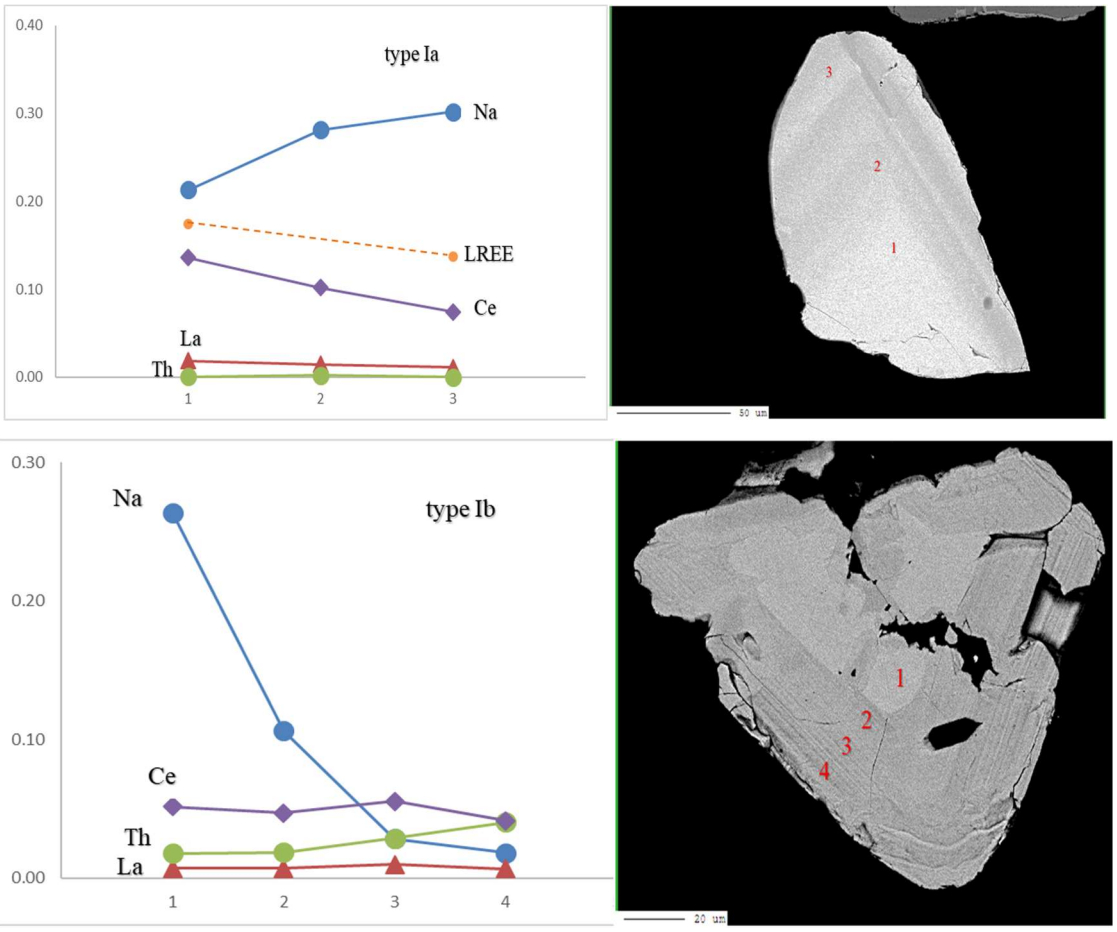

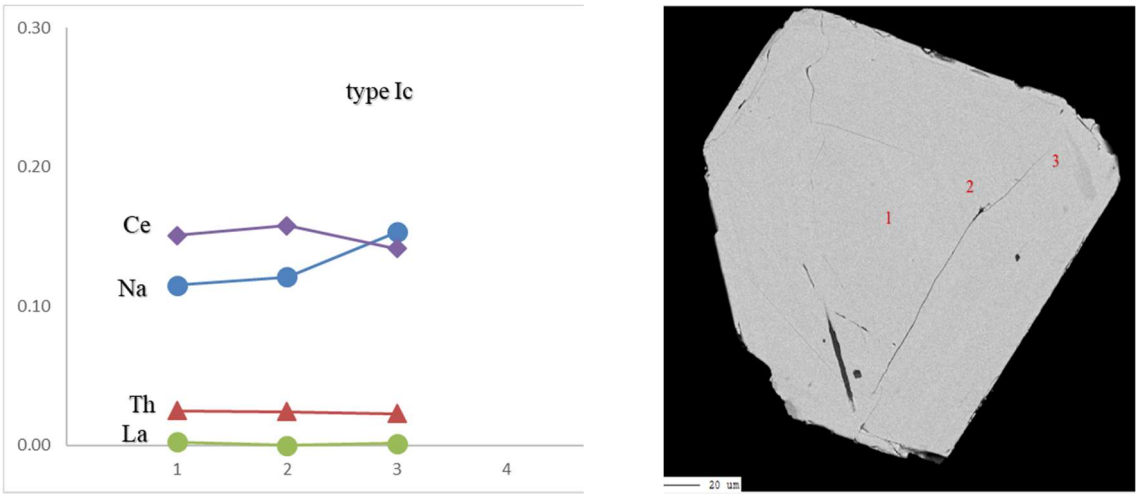

Fig.2.20. Back-scattered electron (BSE) images of perovskite from Grota do Cedro showing zoning pattern and compositions. All occurrences analyzed exhibit a "normal" pattern. Ce, Na, Th, La and LREE decrease towards the rims and Na contents are variable. Type Ic perovskite exhibits higher homogeneity, and constant Na content in some grains.

Incompatible trace element diagrams (Fig.2.21) show similar a pattern across perovskite types, characterized by strong negative anomalies, mainly of K and Ti. Zr values (up to 28865 ppm) are also raised to alkaline rocks from the APIP (up to ~2600 ppm). High Zr/Hf values (up to 311) suggest preferential partitioning of Zr for the mineral. Lu/ Hf values are low (0.0 – 9), suggesting a slight preferential partitioning of Hf. These ratios are not equated with data from PIAP alkaline rocks (Melluso et al., 2008) because of the uncommon composition.

According to Boyton (1984), C1 chondrite-normalized REE patterns exhibit a humped pattern that reflects enrichment in LREE with respect to $MREE_N$ and $HREE_N$ (La up to 17087; Lu up to 21.3). Grota do Cedro perovskite grains are characterized by very low fractionated REE values (La/Yb < 290), the larger variation being shown by type Ia perovskite. Eu anomalies (0.03 to 1.1) and light over heavy rare-earth fractionation fall within the range of kimberlitic perovskite from the APIP (La/Ybn from ~175 to ~2000 and Eu/Eu* in the range 0.88–1.1, after Melluso et al., 2008).

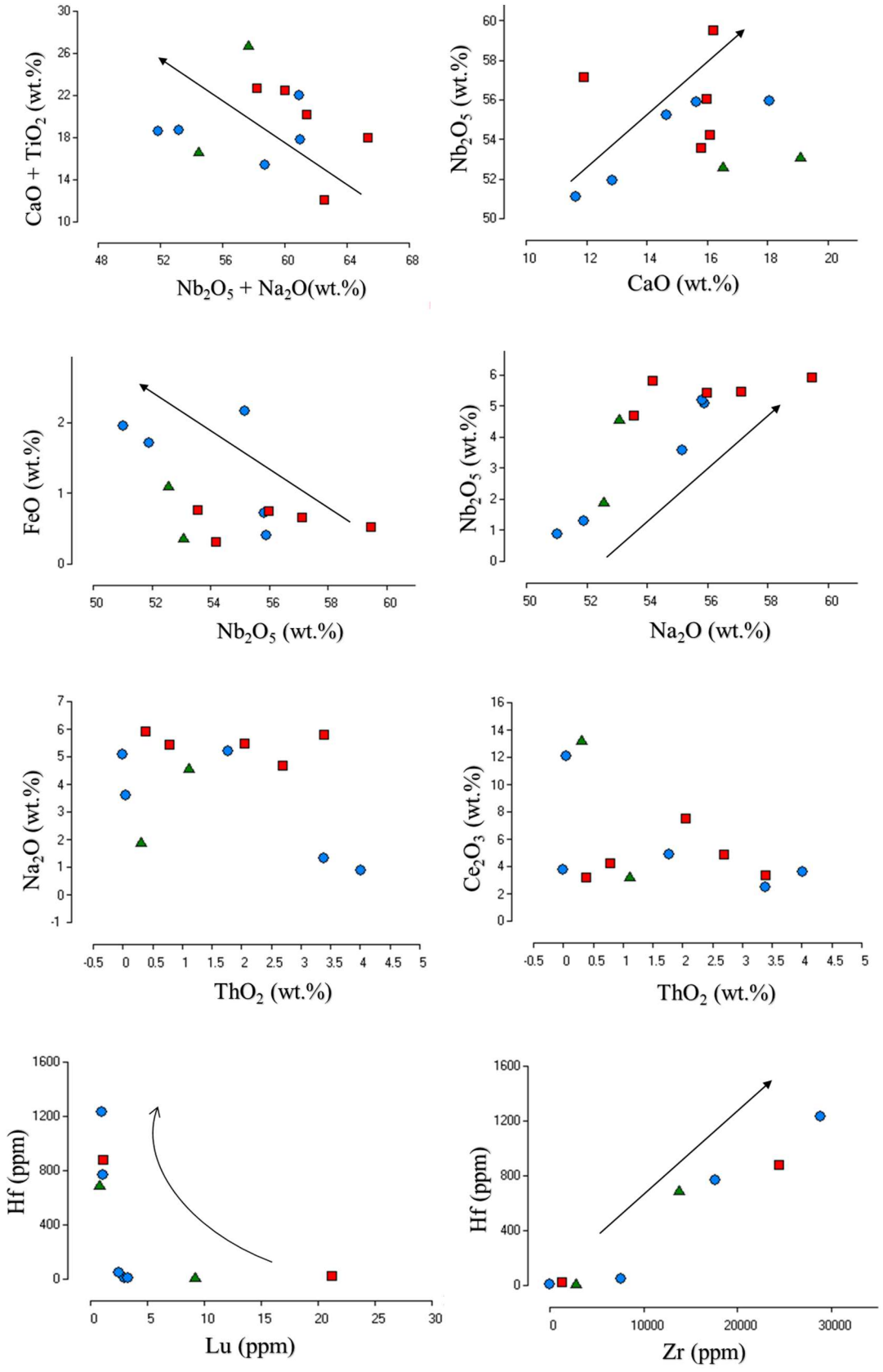

Fig. 2.21. Major and trace element co-variation diagrams for perovskite grains from the Grota do Cedro kimberlite. Arrows indicate positive or negative correlation between elements. The strong negative correlation between Ca+Ti vs Nb+Na indicates substitution of Ti with Nb. Circle (Type Ia); square (Type Ib); triangle (Type Ic).

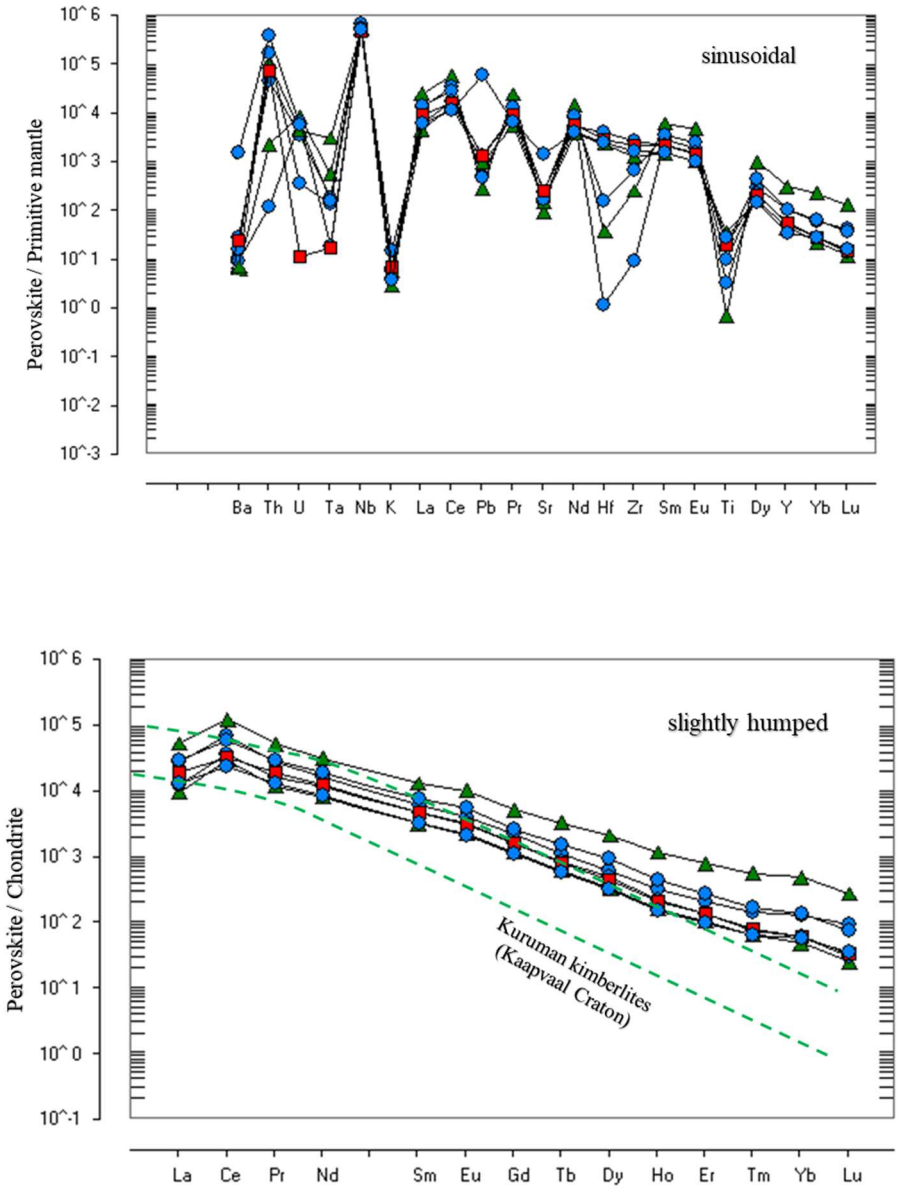

Fig.2.22. A) Primitive mantle-normalized McDonough and Sun, 1995) incompatible elements of perovskite occurrences from the Grota do Cedro kimberlite. B) C1 chondrite-normalized (Boyton, 1984) REE patterns for perovskite occurrences from the Grota do Cedro kimberlite. Green dashed lines: averaged REE_N concentration field of perovskite from the Kuruman kimberlite province, South Africa (Donnelly et al., 2012).

4.5 Pyroxene

The micro- and macrocrystals analysed are anhedral grains ranging from 0.07 to 6.2 mm in diameter and correspond as Morimoto (1990) mainly to diopside and augite end-members (Table 19). They present variable amounts of FeO (up to 12.86 wt%), Cr_2O_3 (up to 1.67 wt%), CaO (up to 24.44 wt%), TiO_2 (up to 3.0 wt%) and MgO (up to 18.92 wt%), and minor amounts of NaO (up to 1.72 wt%) and MnO (up to 0.58 wt%). Some grains exhibit a solid-solution between augite-hedenbergite with highest values of FeO (up to 25.34 wt%), Na_2O (up to 2.57 wt%) and MnO (up to 0.58 wt%), and lowest of Mg# (up to 0.79). One enstatite-ferrosilite solid-solution also was founded.

The clinopyroxenes population has been divided into two groups, a low-Cr (< 1.0 wt%) and high-Cr (> 1.0 wt%). The high-Cr crystals present no significant compositionally variations toward to rims, with exception of one grain, which Al, Cr, Na and Mg# decrease and Fe and Ca increase from core to rim. This grain exhibit core higher Mg# (0.93) value. The low-Cr group display significative variations of the elements from core to rim. They exhibit Al, Na and Mg# decrease and Fe and Ca increase towards the rims. The grains augite-hedenbergite not exhibit compositionally variation.

It is possible to note the distinct behaviour related to major elements between the low-Cr and high-Cr groups (Fig.2.23 d). There is Al and Cr negative correlation for both groups, while in the other elements they present opposite correlations each other (Fig.2.23 a). Due to low Mg# values and relative high Ti amounts of low-Cr groups, these clinopyroxene are similar to grains from piroxenites (Boyd et al., 1984; Chen et al., 2014).

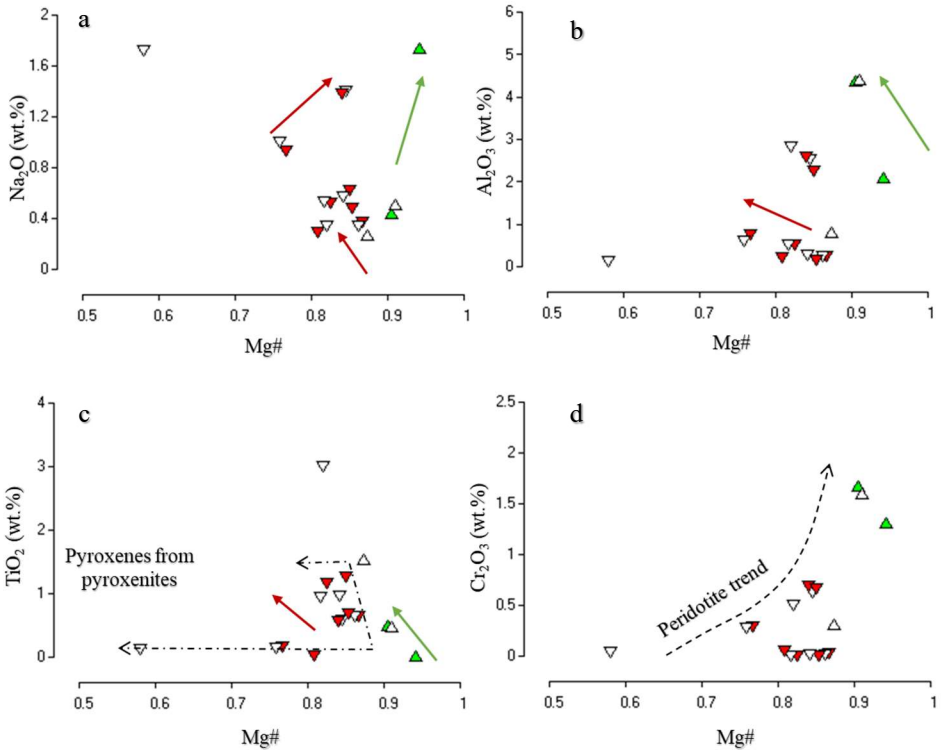

Fig. 2.23 Plot of Mg-number vs Na_2O-Al_2O_3-TiO_2-Cr_2O_3 of clinopyroxene compositions from Grota do Cedro kimberlite. The dashed arrow area in graphic (c) corresponds to clinopyroxenes of megacryst suite from East Griqualand pyroxenites (modified from Janney et al. 2010) and clino- and orthopyroxenes from Mzongwana kimberlite dike (modified from Boyd et al. 1984), both rocks located in southern Africa. The dashed arrow in graphic (d) indicate the trend of clinopyroxenes from worldwide peridotites (Pivin et al., 2009). Symbols: green / red arrows, correlation direction; green triangle, high-Cr clinopyroxene cores (>1.0 wt%); red triangle, low-Cr clinopyroxene cores (< 1.0 wt%); white triangle, clinopyroxene rims.

Clinopyroxenes from Grota do Cedro show variable REE concentrations (Fig.2.24a). On average, they display relative LREE enrichment and HREE depletion resulting in a slightly humped pattern, La and, in some cases, Ce are slightly elevated, however, two grains exhibit flat pattern with very slightly LREE enrichment. In particular the high Cr-clinopyroxene variants are up to hundred enriched with respect to the C1 Condrite.

The fractionated values of rare earth elements (REE) vary from 0.00 – 39.26 for $(La/Yb)_N$, 0.61 to 2.11 for $(La/Nd)_N$, 0.01 to 2.80 for $(La/Sm)_N$ and from 0.16 to 14.12 for $(Sm/Yb)_N$. On the other hand, these clinopyroxenes are characterized by $(Zr/Hf)_N$ values from 15.40 to 34.25. The trace element diagrams (Fig2.24 b) show strong negative anomalies in Ba, K, Pb, Nd, Ti and slightly negative slopes in Hf and Zr.

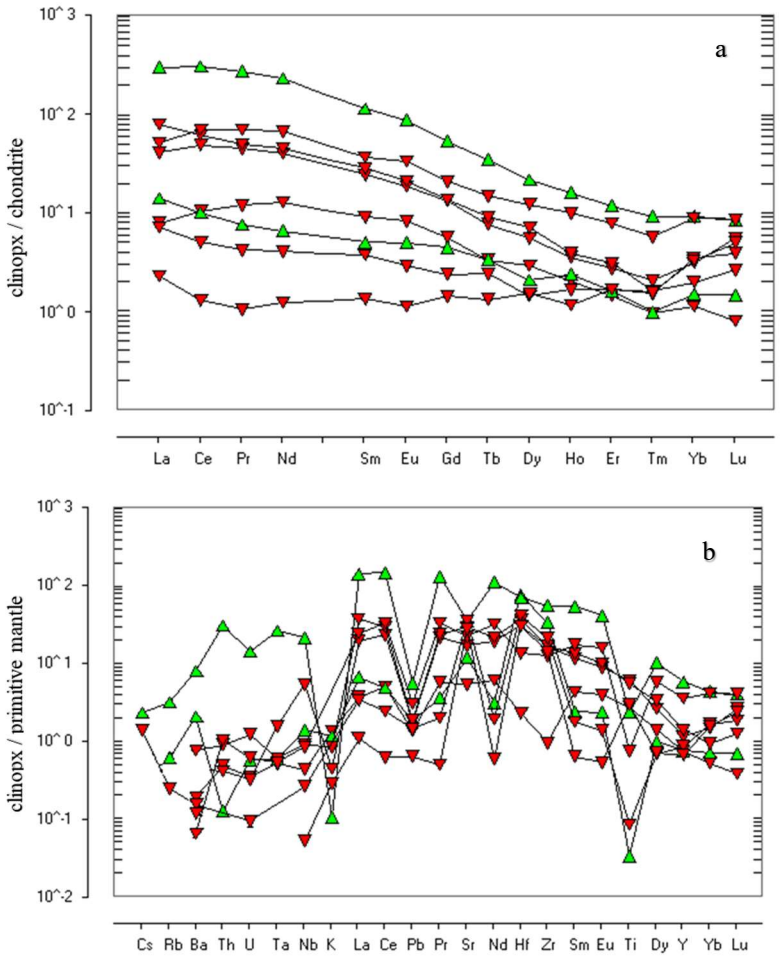

Figure 2.24. a) Chondrite normalised REE patterns (Boynton, 1984), and (b) primitive mantle-normalized incompatible elements pattern (McDonough and Sun, 1995) for low-Cr (red triangles) and high-Cr (green triangles) clinopyroxenes from Grota do Cedro kimberlite.

5. Sr isotope analysis

The Sr-isotope compositions of the Grota do Cedro perovskites are shown in Figs 2.29 and summarized in Table 2.3. Fiveteen analyses of individual perovskite grains from was realized, and due isobaric interferences of ^{87}Rb over ^{87}Sr was considered only nine chemical analyses ranging between 0.705156 and 0.706447. The isobaric ^{87}Rb contribution over ^{87}Sr was corrected by using the ^{85}Rb ion signal and the $^{87}Rb/^{85}Rb$ natural ratio (Ramos et al. 2004), however, we opted to exclude some analyzes that was interpreted to have some uncertainty degree, and for better accuracy of the data were considered values only up to the third decimal place. Due to their very low Rb/Sr ratios (< 0.005) (Sarkar et al., 2014) and the relatively young

age of the kimberlites, no age correction was applied on the measured Sr isotope ratios, furthermore, the date obtained were considered initial.

The isobaric interferences should be corrected for the accuracy of resultant $^{87}Sr/^{86}Sr$ ratios. Munoz et al. (2016) implemented measurements of half-masses ($^{171}Yb^{2+}$) allows the accurate assessment of lanthanide interferences, permitting the determination of Sr isotopes in important REE-rich accessory phases. The appropriate results are achieved in Sr-rich and Rb-poor phases (Rb/Sr <0.02), materials with Rb/Sr ratios > 0.02 are not suitable for the acquisition of accurate Sr isotope ratios via LA-MC-ICP-MS (Ramos et al. 2004), whereas others advocate that an efficient correction can be performed for materials with far greater Rb/Sr ratios (<0.2 Davidson et al. 2001). Due to the very low amounts of Rb (< ~5.7ppm; Donnelly et al., 2012) in perovskites, if interference occurs, this influence will be minimum.

Table 2.3. $^{87}Sr/^{86}Sr$-isotope results for perovskite analyzed in this study.

Perovskite (LA-MC-ICP	
SrO (average): 6078 ppn	
Sr^{87}/Sr^{86}_i	2 sigma
0.705156	0.000551
0.706447	0.000366
0.705486	0.000384
0.705385	0.000406
0.706147	0.000405

6. Discussion

The classification of kimberlitic facies is complex and confused, kimberlite pipes and craters are infilled by a variety of volcaniclastic rocks and many classification were proposed (Clement and Skinner, 1985; Cas et al., 2008; Field and Scott Smith, 1999; Hetman et al., 2004; Scott Smith et al., 2008; Skinner and Marsh, 2004; Sparks et al., 2006). At great depth the exsolution of juvenile volatiles is initiated, in addition, the subsequently explosive eruption of relatively large volumes of kimberlite, result in the emplacement of southern African type (Class 1) kimberlite pipes (Skinner, 2008). The suite of rocks formed change from hypabyssal-

, through transitional-to diatreme-and crater-facies rocks present in three zones, namely root, diatreme and crater zones (Clement, 1982).

However, these emplacement process cannot be applied to Class 2 and 3 kimberlite, which are mainly characterized by shallow crater zones filled with volcaniclastic kimberlite or filled with re-sedimented volcaniclastic kimberlite, respectively. According with some characteristics it is possible suggest which Grota do Cedro kimberlite facies was studied.

These names and textural terms are applied to rocks where the origin is not necessarily well-established (Sparks et al., 2006), however, the classification thus provides a useful starting point. In hypabyssal-facies kimberlite (HFK) olivine may be unaltered or partly altered, microlitic diopside is relatively rare, while in the diatreme-facies kimberlite (DFK) the olivine is completely serpentinized and has abundant microlitic diopside. Segregationary textures and juvenile clasts are common in the diatreme type, in opposite of HFK which exhibit uniform magmatic textures and rare juvenile clasts, like pelletal structures. Calcite primary is characteristic mineral in the groundmass of HFK, while in the DFK is absent. A transitional facies (TFK) can occur between two main end- member varieties localized in the lower parts of the pipe (towards the base of the diatreme zone and towards the top of the root zone) is a relatively new development (e.g. Hetman et al., 2004; Skinner and Marsh, 2004).

The Grota do Cedro kimberlite displays features of volcanoclastic kimberlite, which can be associated of crater (Skinner and Marsh, 2004) or diatreme facies (Cas et al., 2008). In these work, these terms are descriptive and non-genetic, because crater facies could also occur in the diatreme zone, and hypabyssal or coherent kimberlite could occur at any level of a pipe (Cas et al., 2009). The uncored juvenile clasts with lapilli size from Grota do Cedro may be amoeboid in shape with plastic margins (Fig. 2.7), the abundance of secondary calcite within interstitial medium filling or no vesicles and/ or replacing totally the kimberlitic clast (Fig. 2.25), are features that indicate a vulcanoclastic origin (Skinner and Marsh, 2004). Such these lapilli structure are an important component of many Class 2 kimberlites infilling craters and can be recognised in some Class 1 and 3 kimberlites (Sparks et al., 2006). The components of Grota, such as crystals, lithic clasts from different sources and juvenile lapilli, are equated with massive vulcanoclastic kimberlite (MVK) decribed by Sparks et al. (2006) from Orapa and Venetia mines.

Besides the juvenile structures that characterized a vulcanoclatic kimberlite, the carbonate minerals phase of interstitial medium is important feature and the Grota do Cedro

exhibit a secondary calcite, e.g. resulted by a vapour phase or deuteric alteration product. According with Cas et al. (2008), in fragmental kimberlite rocks, carbonate cannot be a segregation product. The carbonates minerals also occur like veins and filling the fractures in altered olivine crystals or replacing totally some clasts. The partially fill by carbonate of the vesicular uncored clasts may suggest a secondary phase for the carbonate minerals.

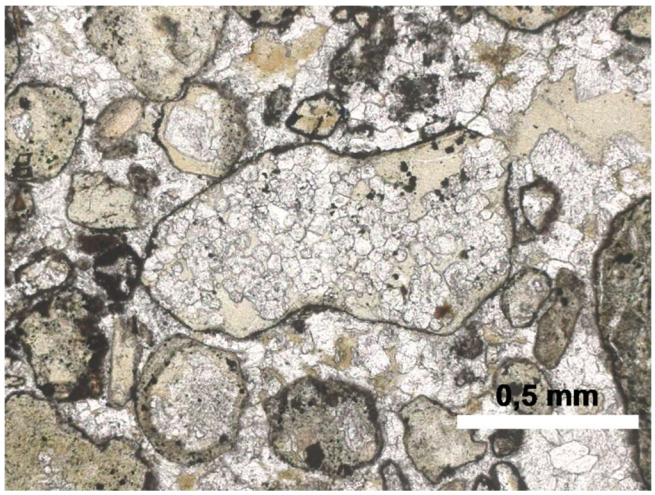

Fig.2.25. Kimberlitic juvenile clast totally replaced by secondary calcite.

The uncored juvenile clasts described in table 2.1 (Fig. 2.6) exhibits wide mineralogical similarities to hypabyssal kimberlites (Mitchell, 2008a). The clasts different compositions, the abundance and size of olivine crystals within and outside of the clasts (material intra-clast) are very differently. The juvenile clasts olivine sizes from Grota are higher (type E and F) or smaller (type A to D) than olivine crystals within material that enclose the clasts (Fig. 2.6 and 2.10). The first can suggest a derivation of the juvenile clast from a separate unit and can be a resulted from more than one magmatic pulse. The size and abundance of the olivine population originally liberated from the magma during eruption may be modified by volcanic process (Webb, 2006), than, the clast types with olivine smaller size, suggest a clastic pyroclastic classification.

The emplacement sequence evidence of the different types that composed the Grota do Cedro kimberlite, can be reconstituted by the mixed of the types (Fig. 2.26). It is important to note that the type E clast is the latest to be part of the system, which encompasses the type D clast and that which encompasses the type A and F clasts. It was not possible to identify the order between the A and F clasts, but these two materials were already in the vent when there was a subsequent injection of the magma corresponding to the type D clast. In the latter, it is

notable its plastic margins resulted in the higher viscosity in relation to the other types, evidenced by the tube-shaped (Fig. 2.6) and the minerals alignment (mainly phlogopite) close to contact with other clasts or interstitial medium.

For the C type (the least abundant) it was not possible to identify the emplacement order, however, it may correspond to one of the last magmatic pulses due phlogopites still remain relatively fresh (Fig 2.8). The differences in compositions and granulometry of the clasts, besides the morphology and contact relations, reveal a complex and dynamic emplacement of Grota do Cedro kimberlite, and may involve differently batches of compositionally distinct kimberlitic magma.

Some of kimberlitic material that compose the clast types is found forming the pelletal structures (Fig. 2.6). During the rising magma there is an incorporation of particles into liquid spheres in addition to rapid unmixing of immiscible liquids (Junqueira-Brod, 1999; Lloyd and Stoppa, 2003; Wilson and Head III, 2007). Gernon et al. (2012) suggest a more detailed mechanism to pelletal formation, involving a fluidized spray granulation during emplacement. The mechanisms involves continuous injection of liquids, solutions or melts into a powdery fluidized bed, which produces a dispersion of larger coated granules (pelletals) that are simultaneously dried by gases. The types 3, 5 and 7 represent very well these mechanisms due well-rouded shapes with layered concentrically aligned.

The elliptical geometry exhibited by type 1 and 8 pelletal lapilli suggests that a major surface tensional envolved and consequently a major variable in fluidized spray granulation (Gernon et al., 2012). The presence of multiple rims of the type 6 and concentrically aligned phenocrysts in external rim is suggestive of a systematic multi-stage layering process. The wide diversity of cored juvenile clasts from Grota do Cedro also suggest differently pulses during the formation of this kimberlite, presenting a strict relation to uncored clasts. A fluidized spray granulation occurs when a new pulse of kimberlite magma intrudes into unconsolidated pyroclastic deposits within the diatreme (Gernon et al., 2012), therefore, each pelletal structure may be related to the magmatic flows that gave origin to the different clasts.

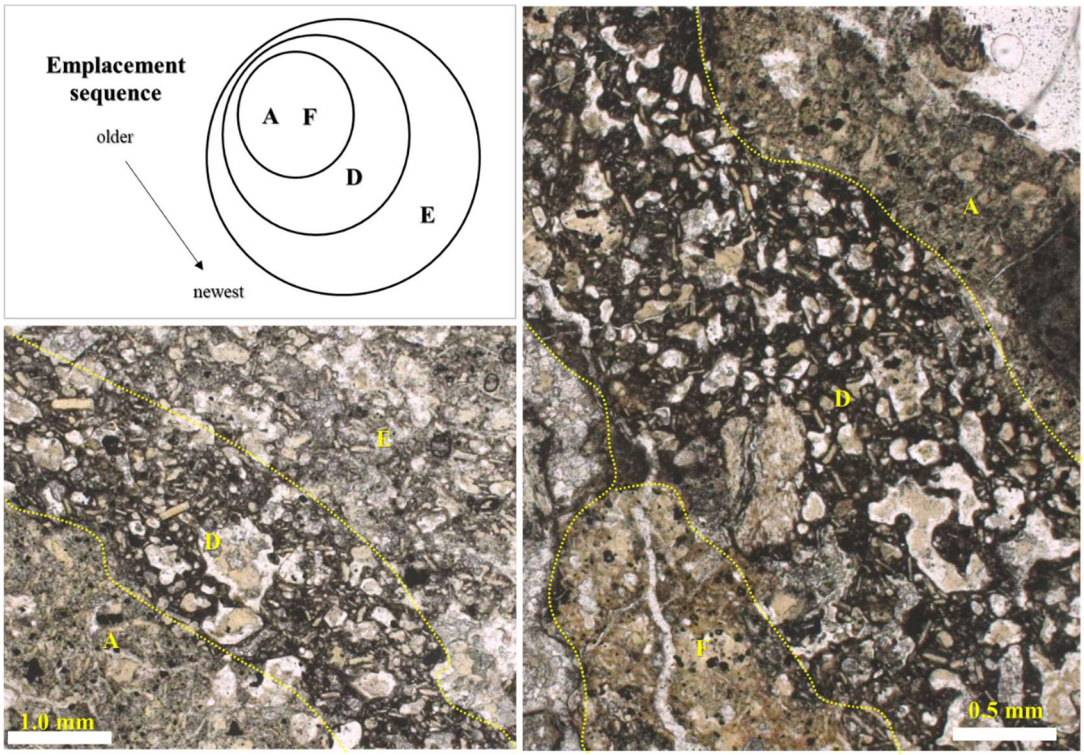

Fig.2.26. The emplacement sequence of uncored clasts from Grota do Cedro kimberlite.

The grain size criterion is not self-sufficient to establish the relationship between megacrysts and macrocrysts due to the fact that both can be derived from larger grains crystals (Pivin et al., 2009), including megacrysts and xenolith-derived fragments, which may have been mechanically reduced during the process of the primary kimberlite material. In this study, most mineral grains available are in fact smaller than 10 mm in diameter and do not fit the strict definition of megacrysts. Therefore, based on major and trace element compositions, the word "megacrysts" can be link to genetic processes rather than just as a description of mineral size.

Process recorded by major elements

In the garnets, the first stage of mantle metasomatic enrichment can be recognized by the abundance of such elements, e.g. high-chromium and low-calcium, with sinusoidal REE patterns (Shchukina et al., 2015). Normally, harzburgite garnets (high Cr_2O_3 and low HREE) evolve with continuous metasomatic event to lherzolitic composition, characterized by a concurrent decrease in CaO-Cr_2O_3, depletion of LREE and enrichment in Al_2O3, TiO_2, Y and

HREE. The Cr content of garnet is a primary indicator of the degree of depletion of the host rock (Griffin et al., 1999).

The mantle garnets analyses from Grota do Cedro correspond to lherzolitic origin, but the amounts of Cr_2O_3 and CaO are moderate (3.63 to 6.42 wt.% and 4.51 to 6.88 wt.%, respectively). There are no significant compositional variation from core to rim, and an addition to intermediate values of Mg# (0.77 – 0.81), which decrease with mantle metasomatism evolution, it is possible to suggest that these garnets represent an intermediate stage of metasomatic enrichment (Fig.2.27). They are very similar (in relation to major elements) to "Lz 3" garnets studied by Shchukina et al. (2017), these garnets type occur through the section of the lithospheric mantle up to 69 kbar, and according to modeling results, the composition of the parental melt in this stage could be close to mica-poor picrites.

The "Lz3" garnets in lherzolite samples are associated but are not in trace element equilibrium with clinopyroxenes (Shchukina et al., 2015). The clinopyroxenes in those lherzolites are in REE equilibrium with a silicate melt that is depleted in LREE and close in composition to the fractionated Turiyno basalt (Shchukina et al., 2015).

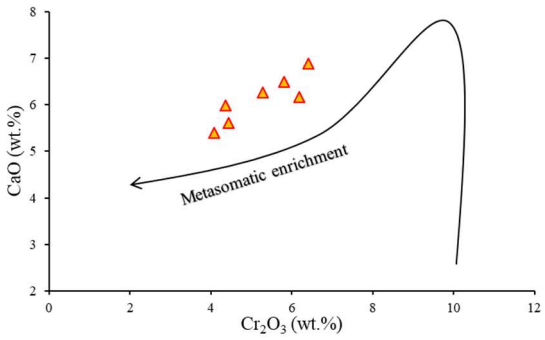

Fig.2.27. The garnet CaO-Cr_2O_3 evolution. The triangles are garnet cores from Grota do Cedro kimberlite and the arrow indicate the metasomatic enrichment from harzburgitic to lherzolitic composition (modified of Shchukina et al., 2017).

The higher Mg#, Cr# and Al_2O_3 values of the high-chromian clinopyroxene group suggest a peridotite origin for this grains, being very similar to worldwide peridotites (Pivin et al., 2009) following this trend. A relatively high TiO_2 content is one of the essential features used to distinguish the megacrysts, irrespective of whether they belong to the low chromium or high-chromium megacryst association (Kostrovitsky et al., 2004). The high TiO_2 values indicate that the low-Cr clinopyroxene group represent disintegrated fragments from

megacrystals, and these features can be equated with worldwide megacrysts peridotites (Pivin et al., 2009). However, two grains from low-Cr group have ~ 0.5 wt.% Cr_2O_3, very low TiO_2 and high Na_2O values being similar to high-Cr group, furthermore, they can also be considered from peridotite xenoliths.

The low-chromium megacrysts can be crystallized from magmas bodies by normal crystallization fractionation in the deep lithosphere in the protokimberlite stage (Gurney et al., 1979). The parental (protokimberlitic) magma may evolve to kimberlitic magma as a result of interaction with the lithospheric mantle and assimilation of rocks enriched in incompatible elements (Agashev et al., 2006). Many origins are attributed to megacrystals, e.g. magmatic origin or from mantle xenoliths, the low Mg# and La/Sm ratios can suggest a fractional crystallization (Kargin et al., 2016; Nimis et al., 2009), however, the chemical composition of the supposed low-Cr megacrysts clinopyroxenes from Grota do Cedro can be from pyroxenites (Table 19) or Fe-rich lherzolite (Ionov et al., 2005).

In relation to chemical characteristics, there is a great similarity between pyroxenes from Grota and the pyroxenes in pyroxenite from Mzongwana kimberlite (Boyd et al., 1984). The pyroxenites are low in Cr_2O_3 and are richer in FeO and TiO than equivalent phases in common garnet lherzolites; in this respect, according Boyd et al. (1984), they are similar to the more Fe-rich discrete nodules. The pyroxenes from Grota are higher in Fe displaying a diopside-hedenbergite and an enstatite-ferrosilite solid-solution, in addition to relative low Mg# (< 0.88) and Cr_2O_3 (< 0.28 wt.%), the pyroxenites can be a possible origin from these low-Cr group. The Cr_2O_3 content is lower in pyroxenite pyroxenes than peridotite pyroxenes whereas TiO_2 contents are higher (Chen et al., 2014).

The evidence that can link the pyroxenite to their kimberlite host is the nature of the abundant phlogopite crystals dispersed in the kimberlite; however, Ti- rich phlogopite grains in the pyroxenites are very similar in composition range and appearance with from kimberlite.

The low-Ti cores phlogopites from Grota do Cedro, additionally to high Mg# values (0.87 to 0.92) can indicate the peridotite origin for this phlogopite type, plotting within phlogopite K-richterite peridotites and metasomatized xenoliths field (Fig. 2.17). Zoning is a typical feature of phlogopite macrocrysts in kimberlites (Mitchel, 1986) and the low metasomatism (T range 950 – 110°C) is accompanied by the introduction of this mineral (W. L. Griffin et al., 1999). The low-Ti types from Grota have variable composition from core to rim suggesting a low metasomatism enrichment. The occurrence of phlogopite inclusion in low-

Cr/high-Ti clinopyroxene suggest that this latter crystallized after or in overlap with phlogopite, which exhibit higher Ti and Fe.

The high-Ti cores (with high and poor Cr) are higher compositionally homogenous than low-Ti and exhibit lower Mg# (~0.86) and may be linked to the crystallization of phlogopite of the kimberlite megacryst suite (Nixon and Boyd, 1973). Another possibility and considering the pyroxenites as a probably mantle xenocrysts source, these crystals maybe from pyroxenites xenoliths, the same source of pyroxenes. The high-Ti phlogopites, which include the classified in this work like high Ti-Cr and the that included in a low-Cr clinopyroxene (with suppose from pyroxenitic origin), have great similarity with pyroxenitic phlogopites from Mzongwana kimberlite (Boyd et al., 1984), e.g. high FeO (up to 10.44 wt.%), TiO_2 (up to 4.28 wt.%) and low Cr_2O_3 (up to 0.48 wt.%).

The spinel anhedral grains from Grota do Cedro can could be from peridotite sources, while the euhedral grains can could be from a primary phase in the rock. Although the composition overlapping between xenolitic macrocrysts and euhedral grains (Schulze, 2001), the chemical composition reflected by patterns in the binary graphic between of the spinels from Grota is very distinct, pointing to different origins. The macrocrystal follow mainly Cr-Al trend, while euhedral grains follow Fe-Ti trend, suggesting for this latter an evolution of spinel compositions during fractional crystallization from the host magma, which increases the Fe/Mg ratio and the Ti content of the melt (Barnes and Roeder, 2001). The anhedral grains plotted within Al-Cr suggesting an equilibrium with pyroxenes and may indicate the origin of these crystals being from mantle xenoliths.

Process recorded by trace elements

Clinopyroxenes typically are LREE-enriched and have high Ti/Eu, indicating kimberlite rather than carbonatite metasomatism (Howarth et al., 2014) and the elevated Ti and Zr contents in clinopyroxenes (TiO_2 > 0.7 wt.%), could reflect the impact of high-temperature melt-related metasomatism (Griffin et al., 1999) most likely of essentially carbonate nature (Sokol et al., 2016).

The pyroxenes analysed from Grota do Cedro display positive correlation between Y and Zr concentrations. The grains that exhibit variable variation compositionally from core to rim follow the low-T metasomatism, and two homogeneous grains follow the high-T metasomatism and are homogeneous. Low-T metasomatism is generally only recorded in zoned

grains, characterized by increases in CaO, Zr, Y, Ti, and distinct Zr *vs*. Y and Zr *vs*. Ti trends (Griffin et al., 1999).

Higher $(La/Yb)_N$ (Howarth et al., 2014) or $(Sm/Er)_N$ (Shchukina et al., 2017) at constant Ti/Eu can be used to distinguish between carbonatite and kimberlite metasomatic process. The $(Sm/Er)_N < 1$ and > 5 characterizes a silicate and carbonatite metasomatism, respectively, while $1 < (Sm/Er)_N < 5$, matching the transitional position between two metasomatism types. The most of pyroxenes from Grota display constant values of Ti/Eu (with exception of one grain) and high $(Sm/Er)_N$ (0.3 – 8.85) and $(La/Yb)_N$ (0.00 – 39.26) indicating that the LREE enrichment is likely related to carbonatite metasomatism.

The lherzolitic garnets from Grota submitted to intermediate stage of mantle metasomatic enrichment with depletion in Cr_2O_3 and enriched in Al_2O_3 and TiO_2, can testifies a silicate composition of the metasomatic agent (Shchukina et al., 2017), and they can be in agreement with the single clinopyroxene grain that follow the silicate metasomatism trend, indicating the influence of a second metasomatic enrichment.

The high LREE concentrations of clinopyroxenes associated with negative Nb, Ta, Zr, Hf and Ti anomalies have been interpreted to result from metasomatism of the subcontinental lithospheric mantle (SCLM) by silicate melts/fluids (Shchukina et al., 2015), or kimberlite melts (Kargin et al., 2016). They could be the final product of a metasomatism of garnet peridotites within the SCLM (Kargin et al., 2017), and maybe the same source that formed the lherzolitic garnets (Fg. 2.28).

Higher $(La/Yb)_N$ at constant Ti/Eu can also be used to distinguish between carbonatite and kimberlite metasomatism. Clinopyroxenes analyzed in this study have show relatively high Ti/Eu values, inconsistent with carbonatite metasomatism, indicating that the LREE enrichment is likely related to kimberlite metasomatism.

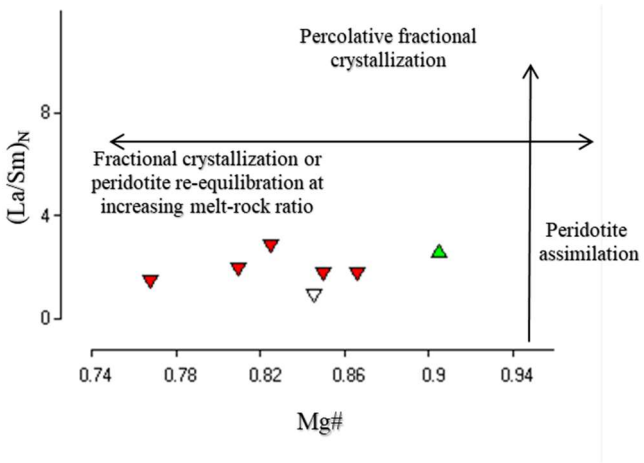

Fig.2.28. Relations between Mg# values and LREE fractionation for clinopyroxene (after Kargin et al., 2016; Nimis et al., 2009)

The metasomatism is a pervasive process in the mantle, as exhibited by mantle xenoliths worldwide (Howarth et al., 2014). The spinel Cr# values increase with the evolution of partial melting, the Grota do Cedro spinel macrocrysts exhibit relative high Cr# (Cr/(Cr + Al) (0.62 – 0.81) with low and high Ti (0.005 to 0.50 wt.%). The high Cr# > 0.6 (Bhat et al., 2017a) or > 0.8 (Schulze, 2001) are characteristics of depleted peridotite. In abyssal peridotites, melt extraction results in TiO_2 depletion (<0.1 wt.%) but increase in Cr# (≤ 0.6) in associated Cr-spinels, the TiO_2 enrichment of the spinel occur when these residual peridotites later react with MORB composition melts (Ti-rich) without increasing their Cr# (Pearce et al., 2000), whereas reaction with boninite melts results in high-Cr and high-Ti spinels.

The high Cr# of macrocrysts spinels analysed point to an existence of "primary fertile" peridotite, and associated with low TiO_2 can indicate higher degrees of partial melting characteristic of Cr-spinels related to subduction zone magmas. When associated with high TiO_2 suggest that these Cr-spinels are related to highly refractory peridotites (i.e., dunites and harzburgites) formed in a supra-subduction setting by hydrous melt extraction and by melt-rock reaction (Bhat et al., 2017; Pearce et al., 2000). The depleted REE patterns relative to PM can be observed in Cr-spinel from Grota (Fig. 2.18) and have been observed in orogenic peridotites, abyssal peridotites and ophiolitic peridotites. In ophiolites, the depleted REE patterns are restricted to refractory mantle peridotites with their petrogenetic interpretation of being mantle-melting residues

The average of isotopic date are compared with perovskites $^{87}Sr/^{86}$ Sr ratios from APIP kimberlites (Guarino et al., 2013) and bulk-rock data from Group I and II kimberlites (Becker and Le Roex, 2006; Skinner et al., 1992, Woodhead et al., 2009). Trace element characteristics, including mobile elements and $^{87}Sr/^{86}Sr$ ratios are typically used to explore crustal contamination in kimberlite magma (Sarkar et al., 2014). Strontium isotope compositions can also be used as supporting evidence against significant crustal contamination of the magma from which the perovskite crystallised.

The Fig. 2.29 shows the perovskite $^{87}Sr/^{86}$ Sr ratios from Grota do Cedro kimberlite and occur an overlapping between APIP perovskites and bulk-rock of Group I. On average, the ratios Grota acquired are higher than Group I kimberlite but equal with APIP rocks. The Grota present slightly higher $^{87}Sr/^{86}Sri$ ratios (0.705156 and 0.706447) than APIP rocks (0.70506–0.70565; data from Guarino et al., 2013) and Group I kimberlites (0.70328 to 0.70537; date from Becker and Le Roex, 2006).

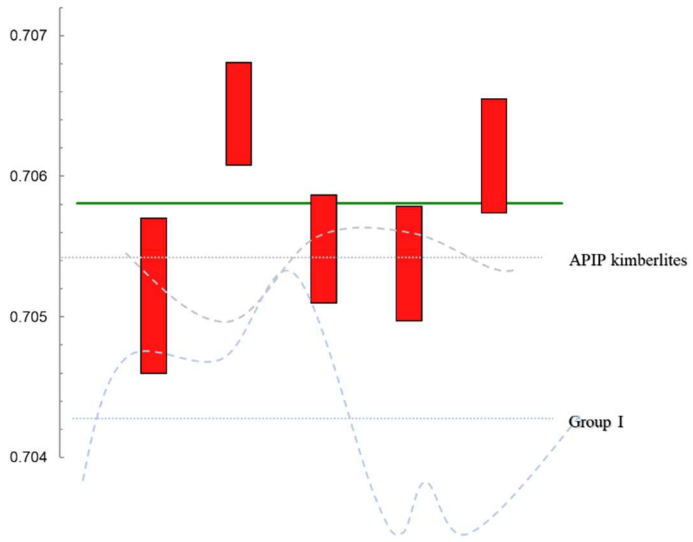

Fig. 2.29. $^{87}Sr/^{86}Sr$ perovskite data from Grota compared with $^{87}Sr/^{86}Sr$ perovskite data for APIP kimberlites (Guarino et al., 2013) and bulk-rock from Group I and Group II kimberlites (Becker and Le Roex, 2006).

These suggested that the Sr isotope compositions from groundmass perovskite are more representative of the uncontaminated kimberlite magma than those from bulk rock studies, which are often contaminated (Paton et al., 2007). Therefore, the major variance between bulk

rock and perovskite analyses is more marked for fragmental, massive volcaniclastic or pyroclastic kimberlites (Sarkar et al., 2014). The Grota kimberlite have uniform Sr isotopic compositions, as it is seen in some APIP rock and Indian and Chinese kimberlites (Guarino et al., 2013; Woodhead et al., 2009), suggesting low upper crustal contamination.

The Grota perovskites show considerable enrichment in REE, Th and Na, and unusual Nb contents. The compositional variation between different perovskite types point to multiple generations of perovskite, and probably reflect different crystallization conditions (Chakhmouradian and Mitchell, 2001), as perovskite can crystallize over a wide range of pressure-temperature conditions, and under differing activities of minor elements.

Sr isotope ratios tend to be insensitive to the timing of perovskite crystallisation due to the very small P–T window in which perovskite crystallises from kimberlite magma (Sarkar et al., 2014). A progressive assimilation of crustal material into the kimberlite magma, through melt-wall-rock interactions over the range of perovskite crystallization temperatures, can result in compositional and isotopic variations in perovskite (Malarkey et al. 2010). Another evidence that can suggest a crustal contamination are La/Yb values of the perovskites (< 290) relative to the whole-rock samples are consistent with low contamination after the crystallization of the perovskite (Mitchell & Reed, 1988).

It is possible that there was no significant contamination of the kimberlite magma from which the perovskite crystallized, and maybe the perovskites from Grota do Cedro represents a pre-shallow level contamination magma characteristic.

APÊNDICE 3 – Kimberlito Régis

Mineralogy and Petrology of the Régis diamondiferous kimberlite pipe, West of Minas Gerais, Brazil

Summary

1. Introduction

Kimberlites are potassium and ultramafic igneous rocks that belong to a suite of volatile-rich, high-MgO, and ultrabasic rocks. Together with lamproites, they are potentially diamondiferous members that occur as small volcanic pipes, dikes and sills. Their typical inequigranular texture is determined by mega-crystals / macro-crystals set in a fine groundmass, often containing ultramafic inclusions from mantle rocks and varying amounts of xenocrystals and crustal xenoliths (Dawson, 1971; LeMaitre et al., 1989; Mitchell, 1986; Skinner and Clement, 1979).

The many crystallization phases undergone by magmatic fragments and the xenocrystals derived from various types of xenoliths, in addition to high alteration degrees (mainly serpentinization of olivine), make it difficult to identify and rebuild the original composition of kimberlitic magmas. This reflects the understanding of the magmas' ascension dynamics and eruption, and their economic interpretation and petrology (McCall (2005).

In Brazil, circa a hundred kimberlitic intrusions and correlated rocks, eg., kamafugites, lamproites and carbonatites, are known to occur in the Alto Paranaíba Igneous Province (APIP), as a result from mafic-alkalic magmatism that took place along a NW-SE lineament in the Minas Gerais State in Late Cretaceous (Gibson et al., 1995). The kimberlite intrusion investigated in this work, known, as Régis or Sucesso 1, is located in the Carmo do Paranaíba district to the south of Patos de Minas city, western Minas Gerais (Fig. 3.1). De Beers discovered the intrusion in the 1970s. Some researchers have studied this occurrence ever since, which resulted in a significant amount of available morphological and chemical data (Chaves et al., 2009; la Terra et al., 2010; Read et al., 2004; Rocha et al., 2013; Thomaz, 2009). Micro-diamonds were recovered from 229.6 meters depth (Cookenboo, 2009), which indicates that the mineral chemistry and emplacement of the Régis kimberlite reflect favorable conditions for diamond preservation.

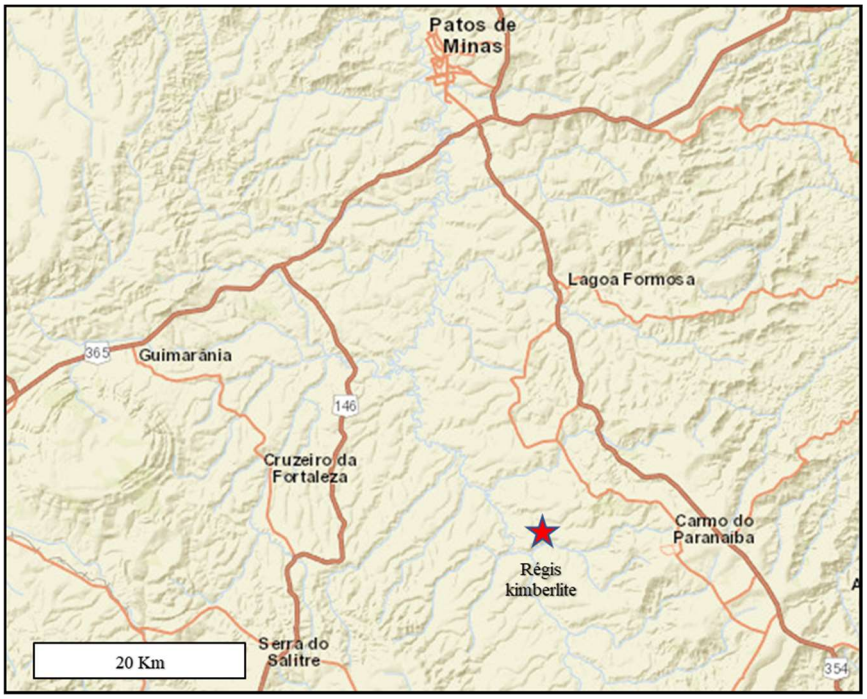

Fig. 3.1 - Location of the Régis kimberlite (red star) near Carmo do Paranaíba and Patos de Minas cities, western Minas Gerais, Brazil.

2. Geology and geological setting of the Charneca kimberlite

The Alto Paranaíba Igneous Province (APIP) forms an elongated, 1,100 km long and 200 km wide NW-SE structure (Haralyi & Hasui 1982; Hasui & Haralyi 1991, Gibson et al., 1995) that separates Paraná and Franciscana basins across southeastern Minas Gerais and southwestern Goiás. It coincides structurally with the southern portion of the Neoproterozoic Brasília Belt (Almeida, 1967; Schobbenhaus and Neves, 2003), and it was established along the Ponta Grossa arch during the Neocretaceous, as a result of an intense mafic-ultramafic, alkaline and ultrapotassic magmatism that generated intrusive and extrusive bodies. (Almeida, 1983, Gibson et al., 1995b).

The arc is well marked by magnetic anomalies, and it is associated to alkaline magmatic manifestations, mostly coinciding with the alkaline intrusive bodies (Almeida et al., 2000). The mega-lineament Az125 corresponds to many of these intrusions, distributed along a N35°W direction (Leonardos & Meyer 1991). The magmatism is attributed to the impact of the Trindade mantle plume beneath a previously metasomatized subcontinental lithospheric mantle in this region (Gibson et al., 1995; Sgarbi et al., 2004; Thompson et al., 1998)

The Régis kimberlite emplaced into the Serra da Saudade formation, which is composed mainly of shales/phyllites of the Bambuí Group, which, in turn, together another Precambrian groups (Araxá, Ibiá, Canastra), are covered by the Mata da Corda Group, an extensive Upper Cretaceous cover of tuff and lava flows of the APIP (Read et al., 2004). Although its outcrops are strongly weathered, this intrusion presents good superficial exposure (la Terra et al., 2010). Reddish/yellowish soils derive from the host rocks.

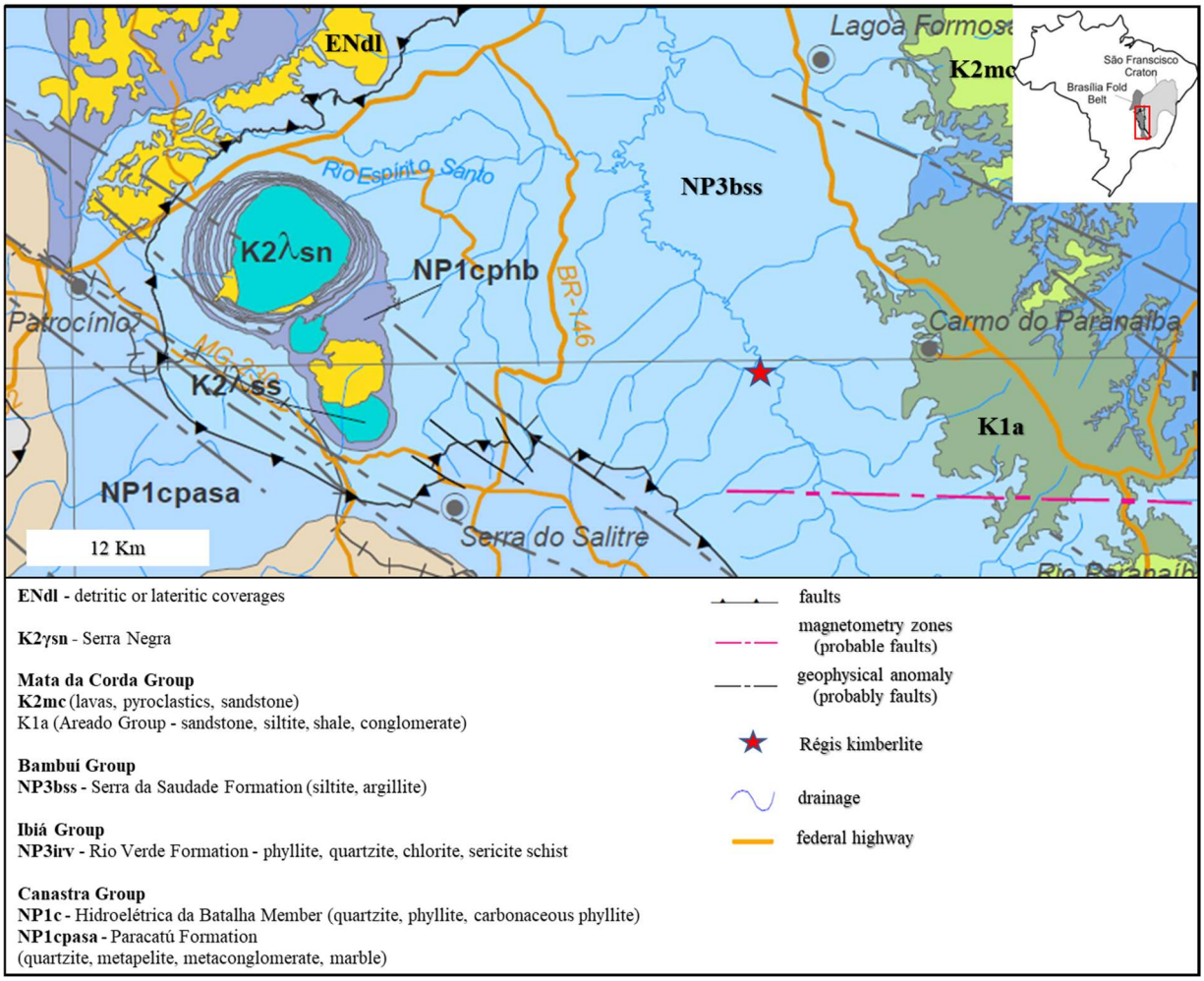

Fig. 3.2. Geological and geotectonic setting of the Régis kimberlite (red star) (Modified from CPRM, 2014).

3. Previous Works

Read et al. (2004) carried out geothermobarometric studies of clinopyroxenes from diamond-bearing kimberlites (Régis and X270) and kamafugites (without diamonds) rocks from the APIP. These authors showed that the kimberlites erupted in the Early Cretaceous through a cooled cratonic lithosphere suitable for the preservation of diamonds. Considering that the alkaline volcanism commenced with kimberlites and culminated with kamafugites, they

revealed short time changes in geothermal conditions at the beginning of the kamafugite magmatism, a diamond stability field being recorded in the range of 880-1000 °C for kimberlites, and a higher, 950-1175 °C temperature range for kamafugites corresponding to a graphite stability field.

Thomaz (2009) also performed geothermobarometry studies of pyroxene and lherzolitic garnets. The results are in accordance with Read et al. (2004), in that a deep region (40 to 53 kb) indicated a cold geothermal region in equilibrium with diamond stability. Two lithological units were then characterized by surface mapping of the Regis kimberlite: a muddy conglomerate and an argillite. The first one crops out at the edge of the intrusion and near the drainage system that intersects it, being composed predominantly of muddy and sandy-muddy conglomerates that correspond to host rock phyllites, besides kimberlitic volcanic materials. The second unit outcrops in the central and upper parts of the intrusion, being composed of clay and silt sedimentary rocks, in alternation with thin gray sand layers. Indicator minerals are rare in both units; only pyrope garnet, cr-diopside and opaque minerals are recognized. Thomaz (2009) also carried out chemical analyses of phlogopite, ilmenite and perovskite. The results indicate similarity with type I kimberlite and lamproite.

Other mineralogical investigations of the Régis kimberlite were performed by Chaves et al. (2012, 2009), who proposed that the Régis kimberlite pipe bears more resemblance with a lamproite pipe. Moreover, mineralogical characteristics, such as the presence of sanidine, indicate a lamproite “trend”.

Other studies (La Terra et al., 2010; Rocha et al., 2013) investigated the morphology of the Régis volcanic conduit by using CSAMT, a gravimetric and magnetometric geophysical method. The intrusion’s depth was estimated to be of about 800 m, and its diameter on surface was about 200 m. The conical configuration was one of the characteristics that prompted Chaves et al. (2012, 2009) to propose a revision of the mineralogical definition of the intrusion.

4. Petrography

The Régis kimberlite shows inequigranular, moderately to poorly sorted clast-supported and matrix-supported textures. Coarse ash- to medium-lapilli-sized juvenile fragments and accessory clasts (country and mantle xenoliths) set in an interstitial medium dominated by carbonates, serpentine and spinel are present (Fig 3.3 and 3.4).

Most of the kimberlitic material we analyze here (85.44 m to 278.93 m) occurs as juvenile clasts, with or without nucleus, different compositions and shapes, within in a fine interstitial medium, with local replaced texture, reflecting a complex emplacement process. Single crystals are rare, being usually rimmed by kimberlitic material or composing uncored clasts.

The cored juvenile clasts range from ash to lapilli size and occur in several shapes, controlled by the size and shape of the core, that often consists of olivine and rare country rock, and by the dynamics of emplacement. Single and multiple symmetrical and asymmetric, complete and incomplete rims were observed. Nine different uncored juvenile clasts were recorded, which were grouped into four types according to the similarities between them and to the difficulty of recognition due to alteration. They range in size from ash to lapilli, with variable shapes, angular to amoeboid margins reflecting different deformation levels.

Country rocks occur in the entire depth of the holes studied. As depth increases, fragments tend to become larger and less angular. Two types of mantle xenoliths are observed, one with abundant phlogopite, other one rich in phlogopite, olivine and perovskite.

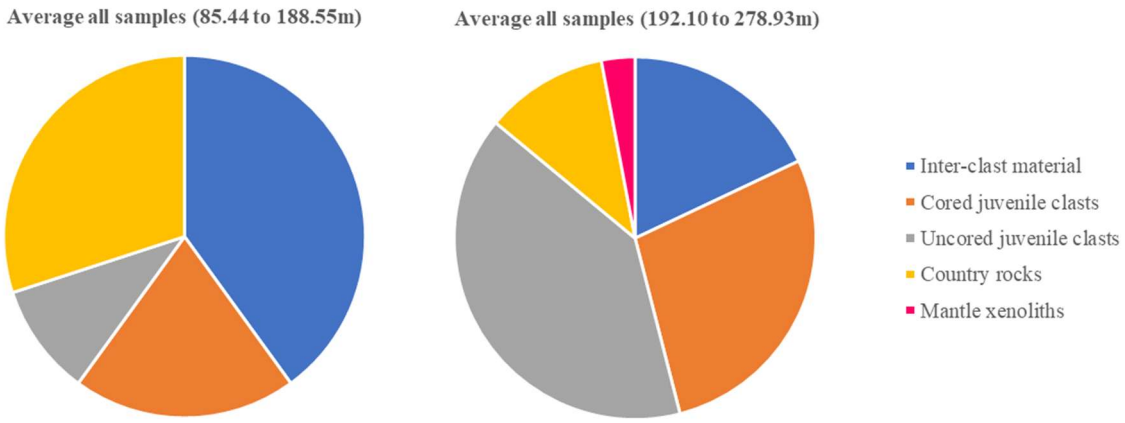

Fig. 3.3 - Estimated average of the main constituents of the Régis kimberlite.

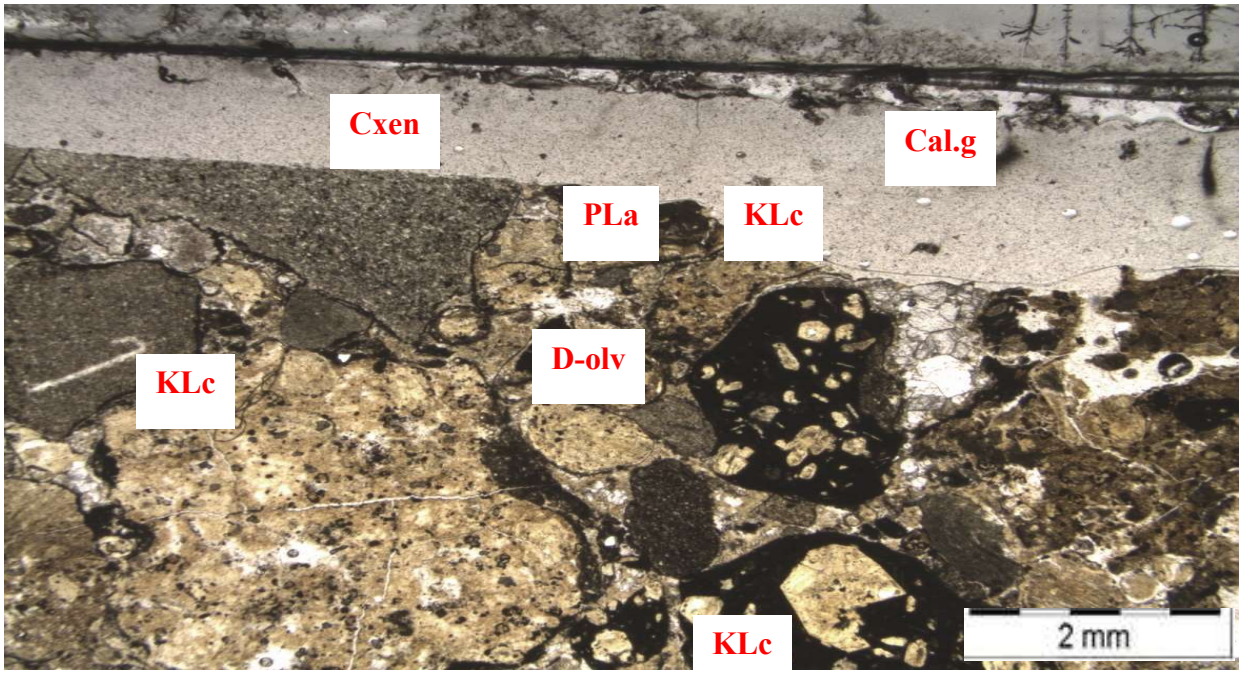

Fig. 3.4 – Clast-supported and matrix-supported textures of Régis kimberlite. KLc: kimberlitic lithic clast; PLa: pelletal ash; D-olv: discrete olivine; Cxen; crustal xenolith; Cal.g: groundmass with well crystallized calcite.

4.1 Texture

At the shallowest hole depths (85.44 to 188.55 m), the Régis kimberlite shows matrix-supported texture, are poorly sorted, with few clast-clast contacts (Fig. 3.5). Ash interstitial medium supports the few clasts present, locally resembling a cement. From 192.10 m to 278.93 m, a clast-supported, very poorly to moderately sorted texture is present. There is an increase in the number of kimberlitic clasts and lapilli structures supported in an interstitial medium dominated by carbonates and serpentine. Intra-clast contacts become more common with depth.

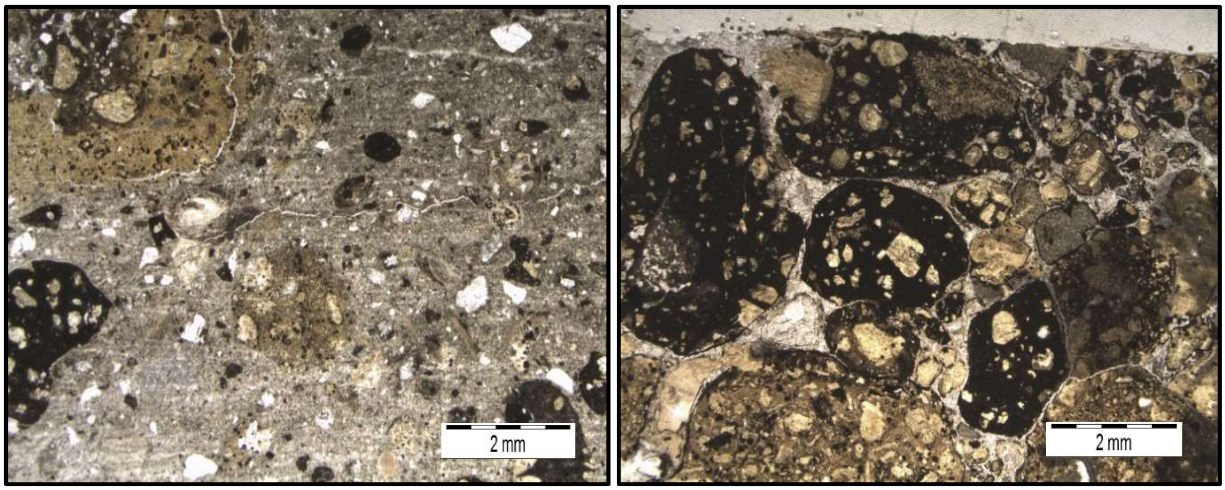

Fig. 3.5. Microscopic textures of Régis kimberlite. On the left, a matrix supported texture with juvenile fragments set in ash interstitial medium (170.32 m). On the right, a clast supported texture, juvenile fragments and lapilli structures in contact (253.44 m).

4.2 Interstitial medium

The dominant interstitial mineral is commonly of the serpentine group. Its origin is generally ambiguous, and whether it is primary, secondary pore-filling cement, or a replacement of original fine-grained ash matrix is contentious (Porritt et al., 2012). The most common interstitial medium observed is light brown and pale yellow in color, with irregular patches of speckled pale-brown serpentine and clay visible in plane-polarized light (Fig. 3.6a). Yellow interstitial medium with cement aspect is dominant, consisting of a cryptocrystalline mixture dominated by serpentine, clays and carbonates (Fig. 3.6b). Locally, extremely large carbonate crystals (up to 12 mm) define a granoblastic texture (Fig 3.6c).

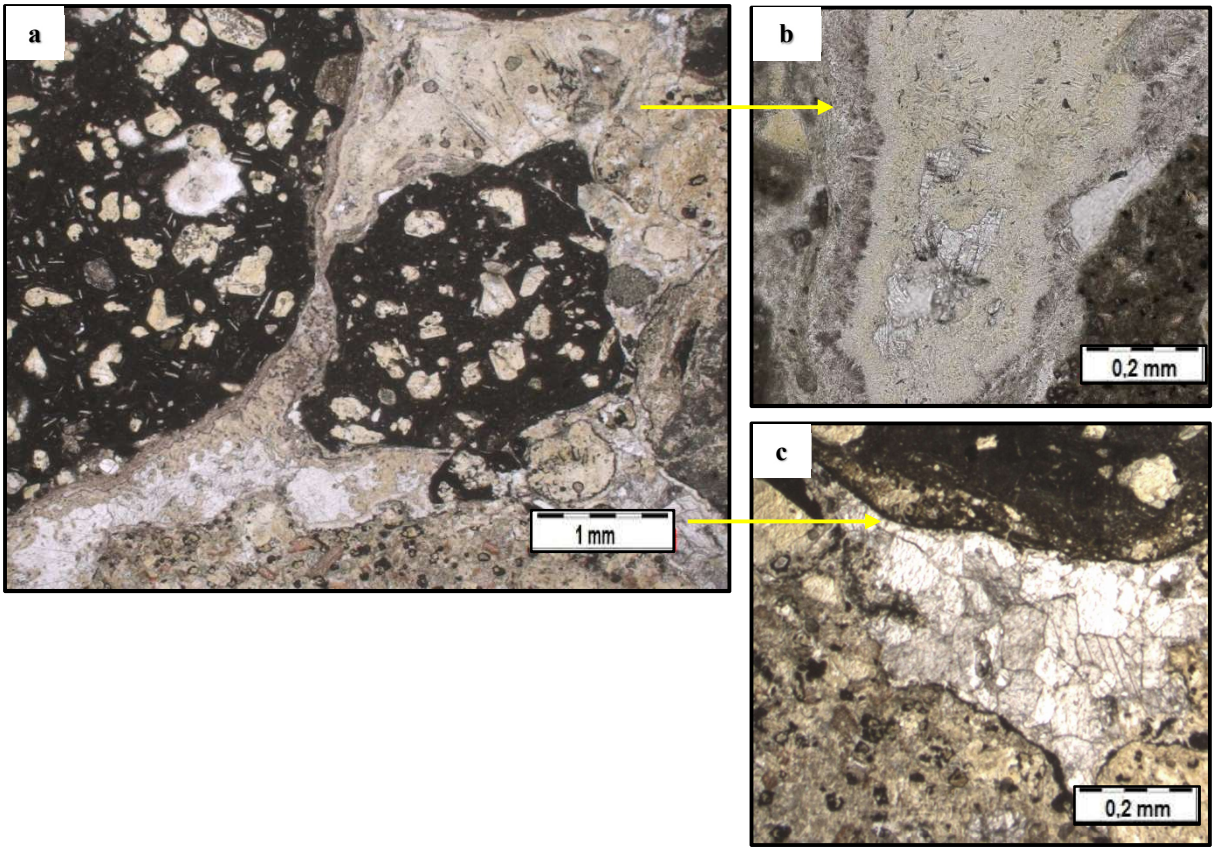

Fig. 3.6. Textures of interstitial medium in the Régis kimberlite (a) cryptocrystalline pale yellow-brown mixture dominated by serpentine, clays and carbonates in the upper portion. The white interstitial medium in the lower portion is dominated by carbonates crystals well-developed; (b) yellow-brown interstitial medium magnification showing fine-grained speckled material. Notice the carbonate crystals developed apparently bellow this texture; (c) white interstitial medium detail with carbonate crystals with granoblastic texture.

4.3 Juvenile clasts

Magma clasts form in vents during explosive eruptions, the term “juvenile” referring to the solidified material, in this case a volcanic rock clast preserved in a deposit (Cas et al., 2008). In volcanological nomenclature, juvenile pyroclasts are generated by disruption, as a direct result of volcanic action (Schmid, 1981). Regarding kimberlites, the term is either magmatic or clastic. “Juvenile clast” is used loosely for juvenile pyroclasts and juvenile pseudo-clasts (produced by alteration and replacement processes). It excludes discrete (free) crystals and xenoliths (Webb, 2006). Juvenile magmaclasts was introduced by Field and Smith (1998), as a non-genetic term that encompasses all juvenile clasts and discrete cognate crystals.

The approach of Cas et al. (2008) was taken for the discrimination among components of the Régis kimberlite. For the description and characterization of juvenile clasts, the non-genetic scheme of Webb (2006) was used, as summarized in tables 3.1 and 3.2.

4.3.1 Kimberlite lithic clasts

The term “kimberlite lithic clast” refers to co-magmatic kimberlite solidified deeper in the vent and then incorporate (Cas et al., 2008). In the Régis kimberlite, nine types of kimberlitic clasts are observed (Fig 3.7), that differ in modal abundance, shape and frequency (Fig 3.8). Table 3.1 summarizes the characteristics of each type. Because of their similarities, they are approached together.

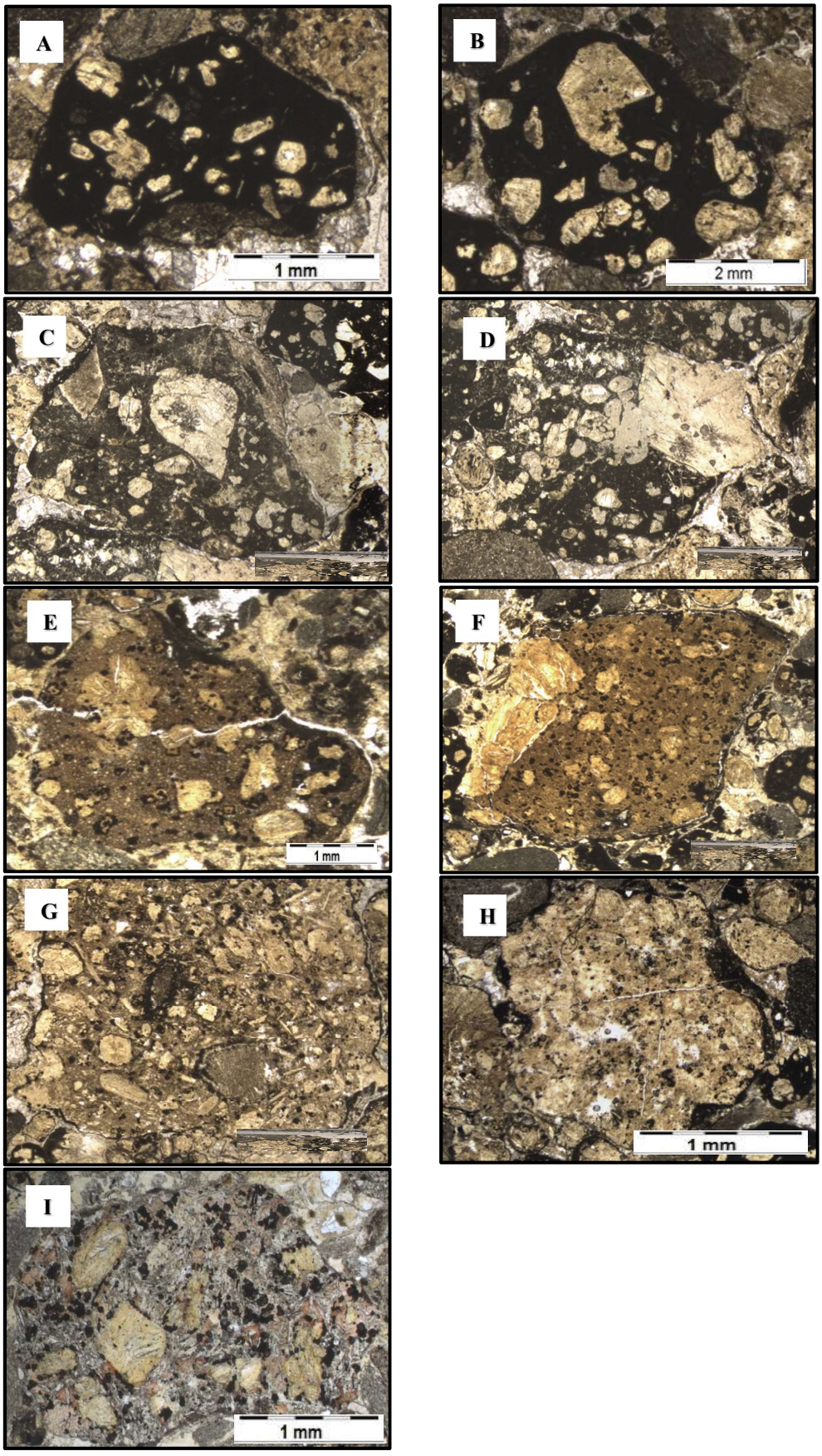

Fig. 3.7 – types of uncored juvenile clasts of the Régis kimberlite, distinguished based on relative modal abundance and shape of minerals; nine types of clasts are identified. However, due to similarities they are further grouped into four groups: AB, CD, EFGH, I.

Table 3.1 - Petrographic characteristics summary of uncored juvenile clasts of the Régis kimberlite.

	MORPHOLOGY	VESICULARITY	CLAST-HOST RELATIONSHIP	MINERALOGY	GROUNDMASS CRYSTALLINITY	SIZE RANGE
A	El-SbQ /SbR- R / SbI	Sparsely vesicular partially filled. Irregular and sometimes with elongate form.	Well-defined margins clast set in a cement and carbonate interstitial medium.	Pseudo-olivine: moderate (18%), euhedral, fine to medium (0.03-0.18mm). Phlogopite: moderate (15%), euhedral, micro to medium crystals (0.04 - 0.26mm). Perovskite: low (3%), sub-euhedral, very fine to microcrystals (<0.04 mm). Spinel: low (3%), sub-euedral, microcrystals (<0.06).	Very poorly crystallized, brown groundmass containing serpentine and fine-grained opaque minerals.	Ash to lapilli (0.4 - 3.09mm)
B	Eq / R / SbI	Very poorly vesicular, angular and elongate forms, partially filled with diopside microlites in the edges.	Diffuse to defined margins set in a cement and carbonate interstitial medium. Ocassionally occurs within clast A.	Pseudo-olivine: moderate (18%), euhedral and multiples intergrowths, fine to coarse crystals (0.11-0.84mm). Perovskite: low (< 1%), sub-euhedral, fine crystals (0.07-0.25mm). Spinels: low (3%), sub-euedral, microcrystals (<0.06).	Very poorly crystallized, brown speckled relict groundmass containing serpentine and fine-grained opaque minerals.	Ash to lapilli (0.8 - 5.2mm)
C	El / Ang / SbI - Ic	Moderately to very poorly vesicular. Veil shape vesicles with carbonate fill and microlitic diopside.	Defined to diffuse margins clast set in a cement and carbonate interstitial medium.	Pseudo-olivine: high (20-30%), euhedral, fine to very coarse crystals (0.22-1.86mm). Perovskite: low (2 - 8%), euhedral, fine crystals (<0.22mm).Spinel: low to moderate (2 - 10%), euhedral, fine microcrystals (<0.06mm).	Very poorly greyish crystallized groundmass, with acicular microlites of diopside and irregular patches of speckled yellow-brown serpentine, carbonates and opaques. Country rock fragments are commom with angular shape.	Lapilli (2.0 - 4.2mm)
D	Eq / R / SbI	Very poorly vesicular, sparsely and irregular shape, partially filled.	Defined margins clast set in a cement and carbonate interstitial medium.	Pseudo-olivine: high (35%), euhedral, fine to coarse (0.14 - 0.60mm). Phlogopite: high (25%), euhedral, micro to fine crystals (< 0.12 mm). Perovskite: low (5%), euhedral, micro to fine crystals (< 0.24). Spinel: low to moderate (10%), euedral, microcrystals and microlites (<0.06). Orange spinel: low (2%), octaedron euhedral, microcrystal (< 0.04mm).	Very poorly greyish crystallized groundmass, with acicular microlites of diopside and irregular patches of speckled yellow-brown serpentine, carbonates and opaques.	Lapilli (2.0 - 3.9mm)
E	SbQ - Eq / SbR / Ic - SbI	Very poorly vesicular, spherical forms and infill.	Defined margins clast set in a cement and carbonate interstitial medium.	Pseudo-olivine: moderate (15%), sub-euhedral and multiple intergrowths, fine to medium (0.1-0.51mm). Perovskite: low (3%), sub-euhedral, microcrystals (<0.08mm). Atoll spinel: low (8%), euedral, microcrystals (<0.07).	Well-crystallized orange groundmass, with opaques and altered phlogopites.	Lapilli (2.5 - 6.50 mm)
F	SbE-Eq / SbA - R / SbI	Sparsely vesicular; no fill.	Diffuse to defined margins set in a cement	Olivine: moderate (15-20%), euhedral single crystals and multiple intergrowths, micro to large crystal (0.13-4.3mm). Pseudo-phlogopite: moderate - high (10-20%), euhedral, microcrystals. Perovskite: low (8%), subehedral, microcrystals. Spinels: low (10%), sub-euedral, microcrystals (<0.06mm). Atoll spinel: Low (5%), euhedral, microcystals (< 0.06mm)	Orange brown poorly-crystallized groundmass.	Lapilli (2.50 - 6.1mm)
G	Eq / R / Ic - Ia	Moderately vesicular. Irregular shape and no fill vesicles.	Diffuse margins; the clast set in a cement and carbonate interstitial medium.	Pseudo-olivine: high (20%), subehedral-anedral, fine to very coarse crystals (0.07-2.0mm). Phlogopite: high (20%), euhedral, micro to coarse crystals (0.03 - 0.77mm). Atoll spinel: moderate (12%), euhedral, microcrystals. Perovskite: moderate (12%), sub-euhedral, fine crystals (< 0.12mm).	Pale orange-yellow very poorly crystallized groundmass.	Lapilli (2.50 - 5.0mm)
H	Eq / R / Ic - Ia	Moderately vesicular. Irregular shape and no fill vesicles.	Diffuse margins; the clast set in a cement and carbonate interstitial medium; irregular and very thik rim probabily by alteration results.	Pseudo-olivine: moderate (10%), subehedral-anedral, medium crystals (0.30-0.46mm). Atoll spinel: low (5-10%), sub-euhedral, microcrystals. Perovskite: low (1%), sub-euhedral, fine crystals (< 0.12mm).	Pale yellow very poorly crystallized groundmass.	Lapilli (2.0 - 4.0mm)
I	El / SbA / Ic	Non-vesicular.	Defined margins set in a cement.	Pseudo-olivine: moderate (15%), sub-euhedral, fine crystals (0.07-0.12mm). Phlogopite: high (20 - 30%), euhedral, micro to coarse crystals (0.03 - 0.66mm). Atoll spinel: moderate (12%), euhedral, microcrystals. Perovskite: moderate (10%), sub-euhedral, fine crystals (< 0.12mm).	Well-crystallized groundmass with splecked minerals.	Ash to lapilli (1.5 - 14mm)

Sphericity: Elongate (El); Subelongate (SbE); Subequant (SbQ); Equant (Eq).

Roundness: Well-rounded (Wr); Rounded (R); Sub-rounded (SbR); Sub-angular (SbA); Angular (Ang).

Irregularity: Smoothly curved (Sc); Subirregular (SbI); Irregular curvilinear (Ic); Irregular ameboid (Ia).

Type A clasts have well-defined margins and are characterized by their elongate to subequant shapes and by being sparsely vesicular. They are composed of a moderate abundance of euhedral olivine and phlogopite phenocrysts (18% and 15%, respectively) and a low abundance of perovskite and spinels micro-crystals (3%) set in a very poorly crystallized brown, opaque oxide groundmass. Type B vesicular juvenile clasts are equant, round, sub-irregular and very poorly vesicular. They have diffuse to defined margins and are composed of a moderate abundance (18%) of olivine phenocrysts which also occurs as multiple intergrowths, and a low abundance of spinels (3%) and perovskite micro-crystals (< 1%), set in a very poorly crystallized, brown speckled relict groundmass of serpentine and opaque minerals.

Type A and B occur mostly together and have similar modal abundances. The main difference between them is the presence of phlogopite. Clasts A bear 15% of well-developed phlogopite crystals occasionally masked by alteration, whereas in clasts B the mineral is absent. In general, clasts A and B show more rounded and/or elongated forms. Bottle shapes were also observed when mixed with other clasts.

Type C clasts have defined margins, elongate shapes, angular and sub-irregular to irregular curvilinear outlines very poorly to moderately vesicular and are composed of a high (20-30%) abundance of olivine phenocrystals and a low to moderate abundance of spinel (2-10%) and perovskite (2-8%) micro-crystals, set in very grayish poorly crystallized groundmass of diopside microlites, serpentine, carbonates and opaque minerals. Country rock fragments are common, in angular shapes. Type D juvenile clasts are composed of a high abundance of euhedral olivine phenocrystals (35%), phlogopite (25%) and a low to moderate abundance of perovskite (5%) and spinel (10%). Octahedron orange spinel micro-crystals are dispersed in a very poorly grayish crystallized groundmass of diopside microlites, serpentine, carbonates and oxide opaque minerals.

Type C and Type D clasts have common characteristics: they occur in low proportions (2% and 4%, respectively), exhibit a peculiar altered groundmass with serpentine patches overgrown with diopside microlites that result in yellow-coloured edges, very coarse olivine pseudomorph phenocrystals (up to 1.86mm), frequent vesicles filled with carbonates and/or diopside microlites. They often occur in angular shapes indicative of little plastic deformation.

Types E,F,G, and H represent the second more abundant group of clasts. Type E has defined margins, subequant to equant shapes, sub-rounded, irregular curvilinear to sub-irregular outlines, are very poorly vesicular, composed of moderate (15%) euhedral / inter-grown phenocrystals of olivine and a low abundance of atoll spinel (8%) and perovskite (3%). The crystals set in an orange groundmass of well-crystallized opaque minerals and altered phlogopite. Type F clasts are composed of single or multiple inter-grown olivine phenocrysts (15-20%), a moderate to high (10-20%) abundance of pseudo-phlogopite crystals, and a low abundance of perovskite, spinel and atoll spinel (8%, 10%, 5%, respectively), set in poorly-crystallized orange brown groundmass. These clasts have diffused margins, subelongate to equant shapes, sub-angular to regular and sub-irregular outlines, being sparsely vesicular.

Equant, rounded, irregular curvilinear to amoeboid outlines, moderately vesicular and diffuse margins characterize Type G clasts.

They are composed of a high abundance of olivine and phlogopite crystals (20%) and a low abundance of atoll spinel and perovskite crystals (12%), set in a very poorly crystallized pale orange-yellow groundmass. Type H clasts have diffuse margins, equant shapes, rounded, irregular amoeboid to curvilinear outlines, are moderately vesicular, composed of a moderate (10%) abundance of pseudo-olivine, a low abundance of atoll spinel (5-10%) and perovskite crystals (1%), set in a poorly crystallized pale yellow groundmass. E,F,G, and H clasts show a light orange-yellow groundmass. Olivine pseudomorphic phenocrystals are mainly subhedral. A greater amount of perovskite and opaque crystals is observed.

A peculiar restricted occurrence that corresponds to a Type I clast was recorded at depths between 192.1 and 212.7 m, composed of a moderate abundance of olivine phenocrystals (15%), atoll spinel (12%) and perovskite micro-crystals (10%). Fresh salmon colored euhedral phlogopite crystals are large (up to 0.66 mm) and highly abundant (20 to 30%). Elongated shapes are common, with sub-angular to rounded and irregular curvilinear outlines. Occasionally, rimmed olivine crystals form pelletal structures, occurring in elongated shapes at a depth of 212.70 m, reflecting plastic deformation as evidenced by crystal alignment and curvilinear margins.

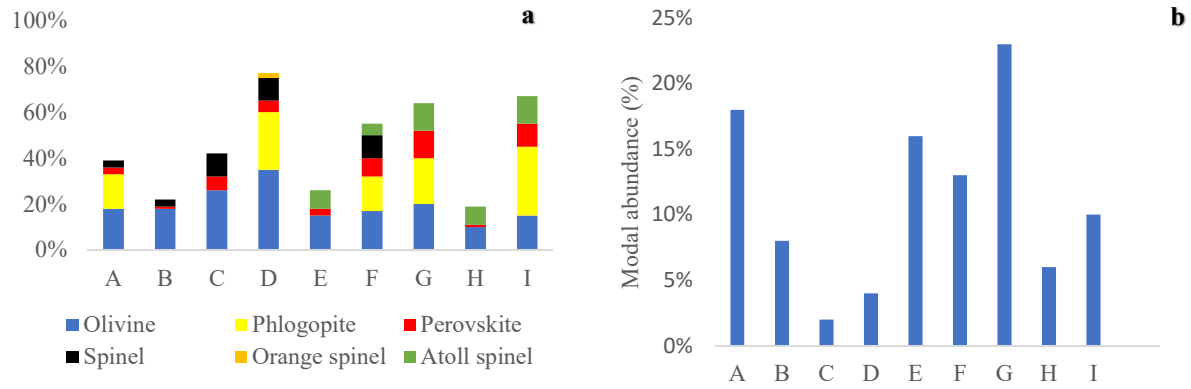

Fig. 3.8 – Diagrams showing the composition (a) and modal abundance b) of uncored juvenile clasts.

4.3.2 Pelletal structures

Pelletal structures encompasses all round to elliptical juvenile clasts of ash, lapilli or bomb size composed of variably crystallized cored kimberlitic materials. Crystal shells can or cannot display flow arrangement. When clasts or crystals have alteration rinds, they are called pseudo- pelletal lapilli (Cas et al., 2008). Pelletal or ash lapilli represent the interface between volatile components and the erupting magma (Lloyd and Stoppa, 2003).

Eight types of cored juvenile pelletal ash / lapilli prevail in the Régis kimberlite, with symmetrical and asymmetrical cores composed almost always by euhedral to subhedral olivine crystals totally replaced with serpentine. However single rim are the most common ones, pelletal structures with multiple rims of different sizes and compositions (Table 3.2, Fig.3.9) are present. Pelletal structures, that first appear at a depth of 85.44 m, prevail between 192.10 m and 253.44 m (25-30%). Yet uncommon, accretionary ash is observed (< 1%) at a depth of 278.88 m, differing by forming spherical aggregates of ash.

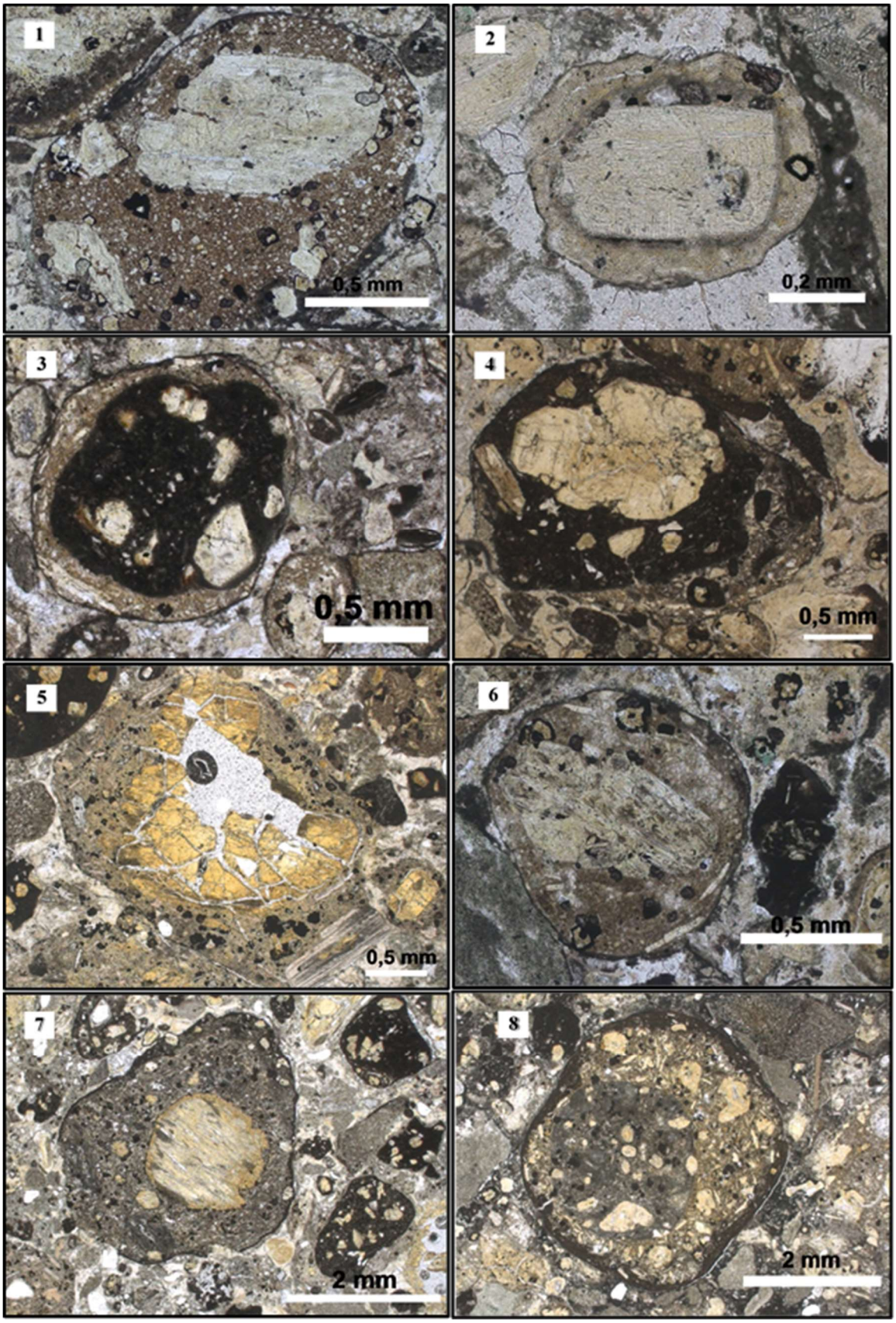

Fig. 3.9 – Cored juvenile clast types of the Régis kimberlite. Eight types are present, from ash to lapilli size. The most common are olivine cores totally replaced by serpentine. Type A clasts are less common. Country rocks are extremely rare. Pelletals follow the nucleous in shape.

Table 3.2 - Petrographic characteristics summary of cored juvenile clasts of the Régis kimberlite.

	MORPHOLOGY	INTERNAL STRUCTURE		VESICULARITY	CLAST-HOST RELATIONSHIP	MINERALOGY	GROUNDMASS CRYSTALLINITY	SIZE RANGE
		Type of core	Rims					
1	SbE / Wr / SbI	Cored: euhedral olivine pseudomorph.	Single, asymetrical, complete, ultra thin to very thin micro-rim.	Non-vesicular.	Defined margin set in a cement and carbonate interstitial medium.	Rim - pseud-olivine: low (3%), subhedral, micro to coarse (0.05-0.9mm). Perovskite: low (5%), euhedral, fine (0.22 - 0.08mm). Spinel: low (1%), euhedral, micro - fine crystals (0.32 - 0.07).	Orange-brownish well-crystallized groundmass	Cored juvenile pelletal ash (1.0 - 1.76 mm)
2	SbE / Wr / SbI	Cored: euhedral olivine pseudomorph.	Single, symetrical, complete, ultra thin rim.	Non-vesicular.	Well-defined margins set in a cement.	Rim - Perovskite: low (<1%), anhedral, microcrystals (0.02-0.07mm). Pseudo-phlogopite: low (4%), subhedral, microcystals (< 0.02mm). Opaques: low (2%), anhedral, microcrystals (< 0.01mm).	Carbonate, opaque minerals, speckled yellow-brown groundmass.	Cored juvenile pelletal ash (0.61 - 1.5 mm)
3	SbQ / SbR / SbI	Cored: kimberlitic clast (type A)	Single, asymetrical, incomplete, super-very thin micro rim.	Non-vesicular.	Well-defined margin set in a cement and carbonate interstitial medium.	Rim - Phlogopite, olivine, perovskite, opaques (clast G) with orientation. Core: Olivine, pseudo-phlogopite, provskite, opaques (clast A).	Core: very pooly crystallized, brown groundmass containing serpentine and fine-grained opaque minerals. Rim: speckled yellow-brown groundmass, carbonates and opaques.	Cored juvenile pelletal ash (1.15 - 1.40mm)
4	SbE / R / SbI	Cored: Olivine	Multiple rims, asymetrical, complete. Very to super thin micro-rim (both oriented).	Non-vesicular.	Defined margin set in a cement and carbonate interstitial medium.	Internal rim: olivine, phlogopite, opaques and perovskite (clast A) oriented. External rim: phlogopite, olivine, perovskite (clast G) crystals oriented.	Internal rim: brown very poorly crystallized groundmass. External rim: orange brown poorly-crystallized groundmass.	Cored juvenile pelletal lapilli (2.0 - 2.80mm)
5	SbE / SubR / SbI	Cored: Olivine	Single rim, asymetrical, incomplete, very thin micro rim.	Non-vesicular.	Diffuse to defined margins set in a cement.	Olivine fine crystals, phlogopite micro to coarse crystals, atoll spinel microcrystals and perovskite fine crystals (clast I).	Well-crystallized groundmass with splecked minerals.	Cored juvenile pelletal lapilli or ash (0.5 - 3.20mm)
6	SbE - Eq / Wr / Sc	Cored: Olivine	Single rim, symetrical, complete, super thin micro-rim.	Non-vesicular.	Defined margin set in a cement and carbonate interstitial medium.	Phlogopite, olivine, perovskite, spinel atoll (clast G) crystals oriented.	Orange brown poorly-crystallized groundmass.	Cored juvenile pelletal ash and lapilli (1.2 - 2mm)
7	Eq / R / SbI	Cored: olivine or country rock fragment	Single rim, symetrical, incomplete, ultra thin rim.	Non-vesicular.	Defined margin set in a cement composed by carbonate and serpentine.	–	Rim: dark criptocrystaline material (type A) or phlogopite, olivine, perovskite, atoll spinel microcrysts (type G clast).	Cored juvenile pelletal ash (0.5mm)
8	Eq / Wr / Sc	core: kimberlitic clast	Multiple rims, asymetrical, complete, ultra thin to thin micro-rims (0.17 - 1.13mm).	Non-vesicular.	Defined margins set in a carbonate cement with perovskite and coutry rocks.	Core: olivine (10%, euhedral, fine to coarse 0.1-0.8mm), perovskite (7%, euhedral, micro to fine <0.14mm) and phlogopite (25%) oriented around olivine groundmass. Internal Rim: olivine (10%, single and intergrowth crystals, fine-coarse 0.17-0.56mm), phlogopite (15%	Core: very poorly crystallized speckled gray groundmass. Internal rim: poorly crystallized opaque yellow speckled groundmass. Extrernal rim: Poorly crystallized oriented phlogopite perovskite brown groundmass	cored juvenile pelletal lapilli (2.0 - 5.3mm)

Sphericity: Elongate (El); Subelongate (SbE); Subequant (SbQ); Equant (Eq).

Roundness: Well-rounded (Wr); Rounded (R); Sub-rounded (SbR); Sub-angular (SbA); Angular (Ang).

Irregularity: Smoothly curved (Sc); Subirregular (SbI); Irregular curvilinear (Ic); Irregular ameboid (Ia).

Type 1 has defined margins and is subequant, well-rounded, sub-irregular, non-vesicular, cored manly by pseudomorphed olivine. A single, asymmetrical, complete ultra-thin to very thin micro-rim is composed of pseudo-olivine (3%), perovskite (5%) and spinel (1%) set in a well-crystallized orange-brownish groundmass. Type 2 has subequant shape, well-rounded and sub-irregular outlines, well-defined margins and is non-vesicular. A single, symmetrical, complete, ultra-thin rim mimic the shape of the core, formed by micro-crystals of perovskite (<1%), pseudo-phlogopite (4%) and spinel (2%) set in a speckled, carbonate and opaque minerals yellow-brown groundmass.

Type 3 juvenile pelletal ash is cored mainly by Type A kimberlitic clasts. It is typically subequant, sub rounded, sub-irregular and non-vesicular, consisting of a single, asymmetrical, incomplete, super-very thin micro rim of phlogopite, olivine, perovskite, opaque minerals (Type G) with orientation arrange. Type 4 clasts have well defined margins and are subelongate, rounded, sub-irregular, non-vesicular and cored by pseudomorphed euhedral olivine. They are characterized by multiple, asymmetrical, complete, very to super thin oriented micro-rims. The internal rim is composed of olivine, phlogopite, opaque minerals and perovskite (Type A), oriented. The external rim is constituted of phlogopite, olivine, and perovskite (Type G) crystals, oriented.

Another characteristic pelletal structure is formed by Type I clasts, occurring at restrict depths (192.1 to 212.7 m) with diffuse margins. They are typically subelongate, sub-rounded, sub-irregular, non-vesicular, cored by pseudomorphed sub-euhedral olivine. The single, asymmetrical, incomplete, very thin micro rim mimic the shape of the cores, consisting of fine pseudomorph crystals of olivine, phlogopite micro to coarse crystals, atoll spinel micro-crystals and fine crystals of perovskite (Type 5). Type 6 has defined margins, subelongate to equant shapes, well-rounded and smoothly curved outlines, is non-vesicular, cored manly pseudomorphed olivine. It occurs with a single, symmetrical, complete, super thin micro-rim that correspond to Type G clasts (phlogopite, olivine, perovskite, spinel atoll with oriented crystals set in poorly crystallized orange brown groundmass).

Type 7 cored juvenile pelletal ashes occur with defined margins, equant shapes, rounded and sub-irregular outlines, are non-vesicular, cored by euhedral pseudomorphed olivine crystals or, less commonly, country rock fragments. The single, symmetrical, incomplete, ultra-thin rim follows the shape of the cores, which are recorded as being of types A (dark cryptocrystalline material) and G clasts (phlogopite, olivine, perovskite, atoll spinel microcrysts).

Another peculiar pelletal structure is formed by Type 8 clasts, with defined margins, typically equant, well-rounded, smoothly curved, non-vesicular and cored by kimberlitic clasts (Type D). It is characterized by multiple, asymmetrical, complete, ultra-thin to thin micro-rims. The internal rim is composed of a poorly crystallized opaque yellow, speckled groundmass and the external rim is constituted of poorly crystallized oriented phlogopite perovskite brown groundmass.

4.4 Accessory lithic clast

4.4.1 Country rocks

The crustal rock fragments of the Régis kimberlite are marbles and mainly phyllites, corresponding to 20-30% at the shallowest depths (88.44 to 188.55 m), with angular shapes and lapilli size, as depth increases (from 192.10 m), the modal abundance decreases to 10% and lithic fragments occur in elongate shapes, rounded outlines, with ash to lapilli sizes, occasionally enclosed by kimberlitic material (Fig. 3.10). Frequency decreases with depth; from 253.40 m below, country rocks correspond to 2 - 4%. However, larger fragments (up to 8 mm) become common.

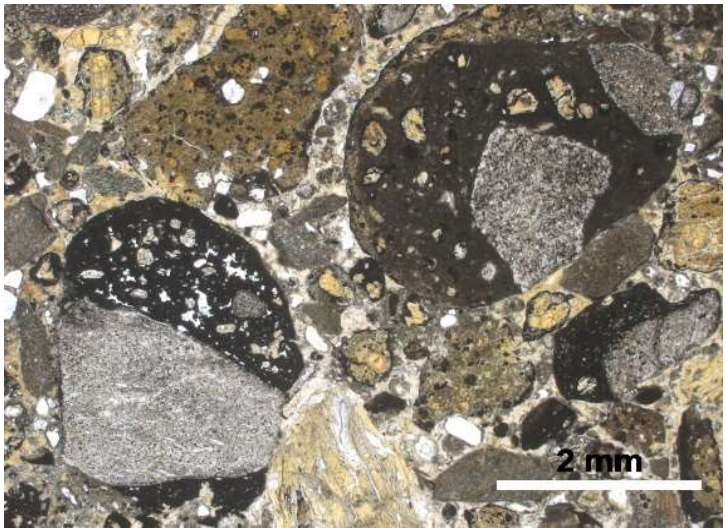

Fig. 3.10 – Country rocks (CR) of the Régis kimberlite enclosed by kimberlitic material.

4.4.2 Mantle xenoliths

Two types of mantle xenoliths were observed at depths from 278.88 to 278.93 m. Major fragments (18 mm) correspond to an opaque-perovskite-orthopyroxene-mica-olivine xenolith with granoblastic texture (Fig. 3.11a). Two minor fragments of other mantle xenolith are recorded, varying from 1.8 to 2 mm, both with granoblastic texture and rounded shapes, one of them enclosed by kimberlitic material (type B, table 3.1). Phlogopite crystals are preserved with little alteration (Fig. 3.11b).

Three other mantle xenoliths were macroscopically and petrographically recorded by Thomaz (2009): lherzolite garnet, dunite and phlogopite-bearing xenolith. The first one occurs at depths of 96.6m and 103.15m (macroscopically) and 91 m (petrographically) in sizes of 15 cm, 3 cm and 8 mm, respectively, composed of purple garnet, cr-diopside, green-yellow olivine and enstatite. Two fragments of dunite were described in hand sample and thin section at depths of 91 m and 135 m with 1.5 cm and 11x4 cm, respectively, being composed mainly of preserved olivine crystals and rare orthopyroxene, cr-diopside and pyrope garnet. A fragment of phlogopite-bearing xenolith was recorded at a depth of 85.44 m, with rounded shape, composed manly to colorless (parallel nicols) phlogopite fine crystals.

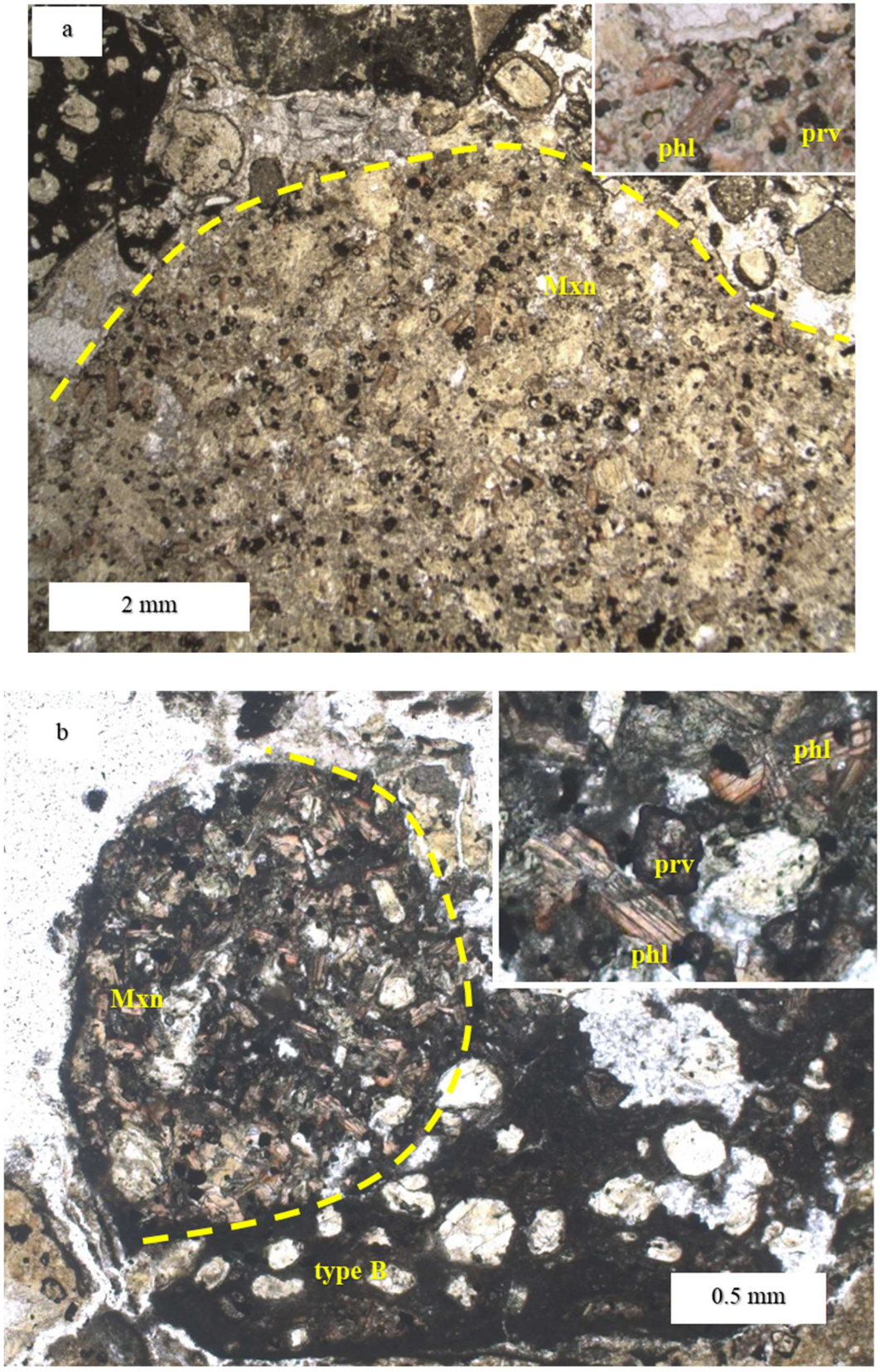

Fig 3.11 – Régis kimberlite mantle xenoliths recorded in this study. (a) opaque-perovskite-orthopyroxene-mica-olivine xenolith with granoblastic texture; (b) phlogopite-opaque-perovskite-olivine xenolith enclosed by type B clast. Notice well preserved phlogopite and perovskite crystals.

5. Mineral Chemistry

5.1 Garnet

The structure of a garnet crystal allows a wide variety of cations to be substituted, in highly-variable abundances, based on chemical composition. Garnet is an important mineral in the study of mantle processes, and an indicator in diamond exploration (Dawson and Stephens, 1975; Griffin et al., 1999; Grütter et al., 2004; Hardman et al., 2018; Nowicki et al., 2007; Schulze, 2003). Owing to the high alteration degree of the Regis kimberlite, only three samples of garnet crystals were analyzed (Table 6). For this reason, some of the data presented here was compiled from Thomaz (2009), who analysed fresh garnet specimens from deeper drill cores (up to ~ 360 m).

Mantle garnet samples studied correspond mainly to the pyrope variety (> 70%), being characterized by a high content of Mg/(Mg+Fe) (0.80 - 0.81), MgO (~ 19.0 wt.%), CaO (~ 5.22 wt.%) and Cr_2O_3 (~3.65 wt.%) (Fig.3.12). Only one of the samples corresponds mainly to almandine (~ 68%) and was identified as being of crustal origin (Mg/(Mg+Fe) = 0.22; 5.55 wt.% MgO; 2.21 wt.% CaO; 0.08 wt.% Cr_2O_3; 32.80 wt.% FeO). In Schulze (2003) and Grütter et al. (2004) classifications, the mantle garnet samples correspond to peridotite ones (Cr_2O_3 > 4.0 wt.% or TiO_2 > 0.50 wt.% if Cr_2O_3 > 1.0 < 4.0 wt.%). Due to the positive correlation between CaO and Cr_2O_3, they are in turn identified as being of lherzolite origin, corresponding to the G9 field.

Pyroxenitic garnet also falls within this field or are undifferentiated (Sculze 2003). However, Grütter et al. (2004) discriminates among them by the smaller amount of Cr_2O_3 (<4.0%) and MGNUM <0.7, (where MGNUM = (MgO/40.3)/(MgO/40.3 + FeO_t/ 71.85) [oxides in wt.%]) as compared to lherzolitic garnet, separating such varieties into the G5 group. Meanwhile, the classic CaO x Cr_2O_3 diagram of Grütter et al. (2004) (Fig. 3.12) separates G5 and G9 fields only by Cr and Ca, disregarding the MGNUM limit. These authors also point out that field overlapping occurs.

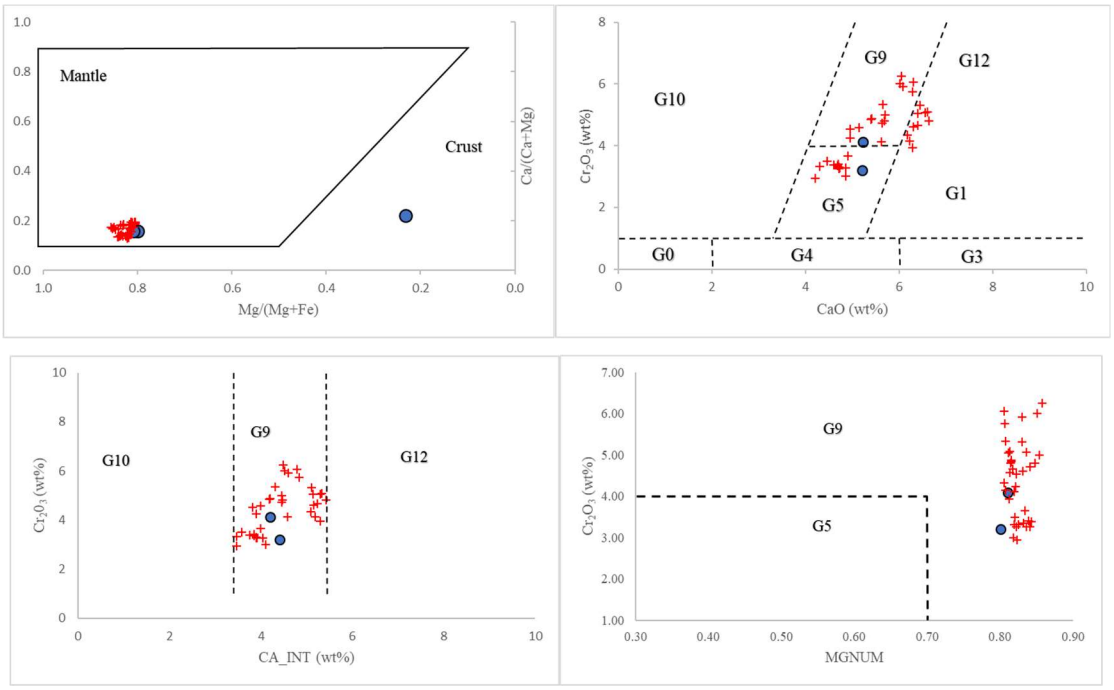

Fig.3.12. Chemical characteristics of garnet from the Régis kimberlite. Data pertaining to this study (circle) is plotted together with dataset from Thomaz (2009) (cross): (a) mantle and crustal garnet after Schulze (2003). (b) Cr_2O_3 vs. CaO diagram for Régis kimberlite garnet, with overlapping G9 and G5 fields, after Grütter et al. (2004). (c) MGNUM vs Cr_2O_3 diagram for the distinction between pyroxenitic (G5) and lherzolitic garnet (G9). (d) CA_INT vs Cr_2O_3 for better separation between G9 and G12 fields.

Trace element chemistry

Trace elements of two peridotitic garnet grains analysed in this study exhibit 0.40 and 4.61 ppm Sr, 6.93 and 7.07 ppm Y, 4.31 and 62.73 ppm Zr, 0.04 and 0.56 ppm Ba, 0.01 and 0.56 ppm Hf, 29.29 and 93.03 ppm Ni, 16.23 and 21.33 pp Zn, and 7.12 and 7.15 ppm Ga, respectively (Table 6). Both grains show little variation in REE_N (N denotes normalization to the chondrite composition of Boynton, 1984) and are characterized by a weakly sinuous pattern, following the terminology of Banas et al. (2009) and Viljoen et al. (2014).

Régis-9 has positive $LREE_N$ slopes, negative $MREE_N$ to Gd slopes and a slight enrichment in $HREE_N$. Régis-5 presents a constant enrichment in REE_N, except for a negative Sm slope (Fig. 3.13). However heterogeneous in terms of other trace elements, their patterns are similar. Their trends are also similar, with negative Sr and Ba anomalies and positive Zr, Hf, Pb, and U anomalies. Both differ in Rb, which is absent in Régis-5, that exhibits lower concentrations of Th, U, Ta and Nb, while Régis-9 presents a discrete content increase in these elements.

The Garnet REE_N patterns studied are similar to both lherzolitic garnet that occurs as inclusions in diamonds in the Premier diamondiferous kimberlite (Viljoen et al., 2014), which are characteristically flat, normal and sinuous, and lherzolitic garnet (Lz3) from the V. Grib kimberlite pipe deposit in the Arkhangelsk diamondiferous province (Shchukina et al., 2015). Similarities are also found with low-Ti garnet varieties analysed by Banas et al. (2009).

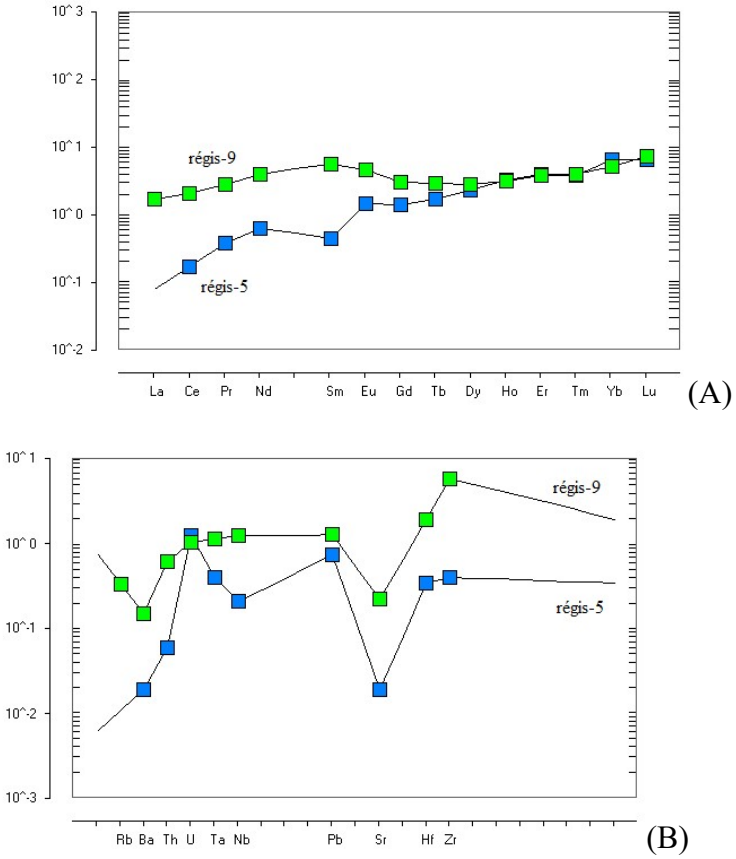

Fig.3.13. A. Chondrite-normalised rare earth element plots (Boynton, 1984); B. primitive mantle-normalized incompatible element variation diagrams (McDonough and Sun, 1995) for Régis kimberlite garnets.

5.2 Spinel

The spinel grains analysed correspond to two populations: euhedral and anhedral. Euhedral spinel corresponds to a primary groundmass and is characterized by euhedral to subhedral habit, small size (0.01 - 0.1 mm) and by occurring as discrete, homogeneous and zoned crystals. Primary groundmass spinel cores are dominated by chromite and are characterized by 7.40 to 53.06 wt% Cr_2O_3, 3.73 to 17.57 wt% TiO_2, 4.26 to 12.51 wt% MgO, 31.62 to 72.23 wt% FeO_t, and 0.72 to 5.45 wt% Al_2O_3 contents, in the range of 0.69 < Cr/(Cr

+ Al) < 0.98 and 0.50 < $Fe^{2+}/(Fe^{2+}$ + Mg) < 0.83. The chemical composition of rims ranges from 2.43 to 38.52 wt% Cr_2O_3, 2.39 to 12.61 wt% TiO_2, 3.53 to 11.63 wt% MgO, 39.84 to 82.87 wt% FeO_t, and 0.64 to 5.55 wt% Al_2O_3 (Table 3). Only two gains are of aluminous spinel composition, (0.13 to 6.20 wt% Cr_2O_3, 10.63 to 17.08 wt% TiO_2, 3.24 to 12.82 wt% MgO, 65.87 to 79.41 wt% FeO_t, and 0.54 to 6.22 wt% Al_2O_3), in the range of 0.03 < Cr/(Cr + Al) < 0.14 and 0.51 < $Fe^{2+}/(Fe^{2+}$ + Mg) < 0.87.

According to Schulze (2001), aluminous spinel corresponds to a Cr/(Cr + Al) < 0.50 (molar) ratio, while chromite refers to a chromian spinel with molar $Fe^{2+}/(Fe^{2+}$ + Mg) > 0.50 (Schulze, 2001).

The anhedral spinel crystals are larger than the primary groundmass (up to 0.3mm). They occur in discrete, homogeneous or zoned forms, slightly rounded and occasionally broken. Their major element composition is very similar to that of euhedral grains, cores being dominated by chromite and characterized by 6.79 to 52.64 wt% Cr_2O_3, 2.38 to 14.95 wt% TiO_2, 4.39 to 10.03 wt% MgO, 36.5 to 68.36 wt% FeO_t, and 0.90 to 4.74 wt% Al_2O_3 values, in the range of 0.77 < Cr/(Cr + Al) < 0.98 and 0.61 < $Fe^{2+}/(Fe^{2+}$ + Mg) < 0.81. The chemical composition of the rims ranges from 0.56 to 10.66 wt% Cr_2O_3, 11.46 to 16.28 wt% TiO_2, 2.03 to 12.41 wt% MgO, 58.30 to 82.67 wt% FeO_t, and 1.27 to 3.37 wt% Al_2O_3.

Chemical discontinuities were observed in both populations, as evidenced by edges of chromite grains being depleted in Cr, Al and Mg and enriched in Fe and Ti as compared to cores, reaching the composition of magnetite. However, such of them cores are enriched in Fe and depleted in Al and Cr as compared to rims. In such cases, Ti and Mg values vary.

According to Mitchell (1995), kimberlite spinel normally falls within the magnesian ulvöspinel trend (Trend 1) and the titanomagnetite trend (Trend 2). In the area of study, spinel is dominated by ulvöspinel of the magmatic trend 1, with minor concentration falling within trend 2 (Fig. 3.14 a). The kimberlite trend is similar to the Fe-Ti trend. Spinel follows this feature, Cr/(Cr+Al) values being nearly constant while Fe^{3+} and TiO_2 increases (Fig 3.14 b). However, Fig 3.14 shows that the kimberlite trend is preserved, but that it differs in the nearly constant $Fe^{2+}/(Mg + Fe^{2+})$ over a wide range in Fe^{3+}. Ti has a tendency to partition into spinel with/in higher magnetite contents, their increased values being a secondary consequence (Barnes and Roeder, 2001).

The euhedral and anhedral chromite spinel [$Fe^{2+}/(Mg + Fe^{2+}) > 0.50$] varieties are characterized by low Ni (up to 0.22 wt% and 0.16 wt%, respectively) and very high TiO_2 values (up to 17.57 wt% and 14.95 wt%, respectively). Figure 3.14 c shows the variation in Ni (wt% NiO) with $Fe^{2+}/(Mg + Fe^{2+})$ and TiO_2 values. The enrichment in Ni is not evident in chromite from Group-I kimberlites. Ti-rich chromian spinel (>3.0 TiO_2 wt%) relates to this group (Schulze, 2001).

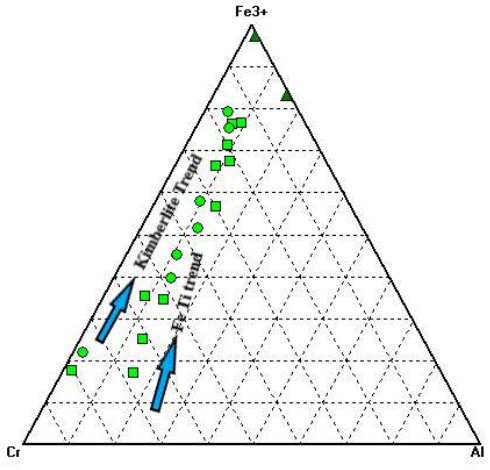

(A)

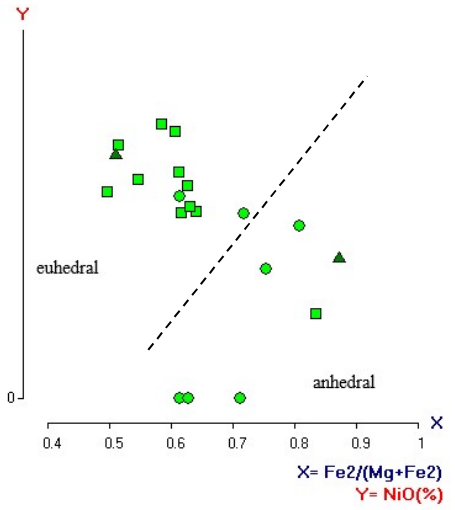

(B)

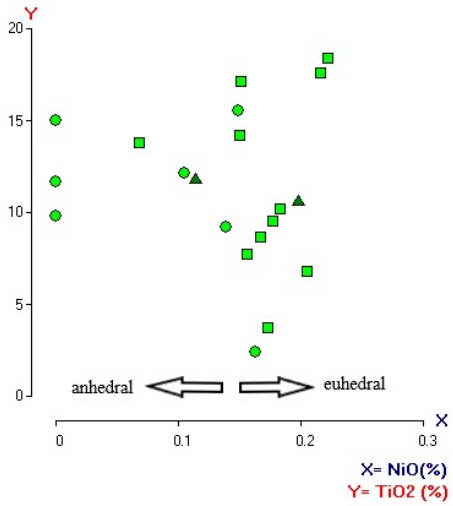

(C)

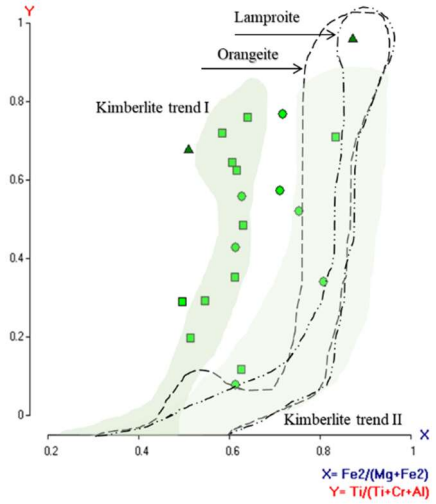

Fig.3.14. A) Fe^{3+} - Cr - Al diagram showing Ti-Fe trends defined by Barnes et al. (2001). B C) Variation of Ni with molar $Fe^{2+}/(Fe^{2+} + Mg)$ and TiO_2 in anhedral and euhedral chromite. Dashed line and arrows separate the greatest concentration fields of two spinel populations analysed. D) Ti/(Ti+Cr+Al) *versus* $Fe^{2+}/(Fe^{2+}+Mg)$ diagram showing greater concentration of chromite in kimberlite trend I as defined by Mitchell (1995).

Trace Element Chemistry

In the Régis kimberlite, chromite presents a large variation in trace elements (Table 3), with two different patterns (sinusoidal and humped), identified by different colors in Fig. 3.15. Such of them exhibit high values of Co, Zr, Nb, Ba and Ta (16.34 to 1149.79 ppm, 9.62 to 1630.50 ppm, 50.48 to 5950.65 ppm, 0.25 to 2628.08 ppm and 0.031 to 1054 ppm, respectively) and significative amounts of Sr, Y, La, Ce and Hf (0.37 to 214.84 ppm, 0.07 to 5.03 ppm, 0.36 to 13.27 ppm, 0.04 to 12.13 ppm and 0.47 to 49.21, respectively).

The sinusoidal pattern consists of very strong positive anomalies of Ta, Nb, Hf and Zr, and negative anomalies of Th, Ce, Sr and Y, while the humped pattern is, on average, more homogeneous, marked by a slightly constant depletion of Ce to Lu, with exception of positive (two analysis) and negative (one analysis) anomalies of Hf and Zr. From Ce to La, only one grain presents a constant decline, with a positive slope for Ba, while the others exhibit enrichment in this range, except for Ba and Th.

$LREE_N$ were detected in grains showing humped trace element composition patterns. Grains with sinusoidal patterns have very low values, the lowest detection limit, remaining, thus, unplotted. In the Régis kimberlite, chromite is enriched in $LREE_N$, with a constant depletion towards $HREE_N$, except only for a negative Pr and positive Tm anomalies.

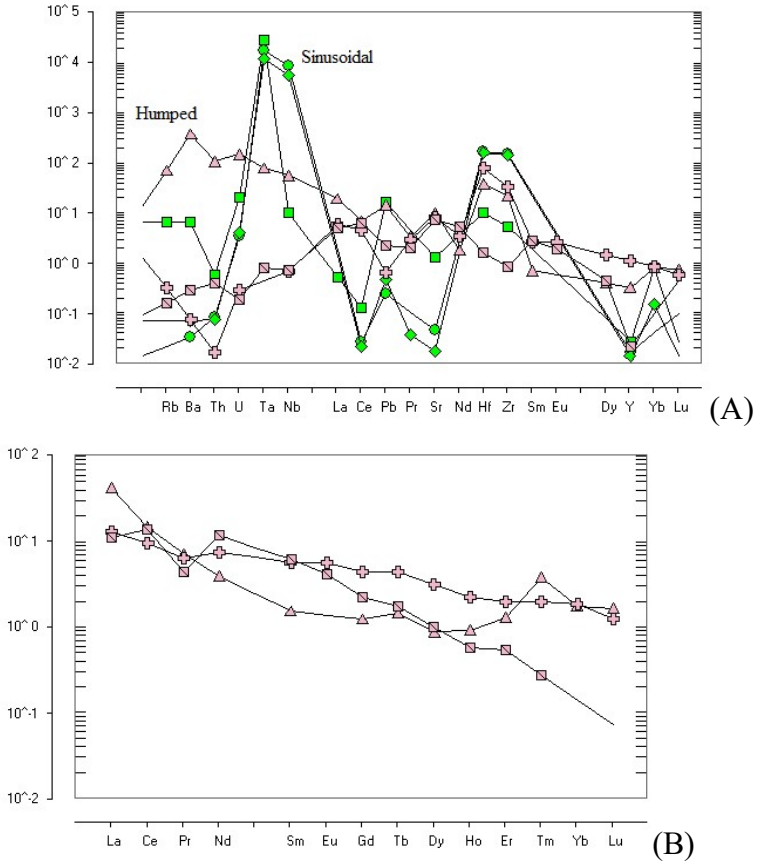

Fig.3.15. A. primitive mantle-normalized incompatible element (McDonough and Sun, 1995) variation diagrams for Régis kimberlite spinel. B. Chondrite-normalised rare earth element plots (Boynton, 1984) for Régis kimberlite spinel. The different colors represent recognized patterns (sinusoidal and humped).

5.3 Ilmenite

In the Régis kimberlite, groundmass microcrysts of ilmenite range from 0.10 mm to 0.30 mm in diameter, exhibiting a composition that is rich in magnesium. They are characteristically high in FeO_t and TiO_2 (38.66 to 44.45 wt.% and 43.46 to 50.03 wt.%, respectively), with significant amounts of MgO (1.88 to 13.46 wt.%) and minor amounts of Al_2O_3 (< 0.46 wt.%) and MnO (< 1.21wt.%) (Table 8)

In order to differentiate between kimberlitic from non-kimberlitic ilmenite, data was plotted in a MgO versus TiO_2 diagram (Haggerty, 1975,1976; Wyatt et al.,2004), which establishes a parabolic arc typical of many kimberlitic ilmenite populations. Reference lines of constant hematite content were added to the scatter plots (Fig. 3.16). Most of the ilmenite falls within the kimberlitic field, with exception of one grain, whose core falls outside and intermediate and rim fall inside this field due to a zoned rim with increased MgO content (1.88

wt.% core and 13.46 wt.%). This feature is characteristic of non-kimberlitic ilmenite (Wyatt et al., 2004).

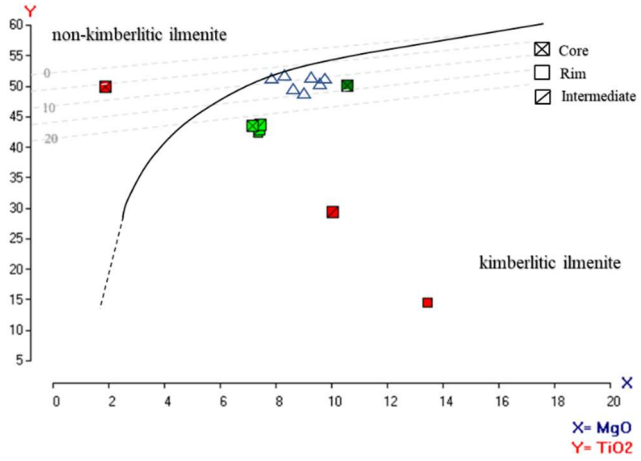

Fig.3.16. MgO *versus* TiO_2 for ilmenite analysed in this study (squares) and from Thomaz (2009) (triangles). Percent Fe_2O_3 as dashed light-grey lines. Black line represents the bounding reference of the kimberlitic ilmenite field after Haggerty (1975, 1976) and Wyatt et al. (2004).

Trace Element Chemistry

In the Régis kimberlite, ilmenite is characterized by containing 4.90 ppm Sc, 80.49 ppm V, 12.36 ppm Co, 109.47 ppm Sr, 5.82 ppm Zr, 10.19 ppm Ba, 0.30 ppm Hf and 0.03 ppm Yb. The pattern displayed by trace elements is weakly sinusoidal (Fig 3.17). A balance between the elements can be noticed, with a slight increase from Ba to Sr. Except for a strong negative K anomaly from La to Nd, contents remain practically constant. From Hf to Yb, there is a depletion, except for a slightly positive Sm and a strong Ti anomalies (Table 8).

Ilmenite REE pattern is humped, characterised by a strong $LREE_N$ enrichment and a constant depletion towards $HREE_N$ (Fig.3.17). The highest enrichments are in La (2.25 ppm), Ce (6.98 ppm), Pr (1.0 ppm) and Nd (4.19 ppm).

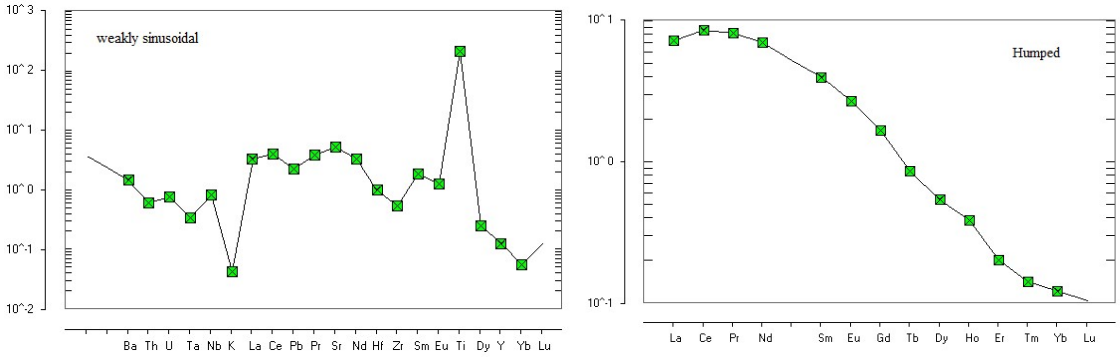

Fig.3.17. Incompatible elements and REE concentrations of kimberlitic ilmenite in the Régis kimberlite normalised to the primitive mantle of McDonough and Sun (1995) and to the chondrite composition of Boyton (1984), respectively.

5.4 Perovskite

Perovskite is a late-stage magmatic product of kimberlitic magmas. Due to symmetry distortions, it can exhibit tetragonal to orthorhombic forms. Hence, many elements (Na, K, Sr, Ba, Ti, Nb, Zr, Th) can occupy perovskite sites. It is, therefore, an important repository of REE and trace elements in kimberlitic magmas (Chakhmouradian and Mitchell, 2001; Sarkar, 2011). Perovskite forms a primary phase and occurs as grains up to 0.40 mm in size inside clasts, in anhedral to subhedral forms, the minor ones rimmed by olivine pseudomorphs.

The table 13 list major and trace-element data on perovskite from the Régis kimberlite. CaO ranges from 37.54 to 39.69 wt.%, TiO_2 from 54.05 to 57.12 wt.% and FeO_T from 0.92 to 1.41 wt.%, with low variation. Significant amounts of La_2O_3 (0.11 to 0.62 wt.%), Ce_2O_3 (0.29 to 1.61 wt.%), Nb_2O_5 (up to 0.41 wt.%) and ThO_2 (up to 0.32 wt%) are present. Based on chemical composition, anhedral forms and subtle zoning patterns, the perovskite can be recognized as type Ia following parameters and terminology from Castillo-Oliver et al. (2016), who distinguished among different perovskite types in kimberlites according to crystal perfection and zoning patterns (texture).

Type Ia perovskite is in good agreement with Type 1 perovskite from Canadian kimberlites (Chakhmouradian and Mitchell, 2001) in and with Group 1 perovskite of Castillo-Oliver et al. (2016). It is characterized by being poor in REE, Nb and Al (up to 2.66 wt.%, 0.46 wt.% and 0.17 wt.%, respectively), with very low Sr and K contents (up to 0.34 and 0.15 wt.%, respectively), as opposite to the ones from Lac de Gras rocks.

The most common alteration observed is the development of TiO_2 rims, while cores remain unaltered. The alteration results in atoll texture due to cation leaching and replacement

with Ti-bearing minerals. Titanium dioxide (TiO_2) is the most common product of perovskite alteration in kimberlites (Chakhmouradian and Mitchell, 2000). Rutile, anatase and brookite can replace perovskite, but further detailed investigation is necessary for such a distinction.

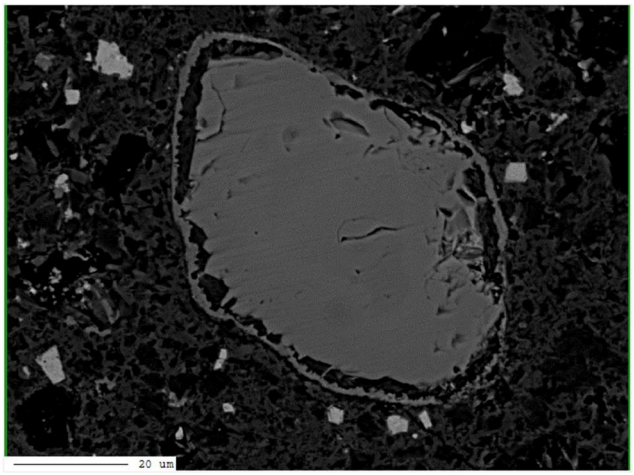

Fig.3.18. BSE image of perovskite alteration pattern in the Régis kimberlite resulting in a characteristic atoll texture with a rim of TiO_2.

Type Ia perovskite exhibits a subtle zoning pattern only visible in back-scattered electron (BSE) images, normally with darker cores and bright rims or bright cores with dark rims. Zoning patterns are common in this mineral and reflects a complex composition variation.

Perovskite occurrences can be grouped based on zonation patterns (Castillo-Oliver et al., 2016; Chakhmouradian and Mitchell, 2001). However, a “universal classification” of perovskite occurrences would be difficult to achieve given the the wide range of chemical compositions possible. However, based on Castillo-Oliver et al. (2016) and Chakhmouradian and Mitchell (2001), a “normal” and a “reverse” pattern was recognized in perovskite specimens from the Régis kimberlite. According to these authors, the normal pattern corresponds to a decrease in LREE and Th (core to rim), with variable Na and Nb content, while the reverse pattern exhibits enrichment in LREE and Th towards the rim, a possible increase in Fe and Nb content, LREE values remaining constant or slightly decreasing.

Figure.3.19 displays a typical zonation. An abrupt decrease in all elements (ΣLREE, Na, Ce, La, Nb and Th) from core to rim characterizes the “normal” pattern (Fig. 3.19- A), normally with bright cores and rims, but also with darker cores and bright rims. In intermediate zones, oscillation of elements occurs, with a slight increase towards the rims (clearly visible in LREE), rim values remaining lower than core values. In darker cores, a slight increase in Ce values is not uncommon while other elements decrease (Fig.3.19 - B). The “reverse” pattern is observed

in bright cores and bright rims, with darker intermediate zones. It is characterized by an increase in ΣLREE, Nb, Th and a decrease in Ce and La towards the rim, with oscillation in intermediate areas. Rim values remain higher than core values, except for Nb and Th.

Variations of Nb and Sr and negative correlation of Na, Fe against Ti (Fig 3.20. a-d) and REE, SrO against CaO (Fig. 3.20 a-d) are low. A similarity is observed with perovskite from Bathlatos and Lucapa 2 kimberlites, which exhibit lower values than other kimberlite bodies in the same province. In general, substitution of minor elements is more intense compared to most South African kimberlites, and lowest in the Régis kimberlite.

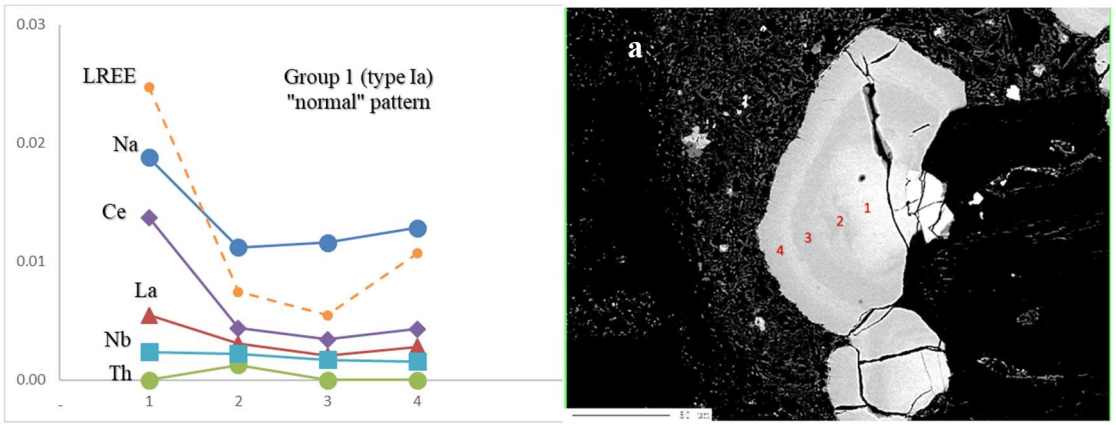

(A)

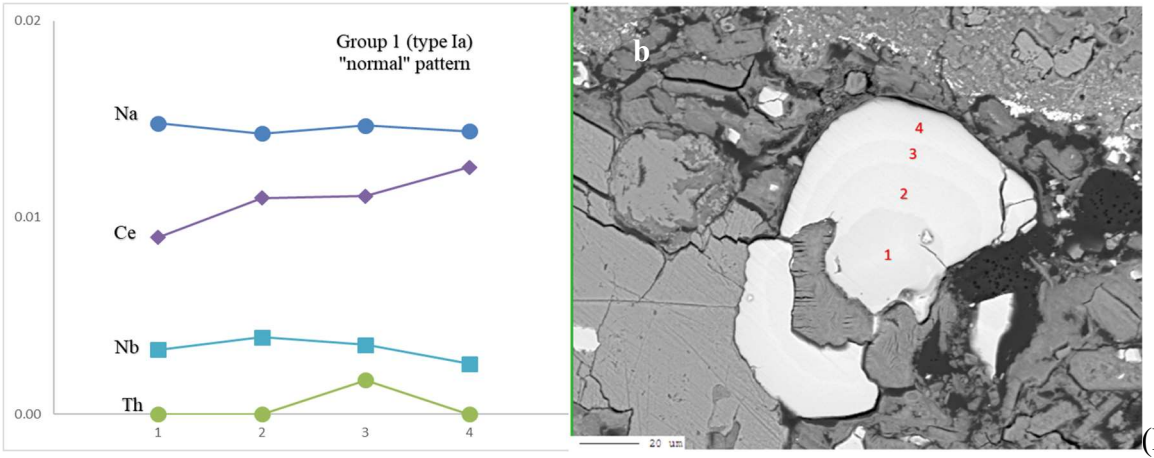

(B)

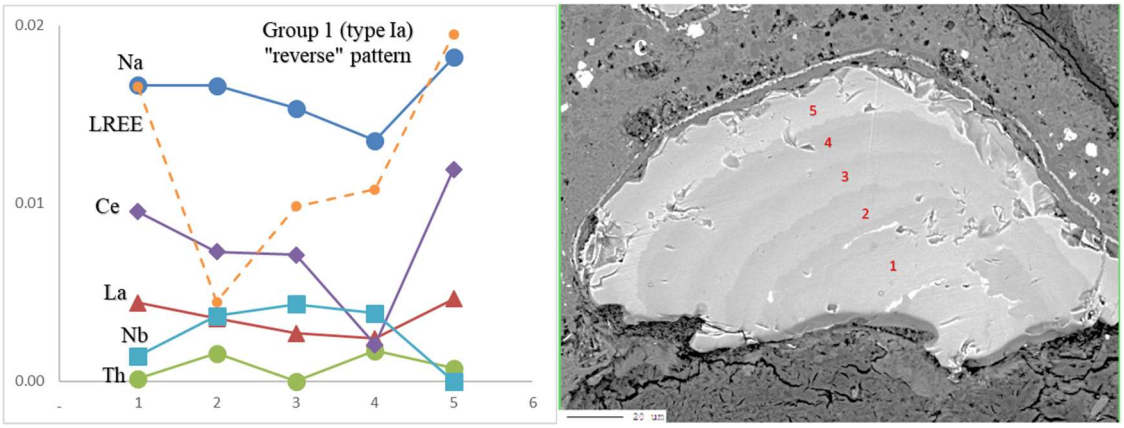

(C)

Fig.3.19. Back-scattered electron (BSE) image of perovskite from the Régis kimberlite showing subtle zoning pattern and composition. The grains analyzed are Type Ia (anhedral with subtle zoning) of Group 1 (REE-, Nb- and Al-poor perovskite).

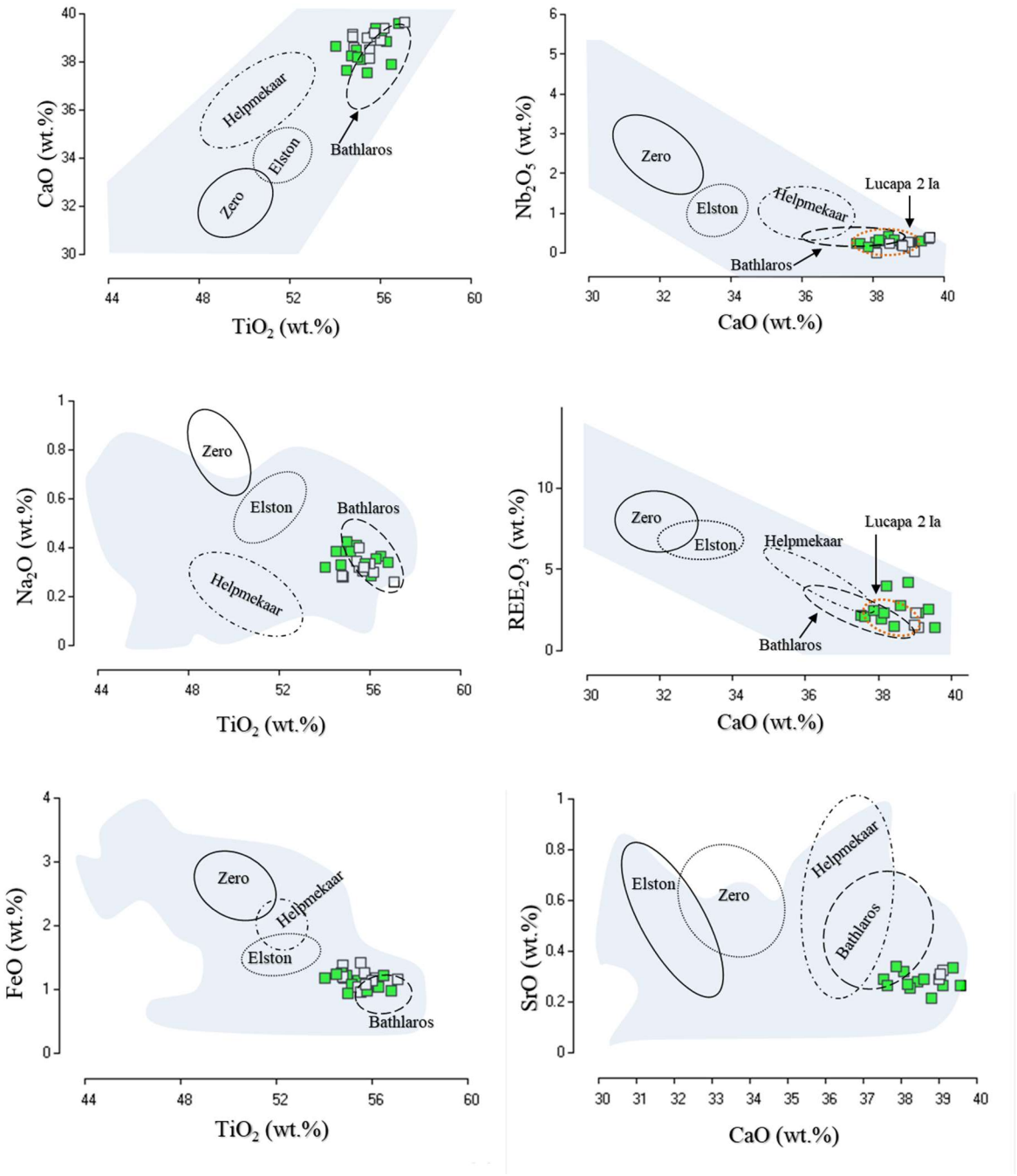

Fig.3.20. Representative major- and trace-elements variation diagrams for perovskites from the Régis kimberlite. Symbol: core, full; rim, empty. Black line delimited areas, Kuruman kimberlites; blue area, worldwide sources (Donnelly et al., 2011). Orange line delimited area, perovskites type Ia from Lucapa I kimberlite (Castillo-Oliver et al., 2016). REE_2O_3 includes La_2O_3, Ce_2O_3 and Nd_2O_3.

Figure 3.21 illustrates primitive mantle-normalized incompatible element concentrations of perovskite for the present study (Table 13). A pattern is characterized by strong Ba and K negative anomalies and by slighter anomalies of Pb, Sr, Hf and Zr. The diagram also confirms that perovskite is a main carrier for REE and other trace elements present in significative values, e.g. Th (335.12 to 2753.86 ppm), U (24.93 to 218.13 ppm) and Ta (202.37 to 693.74 ppm). A positive correlation is observed for Th, Ta, Hf and Ho relative to U, Nb, Zr and Y, respectively, demonstrating higher affinity between pairs. Such features were also observed in Castillo-Oliver et al. (2016) and Chakhmouradian et al. (2013).

Zr/Hf (19 - 24), Nb/Ta (4.7 - 8.8) and low Lu/ Hf ratios (0.02 - 0.06) are in agreement with data from PIAP rocks (Zr/Hf, 16-37; Nb/Ta, 3.8-25.3; Lu/Hf, 0.007-0.12) as defined by Melluso et al., 2008).

REE_N exhibit a humped pattern that reflects enrichment in $LREE_N$ regarding $MREE_N$ and $HREE_N$ (La_N: 6969.29 vs Lu_N: 0.66). In the area of study, perovskite is characterized by moderately fractionated REE values (La/Yb ratios between 329 and 635), which is in accordance with Kuruman kimberlites (La/Ybn from 321 and 2180) and within the range of Paranaíba igneous province rocks (La/Ybn from ~175 to ~2000). Eu anomalies (in the range 0.83 to 0.96) fall close to PIAP perovskite values (Eu/Eu* in the range 0.88-1.1, after Melluso et al. (2008)) displaying the lowest minimum limit.

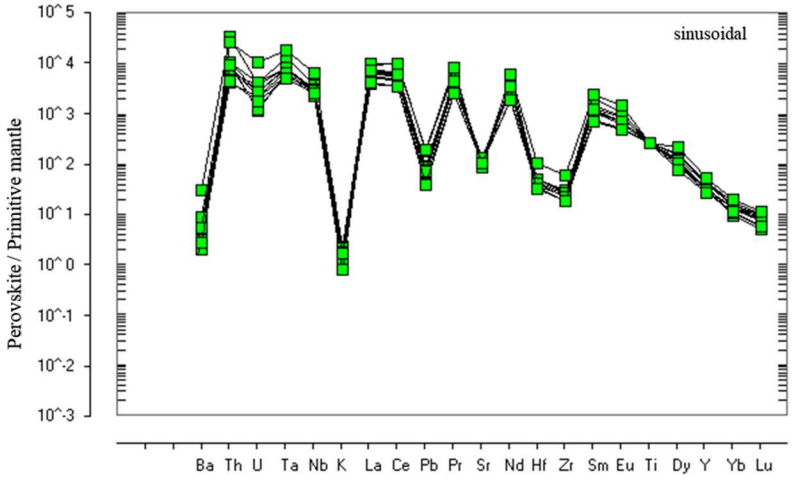

(A)

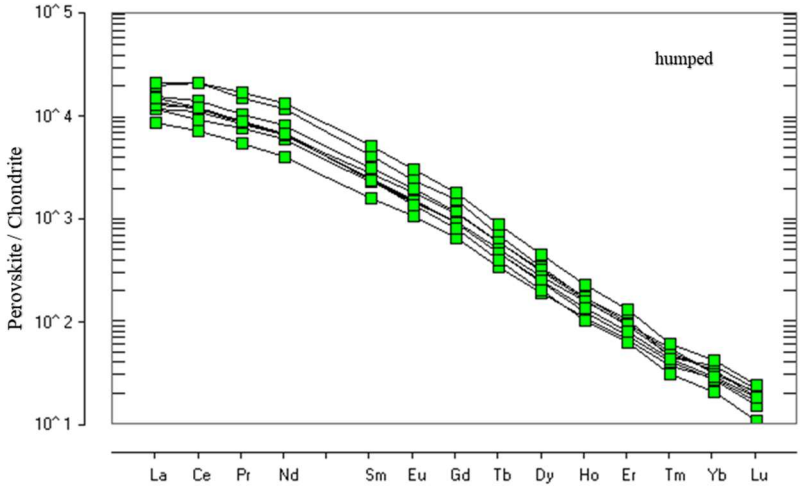

(B)

Fig.3.21. Trace element and REE concentrations of kimberlitic perovskite from Régis kimberlite normalized to the primitive mantle of McDonough and Sun (1995) and to the C1 chondrite composition of Boyton (1984), respectively.

5.5 Pyroxene

The macrocrystals analysed are anhedral grains with up to 1.0 mm in diameter and correspond mainly to augite and diopside end-member (Table 20) and minor enstatite. The clinopyroxene are variable in Cr_2O_3 contents (0 to 1.71 wt%), TiO_2 (0.03 to 2.87 wt%) and Mg# values (0.70 to 0.93), with significative amounts of Al_2O_3 (0.7 to 2.49 wt%) and Na_2O (0.11 to 0.94 wt%). The amounts of Cr# (0.0 to 0.43) and Ca# (0.27 to 0.49) are variable (Fig.3.22). The orthopyroxene exhibit high MgO amounts (up to 36.63 wt%), significative FeO (up to 5.15 wt%) and minor TiO_2 (up to 0.08 wt%), CaO (0.50 wt%) and Cr_2O_3 (up to 0.28 wt%). The Mg# values are high (0.92-0.93) and low Cr# and Ca# (0.19 and 0.01, respectively).

Based mainly in a major chemical composition, the pyroxenes from Régis have great similarity with clinopyroxenes from peridotite xenoliths from Grib kimberlite (Fig. 3.22). The low Ti-Cr and high-Cr plot mainly in the sheared garnet peridotite and garnet peridotite xenoliths fields, respectively, with exception in graphic d, where the low Ti-Cr pyroxene analysed have lower Na_2O values. The clinopyroxene with high-Ti remains outside of delimited field from Grib kimberlite, exhibiting higher values of Ti and lower values of Cr and Na.

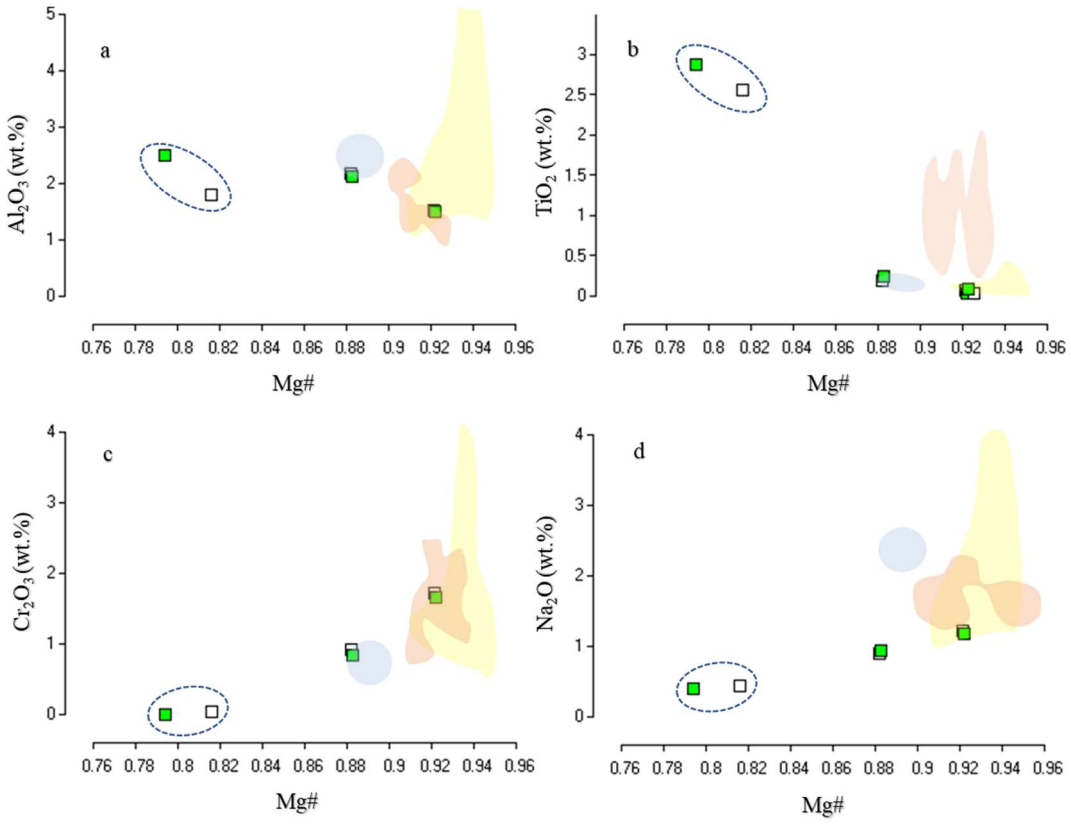

Fig.3.22 Bivariate plots for the clinopyroxene cores (full squares) and rims (empty squares) from Régis kimberlite. The yellow field shows the range for clinopyroxene from garnet peridotite xenoliths in the Grib kimberlite (Kargin et al., 2016). The orange field show the clinopyroxene-phlogopite xenoliths from Grib kimberlite (Kargin et al., 2017). The blue field displays the range for clinopyroxenes from sheared garnet peridotite xenoliths, which were in metasomatic equilibrium with Fe-Ti and carbonate bearing kimberlite magmas from the Grib kimberlite (Kargin et al., 2017). The dashed line area indicates the clinopyroxene with high-Ti.

Trace elements

The trace element from Régis pyroxenes varies according mainly with Cr contents (Fig.3.23). The high-Cr clinopyroxene present the lower values and uniformly variation, with more enrichment from La to Nd and negative anomalie in Zr. The high Ti/low Cr clinopyroxene display similar pattern to low Ti-Cr, displaying stronger negative slopes in K and Hf, and higher positive slopes in Sr, while the low Ti-Cr grain exhibit higher positive anomaly in Pb. The orthopyroxene displays the highest enrichment of almost trace elements, with exception in Pb, Hf and Ti.

From C1 Chondrite-normalized REE pattern (according to Boynton, 1984), the orthopyroxene exhibits the major enrichment related to HREE (10000 times chondrite) and flat pattern in the Sm-Gd. The low Ti-Cr clinopyroxene display ~1200 time chrondrite in LREE and depleting towards MREE remaining with flat pattern in the Eu to Lu. The lower values are exhibit by high-Cr clinopyroxene with up to 100 time chondrite in LREE with continuous depletion towards HREE.

The fractionated values of rare earth elements vary from 0.96 to 257.20 for $(La/Yb)_N$, 3.01 to 14.12 for $(Sm/Er)_N$ and 1.60 to 9.76 for $(Zr/Y)_N$. Abundances of incompatible elements normalized to primitive mantle (Sun & McDonough, 1989) of pyroxene minerals from Régis have comparable behaviour to the REE. The orthopyroxene, exhibit the most enrichment in IE and the high-Cr clinopyroxene the lowest. In addition, these pyroxenes are characterised by $(Zr/Hf)_N$ values from 2.80 to 63.73.

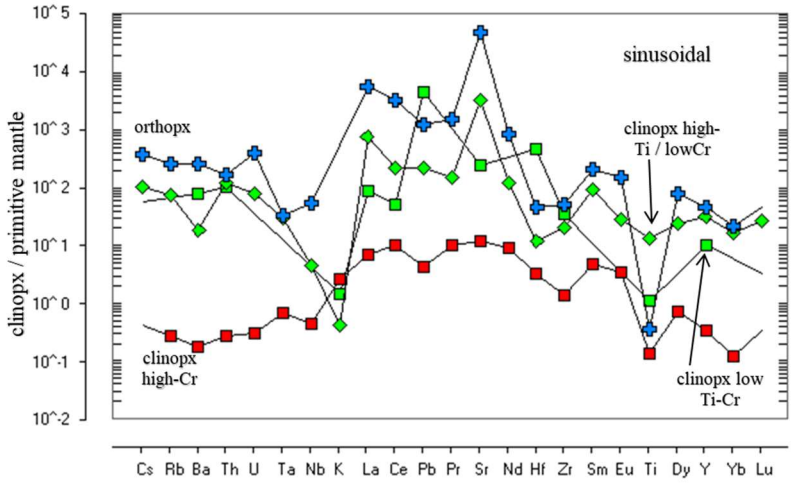

a)

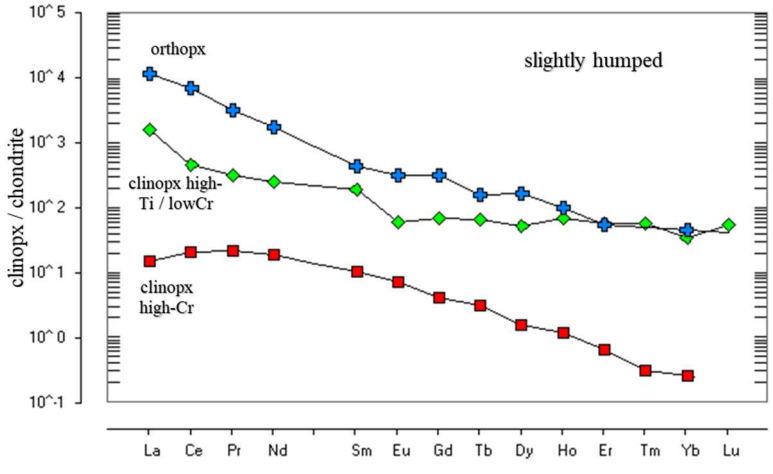

Figure 3.23. (a) primitive mantle-normalized incompatible elements pattern (McDonough and Sun, 1995) and b) Chondrite normalised REE patterns (Boynton, 1984) for pyroxenes cores.

5.6 Phlogopite

Two different phlogopite types from Régis kimberlite were analysed: microcrystals (0.30 to 0.48 mm) and macrocrystals (0.66 and 0.72 mm). They were separated according to differences and similarities of the chemical composition (Table 16). It was recorded two microcrystals groups: low Ti-Cr_m and high-Cr_m, and low Ti-Cr_M megacrystals group. One microcrystal analysed exhibited similar composition with megacrystals, therefore, it was considered derived from Ti-Cr_M group.

Low Ti-Cr_m microcrytals

This group is characterized by low TiO_2 and Cr_2O_3 contents (0.25 to 0.73 wt.% and 0.09 to 0.34 wt.%, respectively), FeO (3.11 to 6.73 wt.%), K_2O (0.64 to 10.52 wt.%), MgO (18.44 to 29.63 wt.%) and Al_2O_3 (5.25 to 14.44 wt.%). The Mg# varies from 0.86 to 0.94. Zoning patterns it is common, on average, it exhibits slightly Ti, Al decrease and Mg increase from core to rim. The dark areas have the lowest values mainly K and Fe.

High-Cr_m microcrytals

Only one grain was analysed of this group, however, Thomaz (2009) analysed eight phlogopite crystals with similar chemical composition characteristic of this group proposed in this study. It is characterized by low TiO_2 and high Cr_2O_3 (0.25 to 0.41 wt.% and 1.18 wt.%, respectively), FeO (3.90 to 6.51 wt.%), K_2O (5.36 to 10.35 wt.%), MgO (25.23 to 29.88 wt.%)

and Al_2O_3 (5.25 to 10.04 wt.%). The Mg# varies from 0.87 to 0.93. The Ti contents increase while Mg decrease from core to rim.

High-Ti_M macrocrystals

The macrocrystals shows high levels of TiO_2 (4.81 to 5.57 wt%), FeO (7.40 to 9.06 wt%), Al_2O_3 (12.89 to 14.44 wt%) and MgO (18.44 – 20.58 wt%), low contents of Cr_2O_3 (0.09 to 0.35 wt.%). The Mg# varies from 0.70 to 0.83. They exhibit highest values of Ti, Fe and Al, and lowest values of MgO and Mg# when compared to microcrystals. This group present low chemical variation within the crystal, on average, there is Ti, Al, Mg slightly decrease and K increase from core to rim.

The phlogopites from Régis kimberlite plotted within or close to groundmass mica field from Zolotitsa kimberlites studied by Beard et al. (2000) (Fig. 3.24a). The low Low Ti-Cr_m cores plotted in the phlogopite K-richterite peridotites field (PKP) defined by Early et al. (1987), while the High-Cr_m plotted within garnet phlogopite peridotites (GPP) and phlogopite peridotite (PP). The high-Ti_M plotted in MARID field. It may be a possibility of Régis phlogopites origins.

Giulliani et al (2016) studied the macrocrysts and groundmass phlogopites from Bultfontein kimberlite, and the most of low Ti-Cr_m phlogopites from Régis plotted in the field of metasomatized mantle xenoliths (MMX), suggesting again a xenolithic origin for this group. The high-Ti_M phlogopites follow the low-Cr groundmass trend, and always remain close to high Ti-Cr megacrysts phlogopite field from Bultfontein kimberlite. The TiO_2 values correlate negatively with Mg# and positively with Al_2O_3, in the Fig.3.24 it is possible to note that high-Ti_M group exhibit higher Mg# and lowest Al_2O_3 values than the microcrystals groups.

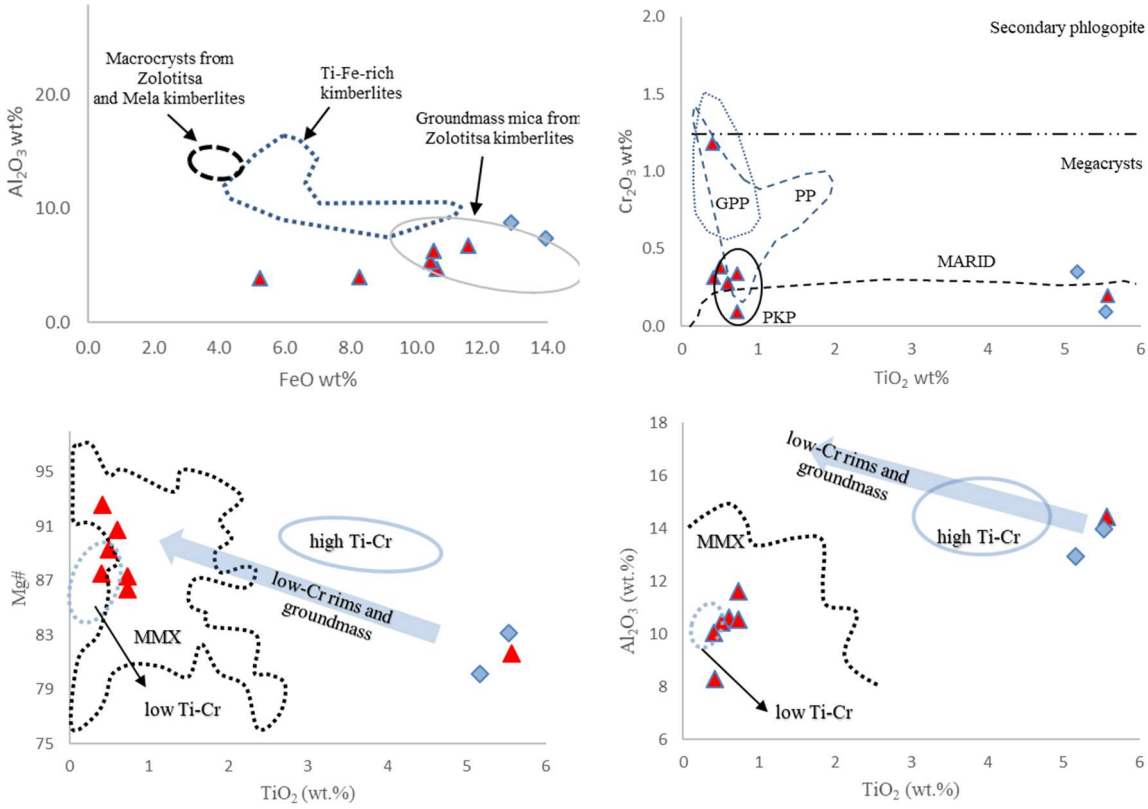

Figure 3.24 – Compositional variation of phlogopite groups from Régis. The red triangle corresponds to microcrystals (low Ti-Cr_m and high-Cr_m) and blue lozenge correspond to macrocrystals (high-Ti_M). Note that there is a microcrystal grain that remains always together with macrocrystals, due similar chemical compositions it is possible that microcrystal is from desegregation of microcrystal or the same rocks. A) Al_2O_3 wt.% vs. FeO wt.% diagram (after Beard et al., 2000); B) Cr_2O_3 wt.% vs. TiO_2 wt.% diagram (after Dawson and Smith, 1975) with xenoliths fields from Erlank et al. 1987. GPP: garnet phlogopite peridotites, PP: phlogopite peridotites, PKP: phlogopite K-richterite peridotites. C) TiO_2 wt.% vs. Mg# diagram (after Giuliani et al., 2016). The delimited fields are the major concentration of macrocrystal phlogopites from Bultfontein kimberlite and metasomatized mantle xenoliths (MMX) from Kimberley (after Giulliani et al. (2016) and Grégoire et al. (2002), respectively). The arrows show compositional trends towards more evolved compositions for low-Cr groundmass, rims and microcrysts phlogopites (after Giulliani et al. (2016).

Trace elements

The two phlogopite populations exhibit similar trace elements contents, however, the macrocrysts mostly display higher values than microcrysts (Fig.3.25). On average, have high levels of Ni (384.61 to 1570.96 ppm), Rb (225.88 to 693.81 ppm) and Ba (97.35 to 2595.2 ppm), significative amounts of V (52.97 to 160.33 ppm), Sr (1.08 to 13.58 ppm), Zr (2.67 to 83.37 ppm) and Nb (7.27 to 24.59 ppm) (Table 16).

The Ti values correlate positively with Ba, Sr, V and Nb, and negatively with Ni (Fig.3.25 a,b,c) and there is similarity with phlogopite crystals from Bultfontein kimberlite

studied by Giulliani et al. (2016). The low Ti-Cr_m cores plot in the field of metasomatized mantle xenoliths (MMX) from the Kimberley and other southern African kimberlites. It appears likely that these cores derived from disaggregation of mantle rocks (Dawson and Stephens, 1975). It is possible to note that these phlogopites cores evolve towards even more distinctive Ni-rich composition with respect to the high-Ti_M group, which are plotted within or very closer to high Ti-Cr macrocrysts from Bultfontein.

The two phlogopite populations exhibit similar sinusoidal patterns of trace elements, wichi is characterized by strong positive slopes in Rb, K, Pb and Ti, and negative slopes in Th, Ce, Pr, Nd and Y, it is possible to note a depletion towards to Lu. The macrocrysts are enriched in $LREE_N$ and depleted in $HREE_N$, with lightly enrichment of one grain in $MREE_N$ (Fig.3.26), exhibiting a slightly humped pattern. The microcrysts phlogopite also display a depletion towards $HREE_N$, however, the pattern is sinusoidal (Fig. 3.26). The most microcrysts analyzed is more enriched in $LREE_N$ in the rims than cores, the $HREE_N$ levels are below detection limit for most grains, but the rims present significative enriched from Tb to Er. It is possible to note that all groups display very slightly enrichment in MHREEN (from Nd to Eu).

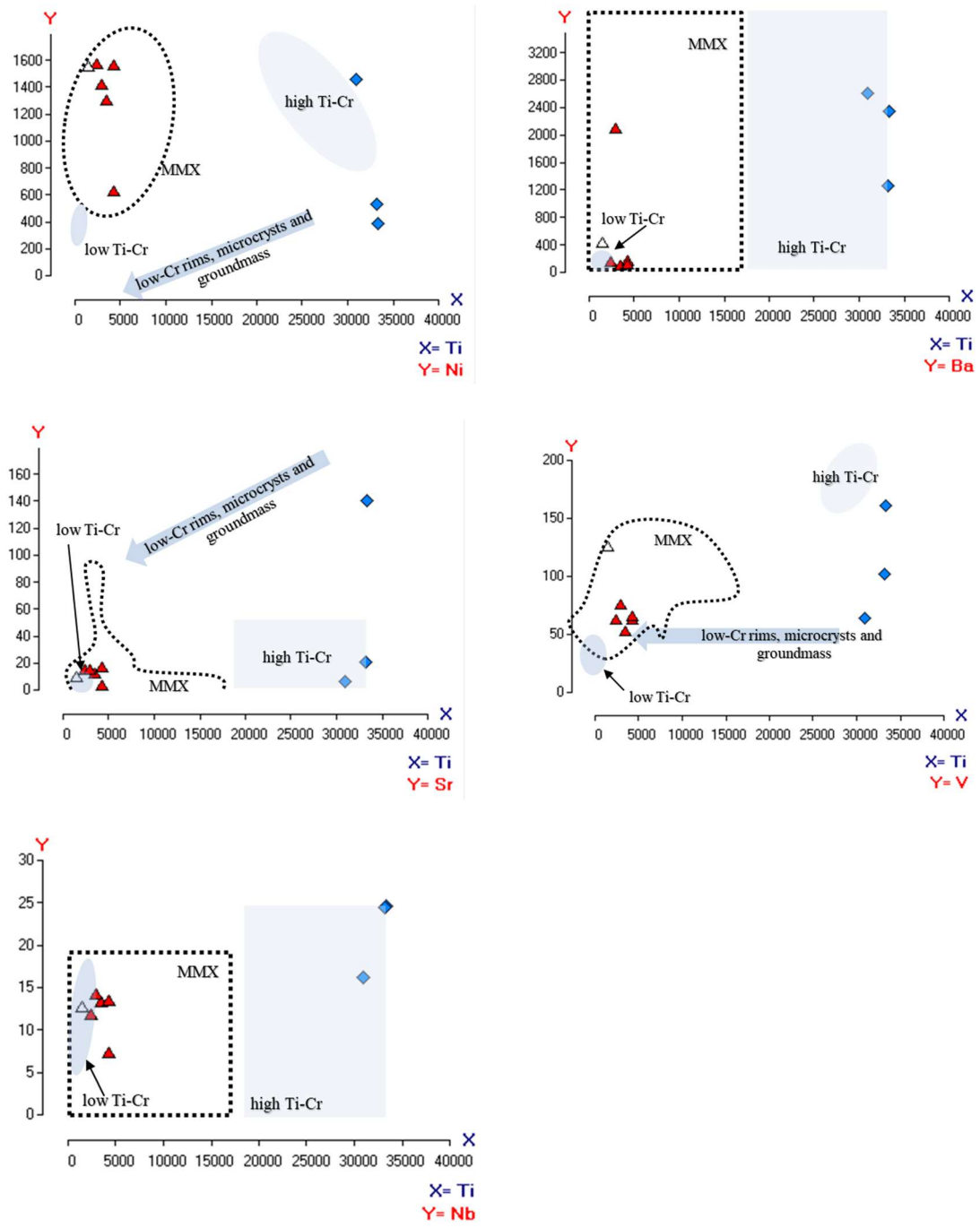

Figure 3.25 – Trace element co-variation diagrams for micro and macrocryst phlogopites from the Régis kimberlite. The microcrysts (low Ti-Cr_m and high-Cr_m groups) and macrocrysts (high-Ti_M) are represented by red triangle and blue lozenge, respectively. Note that the macrocrysts values are higher than microcrysts, with exception in Ni. The microcryst considered derived from Ti-CrM group exhibit higher values than other macrocryst grains. The delimited fields are the major concentration of macrocrystal phlogopites from Bultfontein kimberlite and metasomatized mantle xenoliths (MMX) from Kimberley (after Giulliani et al. (2016), Grégoire et al. (2002)). The arrows show compositional trends towards more evolved compositions for groundmass grains and macrocryst rims (after Giulliani et al. (2016).

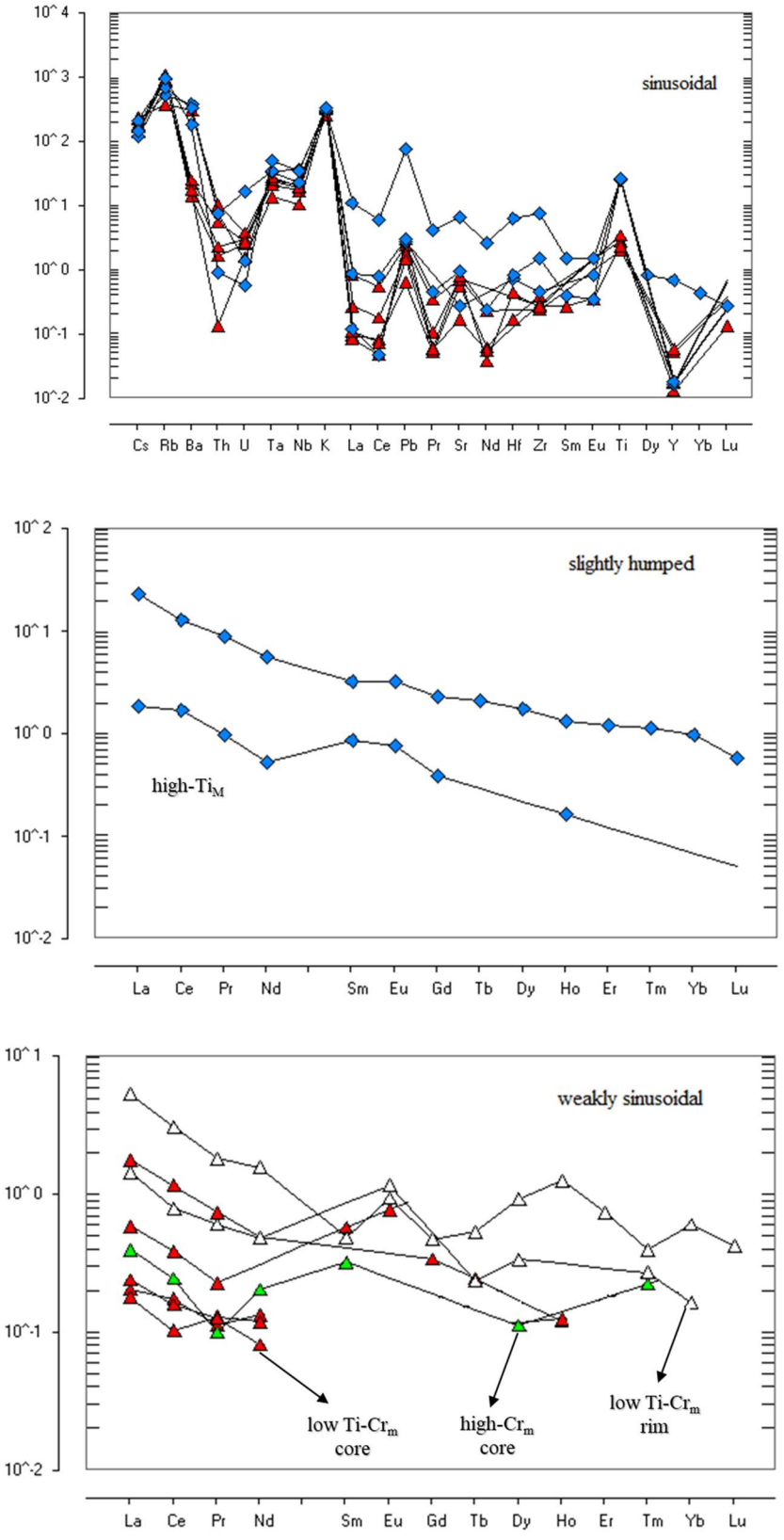

Figgg. 3.26. Trace element concentrations of macrocrysts and groundmass phlogopites from Régis kimberlite. Concentrations are normalized to the C1 chondrite composition of McDonough and Sun (1995).

6. Sr isotope analysis

The Sr-isotope compositions of the Régis perovskites are summarized in Table 3.3. Seventeen analyses of individual perovskite grains from Charneca was realized, and due isobaric interferences of ^{87}Rb over ^{87}Sr was considered only nine chemical analyses ranging between 0.704238 and 0.705644. The isobaric ^{87}Rb contribution over ^{87}Sr was corrected by using the ^{85}Rb ion signal and the $^{87}Rb/^{85}Rb$ natural ratio (Ramos et al. 2004), however, we opted to exclude some analyzes that was interpreted to have some uncertainty degree, and for better accuracy of the data were considered values only up to the third decimal place. Due to their very low Rb/Sr ratios (< 0.005) (Sarkar et al., 2014) and the relatively young age of the kimberlites, no age correction was applied on the measured Sr isotope ratios, furthermore, the data obtained were considered initial.

The isobaric interferences should be corrected for the accuracy of resultant $^{87}Sr/^{86}$ Sr ratios. Munoz et al. (2016) implemented measurements of half-masses ($^{171}Yb^{2+}$) allows the accurate assessment of lanthanide interferences, permitting the determination of Sr isotopes in important REE-rich accessory phases. The appropriate results are achieved in Sr-rich and Rb-poor phases (Rb/Sr <0.02), materials with Rb/Sr ratios > 0.02 are not suitable for the acquisition of accurate Sr isotope ratios via LA-MC-ICP-MS (Ramos et al. 2004), whereas others advocate that an efficient correction can be performed for materials with far greater Rb/Sr ratios (<0.2 Davidson et al. 2001). Due the very low amounts of Rb (< ~5.7ppm; Donnelly et al., 2012) in perovskites, if interference occurs, this influence will be minimum.

Table 3.3. $^{87}Sr/^{86}Sr$-isotope results for perovskite analyzed in this study.

Perovskite (LA-MC-ICP	
SrO (average): 2411 ppm	
Sr^{87}/Sr^{86}_i	2 sigma
0.704927	0.000465
0.704832	0.000701
0.704259	0.000688
0.704430	0.000643
0.704660	0.000764
0.705456	0.000676
0.704724	0.000666
0.704238	0.000761
0.705644	0.000554

7. Discussions

The recognition of different facies that infilled the pipes and craters of the Class 1, 2 and 3 kimberlites were studied by many authors (e.g. Clement and Skinner, 1985; R. Cas et al., 2008; Field and Scott Smith, 1999; Hetman et al., 2004; Scott Smith et al., 2008; Skinner and Marsh, 2004; Sparks et al., 2006). These classes are based in African and Canadian kimberlite models, the classical pipe composed by root, diatreme and crater zones (Clement, 1982; Howthorne, 1975) correspond to the first model found in Africa (Class 1) and the facies that fill which zone are from hypabyssal- (HFK), through transitional- (TFK) to diatreme- (DFK) and crater-facies rocks (CFK), respectively. The other two classes differ mainly by absence of diatreme zones and by the mineralogical different facies that composed each one.

These names and textural terms are applied to rocks where the origin is not necessarily well-established (Sparks et al., 2006), however, the classification thus provides a useful starting point. The association of the facies with specific region of the zones should be applied with care to the Brazilian kimberlites, as these classifications were established through studies done in extensively studied kimberlites. The crater facies could also occur in the diatreme zone, and hypabyssal or coherent kimberlite could occur at any level of a pipe (Cas et al., 2008).

The crater-facies from Régis kimberlite is from 36 to 110m depth, and was well studied by Thomaz (2009) that described samples in situ and had access to fresh samples of this kimberlite in field available from SAMSUL. In the present work, it was described and classified the deeper zones. From 180.90m to 278.93m depth, it was recognized features of diatreme-facies (DFK), it is characterized by completely serpentinized olivine crystals, segregationary textures and juvenile clasts are common and these last composed the most part of Régis diatreme-facies. In addition, many clasts or discrete olivine pseudomorphs are coated by a thin film, which is produced by surface tension (Gernon et al., 2012).

The calcite in these levels are secondary, occurs within interstitial medium like veins, filling the vesicular clasts or olivine fractures. It is possible to observe sharply bounded domains of carbonate, featuring radiating inwards and crystal size increasing inwards suggest a pore-filling phase of carbonate, in addition, also occurs as diffusely bounded patches of both matrix, according with CAS et al. (2008a), in kimberlites this features correspond to a secondary carbonates, in kimberlites, mainly calcite.

The absence of primary calcite and the strong occurrence of secondary phase of this mineral, in addition to abundance of juvenile clasts and country rocks with angular shapes, point to a diatreme-facies from 180.90m to 278.93m depth. The microlitic diopside is abundant in edges clasts and dispersed in interstitial medium in some types clasts, it is interpreted as the product of quenching (Skinner and Marsh, 2004).

The uncored juvenile clasts described in table 3.1 exhibits wide mineralogical similarities to hypabyssal kimberlites (Mitchell, 2008), pseudo-olivine phenocrysts set in a fine groundmass. The different compositions, the abundance and size of olivine crystals within and outside of the clasts (material intra-clast) are very differently. In the most type of juvenile clasts from Régis, the olivine sizes are higher than interstitial medium discrete olivine that enclose the clasts, suggesting a derivation of the juvenile clast from more than one magmatic pulse (Webb, 2006).

The emplacement sequence evidence of the different types that composed the Régis kimberlite, can be reconstituted by the misture of the types (Fig. 3.27). The type C,D clasts correspond to one of the first magmatic pulses at the beginning of the root zone formation, which is formed by the intrusion of several pulses of magma (Hetman et al., 2004). Due to the rapid depressurisation of an intrusive magma column occurs the diatremes formation and many

magmatic pulses are being injected through the vent following explosive breakthrough to surface.

The type C,D clasts are englobed by type B, which is englobed by type A, which is encompassed by type F or G and these last are englobed by clast E or F. It is suggested that the type I clast probably is a late magmatic pulse. No mixing of this clast with any other material was observed and the phlogopites still remain relatively fresh, in addition, very elongated tube-shapes appear “to drag” the kimberlitic material around, resulting in an alignment of the minerals in the clast-interstitial medium constituents interface.

The contacts between type A and B, and type A/B and C/D are diffuse, this may be due to a shorter time between the magmatic pulses, or the younger melt (type A / B) had a temperature high enough to change the edges of the older clasts (type C/D). The high plasticity exhibited by the A / B type may be evidence of this higher temperature.

The wide mineralogy and size of the clasts, besides the morphology and contact relations, reveal a complex and dynamic emplacement of Régis kimberlite, and may involve differently batches of compositionally distinct kimberlitic magma, in addition, these juvenile clasts can be crystallized under potentially higher P-T conditions (Abersteiner et al., 2017)

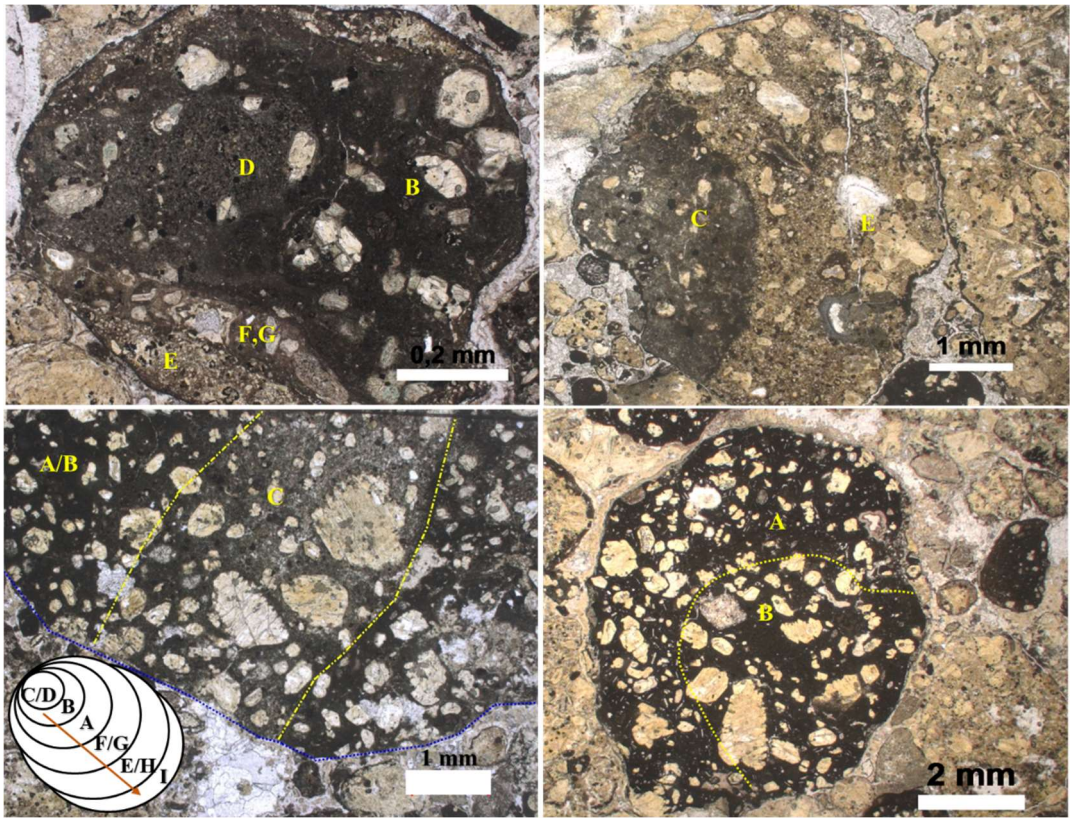

Fig.3.27. The emplacement sequence of uncored clasts from Régis kimberlite.

Some of kimberlitic material that compose the clast types is found forming the pelletal structures (Fig. 3.9). During the rising magma there is an incorporation of particles into liquid spheres in addition to rapid unmixing of immiscible liquids (Wilson and Head III, 2007; Junqueira-Brod T.C, 1999; Lloyd and Stoppa, 2003). The responsible mechanism during emplacement by pelletal formation is attributed to fluidized spray granulation (Gernon et al., 2012). The mechanism involves continuous injection of fluid, volatile-rich melts as dykes into loose, granular deposits close to the diatreme root zone, which produces a dispersion of larger coated granules (pelletals) that are simultaneously dried by gases. The types 3 and 6 represent very well these mechanisms due to well-rouded rounded shapes with layered concentrically aligned.

The elliptical geometry exhibited by type 5 and 1 pelletal lapilli suggests that a major surface tensional is envolved and consequently a major variable in fluidised spray granulation (Gernon et al., 2012). The presence of multiple rims of the type 4 and 1 ly concentrically aligned phenocrysts in external rim is suggestive of a systematic multi-stage layering process. The wide diversity of cored juvenile clasts from Régis also suggest differently pulses during the formation of this kimberlite, presenting a strict relation to uncored clasts. The types 3 and 8 also show the

sequence of emplacement. A fluidised spray granulation occurs when a new pulse of kimberlite magma intrudes into unconsolidated pyroclastic deposits within the diatreme (Gernon et al., 2012), therefore, each pelletal structure rim may be related to the magmatic flows that gave origin to the different clasts.

The type 1, 2, 5 and 7 are pelletal without concentric rim and no alignment, they can be evidence of the initial stage of pelletal formation, according to Junqueira-Brod (1999) model, in the first stage the crystal (nucleous) starts to spin. These pelletals without concentric layers were found in higher dephs (253.4 to 278.93 m), this fact could be another indicator of proximity of hypabyssal-facie.

The dynamical emplacement mechanism that formed the pelletal structures involves multi-stage intrusion, resulting in spatial and temporal variation in the structure and composition of pipe-fill and consequently, could influence local diamond grade and size distributions (Gernon et al., 2012).

The grain size criterion is not self-sufficient to establish the relationship between megacrysts and macrocrysts due to the fact that both can be derived from larger grains crystals (Pivin et al., 2009), including megacrysts and xenolith-derived fragments, which may have been mechanically reduced during the process of the primary kimberlite material. In this study, most mineral grains available are in fact smaller than 10 mm in diameter and do not fit the strict definition of megacrysts. Therefore, based on major and trace element compositions, the word “megacrysts” can be linked to genetic processes rather than just as a description of mineral size.

Process recorded by major elements

The chemical composition of garnet has been linked to the bulk rock composition of lithospheric peridotites (Griffin et al., 1999). According with $Cr_2O_3 > 4.0$ wt.% or $TiO_2 > 0.50$ wt.% if $Cr_2O_3 > 1.0 < 4.0$ wt.% , the Régis mantle garnets are from peridotites, and the positive correlation between CaO and Cr_2O_3 points to lherzolitic origin (Schulze, 2003; Grütter et al., 2004). The Cr content of garnet is a primary indicator of the degree of depletion of the host rock (Griffin et al., 1999) and may be used as an indicator of the extent of initial melt extraction. Garnets with Cr_2O_3 contents ≥ 4 wt.% imply protolith depletion during mantle melt extraction at low pressures (Stachel et al., 1998), this implies in a stabilization during subcretion of the

shallow melting residues beneath early continents and/or introduced during subsequent metasomatism.

The low to moderate chromium (3.2 to 4.6 wt.%) and calcium (< 5.23 wt.%) garnets analysed from Régis correspond to "normal" subcalcic garnets (CaO > 1.8 wt.%) and can reflect melt extraction in excess of 20% (clinopyroxene exhaustion) whilst ultra-depleted garnets (CaO < 1.8 wt.%) derive from residues of ≥ 50% melt extraction (orthopyroxene exhaustion (Griffin et al., 1999). Geotermobarometry studies in garnets from Régis kimberlite indicated a cold mantle region (40 to 53 Kbar) (Thomaz, 2009), which correspond to diamond equilibrium field.

The depletion in Cr_2O_3 and relative low Mg# values (0.80 – 0.85), which decrease with metasomatism evolution, in addition to initial enrichment in Al_2O_3, TiO_2 and HREE (Fig.3.13), it is possible to suggest that the Régis -9 garnets represent an intermediate stage of metasomatic enrichment, while régis-5 have no influence of metasomatic fluids. This features are in agreement with "Lz3" and "Lz1" garnets, respectively, studied by Shchukina et al. (2017), and according to the thermobarometer the "Lz3" garnets occur through the section of the lithospheric mantle from 20 kbar to 69 kbar, with major concentration from 30 to 53 kbar, and according to modeling results, the composition of the parental melt in this stage could be close to mica-poor picrites.

The low Ti-Cr and low Ti/ high-Cr clinopyroxenes overlap in Mg#, Al_2O_3, TiO_2 and Cr_2O_3 contents mainly the sheared garnet peridotite and garnet peridotite xenoliths fields, respectively, being very similar of clinopyroxenes from peridotite xenoliths from Grib kimberlite (Kargin et al., 2016, 2017) (Fig. 3.22). They present great chemical similarity with clinopyroxenes associated with low-Ti garnets and the high-Ti clinopyroxene are very similar to clinopyroxenes associated with high-Ti garnets (Kargin et al., 2016) and megacrystals from Grib kimberlite (Kostrovitsky et al., 2004).

The features above suggest that the clinopyroxenes with low Ti and the orthopyroxene represent disintegrated fragments of peridotite xenoliths (probably garnet peridotite) in addition, the Mg#, Ca# and Cr# values are higher than worldwide megacrysts and similar to worldwide peridotites (Pivin et al., 2009). The high TiO_2 values indicate that the high Ti/ low Cr clinopyroxene represent disintegrated fragments from megacrystals.

The low-chromium megacrysts can crystallize from magmas bodies by normal fractional crystallization fractionation in the deep lithosphere in the protokimberlite stage

(Gurney et al., 1979). Many origins are attributed to megacrystals, e.g. magmatic origin or from mantle xenoliths, the low Mg# and La/Sm ratios can suggest a fractional crystallization (Kargin et al., 2016; Nimis et al., 2009).

The low Ti-Cr_m and high-Cr_m phlogopite cores additionally to high Mg# values (0.87 to 0.92) can indicate the peridotite origin for this phlogopite type, plotting within phlogopite K-richterite peridotites and metasomatized xenoliths field. Zoning is a typical feature of phlogopite macrocrysts in kimberlites (Mitchel, 1986) and the low metasomatism (T range 950 – 110°C) is accompanied by the introduction of this mineral (Griffin et al., 1999). The low-Ti types from Régis have variable composition from core to rim suggesting a low mantle metasomatism enrichment, addition. They , they show great compositional similarities with phlogopites from metasomatized garnet peridotite xenoliths from several kimberlites (e.g. (Erlank et al., 1987; Kostrovitsky et al., 2004).

The high-Ti_M plotted in MARID field and it may be a possibility of Régis phlogopite origin. However, the megacrysts worldwide are strongly richer in Fe and Ti than the peridotite minerals (Pivin et al., 2009) and similar Cr_2O_3 contents to the primary peridotite micas but higher TiO_2, normally the most of them contain less than 0.5 wt.% Cr_2O_3 (Dawson and Smith, 1975). The high-Ti_M type can be dissociated fragments from megacrystals during the kimberlitic melt rise.

Another hypothesis of high-Ti_M phlogopite source is MARID suite. In addition the high values of Ti_2O and , the high FeO and low Cr_2O_3 amounts also testify a MARID source, normally megacryst phlogopites have lower FeO and higher Cr_2O_3 values, compositions similar to MARID phlogopites can occur, but FeO values are up to ~ 7.8 wt.% (Dawson and Smith, 1977). The relative low Mg# values and NiO contents also can be an evidence from MARID source.

The majority of spinel grains analysed from Régis follow Fe-Ti trend, suggesting an evolution of spinel compositions during fractional crystallization from the host magma, which increases the Fe/Mg ratio and the Ti content of the melt (Barnes and Roeder, 2001). The most of spinels from Régis is enriched in Fe^{3+} and Ti, which correspond to late-stage crystallization (Agee et al., 1982). However, the origin of the minerals that composed the kimberlite is controversial, due high mixture with mantle xenoliths during the rise and emplacement of this rocks. Normally spinel macrocrysts and xenocrysts that are low in $Fe^{2+}/(Fe^{2+} + Mg)$ tend to be low in Ti (< 0.1 wt.%) and ferric iron.

The composition overlapping between xenolitic xenolithic macrocrysts and euhedral grains is common. The trends of small euhedral and macrocrysts in terms of Cr/(Cr + Al) and $Fe^{2+}/(Fe^{2+} + Mg)$ is identical to that of spinel-group minerals from xenoliths (Schulze, 2001). However, most of euhedral grains analysed displayed a chemical composition very distinct from anhedral spinels, pointing probably to different origin.

It was observed in some primary Cr-spinel cores with ferrichromite or magnetite rims, and these rims are of metamorphic origin (Bhat et al., 2017a). The ferritchromite and magnetite rims mantling the primary Cr- spinel cores are of metamorphic origin. The magnetite rims are highly in Al, Mg and Cr content as compared to Cr-spinel cores. During the metamorphism the Al, Mg and Cr can be diffuse out of the grains, while Fe and Si were introduce. The peridotitic origin can be suggest for the anhedral spinel analyzed; the Mg# is positively correlated with Cr and due coexistence spinel and silicate phases of this rocks, an extensive $Mg^{2+} - Fe^{2+}$ exchange is probably, resulting in a decreasing of Mg forming magnetite. Another texture recorded in the minor phenocrysts spinels is atoll-textures, characteristic of primary groundmass spinel feature (Roeder and Schulze, 2008)

Process recorded by trace elements

Residual garnets have increasing concentrations from La to Lu with HREE contents of about 10 chondritic units (Shchukina et al., 2015). The depletion in the LREE and relative enrichment in HREE displayed by régis-9 crystal from Régis kimberlite testifies for the silicate composition of the metasomatic agent with high LREE (Shchukina et al., 2017). The positive correlation between Y and Zr concentrations corresponding to the “melt” metasomatic trend (Griffin, Fisher, et al., 1999). The slightly enrichment in LREE with MREE at C1 chondrite unit displayed by régis-5 additionally to Y/Zr (0.62) plot in depleted field garnets from W L Griffin et al. (1999). However, low Y/Zr, (Sm/Er)n < 1 (0.11) and (La/Yb)n (0.01) ratios indicate its residual nature without any influence of metasomatic fluids (Shchukina et al., 2017).

In opposite, the régis-9 garnet exhibit slightly enrichment in MREE and higher Zr/Y (8.87), (Sm/Er)n > 1 (1.34) and (La/Yb)n (0.33) ratios, indicating a major influence of metasomatic fluids. Higher $(La/Yb)_N$ (Howarth et al., 2014) or $(Sm/Er)_N$ (Shchukina et al., 2017) at constant Ti/Eu can be used to distinguish between carbonatite and kimberlite

metasomatism. The régis-9 from Régis present low (Sm/Er)n and (La/Yb)n with variable Ti/Eu indicating a silicate metasomatism.

The high LREE concentrations of clinopyroxenes associated with negative Nb, Ta, Zr, Hf and Ti anomalies have been interpreted to result from metasomatism of the subcontinental lithospheric mantle (SCLM) by silicate melts/fluids (Shchukina et al., 2015), or kimberlite melts (Kargin et al., 2016). All pyroxenes were affected by metasomatism in different intensities, e.g. the high-Cr clinopyroxene display the more homogeneous trace element pattern and the high LREE and strong to subtle negative Nb, Ta, Zr, Hf and Ti anomalies could reflect modification of the SCLM by kimberlite or ultramafic alkaline melts.

The clinopyroxenes from peridotite show subtle negative Sr, Zr and Hf anomalies (Fig.3.23), this mismatch suggests compositional differences between the ultra-alkaline melts migrating at depth and those erupted (Nimis et al., 2009). The clinopyroxene could be the final product of a metasomatism of garnet peridotites within the SCLM (Kargin et al., 2017), and maybe the same source that formed the lherzolitic garnets (Fig. 3.28)

The trace element pattern of the most Fe-rich is the closest to that of the model clinopyroxenes in equilibrium with the Zagadochnaya kimberlites (Nimis et al., 2009) and can suggests a lesser degree of melt–peridotite interaction for its parent liquid. This are in agree with small La/Sm ratios and relative high Mg# values (0.89 and 0.92, respectively) exhibited by these grains, pointing to peridotite re-equilibration at increasing melt-rock ratio. The higher La/Sm ratios exhibited by clinopyroxene megacryst and orthopyroxene (Fig. gg) can be interpreted as formed by fractional crystallization influenced by percolation of metasomatic fluid (Nimis et al., 2009). In relation to megacrystal analysed, the clinopyroxene megacrystal can be formed from protokimberlitic fluids shortly before the kimberlite emplacement (Kopylova et al., 2009). This hypothesis can explain the high La/Sm ratio exhibited by clinopyroxene megacryst and can be the same fluid that posteriorly influenced the kimberlite.

The high relative Ti/Eu and the low La/Yb ratios of clinopyroxene megacryst indicate that the LREE enrichment is likely related to silicate metasomatism, while the low Ti/Eu and higher La/Yb of ortho- and clinopyroxenes are related to carbonatite metasomatism (Fig. 3.28).

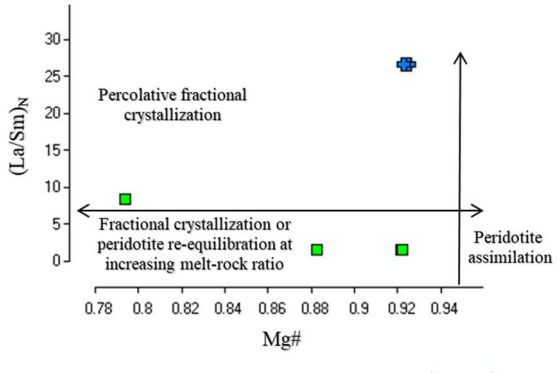

Fig.3.28. Relations between Mg# values and LREE fractionation for clinopyroxene (after Kargin et al., 2016; Nimis et al., 2009)

The assimilation of xenoliths, e.g. peridotite, enriched the kimberlitic melt in silicate and the formation of the low-Cr and Fe-Ti-rich megacrysts occur, in this case, the presence of Mg-ilmenites with high Al and low Mn and Cr. The strong depletion of Ti, Nb, Ta, Zr and Hf may reflect the precipitation of Ti-oxides, such as ilmenite due to preferential fractionation (Golubkova et al., 2013), and can be indicate the presence of garnet-clinopyroxene-ilmenite peridotite xenoliths.

The all silicates analysed (garnet and clinopyroxenes) have light depletion in Hf, Nb, Ta, and Zr, this can suggest the subtle enrichment of these elements in the ilmenites. The Mg-ilmenite grains analysed have relative high concentrations of incompatible elements, such as Ba, Sr, Pb, Th, U, LREE, have and lower abundances of high field strength elements HFSE (Zr, Nb, Ta, Hf). These variations imply that Mg-ilmenite grains were in equilibrium with kimberlite magma (Golubkova et al., 2013). The strong enrichment in LREE can be reflect that the melt was HREE depleted.

Another signature of the metasomatic enrichment is impress within spinels from Régis kimberlite. The Cr# values increase with the evolution of partial melting, the Régis anhedral spinels exhibit variable Cr# (Cr/(Cr + Al) (0.74 – 0.98) and this range can indicate a garnet peridotite source (Schulze, 2001). The high values Cr# (>0.6 or >0.8) and low Ti (Bhat et al., 2017a) are characteristics of depleted peridotite, can indicate a “primary fertile” peridotite.

The high TiO_2 values of anhedral spinels from Régis (2.38 – 50.03 wt.%) associated with high Cr# probably are related to reaction with boninite melts (Pearce et al., 2000). These Cr-spinels are related to highly refractory peridotites (i.e., dunites and harzburgites) formed in

a supra-subduction setting by hydrous melt extraction and by melt-rock reaction (Bhat et al., 2017; Pearce et al., 2000). The depleted REE patterns relative to PM condritic pattern can be observed in spinel from Régis (Fig.3.15) and have also been observed in orogenic peridotites, abyssal peridotites and ophiolitic peridotites. In ophiolites, the depleted REE patterns are restricted to refractory mantle peridotites with their petrogenetic interpretation of being mantle-melting residues (Bhat et al., 2017b).

Trace element characteristics, including mobile elements and $^{87}Sr/^{86}Sr$ ratios are typically used to explore crustal contamination in kimberlite magma (Sarkar et al., 2014). The more evolved and isotopically enriched upper crust would modify the magma to a greater degree, and the bulk rock compositions of kimberlites are sensitive to the effects of contamination and post-emplacement alteration. Strontium isotope compositions can also be used as supporting evidence against significant crustal contamination of the magma from which the perovskite crystallized.

The average of isotopic data are compared with perovskites $^{87}Sr/^{86}$ Sr ratios from APIP kimberlites (Guarino et al., 2013) and bulk-rock data from Group I kimberlites (Becker and Le Roex, 2006; Skinner et al., 1992, Woodhead et al., 2009). The Fig. 3.29 show the perovskite $^{87}Sr/^{86}$ Sr ratios from Régis kimberlite and occur an overlapping between APIP perovskites and bulk-rock of Group I. On average, the ratios Régis are very similar than APIP rocks and Group II, and present slightly lower $^{87}Sr/^{86}Sri$ ratios (0.704238 and 0.705644) than APIP rocks (0.70506–0.70565; data from Guarino et al., 2013) and Group I kimberlites (0.70328 to 0.70537; data from Becker and Le Roex, 2006).

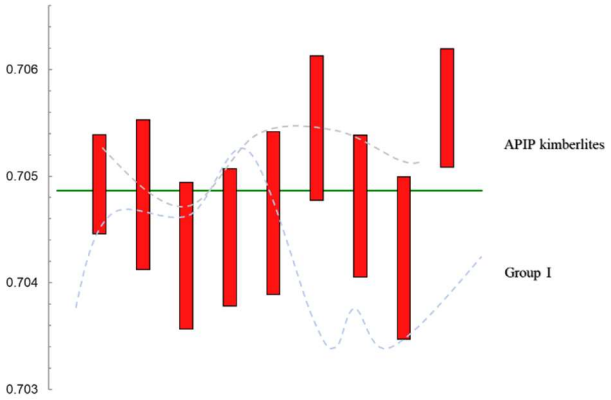

Fig.3.29. $^{87}Sr/^{86}Sr$ perovskite data from Régis compared with $^{87}Sr/^{86}Sr$ perovskite data for APIP kimberlites (Guarino et al., 2013) and bulk-rock from Group I and Group II kimberlites (Becker and Le Roex, 2006).

These suggested that the Sr isotope compositions from groundmass perovskite are more representative of the uncontaminated kimberlite magma than those from bulk rock studies, which are often contaminated (Paton et al., 2007). Therefore, the major variance between bulk rock and perovskite analyses is more marked for fragmental, massive volcaniclastic or pyroclastic kimberlites (Sarkar et al., 2014). The Régis kimberlite do not have uniform Sr isotopic compositions, as is seen in some APIP rocks and Indian and Chinese kimberlites (Guarino et al., 2013; Woodhead et al., 2009), suggesting major upper crustal contamination.

The Régis perovskites also are compositionally similar to another kimberlitic perovskite (e.g. Kuruman kimberlites; Donnelly et al., 2011), and show considerable enrichment in REE, Nb, Th and Na, and typically shows the highest concentrations of REE. The compositional variation between different perovskite types within Régis kimberlite point to multiple generations of perovskite, and probably reflect different crystallization conditions (Chakhmouradian and Mitchell, 2001), as perovskite can crystallize over a wide range of pressure-temperature conditions, and under differing activities of minor elements

The trace element data suggest a light crustal contamination of the Régis kimberlite, specifically the higher La/Yb values of the perovskites (329 and 635). A progressive assimilation of crustal material into the kimberlite magma, through melt-wall-rock interactions over the range of perovskite crystallization temperatures, can result in compositional and isotopic variations in perovskite (Malarkey et al. 2010).

APÊNDICE 4 – Kimberlito Indaiá I

Contribution to the mineral chemistry of the Indaiá I kimberlite, West of Minas Gerais, Brazil

Summary

1. Introduction and geological background

Differences in petrography and composition have been used to divide kimberlites into Groups I and II (Dawson, 1971; Mitchell, 1986, 1995; Smith, 1983). The term “orangeite” was introduced by Mitchell (1986, 1995) as a reference to the first group, which normally shows a higher content of oxide minerals in the groundmass and a slightly lower content of potassium, unlike Group II kimberlites, which can present high potassium minerals (e.g. sanidine) and high amounts of phlogopite, often above 20% (Becker and Le Roex, 2006). This definition is the most used until today. Many classifications, based not only on mineralogy, but also on geochemistry, have been proposed (e.g. Cas et al., 2009; Field and Smith, 1998; Hayman and Cas, 2011; Mitchell, 1995; Skinner and Clement, 1979; Sparks et al., 2006; Woolley et al., 1996). This conflicting use of geological and volcanological terms have given rise to many controversies.

Intrusive complexes of kamafugites, kimberlites and related rocks characterize the Alto Paranaíba Igneous Province (APIP), one of the largest potassic–ultrapotassic provinces in the world, located in the southwest of Minas Gerais, Brazil. The province has been subject of many studies (e.g. Araújo, et.al., 2001; Bizzi & Araujo, 2005; Brod et al., 2004; Carlson et al., 1996; Felgate, 2014; Gibson et al., 1995; Gomes & Comin-Chiaramonti, 2005; Guarino et al., 2013; Melluso et al., 2008; Moraes Rocha et al., 2015, 2014; Nannini, 2016; Pereira, R. S.; Fuck, 2005; Read et al., 2004). The restricted ranges of initial $^{87}Sr/^{86}Sr$ (0.704 – 0.706) and εNd_i values (-4.14 to -6.10) suggest that these rocks are intermediate between Group I and II South African kimberlites (Gibson et al., 1995; Guarino et al., 2013).

In this paper, we introduce a new petrographic characterization of the kimberlitic materials and the major- and trace-element contents of Indaiá I, a coherent kimberlite located to the northeast of Monte Carmelo city (MG), nearby innumerable kimberlitic intrusions that compose the APIP (Fig. 4.1). This work aims to contribute to the textural characterization of Brazilian kimberlites, as well as to increase the knowledge on chemical and geochemical aspects of the PIAP kimberlites, the nature and evolutionary history of the magmas from which they originated.

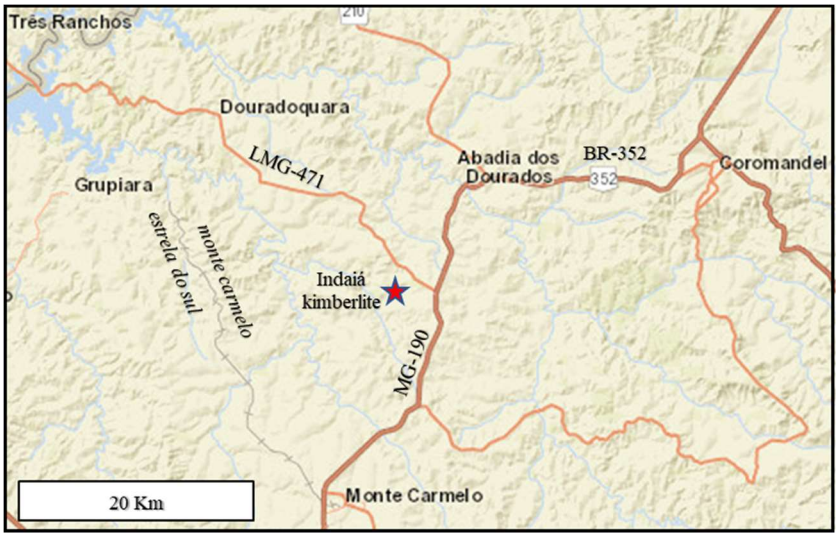

Fig. 4.1. Location of the Indaiá I kimberlite (red star), nearby Monte Carmelo and Abadia dos Dourados cities.

The APIP magmatism emplaced into a Brasília mobile belt (between São Francisco craton and Paraná basin). It consists of metasedimentary sequences of the Canastra, Araxá, Ibiá and Bambuí groups, archean rocks represented by felsic and mafic granulites and orthogneisses, and phanerozoic covers of the Areado and Mata da Corda groups (Dardenne, 2000) (Fig. 4.2). The Indaiá I kimberlite intruded granitoids and Araxá Group rocks, represented by micaceous quartzites, schists, and locally calcitic or dolomitic marble (Dardenne, 2000). Schists vary in composition, including garnet, biotite, hornblende and feldspar among their mineral constituents (Chaves et al., 2008).

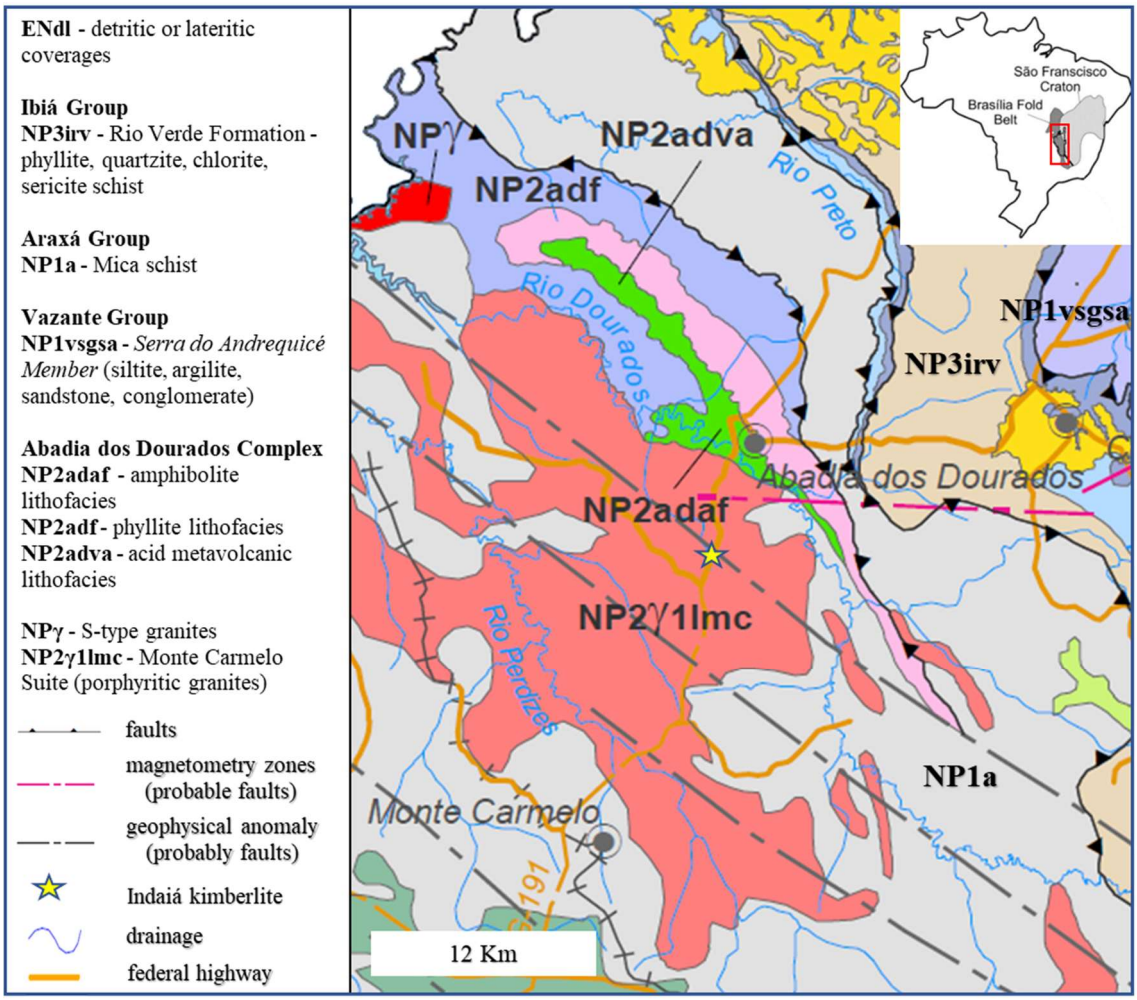

Fig. 4.2. Geology location map and geotectonic setting of the Indaiá-I kimberlite (yellow star) (Modified from CPRM, 2014)

2. Previous works

Since its discovery in 1975, many studies have focused on the Indaiá I kimberlite (Almeida, 2009, Guarino et al., 2013; Melluso et al., 2008; Meyer & Svisero, 1991; Nannini, 2011, 2016; Silva, 2008; Svisero & Haralyi, 1984; Svisero et al., 1984), it has a large amount of mantle xenoliths and is a fresh kimberlite, and this fact facilitates the investigations.

Petrographic descriptions and major elements analyses were carried out by Silva (2008), according to whom the ilmenites present indicate a favourable environment for diamond preservation. However, the absence of indicators such as garnet and Cr-spinel so far do not point to a favourable assemblage to the occurrence of that mineral. Detailed studies of mantle xenoliths (e.g. Cr-spinel peridotite, dunites and harzburgites) from Indaiá I (and other intrusions nearby) were presented by Nannini (2011, 2016), according to whom high Mg# contents in

olivine and Al depletion suggests that APIP mantle xenoliths were affected by intense partial melting, and that $^{87}Sr/^{86}Sr$ ratios in clinopyroxene suggests a metasomatism from asthenosphere or lithosphere with crust material.

Investigations of U-Pb ages and Sr-Nd- isotope geochemistry of perovskites from kimberlites, kamafugites and phlogopite-picrites of the APIP (including Indaiá) were performed by Guarinos et al (2003), which restricted the ages for the rocks (kimberlites ~91–80 Ma, kamafugites ~81–78 Ma, and phlogopite-picrites ~90–82 Ma). Sr–Nd isotopic ratios ($^{87}Sr/^{86}Sr_i$=0.70467–0.70565 and $^{143}Nd/^{144}Nd_i$= 0.51222–0.51233) indicate slightly radiogenic compositions, suggesting incompatibility with classical mantle plume models based on isotopic grounds.

3. Petrographic descriptions

The Indaiá I kimberlite has a matrix-supported inequigranular texture. It is termed a macrocrystal coherent kimberlite, composed of a high (30%) abundance of fine- to coarse-grained, commonly nucleus fresh olivine crystals present in four different forms, as described in detail in the next item. It has a low abundance (5%) of phlogopite phenocrysts (0.5 – 2mm), moderate proportions (13%) of anhedral to euhedral spinels (up to 1mm) and a low abundance of pyroxene crystals (4%), all supported in a groundmass dominated by carbonates, opaque minerals, pseudomorphed laths of melillite altered to carbonate and/or biotite, serpentine, mica and perovskite. Rutile, barite, apatite also is present in minor phases. The term “macrocrystal” refers to kimberlites with high amounts (~25%) of anhedral mantle-derived xenocrystals of (> 0.5mm) olivine (Cas et al., 2008). Phenocrysts can be present in when small relative to the macrocrysts (Mitchell, 2008).

Unusual incipient juvenile structures present are well described in the “juvenile clasts” topic. These are recorded by partial magmatic rims, mainly on olivine, and some spinel and phlogopite crystals or elongate to sub-round magmatic material without kernels. The low proportion (< 4%) of country rock xenoliths is dominated by partially altered granitoid, predominantly in irregular shapes and angular edges, some of the them displaying zonal alteration or alteration halos in the host rock.

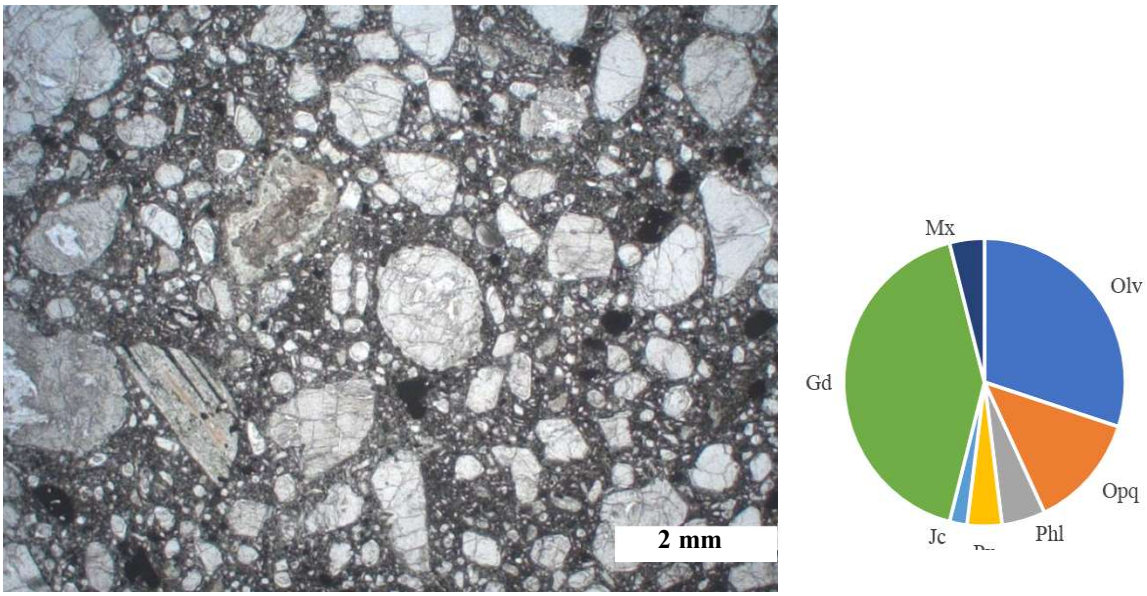

Fig.4.3. Appearance of the Indaiá I macrocrystal coherent kimberlite. Notice the abundant and uniformly distributed matrix-supported olivine, phlogopite and spinels crystals, in a fine groundmass rich mainly in opaque minerals, mica and melilite groundmass. On the right, the average modal abundances of the main constituents of the Indaiá I kimberlite: Olv - olivine (mega, macro, pheno, tablets); Opq - opaque minerals; Phl – phlogopite; Px – pyroxene; Jc – juvenile clasts; Mx – mantle xenoliths; Gd – groundmass.

3.1 Olivine

The two populations of olivine found in kimberlite had long been described as “macrocrysts” (large, sub- angular to rounded) and “phenocrysts” (smaller grains characterized by a sub- or euhedral habit), considered xenocristic and crystallized from kimberlitic melts, respectively (Clement, 1989; Mitchell, 1970, 1986; Moore, 1988; Scott-Smith, 1992). Recent studies have investigated different origins for olivine “phenocrysts” (Arndt et al., 2010, 2006, Brett et al., 2015, 2009; Bussweiler et al., 2015; Kamenetsky et al., 2008), e.g. from disaggregated mantle peridotite and dunite. These new hypotheses of reduced olivine crystallization have important implications on the estimation of primitive kimberlite melt compositions, on dynamical magma ascent and on the understanding of the abundance and distribution of diamonds in kimberlites.

Arndt et al. (2010) investigated the origin of olivines in kimberlite and proposed another form of such crystals besides macrocrystals (which was referred to as nodule) and phenocrystal, the so-called tablets. They are distinct in that 3-5 well developed crystal faces of each grain join at solid angles between 120 and 140°, whereas the remaining faces are irregular or rounded. The crystals originate from recrystallization of anhedral olivine and can be incorporated into

the kimberlite matrix during disaggregation of nodules. We prefer to adopt the term “tablet”, as defined by Arndt et al. (2010). However, we maintain the terms macrocrystal and phenocrystal (Mitchell, 1986; Scott-Smith, 1992; Mitchell, 2008) to designate mantle-derived xenocrystal and grains derived from primary liquidus phases, respectively (Fig. 4.4). The more common alterations is the presence of bowlingite edges, total replacement by serpentine, calcite and/or bowlingite can occur. Rare fully fresh olivine phenocrystals are observed (Fig. 4.5).

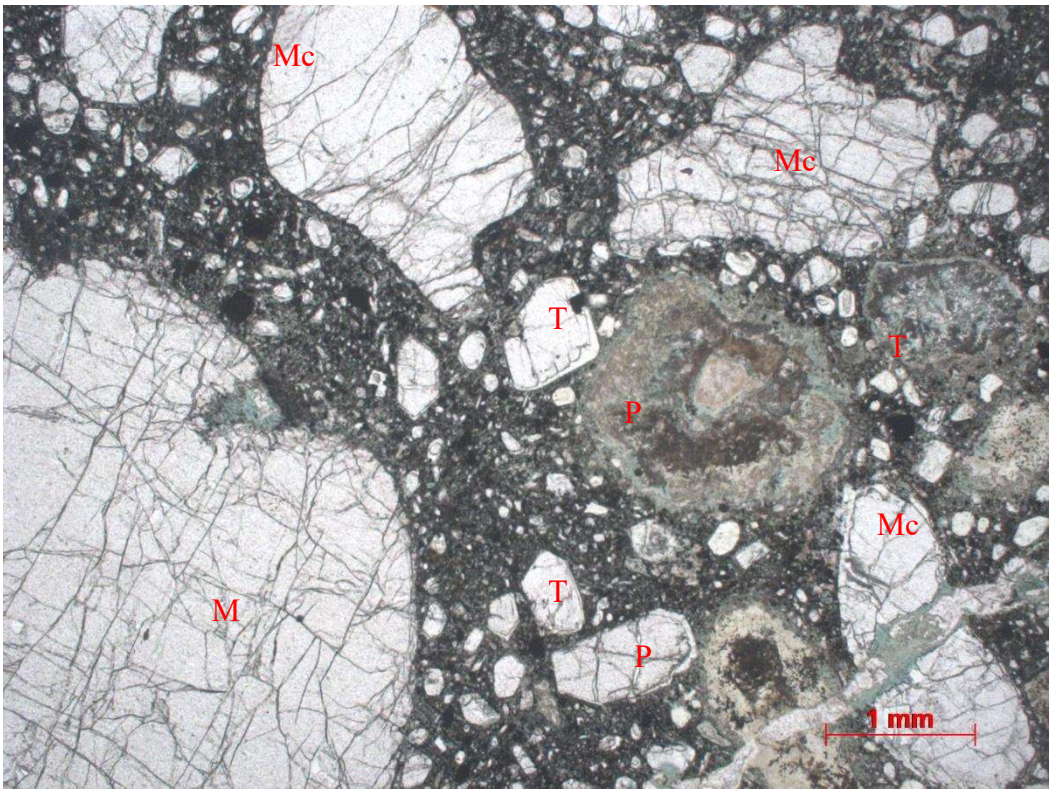

Fig.4.4. Indaiá I olivine population: Mc – macrocrystal; M – megacrystal; P – phenocrystal; T – tablet.

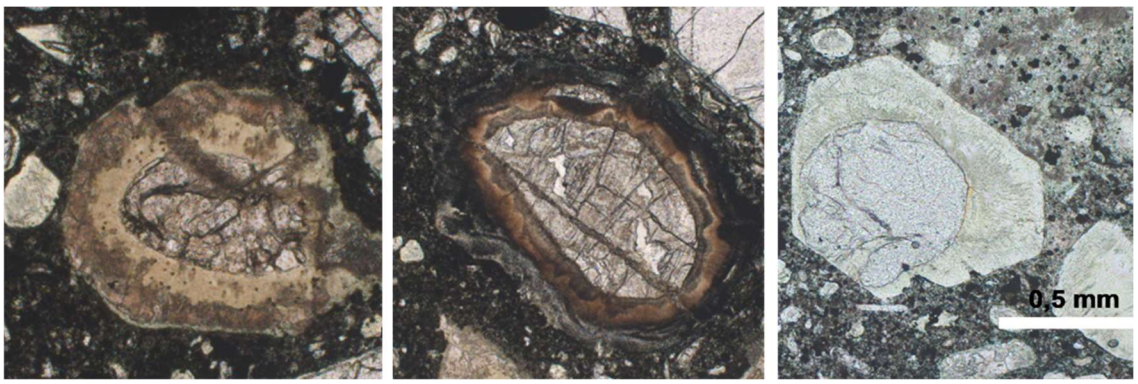

Fig.4.5. Altered olivine rims.

In the Indaiá kimberlite, olivine occurs in four populations (Fig. 4.4, 4.6 and 4.7): macro (19%) and megacrystals (1%) up to 2.5mm and 13mm in size, respectively, are always anhedral and generally fresh; phenocrystals (2%) up to 1.3 mm in size are distinguished based on their subhedral to euhedral habit and varying degrees of alteration, usually with alteration rims. Tablet crystals (5%) are partially differentiated from phenocrystals only by shape, as proposed by Arndt et al. (2010) (Fig. 4.7). Therefore, the abundance between these two forms is inferred. For a correct distinction, additional investigations on zoning and mineral chemistry should be carried out.

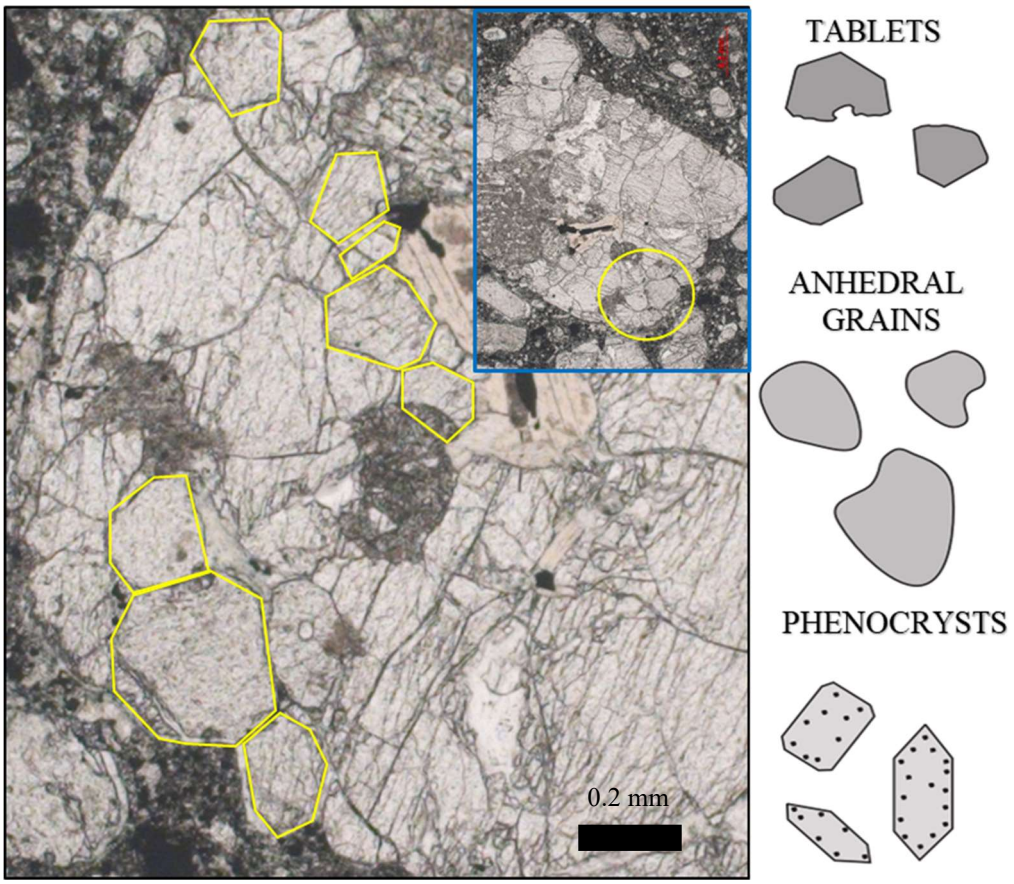

Fig.4.6. Multigranular macrocryst of olivine from the Indaiá I kimberlite. Tablets are highlighted in yellow. On the right, criteria suggested by Arndt et al. (2010) that can be used to distinguish tablets, anhedral grains and phenocrysts.

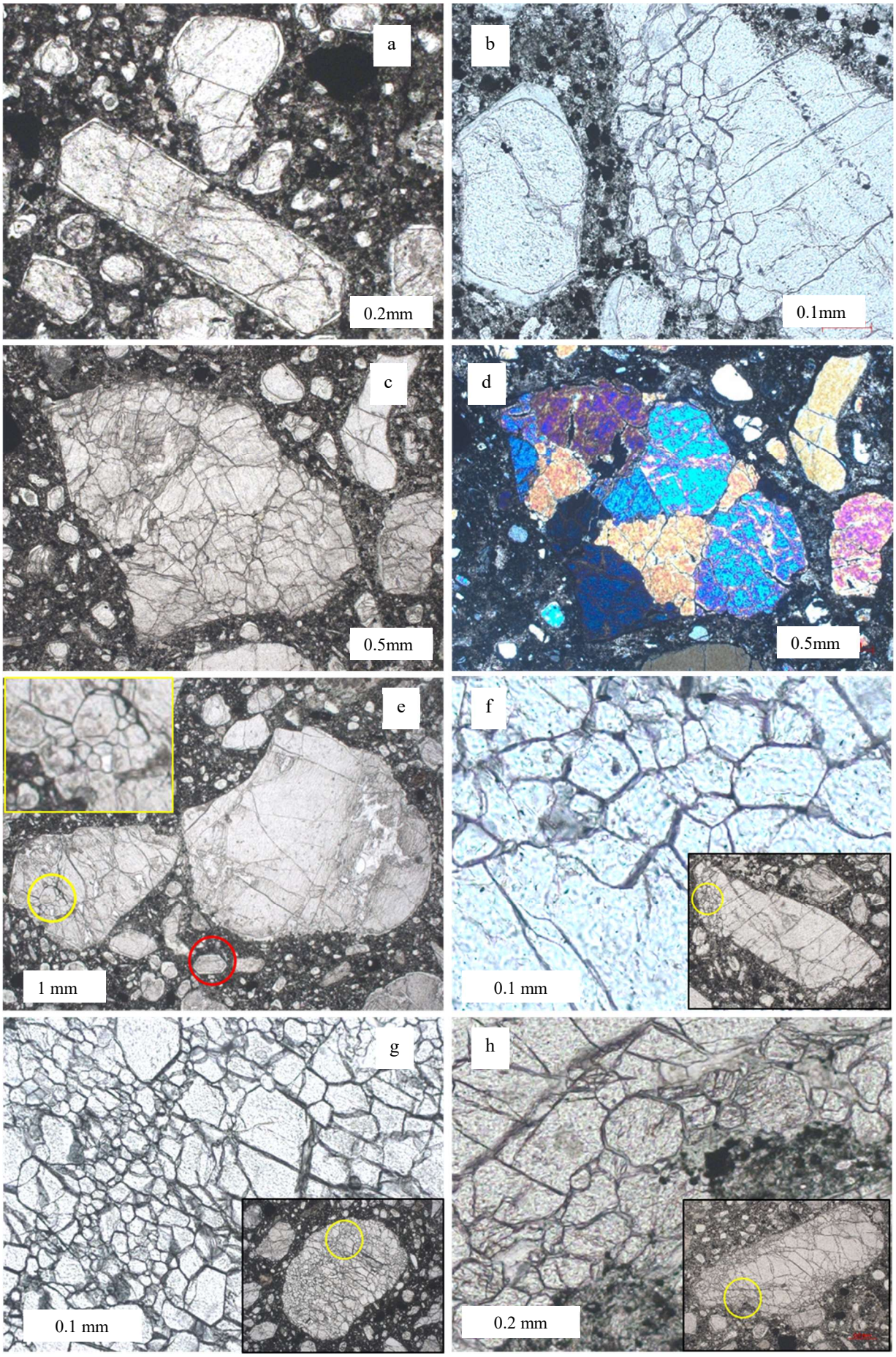
a
0.2mm
b
0.1mm
c
0.5mm
d
0.5mm
e
1 mm
f
0.1 mm
g
0.1 mm
h
0.2 mm

Fig.4.7. Populations described in the Indaiá I kimberlite. (a) Phenocrystal. (b) Probably phenocrystal and macrocrystal partially recrystallized, one of the possible origin for the tablets. (c,d) Irregular aggregate of olivine grains on parallel and crossed nicols. (e) Monogranular macrocryst (right) and in highlight a multigranular macrocryst (left). (f) Megacryst partially recrystallized. (g) Multigranular macrocryst. (h) Megacryst partially recrystallized.

3.2 Juvenile clasts

According to Cas et al. (2008), magma clasts are formed in vents during explosive eruptions, and the term "juvenile" refers to solidified material — in this case, a preserved volcanic rock clast. A non-genetic term that encompasses all juvenile clasts and discrete cognate crystals is "juvenile magmaclast", which was introduced by Field and Smith (1998).

For the discrimination of the different components of the Indaiá I kimberlite, the approach of Cas et al. (2008) was taken. For the description and characterization of juvenile clasts, the non-genetic scheme of Webb (2006) was used, as summarized in tables 4.1 and 4.2. These structures are unusual in coherent kimberlites, and are incipient.

3.2.1 Kimberlite lithic clasts

Kimberlite lithic clast refers to a co-magmatic kimberlite that solidified deeper in the vent and was then incorporated (Cas et al., 2008). Five different types of kimberlitic clasts are observed in the Indaiá I kimberlite that differ in modal abundance, shape and frequency (Fig. 4.7). Table 4.1 summarizes the characteristics of each one.

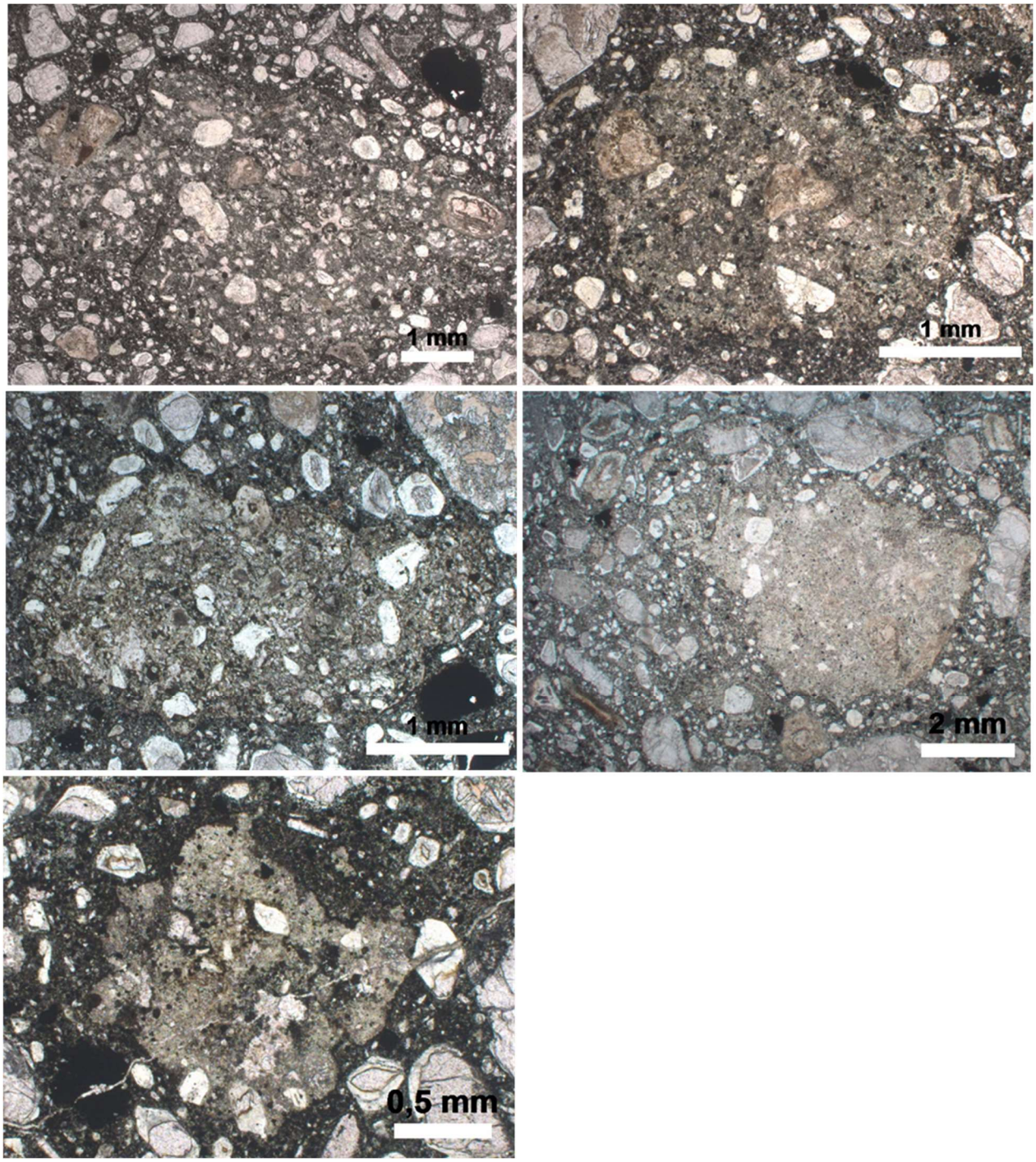

Fig. 4.8. Five types of uncored juvenile clasts (A to E) of Indaiá I kimberlite, distinguished based on relative mineral modal abundance and shapes.

Table 4.1 - Petrographic characteristics summary of uncored juvenile clasts of the Indaiá I kimberlite.

	MORPHOLOGY	VESICULARITY	CLAST-HOST RELATIONSHIP	MINERALOGY	GROUNDMASS CRYSTALLINITY	SIZE RANGE
A	El / SbA / Ic	Sparsely vesicular. Irregular shape and no fill.	Diffuse margins clast set in well-crystallized dark groundmass.	Olivine: high (20%), sub-euhedral, fine to coarse (0.23-0.98mm). Perovskie: low (8%), euhedral, micro to fine crystals (< 0.15mm).	Very poorly crystallized, spinel (13%) serpentine green groundmass.	Lapilli (2.0 - 8.14mm)
B	SbQ / SbR / SbI	Very poorly vesicular. Elongate shape partially filled vesicles by carbonates.	Diffuse margins clast set in well-crystallized dark groundmass.	Olivine: low-moderate (10%), sub-anhedral, fine to medium (0.14 - 0.44mm). Perovskite: low (8%), sub-euhedral, fine (~0.07mm).	Very poorly-crystallized, spinel (3%) serpentine green groundmass.	Lapilli (2.0 - 2.6 mm)
C	El / SbA / Ic	Sparsely vesicular.	Diffuse margins clast set in well-crystallized dark groundmass with olivine phenocrystals (graphic rims and preserved cores).	Olivine: moderate (11%), subhedral, fine to medium (0.11-0.35mm). Perovskite: low (10%), sub-euhedral, micro to fine (~0.08mm). Orthopyroxene: low (<1%), single crystal with preserved core, coarse (0.38mm).	Very poorly crystallized spinel serpentine brown groundmass.	Lapilli (2.0 - 3.4mm)
D	SbE/ SbR / Ic	Non-vesicular	Defined margins clast set in well-crystallized dark groundmass.	Olivine: moderate (10%), euhedral-anhedral and multiple intergrowth crystals, fine to very coarse (0.24 - 1.34mm).	Very poorly-crystallized, opaque perovskite serpentine brown groundmass.	Lapilli (2.0 - 6.78mm)
E	SbE/ Ang / Ic	Non-vesicular	Defined margins clast set in well-crystallized dark groundmass.	Olivine: low (8%), euhedral, fine to medium (0.10-0.25mm).	Well-crystallized, perovskite spinel greenish groundmass.	Ash (1.0 - 2.0 mm)

Sphericity: Elongate (El); Subelongate (SbE); Subequant (SbQ); Equant (Eq).
Roundness: Well-rounded (Wr); Rounded (R); Sub-rounded (SbR); Sub-angular (SbA); Angular (Ang).
Irregularity: Smoothly curved (Sc); Subirregular (SbI); Irregular curvilinear (Ic); Irregular ameboid (Ia).

Type A clasts have diffuse margins and are characterized by elongated shapes, sub-angular, irregular curvilinear outlines sparsely vesicular, with irregular shapes and no fill. They are composed of highly abundant sub- euhedral pseudo-olivine phenocrysts (20%) and minor amounts of perovskite (<8%), set in a very poorly crystallized spinel serpentine green groundmass.

The type B clasts are composed of low-moderate (10%) sub- anhedral olivine and perovskite (8%) set in a very poorly-crystallized, spinel (3%) serpentine green groundmass. Clasts have diffuse margins with subequant and sub-rounded forms, sub-irregular outlines very poorly vesicular, partially filled by carbonates.

Elongate, sub-angular, irregular curvilinear and irregular sparsely vesicular outlines characterize Type C juvenile clasts. They have diffuse margins set in a dark groundmass, with orientated euhedral olivine crystals and preserved cores, being composed of a moderate abundance (11%) of pseudo-olivine, a low abundance (10%) of perovskite and minor amounts of orthopyroxene (< 1%). Groundmass consists in a very poorly-crystallized spinel serpentine brown groundmass.

Juvenile clasts D are composed of subequant, sub-rounded, irregular curvilinear outlines, and are composed mainly by moderate, euhedral to anhedral phenocrystals and multiple intergrowths of olivine (10%) set in a very poorly-crystallized, opaque perovskite serpentine brown groundmass.

Type E clasts have defined margins, sub elongated shapes, angular or irregular curvilinear non-vesicular outlines. They are composed of pseudo-olivine (8%) set in a well-crystallized opaque perovskite serpentine brown groundmass.

Figure 4.9 shows the composition and frequency of uncored juvenile clasts in the Indaiá I kimberlite. Olivine and perovskite phenocrysts are predominant in almost all recorded clasts, except for A clasts, which opaque minerals instead of perovskite prevail.

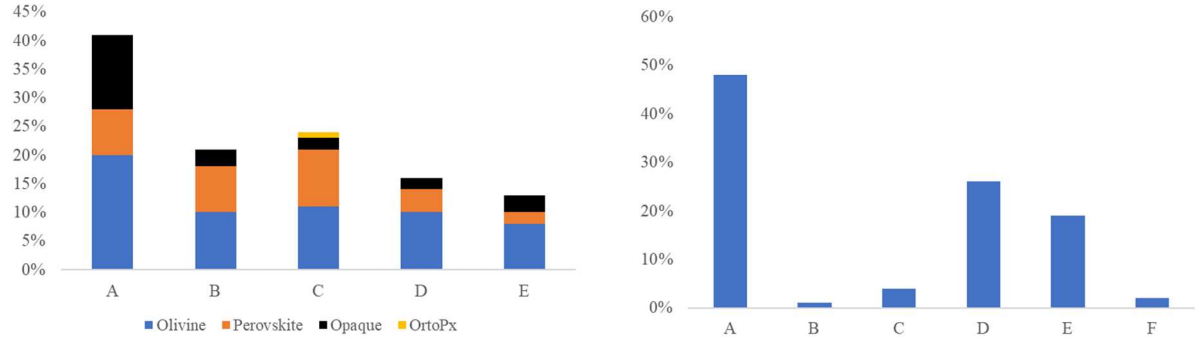

Fig. 4.9. Composition (a) and modal abundance (b) of uncored juvenile clasts. Mineral frequency within juvenile clasts is also conditioned to the alteration degree, and may not reflect the kimberlitic clasts primary composition.

3.2.2 Pelletal structures

This term encompasses all round to elliptical juvenile clasts of ash, lapilli or bomb size, composed of variably crystallized kimberlitic material with core. Crystals shells can or can not show flow orientation. When clasts or crystals have alteration rinds, they are called pseudo-pelletal lapilli (Cas et al., 2008). Pelletal or ash lapilli represent the interface between volatile components and the erupting magma (Lloyd and Stoppa, 2003).

Six types of cored juvenile pelletal ashes/lapilli prevail in the Indaiá I kimberlite (Fig. 4.9), with symmetrical and asymmetrical cores usually composed of euhedral to subhedral olivine crystals totally replaced by serpentine.

Type 1 has diffuse margins and is equant, well rounded, smoothly curved, non-vesicular and cored by altered kimberlitic clast. The single, symmetrical, complete very thin to thin micro-rim is composed of olivine, perovskite, spinel set in a well-crystallized dark groundmass.

Type 2 has subequant shapes, sub-angular and irregular curvilinear outlines, ill-defined margins and are non-vesicular. The multiple rims are symmetrical, complete, super thin micro-rim, the internal rim being composed of olivine, phlogopite and perovskite, the external corresponding to a kimberlitic material groundmass.

Pseudo-olivine cores characterize juvenile pelletal lapilli Type 3, which are typically subequant, well rounded, smoothly curved and non-vesicular. Single, symmetrical, complete, super thin micro rims, composed of oriented crystals of kimberlite groundmass, comprise them.

Type 4 clasts have ill-defined margins and are subequant, well-rounded, smoothly curved, very poorly vesicular and cored by olivine. They are characterized by single,

symmetrical, complete, very-thin micro-rims. The rims are composed of oriented crystals (olivine, phlogopite, opaque minerals) of kimberlite groundmass.

Other pelletal structures correspond to type 5, which are cored by pseudo-olivine, with diffuse margins. They are subequant, rounded, sub-irregular, and non-vesicular. The multiple, symmetrical, complete, super-thin micro rims mimic the shape of the core. The internal rim consists mainly of oriented olivine. The external rim consists of oriented olivine and phlogopite.

Type 6 clasts have ill-defined margins, sub-elongated shapes, well-rounded and smoothly curved outlines, are non-vesicular, cored by phlogopite, and consist of olivine and phlogopite.

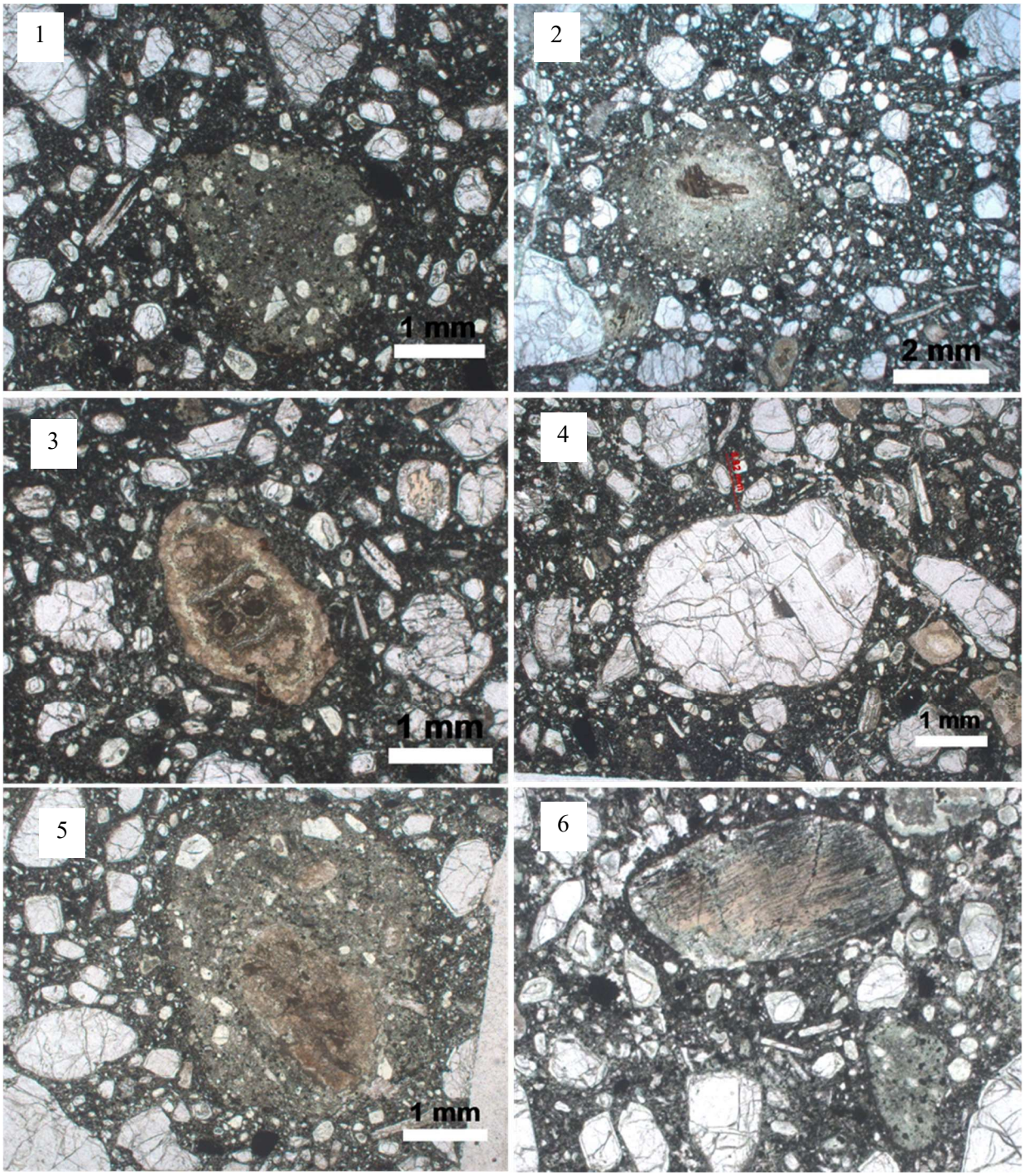

Fig. 4.10. Six types of cored juvenile clasts of the Indaiá I kimberlite. The shape of the pelletals follows the shape of the nucleus. Olivine pseudomorphs are the main constituent of the cores; phlogopite crystals are also very common, but less frequent. These clasts are incipient, margins are diffuse and external rims comprehend the kimberlite groundmass.

Table 4.2 Petrographic characteristics summary of cored juvenile clasts of the Indaiá I kimberlite.

	MORPHOLOGY	INTERNAL STRUCTURE		VESICULARITY	CLAST-HOST RELATIONSHIP	MINERALOGY	GROUNDMASS CRYSTALLINITY	SIZE RANGE
		Type of core	Rims					
1	Eq / Wr / Sc	core: kimberlitic clast	Single, symetrical, complete, very thin to thin micro rim.	Non-vesicular.	Diffuse to defined margins clast set in a well-crystallized dark groundmass.	Core: olivine (5%, sub-anhedral, micro - fine < 0.14mm), perovskite (2%, euhedral, microlites < 0.08mm), spinel (1%, euhedral, microlites). Rim: olivine (12%, sub-euhedral, fine - coarse 0.11 - 0.52mm) , phlogopite (< 2%, euhedral, fine - coarse 0.08 - 0.89 mm), perovskite (5%, euhedral, fine < 0.16 mm), opaque (5%, subhedral, fine < 0.17mm).	Core: very poorly-crystallized serpentine groudmass. Rim: well-crystallized dark groundmass (kimberlitic material).	Cored pelletal lapilli (2.0 - 3.5 mm)
2	SbE / SbA / Ic	core: pseudo-olivine	Multiple rims, symetrical, complete, super thin micro-rims.	Non-vesicular.	Ill-defined margins clast set in a well-crystallized dark groundmass.	Internal rim: olivine (9%) , phlogopite (<1%), perovskite (6%), opaque (10%). External rim: kimberlitic material groundmass.	Internal rim: poorly-crystallized serpentine groudmass. External rim: well-crystallized dark groundmass (kimberlitic	Cored pelletal lapilli (2.0 - 3.19 mm)
3	SbE / Wr / Sc	core: pseudo-olivine	Single, symetrical, complete, super thin micro-rim.	Non-vesicular.	Ill-defined margins clast set in a well-crystallized dark groundmass.	Rim - oriented crystals of kimberlitic material groundmass.	Rim: well-crystallized dark groundmass.	Cored juvenile pelletal lapilli (2.0 - 3.0mm)
4	SbQ / Wr / Sc	core: Olivine	Single, symetrical, complete, very thin micro-rim.	Very poorly vesicular; partially filled.	Ill-defined margins clast set in a well-crystallized dark groundmass.	Rim - oriented crystals (olivine, phlogopite, opaque minerals) of kimberlitic material groundmass.	Rim: well-crystallized dark groundmass.	Cored juvenile pelletal lapilli (2.0 - 3.0mm)
5	SbQ / R / SbI	core: pseudo-olivine	Multiple rims, asymetrical, complete, super thin micro-rims.	Non-vesicular.	Diffuse margins clast set in a well-crystallized dark groundmass.	Internal rim - oriented olivine (13%, sub-anhedral, fine-coarse). External rim: oriented olivine (18%, subhedral, fine-coarse), phlogopite (4%, subhedral, micro to coarse).	Internal rim: poorly-crystallized perovskite spinel serpentinized groundmass. External tim: well-crystallized opaque minerals perovskite dark groundmass.	Cored juvenile pelletal lapilli (~ 3.0mm)
6	SbE / Wr / Sc	core: phlogopite	Single, symetrical, complete, very thin micro-rim.	Non-vesicular.	Ill-defined margins clast set in a well-crystallized dark groundmass.	Rim - olivine (10%, euhedral, fine-coarse crystals with alteration rims);, phlogopite (3%, euhedral, fine crystals).	Rim: well-crystallized opaque perovskite serpentine dark groundmass.	Cored juvenile pelletal lapilli (2.0 - 4.0mm)

Sphericity: Elongate (El); Subelongate (SbE); Subequant (SbQ); Equant (Eq).

Roundness: Well-rounded (Wr); Rounded (R); Sub-rounded (SbR); Sub-angular (SbA); Angular (Ang).

Irregularity: Smoothly curved (Sc); Subirregular (SbI); Irregular curvilinear (Ic); Irregular ameboid (Ia).

4. Mineral Chemistry

4.1 Olivine

The anhedral and euhedral crystals of olivine from the Indaiá kimberlite studied here are up to 1.86 mm wide, with a highly variable content in Fo (80.51 to 92.77 mol%) and Mg# (93 – 81). Their compositional ranges of NiO (0.02 to 0.46 wt%), CaO (0 to 0.97 wt%), MnO (0.08 to 0.36 wt%), and Cr_2O_3 (0 to 0.44 wt%) are presented in Table 10. No obvious correlation was observed between composition and morphology or grain size.

Despite the difficulty in distinguishing phenocrysts from tablets in the graphic Fo vs NiO, the major olivine grains analysed fall within the xenolithic field, represented by cores/rims and tablets from nodule studies by Arndt et al. 2010. Even euhedral grains can not be considered phenocrysts. In Fig.4.11, they are represented by squares, being tablet or phenocrysts.

CaO, MnO and, in some cases, Cr_2O_3 contents are relatively low in cores and somewhat higher on rims. Compared with the composition range from a mafic - ultramafic suite of rocks studied by Sobolev et al. (2007) and nodules studied by Arndt et al. 2010, Indaiá I olivine shows high CaO, MnO and Cr_2O_3 contents, falling mainly within the mafic and ultramafic field (Fig. 4.12).

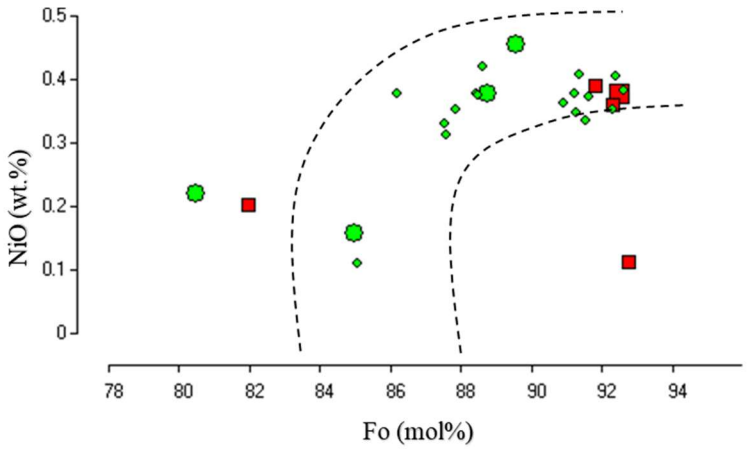

Fig.4.11. Fo vs NiO showing large variation in composition. The delimited area is the field with major concentration of cores / rims and tablets from nodules studied by Arndt et al. 2010. Green, anhedral grains; red squares, euhedral grains; small symbols, <0.5mm crystals; large symbols, >1 mm crystals.

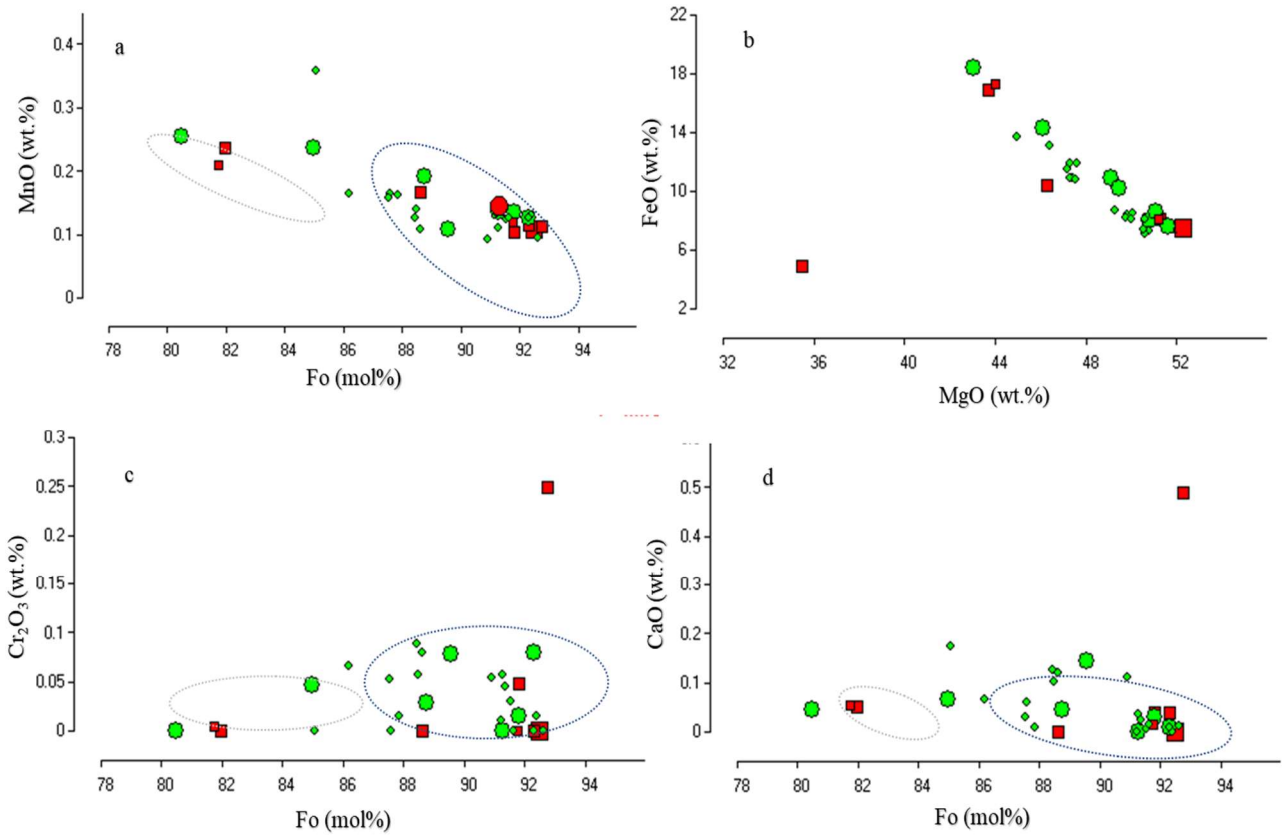

Fig.4.12. Fo *vs* MnO, Cr_2O_3 and CaO, and MgO *vs* FeO for olivine types from the Indaiá kimberlite. Blue and grey fields correspond to major concentration olivine areas of mafic / ultramafic rocks from South Africa (groups I and II, Sobolev et al., 2007) and from Kangamiut (Greenland) (Arndt et al. 2010). Symbols: blue line – higher concentration of olivines from South Africa Group I and II kimberlite. Grey line: olivine data from Kangamiut kimberlite.

As illustrated in the incompatible trace element spidergram (primitive mantle-normalized of Fig. 4.13), the various types of small to large anhedral and euhedral olivine grains show subparallel trends and highly variable patterns, except for Pb, that shows a pronounced positive spike, and Sr, that shows a negative spike. Lanthanide content is low or barely detectable (Table 10). The chondrite-normalized REE pattern (Boynton, 1984) for olivine shows low LREE and MREE. According to Melluso et al. (2008), olivine lanthanide content generally falls below 0.1 times chondrite enriched. In the Indaiá kimberlite, olivine displays, on average, only a very slight enrichment in HREE over LREE. However, one grain displays the opposite pattern, with enrichment of LREE over HREE.

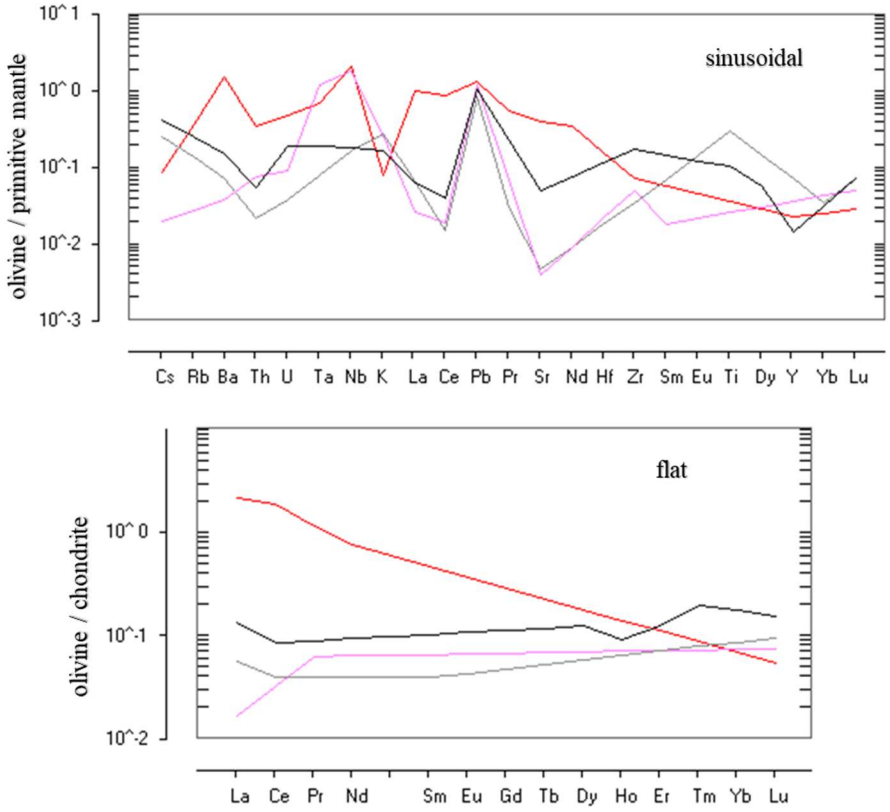

Fig.4.13. A) Primitive mantle-normalized (McDonough and Sun, 1995) incompatible element pattern of olivine from the Indaiá kimberlite; (B) Chondrite-normalised REE patterns (Boynton, 1984) of olivine from the Indaiá kimberlite.

4.2 Ilmenite

Two varieties of ilmenite from the Indaiá kimberlite were studied: groundmass (0.15 to 0.40 mm) and macrocryst (0.57 to 3.40 mm), both rich in Mg (10.01 to 12.10 wt% and 6.98 to 9.48wt%, respectively). The distinction between groundmass and macrocryst ilmenite was initially based on size only (Mitchell, 1995).

Groundmass ilmenite cores exhibit typically high FeO_t and TiO_2 contents (32.57 to 39.11 wt% and 50.12 to 52.19 wt%, respectively), significant contents of Cr_2O_3 (1.42 to 3.97 wt%), V_2O_3 (0.18 to 0.51 wt%), NiO (0.11 to 0.20 wt%), and minor contents of Al_2O_3 (< 0.08 wt%) and MnO (< 0.66wt%) (Table 9). The compositional variation is subtle. However, on average, there is a decrease in Cr_2O_3, FeO_2 and Fe_2O_3 from core to rim.

Macrocryst ilmenite cores are characterized by high FeO_t and TiO_2 (40.45 to 47.02 wt% and 46.01 to 49.25 wt%, respectively), Cr_2O_3 (0.15 to 2.94 wt%), V_2O_3 (0.43 to 0.51 wt%) and NiO (0.1 to 0.13 wt%) contents and by minor contents of Al_2O_3 (< 0.18 wt%) and MnO (<

0.43wt%). Rim and core compositions are practically the same, with a variation of up to ~1 wt%, which indicates homogeneity throughout the crystals.

The MgO versus TiO_2 diagram in Fig. 4.14 shows a parabolic arc typical of many kimberlitic ilmenite populations for differentiation between kimberlitic and non-kimberlitic ones (Haggerty, 1975,1976; Wyatt et al., 2004). Reference lines of constant hematite content are inserted to the scatter plots. Indaiá I ilmenite falls within the kimberlitic field, confirming the origin of the analyzed grains.

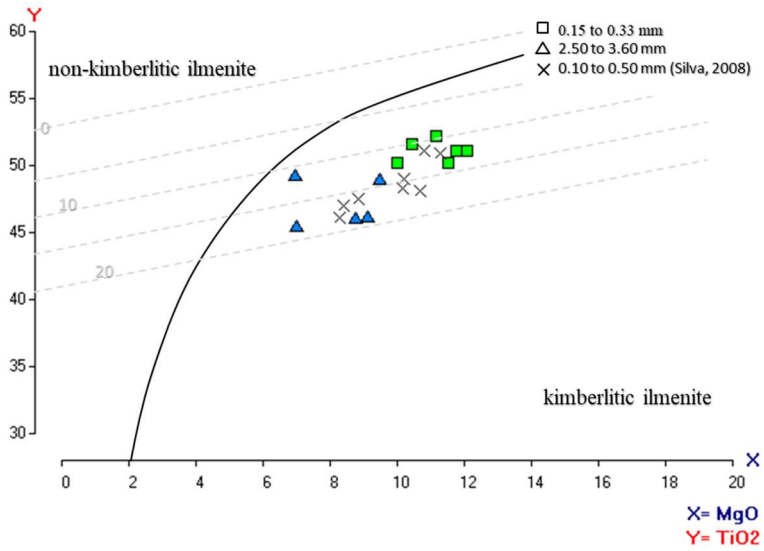

Fig.4.14. Plot of MgO *versus* TiO_2 for Indaiá I ilmenite. Dashed light-grey lines are percent Fe_2O_3 markers. Black line represents the bounding reference of the kimberlitic ilmenite field after Haggerty (1975, 1976) and Wyatt et al. (2004). Blue triangle, 2.50 to 3.60mm macrocrystals; green squares, groundmass 0.15 to 0.33mm ilmenite; cross, Indaiá I phenocrystals from Silva, 2008).

Trace Element Chemistry

In groundmass ilmenite, Sc ranges from 37.82 to 77.08 ppm, Co from 0.59 to 189.23, Zr from 613.89 to 2444.20, Sn from 24.29 to 40.97 ppm, Ba from 7.33 to 51.14 ppm, Hf from 19.56 to 25.50 ppm and Ta from 134.28 to 260.25 ppm. The macrocryst variety shows significative amounts of Sc (26.87 to 53.46 ppm) and Zr (1142.69 to 3882.58 ppm), Sn ranging from 19.96 to 46.10 ppm, Hf from 13.23 to 19.58 ppm and Ta from 137.96 to 367.09 ppm (Table. 9).

NiO, V_2O_3 and Hf contents correlate positively with MgO, while Zr exhibit a negative correlation (Fig.4.15). It can be noticed that the macrocryst variety contains lower amounts of Mg, Ni and Hf and higher amounts of Zr and V compared with groundmass ilmenite.

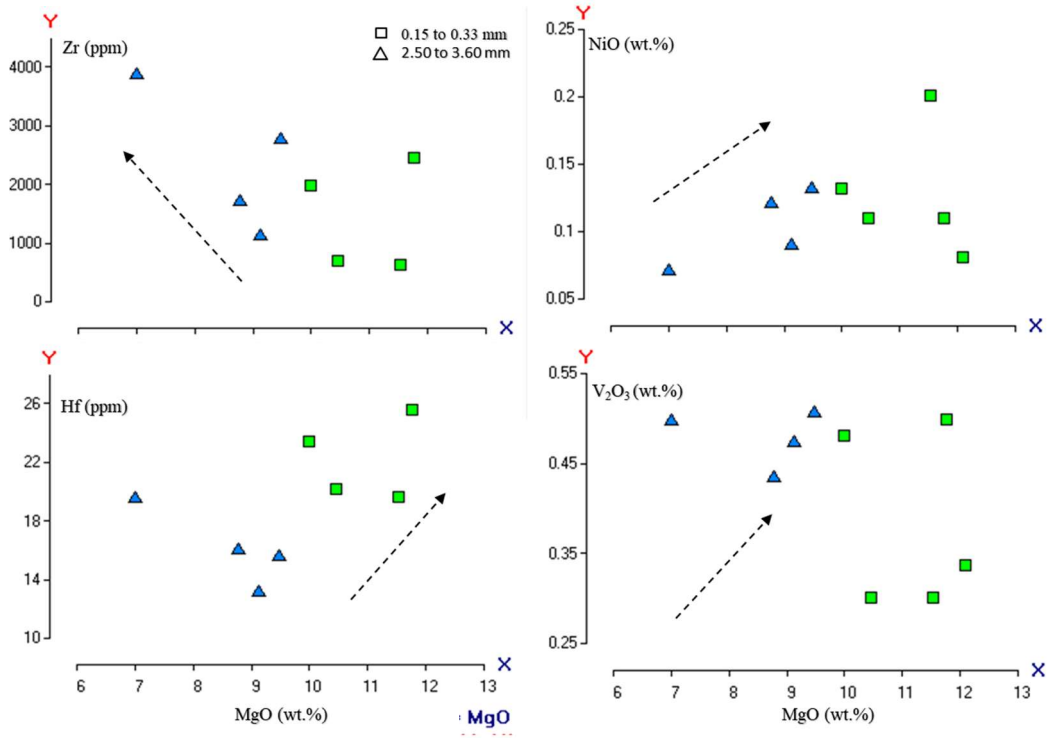

Fig.4.15. MgO *vs* Zr , Hf, NiO and V_2O_3 for macroryst and groundmass ilmenite from the Indaiá I kimberlite. Arrows indicate negative and positive correlation between these elements.

Abundances of incompatible elements normalized to primitive mantle (McDonough and Sun, 1995) are shown in Fig 4.16. In general, both populations display similar patterns, characterized by Ta, Hf, Zr and Y strong positive spikes. Only groundmass ilmenite exhibits a positive Nb slope. Th, La, Ce, Sr, Eu and Y show weaker negative spikes than macrocrystals (Fig. 4.16 B).

As illustrated in the chondrite-normalized REE diagram in Fig 4.16 A both populations are characterized by a flat pattern, most $MREE_N$ falling below detection. However, homogeneity can be noticed between light and heavy elements, and there is slight enrichment and depletion in $LREE_N$ and $HREE_N$, respectively. Only one grain exhibits a higher slope pattern, with a strong Gd peak possibly caused by mineral inclusion. Minor sized ilmenite

grains/crystals present incompatible trace elements and REE values slightly higher than those of larger grains.

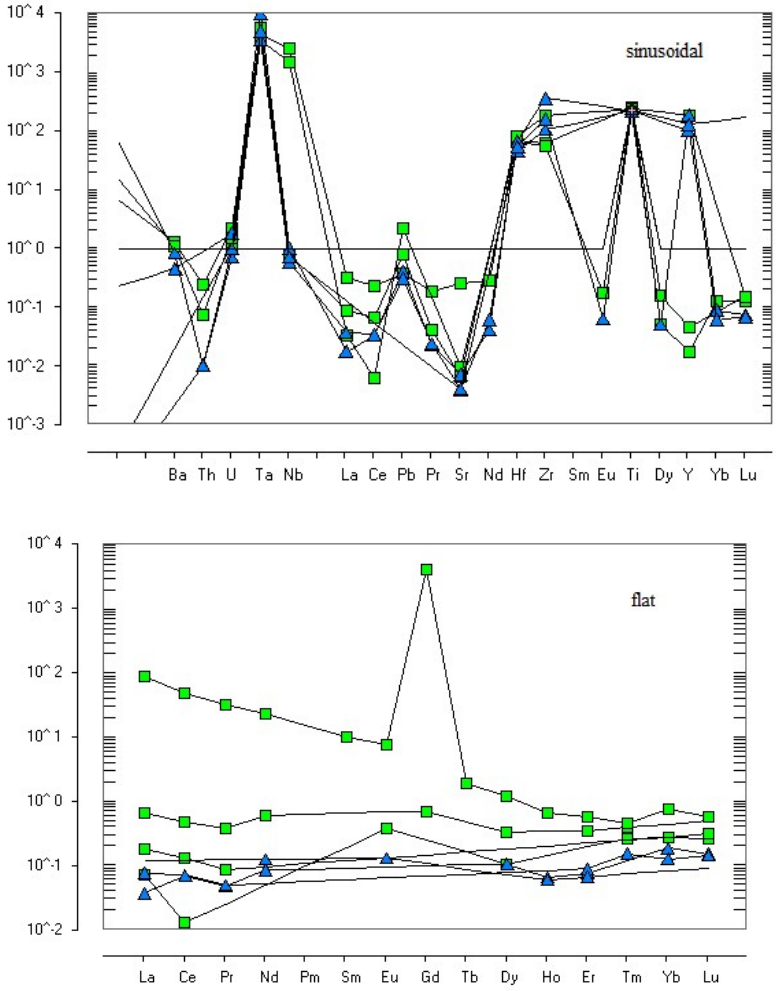

Fig.4.16. A) Primitive mantle-normalized (McDonough and Sun, 1995) incompatible element patterns of ilmenite from the Indaiá kimberlite; (B) Chondrite-normalised REE patterns (Boynton, 1984) of ilmenite from the Indaiá kimberlite. Symbols as in Fig 4.14 ($MgOxTiO_2$).

4.3 Perovskite

The Indaiá I perovskite varieties studied belong to the groundmass of minerals and occur as either anhedral or euhedral grains scattered in the fine-grained matrix of the kimberlite. Strong zoning is a very common feature in euhedral perovskite. Compositional variations are more accentuated than in anhedral grains, which exhibit subtle or none zoning patterns in back-scattered electron (BSE) images (Table 14).

In the Indaiá I kimberlite, perovskite can be interpreted as a primary phase that crystallized directly from the magma. The mineral is not abundant and can be classified in the

following types based on crystal perfection and zoning patterns (texture) in Castillo-Oliver et al. (2016) parameters and terminology:

Type Ia perovskite

Type Ia crystals are anhedral, up to 0.20 mm in size. They occur usually scattered in the groundmass or forming "necklaces" around earlier-formed macrocrysts or phenocrysts of olivine as serpentine pseudomorphs. This perovskite texture is described in many Canadian and South African kimberlites (e.g. Castillo-Oliver et al., 2016; Chakhmouradian and Mitchell, 2000; Donnelly et al., 2012). Zoning is usually less pronounced than type in Ib in back-scattered electron (BSE) images, with bright cores and dark rims.

Type Ia.a perovskite

Type Ia.a perovskite corresponds to anhedral grains that, unlike Ia ones, neither show any zoning pattern in MeV images nor have any correspondent form in Castillo-Oliver et al. (2016) work. They are smaller (up to 0.10 mm) than other perovskite types and are recovered as single grains in heavy mineral concentrates. They are usually more homogeneous in BSE images, yet chemical analyses reveal subtle zoning.

Type Ib perovskite

This type of perovskite occurs as discrete, single euhedral up to 0.12 mm crystals scattered in groundmass exhibiting a very strong zoning pattern in BSE images, with darker cores and bright rims.

Based on major-element composition, these perovskite types can be divided in two groups according to Castillo-Oliver et al. (2016), Chakhmouradian, and Mitchell (2001). In perovskite, zoning patterns reflect compositional variation within the crystal. Chakhmouradian and Mitchell (2000) defined such patterns as normal (decrease in LREE and Th, with varying Na and Nb contents), reverse (enrichment in LREE and Th towards the rim, Fe and Nb content increase and constant or slightly decreasing LREE values) and oscillatory (significant variations in Nb, Na, Ce, Fe and Nd within a single grain).

Owing to the large variation in chemical composition, a "universal classification pattern" for perovskite forms would hardly be achieved. In Indaiá I, perovskite forms do not exactly follow the classification proposed by (Castillo-Oliver et al., 2016; Chakhmouradian and

Mitchell, 2000). Additional LREE analyzes in the rims are necessary. However, zoning patterns could be based in the work of these authors and are described below.

Group 1

Types Ia and Ia.a perovskite from Indaiá I are in good agreement with those found in perovskite I as defined by Chakhmouradian and Mitchell (2001) in Canadian kimberlites, but they can not be equated to the perovskite group 1 of Castillo-Oliver et al. (2016) (Fig. 4.17). They are characterized by significant amounts of Ce_2O_3 (1.66 to 3.86 wt%) and La_2O_3 (0.79 to 1.28 wt%) and low amounts of Nb_2O_5, Na_2O and ThO_2 (0.20 to 0.60 wt%, 0.21 to 0.45 wt%, 0 to 0.58 wt%, respectively). Regarding major-element, the main characteristic that separates Ia and Ia_b perovskite in Indaiá I is the compositional variation. Ia perovskite presents a normal pattern, characterized by increased Nb and Na, La, Th and decreased Ce from core to rim, while Ia_b perovskite displays the opposite: decreased Nb and Na, La, Th and increased Ce from core to rim, characterized by a reverse pattern.

Group 2

Type Ib perovskite I content in Indaiá is also high compared to most Group I grains as defined by Castillo-Oliver et al. (2016) in South African kimberlites and to perovskite II as defined by Chakhmouradian and Mitchell (2001) in Lac de Gras kimberlites. In Indaiá I, Type Ib perovskite is characterized by a high content of Ce_2O_3 (3.95 to 6.11 wt%), significative contents of Nb_2O_5, La_2O_3 and Na_2O (1.22 to 1.87 wt%, 1.45 to 2.0 wt% and 0.71 to 1.04 wt%, respectively) and low amounts ThO_2 (up to 1.0 wt%). All these elements increase in content from core to rim, with exception of Th, whose varying content shows as an oscillatory pattern.

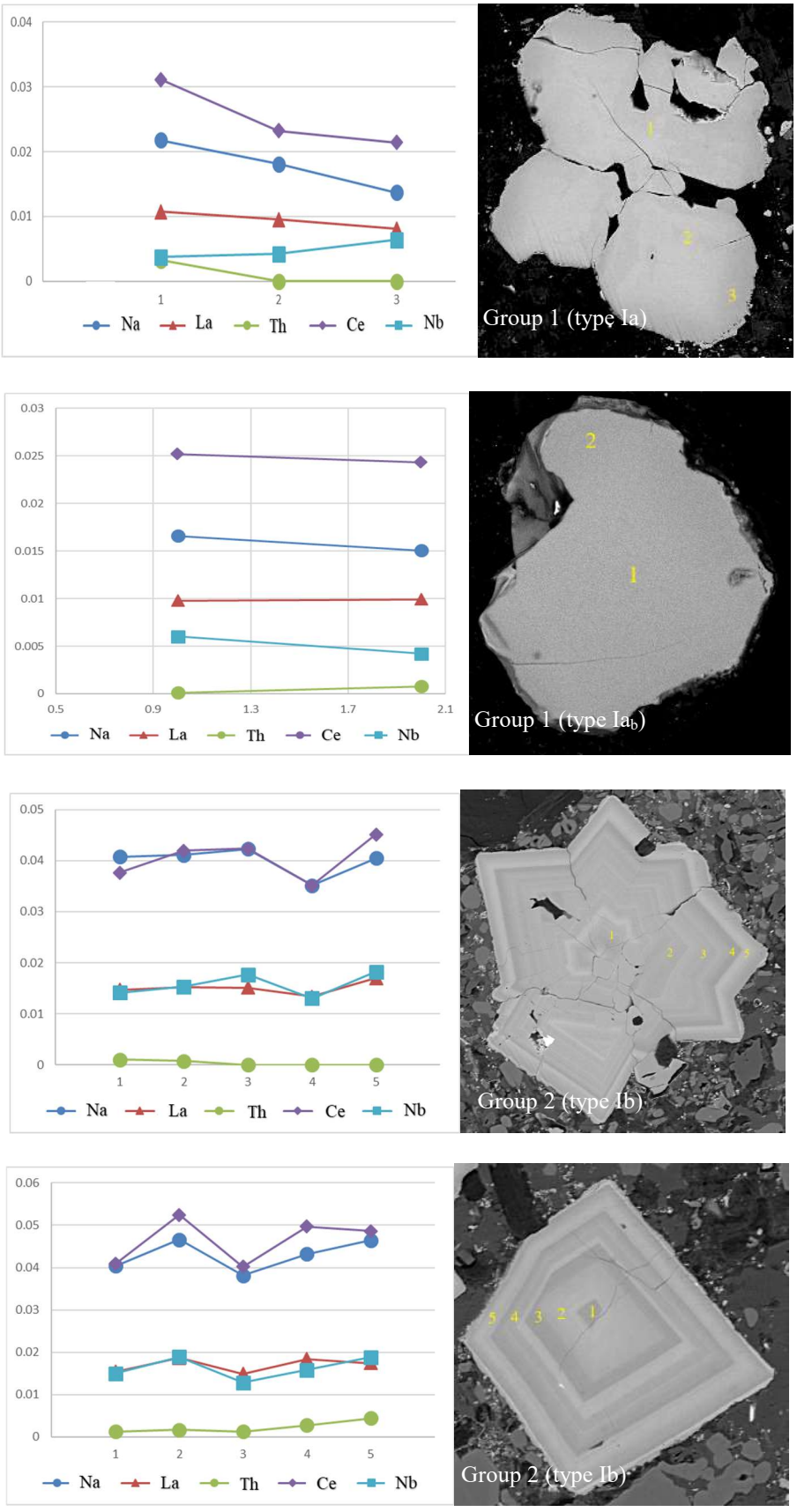

Fig.4.17. Back-scattered electron (BSE) images of perovskite from the Indaiá I kimberlite showing different textural types and compositions. (a) Type Ia is anhedral and occurs scattered in the groundmass or rimmed olivine pseudomorphs, exhibiting subtle normal zoning pattern with bright core and dark rim. (b) Type Ia.a is anhedral and is recovered in heavy

mineral concentrates. They exhibit homogeneity, displaying, however, a subtle Na, La, Ce and Nb increase from core to rim, characteristic of reverse pattern. (c,d) Type Ib crystals are euhedral, with very strong pattern and complex oscillatory zoning patterns. In general, brighter areas are given by higher concentrations of all elements.

Compared with perovskite from the Lunda Norte province (Castillo-Oliver et al., 2016) the perovskite from Indaiá I follows the same trend, but with lower Nb, Na, Th, La and Ce values. Negative correlations of Na, Nb and Fe against Ca are observed (Fig 4.18. a–d), while Na and Nb correlate positively in all analysed grains (Fig 4.18 b). It can be noticed that euhedral crystals (Ib) always exhibit higher values than anhedral crystals (Ia, Ia_b), which display similar trends in the diagram. The chemical values from Indaiá I fall within Lunda Norte kimberlitic province fields (Fig 4.18 a-d) and follow the Alto Paranaiba perovskite trend (Fig. 4.18 e). On average, types Ia and Ia.a from Indaiá I are characterized by Ce and La amounts higher than 1% and by low amounts of Nb, Na and Th.

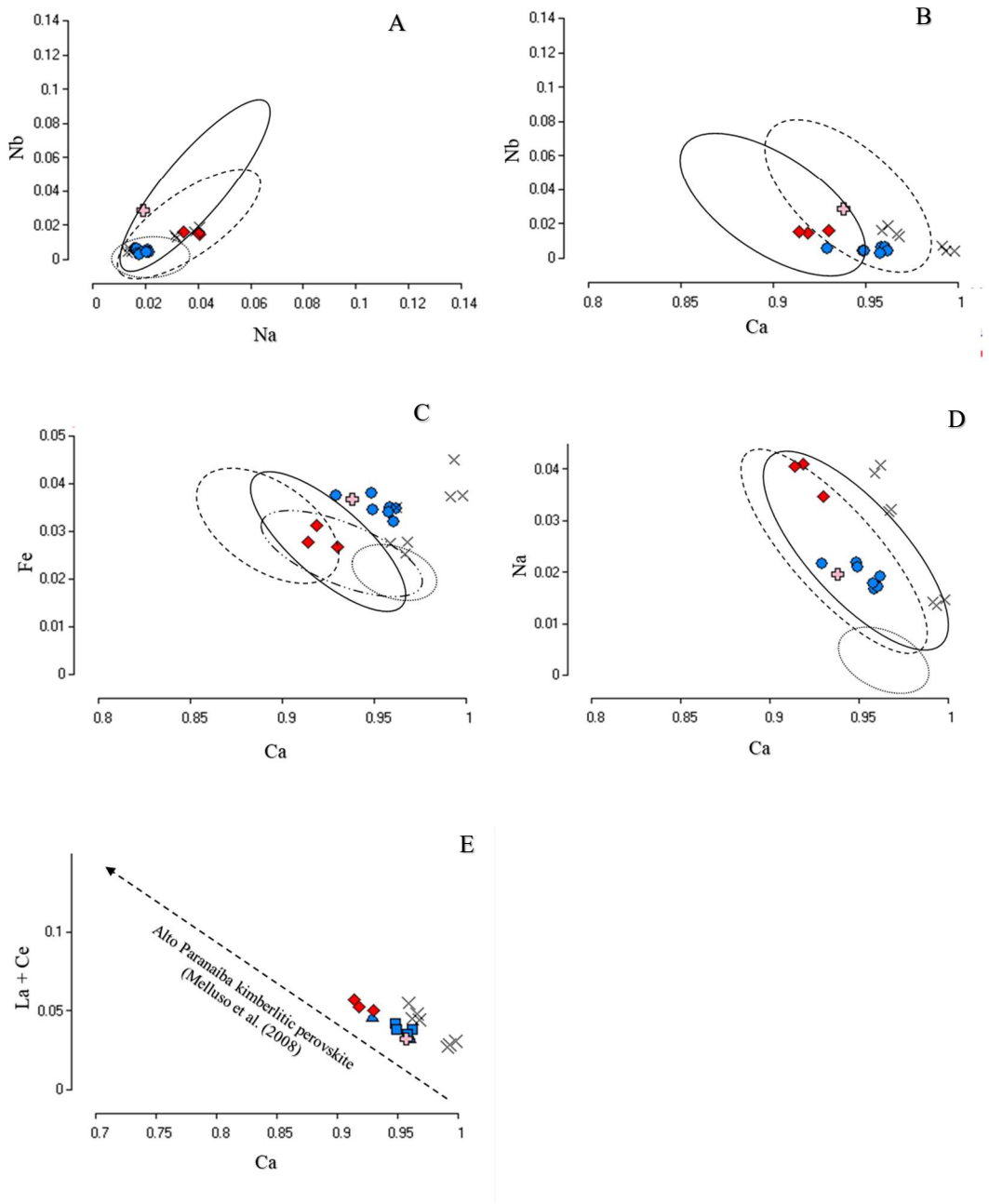

Fig.4.18. Binary diagrams representing the perovskite major-element chemistry of Indaiá I, in atoms per formula unit (apfu). Ca is represented against Nb (a), Na (c), Fe (d), La+Ce (e) and Na against Nb (b). Red lozenge, euhedral perovskite with zoning patterns (Type Ib); blue circle, anhedral perovskite (Type Ia); black cross, groundmass perovskite from Silva (2008); pink cross, perovskite grain from Melluso et al. (2008); dashed lines, perovskite Type Ia field from Calonda, Lucapa II and Mulepe I kimberlites; full line, Type Ib field perovskite from the Mulepe II kimberlite. The Na–Nb (b) diagram shows positive correlation and significantly higher Na and Nb contents in Subtype Ib perovskite. Conversely, negative correlation is found between Ca and Nb, Na, REE and Fe.

Trace Elements

In the Indaiá I kimberlite, perovskite types show varying trace element values of Zr (594.26 ppm), V (85.22 ppm), Ba (31.95 ppm), U (62.76 ppm), Y (239.78 ppm) and Ta (460.38) and, as illustrated in the primitive mantle-normalized incompatible element spidergram (McDonough and Sun, 1995) of Fig 4.19 show strong Ba, K, Pb, Sr and Zr negative anomalies. These features are in accordance with patterns exhibited by kimberlite perovskite types worldwide, such as Chicken Park, Iron Mountain, Udachnaya and Grizzly kimberlites from Chakhmouradian et al. (2013) and by Indaiá I data from Melluso et al. (2008).

The REE diagram (C1 chondrite-normalized, Boyton, 1984) of Fig 4.19B exhibits a humped pattern, reflecting enrichment in $LREE_N$ with respect to the $MREE_N$ and $HREE_N$ (La_N: 9785.83 vs Lu_N:0.74). while perovskite REE patterns from Indaiá I display a quite similar trend, approaching that of perovskite from the Kuruman kimberlite of South Africa (Donnelly et al., 2011).

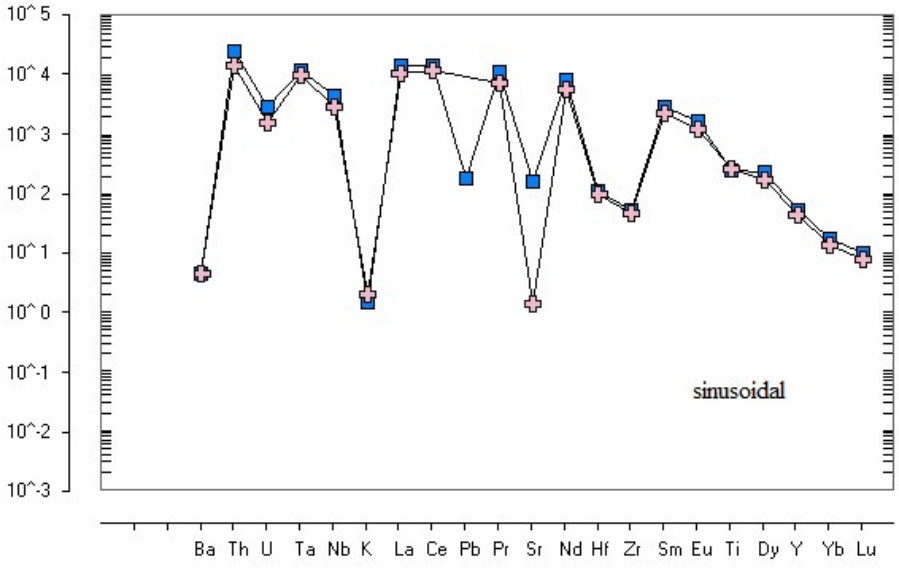

(A)

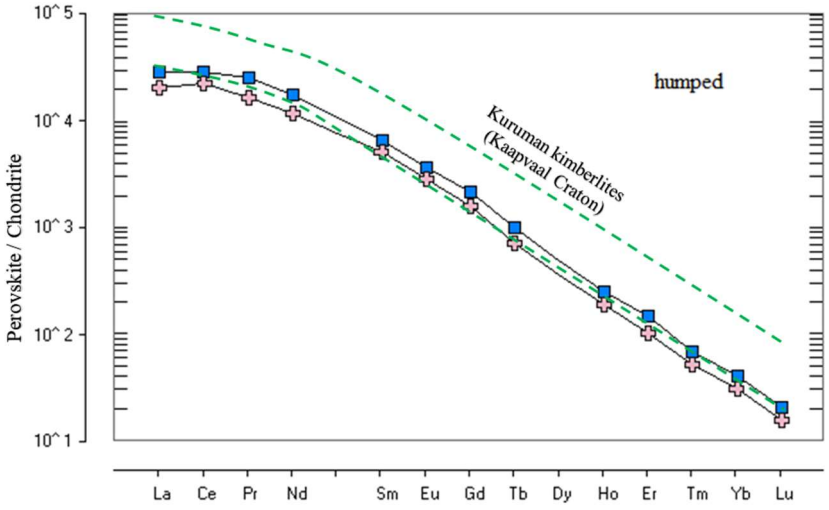

(B)

Fig.4.19. A) Primitive mantle-normalized (McDonough and Sun, 1995) incompatible element pattern of perovskite from the Indaiá kimberlite; (B) Chondrite-normalised REE patterns (Boynton, 1984) of perovskite from the Indaiá kimberlite. Blue squares, our data; Pink crosses, Melluso et al. (2008); Blue area, averaged REE_N concentrations of perovskites from the Kuruman kimberlite province, South Africa (Donnelly et al., 2012).

4.4 Pyroxene

The microcrystals analysed are anhedral grains with up to 0.2 mm in diameter and correspond mainly to augite and diopside end-member (table 21). The clinopyroxene minerals are variable in Cr_2O_3 contents (0 to 2.86 wt%), low TiO_2 (0.05 to 0.38 wt%) and have Mg# values ranging from 0.89 to 0.97. They present significative amounts of Al_2O_3 (0.0 to 3.7 wt%) and Na_2O (0.01 to 1.42 wt%). The amounts of Cr# (0.0 to 0.93) and Ca# (0.0 to 0.50) are variable (Fig.4.19).

Based mainly in a major mineral chemistry, the pyroxenes from Indaiá I can be divided in low-Cr (< 0.5 wt%) and high-Cr (>0.5 wt%), the high Cr content are associated with higher Na_2O content. They have great similarity with clinopyroxenes from phlogopite peridotite xenoliths and Cr-spinel harzburgites from Indaiá I studied by Nannini (2016) (Fig. 4.20e). The Cr and Ti amounts versus Mg# values are in agree with worldwide kimberlites (Pivin et al., 2009).

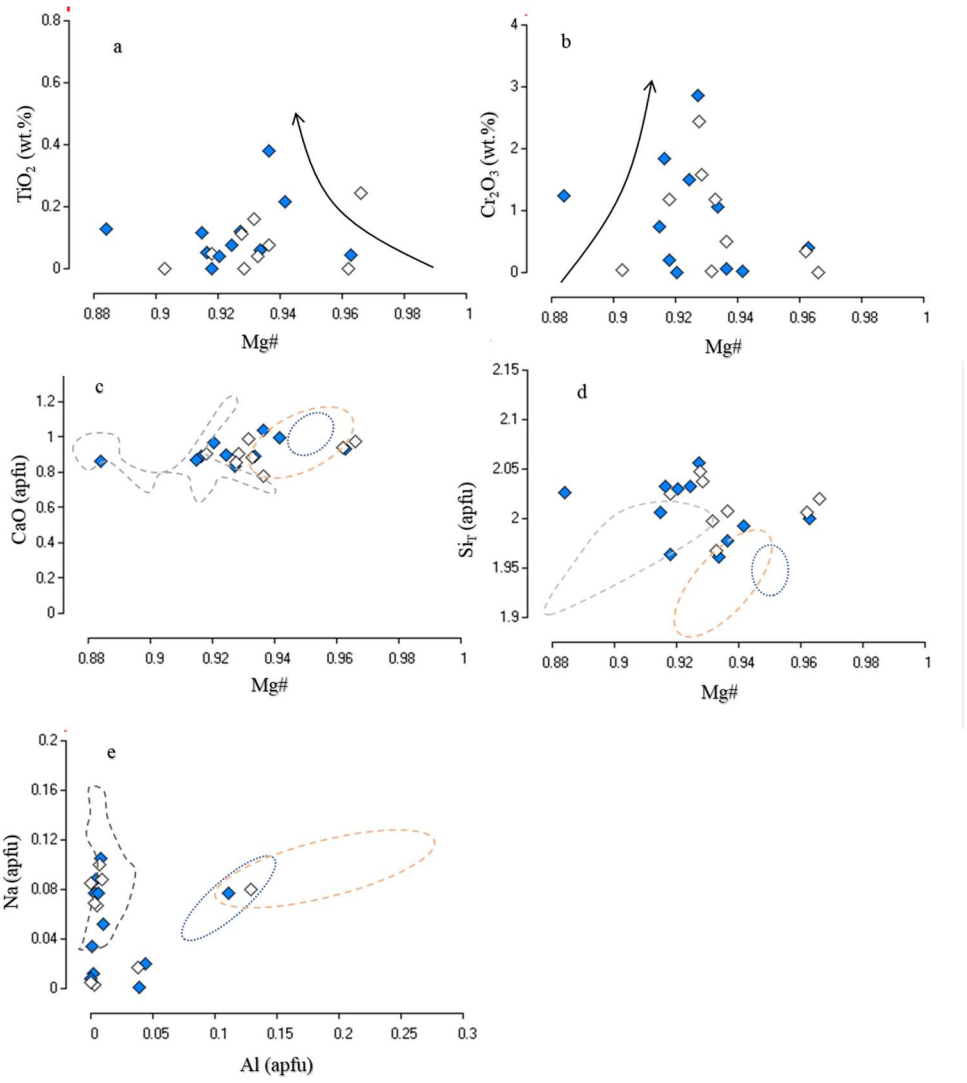

Fig.4.20 Bivariate plots for the clinopyroxene cores (full squares) and rims (empty squares) from Indaiá I kimberlite. The delimited fields correspond to xenoliths from Indaiá I (after Nannini, 2016). Grey field: phlogopite xenoliths. Blue field: Cr-spinel harzburgite and dunites. Orange field: Cr-spinel lherzolite and Cr-spinel harzburgite. The arrows indicate the peridotite trend with major concentrations of worldwide kimberlites (Pivin et al., 2009).

Negative anomalies are also in Ba, K and Ti. The range from Cs to K is variable, with depletion or enrichment. The low Cr clinopyroxene display opposite pattern. They exhibit lower values (below to chondrite) with strong negative anomalies in Ce, Sr Zr, Y and Yb.

The low-Cr clinopyroxenes presented the major REE below to detection limits. The high-Cr clinopyroxenes have enrichment in LREE (up to 100 times chondrite) with constantly depletion towards HREE. From La to Nd there is a slightly enrichment (Fig.4.21). Only one grain exhibits a direct depletion with light slope in Eu.

The fractionated values of rare earth elements (REE) vary from 0.06 to 23.92 for $(La/Yb)_N$, and 4.04 to 9.54 for $(Sm/Er)_N$. In addition, these pyroxenes are characterised by $(Zr/Hf)_N$ values from 0.01 to 3.74.

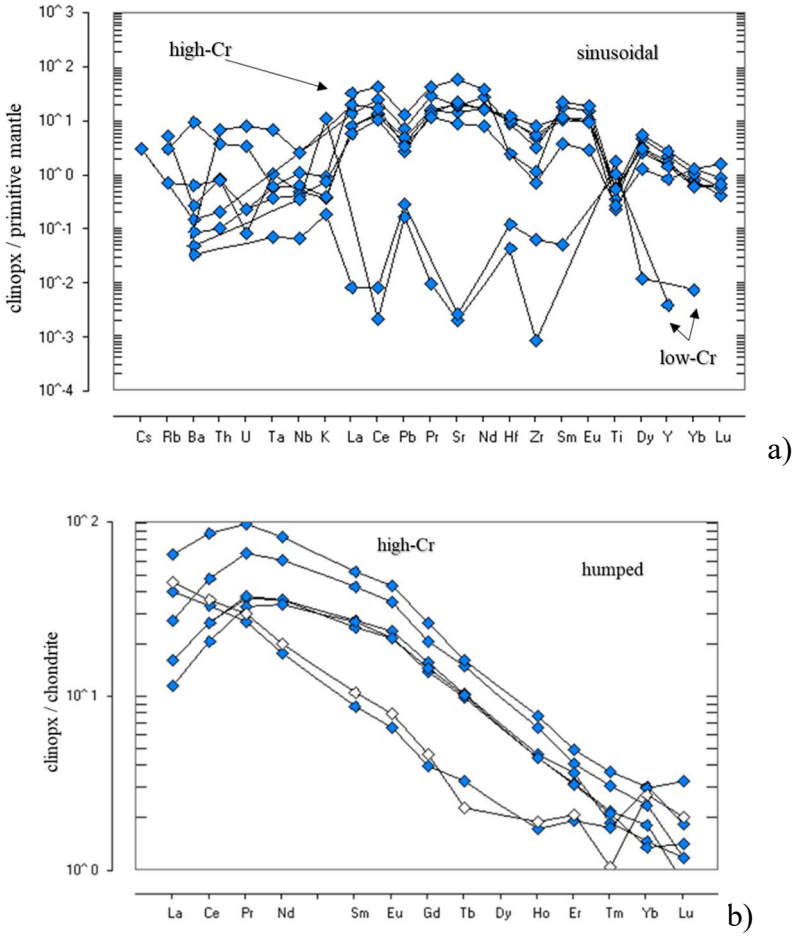

Figure 4.21. (a) primitive mantle-normalized incompatible elements pattern (McDonough and Sun, 1995) and b) Chondrite normalised REE patterns (Boynton, 1984) for pyroxenes cores.

5. Discussions

The classical pipe composed by root, diatreme and crater zones (Clement, 1982; Howthorne, 1975) correspond to the first model funded in Africa (Class 1) and the facies that fill which zone are from hypabyssal- (HFK), through transitional- (TFK) to diatreme- (DFK) and crater-facies rocks (CFK), respectively. The other two classes (Class 2 and 3) differ mainly by absence of diatreme zones and by the mineralogical different facies that composed each one authors (e.g. Clement and Skinner, 1985; R. Cas et al., 2008; Field and Scott Smith, 1999; Hetman et al., 2004; Scott Smith et al., 2008; Skinner and Marsh, 2004; Sparks et al., 2006).

These data come from mature mining operations in these kimberlites, therefore, the association of the facies with specific region of the zones should be applied with care to the Brazilian kimberlites, due the fact that crater facies could also occur in the diatreme zone, and hypabyssal or coherent kimberlite could occur at any level of a pipe (R. Cas et al., 2008). The classification provides a useful starting point, according with some characteristics it is possible suggest which Indaiá I kimberlite facies was studied in this work.

The coherent texture of Indaiá I compose by fresh olivine crystals set in a fine groundmass dominated mainly by carbonates, opaque minerals, perovskite and serpentine, point to hypabyssal-facies (HFK). However, the low abundance of juvenile clasts and incipient pelletal structures, which are characteristic of diatreme-facies, indicate that this kimberlite has a little mixture of different kimberlitic materials. These clasts and pelletals, also named by globular and pelletal segregations (E. M.W. Skinner and Marsh, 2004), can occur in hypabyssal kimberlite.

The first segregationary HFKs, were described by Clement (1975), and initially thought to be a type of DFK, but subsequent discovery of similar rocks in dykes and root zones indicates that they are a variety of HFK (E. M.W. Skinner and Marsh, 2004). However, the low abundance of primary calcite (which is abundant in hypabyssal-facies but tends to disappear as it starts the diatreme-facies) and the occurrence of relatively fresh mantle xenoliths, which in HFK are always highly altered (E. M.W. Skinner and Marsh, 2004), suggest a transitional-facies (TFK) studied for Indaiá I kimberlite. The transitional-facies kimberlite (TFK) grades continuously between two main end- member varieties, the recognition of TFK, localized in the lower parts of the pipe (towards the base of the diatreme zone and towards the top of the root zone) is a relatively new development (e.g. Hetman et al., 2004; Skinner and Marsh, 2004).

In the most, the olivine sizes within the clasts are equal or slightly smaller than outside olivine crystals, this fact may indicate derivation of the juvenile clasts from batches of compositionally distinct kimberlitic magmas (Webb, 2006). The moderate alteration degree of these clasts (and the the cores from pelletals) in contrast to fresh kimberlitic material outside, may be suggest a modification by volcanic process, in this case, a light volcanic process. In addition, the abundance serpentine within the clasts groundmass, can be regarded as a devitrification product of quenched kimberlitic glass (E. M.W. Skinner and Marsh, 2004).

The explosive stage of a volcanism involve fluid, volatile-rich melts that are intruded as dykes into loose, granular deposits close to the diatreme root zone (Gernon et al., 2012), this process can explain the pelletals formation. In the Junqueira-Brod et al. (1999) first stage model, the magma droplet (or a crystal), which already has a rim composed by different material from host, starts to spin, but the rim is no orientation yet.

The lack of different composition pelletals rims from Indaiá I can be due to the available low abundance of different kimberlitic materials that composed the system. An addition to a possible initial volcanic stage, the flow velocity was sufficiently high to transport and rotate little the crystals (nucleus), but not sufficiently for some material adhered it, resulting only in crystals with orientated host kimberlitic material.

P*rocess recorded by major elements*

The grain size criterion is not self-sufficient to establish the relationship between megacrysts and macrocrysts due to the fact that both can be derived from larger grains crystals (Pivin et al., 2009), including megacrysts and xenolith-derived fragments, which may have been mechanically reduced during the process of the primary kimberlite material. In this study, most mineral grains available are in fact smaller than 10 mm in diameter and do not fit the strict definition of megacrysts. Therefore, based in major and trace element compositions, the word “megacrysts” can be link to genetic processes rather than just as a description of mineral size.

The major element compositions of clinopyroxenes analysed overlap in Mg#, Ca, Si, Na contents mainly peridotite xenoliths fields (Nannini, 2016), and Cr-spinel harzburgite and lherzolites are an also possible source for grains with higher Al and Mg #or lower Si (Fig.4.19). The high Cr# and low Ti also suggest a peridotite origin and the chemical composition are in agree with clinopyroxenes from worldwide peridotites (Pivin et al., 2009).

The assimilation of xenoliths enriched the kimberlitic melt in silicate and the formation of the low-Cr and Fe-Ti-rich megacrysts occur, in this case, the presence of Mg-ilmenites. Compositional variation within kimberlitic ilmenites were generalized with the “magmatic” and “reaction” trends. The ilmenite megacrysts, related to the magma differentiation process, are getting richer in ferric iron and poorer in magnesium (Agee et al., 1982). Metasomatic megacrysts, generated by the reactions between kimberlite magmas and mantle peridotites, do not demonstrate such correlations (Golubkova et al., 2013).

The ilmenite macrocrystals analysed have lower MgO and higher FeO than microcrystals, suggesting that are related to the magma differentiation process, while the microcrystals can be formed by metasomatic event and correspond to fragments of higher grains. Metasomatic ilmenite formed at the metasomatic contacts between mantle diapirs and shallower mantle garnet lherzolites, which were substituted by ilmenite–garnet clinopyroxenites after the metasomatic reactions occurred (Golubkova et al., 2013).

Process recorded by trace elements

The (Sc/V) < 1 (0.22 to 0.61) suggest clinopyroxenes from garnet peridotite, consistent with the relative partitioning of these two elements in garnet and clinopyroxene (Nimis et al., 2009), however, websterites and eclogites also display values < 1.

The low-Cr pyroxenes present very low Yb (0 – 0.19) which can suggest events of partial melting (Nimis et al., 2009), this can be in concordance with the high La/Sm ratios (~62.62) and the higher Mg# values exhibited by these clinopyroxenes, and additionally with enrichment in Th and U can be reflect low degrees of metasomatism operated by small volumes of strongly differentiated melts. The high values of this ratio also suggest a percolative fractional crystallization (Kargin et al., 2016) and are in concordance with low Zr/Hf fractionation presented by these clinopyroxenes, suggesting a transient feature of the percolating melt induced by precipitation of and/or reaction with garnet, this fact are related to positive peaks of Zr and Hf in garnets associated with diopsides with negative Zr and Hf anomalies (Solov’eva et al., 2008).

The features described above are in agreement with positive correlation between Zr and Y concentrations corresponding to the “melt” metasomatic trend (W L Griffin et al., 1999). The high-Cr clinopyroxene exhibited high Na_2O and this type are very similar to Type 2 diopside

from from Kaapvaal craton (Grégoire et al., 2003), and this is a characteristic attributed to metasomatic origin in similar kimberlitic xenoliths.

The relative constant Ti/Eu and variable La/Yb point to carbonatite metasomatism for high-Cr clinopyroxenes, the higher LREE content and strong Nb-Ta-Ti anomaly are features typical of this melt. The low-Cr clinopyroxenes do not display these anomalies; can suggesting a silicate metasomatism for low-Cr type.

The strong depletion of Ti, Nb, Ta, Zr and Hf may reflect the precipitation of Ti-oxides, such as ilmenite due to preferential fractionation (Golubkova et al., 2013). The ilmenites from Indaiá I present notable very strong positive anomalies in high field strength elements, e.g. (Zr, Nb, Ta, Hf), suggesting that these grains were not in equilibrium with kimberlitic magma. The equilibrium with kimberlite magma is represent by ilmenites generally with higher concentrations of incompatible elements, such as Sr, Ba, LREE, Pb, Th, U, Zn, have and lower abundances of HFSE (Zr, Nb, Ta, Hf) (Golubkova et al., 2013).

In addition, calculated composition melts which were in equilibrium with Mg-ilmenite megacrysts with flat patterns (Golubkova et al., 2013), resulted in an enriched LREE melt composition.

The all silicates analysed (garnet and clinopyroxenes) have depletion in Hf, Nb, Ta, and Zr, however, ilmenites are rich in this high field strength elements (HFSE). These elements remain relatively constant during the first 80% of crystallization and then increase during the final stages (Jang and Naslund, 2002). These can be explaining the trace elements higher values displayed by microcrysts ilmenites, which can be related to latter crystallization in relation to macrocrysts ilmenites.

The Ba/Ce ratios has been suggested as a possible fingerprint for the influx of new magma during ilmenite crystallization (McBirney, 2002). The macrocrysts ilmenites show the high Ba/Ce ratios; this can indicate an initial stage of crystallization. The ration of Nb, Ta, Hf, or Zr have significative changes during fractionation and normally excluded trace elements like Ba, Cs, Rb, U, Th, or the REEs (Jang and Naslund, 2002). There is a moderate variation between the Zr/Hf, Y/Ho, Nb/Ta and U/Th ratios, indicating the influence of new magma to the intrusion during differentiation.

APÊNDICE 5 – Química mineral

Table 1

Major-element compositions of spinel minerals from Charneca Kimberlite

	CHAR_1_0019 C	CHAR_1_0019 B	CHAR_1_0024 C	CHAR_1_0024 BB	CHAR_1_0024 I	CHAR_1_0026 C	CHAR_1_0026 B	CHAR-6#_0007 C	CHAR-6#_0007 B
SiO2	0.00	0.03	0.00	0.15	0.10	0.00	0.00	0.00	0.00
TiO2	0.43	0.70	0.01	11.00	2.77	2.30	0.85	0.03	0.09
Al2O3	17.84	17.50	43.51	3.96	32.09	11.27	16.01	39.49	38.57
Fe2O3(T)	22.71	23.37	14.17	44.35	23.87	36.54	29.60	15.65	15.68
MnO	0.31	0.30	0.13	0.39	0.21	0.37	0.32	0.20	0.16
MgO	12.60	12.15	17.74	13.07	17.49	10.73	11.91	15.64	16.19
CaO	0.00	0.03	0.02	0.14	0.03	0.00	0.00	0.00	0.01
Na2O									
K2O	0.02	0.02	0.03	0.05	0.00	0.00	0.00	0.00	0.02
Cr2O3	48.10	47.30	25.91	29.78	24.84	41.10	42.06	31.18	30.20
Total	102.01	101.41	101.52	102.90	101.41	102.31	100.75	102.19	100.92
Sum of Atomic	1.850	1.867	1.635	1.923	1.702	1.910	1.887	1.672	1.688
Number of ions on base of 4 oxygen									
Si	0.000	0.001	0.000	0.005	0.003	0.000	0.000	0.000	0.000
Ti	0.010	0.016	0.000	0.265	0.059	0.055	0.020	0.001	0.002
Al	0.647	0.641	1.396	0.149	1.071	0.422	0.592	1.295	1.277
Fe^{3}	0.161	0.162	0.046	0.557	0.248	0.435	0.323	0.017	0.048
Fe^{2}	0.424	0.445	0.277	0.630	0.317	0.537	0.454	0.347	0.320
Mn	0.008	0.008	0.003	0.011	0.005	0.010	0.008	0.005	0.004
Mg	0.578	0.563	0.720	0.624	0.739	0.508	0.558	0.649	0.678
Ca	0.000	0.001	0.001	0.005	0.001	0.000	0.000	0.000	0.000
Na	0.000	0.000	0.000	0.000	0.000	0.000	0.000	0.000	0.000
K	0.001	0.001	0.001	0.002	0.000	0.000	0.000	0.000	0.001
Cr	1.171	1.162	0.558	0.754	0.556	1.033	1.044	0.686	0.671
Ba	0.000	0.000	0.000	0.000	0.000	0.000	0.000	0.000	0.000
Zn	0.000	0.000	0.000	0.000	0.000	0.000	0.000	0.000	0.000
V	0.000	0.000	0.000	0.000	0.000	0.000	0.000	0.000	0.000
Ni	0.000	0.000	0.000	0.000	0.000	0.000	0.000	0.000	0.000
Total:	3.000	3.001	3.001	3.001	3.000	3.000	3.000	3.000	3.000

Trace elements in spinel minerals of Charneca Kimberlite

Concentrations in ppm (µg/g)

Li	0.309	0.96	<0.21	2.09
P	<5.32	13.53	5.01	8.98

Sc	2.34	0.279	6.55	0.9
Co	313.97	382.45	275.95	542.58
Rb	<0.058	<0.059	<0.053	<0.10
Sr	0.0094	0.0175	0.0102	0.147
Y	<0.0072	0.0074	<0.0054	<0.012
Zr	0.5	<0.098	5.28	0.44
Nb	0.366	0.07	8.42	0.072
Sn	0.73	0.4	10.52	<0.38
Sb	<0.069	<0.070	<0.060	<0.13
Ba	<0.047	0.21	<0.051	1.52
La	0.0174	<0.0074	0.0153	0.015
Ce	0.0369	0.0369	0.0133	0.215
Pr	<0.0080	<0.0038	<0.0046	0.014
Nd	<0.061	<0.062	<0.050	0.15
Sm	0.036	<0.038	<0.0210	<0.057
Eu	0.0148	<0.0132	<0.0114	<0.0222
Gd	<0.033	<0.034	<0.037	<0.047
Tb	<0.0046	<0.0054	<0.0057	<0.008
Dy	<0.028	<0.029	<0.024	<0.065
Ho	<0.0067	<0.0060	<0.0056	<0.0115
Er	<0.0134	<0.0148	<0.015	<0.0273
Tm	<0.0054	<0.0063	<0.0049	<0.014
Yb	<0.037	<0.038	<0.021	<0.056
Lu	<0.0055	<0.0077	<0.0049	<0.0087
Hf	<0.046	<0.046	0.125	<0.055
Ta	0.0171	0.0042	1.274	<0.0067
Pb	0.113	0.15	0.064	0.87
Pb	0.159	0.117	0.171	0.44
Pb	0.157	0.145	0.057	0.71
Th	0.0065	<0.00	<0.00	0.012
U	<0.0054	0.0023	<0.00	0.01

Table 2

Major-element compositions of spinel minerals from Grota do Cedro Kimberlite

	GC1-13_0022 C	GC1-13_0022 B	GC1-13_0023 C1	GC1-13_0023 C2	GC1-13_0024 C	GC1-13_0024 B	GC1-A2_0027 I	GC1-A2_0027 C	GC1-A2_0027 B	GC1-A2_0027 C	GC1-A2_0027 B
SiO2	0.15	0.22	0.15	0.34	0.11	0.40	0.03	0.01	0.08	0.22	0.36
TiO2	12.77	14.22	13.78	13.03	4.39	8.34	5.86	6.06	10.92	12.33	11.80
Al2O3	1.36	1.44	1.45	1.50	6.94	3.19	5.61	4.67	2.57	1.64	1.30
Fe2O3(T)	66.88	66.78	65.86	63.49	27.97	47.60	36.74	40.04	59.28	80.26	82.20
MnO	0.62	0.64	0.60	0.60	0.29	0.46	0.41	0.43	0.53	0.86	1.13
MgO	8.42	7.97	6.97	7.65	12.19	12.92	10.35	10.25	10.07	6.05	4.90
CaO	0.32	0.51	0.50	1.09	0.07	0.13	0.06	0.02	0.07	0.20	0.12
Na2O											
K2O	0.01	0.01	0.00	0.01	0.02	0.04	0.01	0.00	0.04	0.06	0.02
Cr2O3	11.73	9.78	10.42	12.15	47.77	24.99	44.08	41.31	19.07	1.20	0.86
BaO											
ZnO	0.02	0.05	0.04	0.04	0.04	0.09	0.08	0.10	0.06	0.06	0.06
V2O3	0.17	0.18	0.17	0.17	0.18	0.10	0.13	0.11	0.11	0.12	0.11
NiO	0.20	0.23	0.19	0.22	0.19	0.11	0.14	0.14	0.12	0.07	0.07
TOTAL	102.64	102.02	100.13	100.28	100.17	98.37	103.49	103.14	102.92	103.06	102.94
Sum of	1.997	2.014	2.066	2.048	1.969	2.002	1.944	1.956	1.965	2.010	2.030
Number of ions on base of 4 oxygen											
Si	0.005	0.007	0.005	0.012	0.004	0.013	0.001	0.000	0.003	0.007	0.012
Ti	0.319	0.359	0.356	0.334	0.108	0.209	0.143	0.148	0.269	0.310	0.300
Al	0.053	0.057	0.059	0.060	0.268	0.125	0.214	0.179	0.099	0.065	0.052
Fe+3	0.983	0.944	0.927	0.913	0.263	0.767	0.366	0.455	0.861	1.264	1.297
Fe+2	0.876	0.928	0.966	0.897	0.504	0.560	0.628	0.635	0.761	0.982	1.027
Mn	0.017	0.018	0.017	0.017	0.008	0.013	0.011	0.012	0.015	0.024	0.032
Mg	0.417	0.398	0.357	0.389	0.595	0.642	0.499	0.498	0.491	0.302	0.247
Ca	0.011	0.018	0.018	0.040	0.003	0.005	0.002	0.001	0.002	0.007	0.004
Na	0.000	0.000	0.000	0.000	0.000	0.000	0.000	0.000	0.000	0.000	0.000
K	0.001	0.000	0.000	0.000	0.001	0.002	0.001	0.000	0.002	0.002	0.001
Cr	0.308	0.259	0.283	0.328	1.238	0.658	1.128	1.064	0.493	0.032	0.023
Ba	0.000	0.000	0.000	0.000	0.000	0.000	0.000	0.000	0.000	0.000	0.000
Zn	0.001	0.001	0.001	0.001	0.001	0.002	0.002	0.002	0.001	0.001	0.002
V	0.004	0.005	0.005	0.005	0.005	0.003	0.003	0.003	0.003	0.003	0.003
Ni	0.005	0.006	0.005	0.006	0.005	0.003	0.004	0.004	0.003	0.002	0.002
Total:	3.002	3.002	3.001	3.002	3.002	3.002	3.001	3.001	3.002	3.002	3.001

	GC1-A2_0031 B	GC1-A2_0031 C	GC1-A2_0031 C1	GC1-A2_0031 C2	GC1-A2_0031 C3	GC1-A2_0032 B	GC1-A2_0032 C	GC1-A2_0035 B	GC1-A2_0035 I	GC1-A2_0035 B	GC1-A2_0036 B
SiO2	0.77	0.45	0.36	0.09	0.53	0.24	0.11	0.07	0.13	1.16	0.11
TiO2	13.88	14.21	15.19	5.09	10.51	10.82	14.76	6.90	10.31	12.47	14.94
Al2O3	1.24	1.26	1.65	4.36	1.31	2.01	0.28	4.13	3.22	4.79	1.80
Fe2O3(T)	74.42	71.74	71.69	38.59	68.26	80.28	81.94	39.37	55.36	72.56	71.65
MnO	0.61	0.60	0.57	0.56	0.61	0.67	0.59	0.44	0.75	0.97	0.52
MgO	7.85	8.15	7.33	8.70	7.74	6.65	2.62	9.44	7.17	4.57	8.84
CaO	0.10	0.11	0.10	0.09	0.18	0.37	0.15	0.08	0.10	0.24	0.07
Na2O											
K2O	0.04	0.06	0.05	0.02	0.03	0.07	0.03	0.00	0.04	0.03	0.02
Cr2O3	2.63	5.53	4.64	44.68	13.93	0.01	1.21	42.69	26.36	2.40	4.63
BaO											
ZnO	0.01	0.04	0.04	0.10	0.07	0.05	0.33	0.07	0.10	0.05	0.04
V2O3	0.12	0.12	0.13	0.15	0.10	0.10	0.40	0.13	0.12	0.14	0.12
NiO	0.10	0.12	0.12	0.11	0.10	0.01	0.08	0.10	0.10	0.06	0.13
TOTAL	101.78	102.38	101.87	102.54	103.37	101.29	102.49	103.41	103.77	99.44	102.87
Sum of	2.014	2.003	2.023	1.993	1.991	2.027	2.091	1.969	1.992	2.075	1.982
Number of ions on base of 4 oxygen											
Si	0.026	0.015	0.012	0.003	0.018	0.008	0.004	0.002	0.004	0.040	0.004
Ti	0.350	0.356	0.385	0.127	0.262	0.275	0.386	0.170	0.257	0.324	0.371
Al	0.049	0.049	0.065	0.170	0.051	0.080	0.011	0.160	0.126	0.195	0.070
Fe+3	1.125	1.057	1.012	0.393	1.020	1.351	1.163	0.385	0.655	1.006	1.056
Fe+2	0.961	0.944	1.007	0.678	0.871	0.914	1.222	0.694	0.879	1.090	0.921
Mn	0.017	0.017	0.016	0.016	0.017	0.019	0.017	0.012	0.021	0.028	0.014
Mg	0.392	0.405	0.368	0.430	0.382	0.334	0.136	0.461	0.354	0.235	0.435
Ca	0.004	0.004	0.004	0.003	0.006	0.013	0.006	0.003	0.004	0.009	0.003
Na	0.000	0.000	0.000	0.000	0.000	0.000	0.000	0.000	0.000	0.000	0.000
K	0.002	0.002	0.002	0.001	0.001	0.003	0.001	0.000	0.002	0.001	0.001
Cr	0.070	0.146	0.124	1.171	0.365	0.000	0.033	1.106	0.691	0.066	0.121
Ba	0.000	0.000	0.000	0.000	0.000	0.000	0.000	0.000	0.000	0.000	0.000
Zn	0.000	0.001	0.001	0.002	0.002	0.001	0.008	0.002	0.002	0.001	0.001
V	0.003	0.003	0.003	0.004	0.003	0.003	0.011	0.003	0.003	0.004	0.003
Ni	0.003	0.003	0.003	0.003	0.003	0.000	0.002	0.003	0.003	0.002	0.003
Total:	3.002	3.002	3.002	3.001	3.001	3.002	3.001	3.001	3.002	3.001	3.001

	GC1-A2_0036 B	SPGC12_0014 C	SPGC12_0015 C	SPGC12_0016 C	SPGC12_0016 B	SPGC12_0017 C	SPGC12_0017 B	SPGC12_0018 B	SPGC12_0027 C	SPGC12_0027 B
SiO2	0.19	0.00	0.00	0.00	0.00	0.00	0.00	0.00	0.00	0.00
TiO2	11.84	0.00	2.50	0.49	0.46	0.19	0.26	0.27	0.43	0.48
Al2O3	1.61	17.10	0.71	8.30	8.18	13.45	13.47	1.09	8.53	7.99
Fe2O3(T)	80.27	20.32	32.89	24.05	22.86	18.16	17.91	26.97	23.18	23.26
MnO	0.85	0.21	0.34	0.29	0.27	0.25	0.25	0.37	0.31	0.31
MgO	5.87	13.97	8.02	11.91	12.73	13.72	13.71	8.98	11.80	12.71
CaO	0.18	0.04	0.01	0.00	0.00	0.00	0.01	0.01	0.01	0.01
Na2O										
K2O	0.05	0.01	0.01	0.00	0.02	0.00	0.00	0.01	0.00	0.00
Cr2O3	1.90	42.35	56.08	53.32	52.06	48.54	48.59	63.63	52.75	52.69
BaO										
ZnO	0.05	0.00	0.00	0.00	0.00	0.00	0.00	0.00	0.00	0.00
V2O3	0.10	0.00	0.00	0.00	0.00	0.00	0.00	0.00	0.00	0.00
NiO	0.06	0.00	0.00	0.00	0.00	0.00	0.00	0.00	0.00	0.00
TOTAL	102.96	94.01	100.56	98.36	96.58	94.31	94.20	101.32	97.02	97.46
Sum of	2.015	1.966	2.076	1.993	2.014	1.998	2.000	2.047	2.018	2.000
Si	0.006	0.000	0.000	0.000	0.000	0.000	0.000	0.000	0.000	0.000
Ti	0.299	0.000	0.065	0.012	0.012	0.005	0.006	0.007	0.011	0.012
Al	0.064	0.659	0.029	0.325	0.323	0.527	0.528	0.044	0.338	0.313
Fe+3	1.272	0.245	0.309	0.252	0.274	0.187	0.180	0.229	0.240	0.275
Fe+2	0.979	0.311	0.642	0.415	0.367	0.318	0.319	0.540	0.411	0.372
Mn	0.024	0.006	0.010	0.008	0.008	0.007	0.007	0.011	0.009	0.009
Mg	0.293	0.681	0.413	0.589	0.636	0.680	0.680	0.456	0.591	0.631
Ca	0.006	0.001	0.000	0.000	0.000	0.000	0.000	0.000	0.000	0.000
Na	0.000	0.000	0.000	0.000	0.000	0.000	0.000	0.000	0.000	0.000
K	0.002	0.000	0.001	0.000	0.001	0.000	0.000	0.000	0.000	0.000
Cr	0.050	1.096	1.532	1.399	1.380	1.276	1.279	1.714	1.401	1.387
Ba	0.000	0.000	0.000	0.000	0.000	0.000	0.000	0.000	0.000	0.000
Zn	0.001	0.000	0.000	0.000	0.000	0.000	0.000	0.000	0.000	0.000
V	0.003	0.000	0.000	0.000	0.000	0.000	0.000	0.000	0.000	0.000
Ni	0.002	0.000	0.000	0.000	0.000	0.000	0.000	0.000	0.000	0.000
Total:	3.002	3.000	3.000	3.000	3.001	3.000	3.000	3.000	3.000	3.000

Trace elements in spinel minerals of Grota do Cedro Kimberlite

Concentrations in ppm (µg/g)

	GC1-13_0022	GC1-A2_0027	GC1-A2_0031	GC1-A2_0032	SPGC12_0014	SPGC12_0015	SPGC12_0016	SPGC12_0017	SPGC12_0018	GC1-A2_0027
	C	C	C	C	C	C	C	C	B	C
Li	0.72	20.91	32.38	23.91	0.75	0.54	1.36	0.84	<77.89	20.91
P	<11.00	<48.07	108.06	2132.03	<9.85	<8.41	<15.14	<14.01	<1895.55	<48.07
Sc	43.72	17.62	41.81	27.10	2.31	5.35	4.82	3.01	<29.97	17.62
Co	134.64	313.52	319.94	233.94	450.70	295.27	388.91	431.16	361.78	313.52
Rb	<0.112	1.75	0.76	5.17	<0.121	0.16	3.31	<0.164	51.26	1.75
Sr	0.08	6.54	10.37	104.53	0.15	0.07	2.07	0.39	7.24	6.54
Y	0.12	0.11	0.37	2.26	0.02	<0.0152	0.10	0.04	<2.22	0.11
Zr	1097.05	47.55	178.45	146.48	<0.27	10.64	5.84	0.49	<36.99	47.55
Nb	2704.91	4.28	12.58	32.03	0.12	2.98	2.08	0.32	8.25	4.28
Sn	43.75	6.38	14.86	14.41	1.32	8.44	6.33	1.56	161.17	6.38
Sb	<0.179	0.78	<0.81	<0.42	<0.133	<0.109	<0.200	<0.192	<24.95	0.78
Ba	<0.105	10.73	34.82	55.99	0.22	0.35	8.59	0.88	318.09	10.73
La	<0.0116	1.14	1.19	5.83	0.03	<0.014	0.67	0.13	5.15	1.14
Ce	0.04	1.55	1.60	7.32	0.04	0.02	1348.00	0.25	5.17	1.55
Pr	0.01	0.27	0.22	0.79	0.02	<0.0098	0.11	<0.0172	<2.01	0.27
Nd	<0.123	0.74	1.19	2.66	<0.111	<0.090	0.41	<0.204	<27.56	0.74
Sm	<0.091	<0.29	<0.47	0.64	<0.091	<0.050	<0.150	<0.131	<14.78	<0.29
Eu	<0.028	<0.107	<0.106	0.11	<0.031	<0.024	<0.040	<0.031	<5.24	<0.107
Gd	<0.057	<0.29	<0.31	0.99	<0.063	<0.051	0.12	<0.090	<10.81	<0.29
Tb	<0.0103	<0.060	<0.053	0.11	<0.0119	0.01	<0.0210	<0.0134	2.57	<0.060
Dy	<0.060	<0.31	<0.30	0.62	<0.069	<0.031	0.11	<0.071	<14.25	<0.31
Ho	0.01	<0.053	0.06	0.08	<0.0107	<0.0096	<0.0203	<0.0174	<2.01	<0.053
Er	0.04	<0.081	<0.148	0.18	<0.037	<0.028	<0.050	<0.029	4.52	<0.081
Tm	<0.0085	<0.049	<0.046	<0.023	<0.0132	<0.0075	<0.0118	<0.0161	<2.40	<0.049
Yb	<0.050	<0.35	<0.45	0.27	<0.066	<0.037	<0.109	<0.078	<11.48	<0.35
Lu	<0.0102	<0.043	<0.054	<0.033	<0.0100	<0.0090	<0.0209	0.02	<1.47	<0.043
Hf	32.98	2.51	7.49	6.60	<0.074	0.34	0.23	<0.083	<10.52	2.51
Ta	215.54	0.47	1.04	0.92	<0.0122	0.31	0.23	<0.0163	<1.73	0.47
Pb	<0.068	<0.24	0.99	3.73	0.20	0.15	0.12	0.08	14.78	<0.24
Pb	<0.041	0.27	<0.33	3.44	0.13	0.19	<0.084	<0.107	<13.65	0.27
Pb	<0.0173	0.22	0.28	3.98	0.14	0.23	0.11	<0.057	9.89	0.22
Th	0.01	0.38	2.51	8.35	0.01	0.00	0.28	0.01	1.78	0.38
U	0.06	0.10	0.43	1.46	<0.00	0.02	0.03	0.01	<0.74	0.10

Table 3

Major-element compositions of spinel minerals from Régis Kimberlite

	regis-4_0006 B	regis-4_0006 C	regis-4_0006 B	regis-4_0007 C	regis-5_0004 C minor	regis-5_0004 C major	regis-9_0015 C	regis-9_0016 B	regis-9_0016 C
SiO2	0.26	0.06	0.77	0.11	0.56	0.01	0.10	0.21	0.15
TiO2	6.79	9.17	11.46	8.62	15.52	50.03	18.39	6.27	10.19
Al2O3	1.43	4.74	1.27	5.45	1.48	0.46	3.16	5.03	3.23
Fe_2O_3(T)	90.05	54.19	82.67	42.29	68.36	38.66	57.71	39.84	45.79
MnO	1.18	2.03	1.56	0.40	0.73	0.44	0.54	0.48	0.58
MgO	1.16	4.39	2.03	12.51	7.71	10.57	12.25	7.06	9.58
CaO	0.16	0.05	0.24	0.12	0.44	0.35	0.11	0.13	0.20
Na2O									
K2O	0.07	0.02	0.09	0.01	0.00	0.00	0.00	0.01	0.03
Cr2O3	0.43	27.11	0.56	32.31	6.79	1.92	8.90	38.52	31.16
BaO									
ZnO	0.11	0.27	0.09	0.07	0.06	0.01	0.02	0.05	0.05
V2O3	0.20	0.16	0.18	0.12	0.18	0.52	0.22	0.19	0.22
NiO	0.11	0.14	0.10	0.17	0.15	0.10	0.22	0.16	0.18
TOTAL	101.95	102.34	101.02	102.18	101.98	103.07	101.62	97.95	101.37
Sum of	2.097	2.047	2.111	1.932	2.017	2.025	1.957	2.096	2.005
Number of ions on base of 4 oxygen									
Si	0.01	0.00	0.03	0.00	0.02	0.00	0.00	0.01	0.01
Ti	0.18	0.24	0.30	0.21	0.39	1.27	0.45	0.16	0.26
Al	0.06	0.19	0.05	0.21	0.06	0.02	0.12	0.21	0.13
Fe+3	1.55	0.60	1.26	0.54	0.93	0.62	0.73	0.38	0.52
Fe+2	1.08	0.95	1.16	0.59	0.99	1.71	0.84	0.78	0.76
Mn	0.03	0.06	0.05	0.01	0.02	0.01	0.01	0.01	0.02
Mg	0.06	0.22	0.11	0.60	0.39	0.53	0.59	0.37	0.48
Ca	0.01	0.00	0.01	0.00	0.02	0.01	0.00	0.00	0.01
Na	0.00	0.00	0.00	0.00	0.00	0.00	0.00	0.00	0.00
K	0.00	0.00	0.00	0.00	0.00	0.00	0.00	0.00	0.00
Cr	0.01	0.73	0.02	0.82	0.18	0.05	0.23	1.06	0.82
Ba	0.00	0.00	0.00	0.00	0.00	0.00	0.00	0.00	0.00
Zn	0.00	0.01	0.00	0.00	0.00	0.00	0.00	0.00	0.00
V	0.01	0.00	0.00	0.00	0.00	0.01	0.01	0.01	0.01
Ni	0.00	0.00	0.00	0.00	0.00	0.00	0.01	0.00	0.00
Total:	3.00	3.00	3.00	3.00	3.00	3.00	3.00	3.00	3.00

Major-element compositions of s

	regis-9_0018 B	regis-9_0018 C	regis-9_0018 B	regis-10_0005 C	regis-10_0005 B	regis-10_0006 C	regis-10_0012 B	regis-10_0012 C	regis-10_0013 C
SiO2	0.02	0.48	1.89	0.13	1.31	0.05	0.06	0.08	0.10
TiO2	9.62	9.47	14.86	17.08	13.41	2.38	8.79	6.75	3.73
Al2O3	4.34	5.25	0.60	2.74	1.94	0.90	5.55	6.61	0.72
Fe_2O_3(T)	46.24	38.31	75.80	65.87	76.69	36.50	46.51	31.62	34.38
MnO	1.41	0.75	0.96	0.54	0.72	0.39	0.44	0.32	0.38
MgO	8.88	11.36	5.21	10.38	7.80	7.91	10.47	11.42	7.85
CaO	0.12	0.17	0.43	0.13	0.27	0.02	0.12	0.03	0.08
Na2O									
K2O	0.02	0.08	0.06	0.02	0.20	0.04	0.00	0.02	0.14
Cr2O3	30.82	35.87	0.32	6.20	0.01	52.64	29.07	42.84	53.06
BaO									
ZnO	0.26	0.10	0.00	0.08	0.04	0.16	0.07	0.09	0.13
V2O3	0.19	0.24	0.12	0.16	0.18	0.42	0.15	0.21	0.47
NiO	0.10	0.18	0.05	0.15	0.09	0.16	0.15	0.21	0.17
TOTAL	102.03	102.26	100.29	103.48	102.65	101.58	101.38	100.20	101.21
Sum of	1.994	1.952	2.081	1.947	1.988	2.054	1.971	1.982	2.067
	Number of ions on base of 4 oxygen								
Si	0.00	0.02	0.07	0.00	0.04	0.00	0.00	0.00	0.00
Ti	0.24	0.23	0.39	0.42	0.33	0.06	0.22	0.17	0.10
Al	0.17	0.20	0.02	0.10	0.08	0.04	0.21	0.26	0.03
Fe+3	0.53	0.37	1.06	0.89	1.16	0.40	0.59	0.28	0.31
Fe+2	0.75	0.67	1.14	0.90	0.96	0.64	0.69	0.60	0.68
Mn	0.04	0.02	0.03	0.01	0.02	0.01	0.01	0.01	0.01
Mg	0.44	0.55	0.27	0.50	0.38	0.40	0.51	0.56	0.40
Ca	0.00	0.01	0.02	0.00	0.01	0.00	0.00	0.00	0.00
Na	0.00	0.00	0.00	0.00	0.00	0.00	0.00	0.00	0.00
K	0.00	0.00	0.00	0.00	0.01	0.00	0.00	0.00	0.01
Cr	0.81	0.92	0.01	0.16	0.00	1.42	0.75	1.12	1.44
Ba	0.00	0.00	0.00	0.00	0.00	0.00	0.00	0.00	0.00
Zn	0.01	0.00	0.00	0.00	0.00	0.00	0.00	0.00	0.00
V	0.01	0.01	0.00	0.00	0.00	0.01	0.00	0.01	0.01
Ni	0.00	0.00	0.00	0.00	0.00	0.00	0.00	0.01	0.00
Total:	3.00	3.00	3.00	3.00	3.01	3.00	3.00	3.00	3.01

spinel minerals from Régis Kimberlite

	regis-10_0013	regis-10_0014	regis-10_0015	regis-10_0015	regis-10_0015	regis-12_0032	regis-12_0032	regis-12_0032
	C2	C	B	C	C2	C1	C	B
SiO2	11.17	0.37	0.18	0.08	0.12	2.26	0.18	3.84
TiO2	2.68	14.17	14.35	12.12	13.75	11.84	17.57	2.39
Al2O3	3.41	2.80	1.96	3.31	2.23	0.54	3.89	0.64
Fe_2O_3(T)	25.80	60.84	72.26	61.95	71.89	79.41	54.22	82.87
MnO	0.28	0.52	1.01	0.84	1.04	0.91	0.94	0.34
MgO	9.10	10.47	4.58	6.18	4.26	3.24	11.30	3.53
CaO	0.16	0.10	0.15	0.08	0.11	0.67	0.13	0.62
Na2O								
K2O	2.02	0.05	0.02	0.01	0.02	0.12	0.03	0.18
Cr2O3	38.73	12.02	6.27	16.49	7.40	0.13	12.70	2.43
BaO								
ZnO	0.09	0.03	0.11	0.07	0.08	0.04	0.10	0.19
V2O3	0.34	0.17	0.18	0.16	0.19	0.12	0.13	0.06
NiO	0.17	0.15	0.07	0.11	0.07	0.11	0.22	0.19
TOTAL	93.95	101.69	101.15	101.40	101.16	99.39	101.41	97.28
Sum of Atomic	2.126	1.978	2.077	2.043	2.080	2.124	1.971	2.140
	Number of ions on base of 4 oxygen							
Si	0.40	0.01	0.01	0.00	0.00	0.08	0.01	0.14
Ti	0.07	0.35	0.37	0.31	0.36	0.31	0.43	0.06
Al	0.14	0.11	0.08	0.13	0.09	0.02	0.15	0.03
Fe+3	0.19	0.85	0.98	0.79	0.98	1.18	0.63	1.50
Fe+2	0.96	0.83	1.10	0.97	1.10	1.17	0.85	0.97
Mn	0.01	0.01	0.03	0.02	0.03	0.03	0.03	0.01
Mg	0.48	0.51	0.24	0.31	0.22	0.17	0.55	0.19
Ca	0.01	0.00	0.01	0.00	0.00	0.03	0.00	0.02
Na	0.00	0.00	0.00	0.00	0.00	0.00	0.00	0.00
K	0.09	0.00	0.00	0.00	0.00	0.01	0.00	0.01
Cr	1.08	0.31	0.17	0.44	0.20	0.00	0.33	0.07
Ba	0.00	0.00	0.00	0.00	0.00	0.00	0.00	0.00
Zn	0.00	0.00	0.00	0.00	0.00	0.00	0.00	0.01
V	0.01	0.00	0.00	0.00	0.01	0.00	0.00	0.00
Ni	0.00	0.00	0.00	0.00	0.00	0.00	0.01	0.01
Total:	3.06	3.00	3.00	3.00	3.00	3.00	3.00	3.01

	regis-12_0033 C2	regis-12_0033 C	regis-12_0034 C	regis-12_0034 B	regis 1-9_0005 C	regis 1-9_0005 B	regis 1-9_0011 C	regis 1_0006 C
SiO2	0.31	0.20	1.03	0.15	0.08	0.10	0.12	0.21
TiO2	10.63	53.63	7.70	12.61	11.62	16.28	9.79	14.95
Al2O3	6.22	0.22	3.27	4.56	4.06	3.37	2.79	3.85
Fe_2O_3(T)	70.25	2.39	60.97	42.71	51.48	58.30	72.23	53.02
MnO	0.57	0.04	1.50	2.50	0.40	0.52	0.69	1.28
MgO	12.82	0.00	7.82	11.63	10.01	12.41	7.13	10.03
CaO	0.13	38.45	2.01	0.16	0.06	0.10	0.02	0.12
Na2O								
K2O	0.04	0.03	0.09	0.04	0.03	0.00	0.04	0.01
Cr2O3	0.28	0.08	10.70	23.32	23.73	10.66	9.80	16.90
BaO								
ZnO	0.08	0.00	0.48	0.24	0.00	0.00	0.00	0.00
V2O3	0.10	0.31	0.07	0.15	0.00	0.00	0.00	0.00
NiO	0.20	0.01	0.16	0.22	0.00	0.00	0.00	0.00
TOTAL	101.62	95.37	95.80	98.29	101.45	101.74	102.60	100.37
Sum of Atomic	1.905	2.136	2.102	2.020	1.986	1.948	1.999	2.006
Si	0.01	0.01	0.04	0.01	0.00	0.00	0.00	0.01
Ti	0.25	1.43	0.20	0.32	0.29	0.40	0.25	0.38
Al	0.23	0.01	0.13	0.18	0.16	0.13	0.11	0.15
Fe+3	1.23	0.90	1.09	0.54	0.64	0.80	1.13	0.64
Fe+2	0.63	0.98	0.70	0.66	0.78	0.78	0.88	0.84
Mn	0.02	0.00	0.04	0.07	0.01	0.01	0.02	0.04
Mg	0.61	0.00	0.41	0.58	0.49	0.60	0.35	0.50
Ca	0.00	1.46	0.08	0.01	0.00	0.00	0.00	0.00
Na	0.00	0.00	0.00	0.00	0.00	0.00	0.00	0.00
K	0.00	0.00	0.00	0.00	0.00	0.00	0.00	0.00
Cr	0.01	0.00	0.30	0.62	0.62	0.27	0.26	0.45
Ba	0.00	0.00	0.00	0.00	0.00	0.00	0.00	0.00
Zn	0.00	0.00	0.01	0.01	0.00	0.00	0.00	0.00
V	0.00	0.01	0.00	0.00	0.00	0.00	0.00	0.00
Ni	0.01	0.00	0.00	0.01	0.00	0.00	0.00	0.00
Total:	3.00	3.00	3.00	3.00	3.00	3.00	3.00	3.00

Table 3 (continuation)

Trace elements in spinel minerals of Régis Kimberlite

Concentrations in ppm (µg/g)

	regis-4_0006 C	regis-5_0004 C major	regis-10_0012 C	regis-10_0014 C	regis-10_0015 C	regis-12_0033 C2
Li	30.69	0.79				<0.37
P	<29.75	18.34	1.43	1.4	56.28	21.84
Sc	28.51	6.86	<9.64	<10.38	526.95	273.92
Mn	15487	473.45	87.08	76.61	82.89	662.69
Co	728.04	19.19	3840.59	3566.06	29651.56	16.34
Rb	4.23	0.104	253.63	230.6	1149.79	0.205
Sr	27.59	152.18	<0.098	<0.098	44.58	173.44
Y	0.127	1009	0.984	0.374	214.84	5.03
Zr	60.64	9.62	0.076	0.067	1.53	379.41
Nb	7.1	0.502	1630.5	1538.88	244.04	0.479
Sn	20.45	0.64	5950.65	3785.5	39	1.37
Sb	0.4	<0.185	68.48	46.68	24.15	<0.139
Ba	46.41	2.01	1.3	<0.158	0.64	0.548
La	0.357	3.49	0.245	0.522	2628.08	4.05
Ce	0.228	11.42	<0.0135	<0.0126	13.27	7.92
Pr	<0.030	1664	0.049	0.0391	12.13	1027
Nd	<0.25	7.15	<0.0080	0.0104	0.897	4.52
Sm	<0.24	1.23	<0.099	<0.125	2.42	1.13
Eu	<0.067	0.31	<0.057	<0.057	0.31	0.425
Gd	<0.20	0.596	<0.0151	<0.0185	<0.069	1.15
Tb	<0.017	0.085	<0.060	<0.056	0.33	0.215
Dy	<0.18	0.331	<0.0105	<0.0082	0.071	1.04
Ho	<0.038	0.0425	<0.043	<0.056	0.29	0.163
Er	<0.055	0.116	<0.0084	0.0134	0.068	0.427
Tm	<0.024	0.0092	<0.032	<0.031	0.28	0.066
Yb	0.39	<0.048	<0.0067	<0.0088	0.126	0.394
Lu	<0.023	<0.0094	<0.049	0.072	0.38	0.0416
Hf	3.01	0.479	<0.0080	<0.0114	0.055	23.15
Ta	1054	0.0316	49.21	46.39	11.44	<0.0081
Pb	2.27	0.378	672.95	453.51	3.07	0.11
Pb	3.29	0.292	0.083	0.126	2.41	0.139
Pb	2.62	0.354	<0.044	0.069	2.11	0.104
Th	0.05	0.0348	0.04	0.074	2.27	0.0014
U	0.439	0.0041	0.0072	0.0066	8.92	0.0063
			0.076	0.0861	3.15	

Table 4

Major-element compositions of garnet minerals from Charneca Kimberlite

	CHAR_GRAOS_0001 C_GRT	CHAR_GRAOS_0001 B_GRT	CHAR_GRAOS_0002 C_GRT	CHAR_GRAOS_0002 B_GRT	CHAR_GRAOS_0003E4 C_GRT	CHAR_GRAOS_0003E4 B_GRT
SiO2	42.53	41.73	41.81	41.25	41.83	42.06
TiO2	0.22	0.21	0.32	0.20	0.21	0.29
Al2O3	22.86	22.73	22.68	22.65	22.58	22.40
Cr2O3	1.49	1.47	1.83	1.56	1.95	2.01
FeO(t)	9.30	9.38	9.70	9.46	8.81	8.70
MnO	0.39	0.40	0.38	0.40	0.41	0.41
MgO	19.44	19.66	19.25	19.45	19.51	19.72
CaO	4.07	4.22	4.16	3.95	4.34	4.40
Na2O	0.05	0.05	0.05	0.06	0.06	0.04
ZnO	0.00	0.00	0.00	0.00	0.00	0.00
NiO	0.00	0.00	0.00	0.00	0.00	0.00
	Reformatted oxide percentages based on 12 oxygens and with Fe2+/Fe3+ calculated assuming full occupancy					
SiO2	42.53	41.73	41.81	41.25	41.83	42.06
TiO2	0.22	0.21	0.32	0.20	0.21	0.29
Al2O3	22.86	22.73	22.68	22.65	22.58	22.40
Cr2O3	1.49	1.47	1.83	1.56	1.95	2.01
Fe2O3	0.00	0.05	0.00	0.00	0.00	0.00
FeO	9.30	9.33	9.70	9.46	8.81	8.70
MnO	0.39	0.40	0.38	0.40	0.41	0.41
MgO	19.44	19.66	19.25	19.45	19.51	19.72
CaO	4.07	4.22	4.16	3.95	4.34	4.40
Na2O	0.05	0.05	0.05	0.06	0.06	0.04
NiO	0.00	0.00	0.00	0.00	0.00	0.00
ZnO	0.00	0.00	0.00	0.00	0.00	0.00
Total	100.31	99.80	100.13	98.92	99.64	99.99

Number of ions on base of 12 oxygen

Si	3.012	2.985	2.983	2.977	2.989	2.997
Al iv	0.000	0.015	0.017	0.023	0.011	0.003
Al vi	1.913	1.902	1.893	1.905	1.894	1.879
Ti	0.012	0.011	0.017	0.011	0.011	0.015
Cr	0.083	0.083	0.103	0.089	0.110	0.113
Fe3+	0.000	0.003	0.000	0.000	0.000	0.000
Fe2+	0.578	0.558	0.596	0.578	0.547	0.529
Mn	0.024	0.024	0.023	0.024	0.025	0.025
Mg	2.053	2.097	2.047	2.093	2.078	2.094
Ca	0.309	0.323	0.318	0.305	0.332	0.336
Na	0.004	0.004	0.004	0.004	0.004	0.003
Ni	0.000	0.000	0.000	0.000	0.000	0.000
Zn	0.000	0.000	0.000	0.000	0.000	0.000
Total	7.984	8.002	7.998	8.005	7.997	7.993

Mol per cent end-members

Almandine	19.52	18.13	19.93	18.63	18.34	17.74
Andradite	0.00	0.15	0.00	0.00	0.00	0.00
Grossular	6.20	6.51	5.47	5.78	5.60	5.56
Pyrope	69.26	70.23	68.63	70.29	69.69	70.19
Spessartine	0.80	0.80	0.77	0.82	0.82	0.82
Uvarovite	4.22	4.18	5.19	4.49	5.54	5.69

Trace elements in garnetl minerals of Charneca Kimberlite

Concentrations in ppm (µg/g)

Li7	0.255	0.267	0.244	0.251	<0.162
Na23	377.6	373.34	424.11	429.05	291.32
P31	63.91	61.17	69.49	62.81	40.51
Sc45	66.99	71.92	70.8	68.06	92.82
Ti49	1551.79	1652.02	1805.54	1719.78	1633.99
V51	167.26	176.9	178.28	171.64	256.41
Co59	45.1	46.25	48.66	45.35	47.71
Ni62	32.56	33.04	33.14	29.48	31.48
Cu65	0.59	<0.26	0.55	0.34	0.67

Zn66	18.83	18.83	20.11	18.67	18.64
Ga71	11.87	12.07	12.34	10.86	10.81
Rb85	<0.045	<0.043	<0.046	<0.046	<0.049
Sr88	0.0207	0.0391	0.0271	0.0273	0.0342
Y89	15.48	15.73	16.12	15.25	15.71
Zr90	10.29	10.66	11.06	10.26	10.67
Nb93	0.0093	0.0144	0.0071	<0.0060	0.0389
Sn118	0.494	0.801	0.95	0.58	0.92
Sb121	<0.059	<0.064	<0.061	<0.061	<0.061
Cs133	<0.0101	<0.0135	<0.0095	<0.0085	<0.0072
Ba137	<0.033	<0.030	<0.033	<0.036	<0.034
La139	<0.0047	<0.0048	<0.0040	<0.0050	<0.0064
Ce140	0.0103	0.0171	0.0053	0.0079	0.0202
Pr141	0.0047	0.0078	<0.0029	0.0034	0.0114
Nd146	0.111	0.121	0.059	0.083	0.155
Sm149	0.196	0.261	0.314	0.305	0.345
Eu151	0.195	0.197	0.23	0.218	0.245
Gd157	0.936	0.782	1.01	0.874	1.07
Tb159	0.252	0.293	0.278	0.274	0.301
Dy161	2.37	2.46	2.34	2.33	2.31
Ho165	0.607	0.62	0.621	0.611	0.632
Er166	1.89	2.04	1.95	1.77	1.97
Tm169	0.287	0.318	0.322	0.288	0.342
Yb172	2.31	2.45	2.33	2.31	2.56
Lu175	0.321	0.355	0.348	0.304	0.35
Hf179	0.209	0.212	0.239	0.192	0.335
Ta181	0.0042	0.0039	<0.0030	<0.0039	0.0051
Pb206	0.05	0.075	0.045	0.071	0.164
Pb207	0.073	0.08	<0.0167	0.112	<0.026
Pb208	0.0475	0.068	0.0296	0.068	0.057
Th232	0.0021	0.00164	<0.00	<0.00200	0.0028
U238	0.0067	0.0059	0.00104	0.00053	0.0044

	CHAR_GRAOS_0003E4B_GRT	CHAR_GRAOS_0003E4C_GRT	CHAR_GRAOS_0005C_GRT	CHAR_GRAOS_0005B_GRT	CHAR_GRAOS_0006C_GRT	CHAR_GRAOS_0006B_GRT
SiO2	41.50	41.94	41.84	41.64	41.62	41.28
TiO2	0.23	0.22	0.24	0.25	0.33	0.38
Al2O3	22.38	22.33	22.44	22.39	22.63	22.46
Cr2O3	2.06	1.95	1.92	1.96	1.82	1.78
FeO(t)	8.81	8.59	8.85	8.66	8.53	8.52
MnO	0.43	0.43	0.43	0.42	0.43	0.44
MgO	19.60	19.49	19.56	19.49	19.93	19.78
CaO	4.54	4.53	4.43	4.52	4.35	4.44
Na2O	0.04		0.06	0.05	0.06	0.06
ZnO	0.00	0.00	0.00	0.00	0.00	0.00
NiO	0.00	0.00	0.00	0.00	0.00	0.00
SiO2	41.50	41.94	41.84	41.64	41.62	41.28
TiO2	0.23	0.22	0.24	0.25	0.33	0.38
Al2O3	22.38	22.33	22.44	22.39	22.63	22.46
Cr2O3	2.06	1.95	1.92	1.96	1.82	1.78
Fe2O3	0.00	0.00	0.00	0.00	0.00	0.02
FeO	8.81	8.59	8.85	8.66	8.53	8.50
MnO	0.43	0.43	0.43	0.42	0.43	0.44
MgO	19.60	19.49	19.56	19.49	19.93	19.78
CaO	4.54	4.53	4.43	4.52	4.35	4.44
Na2O	0.04	0.00	0.06	0.05	0.06	0.06
NiO	0.00	0.00	0.00	0.00	0.00	0.00
ZnO	0.00	0.00	0.00	0.00	0.00	0.00
Total	99.55	99.48	99.72	99.33	99.64	99.08

Si	2.978	3.002	2.992	2.988	2.975	2.972
Al iv	0.022	0.000	0.008	0.012	0.025	0.028
Al vi	1.872	1.886	1.885	1.884	1.883	1.877
Ti	0.013	0.012	0.013	0.013	0.018	0.020
Cr	0.117	0.110	0.109	0.111	0.103	0.101
Fe3+	0.000	0.000	0.000	0.000	0.000	0.001
Fe2+	0.531	0.528	0.538	0.531	0.515	0.512
Mn	0.026	0.026	0.026	0.025	0.026	0.027
Mg	2.097	2.080	2.085	2.085	2.124	2.123
Ca	0.349	0.347	0.339	0.348	0.333	0.342
Na	0.003	0.000	0.004	0.003	0.004	0.004
Ni	0.000	0.000	0.000	0.000	0.000	0.000
Zn	0.000	0.000	0.000	0.000	0.000	0.000
Total	8.004	7.991	7.996	7.998	8.003	8.004

Almandine	16.99	17.71	18.01	17.75	16.55	16.14
Andradite	0.00	0.00	0.00	0.00	0.00	0.04
Grossular	5.83	6.10	5.91	6.05	6.01	6.37
Pyrope	70.40	69.76	69.76	69.77	71.38	71.43
Spessartine	0.88	0.88	0.88	0.85	0.87	0.91
Uvarovite	5.89	5.55	5.45	5.58	5.19	5.11

Concentrations in ppm (µg/g)						
Li7	<0.165			0.291	<0.160	<0.170
Na23	289.81			447.17	364.06	418.48
P31	37.93			62.55	60.6	67.9
Sc45	79.62			73.46	76.21	76.28
Ti49	1518.04			1859.83	1760.15	1917.58
V51	247.98			210.37	206.02	194.27
Co59	45.38			44.95	43.27	51.98
Ni62	29.65			28.99	32.58	32.41
Cu65	0.51			<0.23	0.71	0.52

Zn66	14.64	16.26	14.22	20.89
Ga71	10.29	11.19	10.34	12.57
Rb85	<0.046	<0.048	<0.049	<0.050
Sr88	0.0284	0.035	0.0525	0.0274
Y89	14.77	15.56	13.83	17.78
Zr90	9.92	14.15	11.75	13.91
Nb93	0.0502	0.0143	<0.0073	<0.0072
Sn118	0.69	0.98	0.96	1.03
Sb121	0.064	<0.065	<0.059	<0.065
Cs133	<0.0070	<0.0098	<0.0074	<0.0103
Ba137	<0.041	<0.031	<0.038	0.038
La139	0.0066	<0.0054	<0.0031	0.0041
Ce140	0.0223	0.0186	0.0281	0.0125
Pr141	0.011	0.0102	0.0086	<0.0051
Nd146	0.187	0.159	0.133	0.131
Sm149	0.325	0.288	0.279	0.35
Eu151	0.219	0.225	0.18	0.247
Gd157	0.957	0.99	0.89	1.13
Tb159	0.26	0.306	0.245	0.332
Dy161	2.52	2.64	2.09	2.57
Ho165	0.604	0.671	0.583	0.703
Er166	1.95	1.88	1.64	2.03
Tm169	0.316	0.298	0.249	0.289
Yb172	2.41	2.44	2.19	2.78
Lu175	0.387	0.362	0.283	0.364
Hf179	0.335	0.318	0.212	0.25
Ta181	0.0059	<0.0031	<0.0031	<0.0033
Pb206	0.094	0.08	0.123	0.078
Pb207	0.051	0.062	0.038	0.08
Pb208	0.064	0.081	0.058	0.088
Th232	0.004	0.00088	0.0018	0.00056
U238	0.0046	0.0031	0.0061	0.003

	CHAR_GRAOS_0007 C_GRT	CHAR_GRAOS_0007 B_GRT	CHAR_GRAOS_0010 C_GRT	CHAR_GRAOS_0010 B_GRT	CHAR_GRAOS_0011 C_GRT	CHAR_GRAOS_0011 B_GRT
SiO2	42.02	41.09	41.67	41.89	41.64	41.49
TiO2	0.28	0.24	0.36	0.40	0.41	0.38
Al2O3	22.85	22.62	22.46	22.62	22.46	22.35
Cr2O3	1.56	1.56	1.75	1.67	1.73	1.77
FeO(t)	9.80	9.49	9.74	9.63	9.53	9.64
MnO	0.42	0.39	0.42	0.43	0.42	0.40
MgO	19.21	19.57	19.18	19.33	18.99	19.22
CaO	4.10	4.05	4.30	4.22	4.25	4.26
Na2O	0.07	0.07				
ZnO	0.00	0.00	0.00	0.00	0.00	0.00
NiO	0.00	0.00	0.00	0.00	0.00	0.00
SiO2	42.02	41.09	41.67	41.89	41.64	41.49
TiO2	0.28	0.24	0.36	0.40	0.41	0.38
Al2O3	22.85	22.62	22.46	22.62	22.46	22.35
Cr2O3	1.56	1.56	1.75	1.67	1.73	1.77
Fe2O3	0.00	0.10	0.00	0.00	0.00	0.00
FeO	9.80	9.41	9.74	9.63	9.53	9.64
MnO	0.42	0.39	0.42	0.43	0.42	0.40
MgO	19.21	19.57	19.18	19.33	18.99	19.22
CaO	4.10	4.05	4.30	4.22	4.25	4.26
Na2O	0.07	0.07	0.00	0.00	0.00	0.00
NiO	0.00	0.00	0.00	0.00	0.00	0.00
ZnO	0.00	0.00	0.00	0.00	0.00	0.00
Total	100.24	99.03	99.88	100.19	99.42	99.51

Si	2.991	2.967	2.987	2.988	2.990	2.985
Al iv	0.009	0.033	0.013	0.012	0.010	0.015
Al vi	1.912	1.892	1.885	1.891	1.894	1.880
Ti	0.015	0.013	0.019	0.022	0.022	0.020
Cr	0.088	0.089	0.099	0.094	0.098	0.101
Fe3+	0.000	0.005	0.000	0.000	0.000	0.000
Fe2+	0.603	0.568	0.588	0.584	0.592	0.582
Mn	0.025	0.024	0.026	0.026	0.025	0.025
Mg	2.039	2.106	2.049	2.055	2.033	2.061
Ca	0.313	0.313	0.330	0.323	0.327	0.328
Na	0.004	0.005	0.000	0.000	0.000	0.000
Ni	0.000	0.000	0.000	0.000	0.000	0.000
Zn	0.000	0.000	0.000	0.000	0.000	0.000
Total	7.994	8.011	7.997	7.994	7.991	7.997

Almandine	20.24	17.64	19.47	19.53	19.88	19.12
Andradite	0.00	0.26	0.00	0.00	0.00	0.00
Grossular	6.08	5.80	6.08	6.07	6.04	5.94
Pyrope	68.42	71.00	68.61	68.80	68.28	69.06
Spessartine	0.84	0.80	0.86	0.87	0.85	0.83
Uvarovite	4.42	4.50	4.98	4.73	4.95	5.06

Li7	<0.152	0.334	0.303
Na23	457.36	484.78	506.81
P31	67.58	70.77	69.09
Sc45	70.64	65.58	66.76
Ti49	2068.22	2285.4	2271.18
V51	194.13	215.33	215.21
Co59	49.81	49.26	52.88
Ni62	34.28	37.81	35.31
Cu65	0.73	0.57	0.56

Zn66	21.05	19.88	21.37
Ga71	12.72	12.37	13.2
Rb85	<0.045	<0.048	<0.051
Sr88	0.0301	0.0386	0.0355
Y89	18.04	15.73	16.23
Zr90	15.34	16.59	16.41
Nb93	<0.0072	<0.0083	<0.0070
Sn118	0.97	0.95	1
Sb121	<0.057	<0.061	<0.064
Cs133	<0.0080	<0.0084	<0.0090
Ba137	<0.028	<0.023	<0.040
La139	<0.0040	<0.0064	<0.0040
Ce140	0.0115	0.0178	0.0187
Pr141	0.0111	<0.0040	0.0083
Nd146	0.149	0.146	0.131
Sm149	0.293	0.398	0.389
Eu151	0.218	0.279	0.331
Gd157	1.2	1.22	1.15
Tb159	0.331	0.3	0.297
Dy161	2.57	2.5	2.62
Ho165	0.646	0.612	0.604
Er166	2.01	1.81	1.94
Tm169	0.316	0.268	0.294
Yb172	2.42	2.1	2.3
Lu175	0.34	0.319	0.323
Hf179	0.333	0.398	0.357
Ta181	<0.0031	0.0055	<0.0038
Pb206	0.072	0.108	0.043
Pb207	0.054	0.042	0.087
Pb208	0.061	0.057	0.361
Th232	0.0023	0.0017	0.0022
U238	0.0025	0.0025	0.004

	CHAR_3_0001 C_GRT	CHAR_3_0001 B_GRT	CHAR_3_0002 C_GRT	CHAR_3_0002 B_GRT	CHAR_3_0003 C_GRT	CHAR_3_0003 B_GRT	CHAR_3_0004 C_GRT	CHAR_3_0004 B_GRT	CHAR_3_0005 C_GRT	CHAR_3_0005 B_GRT
SiO2	41.34	42.40	41.80	42.31	41.45	41.53	41.24	41.87	41.21	40.16
TiO2	1.16	1.25	1.13	1.12	1.20	1.26	0.98	0.98	1.31	1.22
Al2O3	21.18	21.39	21.98	22.28	21.02	20.76	20.54	21.12	20.76	20.05
Cr2O3	1.43	1.43	0.43	0.40	1.85	1.61	2.67	2.82	1.71	1.63
FeO(t)	9.54	10.25	10.44	10.45	9.46	9.38	6.96	7.67	9.49	8.09
MnO	0.31	0.32	0.36	0.36	0.33	0.29	0.29	0.31	0.32	0.31
MgO	18.68	18.05	18.19	18.15	18.73	18.66	20.35	19.88	18.65	19.29
CaO	5.08	5.02	4.89	5.12	5.14	5.04	4.64	4.74	5.04	4.86
Na2O	0.08		0.10		0.08		0.08		0.08	
ZnO	0.00	0.00	0.00	0.00	0.00	0.00	0.00	0.00	0.00	0.00
NiO	0.01	0.00	0.01	0.00	0.02	0.00	0.02	0.00	0.02	0.00
SiO2	41.34	42.40	41.80	42.31	41.45	41.53	41.24	41.87	41.21	40.16
TiO2	1.16	1.25	1.13	1.12	1.20	1.26	0.98	0.98	1.31	1.22
Al2O3	21.18	21.39	21.98	22.28	21.02	20.76	20.54	21.12	20.76	20.05
Cr2O3	1.43	1.43	0.43	0.40	1.85	1.61	2.67	2.82	1.71	1.63
Fe2O3	0.65	0.05	0.40	0.22	0.59	0.63	0.50	0.00	0.73	1.18
FeO	8.95	10.21	10.08	10.25	8.92	8.81	6.51	7.67	8.84	7.03
MnO	0.31	0.32	0.36	0.36	0.33	0.29	0.29	0.31	0.32	0.31
MgO	18.68	18.05	18.19	18.15	18.73	18.66	20.35	19.88	18.65	19.29
CaO	5.08	5.02	4.89	5.12	5.14	5.04	4.64	4.74	5.04	4.86
Na2O	0.08	0.00	0.10	0.00	0.08	0.00	0.08	0.00	0.08	0.00
NiO	0.01	0.00	0.01	0.00	0.02	0.00	0.02	0.00	0.02	0.00
ZnO	0.00	0.00	0.00	0.00	0.00	0.00	0.00	0.00	0.00	0.00
Total	98.81	100.11	99.27	100.21	99.25	98.59	97.74	99.39	98.58	95.73

Si	3.000	3.041	3.018	3.025	2.998	3.018	2.999	3.003	3.000	2.994
Al iv	0.000	0.000	0.000	0.000	0.002	0.000	0.001	0.000	0.000	0.006
Al vi	1.814	1.808	1.872	1.879	1.792	1.781	1.762	1.786	1.785	1.760
Ti	0.063	0.067	0.061	0.060	0.065	0.069	0.054	0.053	0.072	0.068
Cr	0.082	0.081	0.024	0.023	0.106	0.093	0.154	0.160	0.098	0.096
Fe3+	0.036	0.002	0.022	0.012	0.032	0.035	0.027	0.000	0.040	0.066
Fe2+	0.543	0.612	0.609	0.613	0.540	0.536	0.396	0.462	0.538	0.438
Mn	0.019	0.019	0.022	0.022	0.020	0.018	0.018	0.019	0.020	0.020
Mg	2.021	1.930	1.958	1.934	2.019	2.022	2.206	2.125	2.024	2.144
Ca	0.395	0.386	0.378	0.392	0.398	0.393	0.362	0.364	0.393	0.388
Na	0.005	0.000	0.007	0.000	0.006	0.000	0.005	0.000	0.006	0.000
Ni	0.001	0.000	0.000	0.000	0.001	0.000	0.001	0.000	0.001	0.000
Zn	0.000	0.000	0.000	0.000	0.000	0.000	0.000	0.000	0.000	0.000
Total	7.975	7.946	7.964	7.960	7.974	7.963	7.978	7.972	7.971	7.981

Almandine	15.86	17.72	17.98	18.14	15.80	14.93	11.23	14.04	15.37	11.59
Andradite	1.85	0.13	1.13	0.62	1.67	1.82	1.41	0.00	2.07	3.44
Grossular	7.54	9.18	10.75	11.85	6.61	7.05	3.10	4.26	6.46	5.02
Pyrope	69.82	68.00	68.09	67.43	69.75	70.73	75.75	72.84	70.29	74.28
Spessartine	0.67	0.68	0.77	0.76	0.69	0.61	0.61	0.64	0.69	0.68
Uvarovite	4.26	4.29	1.28	1.20	5.48	4.85	7.91	8.22	5.13	4.99

Li7	<0.25	0.48	<0.58	<0.29	<0.28
Na23	583.44	765.9	577.15	555.65	604.01
P31	133.11	144.81	129.95	150.01	125.92
Sc45	89.42	77.59	83.61	89.2	84.95
Ti49	7997.4	7674.05	7540.75	6840.75	8555.34
V51	326.36	295.96	320.59	260.31	358.72
Co59	60.81	53.02	56.03	50.63	61.76
Ni62	117.47	43.43	122.16	141.11	120.94
Cu65	1.53	1.06	2.36	1.41	1.23

Zn66	30.45	38.54	31.92	26.43	32.01
Ga71	16.02	28.67	14.38	12.33	16.01
Rb85	<0.059	<0.064	<0.154	0.326	<0.066
Sr88	2.42	1.131	1.36	1.84	1.272
Y89	26.48	33.93	22.73	19.33	23.84
Zr90	73.21	161.35	70.16	74.83	72.96
Nb93	0.341	0.177	0.126	0.264	0.178
Sn118	1.51	1.59	1.5	1.27	1.47
Sb121	<0.091	<0.094	<0.20	<0.101	<0.093
Cs133	<0.0176	<0.0168	0.077	0.036	<0.0169
Ba137	0.488	<0.083	6.58	7.62	<0.061
La139	0.307	0.0758	0.136	0.145	0.064
Ce140	1.11	0.994	0.869	0.987	0.901
Pr141	0.299	0.338	0.268	0.292	0.268
Nd146	2.5	3.5	2.1	2.66	2.74
Sm149	1.44	2.8	1.58	1.56	1.68
Eu151	0.835	1.472	0.803	0.839	0.802
Gd157	2.87	4.31	2.74	2.46	2.96
Tb159	0.602	0.999	0.685	0.564	0.562
Dy161	4.26	7	4.04	3.43	4.31
Ho165	1.008	1.542	0.969	0.805	0.976
Er166	3.08	4.29	2.89	2.09	2.83
Tm169	0.443	0.612	0.463	0.32	0.402
Yb172	3.65	4.24	3.05	2.41	2.86
Lu175	0.521	0.617	0.516	0.371	0.384
Hf179	1.97	4.65	1.78	1.98	1.78
Ta181	0.0249	0.029	0.0225	0.0251	0.0107
Pb206	0.109	0.138	0.366	0.16	0.127
Pb207	0.181	0.117	0.45	0.106	0.098
Pb208	0.15	0.151	0.385	0.164	0.172
Th232	0.0248	0.0149	0.0099	0.058	0.0087
U238	0.0232	0.0163	0.003	0.0213	0.0109

Table 5

Major-element compositions of garnet minerals from Grota do Cedro Kimberlite

	SP_GC11_0002 C_GRT ESQUERDA	SP_GC11_0002 B_GRT ESQUERDA	SP_GC11_0002 C_GRT DIREITA	SP_GC11_0002 B_GRT DIREITA	SP_GC11_00: C_GRT	SP_GC11_00: B_GRT	SP_GC11_00: C_GRT	SP_GC11_00: B_GRT	SP_GC11_00: C_GRT	SP_GC11_001 B_GRT
SiO2	38.73	38.52	38.12	38.10	39.11	38.60	41.40	41.95	39.09	38.64
TiO2	0.06	0.02	0.00	0.03	0.07	0.06	0.01	0.02	0.06	0.02
Al2O3	22.76	22.66	22.23	22.26	22.23	22.11	19.54	21.65	22.67	22.52
Cr2O3	0.02	0.00	0.00	0.02	0.01	0.04	6.18	3.63	0.08	0.05
FeO	27.83	27.38	31.70	31.33	24.48	24.21	7.78	7.84	26.36	26.33
MnO	0.51	0.53	0.32	0.33	0.62	0.57	0.51	0.48	0.49	0.52
MgO	8.74	8.50	6.24	6.16	8.18	8.32	18.15	19.46	9.58	9.61
CaO	1.87	1.98	2.25	2.26	5.15	5.07	6.16	4.66	1.78	1.75
Reformatted oxide percentages based on 12 oxygens and with Fe2+/Fe3+ calculated assuming full occupancy										
SiO2	38.73	38.52	38.12	38.10	39.11	38.60	41.40	41.95	39.09	38.64
TiO2	0.06	0.02	0.00	0.03	0.07	0.06	0.01	0.02	0.06	0.02
Al2O3	22.76	22.66	22.23	22.26	22.23	22.11	19.54	21.65	22.67	22.52
Cr2O3	0.02	0.00	0.00	0.02	0.01	0.04	6.18	3.63	0.08	0.05
Fe2O3	0.00	0.00	0.00	0.00	0.00	0.00	0.00	0.00	0.00	0.00
FeO	27.83	27.38	31.70	31.33	24.48	24.21	7.78	7.84	26.36	26.33
MnO	0.51	0.53	0.32	0.33	0.62	0.57	0.51	0.48	0.49	0.52
MgO	8.74	8.50	6.24	6.16	8.18	8.32	18.15	19.46	9.58	9.61
CaO	1.87	1.98	2.25	2.26	5.15	5.07	6.16	4.66	1.78	1.75
NiO	0.00	0.00	0.00	0.00	0.00	0.00	0.00	0.00	0.00	0.00
ZnO	0.00	0.00	0.00	0.00	0.00	0.00	0.00	0.00	0.00	0.00
Total	100.52	99.59	100.86	100.49	99.85	98.98	99.73	99.69	100.11	99.44
Number of ions on base of 12 oxygen					**Number of ions on base of 12 oxygen**					
Si	2.961	2.966	2.967	2.968	2.997	2.985	2.997	2.996	2.977	2.969
Al iv	0.039	0.034	0.033	0.032	0.003	0.015	0.003	0.004	0.023	0.031
Al vi	2.017	2.031	2.008	2.016	2.009	2.003	1.669	1.824	2.018	2.013
Ti	0.004	0.001	0.000	0.002	0.004	0.004	0.001	0.001	0.004	0.001
Cr	0.001	0.000	0.000	0.001	0.001	0.003	0.354	0.205	0.005	0.003
Fe3+	0.000	0.000	0.000	0.000	0.000	0.000	0.000	0.000	0.000	0.000

Fe2+	1.809	1.806	2.074	2.067	1.586	1.578	0.504	0.509	1.714	1.716
Mn	0.033	0.034	0.021	0.022	0.040	0.037	0.031	0.029	0.032	0.034
Mg	0.996	0.976	0.724	0.715	0.935	0.959	1.959	2.071	1.088	1.101
Ca	0.153	0.163	0.188	0.189	0.423	0.420	0.478	0.357	0.145	0.144
Ni	0.000	0.000	0.000	0.000	0.000	0.000	0.000	0.000	0.000	0.000
Zn	0.000	0.000	0.000	0.000	0.000	0.000	0.000	0.000	0.000	0.000
Total	8.014	8.011	8.015	8.012	7.997	8.004	7.996	7.996	8.005	8.012
Mol per cent end-members				**Mol per cent end-members**					**Mol per cent e**	
Almandine	60.08	60.44	68.56	68.81	53.16	52.55	16.96	17.16	57.53	56.94
Andradite	0.00	0.00	0.00	0.00	0.00	0.00	0.00	0.00	0.00	0.00
Grossular	5.11	5.50	6.32	6.30	14.14	13.95	0.00	1.66	4.64	4.69
Pyrope	33.64	32.89	24.40	24.10	31.32	32.13	65.91	69.84	36.53	37.07
Spessartine	1.11	1.16	0.71	0.73	1.36	1.25	1.05	0.98	1.06	1.14
Uvarovite	0.07	0.01	0.00	0.06	0.03	0.13	16.08	10.36	0.24	0.16

Table 5 (continuation)

l3	SP_GC11_00: C_GRT	SP_GC11_00: B_GRT	SP_GC11_00: C_GRT	SP_GC11_00: B_GRT	SP_GC11_00: C_GRT	SP_GC11_00: B_GRT	SP_GC11_00: C_GRT	SP_GC11_00: B_GRT	GC 11_0012 C_GRT	GC 11_0012 B_GRT	GC 11_0016 C_GRT
SiO2	27.61	28.22	41.36	41.48	41.43	41.77	41.01	40.56	41.69	41.29	39.18
TiO2	0.68	0.66	0.10	0.15	0.16	0.09	0.06	0.04	0.05	0.10	0.06
Al2O3	55.58	56.03	20.83	20.93	21.20	21.44	19.33	19.32	20.84	20.93	22.31
Cr2O3	0.04	0.03	4.44	4.42	4.07	3.76	6.41	6.42	4.37	4.50	0.04
FeO	12.91	12.51	8.69	8.62	7.86	7.82	8.80	8.44	8.96	9.06	26.84
MnO	0.12	0.11	0.51	0.51	0.45	0.49	0.59	0.62	0.43	0.47	0.53
MgO	0.91	0.85	18.08	18.22	18.95	19.77	16.98	17.03	17.69	17.72	9.66
CaO	0.01	0.02	5.61	5.57	5.39	4.51	6.88	6.82	5.98	5.97	1.71
	Reformatted oxide percentages based on 12 oxygens and with Fe2+/Fe3+ calculated assuming full occupancy										
SiO2	27.61	28.22	41.36	41.48	41.43	41.77	41.01	40.56	41.69	41.29	39.18
TiO2	0.68	0.66	0.10	0.15	0.16	0.09	0.06	0.04	0.05	0.10	0.06
Al2O3	55.58	56.03	20.83	20.93	21.20	21.44	19.33	19.32	20.84	20.93	22.31
Cr2O3	0.04	0.03	4.44	4.42	4.07	3.76	6.41	6.42	4.37	4.50	0.04
Fe2O3	0.00	0.00	0.00	0.00	0.00	0.00	0.00	0.00	0.00	0.00	0.00
FeO	12.91	12.51	8.69	8.62	7.86	7.82	8.80	8.44	8.96	9.06	26.84
MnO	0.12	0.11	0.51	0.51	0.45	0.49	0.59	0.62	0.43	0.47	0.53
MgO	0.91	0.85	18.08	18.22	18.95	19.77	16.98	17.03	17.69	17.72	9.66
CaO	0.01	0.02	5.61	5.57	5.39	4.51	6.88	6.82	5.98	5.97	1.71
NiO	0.00	0.00	0.00	0.00	0.00	0.00	0.00	0.00	0.00	0.00	0.00
ZnO	0.00	0.00	0.00	0.00	0.00	0.00	0.00	0.00	0.00	0.00	0.00
Total	97.86	98.41	99.62	99.90	99.51	99.65	100.07	99.25	100.01	100.04	100.33
	Number of ions on base of 12 oxygen										
Si	1.735	1.755	2.988	2.986	2.980	2.989	2.986	2.974	3.002	2.979	2.991
Al iv	1.265	1.245	0.012	0.014	0.020	0.011	0.014	0.026	0.000	0.021	0.009
Al vi	3.447	3.462	1.767	1.767	1.782	1.802	1.648	1.648	1.774	1.764	2.000
Ti	0.032	0.031	0.005	0.008	0.009	0.005	0.004	0.002	0.003	0.005	0.004
Cr	0.002	0.001	0.254	0.252	0.231	0.213	0.369	0.372	0.249	0.257	0.003
Fe3+	0.000	0.000	0.000	0.000	0.000	0.000	0.000	0.000	0.000	0.000	0.000

Fe2+	2.196	2.182	0.560	0.555	0.504	0.495	0.564	0.549	0.578	0.582	1.722
Mn	0.006	0.006	0.031	0.031	0.027	0.030	0.037	0.039	0.026	0.029	0.034
Mg	0.085	0.079	1.947	1.955	2.032	2.109	1.843	1.862	1.899	1.906	1.099
Ca	0.000	0.001	0.434	0.430	0.415	0.346	0.537	0.536	0.461	0.461	0.140
Ni	0.000	0.000	0.000	0.000	0.000	0.000	0.000	0.000	0.000	0.000	0.000
Zn	0.000	0.000	0.000	0.000	0.000	0.000	0.000	0.000	0.000	0.000	0.000
Total	8.770	8.761	7.998	7.998	8.001	7.999	8.001	8.007	7.992	8.003	8.002
nd-members											**Mol per cent e**
Almandine	94.70	95.13	18.84	18.70	16.91	16.61	18.94	18.10	19.49	19.53	57.43
Andradite	0.00	0.00	0.00	0.00	0.00	0.00	0.00	0.00	0.00	0.00	0.00
Grossular	0.00	0.00	1.81	1.76	2.29	0.90	0.00	0.00	2.98	2.57	4.55
Pyrope	4.92	4.49	65.50	65.80	68.22	70.79	61.83	62.59	64.06	64.00	36.75
Spessartine	0.36	0.32	1.06	1.04	0.92	1.00	1.23	1.30	0.88	0.97	1.14
Uvarovite	0.03	0.07	12.80	12.70	11.66	10.71	18.01	18.02	12.59	12.93	0.13

Table 5 (continuation)

	GC 11_0016 B_GRT	GC 11_0019 C_GRT	GC 11_0019 B_GRT	GC 11_0021 C_GRT	GC 11_0021 B_GRT	GC 11_0026 C_GRT	GC 11_0026 B_GRT
SiO2	39.13	28.44	27.44	39.51	40.97	40.99	41.53
TiO2	0.02	0.59	0.75	0.05	0.04	0.05	0.08
Al2O3	22.55	55.60	54.84	19.37	19.84	20.18	20.27
Cr2O3	0.05	0.02	0.02	5.80	5.74	5.29	5.20
FeO	27.04	12.03	13.06	8.33	8.59	8.92	8.70
MnO	0.51	0.10	0.11	0.49	0.49	0.52	0.51
MgO	9.51	0.98	0.86	17.64	17.52	17.71	17.39
CaO	1.82	0.03	0.02	6.49	6.55	6.26	6.40
SiO2	39.13	28.44	27.44	39.51	40.97	40.99	41.53
TiO2	0.02	0.59	0.75	0.05	0.04	0.05	0.08
Al2O3	22.55	55.60	54.84	19.37	19.84	20.18	20.27
Cr2O3	0.05	0.02	0.02	5.80	5.74	5.29	5.20
Fe2O3	0.00	0.00	0.00	0.08	0.00	0.00	0.00
FeO	27.04	12.03	13.06	8.26	8.59	8.92	8.70
MnO	0.51	0.10	0.11	0.49	0.49	0.52	0.51
MgO	9.51	0.98	0.86	17.64	17.52	17.71	17.39
CaO	1.82	0.03	0.02	6.49	6.55	6.26	6.40
NiO	0.00	0.00	0.00	0.00	0.00	0.00	0.00
ZnO	0.00	0.00	0.00	0.00	0.00	0.00	0.00
Total	100.63	97.79	97.10	97.68	99.74	99.92	100.08
		Number of ions on base of 12 oxygen					
Si	2.980	1.775	1.741	2.947	2.981	2.977	2.998
Al iv	0.020	1.225	1.259	0.053	0.019	0.023	0.002
Al vi	2.006	3.463	3.434	1.650	1.685	1.706	1.729
Ti	0.001	0.028	0.036	0.003	0.002	0.003	0.004
Cr	0.003	0.001	0.001	0.342	0.330	0.304	0.297
Fe3+	0.000	0.000	0.000	0.004	0.000	0.000	0.000

Fe2+	1.736	2.160	2.202	0.515	0.547	0.559	0.566
Mn	0.033	0.005	0.006	0.031	0.030	0.032	0.031
Mg	1.080	0.091	0.081	1.961	1.900	1.917	1.871
Ca	0.149	0.002	0.001	0.519	0.511	0.487	0.495
Ni	0.000	0.000	0.000	0.000	0.000	0.000	0.000
Zn	0.000	0.000	0.000	0.000	0.000	0.000	0.000
Total	8.008	8.750	8.761	8.026	8.005	8.008	7.993
nd-members							
Almandine	57.69	94.44	94.91	14.79	18.11	18.15	19.10
Andradite	0.00	0.00	0.00	0.19	0.00	0.00	0.00
Grossular	4.82	0.02	0.00	0.00	0.51	1.06	1.68
Pyrope	36.23	5.15	4.67	66.56	63.75	64.41	63.15
Spessartine	1.10	0.30	0.34	1.05	1.02	1.08	1.05
Uvarovite	0.16	0.08	0.08	17.41	16.62	15.31	15.02

Table 6
Major-element compositions of garnet minerals from Régis Kimberlite

	regis-5_0001 GRT.C	regis-5_0001 GRT.B	regis-9_0001 GRT.C	regis-9_0001 GRT.B	regis-12_0001 GRT.C	regis-12_0001 GRT.B
SiO2	41.11	40.99	40.18	40.94	37.30	36.36
TiO2	0.04	0.04	0.04	0.17	0.02	0.04
Al2O3	21.99	21.87	21.29	20.20	21.90	20.86
Cr2O3	3.20	3.21	4.10	4.62	0.08	0.09
FeO	8.81	9.32	8.29	6.38	32.74	32.40
MnO	0.46	0.49	0.48	0.25	1.38	1.37
MgO	19.91	20.15	19.92	21.68	5.55	5.87
CaO	5.21	5.20	5.23	5.03	2.21	2.04
Na2O	0.02	0.02	0.02	0.02	0.01	0.01
ZnO	0.00	0.00	0.00	0.00	0.02	0.02
NiO	0.00	0.00	0.01	0.01	0.00	0.00
	Reformatted oxide percentages based on 12 oxygens and with Fe2+/Fe3+ calculated assuming full occupancy					
SiO2	41.11	40.99	40.18	40.94	37.30	36.36
TiO2	0.04	0.04	0.04	0.17	0.02	0.04
Al2O3	21.99	21.87	21.29	20.20	21.90	20.86
Cr2O3	3.20	3.21	4.10	4.62	0.08	0.09
Fe2O3	0.53	1.07	0.59	1.18	0.55	1.36
FeO	8.33	8.36	7.76	5.32	32.25	31.17
MnO	0.46	0.49	0.48	0.25	1.38	1.37
MgO	19.91	20.15	19.92	21.68	5.55	5.87
CaO	5.21	5.20	5.23	5.03	2.21	2.04
Na2O	0.018	0.015	0.021	0.015	0.008	0.007
NiO	0.00	0.00	0.01	0.01	0.00	0.00
ZnO	0.00	0.00	0.00	0.00	0.02	0.02
Total	100.81	101.40	99.62	99.42	101.26	99.18
Number of ions on base of 12 oxygen						
Si	2.933	2.915	2.908	2.941	2.928	2.919
Al iv	0.067	0.085	0.092	0.059	0.072	0.081
Al vi	1.785	1.753	1.727	1.656	1.957	1.900
Ti	0.002	0.002	0.002	0.009	0.001	0.002

Cr	0.181	0.180	0.235	0.262	0.005	0.005
Fe3+	0.029	0.057	0.032	0.064	0.032	0.082
Fe2+	0.497	0.497	0.470	0.320	2.117	2.093
Mn	0.028	0.030	0.029	0.016	0.092	0.093
Mg	2.118	2.136	2.149	2.322	0.650	0.702
Ca	0.398	0.396	0.406	0.387	0.186	0.175
Na	0.001	0.001	0.001	0.001	0.001	0.001
Ni	0.000	0.000	0.001	0.000	0.000	0.000
Zn	0.000	0.000	0.000	0.000	0.001	0.001
Total	8.038	8.053	8.051	8.037	8.042	8.055
Mol per cent end-members						
Almandine	13.28	12.11	11.15	7.37	68.34	66.73
Andradite	1.46	2.95	1.65	0.00	1.66	4.23
Grossular	2.89	1.36	0.20	0.00	4.43	1.51
Pyrope	72.20	73.28	73.90	78.94	22.18	24.07
Spessartine	0.94	1.02	1.00	0.53	3.13	3.19
Uvarovite	9.23	9.29	12.10	13.16	0.26	0.28
Trace elements in garnet minerals of Régis Kimberlite						
Concentrations in ppm (µg/g)						
Li7 ppm	<0.61	<0.64	<0.50	<0.51	15.57	11.36
Na23	130.19	113.83	152.27	110.87	60.86	54.56
P31	52.97	42.88	51.71	22.85	70.97	1190.42
Sc45	111.61	102.89	136.99	147.45	167.2	151.97
Ti49	253.59	233.25	419.91	227.14	148.82	152.34
V51	225.93	232.45	296.3	367.13	105.33	101.63
Cr52	24552.65	23851.38	34556.95	40139.91	536.77	498.68
Co59	50.75	51.5	51.81	59.51	34.94	30.26
Ni62	29.29	30.49	93.03	66.57	<2.50	2.56
Cu65	0.89	0.56	<0.42	0.48	0.5	0.62
Zn66	16.23	14.94	21.33	22.92	134.12	121.26
Ga71	7.12	7.53	7.15	9.51	12.12	10.5
Rb85	<0.123	<0.123	0.208	0.119	<0.084	<0.081
Sr88	0.396	0.536	4.61	1.05	0.092	1.84
Y89	6.93	6.56	7.07	5.41	610.8	543.49
Zr90	4.31	4.39	62.73	4.14	6.8	7.82
Nb93	0.141	0.048	0.83	0.85	<0.012	0.021
Sn118	1.19	0.9	1.32	0.92	0.42	0.64

Sb121	<0.153	<0.141	<0.26	<0.29	<0.118	0.136
Cs133	<0.028	<0.030	<0.020	<0.028	<0.026	<0.019
Ba137	0.131	0.246	1.02	<0.112	<0.082	0.17
La139	<0.0169	0.039	0.56	0.099	0.023	3.62
Ce140	0.145	0.108	1.77	0.89	<0.011	11.35
Pr141	0.048	0.0447	0.355	0.19	0.041	1.96
Nd146	0.393	0.415	2.51	0.95	0.64	33.16
Sm149	0.091	0.181	1.14	0.094	6.02	10.57
Eu151	0.11	0.075	0.359	<0.025	0.199	0.296
Gd157	0.383	0.351	0.83	0.165	24.87	28.07
Tb159	0.083	0.095	0.146	0.039	9.07	9.3
Dy161	0.779	0.832	0.93	0.465	87.13	80.63
Ho165	0.246	0.254	0.236	0.175	22.7	18.82
Er166	0.863	0.836	0.85	0.75	67.5	52.63
Tm169	0.13	0.155	0.134	0.126	9.96	7.61
Yb172	1.44	1.47	1.15	1.2	65.02	49.33
Lu175	0.219	0.181	0.247	0.23	8.03	6.01
Hf179	0.099	0.1	0.56	0.112	0.182	0.412
Ta181	0.0151	<0.0054	0.043	0.045	0.089	0.0203
Pb206	0.126	0.092	0.299	<0.053	0.274	0.38
Pb207	<0.066	0.166	0.288	0.062	0.161	0.213
Pb208	0.113	0.107	0.195	0.111	0.163	0.223
Th232	0.0049	0.0019	0.0495	0.0124	0.0105	0.06
U238	0.0257	0.0123	0.0214	0.0214	0.0047	0.13

Table 7

Major-element compositions of ilmenite minerals from Charneca Kimberlite

	CHAR_GRAOS_0013 C_ilmenita	CHAR_GRAOS_0013 B_ilmenita	CHAR_GRAOS_0014 C_ilmenita	CHAR_GRAOS_0014 B_ilmenita	CHAR_GRAOS_0015 C_ilmenita	CHAR_GRAOS_0015 B_ilmenita
SiO2	0.05	0.04	0.01	0.04	0.16	0.07
TiO2	50.40	49.35	48.93	52.35	50.57	49.97
Al2O3	0.10	0.10	0.07	0.33	1.08	0.97
FeO(T)	36.72	36.74	37.24	34.47	37.42	37.11
MnO	0.28	0.31	0.27	0.30	0.22	0.20
MgO	9.81	9.80	9.70	11.24	10.13	10.05
CaO	0.03	0.00	0.05	0.03	0.05	0.01
Na2O	0.02	0.02	0.00	0.03	0.05	0.01
K2O	0.00	0.00	0.00	0.01	0.00	0.00
Cr2O3	2.01	1.95	1.73	1.66	0.11	0.10
ZnO	0.00	0.01	0.03	0.01	0.02	0.05
Nb2O3	0.42	0.44	0.41	0.42	0.04	0.00
Sum:	99.84	98.77	98.45	100.89	99.85	98.53
Sum of Atomic mol pr	1.405	1.419	1.424	1.377	1.393	1.412
Number of ions on base of 3 oxygen						
Si	0.001	0.001	0.000	0.001	0.004	0.002
Ti	0.887	0.877	0.872	0.903	0.882	0.883
Al	0.003	0.003	0.002	0.009	0.029	0.027
Fe+3	0.179	0.199	0.215	0.148	0.196	0.201
Fe+2	0.540	0.527	0.523	0.513	0.530	0.528
Mn	0.006	0.006	0.005	0.006	0.004	0.004
Mg	0.342	0.345	0.343	0.384	0.350	0.352
Ca	0.001	0.000	0.001	0.001	0.001	0.000
Na	0.001	0.001	0.000	0.001	0.002	0.000
K	0.000	0.000	0.000	0.000	0.000	0.000
Cr	0.037	0.036	0.032	0.030	0.002	0.002

Zn	0.000	0.000	0.001	0.000	0.000	0.001
Nb	0.005	0.005	0.005	0.005	0.000	0.000
Total:	2.001	2.001	2.000	2.001	2.002	2.000

Trace elements in ilmenite minerals of Charneca Kimberlite

trations in ppm (µg/g

Li7	0.84	0.78	0.95	1.02	1.33	1.20
P31	2.05	<0.70	1.93	2.65	2.39	2.09
Sc45	22.25	17.98	26.36	28.10	16.85	15.63
V51	1853.09	1716.85	1838.34	2011.09	1684.70	1679.51
Co59	110.35	100.72	148.56	153.71	177.70	161.18
Ni60	693.98	539.65	727.37	719.18	501.72	454.65
Sr88	0.04	0.03	0.05	0.04	0.06	0.05
Y89	0.04	0.05	0.04	0.07	0.10	0.10
Zr91	558.04	455.64	596.38	655.72	253.40	236.09
Nb93	3057.34	2596.37	3809.66	4281.07	325.61	304.57
Sn118	23.70	18.30	28.42	30.89	8.77	8.17
Sb121	0.04	<0.0145	0.03	0.03	<0.0166	<0.0168
Ba137	0.04	0.07	0.06	0.10	0.05	0.09
La139	<0.00118	0.00	0.00	0.00	0.00	0.00
Ce140	0.00	0.01	0.02	0.01	0.03	0.02
Pr141	<0.00060	0.00	0.00	0.00	0.00	0.00
Nd143	0.03	0.02	0.02	0.02	0.05	0.04
Sm147	<0.0047	0.01	0.01	<0.0094	0.02	0.02
Eu151	<0.0017	0.00	0.00	0.01	0.00	0.01
Gd157	<0.0062	<0.0055	<0.0059	0.01	0.02	0.02
Tb159	0.00	0.00	0.00	0.00	0.00	0.00
Dy161	<0.0051	0.01	0.01	0.02	0.03	0.03
Ho165	0.00	0.00	0.00	0.00	0.00	0.00
Er166	0.01	0.01	0.01	0.01	0.02	0.02
Tm169	<0.00050	0.00	0.00	0.00	0.00	0.00
Yb173	0.02	<0.0052	0.01	0.01	0.01	0.02
Lu175	0.00	0.00	0.00	0.00	0.00	0.00
Hf178	17.19	13.99	16.30	18.51	9.86	9.14
Ta181	289.12	258.13	384.48	422.04	25.56	23.22
Pb206	0.04	0.02	0.04	0.06	0.05	0.05
Pb207	0.03	0.02	0.04	0.05	0.04	0.06
Pb208	0.03	0.02	0.04	0.04	0.04	0.06
Th232	0.00	0.00	0.00	0.00	0.00	0.00
U238	0.02	0.01	0.02	0.02	0.02	0.02

	CHAR_GRAOS_0019 C_ilmenita	CHAR_GRAOS_0019 B_ilmenita	CHAR_GRAOS_0020 C_ilmenita	CHAR_GRAOS_0020 B_ilmenita	CHAR_GRAOS_0021 C_ilmenita	CHAR_GRAOS_0021 B_ilmenita
SiO2	0.00	0.05	0.03	0.01	0.02	0.00
TiO2	50.04	49.96	44.83	44.94	49.07	49.09
Al2O3	0.52	0.52	0.04	0.01	0.21	0.15
FeO(T)	38.01	37.84	45.01	44.84	38.10	38.44
MnO	0.22	0.23	0.28	0.25	0.29	0.29
MgO	9.33	9.44	6.18	6.46	9.57	9.47
CaO	0.00	0.02	0.01	0.02	0.06	0.00
Na2O	0.00	0.02	0.00	0.01	0.00	0.00
K2O	0.00	0.00	0.00	0.02	0.01	0.02
Cr2O3	1.52	1.52	1.87	1.91	1.77	1.89
ZnO	0.04	0.05	0.04	0.00	0.03	0.03
Nb2O3	0.09	0.15	0.54	0.52	0.38	0.30
Sum:	99.77	99.79	98.83	99.00	99.51	99.69
Sum of Atomic mol prc	1.407	1.405	1.453	1.448	1.410	1.409
Number of ions on base of 3 oxygen						
Si	0.000	0.001	0.001	0.000	0.001	0.000
Ti	0.881	0.879	0.816	0.815	0.866	0.866
Al	0.014	0.014	0.001	0.000	0.006	0.004
Fe+3	0.193	0.195	0.324	0.326	0.223	0.225
Fe+2	0.551	0.545	0.587	0.577	0.524	0.528
Mn	0.004	0.005	0.006	0.005	0.006	0.006
Mg	0.326	0.329	0.223	0.232	0.335	0.331
Ca	0.000	0.000	0.000	0.001	0.001	0.000
Na	0.000	0.001	0.000	0.001	0.000	0.000
K	0.000	0.000	0.000	0.001	0.000	0.001
Cr	0.028	0.028	0.036	0.036	0.033	0.035

Zn	0.001	0.001	0.001	0.000	0.001	0.001
Nb	0.001	0.002	0.007	0.006	0.005	0.004
Total:	2.000	2.001	2.000	2.001	2.000	2.000

Trace elements in ilmenite minerals of Charneca Kimberlite

Li7	1.39	1.04	1.30	1.67
P31	3.40	4.10	4.25	2.49
Sc45	14.12	30.28	29.25	15.64
V51	1425.68	1822.77	1873.86	1389.08
Co59	187.05	148.24	188.17	187.34
Ni60	748.45	451.42	941.77	527.44
Sr88	0.05	0.05	0.07	0.07
Y89	0.07	0.02	0.05	0.09
Zr91	532.85	464.07	717.92	462.55
Nb93	861.06	4137.27	2877.49	562.87
Sn118	17.73	47.60	41.15	13.56
Sb121	<0.026	<0.023	0.05	0.03
Ba137	0.02	0.03	0.02	0.05
La139	<0.0024	0.00	<0.0023	0.00
Ce140	0.03	0.01	0.01	0.04
Pr141	0.01	<0.00115	0.00	0.01
Nd143	0.05	0.04	0.03	0.04
Sm147	<0.0091	<0.0115	0.01	<0.0122
Eu151	0.03	<0.0025	0.00	0.01
Gd157	<0.0090	<0.0103	<0.0104	0.02
Tb159	0.00	0.00	0.00	0.00
Dy161	0.02	<0.0068	0.01	0.03
Ho165	0.00	0.00	0.00	0.01
Er166	0.01	0.01	0.01	0.02
Tm169	<0.00211	<0.00111	0.00	0.00
Yb173	0.02	0.01	0.02	0.02
Lu175	<0.00157	0.00	0.00	0.00
Hf178	22.52	12.28	21.79	17.26
Ta181	77.17	380.36	272.23	50.21
Pb206	0.02	0.05	0.12	0.06
Pb207	0.02	0.05	0.08	0.06
Pb208	0.02	0.07	0.09	0.05
Th232	0.00	<0.00068	<0.00	0.00
U238	0.05	0.05	0.05	0.04

	CHAR_GRAOS_0022 C_ilmenita	CHAR_GRAOS_0022 B_ilmenita	CHAR_GRAOS_0023 C_ilmenita	CHAR_GRAOS_0023 B_ilmenita	CHAR_1_0016 ILM.C	CHAR_1_0016 ILM.B
SiO2	0.03	0.00	0.00	0.02	0.01	0.01
TiO2	51.20	52.63	53.91	53.03	52.33	52.07
Al2O3	0.61	0.63	0.43	0.42	0.31	0.26
FeO(T)	36.87	35.83	33.76	34.74	29.07	28.60
MnO	0.25	0.28	0.27	0.28	0.39	0.39
MgO	10.36	10.93	11.61	11.68	12.33	11.77
CaO	0.00	0.06	0.04	0.04	0.00	0.01
Na2O	0.03	0.00	0.00	0.02	0.03	0.09
K2O	0.01	0.00	0.00	0.00	0.00	0.00
Cr2O3	0.16	0.18	0.51	0.53	1.30	1.39
ZnO	0.00	0.01	0.03	0.00	0.03	0.03
Nb2O3	0.04	0.00	0.10	0.08	0.12	0.22
Sum:	99.55	100.54	100.66	100.84	95.92	94.84
Sum of Atomic mol prc	1.399	1.381	1.376	1.371	1.432	1.455
Number of ions on base of 3 oxygen						
Si	0.001	0.000	0.000	0.000	0.000	0.000
Ti	0.897	0.910	0.929	0.911	0.938	0.949
Al	0.017	0.017	0.012	0.011	0.009	0.007
Fe+3	0.185	0.160	0.121	0.156	0.087	0.064
Fe+2	0.533	0.528	0.526	0.507	0.492	0.515
Mn	0.005	0.005	0.005	0.005	0.008	0.008
Mg	0.360	0.374	0.396	0.397	0.438	0.425
Ca	0.000	0.001	0.001	0.001	0.000	0.000
Na	0.001	0.000	0.000	0.001	0.001	0.004
K	0.000	0.000	0.000	0.000	0.000	0.000
Cr	0.003	0.003	0.009	0.010	0.025	0.027

Zn	0.000	0.000	0.001	0.000	0.000	0.001
Nb	0.000	0.000	0.001	0.001	0.001	0.003
Total:	2.001	2.000	2.000	2.001	2.001	2.003

Trace elements in ilmenite minerals of Charneca Kimberlite

Li7	1.93	14.32	3.68
P31	4.07	31.19	4.76
Sc45	18.08	30.40	24.71
V51	1541.04	1701.43	1458.16
Co59	200.30	163.20	201.12
Ni60	635.57	832.65	992.66
Sr88	0.08	4.49	0.62
Y89	0.10	0.13	0.32
Zr91	710.03	1144.93	889.55
Nb93	972.67	1514.15	827.82
Sn118	17.61	25.76	17.14
Sb121	0.02	0.05	<0.027
Ba137	0.06	42.87	44.83
La139	0.00	0.20	0.34
Ce140	0.03	0.37	1.76
Pr141	0.00	0.03	0.07
Nd143	0.04	0.17	0.31
Sm147	0.02	0.03	0.10
Eu151	0.01	0.01	0.03
Gd157	0.02	0.02	0.08
Tb159	0.00	0.01	0.01
Dy161	0.02	0.04	0.09
Ho165	0.00	0.01	0.02
Er166	0.02	0.01	0.05
Tm169	0.00	0.00	0.01
Yb173	0.01	0.03	0.06
Lu175	0.00	0.00	0.01
Hf178	29.19	44.42	34.21
Ta181	97.85	169.20	95.70
Pb206	0.07	0.33	0.58
Pb207	0.08	0.22	0.49
Pb208	0.06	0.19	0.51
Th232	0.00	0.01	0.12
U238	0.03	0.05	0.16

	CHAR_1_0017 ILM.C	CHAR_1_0017 ILM.B	CHAR_1_0018 ILM.C	CHAR_1_0018 ILM.B	CHAR_1_0021 ILM.C	CHAR_1_0021 ILM.B	CHAR_1_0022 ILM.C	CHAR_1_0022 ILM.B
SiO2	0.00	0.10	0.03	0.01	0.03	0.00	0.02	0.04
TiO2	48.91	49.16	50.86	49.42	49.11	50.02	49.06	50.19
Al2O3	0.38	0.49	0.53	0.50	0.21	0.14	1.00	0.89
FeO(T)	36.64	37.17	37.66	37.09	36.31	33.54	35.22	34.90
MnO	0.29	0.26	0.30	0.35	0.29	0.31	0.21	0.21
MgO	10.02	10.37	10.00	10.38	10.97	11.85	11.20	11.78
CaO	0.10	0.06	0.05	0.09	0.04	0.08	0.06	0.07
Na2O	0.00	0.01	0.01	0.02	0.01	0.00	0.00	0.00
K2O	0.00	0.00	0.01	0.00	0.01	0.00	0.00	0.00
Cr2O3	1.92	1.85	0.08	0.08	1.58	1.44	1.73	1.65
ZnO	0.00	0.03	0.02	0.02	0.00	0.02	0.07	0.00
Nb2O3	0.06	0.10	0.06	0.10	0.53	0.49	0.00	0.05
Sum:	98.33	99.60	99.61	98.06	99.09	97.90	98.56	99.78
Sum of Atomic mc	1.418	1.397	1.401	1.417	1.401	1.409	1.399	1.378
Number of ions on base of 3 oxygen								
Si	0.000	0.002	0.001	0.000	0.001	0.000	0.000	0.001
Ti	0.869	0.860	0.892	0.877	0.862	0.883	0.859	0.866
Al	0.011	0.013	0.015	0.014	0.006	0.004	0.027	0.024
Fe+3	0.216	0.227	0.197	0.229	0.234	0.198	0.221	0.211
Fe+2	0.508	0.495	0.538	0.503	0.474	0.460	0.464	0.458
Mn	0.006	0.005	0.006	0.007	0.006	0.006	0.004	0.004
Mg	0.353	0.359	0.348	0.365	0.381	0.414	0.389	0.403
Ca	0.003	0.002	0.001	0.002	0.001	0.002	0.001	0.002
Na	0.000	0.001	0.000	0.001	0.000	0.000	0.000	0.000
K	0.000	0.000	0.000	0.000	0.000	0.000	0.000	0.000
Cr	0.036	0.034	0.001	0.002	0.029	0.027	0.032	0.030

Zn	0.000	0.001	0.000	0.000	0.000	0.000	0.001	0.000
Nb	0.001	0.001	0.001	0.001	0.006	0.006	0.000	0.001
Total:	2.000	2.000	2.000	2.001	2.001	2.000	2.000	2.000

Trace elements in ilmenite minerals of Charneca Kimberlite

Li7	1.62	1.86	1.80	1.67
P31	<1.70	<1.72	2.71	2.26
Sc45	19.37	31.72	22.14	29.12
V51	1411.58	1766.72	2131.94	1840.48
Co59	172.43	180.70	208.84	170.77
Ni60	286.29	760.29	1845.01	919.00
Sr88	0.09	0.09	0.53	0.11
Y89	0.12	0.20	0.29	0.14
Zr91	595.47	636.53	259.14	1019.91
Nb93	740.18	3843.76	199.97	2339.21
Sn118	13.86	37.90	8.58	35.29
Sb121	0.05	<0.033	<0.033	<0.029
Ba137	0.16	0.10	6.89	0.19
La139	0.01	<0.0045	0.16	<0.0028
Ce140	0.06	0.06	0.62	0.07
Pr141	0.01	0.00	0.05	0.01
Nd143	0.04	0.04	0.25	<0.029
Sm147	<0.0168	0.02	0.06	0.02
Eu151	0.01	0.01	0.03	0.02
Gd157	0.03	0.03	0.05	<0.0101
Tb159	0.00	0.01	0.01	0.00
Dy161	0.02	0.02	0.05	0.03
Ho165	0.01	0.01	0.01	<0.0021
Er166	0.02	0.02	0.03	0.03
Tm169	0.00	0.00	0.01	0.00
Yb173	0.02	0.02	0.06	0.04
Lu175	0.00	0.01	0.01	<0.0019
Hf178	21.52	16.91	9.09	30.54
Ta181	80.80	466.32	18.46	271.59
Pb206	0.15	0.15	0.81	0.23
Pb207	0.11	0.15	0.71	0.13
Pb208	0.17	0.15	0.70	0.10
Th232	0.00	0.00	0.07	0.01
U238	0.05	0.04	0.10	0.07

	CHAR_1_0023 ILM.C	CHAR_1_0023 ILM.B	CHAR_1_0025 ILM.C	CHAR_1_0025 ILM.B	CHAR_1_0027 ILM.C	CHAR_1_0027 ILM.B	CHAR_1_0029 ILM.C	CHAR_1_0029 ILM.B	CHAR_1_0030 ILM.C	CHAR_1_0030 ILM.B	CHARNECA - 6#_0(ILM.B	CHARNECA _6# ILM.C
SiO2	0.00	0.03	0.00	0.01	0.04	0.00	0.00	0.01	0.00	0.00	0.00	0.04
TiO2	48.19	49.23	48.37	48.48	43.60	44.17	50.09	50.49	48.70	49.05	51.14	51.54
Al2O3	0.23	0.21	0.05	0.01	0.00	0.02	0.18	0.18	0.17	0.12	0.33	0.34
FeO(T)	36.51	36.55	38.47	37.95	42.96	41.80	35.04	34.94	34.69	34.89	32.72	33.26
MnO	0.30	0.29	0.35	0.37	0.31	0.28	0.36	0.37	0.32	0.36	0.45	0.43
MgO	10.45	10.32	9.40	9.00	7.44	8.21	11.52	11.80	11.74	10.76	12.61	12.93
CaO	0.02	0.10	0.00	0.03	0.02	0.02	0.06	0.03	0.04	0.00	0.10	0.08
Na2O	0.01	0.00	0.00	0.00	0.01	0.02	0.03	0.01	0.00	0.00	0.00	0.01
K2O	0.01	0.00	0.00	0.00	0.00	0.00	0.00	0.01	0.00	0.00	0.01	0.00
Cr2O3	1.95	2.03	2.08	2.08	2.57	2.50	1.53	1.57	1.56	1.54	0.58	0.27
ZnO	0.01	0.00	0.05	0.01	0.01	0.02	0.02	0.02	0.00	0.03	0.00	0.06
Nb2O3	0.34	0.29	0.43	0.49	0.47	0.40	0.47	0.40	0.33	0.53	0.16	0.12
Sum:	98.02	99.04	99.20	98.42	97.43	97.44	99.31	99.82	97.55	97.29	98.10	99.08
Sum of	1.420	1.408	1.417	1.432	1.458	1.449	1.393	1.384	1.413	1.429	1.396	1.380
Number of ions on base of 3 oxygen												
Si	0.000	0.001	0.000	0.000	0.001	0.000	0.000	0.000	0.000	0.000	0.000	0.001
Ti	0.857	0.868	0.858	0.870	0.796	0.801	0.874	0.875	0.861	0.878	0.894	0.891
Al	0.007	0.006	0.001	0.000	0.000	0.001	0.005	0.005	0.005	0.003	0.009	0.009
Fe+3	0.240	0.216	0.239	0.215	0.351	0.344	0.213	0.212	0.239	0.206	0.190	0.202
Fe+2	0.482	0.500	0.520	0.541	0.521	0.500	0.467	0.462	0.443	0.488	0.446	0.437
Mn	0.006	0.006	0.007	0.008	0.006	0.006	0.007	0.007	0.006	0.007	0.009	0.008
Mg	0.368	0.360	0.330	0.320	0.269	0.295	0.398	0.405	0.411	0.382	0.437	0.443
Ca	0.001	0.002	0.000	0.001	0.000	0.001	0.001	0.001	0.001	0.000	0.003	0.002
Na	0.000	0.000	0.000	0.000	0.000	0.001	0.001	0.000	0.000	0.000	0.000	0.001
K	0.000	0.000	0.000	0.000	0.000	0.000	0.000	0.000	0.000	0.000	0.000	0.000
Cr	0.036	0.038	0.039	0.039	0.049	0.048	0.028	0.029	0.029	0.029	0.011	0.005

Zn	0.000	0.000	0.001	0.000	0.000	0.000	0.000	0.000	0.000	0.001	0.000	0.001
Nb	0.004	0.003	0.005	0.006	0.006	0.005	0.006	0.005	0.004	0.006	0.002	0.001
Total:	2.000	2.000	2.000	2.000	2.000	2.001	2.001	2.000	2.000	2.000	2.000	2.000

Trace elements in ilmenite minerals of Charneca Kimberlite

Li7	1.65	1.15	1.78	1.82
P31	4.67	5.89	3.16	5.58
Sc45	32.52	36.46	32.23	32.78
V51	1854.32	2075.51	1731.83	1824.55
Co59	176.96	167.00	182.05	200.60
Ni60	668.44	688.29	919.35	1010.47
Sr88	0.10	0.08	0.08	0.09
Y89	0.04	0.04	0.16	0.12
Zr91	527.57	611.90	692.43	774.51
Nb93	3482.67	3999.66	2905.44	3126.16
Sn118	39.64	48.06	32.95	34.61
Sb121	0.05	0.07	<0.032	0.03
Ba137	0.23	0.18	0.15	0.08
La139	<0.0036	0.01	0.00	0.01
Ce140	0.01	0.02	0.08	0.06
Pr141	<0.0026	<0.0021	0.01	0.00
Nd143	<0.026	0.03	0.06	0.05
Sm147	<0.0234	<0.0177	0.04	<0.014
Eu151	<0.0035	<0.0037	0.01	0.01
Gd157	0.01	<0.0125	0.02	0.03
Tb159	0.00	<0.00221	0.01	0.01
Dy161	<0.0111	<0.0125	0.05	0.03
Ho165	0.00	<0.00174	0.01	0.00
Er166	<0.0074	<0.0056	0.03	0.03
Tm169	0.00	<0.0023	0.00	0.00
Yb173	0.02	<0.0154	0.03	0.02
Lu175	0.00	0.00	0.01	0.00
Hf178	14.81	15.77	21.88	22.46
Ta181	434.98	355.71	264.70	280.15
Pb206	0.24	0.21	0.08	0.14
Pb207	0.20	0.23	0.15	0.09
Pb208	0.20	0.21	0.10	0.07
Th232	0.00	0.00	0.00	<0.00
U238	0.03	0.07	0.03	0.04

table 8

Major-element compositions of ilmenite minerals from Régis Kimberlite

	regis-10_0001 ILM.B	regis-10_0001 ILM.C	regis-10_0001 ILM.B	regis-10_0002 ILM.C	regis-10_0003 ILM.B	regis-10_0003 ILM.IT1	regis-10_0003 ILM.INT2	regis-10_0003 ILM.C	regis 1_0007 ILM.C
SiO2	0.98	0.46	0.47	0.46	0.07	0.04	0.06	0.05	1.64
TiO2	19.68	21.83	21.25	49.89	42.35	42.77	43.53	43.46	13.09
Al2O3	0.37	0.09	0.08	0.00	0.20	0.13	0.11	0.08	0.96
FeO(T)	67.46	65.40	66.98	44.45	40.24	40.28	42.13	42.27	73.77
MnO	0.81	0.87	0.90	1.21	0.29	0.24	0.26	0.29	1.08
MgO	1.27	1.08	1.11	1.88	7.39	7.42	7.45	7.17	3.27
CaO	0.47	0.43	0.45	0.55	0.07	0.04	0.04	0.01	0.58
Na2O	0.02	0.01	0.00	0.29	0.00	0.01	0.01	0.01	0.10
K2O	0.03	0.01	0.04	0.10	0.00	0.00	0.02	0.00	0.15
Cr2O3	1.50	1.40	1.53	0.00	2.34	2.38	2.40	2.41	0.05
ZnO	0.05	0.01	0.00	0.06	0.00	0.01	0.01	0.00	0.16
Nb2O3	0.03	0.02	0.05	0.07	0.40	0.44	0.40	0.38	0.00
Sum:	92.68	91.59	92.87	98.95	93.35	93.76	96.41	96.13	94.85
Carmichael (1967)									
Sum of Atc	1.561	1.589	1.566	1.504	1.517	1.512	1.472	1.479	1.483
Number of ions on base of 3 oxygen									
Si	0.026	0.012	0.012	0.011	0.002	0.001	0.001	0.001	0.040
Ti	0.385	0.434	0.417	0.940	0.804	0.810	0.802	0.805	0.243
Al	0.011	0.003	0.002	0.000	0.006	0.004	0.003	0.002	0.028
Fe+3	1.136	1.074	1.107	0.091	0.330	0.322	0.338	0.333	1.401
Fe+2	0.329	0.372	0.353	0.840	0.520	0.526	0.525	0.537	0.122
Mn	0.018	0.019	0.020	0.026	0.006	0.005	0.005	0.006	0.023
Mg	0.049	0.042	0.043	0.070	0.278	0.278	0.272	0.263	0.120
Ca	0.013	0.012	0.013	0.015	0.002	0.001	0.001	0.000	0.015
Na	0.001	0.000	0.000	0.014	0.000	0.001	0.000	0.000	0.005
K	0.001	0.000	0.001	0.003	0.000	0.000	0.000	0.000	0.005
Cr	0.031	0.029	0.032	0.000	0.047	0.047	0.046	0.047	0.001
Zn	0.001	0.000	0.000	0.001	0.000	0.000	0.000	0.000	0.003
Nb	0.000	0.000	0.001	0.001	0.005	0.006	0.005	0.005	0.000

Total:	2.001	2.001	2.001	2.012	2.000	2.000	2.001	2.000	2.006

Trace elements in ilmenite minerals of Régis Kimberlite

Concentrations in ppm (µg/g)

Li7	0.50
P31	25.51
Sc45	4.90
V51	80.49
Co59	12.36
Sr88	109.47
Y89	0.57
Zr91	5.82
Nb93	0.57
Sn118	0.42
Sb121	<0.102
Ba137	10.19
La139	2.25
Ce140	6.98
Pr141	1.00
Nd143	4.19
Sm147	0.78
Eu151	0.20
Gd157	0.43
Tb159	0.04
Dy161	0.18
Ho165	0.03
Er166	0.04
Tm169	0.00
Yb173	0.03
Lu175	<0.0045
Hf178	0.30
Ta181	0.01
Pb206	0.31
Pb207	0.38
Pb208	0.35
Th232	0.05
U238	0.02

Table 9

Major-element compositions of ilmenite minerals from Indaiá Kimberlite

	SP_ID 4_0006 C_ilmenita	SP_ID 4_0006 B_ilmenita	SP_ID 4_0014 C_ilmenita	SP_ID 4_0014 B_ilmenita	SP_ID 4_0001 C_ILM	SP_ID 4_0001 B_ILM	IDIA-1_0002 graoMAIOR C	IDIA-1_0002 graoMAIOR B	IDIA-1_0002 graoMENOR C	IDIA-1_0002 graoMENOR B
SiO2	0.00	0.00	0.02	0.00	0.00	0.00	0.03	0.03	0.02	0.05
TiO2	51.58	51.35	52.19	50.31	50.14	51.32	45.42	48.77	48.97	49.79
Al2O3	0.04	0.08	0.05	0.04	0.08	0.10	0.01	0.04	0.18	0.11
FeO(T)	34.64	34.33	32.57	32.21	33.76	33.51	47.02	45.52	40.45	38.39
MnO	0.30	0.28	0.33	0.34	0.30	0.30	0.33	0.39	0.33	0.57
MgO	10.46	10.41	11.19	11.17	11.54	11.68	7.01	7.65	9.48	10.47
CaO	0.00	0.01	0.00	0.01	0.03	0.03	0.01	0.01	0.00	0.06
Na2O	0.02	0.00	0.02	0.02						
K2O	0.01	0.01	0.00	0.00	0.01	0.00	0.00	0.01	0.00	0.01
Cr2O3	1.71	1.72	3.65	3.55	3.97	3.82	1.52	1.44	2.66	2.40
ZnO	0.02	0.01	0.03	0.03			0.01	0.01	0.03	0.04
Nb2O3	0.25	0.24	0.14	0.21						
total	99.15	98.43	100.18	97.89	100.04	100.75	101.93	104.41	102.76	102.52
total	1.410	1.419	1.389	1.418	1.384	1.374	1.399	1.363	1.367	1.361
Number of ions on base of 3 oxygen										
Si	0.000	0.000	0.000	0.000	0.000	0.000	0.001	0.001	0.000	0.001
Ti	0.910	0.912	0.908	0.893	0.869	0.883	0.795	0.833	0.838	0.848
Al	0.001	0.002	0.001	0.001	0.002	0.003	0.000	0.001	0.005	0.003
Fe+3	0.141	0.138	0.114	0.143	0.184	0.163	0.370	0.297	0.259	0.244
Fe+2	0.538	0.540	0.516	0.493	0.466	0.478	0.546	0.567	0.510	0.483
Mn	0.006	0.006	0.006	0.007	0.006	0.006	0.007	0.007	0.006	0.011
Mg	0.366	0.366	0.386	0.393	0.396	0.398	0.243	0.259	0.321	0.354
Ca	0.000	0.000	0.000	0.000	0.001	0.001	0.000	0.000	0.000	0.001
Na	0.001	0.000	0.001	0.001	0.000	0.000	0.000	0.000	0.000	0.000
K	0.000	0.000	0.000	0.000	0.000	0.000	0.000	0.000	0.000	0.000
Cr	0.032	0.032	0.067	0.066	0.072	0.069	0.028	0.026	0.048	0.043
Zn	0.000	0.000	0.000	0.000	0.000	0.000	0.000	0.000	0.001	0.001
Nb	0.003	0.003	0.002	0.003	0.000	0.000	0.000	0.000	0.000	0.000
Total:	2.002	2.000	2.001	2.001	2.001	2.000	2.000	2.001	2.001	2.001

Trace elements in ilmenite minerals of Indaiá Kimberlite

	SP_ID 4_0006 C_ilmenita	SP_ID 4_0006 B_ilmenita	SP_ID 4_0014 C_ilmenita	SP_ID 4_0014 B_ilmenita	SP_ID 4_0001 C_ILM	SP_ID 4_0001 B_ILM	IDIA-1_0002 grãoMAIOR C	IDIA-1_0002 grãoMAIOR B	IDIA-1_0002 grãoMENOR C	IDIA-1_0002 grãoMENOR B
Li7	1.3				2.4		2.71		<18.22	
P31	29.5				<6.39		<10.72		<385.51	
Sc45	40.8				37.8		53.46		39.60	
V51	1674.9				1592.4		24782.81		11529.21	
Co59	175.4				189.2		<0.062		<2.60	
Ni60	850.0				1530.0		0.363		5.77	
Sr88	5.3				0.2		0.151		<0.31	
Y89	0.2				0.1		832.18		714.22	
Zr91	685.2				613.9		3882.58		2773.12	
Nb93	1746.2				1030.6		0.69		<3.84	
Sn118	31.3				24.3		46.10		36.30	
Sb121	<0.164				<0.095		<0.074		<3.20	
Ba137	8.9				<0.116		3.11		85.69	
La139	0.2				0.0		0.0121		0.63	
Ce140	0.4				0.0		0.0591		1.06	
Pr141	0.0				<0.0065		0.0062		<0.174	
Nd143	0.4				<0.076		0.054		<2.02	
Sm147	<0.085				<0.057		<0.025		<1.58	
Eu151	<0.022				0.0		<0.0086		<0.38	
Gd157	0.2				<0.024		<0.030		<1.35	
Tb159	<0.0102				<0.0063		<0.0043		<0.122	
Dy161	0.1				0.0		0.036		0.91	
Ho165	<0.0122				<0.0076		0.0050		<0.195	
Er166	0.1				<0.024		0.0168		<0.38	
Tm169	0.0				0.0		<0.0029		<0.087	
Yb173	<0.063				0.1		0.041		<1.05	
Lu175	<0.0106				0.0		0.0052		<0.140	
Hf178	20.1				19.6		19.58		15.61	
Ta181	169.2				134.3		367.09		168.58	
Pb206	<0.056				0.3		0.083		2.29	
Pb207	0.1				0.3		0.062		<1.47	
Pb208	0.1				0.4		0.064		1.70	
Th232	0.0				<0.00		<0.0018		<0.00	
U238	0.0				0.0		0.0382		0.075	

Table 9 (continuation)

	IDIA-1_0003 graoMAIOR C	IDIA-1_0003 graoMAIOR B	IDIA-1_0003 graoMENOR C	IDIA-1_0003 graoMENOR B	IDIA-1_0004 Centro	IDIA-1_0004 B.escura	IDIA-1_0004 B.clara	IDIA-1_0005 Centro	IDIA-1_0005 Borda
SiO2	0.12	0.26	0.07	0.06	0.02	0.05	0.07	0.08	0.03
TiO2	51.06	51.25	51.06	52.89	50.12	54.57	16.37	46.12	46.17
Al2O3	0.08	0.06	0.03	0.06	0.07	0.09	1.46	0.06	0.06
FeO(T)	35.86	36.20	34.25	36.54	39.11	1.80	68.38	42.13	45.32
MnO	0.61	0.63	0.66	0.62	0.33	0.04	1.13	0.43	0.33
MgO	11.77	11.75	12.10	11.84	10.01	0.00	11.93	9.13	7.34
CaO	0.03	0.53	0.58	0.05	0.03	35.70	0.35	0.54	0.01
Na2O									
K2O	0.01	0.00	0.00	0.00	0.00	0.04	0.00	0.02	0.00
Cr2O3	1.42	1.75	2.51	0.74	1.87	0.06	2.21	2.48	2.65
ZnO	0.03	0.03	0.02	0.01	0.03	0.01	0.05	0.02	0.00
Nb2O3									
total	101.61	103.06	101.70	103.30	102.20	92.64	102.22	101.57	102.48
total	1.360	1.341	1.355	1.340	1.370	1.478	1.301	1.381	1.389
Number of ions on base of 3 oxygen									
Si	0.003	0.006	0.002	0.001	0.001	0.001	0.001	0.002	0.001
Ti	0.870	0.860	0.866	0.887	0.860	1.010	0.267	0.797	0.803
Al	0.002	0.001	0.001	0.001	0.002	0.003	0.037	0.002	0.002
Fe+3	0.217	0.225	0.212	0.199	0.233	-0.032	1.385	0.345	0.332
Fe+2	0.462	0.450	0.434	0.482	0.512	0.069	-0.147	0.464	0.544
Mn	0.012	0.012	0.013	0.012	0.006	0.001	0.021	0.008	0.006
Mg	0.397	0.391	0.407	0.394	0.340	0.000	0.385	0.313	0.253
Ca	0.001	0.013	0.014	0.001	0.001	0.941	0.008	0.013	0.000
Na	0.000	0.000	0.000	0.000	0.000	0.000	0.000	0.000	0.000
K	0.000	0.000	0.000	0.000	0.000	0.001	0.000	0.001	0.000
Cr	0.026	0.031	0.045	0.013	0.034	0.001	0.038	0.045	0.048
Zn	0.001	0.000	0.000	0.000	0.001	0.000	0.001	0.000	0.000
Nb	0.000	0.000	0.000	0.000	0.000	0.000	0.000	0.000	0.000
Total:	2.001	2.001	2.000	2.000	2.001	2.001	2.001	2.001	2.001

Trace elements in ilmenite minerals of Indaiá Kimberlite

	IDIA-1_0003 grãoMAIOR C	IDIA-1_0004 Centro	IDIA-1_0005 Centro	IDIA-1_0006 Centro
Li7	4.27	2.35	2.23	3.20
P31	314.83	<11.99	<8.04	36.88
Sc45	77.02	42.99	26.87	30.75
V51	12919.38	16255.99	10141.49	10837.80
Co59	0.594	<0.085	<0.051	<0.094
Ni60	307.17	0.591	0.742	0.050
Sr88	1157.0	0.141	0.083	0.085
Y89	988.00	816.33	447.52	572.99
Zr91	2444.20	1957.87	1142.69	1714.52
Nb93	0.81	0.549	0.404	0.49
Sn118	40.97	34.19	19.96	25.51
Sb121	<0.098	<0.111	<0.060	<0.115
Ba137	51.14	7.33	5.72	<0.056
La139	28.57	0.0602	0.0250	<0.0046
Ce140	40.53	0.114	0.0604	<0.0072
Pr141	3.95	0.0111	0.0064	<0.0078
Nd143	14.53	<0.051	<0.028	0.079
Sm147	2.05	<0.031	<0.033	<0.043
Eu151	0.591	<0.0118	<0.0097	0.0101
Gd157	1083.0	<0.027	<0.0136	<0.045
Tb159	0.0944	<0.0064	<0.0030	<0.0086
Dy161	0.410	<0.026	<0.0158	<0.040
Ho165	0.0492	<0.0073	<0.0030	0.0045
Er166	0.128	<0.0200	0.0197	0.0147
Tm169	0.0158	<0.0048	0.0052	<0.0075
Yb173	0.163	<0.039	0.028	<0.045
Lu175	0.0198	0.0105	0.0049	<0.0057
Hf178	25.50	23.38	13.23	16.05
Ta181	260.25	220.59	137.96	189.19
Pb206	2.39	0.107	0.037	<0.049
Pb207	2.07	0.090	<0.032	0.054
Pb208	2.39	0.122	0.048	<0.030
Th232	0.528	0.0062	0.00086	0.00084
U238	0.743	0.0317	0.0151	0.0209

Table 9 (continuation)

	IDIA-1_0006 Centro	IDIA-1_0006 Borda	IDI A2_0009 C	IDI A2_0009 B
SiO2	0.03	0.22	0.00	0.03
TiO2	46.01	50.54	49.25	49.97
Al2O3	0.03	0.74	0.15	0.08
FeO(T)	41.63	15.62	44.78	44.64
MnO	0.32	0.22	0.35	0.34
MgO	8.78	3.80	6.98	7.21
CaO	0.00	22.19	0.02	0.00
Na2O				
K2O	0.01	0.03	0.00	0.01
Cr2O3	2.94	1.82	0.15	0.16
ZnO	0.02	0.00	0.00	0.00
Nb2O3				
total	100.33	95.51	101.68	102.44
total	1.403	1.439	1.405	1.394
Number of ions on base of 3 oxygen				
Si	0.001	0.005	0.000	0.001
Ti	0.809	0.911	0.867	0.872
Al	0.001	0.021	0.004	0.002
Fe+3	0.316	0.106	0.260	0.249
Fe+2	0.497	0.206	0.616	0.617
Mn	0.006	0.004	0.007	0.007
Mg	0.306	0.136	0.243	0.249
Ca	0.000	0.569	0.001	0.000
Na	0.000	0.000	0.000	0.000
K	0.000	0.001	0.000	0.000
Cr	0.054	0.034	0.003	0.003
Zn	0.000	0.000	0.000	0.000
Nb	0.000	0.000	0.000	0.000
Total:	2.001	2.001	2.000	2.000

Table 10

Major-element compositions of olivine minerals from Indaiá Kimberlite

	IDI-A1_0001 OL.BORDA	IDI-A1_0001 OL.INT	IDI-A1_0001 OL.INT	IDI-A1_0001 OL.INT	IDI-A1_0001 OL.INT	IDI-A1_0001 OL.CENTRO	IDI-A1_0002 mega.olv.borda	IDI-A1_0002 mega.olv.borda	IDI-A1_0002 mega.olv.borda	IDI-A1_0002 macro.olv.inter
SiO2	40.10	40.14	40.17	40.19	40.47	40.27	39.56	40.13	39.44	40.70
TiO2	0.04	0.01	0.00	0.00	0.00	0.00	0.10	0.03	0.00	0.06
Al2O3	0.01	0.00	0.00	0.00	0.00	0.00	0.00	0.02	0.00	0.00
Cr2O3	0.02	0.00	0.03	0.00	0.05	0.03	0.03	0.08	0.13	0.00
FeOt	11.86	11.79	10.82	10.31	9.77	10.87	14.30	14.15	14.07	8.41
MnO	0.16	0.14	0.14	0.18	0.15	0.19	0.24	0.20	0.20	0.12
MgO	48.13	48.52	49.26	49.52	49.95	49.16	46.17	46.95	46.87	51.25
CaO	0.03	0.02	0.02	0.03	0.00	0.04	0.08	0.07	0.07	0.03
Na2O	0.01	0.00	0.00	0.02	0.01	0.01	0.00	0.01	0.01	0.00
K2O	0.01	0.00	0.01	0.00	0.00	0.00	0.01	0.01	0.00	0.00
NiO	0.31	0.34	0.36	0.38	0.37	0.38	0.16	0.15	0.17	0.35
TOTAL	100.69	100.97	100.80	100.63	100.76	100.95	100.64	101.80	100.97	100.92
	Number of ions on base of 4 oxygen									
Si	0.988	0.986	0.984	0.984	0.987	0.985	0.986	0.987	0.979	0.985
Ti	0.001	0.000	0.000	0.000	0.000	0.000	0.002	0.001	0.000	0.001
Al	0.000	0.000	0.000	0.000	0.000	0.000	0.000	0.001	0.000	0.000
Cr	0.000	0.000	0.000	0.000	0.001	0.001	0.001	0.001	0.003	0.000
Fe2+	0.244	0.242	0.222	0.211	0.199	0.222	0.298	0.291	0.292	0.170
Mn	0.003	0.003	0.003	0.004	0.003	0.004	0.005	0.004	0.004	0.003
Mg	1.767	1.776	1.799	1.808	1.816	1.793	1.715	1.721	1.735	1.848
Ca	0.001	0.001	0.000	0.001	0.000	0.001	0.002	0.002	0.002	0.001
Na	0.000	0.000	0.000	0.001	0.000	0.001	0.000	0.001	0.001	0.000
K	0.000	0.000	0.000	0.000	0.000	0.000	0.000	0.000	0.000	0.000
Ni	0.006	0.007	0.007	0.007	0.007	0.007	0.003	0.003	0.003	0.007
	3.005	3.008	3.009	3.009	3.006	3.007	3.009	3.009	3.016	3.007
Mg#	0.88	0.88	0.89	0.89	0.90	0.89	0.85	0.85	0.85	0.91
Fa	12.29	12.12	11.10	10.62	10.02	11.21	15.01	14.64	14.59	8.54
Fo	87.71	87.88	88.90	89.38	89.98	88.79	84.99	85.36	85.41	91.46

Table 10 (continuation)

IDI-A1_0002 macro.olv.C	IDI-A1_0002 macro.olv.INT	IDI-A1_0002 micro.ol.borda	IDI-A1_0002 micro.ol.centro	IDI-A1_0003 MACRO.BORD	IDI-A1_0003 MACRO.BORD	IDI-A1_0003 MACRO.CENT	IDI-A1_0003 MACRO.BORD	IDI-A1_0003 MICRO.BORD	IDI-A1_0003 MICRO.CENTF	IDI-A1_0003 MICRO.BORD
40.83	40.89	39.95	41.06	40.47	40.26	40.09	39.51	39.76	38.86	40.21
0.00	0.00	0.00	0.00	0.03	0.03	0.03	0.04	0.09	0.04	0.08
0.01	0.00	0.01	0.02	0.02	0.01	0.02	0.01	0.00	0.00	0.28
0.00	0.00	0.05	0.05	0.11	0.12	0.08	0.00	0.14	0.00	0.05
7.45	7.64	12.08	8.03	10.56	10.06	10.15	12.24	14.30	16.89	5.70
0.11	0.11	0.16	0.10	0.14	0.12	0.11	0.17	0.21	0.24	0.16
52.32	51.99	47.96	51.29	49.14	49.31	49.51	48.05	45.53	43.73	35.86
0.00	0.01	0.07	0.04	0.14	0.13	0.14	0.11	0.11	0.05	0.67
0.01	0.01	0.00	0.01	0.02	0.01	0.02	0.01	0.01	0.02	0.01
0.01	0.00	0.00	0.00	0.00	0.01	0.00	0.00	0.00	0.00	0.03
0.38	0.38	0.32	0.39	0.46	0.45	0.45	0.38	0.17	0.20	0.24
101.11	101.02	100.61	100.98	101.10	100.52	100.61	100.53	100.31	100.02	83.29
0.982	0.985	0.986	0.990	0.988	0.986	0.982	0.978	0.993	0.987	1.146
0.000	0.000	0.000	0.000	0.001	0.001	0.001	0.001	0.002	0.001	0.002
0.000	0.000	0.000	0.001	0.001	0.000	0.001	0.000	0.000	0.000	0.009
0.000	0.000	0.001	0.001	0.002	0.002	0.002	0.000	0.003	0.000	0.001
0.150	0.154	0.249	0.162	0.215	0.206	0.208	0.253	0.299	0.359	0.136
0.002	0.002	0.003	0.002	0.003	0.002	0.002	0.004	0.004	0.005	0.004
1.876	1.867	1.765	1.844	1.788	1.801	1.808	1.774	1.696	1.656	1.523
0.000	0.000	0.002	0.001	0.004	0.003	0.004	0.003	0.003	0.001	0.020
0.001	0.000	0.000	0.000	0.001	0.001	0.001	0.000	0.000	0.001	0.001
0.000	0.000	0.000	0.000	0.000	0.000	0.000	0.000	0.000	0.000	0.001
0.007	0.007	0.006	0.008	0.009	0.009	0.009	0.008	0.003	0.004	0.006
3.011	3.008	3.007	3.002	3.002	3.003	3.008	3.013	3.000	3.009	2.843
0.93	0.92	0.87	0.92	0.89	0.90	0.90	0.87	0.85	0.82	0.92
7.50	7.72	12.53	8.17	10.88	10.38	10.41	12.66	15.16	18.01	8.40
92.50	92.28	87.47	91.83	89.12	89.62	89.59	87.34	84.84	81.99	91.60

IDI-A1_0004 OLV.BORDA	IDI-A1_0004 OLV.INT	IDI-A1_0004 OLV.INT 2	IDI-A1_0004 OLV.CENTRO	IDI-A1_0004 OLV2.BORDA.	IDI-A1_0004 OLV2.CENTRO	IDI-A1_0004 OLV2.BORDA	IDI-A1_0011 PERFIL.B	IDI-A1_0011 PERFIL.INT	IDI-A1_0011 PERFIL.INT	IDI-A1_0011 PERFIL.INT
39.63	39.18	38.99	38.92	38.57	41.18	40.14	42.18	39.28	39.75	40.48
0.01	0.00	0.01	0.00	0.06	0.00	0.06	0.08	0.06	0.02	0.01
0.01	0.00	0.01	0.00	0.15	0.00	0.01	0.04	0.00	0.02	0.00
0.05	0.07	0.02	0.00	0.00	0.00	0.02	0.01	0.10	0.00	0.00
14.28	17.45	18.21	18.33	5.28	7.52	14.25	2.78	14.41	12.41	9.74
0.24	0.21	0.23	0.25	0.18	0.11	0.28	0.25	0.20	0.18	0.12
46.16	43.69	43.52	43.07	34.09	51.72	46.49	53.65	46.00	47.61	49.98
0.06	0.03	0.01	0.04	0.31	0.04	0.12	0.97	0.12	0.04	0.00
0.00	0.01	0.02	0.00	0.02	0.01	0.01	0.01	0.02	0.02	0.00
0.00	0.00	0.00	0.00	0.03	0.00	0.00	0.03	0.01	0.00	0.00
0.16	0.21	0.21	0.22	0.02	0.36	0.13	-	-	-	-
100.60	100.85	101.23	100.84	78.70	100.94	101.51	100.01	100.19	100.04	100.33
0.988	0.988	0.984	0.986	1.158	0.991	0.990	1.003	0.984	0.987	0.989
0.000	0.000	0.000	0.000	0.001	0.000	0.001	0.001	0.001	0.000	0.000
0.000	0.000	0.000	0.000	0.005	0.000	0.000	0.001	0.000	0.001	0.000
0.001	0.001	0.000	0.000	0.000	0.000	0.000	0.000	0.002	0.000	0.000
0.298	0.368	0.384	0.388	0.133	0.151	0.294	0.055	0.302	0.258	0.199
0.005	0.004	0.005	0.005	0.005	0.002	0.006	0.005	0.004	0.004	0.003
1.715	1.643	1.637	1.627	1.525	1.856	1.710	1.902	1.718	1.762	1.820
0.002	0.001	0.000	0.001	0.010	0.001	0.003	0.025	0.003	0.001	0.000
0.000	0.001	0.001	0.000	0.001	0.000	0.000	0.001	0.001	0.001	0.000
0.000	0.000	0.000	0.000	0.001	0.000	0.000	0.001	0.000	0.000	0.000
0.003	0.004	0.004	0.004	0.000	0.007	0.003	0.000	0.000	0.000	0.000
3.008	3.007	3.012	3.009	2.839	3.002	3.006	2.995	3.015	3.013	3.011
0.85	0.82	0.81	0.81	0.92	0.92	0.85	0.97	0.85	0.87	0.90
15.00	18.48	19.20	19.49	8.24	7.65	14.92	3.08	15.12	12.92	9.97
85.00	81.52	80.80	80.51	91.76	92.35	85.08	96.92	84.88	87.08	90.03

Table 10 (continuation)

IDI-A1_0011 PERFIL.C	IDI-A1_0011 PERFIL.C	IDI-A1_0011 PERFIL.INT	IDI-A1_0011 PERFIL.INT	IDI-A1_0011 PERFIL.B	IDI-A1_0011 PERFIL.B	IDI-A1_0012 B	IDI-A1_0012 INT	IDI-A1_0012 C	IDI-A1_0013 grão1 B.	IDI-A1_0013 grão1 INT
41.14	40.61	40.40	40.88	39.77	39.29	39.37	39.87	19.99	38.27	38.77
0.00	0.01	0.02	0.05	0.05	0.04	0.04	0.06	0.02	0.00	0.13
0.01	0.00	0.00	0.01	0.00	0.00	0.01	0.02	0.00	0.02	0.05
0.01	0.08	0.01	0.06	0.02	0.07	0.07	0.00	0.00	0.04	0.00
7.92	7.53	7.50	7.23	13.37	14.31	14.37	11.73	10.39	14.12	8.69
0.13	0.12	0.08	0.11	0.18	0.21	0.22	0.17	0.17	0.28	0.13
50.83	51.66	51.95	52.00	47.03	46.24	45.42	47.91	46.32	47.75	48.92
0.03	0.01	0.01	0.01	0.07	0.07	0.04	0.08	0.00	0.39	0.05
0.00	0.00	0.01	0.01	0.02	0.00	0.00	0.02	0.00	0.02	0.00
0.02	0.00	0.00	0.00	0.00	0.00	0.00	0.03	0.00	0.04	0.00
-	-	-	-	-	-	-				
100.09	100.02	99.99	100.36	100.51	100.24	99.54	99.90	76.89	100.93	96.74
0.998	0.986	0.981	0.987	0.987	0.983	0.991	0.988	0.678	0.955	0.980
0.000	0.000	0.000	0.001	0.001	0.001	0.001	0.001	0.001	0.000	0.002
0.000	0.000	0.000	0.000	0.000	0.000	0.000	0.000	0.000	0.001	0.002
0.000	0.002	0.000	0.001	0.000	0.001	0.001	0.000	0.000	0.001	0.000
0.161	0.153	0.152	0.146	0.277	0.299	0.303	0.243	0.295	0.295	0.184
0.003	0.003	0.002	0.002	0.004	0.004	0.005	0.004	0.005	0.006	0.003
1.839	1.870	1.881	1.873	1.740	1.725	1.705	1.770	2.343	1.776	1.844
0.001	0.000	0.000	0.000	0.002	0.002	0.001	0.002	0.000	0.010	0.001
0.000	0.000	0.001	0.000	0.001	0.000	0.000	0.001	0.000	0.001	0.000
0.001	0.000	0.000	0.000	0.000	0.000	0.000	0.001	0.000	0.001	0.000
0.000	0.000	0.000	0.000	0.000	0.000	0.000	0.000	0.000	0.000	0.000
3.002	3.013	3.018	3.011	3.012	3.016	3.007	3.011	3.321	3.045	3.016
0.92	0.92	0.92	0.93	0.86	0.85	0.85	0.88	0.89	0.86	0.91
8.16	7.67	7.57	7.34	13.91	14.98	15.27	12.23	11.34	14.47	9.18
91.84	92.33	92.43	92.66	86.09	85.02	84.73	87.77	88.66	85.53	90.82

Table 10 (continuation)

IDI-A1_0013 grão1 C	IDI-A1_0013 grão1 INT2	IDI-A1_0013 grão1 INT3	IDI-A1_0013 grão2 B.	IDI-A1_0013 grão2 INT2	IDI-A1_0013 grão2 INT3	IDI-A1_0013 grão2 C	IDI-A1_0013 grão3 B	IDI-A1_0013 grão3 INT1	IDI-A1_0013 grão3 INT2	IDI-A1_0013 grão3 C
40.36	40.29	40.96	40.24	39.74	38.80	38.83	39.03	39.92	40.31	40.13
0.01	0.03	0.06	0.00	0.00	0.06	0.00	0.00	0.02	0.00	0.00
0.00	0.00	0.28	0.01	0.00	0.01	0.00	0.00	0.00	0.00	0.00
0.00	0.04	0.00	0.03	0.01	0.00	0.00	0.02	0.01	0.00	0.00
8.53	8.60	8.20	14.45	13.84	17.27	17.29	13.75	10.63	8.10	8.07
0.13	0.13	0.11	0.21	0.19	0.23	0.21	0.24	0.16	0.12	0.12
51.13	50.91	48.90	45.14	45.65	43.80	44.01	46.08	48.25	51.09	51.25
0.00	0.00	0.06	0.06	0.07	0.06	0.05	0.07	0.06	0.02	0.01
0.00	0.00	0.00	0.02	0.00	0.00	0.00	0.01	0.00	0.00	0.00
0.00	0.00	0.01	0.00	0.00	0.00	0.00	0.00	0.00	0.00	0.00
100.16	100.01	98.59	100.16	99.50	100.24	100.40	99.21	99.05	99.65	99.58
0.983	0.983	1.009	1.005	0.998	0.984	0.983	0.984	0.992	0.985	0.982
0.000	0.001	0.001	0.000	0.000	0.001	0.000	0.000	0.000	0.000	0.000
0.000	0.000	0.008	0.000	0.000	0.000	0.000	0.000	0.000	0.000	0.000
0.000	0.001	0.000	0.001	0.000	0.000	0.000	0.000	0.000	0.000	0.000
0.174	0.176	0.169	0.302	0.290	0.366	0.366	0.290	0.221	0.166	0.165
0.003	0.003	0.002	0.005	0.004	0.005	0.004	0.005	0.003	0.002	0.002
1.857	1.853	1.795	1.681	1.708	1.656	1.661	1.733	1.788	1.861	1.869
0.000	0.000	0.002	0.002	0.002	0.002	0.001	0.002	0.002	0.001	0.000
0.000	0.000	0.000	0.001	0.000	0.000	0.000	0.000	0.000	0.000	0.000
0.000	0.000	0.000	0.000	0.000	0.000	0.000	0.000	0.000	0.000	0.000
0.000	0.000	0.000	0.000	0.000	0.000	0.000	0.000	0.000	0.000	0.000
3.017	3.016	2.986	2.995	3.002	3.015	3.017	3.015	3.007	3.015	3.018
0.91	0.91	0.91	0.85	0.85	0.82	0.82	0.85	0.89	0.92	0.92
8.68	8.77	8.71	15.41	14.71	18.31	18.24	14.56	11.14	8.28	8.23
91.32	91.23	91.29	84.59	85.29	81.69	81.76	85.44	88.86	91.72	91.77

Table 10 (continuation)

SP_ID3_0001 B_OLIVINA	SP_ID3_0001 C_OLIVINA	SP_ID3_0003 B_CLARA	SP_ID3_0003 INT_CLARO	SP_ID3_0003 CENTRO	SP_ID3_0003 INT_ESCURO	SP_ID3_0003 B_ESCURO	SP_ID 4_0008 C_OLIVINA	SP_ID 4_0008 B_OLIVINA	SP_ID 6_0011 C_OLIVINA	SP_ID 6_0011 B_OLIVINA
39.88	39.77	38.68	39.51	39.78	40.95	41.00	40.17	38.96	39.58	39.54
0.01	0.00	0.05	0.01	0.04	0.00	0.00	0.03	0.03	0.06	0.00
0.01	0.01	0.00	0.03	0.00	0.00	0.02	0.03	0.00	0.01	0.01
0.04	0.00	0.07	0.05	0.05	0.01	0.00	0.09	0.09	0.00	0.01
12.18	11.83	13.48	13.45	11.84	7.92	7.65	10.90	13.48	13.70	13.80
0.19	0.16	0.21	0.20	0.16	0.10	0.11	0.12	0.22	0.36	0.34
46.10	47.66	46.30	45.85	47.35	50.41	50.12	47.48	46.80	45.01	44.74
0.06	0.06	0.04	0.09	0.03	0.00	0.03	0.12	0.06	0.17	0.18
0.00	0.02	0.00	0.01	0.00	0.00	0.00	0.01	0.03	0.00	0.01
0.00	0.00	0.00	0.00	0.02	0.00	0.02	0.02	0.00	0.00	0.00
0.27	0.31	0.15	0.21	0.33	0.41	0.39	0.38	0.19	0.11	0.10
98.74	99.82	98.99	99.41	99.59	99.80	99.33	99.35	99.87	99.00	98.73
1.002	0.988	0.978	0.993	0.991	0.998	1.002	0.998	0.977	0.999	1.001
0.000	0.000	0.001	0.000	0.001	0.000	0.000	0.000	0.001	0.001	0.000
0.000	0.000	0.000	0.001	0.000	0.000	0.000	0.001	0.000	0.000	0.000
0.001	0.000	0.001	0.001	0.001	0.000	0.000	0.002	0.002	0.000	0.000
0.256	0.246	0.285	0.283	0.247	0.161	0.156	0.226	0.283	0.289	0.292
0.004	0.003	0.004	0.004	0.003	0.002	0.002	0.003	0.005	0.008	0.007
1.727	1.766	1.746	1.718	1.758	1.832	1.827	1.759	1.749	1.694	1.689
0.002	0.002	0.001	0.002	0.001	0.000	0.001	0.003	0.002	0.005	0.005
0.000	0.001	0.000	0.000	0.000	0.000	0.000	0.000	0.002	0.000	0.000
0.000	0.000	0.000	0.000	0.001	0.000	0.001	0.001	0.000	0.000	0.000
0.006	0.006	0.003	0.004	0.007	0.008	0.008	0.008	0.004	0.002	0.002
2.992	3.006	3.017	3.002	3.002	2.994	2.990	2.993	3.019	2.997	2.996
0.87	0.88	0.86	0.86	0.88	0.92	0.92	0.88	0.86	0.85	0.85
13.08	12.37	14.23	14.31	12.44	8.19	7.99	11.52	14.11	14.91	15.06
86.92	87.63	85.77	85.69	87.56	91.81	92.01	88.48	85.89	85.09	84.94

Table 10 (continuation)

SP_ID9_0001 C_OLIVINA	SP_ID9_0001 B_OLIVINA	SP_ID9_0002 C_OLIVINA	SP_ID9_0002 B_OLIVINA	SP_ID9_0005 C_OLIVINA	SP_ID9_0005 B_OLIVINA	SP_ID9_0006 C_OLIVINA	SP_ID9_0006 B_OLIVINA	SP_ID9#_0001 C_OLIVINA	SP_ID9#_0001 B_OLIVINA
40.11	39.99	40.48	39.95	40.07	39.80	40.09	40.34	40.85	39.56
0.01	0.01	0.01	0.02	0.01	0.00	0.00	0.04	0.00	0.00
0.02	0.03	0.00	0.01	0.02	0.03	0.01	0.00	0.00	0.02
0.06	0.04	0.01	0.07	0.08	0.08	0.06	0.03	0.01	0.11
10.83	10.80	8.37	8.29	10.74	10.64	8.41	8.32	7.28	13.86
0.14	0.13	0.13	0.14	0.11	0.11	0.11	0.13	0.13	0.20
47.35	47.12	49.82	49.69	47.54	47.53	50.09	49.20	50.79	45.23
0.10	0.13	0.00	0.01	0.12	0.10	0.03	0.04	0.00	0.04
0.00	0.01	0.01	0.00	0.02	0.03	0.00	0.02	0.00	0.00
0.00	0.00	0.00	0.01	0.00	0.00	0.02	0.01	0.00	0.02
0.37	0.41	0.38	0.38	0.42	0.41	0.35	0.37	0.40	0.22
98.99	98.67	99.21	98.56	99.13	98.73	99.17	98.49	99.47	99.27
1.000	1.000	0.995	0.990	0.997	0.995	0.987	0.999	0.997	0.997
0.000	0.000	0.000	0.000	0.000	0.000	0.000	0.001	0.000	0.000
0.000	0.001	0.000	0.000	0.001	0.001	0.000	0.000	0.000	0.001
0.001	0.001	0.000	0.001	0.002	0.001	0.001	0.001	0.000	0.002
0.226	0.226	0.172	0.172	0.224	0.222	0.173	0.172	0.149	0.292
0.003	0.003	0.003	0.003	0.002	0.002	0.002	0.003	0.003	0.004
1.759	1.757	1.826	1.835	1.764	1.771	1.839	1.816	1.847	1.700
0.003	0.003	0.000	0.000	0.003	0.003	0.001	0.001	0.000	0.001
0.000	0.001	0.001	0.000	0.001	0.001	0.000	0.001	0.000	0.000
0.000	0.000	0.000	0.000	0.000	0.000	0.000	0.000	0.000	0.000
0.008	0.008	0.007	0.007	0.008	0.008	0.007	0.007	0.008	0.005
2.992	2.991	2.997	3.002	2.994	2.997	3.005	2.993	2.995	2.997
0.89	0.88	0.91	0.91	0.89	0.89	0.91	0.91	0.92	0.85
11.50	11.51	8.74	8.69	11.35	11.26	8.71	8.79	7.57	14.85
88.50	88.49	91.26	91.31	88.65	88.74	91.29	91.21	92.43	85.15

Table 10 (continuation)

SP_ID9#_0004 C_OLIVINA	SP_ID9#_0004 B_OLIVINA	SP_ID9#_0006 C_OLIVINA	SP_ID9#_0006 B_OLIVINA	SP_ID9#_0007 C_OLIVINA	SP_ID9#_0007 B_OLIVINA	SP_ID9#_0008 C_OLIVINA	SP_ID9#_0008 B_OLIVINA	SP_ID9#_0009 C_OLIVINA
40.91	39.54	40.46	40.40	40.52	40.49	41.04	39.27	40.31
0.00	0.00	0.00	0.04	0.03	0.01	0.00	0.07	0.00
0.00	0.00	0.01	0.04	0.04	0.05	0.01	0.00	0.00
0.00	0.03	0.04	0.00	0.05	0.05	0.00	0.06	0.03
7.09	13.26	8.20	8.10	8.67	8.20	7.35	13.66	8.08
0.09	0.20	0.14	0.16	0.09	0.12	0.12	0.19	0.12
50.64	45.23	49.77	49.89	49.28	49.47	50.54	45.59	50.00
0.01	0.04	0.02	0.03	0.11	0.08	0.01	0.06	0.00
0.01	0.01	0.00	0.00	0.02	0.02	0.00	0.02	0.01
0.00	0.00	0.00	0.00	0.01	0.00	0.00	0.00	0.01
0.38	0.19	0.41	0.39	0.36	0.38	0.35	0.16	0.33
99.14	98.51	99.05	99.06	99.18	98.87	99.42	99.08	98.90
1.000	1.001	0.996	0.994	0.998	0.998	1.001	0.991	0.993
0.000	0.000	0.000	0.001	0.001	0.000	0.000	0.001	0.000
0.000	0.000	0.000	0.001	0.001	0.001	0.000	0.000	0.000
0.000	0.001	0.001	0.000	0.001	0.001	0.000	0.001	0.001
0.145	0.281	0.169	0.167	0.179	0.169	0.150	0.288	0.166
0.002	0.004	0.003	0.003	0.002	0.002	0.003	0.004	0.003
1.845	1.707	1.826	1.830	1.809	1.818	1.838	1.715	1.837
0.000	0.001	0.001	0.001	0.003	0.002	0.000	0.002	0.000
0.001	0.001	0.000	0.000	0.001	0.001	0.000	0.001	0.001
0.000	0.000	0.000	0.000	0.000	0.000	0.000	0.000	0.000
0.008	0.004	0.008	0.008	0.007	0.007	0.007	0.003	0.007
2.993	2.995	2.996	2.997	2.994	2.993	2.992	3.004	3.000
0.93	0.86	0.91	0.91	0.91	0.91	0.92	0.85	0.92
7.37	14.31	8.60	8.50	9.07	8.62	7.66	14.56	8.43
92.63	85.69	91.40	91.50	90.93	91.38	92.34	85.44	91.57

Table 10 (continuation)

SP_ID9#_0009 B_OLIVINA	IDI A2_0010 C_OLIVINA	IDI A2_0010 B_OLIVINA	IDI A2_0011 C_OLIVINA	INDAIA _1_0002 C_OLIVINA	INDAIA _1_0002 B_OLIVINA	INDAIA _1_0003 C_OLIVINA	INDAIA _1_0003 B_OLIVINA
39.30	38.90	37.77	37.78	40.00	39.70	57.25	57.99
0.05	0.02	0.04	0.04	0.04	0.02	0.02	0.08
0.01	0.01	0.00	0.04	0.03	0.01	0.14	0.38
0.00	0.00	0.09	0.07	0.01	0.00	0.25	0.44
13.64	8.07	13.83	13.07	11.46	10.80	4.82	4.76
0.24	0.13	0.19	0.16	0.16	0.17	0.11	0.12
45.36	50.63	46.10	46.42	47.22	46.67	35.51	34.58
0.05	0.01	0.12	0.06	0.01	0.02	0.49	0.66
0.00	0.01	0.00	0.00	0.00	0.00	0.05	0.06
0.00	0.00	0.00	0.03	0.02	0.00	0.01	0.00
0.15	0.37	0.20	0.38	0.35	0.31	0.11	0.10
98.80	98.15	98.34	98.04	99.30	97.71	98.76	99.18
0.994	0.969	0.966	0.966	0.997	1.002	1.325	1.335
0.001	0.000	0.001	0.001	0.001	0.000	0.000	0.001
0.000	0.000	0.000	0.001	0.001	0.000	0.004	0.010
0.000	0.000	0.002	0.001	0.000	0.000	0.005	0.008
0.289	0.168	0.296	0.279	0.239	0.228	0.093	0.092
0.005	0.003	0.004	0.004	0.003	0.004	0.002	0.002
1.711	1.881	1.757	1.770	1.754	1.756	1.225	1.187
0.001	0.000	0.003	0.002	0.000	0.001	0.012	0.016
0.000	0.000	0.000	0.000	0.000	0.000	0.002	0.003
0.000	0.000	0.000	0.001	0.001	0.000	0.000	0.000
0.003	0.007	0.004	0.008	0.007	0.006	0.002	0.002
3.002	3.023	3.028	3.025	2.995	2.991	2.669	2.654
0.85	0.92	0.85	0.86	0.88	0.88	0.93	0.93
14.65	8.33	14.57	13.79	12.13	11.65	7.23	7.34
85.35	91.67	85.43	86.21	87.87	88.35	92.77	92.66

Table 10 (continuation) **Trace elements in olivine minerals of Indaiá Kimberlite**

Concentrations in ppm (µg/g)	IDI-A1_0001	IDI-A1_0002	INDAIA _1_0003	IDI-A1_0013
	OL.CENTRO	macro.olv.C	C_OLIVINA	grão1 INT3
Li7	3.81	1.78	3.95	2.76
P31	74.42	13.17	341.11	93.55
Ca42	<226.70	<236.70	999.92	<209.92
Sc45	2.54	2.17	11.08	1.64
Ti49	86.29	34.08	171.45	115.07
V51	<3.26	<3.55	<2.58	<3.17
Cr52	53.34	47.06	462.41	102.91
Mn55	2280.69	1370.63	1785.57	1323.05
Co59	201.84	153.03	150.33	155.84
Ni60	3187.26	3210.12	1598.17	2553.04
Cu65	1.69	1.57	3.2	1.92
Zn66	205.88	122.75	116.24	125.75
Ga71	<0.106	0.16	<0.105	<0.106
Rb85	0.228	<0.108	<0.072	<0.091
Sr88	8.46	0.082	1.06	0.101
Y89	0.101	<0.0149	0.065	<0.0130
Zr90	0.814	0.558	1.9	0.378
Nb93	1.47	1.23	0.125	0.113
Mo95	<0.098	<0.145	<0.069	<0.094
Sn118	1.25	0.96	0.92	1.03
Sb121	<0.138	<0.150	<0.092	<0.122
Cs133	<0.0198	<0.0097	<0.0098	<0.0155
Ba137	10.69	0.268	1.06	0.512
La139	0.684	0.0182	0.043	<0.0081
Ce140	1.55	0.0337	0.071	0.027
Pr141	0.143	<0.01	<0.0044	0.0079
Nd143	0.461	<0.065	<0.060	<0.075
Sm147	<0.074	0.0079	<0.036	<0.031
Eu151	<0.023	<0.0132	<0.0117	<0.0094
Gd157	<0.065	<0.039	<0.029	<0.034
Tb159	<0.0217	<0.0050	<0.0051	<0.0054
Dy161	<0.049	<0.027	0.041	<0.029
Ho165	<0.0109	<0.0062	0.0068	<0.0063
Er166	0.024	0.0154	0.027	<0.0175
Tm169	<0.0202	<0.0080	0.0066	<0.0063
Yb172	<0.0246	<0.031	<0.024	0.016
Lu175	<0.0125	<0.0066	0.0051	<0.0071
Hf179	<0.047	<0.021	<0.021	<0.032
Ta181	0.0272	0.0466	<0.0033	<0.0049
Pb206	0.222	0.27	0.16	0.135
Pb207	0.223	0.219	0.107	0.131
Pb208	0.21	0.189	0.161	0.133
Th232	0.0293	0.0063	0.0046	0.0018
U238	0.0102	0.0019	0.0041	0.00079

Table 11

Major-element compositions of perovskite minerals from Charneca Kimberlite

	CHAR_1_0020 PRV ZONADA_C	CHAR_1_0020 PRV ZONADA_INT	CHAR_1_0020 PRV ZONADA_B	CHAR_1_0028 PRV_C	CHAR_1_0028 PRV_INT	CHAR_1_0028 PRV_B	CHAR-5PRV_0001 PRV_C
SiO2	0.00	0.00	0.00	0.00	0.00	0.00	0.00
TiO2	55.03	54.77	55.36	54.23	55.08	55.05	55.02
Al2O3	0.12	0.14	0.11	0.09	0.17	0.15	0.12
FeO(T)	1.07	1.23	1.12	1.07	1.08	1.13	1.13
MnO	0.02	0.03	0.01	0.02	0.03	0.03	0.04
MgO	0.00	0.00	0.00	0.00	0.00	0.00	0.00
CaO	37.46	39.21	37.87	37.33	37.52	37.99	37.47
Na2O	0.40	0.21	0.33	0.47	0.39	0.33	0.44
K2O	0.03	0.03	0.01	0.03	0.06	0.06	0.02
Cr2O3	0.02	0.02	0.03	0.06	0.05	0.06	0.11
La2O3	0.63	0.38	0.65	0.86	0.78	0.59	0.76
ZnO	0.01	0.00	0.02	0.01	0.00	0.03	0.03
ThO2	0.35	0.22	0.04	0.39	0.00	0.02	0.47
Ce2O3	1.54	0.59	1.56	2.03	1.50	1.52	1.89
Nb2O5	0.44	0.56	0.48	0.43	0.20	0.30	0.37
Sm2O3	0.08	0.08	0.07	0.07	0.08	0.06	0.07
Nd2O3	0.71	0.67	0.62	0.66	0.67	0.54	0.62
SrO	0.35	0.39	0.34	0.34	0.37	0.36	0.33
Pr2O3	0.19	0.18	0.16	0.18	0.18	0.15	0.17
Sum	98.46	98.72	98.80	98.21	98.09	98.31	98.99
Sum of Atomic mol pr	1.4287	1.4021	1.4200	1.4395	1.4311	1.4229	1.4258
Number of ions on base of 3 oxygen							
Si	0.000	0.000	0.000	0.000	0.000	0.000	0.000

Ti	0.984	0.961	0.984	0.983	0.992	0.985	0.987
Al	0.003	0.004	0.003	0.003	0.005	0.004	0.003
Fe+3	0.008	0.044	0.003	0.003	0.007	0.007	0.006
Fe+2	0.029	0.020	0.025	0.019	0.029	0.016	0.028
Mn	0.000	0.001	0.000	0.000	0.001	0.001	0.001
Mg	0.000	0.000	0.000	0.000	0.000	0.000	0.000
Ca	0.954	0.980	0.959	0.963	0.963	0.968	0.957
Na	0.019	0.010	0.015	0.022	0.018	0.015	0.020
K	0.001	0.001	0.000	0.001	0.002	0.002	0.001
Cr	0.000	0.000	0.001	0.001	0.001	0.001	0.002
La	0.006	0.003	0.006	0.008	0.007	0.005	0.007
Zn	0.000	0.000	0.000	0.000	0.000	0.000	0.000
Th	0.002	0.001	0.000	0.002	0.000	0.000	0.003
Ce	0.013	0.005	0.013	0.018	0.013	0.013	0.017
Nb	0.005	0.006	0.005	0.005	0.002	0.003	0.004
Nd	0.006	0.006	0.005	0.006	0.006	0.005	0.005
Sr	0.005	0.005	0.005	0.005	0.005	0.005	0.005
Pr	0.002	0.002	0.001	0.002	0.002	0.001	0.001
Total:	2.022	2.009	2.021	2.028	2.027	2.023	2.026

Trace elements in perovskites minerals of Charneca Kimberlite

Concentrations in ppm (µg/g)							
Li	1.03	<1.85	<0.89	<0.25	0.50	<0.21	<0.28
Na	3127.09	3835.67	2962.99	3548.10	3611.44	3038.77	3537.35
P	<17.99	<38.90	<19.44	5.95	6.40	5.79	7.62
Sc	2.75	3.26	3.22	2.84	3.08	3.04	3.03
V	84.43	86.64	86.11	98.10	104.37	83.76	97.35
Cr	317.68	342.88	409.05	667.78	631.49	464.58	754.36
Co	1.00	<1.07	0.59	0.93	0.88	0.70	0.79
Sr	2931.49	3324.63	2908.52	2868.41	3167.80	3029.89	2832.45
Y	155.62	182.63	154.45	142.64	153.86	142.59	140.00
Zr	306.77	440.74	371.25	314.04	349.79	354.32	293.75

Nb	2281.32	2712.31	2337.05	2517.47	2549.65	2705.27	2320.75
Sn	3.09	5.24	6.09	3.72	4.37	3.99	3.62
Sb	<0.27	<0.50	<0.29	<0.077	0.09	<0.072	<0.097
Ba	38.94	33.67	33.83	29.29	33.55	31.69	26.29
La	6969.29	6394.54	6342.58	6056.26	6151.87	5613.13	5567.44
Ce	15303.50	13972.29	13744.43	14901.96	14382.07	12637.42	13249.05
Pr	1583.81	1523.84	1407.96	1547.77	1541.06	1306.73	1431.59
Nd	6082.75	5750.85	5314.70	5645.36	5766.51	4631.56	5333.24
Sm	659.26	674.75	611.15	628.21	658.39	544.11	616.69
Eu	143.57	149.13	135.31	146.20	149.23	129.64	141.68
Gd	307.01	344.14	288.80	290.68	305.73	262.76	288.79
Tb	26.70	30.23	25.21	24.32	26.19	23.55	25.05
Dy	91.48	106.41	90.99	84.77	89.17	83.94	84.45
Ho	9.70	12.88	9.90	9.23	9.88	9.43	9.29
Er	15.50	20.26	16.47	16.39	16.54	16.04	15.74
Tm	1.35	1.64	1223.00	1175.00	1226.00	1161.00	1200.00
Yb	4.75	6.29	5.88	5.05	5.59	5.44	5.12
Lu	0.47	0.66	0.49	0.47	0.49	0.50	0.47
Hf	16.14	25.85	18.64	17.49	18.67	18.55	16.68
Ta	331.98	419.50	362.15	364.19	378.16	329.85	370.67
Pb	10.74	12.53	10.86	10.43	11.36	10.43	10.45
Pb	8.15	8.89	6.68	7.15	7.69	6.89	7.64
Pb	17.50	21.01	17.68	16.27	17.92	14.04	15.82
Th	992.83	1137.20	1075.85	998.86	1043.27	759.28	872.73
U	64.33	57.03	53.36	54.08	57.91	51.78	54.98

Table 11 (continuation)

	CHAR-5PRV_0001 PRV_INT	CHAR-5PRV_0001 PRV_INT	CHAR-5PRV_0001 PRV_B	CHAR-5PRV_0002 PRV_C	CHAR-5PRV_0002 PRV_INT 1	CHAR-5PRV_0002 PRV_INT 2	CHAR-5PRV_0002 PRV_B
SiO2	0.00	0.00	0.00	0.00	0.00	0.00	0.19
TiO2	54.95	54.13	53.73	53.40	54.74	54.06	54.28
Al2O3	0.15	0.15	0.09	0.14	0.12	0.10	0.36
FeO(T)	1.16	1.62	1.20	1.20	1.17	1.11	1.57
MnO	0.05	0.00	0.01	0.04	0.03	0.04	0.02
MgO	0.00	0.00	0.00	0.00	0.00	0.00	0.00
CaO	37.55	39.38	38.77	37.45	38.05	38.27	38.13
Na2O	0.44	0.23	0.33	0.48	0.37	0.37	0.29
K2O	0.04	0.03	0.04	0.05	0.05	0.05	0.14
Cr2O3	0.05	0.02	0.04	0.14	0.03	0.06	0.02
La2O3	0.67	0.28	0.48	0.76	0.63	0.63	0.50
ZnO	0.00	0.00	0.02	0.01	0.00	0.00	0.02
ThO2	0.21	0.25	0.34	0.00	0.20	0.04	0.01
Ce2O3	1.82	0.52	1.05	1.76	1.37	1.55	1.08
Nb2O5	0.33	0.47	0.53	0.37	0.33	0.40	0.30
Sm2O3	0.06	0.05					
Nd2O3	0.53	0.41					
SrO	0.36	0.38					
Pr2O3	0.14	0.11					
Sum	98.48	97.98	96.62	95.81	97.09	96.67	96.91
Sum of Atomic mol ı	1.4280	1.4051	1.4291	1.4559	1.4312	1.4367	1.4248
Number of ions on base of 3 oxygen							
Si	0.000	0.000	0.000	0.000	0.000	0.000	0.005

Ti	0.987	0.956	0.961	0.973	0.981	0.972	0.968
Al	0.004	0.004	0.002	0.004	0.003	0.003	0.010
Fe+3	0.002	0.066	0.051	0.024	0.014	0.031	0.028
Fe+2	0.025	0.035	0.027	0.000	0.009	0.009	0.004
Mn	0.001	0.000	0.000	0.001	0.001	0.001	0.000
Mg	0.000	0.000	0.000	0.000	0.000	0.000	0.000
Ca	0.961	0.991	0.988	0.972	0.971	0.980	0.969
Na	0.020	0.011	0.015	0.023	0.017	0.017	0.013
K	0.001	0.001	0.001	0.002	0.002	0.002	0.004
Cr	0.001	0.000	0.001	0.003	0.001	0.001	0.000
La	0.006	0.002	0.004	0.007	0.006	0.006	0.004
Zn	0.000	0.000	0.000	0.000	0.000	0.000	0.000
Th	0.001	0.001	0.002	0.000	0.001	0.000	0.000
Ce	0.016	0.004	0.009	0.016	0.012	0.014	0.009
Nb	0.004	0.005	0.006	0.004	0.004	0.004	0.003
Nd	0.005	0.003					
Sr	0.005	0.005					
Pr	0.001	0.001					
Total:	2.027	2.009	2.014	2.028	2.020	2.022	2.019

Trace elements in perovskites minerals of Charneca Kimberlite

Concentrations in ppm (µg/g)		
Li	<0.32	<0.30
Na	3076.01	2632.92
P	<6.02	7.85
Sc	3.80	3.80
V	95.28	95.21
Cr	446.41	262.82
Co	0.60	0.78
Sr	3038.31	3223.74
Y	147.77	143.24
Zr	362.73	490.98

Nb	2435.20	2643.60
Sn	4.08	4.89
Sb	<0.097	<0.095
Ba	29.63	40.64
La	4923.17	4259.73
Ce	11100.31	8884.43
Pr	1215.54	940.66
Nd	4567.45	3523.37
Sm	540.97	439.24
Eu	126.32	112.09
Gd	262.87	245.40
Tb	23.14	22.79
Dy	82.57	83.59
Ho	9.13	9.28
Er	15.59	15.99
Tm	1294.00	1265.00
Yb	5.83	5.65
Lu	0.52	0.50
Hf	20.22	29.00
Ta	335.68	289.13
Pb	10.28	9.54
Pb	6.96	6.78
Pb	13.13	10.69
Th	735.35	469.84
U	52.65	46.95

Table 11 (continuation)

	CHAR-5PRV_0003 PRV_C	CHAR-5PRV_0004 PRV_C	CHAR-5PRV_0004 PRV_B	CHAR-5PRV_0005 PRV_C	CHAR-5PRV_0005 PRV_B	CHAR-5PRV_0006 PRV_C	CHAR-5PRV_0006 PRV_B
SiO2	0.00	0.00	0.09	0.00	0.98	0.00	0.00
TiO2	53.97	53.49	55.09	53.76	92.09	54.82	54.65
Al2O3	0.14	0.13	0.12	0.11	0.00	0.11	0.13
FeO(T)	1.13	1.15	1.24	1.14	1.46	1.32	1.37
MnO	0.03	0.01	0.00	0.03	0.08	0.01	0.02
MgO	0.00	0.00	0.00	0.00	0.05	0.00	0.00
CaO	37.59	36.98	38.29	37.82	0.47	37.16	38.85
Na2O	0.41	0.51	0.33	0.42	0.01	0.38	0.27
K2O	0.05	0.05	0.03	0.04	0.01	0.06	0.04
Cr2O3	0.10	0.07	0.03	0.06	0.06	0.00	0.00
La2O3	0.73	0.88	0.41	0.73	0.00	0.82	0.43
ZnO	0.01	0.00	0.00	0.00	0.02	0.00	0.00
ThO2	0.06	0.09	0.00	0.00	0.00	0.21	0.06
Ce2O3	1.41	2.07	0.93	1.48	0.01	1.54	0.80
Nb2O5	0.34	0.41	0.44	0.58	0.66	0.31	0.15
Sm2O3	0.06	0.08	0.00	0.06	0.00	0.03	
Nd2O3	0.49	0.72		0.54		0.22	
SrO	0.35	0.34		0.35		0.38	
Pr2O3	0.13	0.18		0.14		0.06	
Sum	96.94	97.08	97.01	97.19	95.91	97.40	96.76
Sum of Atomic mol ı	1.4428	1.4555	1.4223	1.4393	1.6528	1.4402	1.4216
Number of ions on base of 3 oxygen							
Si	0.000	0.000	0.002	0.000	0.027	0.000	0.000

Ti	0.979	0.980	0.981	0.973	1.906	0.992	0.973
Al	0.004	0.004	0.003	0.003	0.000	0.003	0.004
Fe+3	0.016	0.009	0.012	0.025	1.881	0.008	0.040
Fe+2	0.007	0.015	0.012	0.002	1.915	0.034	0.012
Mn	0.001	0.000	0.000	0.001	0.002	0.000	0.000
Mg	0.000	0.000	0.000	0.000	0.002	0.000	0.000
Ca	0.971	0.965	0.971	0.975	0.014	0.957	0.985
Na	0.019	0.024	0.015	0.020	0.000	0.018	0.012
K	0.001	0.001	0.001	0.001	0.000	0.002	0.001
Cr	0.002	0.001	0.001	0.001	0.001	0.000	0.000
La	0.007	0.008	0.004	0.006	0.000	0.007	0.004
Zn	0.000	0.000	0.000	0.000	0.000	0.000	0.000
Th	0.000	0.001	0.000	0.000	0.000	0.001	0.000
Ce	0.012	0.018	0.008	0.013	0.000	0.014	0.007
Nb	0.004	0.005	0.005	0.006	0.008	0.003	0.002
Nd	0.004	0.006		0.005		0.002	
Sr	0.005	0.005		0.005		0.005	
Pr	0.001	0.002		0.001		0.001	
Total:	2.025	2.032	2.015	2.024	1.995	2.025	2.015

Trace elements in perovskites minerals of Charneca Kimberlite

Concentrations in ppm (µg/g)				
Li	<0.32	0.46	<0.21	0.37
Na	3263.52	3588.51	3203.18	2195.72
P	27.05	<5.56	<3.84	8.74
Sc	4.72	3.23	3.64	4.29
V	104.11	98.18	102.80	85.54
Cr	464.99	481.15	571.44	12.08
Co	0.81	0.98	2.20	0.78
Sr	2943.33	2869.70	2986.79	3211.75
Y	158.71	145.13	152.01	133.41
Zr	443.97	339.12	359.23	479.75

Nb	2848.63	2269.74	2729.51	2460.41
Sn	5.67	3.70	4.10	5.07
Sb	0.14	<0.094	<0.069	<0.084
Ba	207.07	26.54	65.88	76.89
La	4804.09	5721.84	5110.05	2991.87
Ce	10470.94	14234.02	11200.32	5225.18
Pr	1125.76	1560.26	1191.20	520.81
Nd	4185.59	6132.81	4603.22	1913.56
Sm	505.42	688.51	540.11	272.35
Eu	123.28	154.06	126.01	77.79
Gd	263.69	319.20	276.87	168.19
Tb	24.34	26.90	25.58	17.19
Dy	89.84	91.55	84.31	68.14
Ho	10.64	9.55	9.43	8.29
Er	17.88	15.78	15.04	13.53
Tm	1372.00	1137.00	1146.00	1043.00
Yb	5.83	4.79	5.37	5.01
Lu	0.61	0.41	0.49	0.44
Hf	21.86	18.27	18.59	24.03
Ta	369.05	369.42	343.61	206.60
Pb	27.28	11.29	13.57	13.68
Pb	22.18	7.57	11.97	11.79
Pb	31.48	18.56	17.11	14.43
Th	773.45	1097.78	629.94	203.30
U	56.78	53.50	54.98	40.50

Table 12

Major-element compositions of perovskites minerals from Grota do Cedro Kimberlite

	GC 11_0001 PRV_C	GC 11_0001 PRV_B	GC 11_0001 PRV_INT	GC 11_0002 PRV_C	GC 11_0002 PRV_B	GC 11_0002 PRV_INT	GC 11_0003 PRV_C	GC 11_0003 PRV_B	GC 11_0003 PRV_INT	GC 11_0004 PRV_C
SiO2	0.00	0.00	0.00	0.00	0.02	0.00	0.01	0.32	4.64	0.00
TiO2	0.15	0.27	0.20	0.71	0.94	0.65	3.92	5.27	5.55	7.65
Al2O3	0.02	0.03	0.00	0.03	0.01	0.00	0.03	0.05	0.40	0.00
FeO(T)	1.10	0.73	0.97	2.15	1.63	1.34	0.40	0.43	0.77	0.37
MnO	0.37	0.30	0.31	0.53	0.44	0.29	0.05	0.05	0.02	0.07
MgO	1.55	1.51	1.62	0.42	0.41	0.28	0.45	0.25	1.74	0.00
CaO	16.55	15.54	16.27	14.68	14.38	15.14	18.08	18.00	16.47	19.11
Na2O	1.91	2.52	1.99	3.56	4.83	5.28	5.05	4.76	4.39	4.58
K2O	0.09	0.15	0.13	0.18	0.25	0.29	0.19	0.21	0.30	0.18
Cr2O3	0.00	0.00	0.00	0.00	0.00	0.00	0.00	0.00	0.00	0.00
La2O3	2.16	1.98	2.09	1.64	1.30	1.00	0.60	0.54	0.40	0.34
ZnO	0.04	0.04	0.00	0.00	0.00	0.02	0.04	0.00	0.00	0.02
ThO2	0.32	0.21	0.00	0.05	0.27	0.00	0.01	0.16	0.77	1.13
Ce2O3	13.26	12.32	13.74	12.04	9.23	6.88	3.69	2.89	1.97	3.27
Nb2O5	52.59	53.42	52.27	55.20	57.63	59.55	55.93	54.07	50.15	53.11
Sm2O3	0.31			0.14	0.15		0.18			0.07
Nd2O3	2.28			1.20	1.31		1.37			0.59
SrO	0.24			0.36	0.40		0.60			0.38
Pr2O3	0.77			0.41	0.44		0.42			0.18
ZrO2	0.38			0.01	0.01		1.03			1.87
Total:	94.07	89.01	89.58	93.31	93.64	90.72	92.08	87.01	87.57	92.91
Sum of Atomic mol proportion:	1.9	1.9	1.9	1.9	1.8	1.8	1.7	1.7	1.7	1.7

Number of ions on base of 3 oxygen **Number of ions on bas**

Si	0.000	0.000	0.000	0.000	0.001	0.000	0.000	0.009	0.130	0.000
Ti	0.003	0.006	0.005	0.017	0.021	0.014	0.085	0.115	0.117	0.163
Al	0.001	0.001	0.000	0.001	0.000	0.000	0.001	0.002	0.013	0.000
Fe+3	0.658	0.614	0.652	0.557	0.512	0.516	0.504	0.459	0.338	0.428
Fe+2	0.630	0.595	0.626	0.502	0.471	0.483	0.494	0.448	0.320	0.419
Mn	0.010	0.008	0.008	0.014	0.011	0.007	0.001	0.001	0.001	0.002
Mg	0.072	0.071	0.076	0.019	0.018	0.012	0.019	0.011	0.072	0.000
Ca	0.551	0.522	0.547	0.485	0.463	0.478	0.558	0.561	0.493	0.580
Na	0.115	0.153	0.121	0.213	0.281	0.302	0.282	0.268	0.238	0.252
K	0.003	0.006	0.005	0.007	0.009	0.011	0.007	0.008	0.011	0.006
Cr	0.000	0.000	0.000	0.000	0.000	0.000	0.000	0.000	0.000	0.000
La	0.025	0.023	0.024	0.019	0.014	0.011	0.006	0.006	0.004	0.004
Zn	0.001	0.001	0.000	0.000	0.000	0.001	0.001	0.000	0.000	0.000
Th	0.002	0.001	0.000	0.000	0.002	0.000	0.000	0.001	0.005	0.007
Ce	0.151	0.141	0.158	0.136	0.102	0.074	0.039	0.031	0.020	0.034
Nb	0.739	0.757	0.742	0.770	0.783	0.793	0.728	0.711	0.633	0.680
Sm	0.003	0.000	0.000	0.002	0.002	0.000	0.002	0.000	0.000	0.001
Nd	0.025	0.000	0.000	0.013	0.014	0.000	0.014	0.000	0.000	0.006
Sr	0.004	0.000	0.000	0.006	0.007	0.000	0.010	0.000	0.000	0.006
Pr	0.009	0.000	0.000	0.005	0.005	0.000	0.004	0.000	0.000	0.002
Zr	0.006	0.000	0.000	0.000	0.000	0.000	0.015	0.000	0.000	0.026
Total:	1.749	1.710	1.711	1.762	1.775	1.736	1.782	1.734	1.755	1.777

Trace elements in perovskites minerals of Grota do Cedro Kimberlite

Concentrations in ppm (µg/g)

Li	1.19	0.91	0.83	30.39	0.61
Na	15689.55	34787.64	42702.41	46592.47	38300.48
Mg	11315.68	2420.98	2306.26	12452.02	137.85
Al	104.23	136.49	164.19	1218.63	<0.38
Si	1529.43	<267.21	<220.17	16483.79	434.46
P	154.11	<5.15	<3.97	58.74	<4.76
Ca42	118283	104918.09	110206.88	129217.91	136579.33
Ca44	116781.77	99697.65	104873.47	123561.98	132827.63
Sc	467.58	24.36	24.44	260.29	27.44

Ti46	1248.33	3446.48	3643.83	2708.15	39447.55
Ti49	1333.23	3738.49	3834.87	2927.01	42927.79
V51	75.73	143.42	160.39	193.12	92.94
Cr	0.72	0.57	<0.30	18.46	<0.33
Mn	2647.51	2614.7	2576	1119.89	320.01
Fe	8535.53	11454.11	11662.89	9066.71	2831.87
Co	<0.175	0.366	0.242	5.69	<0.130
Sr	1987.54	3015.43	3361.67	5061.57	3237.59
Y	1392.18	476.08	483.17	465.88	203.36
Zr	2842.42	104.97	69.24	7648.68	13878.22
Nb	368263.47	390791.69	403870.47	466363.22	391265.66
Sn	21.12	111.45	96.49	78.5	932
Sb	4.52	2.23	2.19	12.43	10.64
Ba	43.73	62.38	63.78	194.41	49.01
La	17087.44	9033.08	9563.68	9403.63	3092
Ce	102202.02	58851.11	64840.26	48885.13	25018.61
Pr	6588.13	3470.41	3774.01	3618.08	1502.7
Nd	19552.02	10299.01	11272.04	11767.47	5100.7
Sm	2647.38	1222.25	1327.77	1554.34	645.47
Eu	772.62	302.64	311.28	415.38	170.42
Gd	1386.43	607.94	607.49	720.25	321.92
Tb	161.3	54.15	55.32	76.54	30.11
Dy	710.68	208.88	218.7	308.51	110.59
Ho	87.26	23.85	24	32.72	11.86
Er	171.88	45.54	45.4	58.97	22.9
Tm	18.95	4.74	5	5.71	2.17
Yb	106.01	27.76	30.77	29.26	10.43
Lu	9.22	3.04	3.31	2.55	0.85
Hf	11.32	0.337	0.367	46.39	694.63
Ta	21.59	0.745	0.453	6.82	119.7
Pb	54.88	88.1	78.98	47.89	81.85
Pb	40.81	78.72	74.13	41.4	72.56
Pb	44.03	81.57	76.58	76.53	154.62
Th	189.03	10.19	5.38	3877.69	9268.5
U	180.45	136.74	96.06	76.43	92.37

Table 12 (continuation)

	GC 11_0004 PRV_B	GC 11_0004 PRV_INT	GC 11_0005 PRV ZONADA	GC 11_0005 PRV ZONADA	GC 11_0005 PRV ZONADA	GC 11_0008 PRV_B	GC 11_0008 PRV_INT2	GC 11_0008 PRV_C	GC 11_0009 PRV_B	GC 11_0009 PRV_INT	GC 11_0009 PRV_INT2
SiO2	0.00	0.00	1.04	0.00	0.04	0.00	0.04	0.10	3.87	3.35	2.59
TiO2	7.20	8.13	0.12	0.15	0.12	1.21	2.06	1.76	5.73	6.75	6.46
Al2O3	0.00	0.02	0.01	0.00	0.00	0.03	0.00	0.00	0.06	0.02	0.04
FeO(T)	0.36	0.38	1.56	0.64	0.66	0.29	0.43	0.52	2.53	2.36	1.55
MnO	0.05	0.04	0.11	0.16	0.14	0.04	0.01	0.00	0.07	0.04	0.05
MgO	0.00	0.00	0.32	0.45	0.46	0.00	0.00	0.00	0.10	0.08	0.04
CaO	18.91	18.77	10.42	12.13	11.93	15.55	15.95	16.21	9.46	10.16	13.03
Na2O	4.59	4.69	2.39	5.79	5.46	6.51	5.97	5.91	0.29	0.44	1.78
K2O	0.21	0.19	0.26	0.36	0.40	0.55	0.48	0.48	0.05	0.02	0.08
Cr2O3	0.00	0.00	0.00	0.00	0.00	0.00	0.00	0.01	0.00	0.00	0.00
La2O3	0.32	0.36	1.23	1.46	1.47	0.36	0.50	0.47	0.54	0.81	0.62
ZnO	0.00	0.00	0.00	0.00	0.00	0.00	0.02	0.00	0.04	0.00	0.00
ThO2	1.18	1.43	2.07	2.30	2.06	0.00	0.18	0.38	5.42	3.80	2.65
Ce2O3	2.90	3.60	5.94	7.65	7.45	2.11	2.97	3.20	3.46	4.59	4.16
Nb2O5	53.13	54.37	57.81	57.85	57.12	62.30	60.75	59.47	49.73	48.27	51.84
Sm2O3								0.015			
Nd2O3								0.002			
SrO											
Pr2O3											
ZrO2								0.18			
Total:	88.86	91.98	83.27	88.93	87.32	88.96	89.35	88.71	81.34	80.70	84.90
Sum of Atomic mol proportion:	1.7	1.7	2.0	1.9	1.9	1.7	1.7	1.7	2.0	2.0	1.9

e of 3 oxygen **Number of ions on bas**

Si	0.000	0.000	0.034	0.000	0.001	0.000	0.001	0.003	0.126	0.111	0.080
Ti	0.155	0.170	0.003	0.003	0.003	0.026	0.045	0.039	0.141	0.168	0.150
Al	0.000	0.000	0.000	0.000	0.000	0.001	0.000	0.000	0.002	0.001	0.002
Fe+3	0.434	0.400	0.389	0.444	0.445	0.461	0.458	0.477	0.140	0.151	0.244
Fe+2	0.425	0.391	0.346	0.427	0.427	0.454	0.447	0.464	0.071	0.086	0.204
Mn	0.001	0.001	0.003	0.004	0.004	0.001	0.000	0.000	0.002	0.001	0.001
Mg	0.000	0.000	0.015	0.021	0.022	0.000	0.000	0.000	0.005	0.004	0.002
Ca	0.578	0.560	0.365	0.406	0.406	0.479	0.493	0.506	0.330	0.360	0.430
Na	0.254	0.253	0.151	0.350	0.336	0.363	0.334	0.334	0.018	0.028	0.106
K	0.008	0.007	0.011	0.014	0.016	0.020	0.018	0.018	0.002	0.001	0.003
Cr	0.000	0.000	0.000	0.000	0.000	0.000	0.000	0.000	0.000	0.000	0.000
La	0.003	0.004	0.015	0.017	0.017	0.004	0.005	0.005	0.007	0.010	0.007
Zn	0.000	0.000	0.000	0.000	0.000	0.000	0.000	0.000	0.001	0.000	0.000
Th	0.008	0.009	0.015	0.016	0.015	0.000	0.001	0.003	0.040	0.029	0.019
Ce	0.030	0.037	0.071	0.087	0.087	0.022	0.031	0.034	0.041	0.056	0.047
Nb	0.686	0.685	0.854	0.816	0.819	0.810	0.791	0.783	0.733	0.721	0.722
Sm	0.000	0.000	0.000	0.000	0.000	0.000	0.000	0.000	0.000	0.000	0.000
Nd	0.000	0.000	0.000	0.000	0.000	0.000	0.000	0.000	0.000	0.000	0.000
Sr	0.000	0.000	0.000	0.000	0.000	0.000	0.000	0.000	0.000	0.000	0.000
Pr	0.000	0.000	0.000	0.000	0.000	0.000	0.000	0.000	0.000	0.000	0.000
Zr	0.000	0.000	0.000	0.000	0.000	0.000	0.000	0.003	0.000	0.000	0.000
Total:	1.732	1.735	1.581	1.752	1.743	1.733	1.730	1.739	1.517	1.554	1.609

Trace elements in perovskites minerals of Grota do Cedro Kimberlite

Concentrations in ppm (μg/g)

Li7 ppm	63.49
Na23	259.98
Mg24	432176.38
Al27	1024600.38
Si29	1722360.75
P31	1531.69
Ca42	115853
Ca44	118029.45
Sc45	660.78

Ti46	1977.78
Ti49	2195.28
V51	1324.43
Cr52	1378.33
Mn55	32997.04
Fe56	1818672.75
Co59	305.15
Sr88	0.29
Y89	2042.2
Zr91	1307.28
Nb93	<5.38
Sn118	5.81
Sb121	<1.03
Ba137	<1.03
La139	<0.56
Ce140	<2.66
Pr141	<0.58
Nd143	21.15
Sm147	126.31
Eu151	1.89
Gd157	329.05
Tb159	65.47
Dy161	378.13
Ho165	69.5
Er166	179.77
Tm169	23.94
Yb173	159.06
Lu175	21.26
Hf178	19.73
Ta181	0.244
Pb206	1.05
Pb207	<0.58
Pb208	1.2
Th232	0.076
U238	0.122

Table 12 (continuation)

	GC 11_0009 PRV_C	GC 11_0013 PRV_C	GC 11_0013 PRV_B	GC 11_0014 PRV_B	GC 11_0014 PRV_INT1	GC 11_0014 PRV_C	GC 11_0014 PRV_INT2	GC 11_0015 PRV_C	GC 11_0015 PRV_INT	GC 11_0015 PRV_B	GC 11_0020 PRV_C
SiO2	0.42	0.00	1.58	0.09	0.04	0.10	0.00	3.03	2.93	2.30	2.63
TiO2	6.81	2.14	1.88	1.39	3.11	4.09	1.68	6.88	7.25	5.78	5.74
Al2O3	0.00	0.00	0.04	0.00	0.00	0.00	0.04	0.04	0.04	0.03	0.03
FeO(T)	0.76	0.71	1.90	0.66	0.65	0.75	0.59	1.94	1.88	1.73	1.71
MnO	0.07	0.07	0.04	0.00	0.06	0.05	0.05	0.05	0.08	0.05	0.03
MgO	0.00	0.00	0.12	0.00	0.00	0.00	0.00	0.03	0.00	0.02	0.03
CaO	15.80	15.65	11.59	15.66	15.43	16.01	14.90	11.66	12.09	12.10	12.87
Na2O	4.66	5.17	1.60	6.49	5.66	5.42	6.38	0.87	1.26	1.25	1.29
K2O	0.21	0.47	0.20	0.33	0.24	0.21	0.32	0.13	0.11	0.12	0.11
Cr2O3	0.00	0.00	0.00	0.00	0.00	0.00	0.00	0.00	0.00	0.00	0.00
La2O3	0.66	0.58	0.45	0.64	0.91	0.98	0.66	0.51	0.47	0.49	0.44
ZnO	0.00	0.01	0.03	0.04	0.01	0.00	0.00	0.00	0.01	0.00	0.00
ThO2	2.69	1.79	2.72	0.58	0.79	0.79	0.51	4.02	3.51	2.62	3.40
Ce2O3	4.82	4.84	2.83	2.34	4.73	4.21	3.87	3.53	3.99	3.28	2.43
Nb2O5	53.57	55.86	55.02	58.89	56.32	56.01	58.06	51.06	51.12	53.23	51.91
Sm2O3		0.11				0.11					0.08
Nd2O3		0.85				0.91					0.63
SrO		0.41				0.65					3.44
Pr2O3		0.25				0.29					0.20
ZrO2		3.90				3.31					2.39
Total:	90.48	92.80	80.00	87.10	87.96	93.88	87.05	83.75	84.73	83.01	89.36
Sum of Atomic mol proportion:	1.8	1.8	2.0	1.8	1.8	1.8	1.8	1.9	1.9	1.9	1.9

e of 3 oxygen **Number of ions on bas**

Si	0.012	0.000	0.051	0.003	0.001	0.003	0.000	0.095	0.091	0.072	0.082
Ti	0.150	0.049	0.046	0.031	0.070	0.091	0.038	0.162	0.169	0.136	0.135
Al	0.000	0.000	0.001	0.000	0.000	0.000	0.001	0.001	0.002	0.001	0.001
Fe+3	0.353	0.478	0.366	0.478	0.442	0.432	0.457	0.188	0.193	0.246	0.260
Fe+2	0.334	0.460	0.314	0.462	0.426	0.414	0.443	0.137	0.144	0.200	0.216
Mn	0.002	0.002	0.001	0.000	0.002	0.001	0.001	0.001	0.002	0.001	0.001
Mg	0.000	0.000	0.006	0.000	0.000	0.000	0.000	0.002	0.000	0.001	0.002
Ca	0.494	0.507	0.404	0.495	0.495	0.506	0.479	0.391	0.401	0.406	0.430
Na	0.264	0.303	0.101	0.371	0.329	0.310	0.371	0.053	0.075	0.076	0.078
K	0.008	0.018	0.008	0.012	0.009	0.008	0.012	0.005	0.004	0.005	0.005
Cr	0.000	0.000	0.000	0.000	0.000	0.000	0.000	0.000	0.000	0.000	0.000
La	0.007	0.006	0.005	0.007	0.010	0.011	0.007	0.006	0.005	0.006	0.005
Zn	0.000	0.000	0.001	0.001	0.000	0.000	0.000	0.000	0.000	0.000	0.000
Th	0.018	0.012	0.020	0.004	0.005	0.005	0.003	0.029	0.025	0.019	0.024
Ce	0.052	0.054	0.034	0.025	0.052	0.045	0.043	0.040	0.045	0.038	0.028
Nb	0.707	0.764	0.809	0.785	0.763	0.747	0.788	0.723	0.716	0.754	0.731
Sm	0.000	0.001	0.000	0.000	0.000	0.001	0.000	0.000	0.000	0.000	0.001
Nd	0.000	0.009	0.000	0.000	0.000	0.010	0.000	0.000	0.000	0.000	0.007
Sr	0.000	0.007	0.000	0.000	0.000	0.011	0.000	0.000	0.000	0.000	0.062
Pr	0.000	0.003	0.000	0.000	0.000	0.003	0.000	0.000	0.000	0.000	0.002
Zr	0.000	0.057	0.000	0.000	0.000	0.048	0.000	0.000	0.000	0.000	0.036
Total:	1.731	1.810	1.539	1.750	1.753	1.818	1.760	1.559	1.585	1.561	1.674

Trace elements in perovskites minerals of Grota do Cedro Kimberlite

Concentrations in ppm (μg/g)

Li7 ppm	0.63	0.64	<0.168
Na23	41710.39	40067.86	6847.52
Mg24	437.89	417.72	702
Al27	8.9	<0.32	254.52
Si29	<218.60	1714.59	18537.72
P31	5.56	53.97	692.65
Ca42	111850.66	107205.11	91981.99
Ca44	105346.46	101989.36	90306.89
Sc45	164.41	137.99	58.97

Ti46	10583.02	16933.52	27535.63
Ti49	10951.88	18377.15	29806.86
V51	75.03	62.81	121.15
Cr52	<0.29	0.29	0.88
Mn55	376.4	424.43	407.76
Fe56	4958.53	4399.4	15042.3
Co59	<0.116	<0.110	0.524
Sr88	3437.36	5486.52	29117.14
Y89	241.73	258.87	157.38
Zr91	28865.13	24477.2	17682.47
Nb93	381240.91	341177.38	363466.78
Sn118	496.5	1207.03	582.87
Sb121	3.79	9.99	61.4
Ba137	116.02	172.39	10587.52
La139	4059.74	6302.76	4139.66
Ce140	31219.21	27885.1	19543.69
Pr141	2106.61	2442.93	1697.67
Nd143	7258.76	7780.88	5384.84
Sm147	962.34	945.5	670.94
Eu151	241.32	231.38	159.78
Gd157	434.96	422.09	293.76
Tb159	42.65	39.85	28.37
Dy161	163.39	149.78	106.98
Ho165	16.8	15.77	11.49
Er166	29.52	29.56	21.93
Tm169	2.56	2.7	2.13
Yb173	12.99	13.41	12.83
Lu175	1.02	1.1	1.17
Hf178	1230.93	876.91	764.58
Ta181	5.28	0.693	6.07
Pb206	94.12	154.77	9219.73
Pb207	87.72	149.57	8699.06
Pb208	205.09	210.97	9459.49
Th232	14209.32	6144.43	32653.03
U238	7.89	0.243	125.96

Table 12 (continuation)

	GC 11_0020 PRV_INT	GC 11_0020 PRV_B	GC 11_0029 PRV_B	GC 11_0029 PRV_INT	GC 11_0029 PRV_INT	GC 11_0029 PRV_C
SiO2	3.38	3.31	1.10	2.97	2.43	0.00
TiO2	4.92	4.15	6.44	6.62	6.95	6.37
Al2O3	0.02	0.02	0.02	0.05	0.00	0.00
FeO(T)	2.18	2.26	0.52	1.26	1.07	0.30
MnO	0.04	0.01	0.03	0.11	0.09	0.06
MgO	0.06	0.07	0.00	0.00	0.00	0.00
CaO	10.94	10.52	15.13	12.56	12.86	16.11
Na2O	0.53	0.43	5.05	2.51	3.03	5.79
K2O	0.10	0.07	0.21	0.13	0.16	0.19
Cr2O3	0.00	0.00	0.00	0.00	0.00	0.00
La2O3	0.35	0.52	0.45	0.46	0.49	0.50
ZnO	0.00	0.00	0.00	0.00	0.02	0.05
ThO2	4.52	5.01	3.20	3.79	4.47	3.39
Ce2O3	2.53	2.58	3.53	2.94	3.36	3.32
Nb2O5	50.46	51.44	53.40	51.76	50.89	54.21
Sm2O3						
Nd2O3						
SrO						
Pr2O3						
ZrO2						
Total:	80.03	80.40	89.08	85.16	85.81	90.30
Sum of Atomic mol proportion:	2.0	2.0	1.8	1.8	1.8	1.7

e of 3 oxygen

Si	0.110	0.108	0.032	0.091	0.074	0.000
Ti	0.120	0.102	0.142	0.152	0.160	0.139
Al	0.001	0.001	0.001	0.002	0.000	0.000
Fe+3	0.214	0.223	0.315	0.203	0.218	0.371
Fe+2	0.155	0.161	0.302	0.171	0.190	0.364
Mn	0.001	0.000	0.001	0.003	0.002	0.001
Mg	0.003	0.004	0.000	0.000	0.000	0.000
Ca	0.381	0.367	0.476	0.411	0.422	0.500
Na	0.033	0.027	0.287	0.149	0.180	0.325
K	0.004	0.003	0.008	0.005	0.006	0.007
Cr	0.000	0.000	0.000	0.000	0.000	0.000
La	0.004	0.006	0.005	0.005	0.006	0.005
Zn	0.000	0.000	0.000	0.000	0.000	0.001
Th	0.033	0.037	0.021	0.026	0.031	0.022
Ce	0.030	0.031	0.038	0.033	0.038	0.035
Nb	0.741	0.757	0.708	0.715	0.705	0.710
Sm	0.000	0.000	0.000	0.000	0.000	0.000
Nd	0.000	0.000	0.000	0.000	0.000	0.000
Sr	0.000	0.000	0.000	0.000	0.000	0.000
Pr	0.000	0.000	0.000	0.000	0.000	0.000
Zr	0.000	0.000	0.000	0.000	0.000	0.000
Total:	1.520	1.503	1.732	1.625	1.652	1.753

Major-element compositions of perovskites minerals from Régis Kimberlite

	regis 1-9_0002 PRV_C	regis 1-9_0002 PRV_B	regis 1-9_0003 PRV_C	regis 1-9_0003 PRV_B	regis 1-9_0006 PRV_C	regis 1-9_0007 PRV_C	regis 1-9_0007 PRV_INT	regis 1-9_0007 PRV_INT	regis 1-9_0007 PRV_B	
SiO2	0.03	0.05	0.00	0.01	0.02	0.00	0.00	0.00	0.03	SiO2
TiO2	56.07	54.85	54.98	54.80	54.74	54.05	54.47	54.76	55.55	TiO2
Al2O3	0.12	0.13	0.08	0.12	0.14	0.10	0.16	0.16	0.17	Al2O3
FeO(T)	1.16	1.16	1.21	1.38	1.26	1.16	1.41	1.40	1.42	FeO(T)
MnO	0.04	0.04	0.02	0.04	0.04	0.02	0.03	0.04	0.05	MnO
CaO	39.11	38.59	38.46	39.10	38.24	38.61	38.75	38.36	38.48	CaO
Na2O	0.28	0.28	0.38	0.28	0.33	0.32	0.31	0.32	0.32	Na2O
K2O	0.06	0.15	0.05	0.05	0.07	0.04	0.07	0.04	0.08	K2O
Cr2O3	0.04	0.05	0.01	0.00	0.00	0.00	0.00	0.00	0.00	Cr2O3
La2O3	0.24	0.40	0.54	0.29	0.54	0.52	0.57	0.59	0.51	La2O3
ZnO	0.00	0.00	0.02	0.00	0.08	0.02	0.00	0.00	0.01	ZnO
ThO2	0.00	0.16	0.10	0.00	0.24	0.01	0.00	0.32	0.00	ThO2
Ce2O3	0.43	0.76	1.03	0.45	1.20	1.03	1.27	1.28	1.46	Ce2O3
Nb2O5	0.11	0.29	0.41	0.26	0.29	0.30	0.37	0.33	0.24	Nb2O5
Sm2O3	0.06		0.04	0.03	0.10	0.07				Sm2O3
Nd2O3	0.48		0.29	0.26	0.84	0.58				Nd2O3
SrO	0.26		0.28	0.32	0.25	0.29				SrO
Pr2O3	0.13		0.08	0.07	0.22	0.15				Pr2O3
Total	98.61	96.90	97.98	97.47	98.59	97.28	97.41	97.59	98.30	Total
Sum of Atc	1.403	1.422	1.422	1.415	1.426	1.434	1.420	1.422	1.411	Sum of A
Number of ions on base of 3 oxygen										**Number**
Si	0.001	0.001	0.000	0.000	0.001	0.000	0.000	0.000	0.001	Si
Ti	0.985	0.976	0.979	0.971	0.977	0.970	0.968	0.975	0.982	Ti
Al	0.003	0.004	0.002	0.003	0.004	0.003	0.005	0.004	0.005	Al
Fe+3	0.016	0.025	0.021	0.043	0.022	0.041	0.041	0.026	0.015	Fe+3
Fe+2	0.006	0.002	0.003	0.016	0.003	0.018	0.013	0.002	0.013	Fe+2

Mn	0.001	0.001	0.000	0.001	0.001	0.000	0.001	0.001	0.001	Mn
Ca	0.978	0.978	0.975	0.986	0.972	0.987	0.981	0.972	0.969	Ca
Na	0.013	0.013	0.018	0.013	0.015	0.015	0.014	0.015	0.014	Na
K	0.002	0.005	0.001	0.002	0.002	0.001	0.002	0.001	0.002	K
Cr	0.001	0.001	0.000	0.000	0.000	0.000	0.000	0.000	0.000	Cr
La	0.002	0.003	0.005	0.002	0.005	0.005	0.005	0.005	0.004	La
Zn	0.000	0.000	0.000	0.000	0.001	0.000	0.000	0.000	0.000	Zn
Th	0.000	0.001	0.001	0.000	0.001	0.000	0.000	0.002	0.000	Th
Ce	0.004	0.007	0.009	0.004	0.010	0.009	0.011	0.011	0.013	Ce
Nb	0.001	0.003	0.004	0.003	0.003	0.003	0.004	0.004	0.003	Nb
Sm	0.001	0.000	0.000	0.000	0.001	0.001	0.000	0.000	0.000	Sm
Nd	0.004	0.000	0.002	0.002	0.007	0.005	0.000	0.000	0.000	Nd
Sr	0.004	0.000	0.004	0.004	0.003	0.004	0.000	0.000	0.000	Sr
Pr	0.001	0.000	0.001	0.001	0.002	0.001	0.000	0.000	0.000	Pr
Total:	2.022	2.015	2.026	2.019	2.031	2.028	2.019	2.017	2.021	Total:

Trace elements in perovskite minerals of Régis Kimberlite

Concentrations in ppm (µg/g)

Li	<0.58	<0.59	<0.60	1.75	1.08	Li
Na	3033.93	2802.48	2891.87	95006.78	3187.04	Na
Mg	753.74	437.98	312.24	24312.22	8578.72	Mg
P	<7.32	<7.63	<7.57	23.62	<8.36	P
Sc	4.3	3.6	3.55	3.03	5.53	Sc
V	125.19	151.42	165.25	106.03	160.7	V
Cr	211.39	268.18	227.41	8.48	2238.78	Cr
Mn	279.31	199.22	216.89	259.53	414.26	Mn
Fe	8131.09	7313.15	8810.27	8882.54	21505.31	Fe
Co	1.38	0.77	0.6	2.45	8.17	Co
Sr	2231.38	2343.76	2742.42	2126.29	2424.8	Sr
Y	192.35	132.32	138.12	196.63	193.63	Y
Zr	310.99	245.07	274.91	273.4	328.8	Zr
Nb	2135.56	1935.48	1955.16	2475.58	2089.35	Nb
Sn	3.31	4.05	4.03	2761.06	3.61	Sn

Trace ele

Concentr

Sb	<0.122	<0.129	<0.126	<0.36	<0.149	Sb
Ba	26.1	22.34	25.59	214.07	30.16	Ba
La	4318.57	2735.7	2694.28	6236.71	4926.69	La
Ce	9630.4	6025.32	5679.64	17397.52	11729.92	Ce
Pr	1083.71	677.82	600.37	1851.72	1301.8	Pr
Nd	4121.33	2469.03	2211.7	7213.73	4968.17	Nd
Sm	550.08	317.32	291.35	822.93	618.04	Sm
Eu	137.84	81.02	77.03	176.61	149	Eu
Gd	297.73	171.95	174.13	410.41	310.63	Gd
Tb	28.76	16.69	17.68	33.99	29.08	Tb
Dy	104.75	63.69	65.53	112.83	106.19	Dy
Ho	12.12	8.19	7.89	12.55	12.86	Ho
Er	19.84	14.75	13.92	22.99	21.26	Er
Tm	1.62	1.24	1.27	1.49	1.68	Tm
Yb	7.36	6.19	6.07	8.1	7.23	Yb
Lu	0.609	0.56	0.537	0.73	0.67	Lu
Hf	14.84	12.04	13.21	13.3	15.25	Hf
Ta	325.51	220.76	202.37	523.43	321.06	Ta
Pb	9.62	8.36	8.2	14.61	11.09	Pb
Pb	5.5	5.48	5.03	8.57	6.13	Pb
Pb	10.27	8.5	8.97	28.35	14.5	Pb
Th	540.91	354.78	335.12	2753.86	869.72	Th
U	76.25	45.49	44.94	83.24	89.56	U

regis 1-9_0009 PRV_C	regis 1-9_0009 PRV_INT	regis 1-9_0009 PRV_INT	regis 1-9_0009 PRV_B	regis 1-9_0010 PRV_B GRAO1	regis 1-9_0010 PRV_INT GRAO1		regis 1-9_001 PRV_C GRAO1	regis 1-9_0010 PRV_C		regis 1-9_001 PRV_INT
0.00	0.00	0.00	0.02	0.02	0.01	SiO2	0.00	0.02	SiO2	0.00
55.43	56.13	56.14	54.79	56.19	55.55	TiO2	55.18	54.53	TiO2	55.43
0.13	0.08	0.14	0.15	0.10	0.10	Al2O3	0.14	0.15	Al2O3	0.08
1.12	0.99	1.09	1.19	1.18	1.07	FeO(T)	1.07	1.22	FeO(T)	1.07
0.04	0.05	0.03	0.04	0.04	0.01	MnO	0.02	0.06	MnO	0.03
37.54	39.06	39.46	39.01	39.36	39.32	CaO	38.09	37.64	CaO	39.33
0.41	0.25	0.26	0.28	0.30	0.26	Na2O	0.38	0.38	Na2O	0.28
0.05	0.04	0.06	0.06	0.08	0.04	K2O	0.05	0.05	K2O	0.02
0.06	0.04	0.06	0.09	0.04	0.05	Cr2O3	0.08	0.09	Cr2O3	0.00
0.62	0.36	0.24	0.32	0.25	0.17	La2O3	0.52	0.62	La2O3	0.25
0.00	0.00	0.00	0.00	0.00	0.00	ZnO	0.01	0.00	ZnO	0.01
0.00	0.24	0.00	0.00	0.24	0.00	ThO2	0.08	0.07	ThO2	0.18
1.57	0.51	0.41	0.50	0.50	0.32	Ce2O3	1.24	1.61	Ce2O3	0.57
0.22	0.21	0.17	0.15	0.28	0.17	Nb2O5	0.25	0.23	Nb2O5	0.46
0.06			0.04			Sm2O3	0.05	0.05	Sm2O3	
0.47			0.30			Nd2O3	0.43	0.44	Nd2O3	
0.29			0.29			SrO	0.32	0.26	SrO	
0.12			0.08			Pr2O3	0.11	0.11	Pr2O3	
98.13	97.95	98.04	97.30	98.57	97.07	Total	98.01	97.55	Total	97.71
1.434	1.403	1.396	1.418	1.393	1.408	proportion:	1.428	1.440	Sum of A	1.404
of ions on base of 3 oxygen				**Number of ions on base of 3 oxygen**						**Number of ions on bas**
0.000	0.000	0.000	0.000	0.001	0.000	Si	0.000	0.001	Si	0.000
0.995	0.986	0.982	0.973	0.980	0.979	Ti	0.986	0.983	Ti	0.974
0.004	0.002	0.004	0.004	0.003	0.003	Al	0.004	0.004	Al	0.002
0.012	0.011	0.023	0.038	0.021	0.029	Fe+3	0.005	0.008	Fe+3	0.032
0.034	0.008	0.002	0.014	0.002	0.008	Fe+2	0.016	0.016	Fe+2	0.011

0.001	0.001	0.001	0.001	0.001	0.000	Mn	0.000	0.001	Mn	0.001
0.960	0.978	0.983	0.987	0.978	0.987	Ca	0.970	0.967	Ca	0.985
0.019	0.011	0.012	0.013	0.013	0.012	Na	0.018	0.018	Na	0.013
0.001	0.001	0.002	0.002	0.002	0.001	K	0.001	0.002	K	0.001
0.001	0.001	0.001	0.002	0.001	0.001	Cr	0.001	0.002	Cr	0.000
0.005	0.003	0.002	0.003	0.002	0.001	La	0.005	0.005	La	0.002
0.000	0.000	0.000	0.000	0.000	0.000	Zn	0.000	0.000	Zn	0.000
0.000	0.001	0.000	0.000	0.001	0.000	Th	0.000	0.000	Th	0.001
0.014	0.004	0.003	0.004	0.004	0.003	Ce	0.011	0.014	Ce	0.005
0.002	0.002	0.002	0.002	0.003	0.002	Nb	0.003	0.002	Nb	0.005
0.000	0.000	0.000	0.000	0.000	0.000	Sm	0.000	0.000	Sm	0.000
0.004	0.000	0.000	0.003	0.000	0.000	Nd	0.004	0.004	Nd	0.000
0.004	0.000	0.000	0.004	0.000	0.000	Sr	0.004	0.004	Sr	0.000
0.001	0.000	0.000	0.001	0.000	0.000	Pr	0.001	0.001	Pr	0.000
2.034	2.010	2.011	2.021	2.012	2.010	Total:	2.030	2.033	Total:	2.010

ements in perovskite minerals of Régis Kimberlite rations in ppm (µg/g)	**Trace elements in perovskite minerals of Régis Kimberlite Concentrations in ppm (µg/g)**				**Trace elements in pero Concentrations in ppm**
<0.61	<0.65	Li	2.39	<0.58	Li
3142.99	2883.54	Na	13558.51	2993.39	Na
349.34	337.91	Mg	3792.19	389.45	Mg
<7.78	7.94	P	<10.84	<7.14	P
3.28	3.66	Sc	3.91	3.56	Sc
176.37	177.74	V	141.97	145.35	V
705.99	500.15	Cr	144.31	290.99	Cr
243.64	238.73	Mn	271.09	250.61	Mn
8862.34	8388.19	Fe	8716.7	7431.91	Fe
1.08	0.89	Co	1.39	1.03	Co
2442.52	2413.12	Sr	2703.76	2227.39	Sr
143.97	140.72	Y	182.46	159.12	Y
200.1	237.8	Zr	268.24	223.92	Zr
1806.65	2032.86	Nb	1839.74	1809.57	Nb
3.51	3.98	Sn	644.33	3.24	Sn

<0.137	<0.134	Sb	<0.18	<0.120	Sb
19.34	21.89	Ba	44.15	21.78	Ba
3689.2	2950.24	La	3673.56	3726.9	La
9026.94	6372.07	Ce	7664.59	8669.66	Ce
1053.66	690.28	Pr	949.38	981.91	Pr
4042.51	2573.64	Nd	3664.11	3767.8	Nd
492.17	338.1	Sm	455.88	472.61	Sm
115.55	86.16	Eu	111.01	113.54	Eu
242.36	180.1	Gd	248.24	241.3	Gd
22.49	17.25	Tb	24.9	22.83	Tb
80.47	66.39	Dy	91.46	83.06	Dy
9.09	8.41	Ho	11.73	10.26	Ho
16.06	15.39	Er	20.66	17.67	Er
1.36	1.32	Tm	1.85	1.4	Tm
5.99	6.05	Yb	6.78	6.77	Yb
0.517	0.568	Lu	0.7	0.552	Lu
9.47	11.89	Hf	11.06	9.93	Hf
266.07	237.95	Ta	289.73	253.29	Ta
8.65	7.64	Pb	8.69	7.5	Pb
5.48	4.78	Pb	6.09	4.39	Pb
12.39	8.77	Pb	10.85	10.78	Pb
704.75	391.47	Th	649.49	699.06	Th
49.23	47.56	U	58.39	52.47	U

regis 1-9_001 PRV_INT	regis 1-9_001 PRV_B	regis 1_0001 PRV_C	regis 1_0001 PRV_INT	regis 1_0001 PRV_B		regis 1_0002 PRV_B	regis 1_0002 PRV_INT	regis 1_0002 PRV_INT	regis 1_0002 PRV_INT	regis 1_0002 PRV_C	
0.03	0.00	0.00	0.00	0.00	SiO2	0.00	0.00	0.00	0.01	0.00	SiO2
55.80	55.72	55.00	55.63	55.43	TiO2	55.52	55.79	55.84	56.20	56.53	TiO2
0.11	0.09	0.12	0.13	0.13	Al2O3	0.12	0.12	0.11	0.10	0.14	Al2O3
1.05	1.25	0.92	0.99	1.04	FeO(T)	0.95	1.02	0.91	1.06	1.21	FeO(T)
0.02	0.02	0.04	0.02	0.05	MnO	0.05	0.02	0.04	0.04	0.03	MnO
39.69	39.04	38.18	38.10	39.00	CaO	38.12	39.30	38.99	38.39	37.89	CaO
0.25	0.30	0.42	0.47	0.34	Na2O	0.40	0.30	0.34	0.37	0.36	Na2O
0.03	0.04	0.03	0.07	0.04	K2O	0.05	0.03	0.03	0.03	0.02	K2O
0.03	0.05	0.00	0.04	0.00	Cr2O3	0.04	0.01	0.02	0.05	0.04	Cr2O3
0.25	0.31	0.48	0.53	0.27	La2O3	0.53	0.28	0.31	0.41	0.51	La2O3
0.00	0.00	0.03	0.00	0.00	ZnO	0.02	0.00	0.00	0.00	0.00	ZnO
0.03	0.00	0.00	0.25	0.29	ThO2	0.14	0.32	0.00	0.29	0.03	ThO2
0.29	0.69	1.55	1.29	0.52	Ce2O3	1.37	0.24	0.83	0.85	1.11	Ce2O3
0.28	0.27	0.30	0.25	0.25	Nb2O5	0.00	0.36	0.41	0.35	0.13	Nb2O5
	0.06	0.06			Sm2O3					0.05	Sm2O3
	0.48	0.46			Nd2O3					0.48	Nd2O3
	0.31	0.27			SrO					0.34	SrO
	0.13	0.12			Pr2O3					0.13	Pr2O3
97.87	98.77	98.00	97.76	97.37	Total	97.31	97.81	97.84	98.15	99.01	Total
1.397	1.405	1.430	1.421	1.410	roportion:	1.427	1.401	1.407	1.409	1.415	Sum of At
e of 3 oxygen			**Number of ions on base of 3 oxygen**							**Number c**	
0.001	0.000	0.000	0.000	0.000	Si	0.000	0.000	0.000	0.000	0.000	Si
0.976	0.980	0.985	0.990	0.979	Ti	0.992	0.978	0.984	0.991	1.002	Ti
0.003	0.003	0.003	0.004	0.004	Al	0.003	0.003	0.003	0.003	0.004	Al
0.033	0.023	0.009	0.004	0.023	Fe+3	0.002	0.024	0.013	0.006	0.021	Fe+3
0.012	0.002	0.010	0.024	0.003	Fe+2	0.021	0.004	0.005	0.026	0.045	Fe+2

0.000	0.000	0.001	0.000	0.001	Mn	0.001	0.000	0.001	0.001	0.001	Mn
0.988	0.978	0.974	0.966	0.981	Ca	0.970	0.982	0.978	0.964	0.956	Ca
0.011	0.014	0.019	0.022	0.016	Na	0.018	0.014	0.015	0.017	0.017	Na
0.001	0.001	0.001	0.002	0.001	K	0.002	0.001	0.001	0.001	0.001	K
0.001	0.001	0.000	0.001	0.000	Cr	0.001	0.000	0.000	0.001	0.001	Cr
0.002	0.003	0.004	0.005	0.002	La	0.005	0.002	0.003	0.004	0.004	La
0.000	0.000	0.001	0.000	0.000	Zn	0.000	0.000	0.000	0.000	0.000	Zn
0.000	0.000	0.000	0.001	0.002	Th	0.001	0.002	0.000	0.002	0.000	Th
0.003	0.006	0.014	0.011	0.004	Ce	0.012	0.002	0.007	0.007	0.010	Ce
0.003	0.003	0.003	0.003	0.003	Nb	0.000	0.004	0.004	0.004	0.001	Nb
0.000	0.000	0.000	0.000	0.000	Sm	0.000	0.000	0.000	0.000	0.000	Sm
0.000	0.004	0.004	0.000	0.000	Nd	0.000	0.000	0.000	0.000	0.004	Nd
0.000	0.004	0.004	0.000	0.000	Sr	0.000	0.000	0.000	0.000	0.005	Sr
0.000	0.001	0.001	0.000	0.000	Pr	0.000	0.000	0.000	0.000	0.001	Pr
2.009	2.023	2.032	2.023	2.013	Total:	2.024	2.008	2.015	2.015	2.030	Total:

vskite minerals of Régis Kimberlite (µg/g)

<0.70	<0.61	Li
3670.39	3452.46	Na
425.54	393.2	Mg
<9.41	8.57	P
3.52	3.31	Sc
152.28	180.58	V
334.7	828.14	Cr
260.18	237.62	Mn
8100.74	7910.74	Fe
1.24	0.84	Co
2594.36	2274.17	Sr
169.46	149.24	Y
233.97	202.25	Zr
1889.63	1972.19	Nb
3.55	3.51	Sn

Trace elements in perovskite minerals of Régis Kimberlite
Concentrations in ppm (µg/g)

Trace ele
Concentra

<1.37	Li
3112.86	Na
2772.9	Mg
49.84	P
5.75	Sc
121.04	V
401.3	Cr
318.93	Mn
22756.58	Fe
8.66	Co
2833.96	Sr
145.76	Y
294.11	Zr
1578.89	Nb
5.04	Sn

<0.159	<0.132	Sb	<0.30	Sb
23.91	21.31	Ba	60.47	Ba
4258.57	4138.17	La	4721.98	La
9610.23	10094.31	Ce	10057.14	Ce
1119.08	1067.8	Pr	1112.09	Pr
4132.56	3971.05	Nd	4098.53	Nd
498.18	482	Sm	473.19	Sm
114.22	112.46	Eu	102.29	Eu
246.96	246.13	Gd	213.53	Gd
23.28	22.8	Tb	19.26	Tb
80.35	82.14	Dy	66.85	Dy
10.18	9.95	Ho	7.73	Ho
17.87	17.38	Er	13.54	Er
1.5	1.45	Tm	1.03	Tm
6.85	6.4	Yb	4.5	Yb
0.642	0.62	Lu	0.369	Lu
11.19	10.42	Hf	15.15	Hf
293.48	321.02	Ta	252.35	Ta
8.98	8.58	Pb	6.63	Pb
5.75	5.24	Pb	4.96	Pb
12.47	13.33	Pb	12.12	Pb
749.4	855.05	Th	879.85	Th
52.23	57.31	U	24.93	U

regis 1_0003 PRV_C	regis 1_0003 PRV_INT	regis 1_0003 PRV_B	regis 1_0004 PRV_C	regis 1_0004 PRV_INT	regis 1_0004 PRV_INT	regis 1_0004 PRV_B	regis 1_0005 PRV_C	regis 1_0005 PRV_B
0.00	0.01	0.00	0.00	0.00	0.00	0.04	0.00	0.00
56.28	56.76	56.01	55.80	55.76	56.50	55.75	56.83	57.12
0.11	0.08	0.09	0.05	0.10	0.12	0.12	0.08	0.11
1.02	1.02	1.12	0.97	1.05	0.93	1.07	0.97	1.15
0.02	0.03	0.02	0.02	0.03	0.02	0.05	0.02	0.01
38.83	39.44	38.86	39.39	39.98	39.23	39.17	39.58	39.61
0.35	0.31	0.33	0.33	0.23	0.31	0.32	0.34	0.26
0.07	0.06	0.09	0.06	0.01	0.03	0.10	0.05	0.06
0.01	0.00	0.02	0.02	0.00	0.02	0.00	0.03	0.02
0.42	0.14	0.30	0.20	0.08	0.32	0.23	0.24	0.11
0.00	0.00	0.00	0.00	0.00	0.03	0.05	0.00	0.00
0.22	0.01	0.10	0.15	0.00	0.00	0.11	0.11	0.06
0.83	0.36	0.54	0.30	0.22	0.55	0.63	0.49	0.40
0.21	0.23	0.17	0.29	0.21	0.31	0.02	0.34	0.37
0.12			0.06				0.04	
0.94			0.51				0.28	
0.21			0.33				0.26	
0.25			0.14				0.08	
99.90	98.45	97.67	98.61	97.68	98.37	97.66	99.73	99.29
1.404	1.391	1.407	1.403	1.395	1.396	1.406	1.385	1.380
of ions on base of 3 oxygen								
0.000	0.000	0.000	0.000	0.000	0.000	0.001	0.000	0.000
0.989	0.988	0.987	0.980	0.974	0.988	0.981	0.986	0.987
0.003	0.002	0.002	0.001	0.003	0.003	0.003	0.002	0.003
0.003	0.010	0.011	0.025	0.042	0.008	0.023	0.011	0.010
0.017	0.010	0.011	0.006	0.021	0.010	0.002	0.008	0.012

0.000	0.001	0.000	0.000	0.001	0.000	0.001	0.000	0.000
0.972	0.978	0.975	0.985	0.994	0.977	0.982	0.978	0.975
0.016	0.014	0.015	0.015	0.010	0.014	0.014	0.015	0.011
0.002	0.002	0.003	0.002	0.000	0.001	0.003	0.002	0.002
0.000	0.000	0.000	0.000	0.000	0.000	0.000	0.001	0.000
0.004	0.001	0.003	0.002	0.001	0.003	0.002	0.002	0.001
0.000	0.000	0.000	0.000	0.000	0.001	0.001	0.000	0.000
0.001	0.000	0.001	0.001	0.000	0.000	0.001	0.001	0.000
0.007	0.003	0.005	0.003	0.002	0.005	0.005	0.004	0.003
0.002	0.002	0.002	0.003	0.002	0.003	0.000	0.004	0.004
0.001	0.000	0.000	0.000	0.000	0.000	0.000	0.000	0.000
0.008	0.000	0.000	0.004	0.000	0.000	0.000	0.002	0.000
0.003	0.000	0.000	0.004	0.000	0.000	0.000	0.003	0.000
0.002	0.000	0.000	0.001	0.000	0.000	0.000	0.001	0.000
2.030	2.012	2.015	2.022	2.007	2.013	2.016	2.019	2.009

ments in perovskite minerals of Régis Kimberlite
ations in ppm (µg/g)

1.72	<0.55	<0.30
4834.24	2758.38	2050.95
2800.91	1882.36	263.24
<16.08	72.87	9.13
5.15	3.84	3.38
146.39	110.49	180.75
3060.07	311.43	662.45
341.42	189.13	182.75
7799.32	10801.07	7920.16
1.85	2.2	0.87
1812.3	2791.8	2210.16
238.12	139.44	123.32
679.34	246.14	212.64
4494.22	1580.74	1724.38
4.1	5.63	3.4

<0.22	<0.113	<0.088
14.36	37.73	19.35
6601.27	4787.5	2790.17
17614.15	10619.43	5947.1
2146.66	1177.56	662.45
8102.37	4402.53	2385.2
1032.11	513.35	305.33
230.27	116.58	76.52
473.71	237.22	162.72
42.61	21.2	14.94
150.25	74.24	55.28
17.22	8.47	7.13
28.35	14.62	13.19
2.05	1.05	1.03
9.06	4.92	5.31
0.81	0.413	0.42
31.89	12.54	9.64
693.74	241.91	190.24
24.91	6.06	5.62
10.55	4.1	3.42
31.17	11.56	6.24
2183.56	781.7	366.09
218.13	25.2	38.63

Table 14

Major-element compositions of perovskites minerals from Indaia I Kimberlite

	ID 3_0001 PRV_B	ID 3_0001 PRV_C	ID 3_0002 PRV_B	ID 3_0002 PRV_C	ID 3_0003 PRV_C	IDI A2_0013 PRV_B	IDI A2_0013 PRV_INT	IDI A2_0013 PRV_C	IDI A2_0013 PRV_C_GRAO 2	IDI A2_0014 PRV_C	IDI A2_0014 PRV_INT	IDI A2_0014 PRV_INT
SiO2	0.00	0.00	0.00	0.00	0.00	0.00	0.00	0.00	0.00	0.00	0.00	0.00
TiO2	53.54	52.42	52.21	52.09	52.49	53.52	52.14	52.08	51.82	51.97	50.51	51.67
Al2O3	0.19	0.20	0.18	0.19	0.28	0.23	0.25	0.19	0.22	0.03	0.06	0.05
FeO(T)	1.68	1.68	1.58	1.54	1.78	1.76	1.73	1.82	1.67	1.46	1.60	1.37
MnO	0.05	0.00	0.02	0.06	0.02	0.01	0.03	0.02	0.04	0.02	0.01	0.01
MgO	0.00	0.00	0.00	0.00	0.00	0.00	0.00	0.00	0.00	0.00	0.00	0.00
CaO	36.52	36.17	35.22	36.11	34.66	37.28	36.22	35.62	36.13	33.55	33.20	33.16
Na2O	0.32	0.35	0.45	0.35	0.44	0.29	0.38	0.45	0.40	0.82	0.82	0.85
K2O	0.01	0.04	0.04	0.03	0.06	0.03	0.03	0.05	0.03	0.05	0.05	0.05
Cr2O3	0.00	0.02	0.07	0.03	0.00	0.00	0.06	0.07	0.04	0.07	0.04	0.04
La2O3	1.10	1.07	1.28	1.02	1.19	0.90	1.04	1.17	1.08	1.56	1.58	1.59
ZnO	0.00	0.00	0.00	0.00	0.00	0.00	0.00	0.00	0.00	0.01	0.00	0.02
ThO2	0.14	0.02	0.24	0.29	0.57	0.00	0.01	0.58	0.29	0.17	0.13	0.00
Ce2O3	2.72	2.78	3.17	2.54	3.86	2.42	2.56	3.42	3.11	4.02	4.41	4.49
Nb2O5	0.38	0.54	0.37	0.56	0.48	0.59	0.37	0.33	0.32	1.22	1.30	1.52
Nd2O3												
SrO												
Pr2O3												
Sm2O3												
Sum:	96.65	95.29	94.83	94.80	95.83	97.04	94.82	95.81	95.15	94.95	93.71	94.80
Sum:	1.47	1.49	1.51	1.49	1.50	1.45	1.49	1.49	1.49	1.54	1.56	1.55

Number of ions on base of 3 oxygen

Si	0.000	0.000	0.000	0.000	0.000	0.000	0.000	0.000	0.000	0.000	0.000	0.000
Ti	0.982	0.976	0.985	0.973	0.989	0.972	0.972	0.974	0.969	0.999	0.988	1.001
Al	0.006	0.006	0.005	0.006	0.008	0.007	0.007	0.006	0.006	0.001	0.002	0.001
Fe+3	0.007	0.018	0.005	0.021	0.021	0.028	0.026	0.013	0.029	0.049	0.028	0.056
Fe+2	0.027	0.017	0.038	0.011	0.058	0.008	0.010	0.025	0.006	0.080	0.063	0.086
Mn	0.001	0.000	0.000	0.001	0.000	0.000	0.001	0.000	0.001	0.000	0.000	0.000
Mg	0.000	0.000	0.000	0.000	0.000	0.000	0.000	0.000	0.000	0.000	0.000	0.000
Ca	0.954	0.959	0.946	0.961	0.930	0.964	0.962	0.949	0.962	0.919	0.925	0.915
Na	0.015	0.017	0.022	0.017	0.021	0.014	0.018	0.022	0.019	0.041	0.041	0.042
K	0.000	0.001	0.001	0.001	0.002	0.001	0.001	0.002	0.001	0.002	0.002	0.001
Cr	0.000	0.000	0.001	0.001	0.000	0.000	0.001	0.001	0.001	0.001	0.001	0.001
La	0.010	0.010	0.012	0.009	0.011	0.008	0.010	0.011	0.010	0.015	0.015	0.015
Zn	0.000	0.000	0.000	0.000	0.000	0.000	0.000	0.000	0.000	0.000	0.000	0.000
Th	0.001	0.000	0.001	0.002	0.003	0.000	0.000	0.003	0.002	0.001	0.001	0.000
Ce	0.024	0.025	0.029	0.023	0.035	0.021	0.023	0.031	0.028	0.038	0.042	0.042
Nb	0.004	0.006	0.004	0.006	0.005	0.006	0.004	0.004	0.004	0.014	0.015	0.018
Nd												
Sr												
Pr												
Sm												
Total:	2.032	2.035	2.041	2.032	2.043	2.029	2.034	2.040	2.037	2.062	2.066	2.067

Table 14 (continuation)

	IDI A2_0014 PRV_INT	IDI A2_0014 PRV_B	IDI A2_0015 PRV_B	IDI A2_0015 PRV_INT	IDI A2_0015 PRV_INT	IDI A2_0015 PRV_INT	IDI A2_0015 PRV_C	IDI A2_0015 PRV_B GRAO2	IDI A2_0015 PRV_INT GRAO 2	IDI A2_0015 PRV_C GRAO 2
SiO2	0.00	0.00	0.03	0.00	0.00	0.00	0.00	0.01	0.01	0.00
TiO2	53.17	50.29	49.93	51.23	51.67	50.92	52.07	50.64	50.84	52.29
Al2O3	0.06	0.05	0.04	0.05	0.04	0.04	0.05	0.05	0.07	0.06
FeO(T)	1.26	1.42	1.45	1.35	1.29	1.25	1.29	1.57	1.41	1.26
MnO	0.05	0.01	0.00	0.00	0.02	0.01	0.02	0.00	0.00	0.02
MgO	0.00	0.00	0.00	0.00	0.00	0.00	0.00	0.00	0.00	0.00
CaO	34.11	33.01	31.91	32.38	33.70	32.12	33.25	31.12	33.21	34.39
Na2O	0.72	0.80	0.91	0.86	0.77	0.92	0.81	1.04	0.89	0.71
K2O	0.03	0.09	0.05	0.04	0.04	0.04	0.02	0.09	0.05	0.03
Cr2O3	0.07	0.05	0.00	0.07	0.07	0.02	0.04	0.00	0.05	0.12
La2O3	1.44	1.76	1.78	1.91	1.58	1.93	1.63	1.99	1.72	1.45
ZnO	0.02	0.01	0.03	0.00	0.00	0.00	0.00	0.03	0.00	0.00
ThO2	0.00	0.00	0.73	0.46	0.21	0.28	0.21	1.00	0.04	0.05
Ce2O3	3.81	4.72	5.02	5.21	4.28	5.46	4.35	6.11	4.56	3.95
Nb2O5	1.14	1.54	1.57	1.34	1.11	1.59	1.29	1.87	1.54	1.36
Nd2O3										
SrO										
Pr2O3										
Sm2O3										
Sum:	95.88	93.74	93.44	94.90	94.78	94.57	95.04	95.49	94.41	95.68
Sum:	1.51	1.57	1.59	1.57	1.54	1.58	1.54	1.58	1.56	1.52
Number of ions on base of 3 oxygen										
Si	0.000	0.000	0.001	0.000	0.000	0.000	0.000	0.000	0.000	0.000
Ti	1.007	0.989	0.995	1.005	0.997	1.006	1.005	1.005	0.990	0.994
Al	0.002	0.001	0.001	0.002	0.001	0.001	0.001	0.002	0.002	0.002
Fe+3	0.059	0.033	0.057	0.071	0.043	0.075	0.063	0.091	0.038	0.036
Fe+2	0.086	0.064	0.089	0.100	0.071	0.102	0.091	0.126	0.069	0.063
Mn	0.001	0.000	0.000	0.000	0.000	0.000	0.001	0.000	0.000	0.000
Mg	0.000	0.000	0.000	0.000	0.000	0.000	0.000	0.000	0.000	0.000
Ca	0.920	0.924	0.905	0.904	0.926	0.903	0.914	0.880	0.921	0.931
Na	0.035	0.040	0.046	0.043	0.038	0.047	0.040	0.053	0.044	0.035
K	0.001	0.003	0.002	0.001	0.001	0.001	0.001	0.003	0.002	0.001
Cr	0.001	0.001	0.000	0.001	0.001	0.000	0.001	0.000	0.001	0.002
La	0.013	0.017	0.017	0.018	0.015	0.019	0.015	0.019	0.016	0.014
Zn	0.000	0.000	0.000	0.000	0.000	0.000	0.000	0.000	0.001	0.000
Th	0.000	0.000	0.004	0.003	0.001	0.002	0.001	0.006	0.000	0.000
Ce	0.035	0.045	0.049	0.050	0.040	0.052	0.041	0.059	0.043	0.037
Nb	0.013	0.018	0.019	0.016	0.013	0.019	0.015	0.022	0.018	0.016
Nd										
Sr										
Pr										
Sm										
Total:	2.056	2.070	2.072	2.072	2.062	2.078	2.064	2.084	2.070	2.057

Table 14 (continuation)

	IDIA2_0016 PRV_C	IDIA2_0016 PRV_B	IDIA2_0016 PRV_C GRAO2	IDIA2_0016 PRV_B GRAO2
SiO2	0.01	0.00	0.03	0.00
TiO2	52.48	53.39	52.24	52.89
Al2O3	0.26	0.19	0.21	0.21
FeO(T)	1.64	1.69	1.65	1.81
MnO	0.05	0.03	0.02	0.00
MgO	0.00	0.00	0.00	0.00
CaO	36.26	36.58	35.66	37.45
Na2O	0.37	0.37	0.43	0.21
K2O	0.04	0.06	0.05	0.06
Cr2O3	0.10	0.00	0.09	0.00
La2O3	1.05	0.96	1.15	0.79
ZnO	0.01	0.00	0.00	0.00
ThO2	0.17	0.40	0.59	0.17
Ce2O3	2.82	2.66	3.02	1.66
Nb2O5	0.20	0.46	0.36	0.60
Nd2O3			1.27	
SrO			0.39	
Pr2O3			0.34	
Sm2O3			0.14	
Sum:	95.45	96.79	97.63	95.85
Sum:	1.48	1.46	1.49	1.46

Number of ions on base of 3 oxygen

Si	0.000	0.000	0.001	0.000
Ti	0.974	0.978	0.977	0.965
Al	0.008	0.005	0.006	0.006
Fe+3	0.019	0.011	0.007	0.045
Fe+2	0.015	0.023	0.027	0.008
Mn	0.001	0.001	0.000	0.000
Mg	0.000	0.000	0.000	0.000
Ca	0.958	0.955	0.949	0.973
Na	0.018	0.017	0.021	0.010
K	0.001	0.002	0.001	0.002
Cr	0.002	0.000	0.002	0.000
La	0.010	0.009	0.010	0.007
Zn	0.000	0.000	0.000	0.000
Th	0.001	0.002	0.003	0.001
Ce	0.025	0.024	0.027	0.015
Nb	0.002	0.005	0.004	0.007
Nd			0.011	
Sr			0.006	
Pr			0.003	
Sm			0.001	
Total:	2.034	2.032	2.058	2.022

Trace elements in perovskite minerals of Indaia Kimberlite
Concentrations in ppm (µg/g)

Li	<0.38
Na	3541.83
Mg	412.49
Al	1412.27
Si	<342.82
P	8.27
Sc	5.80
Ti	325801.16
V	85.22
Cr	923.92
Mn	182.52
Fe	12997.99
Co	1.09
Sr	3278.02
Y	239.78
Zr	594.26
Nb	2967.89
Sn	5.66
Sb	<0.086
Ba	31.95
La	9785.83
Ce	25565.94
Pr	2904.92
Nd	10862.68
Sm	1217.40
Eu	260.25
Gd	545.79
Tb	47.88
Dy	165.46
Ho	17.97
Er	30.44
Tm	2.15
Yb	8.37
Lu	0.739
Hf	33.78
Ta	460.38
Pb	13.23
Pb	9.14
Pb	28.40
Th	2122.53
U	62.76

Table 15

Major-element compositions of phlogopite minerals from Grota do Cedro Kimberlite

	GC1-13_0007	GC1-13_0007	GC1-13_0002	GC1-13_0002	GC1-13_0002	GC1-13_0003	GC1-13_0003	GC1-13_0003	GC1-A2_0001	GC1-A2_0001	SP_GC3_0008	SP_GC6#_0011
	inclusa.B	inclusa.C	INT	C	B	escuro.C	claro.C	claroB	B	C	C	inclusa em px
SiO2	40.72	41.76	42.43	43.26	42.16	42.30	42.00	38.29	38.79	38.16	38.95	37.48
TiO2	1.71	1.52	0.56	0.56	0.43	0.19	0.48	4.93	4.28	4.15	3.80	4.03
Al2O3	10.91	11.01	10.19	10.34	10.11	5.13	10.53	12.40	13.69	13.47	12.82	11.64
FeOt	7.81	7.75	5.08	5.07	4.89	4.79	5.73	6.21	6.04	6.28	5.23	10.44
MnO	0.02	0.04	0.05	0.04	0.04	0.01	0.01	0.04	0.05	0.04	0.04	0.17
MgO	23.18	22.44	26.41	25.96	27.07	32.81	25.64	23.09	21.41	22.09	21.00	18.66
CaO	0.05	0.00	0.06	0.09	0.06	0.05	0.02	0.26	0.06	0.09	0.02	0.20
Na2O	0.10	0.08	0.06	0.05	0.07	0.03	0.09	0.17	0.12	0.12	0.16	0.10
K2O	10.35	10.24	9.57	9.45	9.56	4.96	10.39	9.34	10.13	9.93	10.31	10.03
SrO			0.00	0.00	0.00	0.00	0.00	0.00	0.19	0.19	0.01	
BaO	0.10	0.06	0.02	0.07	0.02	0.00	0.00	0.17	0.38	0.47	0.11	0.00
Rb2O			0.06	0.06	0.06	0.07	0.07	0.07	0.57	0.57	0.06	
Cs2O			0.00	0.00	0.00	0.00	0.00	0.00	0.01	0.01	0.00	
ZnO	0.00	0.01	0.00	0.04	0.01	0.01	0.00	0.00	0.04	0.00	0.00	0.00
SnO2			0.00	0.00	0.00	0.00	0.00	0.00	0.03	0.03	0.00	
Ga2O3			0.00	0.00	0.00	0.01	0.01	0.01	0.18	0.18	0.00	
F	0.00	0.00	0.00	0.01	0.00	0.00	0.00	0.00	0.00	0.01	0.12	0.00
Cl	0.04	0.02	0.01	0.01	0.01	0.02	0.02	0.00	0.00	0.00	0.01	0.00
Cr2O3			0.29	0.29	0.29	0.19	0.19	0.19	0.48	0.48	0.33	
NiO			0.16	0.16	0.16	0.17	0.17	0.17	0.04	0.04	0.06	
CuO			0.00	0.00	0.00	0.00	0.00	0.00	0.00	0.00	0.00	
Li2O*	2.13	2.43	2.63	2.86	2.55	2.59	2.50	1.44	1.58	1.40	1.63	1.20
H2O*	2.73	4.27	4.34	4.39	4.34	4.24	4.31	4.23	4.26	4.22	4.10	4.02
Subtota	99.86	101.63	101.91	102.71	101.83	97.57	102.17	101.02	102.33	101.93	98.75	97.97
O=F,Cl	0.01	0.00	0.00	0.00	0.00	0.01	0.01	0.00	0.00	0.01	0.05	0.00
Total	99.85	101.62	101.91	102.70	101.83	97.57	102.16	101.02	102.33	101.92	98.70	97.97
Number of ions on base of 22oxygen												
Si	4.452	5.860	5.857	5.908	5.827	5.976	5.829	5.423	5.459	5.408	5.618	5.593
Al iv	0.937	1.821	1.658	1.664	1.647	0.854	1.722	2.070	2.271	2.250	2.180	2.047
Al vi	0.000	0.000	0.000	0.000	0.000	0.000	0.000	0.000	0.000	0.000	0.000	0.000
Ti	0.141	0.160	0.058	0.057	0.045	0.020	0.050	0.525	0.453	0.442	0.412	0.452

Cr	0.000	0.000	0.031	0.031	0.031	0.022	0.021	0.022	0.054	0.054	0.038	0.000
Fe	1.428	0.910	0.586	0.579	0.565	0.566	0.665	0.736	0.711	0.744	0.631	1.303
Mn	0.004	0.004	0.005	0.005	0.005	0.002	0.001	0.005	0.006	0.005	0.005	0.021
Mg	7.554	4.694	5.434	5.285	5.577	6.909	5.304	4.875	4.492	4.667	4.515	4.151
Zn	0.000	0.001	0.000	0.004	0.001	0.002	0.000	0.000	0.004	0.000	0.000	0.000
Sn	0.000	0.000	0.000	0.000	0.000	0.000	0.000	0.000	0.002	0.002	0.000	0.000
Ga	0.000	0.000	0.000	0.000	0.000	0.001	0.001	0.001	0.016	0.016	0.000	0.000
Ni	0.000	0.000	0.017	0.017	0.017	0.019	0.019	0.019	0.004	0.004	0.007	0.000
Cu	0.000	0.000	0.000	0.000	0.000	0.000	0.000	0.000	0.000	0.000	0.000	0.000
Li*	1.877	1.373	1.458	1.573	1.416	1.471	1.397	0.819	0.895	0.798	0.944	0.723
Ca	0.011	0.000	0.009	0.014	0.009	0.007	0.002	0.040	0.009	0.013	0.003	0.032
Na	0.044	0.023	0.016	0.013	0.020	0.007	0.024	0.046	0.032	0.033	0.045	0.030
K	2.886	1.833	1.685	1.646	1.685	0.894	1.839	1.687	1.818	1.795	1.897	1.909
Sr	0.000	0.000	0.000	0.000	0.000	0.000	0.000	0.000	0.015	0.015	0.001	0.000
Ba	0.008	0.003	0.001	0.004	0.001	0.000	0.000	0.010	0.021	0.026	0.006	0.000
Rb	0.000	0.000	0.005	0.005	0.005	0.006	0.006	0.006	0.051	0.052	0.006	0.000
Cs	0.000	0.000	0.000	0.000	0.000	0.000	0.000	0.000	0.001	0.001	0.000	0.000
OH*	3.986	3.995	3.999	3.995	3.998	3.994	3.994	4.000	3.998	3.993	3.942	4.000
F	0.001	0.000	0.000	0.002	0.000	0.000	0.001	0.000	0.001	0.007	0.054	0.000
Cl	0.013	0.005	0.001	0.003	0.002	0.006	0.005	0.000	0.001	0.000	0.004	0.000
TOTAL	23.343	20.683	20.823	20.806	20.853	20.755	20.882	20.284	20.314	20.326	20.306	20.262

Trace elements in phlogopite minerals of Grota do Cedro Kimberlite

Concentrations in ppm (µg/g)

Li7	4.87	2.98	389.44	4.05
Be9	3.44	5.19	15.98	<0.160
B11	10.35	6.33	1265.33	5.01
P31	24.97	<6.74	<2179.20	10.36
Ca42	<291.92	189.3	<54954.73	<209.14
Sc45	2.31	0.894	980.18	25.06
Ti49	3322.93	2315.75	119822.84	24750.29
V51	63.87	52.01	7962.01	51.74
Cr52	1963.3	1330.92	3301.98	2268.41
Mn55	311.14	221.73	343.45	399.21
Co59	48.65	47.31	<56.62	66.72
Ni60	1231.71	1329.07	302.05	450.84

Cu65	7.66	4.58	<88.65	1.9
Zn66	45.89	57	491.5	46.72
Ga71	21.21	63.07	1331.98	29.86
Rb85	530.04	615.78	5198.07	571.97
Sr88	34.43	10.92	1588.39	51.41
Y89	0.127	0.0726	<3.98	0.123
Zr90	7.86	2.46	82.68	54.43
Nb93	10.57	7.47	465.03	20.54
Mo95	0.24	<0.075	<24.96	<0.105
Sn118	1.41	1.05	250.13	2.33
Sb121	<0.25	<0.112	<45.59	<0.155
Cs133	4.08	3.9	84.64	3.96
Ba137	200.27	91.29	52783.13	5683.83
La139	0.328	0.0351	<2.79	0.051
Ce140	0.584	0.065	<2.39	0.0159
Pr141	<0.015	<0.0065	<2.06	0.0105
Nd143	0.24	<0.050	<24.76	<0.078
Sm147	<0.097	<0.043	<25.66	<0.098
Eu151	<0.027	<0.0146	17.92	0.218
Gd157	<0.095	<0.046	<18.06	<0.064
Tb159	<0.0103	<0.0051	<3.17	<0.0119
Dy161	<0.060	<0.033	<16.31	<0.058
Ho165	<0.0158	0.0056	<3.13	<0.0112
Er166	<0.052	<0.0231	<10.10	<0.031
Tm169	<0.0144	<0.0049	<2.47	<0.0096
Yb172	<0.051	<0.033	<12.63	<0.056
Lu175	<0.014	<0.0076	<3.07	<0.0108
Hf179	0.26	0.04	14.39	1.64
Ta181	0.85	0.448	17.06	1.015
Pb206	0.69	0.299	795.17	<0.051
Pb207	0.47	0.273	716.66	0.086
Pb208	0.546	0.26	692.59	0.12
Th232	0.193	0.0754	0.41	0.0052
U238	0.087	0.0919	1.67	0.0032

Table 16
Major-element compositions of phlogopite minerals from Régis Kimberlite

	regis-5_0003 C	regis-5_0003 B	regis-9_0002 MICA B parte clara	regis-9_0002 MICA C	regis-9_0002 MICA B	regis-12_0004 B.	regis-12_0004 INT	regis-12_0004 C
SiO2	42.30	41.71	40.20	41.26	40.12	42.17	45.14	41.77
TiO2	0.60	0.46	0.51	0.42	0.38	0.41	0.25	0.41
Al2O3	10.63	10.27	9.60	8.28	8.40	9.97	5.25	10.04
FeOt	4.72	4.93	4.11	4.04	4.25	6.48	3.90	6.51
MnO	0.01	0.03	0.02	0.02	0.04	0.03	0.11	0.00
MgO	26.11	26.66	28.42	28.43	29.63	25.23	29.88	25.65
CaO	0.02	0.05	0.05	0.07	0.02	0.01	0.03	0.04
Na2O	0.07	0.10	0.06	0.04	0.06	0.10	0.06	0.07
K2O	10.52	10.27	9.09	7.83	8.13	10.09	5.36	10.35
SrO	0.00	0.00	0.00	0.00	0.00	0.00	0.00	0.00
BaO	0.00	0.01	0.01	0.03	0.05	0.00	0.01	0.00
Rb2O	0.06	0.06	0.06	0.06	0.06	0.04	0.04	0.04
Cs2O	0.00	0.00	0.00	0.00	0.00	0.00	0.00	0.00
ZnO	0.02	0.00	0.01	0.03	0.02	0.00	0.04	0.00
Ga2O3	0.00	0.00	0.00	0.00	0.00	0.00	0.00	0.00
F	0.00	0.01	0.00	0.00	0.01	0.02	0.01	0.00
Cl	0.02	0.02	0.00	0.01	0.02	0.05	0.01	0.01
Cr2O3	0.28	0.28	0.32	0.32	0.32	1.18	1.18	1.18
NiO	0.17	0.17	0.20	0.20	0.20	0.20	0.20	0.20
CuO	0.00	0.00	0.00	0.00	0.00	0.00	0.00	0.00
Li2O*	2.59	2.42	1.99	2.29	1.96	2.55	3.40	2.44
H2O*	4.35	4.30	4.21	4.19	4.17	4.31	4.35	4.32
Subtotal	102.45	101.74	98.85	97.52	97.82	102.84	99.22	103.04
O=F,Cl	0.00	0.01	0.00	0.00	0.01	0.02	0.01	0.00
Total	102.45	101.73	98.85	97.52	97.81	102.83	99.22	103.04
Number of ions on base of 22oxygen								
Si	5.829	5.800	5.727	5.899	5.761	5.839	6.215	5.788
Al iv	1.726	1.683	1.612	1.395	1.422	1.627	0.852	1.640
Al vi	0.000	0.000	0.000	0.000	0.000	0.000	0.000	0.000
Ti	0.062	0.048	0.055	0.045	0.041	0.043	0.025	0.042

Cr	0.030	0.030	0.035	0.036	0.036	0.129	0.129	0.129
Fe	0.544	0.573	0.490	0.483	0.510	0.750	0.449	0.754
Mn	0.001	0.003	0.003	0.003	0.005	0.003	0.012	0.001
Mg	5.363	5.527	6.035	6.059	6.342	5.208	6.133	5.298
Zn	0.002	0.000	0.001	0.003	0.002	0.000	0.004	0.000
Sn	0.000	0.000	0.000	0.000	0.000	0.000	0.000	0.000
Ga	0.000	0.000	0.000	0.000	0.000	0.000	0.000	0.000
Ni	0.018	0.018	0.023	0.023	0.023	0.022	0.022	0.022
Cu	0.000	0.000	0.000	0.000	0.000	0.000	0.000	0.000
Li*	1.434	1.353	1.138	1.317	1.133	1.421	1.885	1.358
Ca	0.003	0.007	0.008	0.011	0.003	0.002	0.005	0.006
Na	0.018	0.027	0.016	0.011	0.016	0.028	0.016	0.020
K	1.849	1.822	1.652	1.428	1.489	1.782	0.941	1.829
Sr	0.000	0.000	0.000	0.000	0.000	0.000	0.000	0.000
Ba	0.000	0.000	0.000	0.002	0.003	0.000	0.000	0.000
Rb	0.006	0.006	0.005	0.005	0.005	0.004	0.004	0.004
Cs	0.000	0.000	0.000	0.000	0.000	0.000	0.000	0.000
OH*	3.995	3.992	4.000	3.998	3.993	3.980	3.994	3.997
F	0.000	0.004	0.000	0.000	0.003	0.009	0.002	0.000
Cl	0.005	0.004	0.000	0.002	0.004	0.011	0.003	0.003
TOTAL	20.885	20.898	20.800	20.721	20.792	20.857	20.692	20.891

Trace elements in phlogopite minerals of Régis Kimberlite
Concentrations in ppm (µg/g)

Li7 ppm	4.61	4.97	3.66
Be9	0	0	6.71
B11	0	0	6.86
P31	14.32	25.03	<6.74
Ca42	268.87	385.74	<175.41
Sc45	1.08	1.13	1.9
Ti49	2693.6	2678.37	3506.5
V51	52.97	62.61	125.08
Cr52	1882.23	2155.61	8079.63
Mn55	212.43	324.53	314.03
Co59	47.92	53.14	61.91
Ni60	1299.08	1570.96	1552.9
Cu65	5.03	4.52	5.19

Zn66	41.03	46.3	85.05
Ga71	54.35	14.6	28.24
Rb85	578.93	541.08	404.11
Sr88	11.79	14.77	9.48
Y89	0.059	0.238	0.1
Zr90	4.28	2.67	7.65
Nb93	13.21	11.79	12.7
Mo95	0	0	<0.061
Sn118	0.66	1.36	1.24
Sb121	<0.096	<0.180	<0.096
Cs133	4.79	4.09	3.53
Ba137	97.35	151.78	426.28
La139	0.065	0.56	0.125
Ce140	0.145	0.96	0.203
Pr141	0.014	0.092	0.0125
Nd143	0.082	0.298	0.125
Sm147	<0.061	<0.051	0.064
Eu151	<0.013	<0.016	<0.0193
Gd157	<0.048	0.09	<0.039
Tb159	<0.0061	0.0119	<0.0073
Dy161	<0.029	<0.042	0.037
Ho165	<0.0070	0.0088	<0.0080
Er166	<0.025	<0.023	<0.024
Tm169	<0.0069	<0.0074	0.0074
Yb172	<0.030	<0.028	<0.049
Lu175	0.0095	<0.0098	<0.0073
Hf179	0.051	<0.064	0.154
Ta181	0.911	0.81	0.915
Pb206	0.247	0.48	0.542
Pb207	0.175	0.33	0.439
Pb208	0.1	0.382	0.533
Th232	0.139	0.191	0.217
U238	0.054	0.064	0.077

Table 16 (continuation)

	regis-12_0006 B	regis-12_0006 C	regis-12_0006 INT	regis-12_0007 B	regis-12_0007 C	regis-12_0007 INT	regis-12_0023 B	regis-12_0023 C	regis-12_0023 B.lateral Escura
SiO2	41.54	41.71	41.56	45.15	43.32	42.79	44.89	42.55	58.54
TiO2	0.65	0.50	0.53	0.65	0.72	0.67	0.58	0.73	0.06
Al2O3	10.34	10.45	9.73	10.11	11.60	11.36	9.89	10.55	0.62
FeOt	5.39	5.40	4.98	6.34	6.73	6.29	6.28	6.29	3.11
MnO	0.03	0.06	0.03	0.06	0.03	0.04	0.09	0.06	0.16
MgO	25.69	25.66	23.83	22.69	24.03	23.95	22.82	24.53	29.29
CaO	0.03	0.01	0.07	0.04	0.04	0.02	0.09	0.04	0.11
Na2O	0.14	0.07	0.08	0.08	0.08	0.06	0.06	0.05	0.11
K2O	10.63	10.34	9.16	8.72	10.20	10.30	8.48	9.50	0.64
SrO	0.01	0.00	0.00	0.01	0.00	0.00	0.00	0.00	0.00
BaO	0.02	0.40	0.28	0.04	0.02	0.06	0.04	0.00	0.01
Rb2O	0.02	0.03	0.02	0.04	0.08	0.04	0.06	0.06	0.06
Cs2O	0.00	0.00	0.00	0.00	0.00	0.00	0.00	0.00	0.00
ZnO	0.03	0.00	0.02	0.02	0.00	0.05	0.03	0.00	0.01
Ga2O3	0.01	0.01	0.01	0.00	0.00	0.00	0.01	0.01	0.01
F	0.00	0.01	0.01	0.01	0.01	0.00	0.01	0.01	0.00
Cl	0.03	0.00	0.02	0.00	0.02	0.03	0.01	0.02	0.01
Cr2O3	0.31	0.38	0.31	0.21	0.34	0.21	0.09	0.09	0.09
NiO	0.17	0.18	0.17	0.12	0.20	0.12	0.08	0.08	0.08
CuO	0.00	0.00	0.00	0.00	0.00	0.00	0.00	0.00	0.00
Li2O*	2.37	2.42	2.38	3.41	2.88	2.73	3.33	2.66	7.25
H2O*	4.28	4.30	4.14	4.39	4.42	4.36	4.36	4.31	4.91
Subtotal	101.68	101.91	97.33	102.09	104.73	103.08	101.19	101.55	105.08
O=F,Cl	0.01	0.00	0.01	0.00	0.01	0.01	0.00	0.01	0.00
Total	101.67	101.91	97.32	102.08	104.72	103.07	101.19	101.54	105.07
Si	5.805	5.817	6.005	6.160	5.856	5.875	6.173	5.908	7.151
Al iv	1.703	1.718	1.657	1.626	1.848	1.839	1.603	1.727	0.089
Al vi	0.000	0.000	0.000	0.000	0.000	0.000	0.000	0.000	0.000
Ti	0.068	0.052	0.058	0.067	0.074	0.069	0.060	0.076	0.006

Cr	0.034	0.042	0.035	0.023	0.036	0.023	0.010	0.010	0.009
Fe	0.630	0.630	0.602	0.723	0.761	0.722	0.722	0.730	0.318
Mn	0.003	0.007	0.003	0.007	0.004	0.005	0.010	0.007	0.016
Mg	5.352	5.334	5.133	4.614	4.843	4.902	4.678	5.078	5.334
Zn	0.003	0.000	0.002	0.002	0.000	0.005	0.003	0.000	0.001
Sn	0.000	0.000	0.000	0.000	0.000	0.000	0.000	0.000	0.000
Ga	0.000	0.000	0.000	0.000	0.000	0.000	0.001	0.001	0.001
Ni	0.020	0.020	0.020	0.013	0.022	0.013	0.009	0.009	0.008
Cu	0.000	0.000	0.000	0.000	0.000	0.000	0.000	0.000	0.000
Li*	1.332	1.357	1.381	1.869	1.566	1.507	1.843	1.486	3.562
Ca	0.004	0.001	0.011	0.006	0.005	0.003	0.013	0.007	0.015
Na	0.037	0.018	0.024	0.020	0.021	0.016	0.016	0.013	0.025
K	1.895	1.839	1.688	1.517	1.759	1.804	1.487	1.683	0.100
Sr	0.001	0.000	0.000	0.001	0.000	0.000	0.000	0.000	0.000
Ba	0.001	0.022	0.016	0.002	0.001	0.003	0.002	0.000	0.001
Rb	0.002	0.002	0.002	0.003	0.007	0.003	0.005	0.006	0.005
Cs	0.000	0.000	0.000	0.000	0.000	0.000	0.000	0.000	0.000
OH*	3.993	3.997	3.989	3.997	3.990	3.993	3.996	3.990	3.998
F	0.000	0.003	0.005	0.002	0.005	0.000	0.003	0.005	0.000
Cl	0.007	0.000	0.006	0.001	0.005	0.007	0.002	0.005	0.002
TOTAL	20.890	20.860	20.638	20.654	20.804	20.790	20.636	20.740	20.640

Trace elements in phlogopite minerals of Régis Kimberlite
Concentrations in ppm (µg/g)

Li7	4.52	6.21		5.23	5.35			4.98	
Be9	0	0		0	0			0	
B11	0	0		0	0			0	
P31	83.24	22.21		291.74	<9.68			8.84	
Ca42	1335.45	442.26		4695.33	212.42			256.38	
Sc45	1.37	1.36		1.48	1.1			1.05	
Ti49	3497.15	3446.63		3783.04	3433.25			3467.96	
V51	66.95	75.64		54.86	62.27			65.01	
Cr52	2120.85	2613.87		1427.79	2334.29			639.53	
Mn55	293.68	449.64		548.82	286.18			587.25	
Co59	54.34	56.02		32.1	56.07			47.76	
Ni60	1365.35	1414.84		912.93	1559.75			627.07	
Cu65	3.56	6.73		9.94	4.08			3.05	

Zn66	61.79	70.72	37.84	53.48	62.27
Ga71	39.07	39.34	14.17	24.02	74.13
Rb85	224.88	235.38	362.32	693.81	568.35
Sr88	56.49	14.96	105.55	3.5	16.66
Y89	0.412	0.269	1.66	0.078	0.082
Zr90	3.32	3.07	4.62	3.22	2.92
Nb93	14.39	14.18	8.81	13.48	7.27
Mo95	0	0	0	0	0
Sn118	0.94	1.01	0.49	1.08	0.9
Sb121	<0.101	0.125	<0.073	<0.103	<0.099
Cs133	5.22	5.08	2.53	3.73	3.02
Ba137	2137.14	2091.06	160.78	173.77	120.31
La139	0.456	0.185	1.68	0.057	0.076
Ce140	0.65	0.318	2.54	0.085	0.131
Pr141	0.075	0.0284	0.226	0.0162	0.0157
Nd143	0.296	<0.067	0.96	0.073	0.05
Sm147	<0.07	0.115	0.097	<0.068	<0.055
Eu151	0.087	0.058	0.07	<0.028	<0.0188
Gd157	<0.042	<0.060	0.125	<0.053	<0.056
Tb159	0.0114	<0.0092	0.0259	<0.0111	<0.0091
Dy161	0.111	<0.063	0.303	<0.062	<0.046
Ho165	<0.0090	<0.0107	0.092	<0.0096	0.0092
Er166	<0.032	<0.027	0.158	0.039	<0.022
Tm169	0.009	<0.0104	0.0131	<0.0111	<0.0082
Yb172	0.035	<0.040	0.129	<0.046	<0.047
Lu175	<0.0094	<0.0088	0.0138	<0.0124	<0.0070
Hf179	0.109	<0.063	0.193	<0.058	0.132
Ta181	1.116	0.985	0.585	1.083	0.529
Pb206	0.246	0.161	1.26	0.576	0.291
Pb207	0.177	0.207	0.98	0.388	0.25
Pb208	0.191	0.266	1.061	0.492	0.226
Th232	1.123	0.861	0.5	0.456	0.0114
U238	0.0435	0.0805	0.138	0.0574	0.0338

Table 16 (continuation)

	regis 1-9_0001 B	regis 1-9_0001 C	regis 1-9_0008 C	regis 1-9_0008 B	regis 1-9_0012 C
SiO2	38.80	38.34	37.66	38.05	37.30
TiO2	4.81	5.17	5.57	5.34	5.54
Al2O3	12.89	12.92	14.44	14.26	13.97
FeOt	9.06	8.75	7.46	7.42	7.40
MnO	0.05	0.04	0.03	0.06	0.07
MgO	19.26	19.87	18.67	18.44	20.58
CaO	0.00	0.04	0.01	0.02	0.03
Na2O	0.23	0.22	0.12	0.13	0.22
K2O	10.08	9.94	9.01	9.04	10.18
SrO	0.00	0.00	0.02	0.02	0.00
BaO	0.19	0.15	0.45	0.31	0.00
Rb2O	0.04	0.04	0.05	0.05	0.07
Cs2O	0.00	0.00	0.00	0.00	0.00
ZnO	0.01	0.00	0.06	0.00	0.01
Ga2O3	0.00	0.00	0.00	0.00	0.01
F	0.09	0.08	0.09	0.09	0.00
Cl	0.01	0.00	0.00	0.01	0.00
Cr2O3	0.35	0.35	0.20	0.20	0.09
NiO	0.19	0.19	0.05	0.05	0.07
CuO	0.00	0.00	0.00	0.00	0.00
Li2O*	1.58	1.45	1.26	1.37	0.00
H2O*	4.16	4.17	4.11	4.10	4.13
Subtotal	101.81	101.71	99.25	98.96	99.66
O=F,Cl	0.04	0.03	0.04	0.04	0.00
Total	101.76	101.68	99.22	98.92	99.66
Si	5.527	5.462	5.442	5.501	5.417
Al iv	2.164	2.170	2.459	2.430	2.391
Al vi	0.000	0.000	0.000	0.000	0.000
Ti	0.515	0.554	0.605	0.581	0.605

Cr	0.039	0.039	0.023	0.023	0.011
Fe	1.079	1.043	0.902	0.897	0.899
Mn	0.006	0.005	0.003	0.007	0.008
Mg	4.090	4.220	4.022	3.974	4.455
Zn	0.001	0.000	0.006	0.000	0.002
Sn	0.000	0.000	0.000	0.000	0.000
Ga	0.000	0.000	0.000	0.000	0.001
Ni	0.021	0.021	0.006	0.006	0.008
Cu	0.000	0.000	0.000	0.000	0.000
Li*	0.907	0.832	0.730	0.796	0.000
Ca	0.000	0.006	0.002	0.004	0.004
Na	0.063	0.060	0.033	0.036	0.063
K	1.831	1.806	1.661	1.667	1.886
Sr	0.000	0.000	0.001	0.001	0.000
Ba	0.011	0.009	0.026	0.018	0.000
Rb	0.003	0.003	0.005	0.005	0.006
Cs	0.000	0.000	0.000	0.000	0.000
OH*	3.955	3.966	3.959	3.958	4.000
F	0.042	0.034	0.041	0.040	0.000
Cl	0.002	0.000	0.000	0.002	0.000
TOTAL	20.259	20.230	19.926	19.944	19.754

Trace elements in phlogopite minerals of Régis Kimberlite
Concentrations in ppm (µg/g)

Li7	4.16	9.99	4.54
Be9	7.51	1.49	0.64
B11	5.14	21.13	<2.62
P31	9.45	1191.4	20.74
Ca42	534.79	6402.79	239.4
Sc45	1.78	13.58	8.09
Ti49	2804.57	22876.43	22696.63
V51	63.8	160.33	101.08
Cr52	2367.55	1362.91	628.58
Mn55	238.11	650.3	472.34
Co59	56.55	69.89	83.39
Ni60	1455.24	384.61	530.53
Cu65	2.89	33.66	2.36

Zn66	54.19	91.01	86.64
Ga71	25.39	28.85	54.08
Rb85	327.38	443.49	597.89
Sr88	5.76	140.28	20.34
Y89	0.075	3.11	0.081
Zr90	4.94	83.37	16.98
Nb93	16.07	24.59	24.37
Mo95	<0.077	0.129	<0.105
Sn118	1.53	1.83	1.95
Sb121	<0.119	0.384	<0.114
Cs133	4.68	2.63	3.14
Ba137	2595.2	2330.24	1244.17
La139	0.083	7.42	0.592
Ce140	0.083	10.5	1.39
Pr141	<0.0069	1.117	0.122
Nd143	<0.105	3.43	0.32
Sm147	<0.052	0.636	0.172
Eu151	0.137	0.241	0.057
Gd157	0.07	0.617	0.104
Tb159	<0.0080	0.101	<0.0110
Dy161	<0.038	0.584	<0.0283
Ho165	<0.0068	0.097	0.012
Er166	<0.0260	0.262	<0.0176
Tm169	<0.0081	0.0376	<0.009
Yb172	<0.030	0.206	<0.042
Lu175	<0.0089	0.0194	<0.0079
Hf179	0.212	1.85	0.25
Ta181	1.27	1.37	1.92
Pb206	0.48	12.29	0.36
Pb207	0.408	11.11	0.43
Pb208	0.426	11.83	0.478
Th232	0.642	0.62	0.075
U238	0.0289	0.352	0.0125

Table 17
Major-element compositions of phlogopite minerals from Indaiá Kimberlite

	IDIA-1_0001 C	IDIA-1_0001 B	ID 3_0004 B	ID 3_0004 C
SiO2	41.18	40.95	39.58	39.97
TiO2	0.48	0.58	3.49	3.54
Al2O3	9.76	9.65	11.74	11.66
FeOt	7.36	8.85	7.78	8.16
MnO	0.10	0.03	0.07	0.05
MgO	24.99	24.09	21.28	20.03
CaO	0.09	0.12	0.02	0.05
Na2O	0.08	0.08	0.09	0.06
K2O	9.38	9.99	10.16	10.24
SrO	0.00	0.00	0.00	0.00
BaO	0.14	0.16	0.05	0.06
Rb2O	0.07	0.07	0.07	0.07
ZnO	0.02	0.02	0.04	0.00
Ga2O3	0.01	0.01	0.01	0.01
F	0.00	0.01	0.19	0.11
Cl	0.00	0.00	0.04	0.02
Cr2O3	0.11	0.11	0.05	0.05
NiO	0.06	0.06	0.06	0.06
Li2O*	2.27	2.20	1.81	1.92
H2O*	4.22	4.20	4.09	4.12
Subtotal	100.33	101.18	100.62	100.18
O=F,Cl	0.00	0.01	0.09	0.05
Total	100.33	101.18	100.53	100.13
Number of ions on base of 22oxygen				
Si	5.8513	5.8327	5.6592	5.7372
Al iv	1.6346	1.6201	1.9786	1.9727
Al vi	0.0000	0.0000	0.0000	0.0000
Ti	0.0509	0.0618	0.3753	0.3821
Cr	0.0121	0.0121	0.0054	0.0055
Fe	0.8746	1.0542	0.9303	0.9796

Mn	0.0125	0.0030	0.0084	0.0056
Mg	5.2932	5.1150	4.5356	4.2858
Zn	0.0021	0.0024	0.0043	0.0003
Sn	0.0000	0.0000	0.0000	0.0000
Ga	0.0007	0.0007	0.0006	0.0007
Ni	0.0074	0.0074	0.0071	0.0071
Cu	0.0000	0.0000	0.0000	0.0000
Li*	1.2954	1.2607	1.0394	1.1081
Ca	0.0141	0.0180	0.0032	0.0074
Na	0.0232	0.0232	0.0257	0.0179
K	1.7000	1.8150	1.8529	1.8748
Sr	0.0001	0.0001	0.0004	0.0004
Ba	0.0079	0.0089	0.0028	0.0035
Rb	0.0068	0.0061	0.0061	0.0062
Cs	0.0000	0.0000	0.0000	0.0000
OH*	4.0000	3.9943	3.9055	3.9440
F	0.0000	0.0045	0.0854	0.0509
Cl	0.0000	0.0012	0.0091	0.0052
TOTAL	20.7869	20.8415	20.4353	20.3947

Trace elements in phlogopite minerals of Indaiá Kimberlite
Concentrations in ppm (µg/g)

Li7 ppm		11.5		16.18
Be9		5.05		4.37
B11		6.08		5.21
P31	<9.65		<9.54	
Ca42	<164.82			490.45
Sc45		1.25		1.23
Ti49		2763.88		8844.73
V51		47.45		100.2
Cr52		734.41		328.93
Mn55		332.11		330.1
Co59		64.15		78.08
Ni60		507.04		484.49
Cu65		0.89		1.43
Zn66		88.32		86.21

Ga71		56.95		47.6
Rb85		684.87		611.56
Sr88		13.32		37.61
Y89		0.0438		0.0507
Zr90		3.84		3.03
Nb93		7.17		10.02
Mo95	<0.056		<0.099	
Sn118		1.02		1.36
Sb121	<0.090		<0.105	
Cs133		3.66		3.12
Ba137		1008.68		1822.24
La139		0.0213		0.0287
Ce140		0.0443		0.0391
Pr141	<0.0057		<0.0072	
Nd143	<0.044		<0.044	
Sm147		0.023	<0.017	
Eu151		0.0513		0.081
Gd157	<0.0215		<0.0154	
Tb159	<0.0048		<0.0064	
Dy161	<0.0180		<0.022	
Ho165	<0.0059		<0.0069	
Er166	<0.0134		<0.0118	
Tm169	<0.0043		<0.00219	
Yb172	<0.0180		<0.0182	
Lu175	<0.0050		<0.0045	
Hf179		0.178		0.125
Ta181		0.311		0.568
Pb206		0.076		0.073
Pb207		0.07		0.067
Pb208		0.142		0.111
Th232		3.63		2.314
U238		0.045		0.0255

Table 18

Major-element compositions of pyroxene minerals from Charneca Kimberlite

	CHAR-6#_0001	CHAR-6#_0001	CHAR-6#_0002	CHAR-6#_0002	CHAR-6#_0003	CHAR-6#_0003	CHAR-6#_0004	CHAR-6#_0004	CHAR-6#_0005	CHAR-6#_0005
	PX.C	PX.B	PX.C	PX.B	PX.C	PX.B	PX.C	PX.B	PX.C	PX.B
SiO2	54.33	54.34	54.76	54.68	54.77	54.59	54.79	54.39	54.45	54.29
TiO2	0.15	0.14	0.02	0.10	0.05	0.07	0.07	0.08	0.03	0.06
Al2O3	1.97	1.87	1.63	1.61	1.91	1.89	1.88	1.90	1.62	1.66
Cr2O3	1.68	1.88	1.02	1.22	2.46	2.58	2.75	2.46	1.40	1.45
FeOT	2.39	2.22	2.16	2.32	2.16	2.22	2.14	2.14	2.19	2.19
MnO	0.08	0.08	0.08	0.06	0.08	0.08	0.07	0.07	0.07	0.09
MgO	16.44	16.56	17.22	17.13	16.12	15.95	16.06	16.31	17.07	17.24
CaO	19.80	19.84	21.18	20.71	19.54	19.56	19.31	19.46	20.59	20.76
Na2O	1.98	2.05	1.42	1.63	2.31	2.36	2.32	2.27	1.54	1.64
K2O	0.02	0.03	0.02	0.01	0.02	0.00	0.03	0.03	0.01	0.04
TOTAL	98.84	99.02	99.51	99.47	99.42	99.29	99.42	99.12	98.98	99.42
Fe2O3	1.44	1.93	1.34	1.75	1.40	1.55	0.94	1.93	1.24	2.43
FeO	1.10	0.48	0.95	0.75	0.90	0.83	1.29	0.40	1.07	0.00
Total	98.98	99.21	99.65	99.64	99.56	99.45	99.51	99.31	99.11	99.66
Number of ions on base of 6 oxygen										
TSi	2.004	2.003	1.996	1.997	2.021	2.020	2.028	2.012	2.002	1.985
TAl	0.000	0.000	0.004	0.003	0.000	0.000	0.000	0.000	0.000	0.015
TFe3	0.000	0.000	0.000	0.000	0.000	0.000	0.000	0.000	0.000	0.000
SOMA T	2.004	2.003	2.000	2.000	2.021	2.020	2.028	2.012	2.002	2.000
M1Al	0.086	0.081	0.067	0.066	0.083	0.082	0.082	0.083	0.070	0.057
M1Ti	0.004	0.004	0.001	0.003	0.001	0.002	0.002	0.002	0.001	0.002
M1Fe3	0.040	0.054	0.037	0.048	0.039	0.043	0.026	0.054	0.034	0.067
M1Zr	0.000	0.000	0.000	0.000	0.000	0.000	0.000	0.000	0.000	0.000
M1Mg	0.870	0.861	0.896	0.883	0.877	0.873	0.886	0.861	0.894	0.874

M1Fe2	0.000	0.000	0.000	0.000	0.000	0.000	0.004	0.000	0.000	0.000
M1Mn	0.000	0.000	0.000	0.000	0.000	0.000	0.000	0.000	0.000	0.000
SOMA M1	1.000	1.000	1.000	1.000	1.000	1.000	1.000	1.000	1.000	1.000
M2Mg	0.034	0.049	0.040	0.049	0.010	0.007	0.000	0.038	0.041	0.066
M2Fe2	0.034	0.015	0.029	0.023	0.028	0.026	0.036	0.013	0.033	0.000
M2Mn	0.003	0.003	0.003	0.002	0.003	0.002	0.002	0.002	0.002	0.003
M2Ca	0.783	0.783	0.827	0.810	0.772	0.775	0.766	0.771	0.811	0.813
M2Na	0.142	0.146	0.100	0.115	0.165	0.169	0.166	0.163	0.110	0.116
M2K	0.001	0.002	0.001	0.001	0.001	0.000	0.001	0.002	0.001	0.002
SOMA M2	0.996	0.998	1.000	1.000	0.979	0.980	0.972	0.988	0.998	1.000
Sum_cat	4.000	4.000	4.000	4.000	4.000	4.000	4.000	4.000	4.000	4.000

Jd	8.93	8.44	6.91	6.83	8.75	8.65	8.72	8.65	7.32	5.94
Ae	4.16	5.56	3.44	4.87	4.09	4.51	2.80	5.61	3.58	5.97
En	45.14	44.44	46.50	45.86	46.08	45.66	47.03	44.88	46.54	45.46
Fs	0.00	0.00	0.00	0.00	0.00	0.00	0.20	0.00	0.00	0.00
Mn	0.14	0.13	0.13	0.10	0.13	0.13	0.12	0.12	0.12	0.14
Wo	40.79	40.61	42.94	42.06	40.66	40.66	40.73	40.28	42.25	42.30
	99.16	99.19	99.93	99.72	99.71	99.60	99.58	99.54	99.81	99.82
Jd	8.64	8.18	6.66	6.58	8.58	8.51	8.56	8.44	7.05	5.71
Ae	4.03	5.39	3.33	4.49	4.01	4.44	2.75	5.47	3.45	5.82
Es	0.00	0.00	0.36	0.32	0.00	0.00	0.00	0.00	0.00	0.88
CaTiTs	0.00	0.00	0.00	0.00	0.00	0.00	0.00	0.00	0.00	0.04
CaTs	0.00	0.00	0.00	0.00	0.00	0.00	0.00	0.00	0.00	0.00
Wo	39.45	39.37	41.20	40.39	39.90	40.01	40.00	39.29	40.69	40.21
En	45.57	45.72	46.81	46.67	45.80	45.40	46.29	45.82	46.94	46.99
Fs	1.50	0.55	1.42	1.00	1.36	1.23	1.99	0.53	1.61	0.00
MnFs	0.00	0.00	0.09	0.00	0.06	0.03	0.01	0.01	0.07	0.07
Fe2+-NaT	0.82	0.78	0.14	0.54	0.28	0.39	0.41	0.45	0.18	0.28
Fe2-NaZ	0.00	0.00	0.00	0.00	0.00	0.00	0.00	0.00	0.00	0.00
	100.00	100.00	100.00	100.00	100.00	100.00	100.00	100.00	100.00	100.00

nomenc final morimoto (1990)	augita com Na	augita com Na	diopsídio com I	augita com Na	augita com Na	augita com Na	augita com Na	augita com Na	augita com Na	augita com Na
Jd	9.01	8.51	6.91	6.84	8.77	8.68	8.76	8.69	7.34	5.95
Ae	4.20	5.61	3.44	4.89	4.10	4.53	2.81	5.63	3.59	5.99
WEF	86.80	85.88	89.64	88.27	87.13	86.79	88.44	85.67	89.07	88.06
	100.00	100.00	100.00	100.00	100.00	100.00	100.00	100.00	100.00	100.00

Trace elements in pyroxene minerals of Charneca Kimberlite

	Concentrations in ppm (µg/g)								
Li7	0.81	0.911	0.907	0.884	0.974	0.799	0.853	0.836	1.04
Be9	0.146	<0.138	0.35	0.11	<0.054	0.421	0.36	0.45	0.349
B11	3.06	2.47	2.43	3.07	2.11	1.61	3.27	2.76	1.73
P31	<4.60	9.43	27.52	9.82	11.27	26.18	27.29	25.16	46.23
Sc45	21.88	23.5	22.83	16.76	16.31	19.88	21.48	22.17	23.76
Ti49	940.87	969.73	239.36	295.8	300.37	236.13	251.6	252.26	269.64
V51	420.07	468.5	468.9	317.81	307.16	421.4	478.71	496.71	533.89
Cr52	11999.44	12905.79	20180.09	7324.57	6942.19	16766.23	19035.44	19175.64	21449.48
Mn55	690.03	709.71	552.55	540.38	547.43	590.71	615.19	637.97	649.64
Co59	19.39	20.86	17.31	18.74	17.47	17.46	18.71	18.78	19.93
Ni60	360.17	385.1	324.69	362.27	326.97	319.45	345.11	353.73	368.24
Cu65	2.64	3.21	1.71	1.31	1.51	1.61	1.62	1.71	1.77
Zn66	11.53	12.97	11.18	12.35	11.23	10.88	11.22	11.58	14
Ga71	7.08	7.88	5.33	5.32	4.72	5.55	5.83	5.88	6.07
Rb85	<0.038	<0.035	<0.034	<0.035	<0.039	<0.040	<0.031	<0.039	<0.038
Sr88	64.39	68.8	126.89	41.02	35.01	169.12	161.63	138.63	201.31
Y89	1.146	1.209	0.792	0.828	0.774	0.803	1.085	0.693	1.54

Zr90	5.9	6.61	6.99	2.2	2	6.11	8.7	5.57	12.94
Nb93	0.0881	0.1035	1.652	0.454	0.211	1.589	1.616	1.64	1.62
Mo95	<0.033	<0.041	<0.028	<0.030	<0.037	<0.045	0.042	<0.034	<0.045
Sn118	0.631	0.824	0.664	0.532	0.55	0.667	0.726	0.756	0.845
Sb121	<0.050	<0.055	0.103	<0.050	<0.052	<0.060	0.051	<0.056	<0.055
Cs133	<0.0089	<0.0082	<0.0070	<0.0094	<0.0090	<0.0092	<0.0068	<0.0090	<0.0091
Ba137	2.31	1.646	1.57	1.085	1.099	2.05	1.838	1.729	1.98
La139	1.406	1.438	4.22	1.664	1.327	6.39	5.42	4.89	6.79
Ce140	4.66	4.73	12.12	4.49	3.73	17.35	15.84	13.18	19.45
Pr141	0.775	0.738	1.551	0.581	0.513	2.002	1.972	1.598	2.378
Nd143	4.07	3.94	6.62	2.35	2.39	7.79	8.23	6.43	9.55
Sm147	1.158	1.061	1.099	0.552	0.495	1.199	1.26	1.084	1.542
Eu151	0.349	0.358	0.298	0.162	0.142	0.248	0.311	0.285	0.451
Gd157	0.811	0.772	0.484	0.397	0.341	0.463	0.618	0.533	0.88
Tb159	0.1041	0.0917	0.0495	0.0499	0.0508	0.054	0.0619	0.0572	0.1022
Dy161	0.387	0.406	0.267	0.222	0.232	0.197	0.306	0.17	0.411
Ho165	0.0599	0.0457	0.0396	0.0394	0.0385	0.0315	0.038	0.0295	0.0627
Er166	0.112	0.106	0.099	0.072	0.07	0.076	0.088	0.0601	0.157
Tm169	0.0124	0.0066	0.0144	0.0049	0.0084	0.0082	0.0102	0.0045	0.0155
Yb172	0.041	0.053	0.084	0.026	0.033	0.049	0.081	0.0283	0.113
Lu175	0.0049	<0.0039	0.0099	<0.0042	0.0045	<0.0063	0.0086	0.0062	0.0152
Hf179	0.387	0.426	0.127	0.134	0.179	0.099	0.143	0.139	0.238
Ta181	0.0084	0.0115	0.1022	0.0129	0.0094	0.0933	0.0981	0.1027	0.1087
Pb206	0.294	0.304	0.961	0.374	0.337	1.39	1.272	1.123	1.51
Pb207	0.27	0.299	0.991	0.401	0.329	1.45	1.061	1.009	1.34
Pb208	0.294	0.362	1.57	0.413	0.352	1.53	1.2	1.065	1.48
Th232	0.0562	0.0354	0.311	0.0872	0.0794	0.392	0.361	0.338	0.443
U238	0.00178	0.005	0.138	0.0354	0.0185	0.142	0.143	0.143	0.149

Table 19

Major-element compositions of pyroxene minerals from Grota do Cedro Kimberlite

	GC1-13_0005 PX.B	GC1-13_0005 PX.C	GC1-13_0018 PX.INT	GC1-13_0018 PX.B	SP_GC3_0006 PX.C	SP_GC3_0006 PX.B	SP_GC6#_0009 PX.C	SP_GC6#_0009 PX.B	SP_GC6#_0011 PX.C
SiO2	54.03	53.95	55.29	52.49	51.55	48.48	50.24	49.99	52.14
TiO2	0.57	0.56	0.01	1.54	1.25	3.00	0.49	0.47	1.14
Al2O3	2.50	2.57	2.10	0.79	2.24	2.82	4.37	4.39	0.48
Cr2O3	0.62	0.68	1.31	0.30	0.66	0.50	1.67	1.59	0.00
FeOT	6.17	6.45	1.72	4.03	4.96	5.61	2.75	2.61	5.47
MnO	0.17	0.17	0.07	0.12	0.11	0.08	0.03	0.04	0.14
MgO	19.48	19.72	16.38	16.07	16.15	14.59	14.89	15.12	14.88
CaO	14.34	13.74	21.27	24.13	21.02	23.09	23.79	23.94	24.01
Na2O	1.40	1.38	1.74	0.27	0.62	0.34	0.43	0.50	0.51
K2O	0.04	0.05	0.03	0.01	0.01	0.00	0.00	0.01	0.03
TOTAL	99.32	99.26	99.92	99.74	98.57	98.51	98.67	98.67	98.81
Fe2O3	1.04	1.01	0.33	0.91	1.04	2.41	1.45	2.70	2.20
FeO	5.24	5.54	1.42	3.21	4.02	3.44	1.44	0.18	3.49
Total novo	99.42	99.36	99.96	99.83	98.68	98.75	98.82	98.94	99.03
Number of ions on base of 6 oxygen									
TSi	1.97	1.97	2.01	1.94	1.92	1.83	1.88	1.87	1.95
TAl	0.03	0.03	0.00	0.03	0.08	0.13	0.12	0.13	0.02
TFe3	0.00	0.00	0.00	0.03	0.00	0.04	0.00	0.00	0.03
SOMA T	2.00	2.00	2.01	2.00	2.00	2.00	2.00	2.00	2.00
M1Al	0.07	0.08	0.09	0.00	0.02	0.00	0.08	0.06	0.00
M1Ti	0.02	0.02	0.00	0.04	0.03	0.08	0.01	0.01	0.03
M1Fe3	0.03	0.03	0.01	0.00	0.03	0.02	0.04	0.08	0.03
M1Zr	0.00	0.00	0.00	0.00	0.00	0.00	0.00	0.00	0.00
M1Mg	0.88	0.88	0.89	0.88	0.90	0.82	0.83	0.84	0.83

M1Fe2	0.00	0.00	0.01	0.07	0.02	0.07	0.03	0.00	0.11
M1Mn	0.00	0.00	0.00	0.00	0.00	0.00	0.00	0.00	0.00
SOMA M1	1.00	1.00	1.00	1.00	1.00	1.00	1.00	1.00	1.00
M2Mg	0.18	0.19	0.00	0.00	0.00	0.00	0.00	0.00	0.00
M2Fe2	0.16	0.17	0.03	0.03	0.11	0.04	0.01	0.00	0.00
M2Mn	0.01	0.01	0.00	0.00	0.00	0.00	0.00	0.00	0.00
M2Ca	0.56	0.54	0.83	0.95	0.84	0.93	0.96	0.96	0.96
M2Na	0.10	0.10	0.12	0.02	0.04	0.02	0.03	0.04	0.04
M2K	0.00	0.00	0.00	0.00	0.00	0.00	0.00	0.00	0.00
SOMA M2	1.00	1.00	0.99	1.00	1.00	1.00	1.00	1.00	1.00
Sum_cat	4.00	4.00	4.00	4.00	4.00	4.00	4.00	4.00	4.00
Jd	9.02	9.38	9.33	3.33	1.09	6.23	3.26	3.69	0.50
Ae	1.07	0.76	0.95	2.64	0.00	2.18	0.00	0.00	0.48
En	53.64	54.46	46.01	45.66	48.63	43.63	42.87	42.81	41.16
Fs	0.00	0.00	0.61	3.78	0.83	3.81	1.78	0.20	5.42
Mn	0.31	0.32	0.11	0.19	0.19	0.14	0.05	0.06	0.22
Wo	34.03	33.16	42.95	48.39	45.49	47.26	46.42	44.20	46.60
	98.07	98.09	99.96	103.98	96.24	103.24	94.37	90.97	94.37
Jd	7.43	7.61	9.18	0.00	2.23	0.00	3.18	3.70	0.00
Ae	0.51	0.71	0.93	6.59	4.63	8.66	2.73	0.70	2.51
Es	3.36	3.49	0.00	6.59	7.56	11.07	6.83	8.30	5.36
CaTiTs	0.00	0.00	0.00	0.00	0.00	2.77	0.00	0.96	0.00
CaTs	0.00	0.00	0.00	0.00	0.00	0.00	4.63	2.69	0.00
Wo	26.35	25.14	42.27	44.43	38.32	39.88	42.11	42.05	45.43
En	52.99	53.69	45.29	44.22	45.01	41.14	41.66	42.20	41.48
Fs	7.19	7.69	2.19	2.82	4.55	2.65	1.58	0.11	3.87
MnFs	0.00	0.00	0.10	0.00	0.00	0.00	0.00	0.00	0.00
Fe2+-NaT	3.19	3.10	0.04	8.53	6.97	11.14	2.73	0.70	6.37
Fe2-NaZ	0.00	0.00	0.00	0.00	0.00	0.00	0.00	0.00	0.00

	101.03	101.42	100.00	113.18	109.27	117.32	105.45	101.41	105.02
nomenc final morimoto (1990)	augita	augita	diopsídio	diopsídio	diopsídio	diopsídio	diopsídio	diopsídio	diopsídio
Jd	9.20	9.57	9.33	3.62	1.13	7.21	3.45	4.05	0.54
Ae	1.09	0.77	0.95	2.86	0.00	2.52	0.00	0.00	0.52
WEF	89.71	89.66	89.72	106.48	98.87	109.73	96.55	95.95	101.06
	100.00	100.00	100.00	112.97	100.00	119.46	100.00	100.00	102.12

Trace elements in pyroxene minerals of Grota do Cedro Kimberlite

Concentrations in ppm (µg/g)

Li7	1.81	<0.51	<0.44	2.67	<0.47
Be9	<0.24	2.44	23.02	1.95	1.12
B11	<2.87	3.55	<2.76	5.03	<2.71
P31	21.27	50.23	<10.14	128.52	564.88
Sc45	18.32	264.31	189.24	142.98	161.26
Ti49	2810.45	8442.54	2295.74	4383.1	6014.09
V51	210.52	82.46	48.96	221.25	42.84
Cr52	4221.9	6181.38	1.22	9689.46	<0.75
Mn55	1251.86	752.05	1523.61	294.06	923.99
Co59	48.9	20.83	2.6	43.13	28.85
Ni60	507.37	194.76	0.27	435.43	14.4
Cu65	5.74	2.11	<0.50	4.83	0.5
Zn66	37.08	21.46	47.33	25.95	35.6
Ga71	6.11	5.34	3.31	5.94	3.08
Rb85	<0.092	0.385	<0.134	1.98	<0.119
Sr88	109.78	245.47	348.41	723.34	596.52
Y89	3.34	3.36	5.13	25.68	6.26
Zr90	10.37	361.81	177.81	597.49	181.49
Nb93	0.296	0.957	3.66	14.62	0.631

Mo95	<0.100	0.129	0.117	0.64	<0.145
Sn118	1	1.83	2.78	4.39	1.66
Sb121	<0.138	<0.165	<0.176	<0.199	0.203
Cs133	<0.0176	<0.023	<0.031	0.051	<0.032
Ba137	1.32	14.2	<0.147	54.83	5.25
La139	2.52	4.5	13.05	94.16	24.98
Ce140	8.71	8.37	40.09	251.68	50.86
Pr141	1.501	0.95	5.61	33.98	6.22
Nd143	7.93	4.07	24.68	141.75	27.93
Sm147	1.82	1.01	4.83	22.65	5.64
Eu151	0.626	0.377	1.4	6.56	1.59
Gd157	1.5	1.19	3.57	14.18	3.63
Tb159	0.164	0.163	0.373	1.69	0.441
Dy161	0.972	0.693	1.83	7.13	2.34
Ho165	0.152	0.176	0.264	1.19	0.29
Er166	0.315	0.352	0.59	2.56	0.67
Tm169	0.0324	0.0331	0.069	0.307	0.054
Yb172	0.243	0.325	0.67	1.99	0.429
Lu175	0.0268	0.049	0.185	0.281	0.088
Hf179	0.673	22.19	8.8	20.64	10.71
Ta181	0.0197	0.0225	0.06	1	0.0231
Pb206	0.174	0.298	0.256	0.91	0.366
Pb207	0.248	0.265	0.324	0.74	0.421
Pb208	0.212	0.287	0.279	0.868	0.29
Th232	0.0405	0.0106	0.034	2.52	0.075
U238	0.0074	0.0122	0.0068	0.298	0.026

Table 19 (continuation)

	SP_GC6#_0011 PX.B	SP_GC6#_0030 PX.C	SP_GC6#_0030 PX.B	SP_GC6#_0032 PX.C escuro	SP_GC6#_0032 PX.B clara	SP_GC12_0012 PX.C (abx)	SP_GC12_0012 PX.B (abx)	GC_1_0001 PX.C	GC_1_0001 PX.B
SiO2	52.38	52.94	53.30	53.88	52.43	53.57	53.78	53.40	52.94
TiO2	0.92	0.16	0.14	0.02	0.11	0.62	0.62	0.67	0.95
Al2O3	0.50	0.72	0.58	0.18	0.11	0.22	0.24	0.15	0.24
Cr2O3	0.00	0.28	0.27	0.05	0.03	0.02	0.00	0.00	0.00
FeOT	5.78	7.27	7.48	5.71	12.86	4.20	4.34	4.60	5.00
MnO	0.13	0.21	0.21	0.43	0.54	0.15	0.16	0.17	0.17
MgO	14.80	13.91	13.61	14.69	10.44	15.87	15.80	15.77	15.51
CaO	24.21	22.87	22.39	24.20	21.06	24.36	24.64	24.44	23.85
Na2O	0.53	0.93	1.00	0.28	1.72	0.36	0.33	0.47	0.57
K2O	0.01	0.00	0.01	0.00	0.01	0.01	0.02	0.01	0.00
TOTAL	99.26	99.28	98.99	99.44	99.32	99.38	99.94	99.69	99.23
Fe2O3	2.55	2.69	1.60	0.24	4.64	1.04	1.08	2.18	2.05
FeO	3.49	4.85	6.04	5.50	8.69	3.27	3.37	2.64	3.16
Total novo	99.51	99.55	99.15	99.47	99.78	99.48	100.05	99.90	99.44
Number of ions on base of 6 oxygen									
TSi	1.95	1.98	2.00	2.00	1.99	1.98	1.98	1.97	1.96
TAl	0.02	0.02	0.00	0.00	0.00	0.01	0.01	0.01	0.01
TFe3	0.03	0.00	0.00	0.00	0.00	0.01	0.01	0.03	0.03
SOMA T	2.00	2.00	2.00	2.00	2.00	2.00	2.00	2.00	2.00
M1Al	0.00	0.01	0.02	0.01	0.00	0.00	0.00	0.00	0.00
M1Ti	0.03	0.00	0.00	0.00	0.00	0.02	0.02	0.02	0.03
M1Fe3	0.04	0.08	0.05	0.01	0.13	0.02	0.02	0.03	0.03
M1Zr	0.00	0.00	0.00	0.00	0.00	0.00	0.00	0.00	0.00
M1Mg	0.82	0.77	0.76	0.81	0.59	0.87	0.87	0.87	0.86

M1Fe2	0.11	0.14	0.17	0.17	0.28	0.09	0.10	0.08	0.09
M1Mn	0.00	0.00	0.00	0.00	0.00	0.00	0.00	0.00	0.00
SOMA M1	1.00	1.00	1.00	1.00	1.00	1.00	1.00	1.00	1.00
M2Mg	0.00	0.00	0.00	0.00	0.00	0.00	0.00	0.00	0.00
M2Fe2	0.00	0.01	0.02	0.00	0.00	0.01	0.00	0.00	0.01
M2Mn	0.00	0.01	0.01	0.01	0.02	0.00	0.01	0.00	0.01
M2Ca	0.96	0.91	0.90	0.96	0.86	0.96	0.97	0.96	0.95
M2Na	0.04	0.07	0.07	0.02	0.13	0.03	0.02	0.03	0.04
M2K	0.00	0.00	0.00	0.00	0.00	0.00	0.00	0.00	0.00
SOMA M2	1.00	1.00	1.00	1.00	1.00	1.00	1.00	1.00	1.00
Sum_cat	4.00	4.00	4.00	4.00	4.00	4.00	4.00	4.00	4.00
Jd	0.00	0.71	2.31	0.80	0.00	0.00	0.05	0.00	0.12
Ae	0.80	6.09	4.54	0.66	12.36	0.10	0.00	0.28	0.16
En	40.85	39.22	38.40	40.82	29.57	43.46	43.01	42.71	42.32
Fs	5.40	7.07	8.48	8.57	13.81	4.72	5.10	4.02	4.45
Mn	0.21	0.33	0.34	0.69	0.87	0.23	0.25	0.27	0.27
Wo	46.64	46.13	45.45	48.36	42.66	47.63	47.82	46.76	46.08
	93.90	99.56	99.52	99.90	99.26	96.14	96.23	94.03	93.41
Jd	0.00	0.71	2.29	0.80	0.00	0.00	0.00	0.00	0.00
Ae	1.31	5.15	4.27	0.66	12.12	0.83	0.99	0.31	1.18
Es	5.28	2.42	0.25	0.00	0.73	2.34	2.51	3.48	3.97
CaTiTs	0.00	0.00	0.00	0.00	0.00	0.00	0.00	0.00	0.00
CaTs	0.00	0.00	0.00	0.00	0.00	0.00	0.00	0.00	0.00
Wo	45.66	44.60	44.90	48.37	42.55	47.09	47.34	46.57	45.45
En	41.09	38.77	38.09	40.85	29.60	43.75	43.36	43.37	42.92
Fs	4.15	7.37	9.29	8.55	13.66	4.19	4.32	3.14	3.58
MnFs	0.00	0.11	0.15	0.66	0.71	0.00	0.00	0.00	0.00
Fe2+-NaT	5.13	0.88	0.76	0.10	0.63	3.45	3.45	3.75	5.26
Fe2-NaZ	0.00	0.00	0.00	0.00	0.00	0.00	0.00	0.00	0.00

	102.61	100.00	100.00	100.00	100.00	101.66	101.97	100.62	102.37

nomenc final
morimoto
(1990)

	diopsídio	diopsídio	diopsídio	diopsídio	diopsídio com F	diopsídio	diopsídio	diopsídio	diopsídio
Jd	0.00	0.72	2.32	0.80	0.00	0.00	0.06	0.00	0.13
Ae	0.86	6.12	4.56	0.66	12.45	0.11	0.00	0.30	0.18
WEF	99.14	93.16	93.12	98.54	87.55	99.89	100.06	99.70	100.30
	100.00	100.00	100.00	100.00	100.00	100.00	100.11	100.00	100.61

Trace elements in pyroxene minerals of Grota do Cedro Kimberlite
Concentrations in ppm (µg/g)

Li7	0.78	0.46	<0.50
Be9	1.05	0.96	0.83
B11	3.14	1.73	<3.67
P31	<10.76	8.11	<12.05
Sc45	71.52	117.12	210.5
Ti49	769.8	4766.39	2864.16
V51	188.16	52.41	33.79
Cr52	1975.28	38.49	<0.96
Mn55	1667.03	1104.93	1280.31
Co59	39.95	31.33	28.52
Ni60	126.3	138.99	17.13
Cu65	<0.52	0.55	0.49
Zn66	63.29	23.42	20.88
Ga71	2.41	2.81	1.78
Rb85	<0.138	0.154	<0.137
Sr88	455.81	728.83	576.22
Y89	15.8	3.88	2.95
Zr90	135.99	230.5	151.24
Nb93	0.578	0.181	0.036

Mo95	<0.161	<0.097	<0.127
Sn118	3.13	1.82	1.1
Sb121	<0.192	<0.117	<0.179
Cs133	<0.038	0.03	<0.032
Ba137	0.45	1.06	0.81
La139	16.25	2.28	0.734
Ce140	57.38	4.2	1.086
Pr141	8.67	0.526	0.132
Nd143	41	2.51	0.77
Sm147	7.33	0.75	0.271
Eu151	2.52	0.219	0.086
Gd157	5.53	0.64	0.381
Tb159	0.72	0.118	0.065
Dy161	4.04	0.48	0.504
Ho165	0.73	0.124	0.086
Er166	1.7	0.366	0.365
Tm169	0.191	0.051	0.0524
Yb172	1.9	0.76	0.713
Lu175	0.282	0.129	0.165
Hf179	3.97	12.17	8.78
Ta181	0.0205	<0.0092	<0.0129
Pb206	0.6	0.172	0.224
Pb207	0.399	0.248	0.122
Pb208	0.475	0.226	0.1
Th232	0.086	<0.0034	<0.00
U238	0.0129	0.002	<0.00

Tabela 20

Major-element compositions of pyroxene minerals from Régis Kimberlite

	regis-5_0006	regis-5_0006	regis-9_0013	regis-9_0013	regis-10_0005	regis-10_0005	regis-10_0009	regis-10_0009
	PX.B	PX.C	PX.B	PX.C	PX.B	PX.C	PX.B	PX.C
SiO2	55.36	55.10	54.38	54.67	50.74	48.69	56.65	57.48
TiO2	0.19	0.24	0.06	0.03	2.54	2.87	0.02	0.08
Al2O3	2.17	2.12	1.51	1.50	1.78	2.49	0.67	0.80
Cr2O3	0.92	0.82	1.71	1.66	0.03	0.00	0.21	0.28
FeOT	4.96	5.11	2.71	2.66	5.72	6.51	5.15	5.13
MnO	0.16	0.13	0.07	0.08	0.09	0.11	0.10	0.11
MgO	21.47	22.21	18.44	18.28	14.51	14.35	36.63	35.24
CaO	13.25	13.20	19.33	19.17	23.97	23.60	0.49	0.50
Na2O	0.90	0.94	1.21	1.16	0.43	0.40	0.11	0.12
K2O	0.05	0.05	0.08	0.08	0.04	0.01	0.01	0.00
TOTAL	99.42	99.91	99.50	99.29	99.85	99.03	100.04	99.73
Fe2O3	0.15	0.15	1.33	0.15	1.69	3.88	4.37	0.49
FeO	4.97	4.97	1.51	2.52	4.20	3.02	1.22	4.69
Total	99.58	99.93	99.63	99.31	100.01	99.42	100.48	99.78
Number of ions on base of 6 oxygen								
TSi	2.0067	1.9804	1.9923	2.0080	1.8827	1.8238	1.9333	1.9793
TAl	0.0000	0.0196	0.0077	0.0000	0.0779	0.1099	0.0269	0.0207
TFe3	0.0000	0.0000	0.0000	0.0000	0.0393	0.0663	0.0398	0.0000
SOMA T	2.0067	2.0000	2.0000	2.0080	2.0000	2.0000	2.0000	2.0000
M1Al	0.0927	0.0702	0.0573	0.0649	0.0000	0.0000	0.0000	0.0117
M1Ti	0.0051	0.0065	0.0017	0.0008	0.0693	0.0783	0.0006	0.0021
M1Fe3	-0.0510	0.0041	0.0367	0.0042	0.0078	0.0431	0.0725	0.0127
M1Zr	0.0000	0.0000	0.0000	0.0000	0.0000	0.0000	0.0000	0.0000
M1Mg	0.9531	0.9192	0.9043	0.9301	0.8026	0.8013	0.9269	0.9735

M1Fe2	0.0000	0.0000	0.0000	0.0000	0.1203	0.0774	0.0000	0.0000
M1Mn	0.0000	0.0000	0.0000	0.0000	0.0000	0.0000	0.0000	0.0000
SOMA M1	1.0000	1.0000	1.0000	1.0000	1.0000	1.0000	1.0000	1.0000
M2Mg	0.2070	0.2708	0.1029	0.0708	0.0000	0.0000	0.9367	0.8356
M2Fe2	0.2013	0.1495	0.0463	0.0775	0.0101	0.0172	0.0347	0.1351
M2Mn	0.0048	0.0039	0.0022	0.0026	0.0028	0.0034	0.0028	0.0033
M2Ca	0.5146	0.5083	0.7588	0.7544	0.9530	0.9471	0.0179	0.0184
M2Na	0.0631	0.0654	0.0862	0.0828	0.0307	0.0290	0.0074	0.0078
M2K	0.0025	0.0022	0.0037	0.0039	0.0018	0.0006	0.0006	0.0000
SOMA M2	0.9933	1.0001	1.0000	0.9920	0.9984	0.9974	1.0000	1.0001
Sum_cat	4.000	4.000	4.000	4.000	3.998	3.997	4.000	4.000
Jd	7.08	7.54	6.24	7.10	4.02	1.82	0.00	1.12
Ae	6.84	0.00	2.96	0.46	3.29	2.39	1.35	0.00
En	63.55	58.84	49.21	50.85	41.88	40.24	92.49	96.31
Fs	0.00	0.00	0.00	0.00	6.28	3.89	0.00	0.00
Mn	0.32	0.25	0.12	0.14	0.15	0.18	0.28	0.32
Wo	34.50	32.54	41.29	41.28	47.67	42.60	2.19	1.82
	112.30	99.17	99.82	99.82	103.30	91.11	96.31	99.58
Jd	6.73	6.77	5.74	6.57	0.00	0.00	0.00	0.78
Ae	5.23	1.30	2.92	0.42	10.10	6.87	0.66	0.43
Es	0.00	1.71	0.76	0.00	10.88	11.19	6.42	1.69
CaTiTs	0.00	0.00	0.00	0.00	0.26	2.93	0.00	0.00
CaTs	2.79	0.27	0.00	0.00	0.00	0.00	0.00	0.39
Wo	25.02	24.48	37.59	38.19	42.18	40.44	0.00	0.00
En	59.56	59.62	50.40	50.68	40.22	40.19	91.03	90.43
Fs	10.07	7.16	2.23	3.88	3.20	2.29	1.67	6.65
MnFs	0.00	0.00	0.02	0.09	0.00	0.00	0.11	0.06
Fe2+-NaT	1.05	1.30	0.34	0.17	13.35	9.84	0.12	0.43
Fe2-NaZ	0.00	0.00	0.00	0.00	0.00	0.00	0.00	0.00

	110.47	102.60	100.00	100.00	120.19	113.74	100.00	100.85
nomenc final morimoto (1990)	augita com	augita com	augita com	augita com	diopsídio	diopsídio com f	enstatita	augita
Jd	7.18	7.60	6.25	7.11	4.54	2.20	0.00	1.12
Ae	6.93	0.00	2.96	0.46	3.71	2.89	1.47	0.00
WEF	99.75	92.40	90.78	92.43	108.25	105.09	98.53	98.88
	113.86	100.00	100.00	100.00	116.50	110.18	100.00	100.00

Trace elements in pyroxene minerals of Régis Kimberlite
Concentrations in ppm (µg/g)

Li7 ppm	<1142.79	0.98	0.7	14.86	23.79	<59.43
Be9				8.22	<5.73	<33.19
B11				816.76	448.56	1713.53
P31	<25130.04	16.73	16.37	849.23	823.1	4384.27
Sc45	450.39	13.41	13.43	17.3	11.24	24.04
Ti49	3759.33	222.26	212.11	428.58	2624.84	4733.54
V51	231.06	265.19	295.01	19.08	86.2	439.41
Cr52	19992.74	12331.81	12800.55	167.62	785.22	50392.34
Mn55	879.47	755.31	738.99	155942.06	26606.55	279874.59
Co59	<603.99	31.54	31.3	22.67	56.28	110.89
Ni60	<5652.50	544.45	521	271.97	1169.81	1687.57
Cu65	4121.92	1.31	1.35	43.51	296.1	389.19
Zn66	39.33	17.46	18.37	138.87	438.84	839.4
Ga71	60.35	3.59	3.82	10.89	16.43	30.73

Rb85	<248.83	0.115	0.18	48.21	141.85	164.28
Sr88	5200.05	267.83	259.05	245.4	5.25	337.6
Y89	45.91	1.62	1.59	146.06	97.99	212.43
Zr90	380.16	15.46	15.53	233.24	678.14	567.9
Nb93	<38.12	0.313	0.319	3.12	25.68	37.1
Mo95				2.74	<3.07	<8.04
Sn118	2877.51	1.1	0.48	12807.2	22667.7	21583.42
Sb121	<318.17	<0.26	<0.24	5.44	4	28.07
Cs133	<56.40	<0.025	<0.025	2.31	3.55	8.19
Ba137	538.19	1.25	1.3	131.49	442.76	1748.49
La139	61.26	4.91	4.93	508.49	1164.44	3757.69
Ce140	91.67	17.18	17.63	391.61	1277.05	5745.92
Pr141	<24.78	2.55	2.74	39.86	104.46	408.93
Nd143	<117.89	11.58	11.95	157.14	221.54	1077.75
Sm147	<171.18	2.03	2.09	38.63	27.69	88.92
Eu151	<36.41	0.6	0.57	4.61	7.94	24.1
Gd157	<108.64	1.23	1.15	18.5	24.98	87.71
Tb159	<21.43	0.108	0.159	3.21	2.98	8.03
Dy161	<116.61	0.55	0.53	17.44	13.77	54.86
Ho165	<30.73	0.054	0.092	5.18	3.81	7.47
Er166	39.21	0.079	0.148	12.8	7.16	12
Tm169	<18.99	<0.0098	0.0109	1.95	1.38	<1.32
Yb172	<129.01	0.063	0.058	7.69	6.56	9.85
Lu175	<25.59	<0.0097	<0.0096	1.88	0.6	<1.57
Hf179	135.68	0.57	0.99	3.66	15.89	13.77
Ta181	<10.86	0.0163	0.0279	1.15	1.44	1.29
Pb206	549.22	0.64	0.59	31.47	246.88	168.94
Pb207	607.37	0.51	0.56	39.68	302.06	212.05
Pb208	684.71	0.492	0.678	34.66	278.53	192.05
Th232	8.65	0.0272	0.0229	10.02	18.4	13.89
U238	<61.91	0.0062	0.0066	1.68	5.9	8.43

Table 21

Major-element compositions of pyroxene minerals from Indaiá Kimberlite

	SP_ID 6_0012 PX.C	SP_ID 6_0012 PX.B	SP_ID 6_0015 PX.C	SP_ID 6_0015 PX.B	SP_ID 6_0017 PX.C	SP_ID 6_0017 PX.B	SP_ID 6_0019 PX.C	SP_ID 6_0019 PX.B	SP_ID 6_0020 PX.C
SiO2	54.47	54.48	54.26	54.61	53.86	50.52	54.24	54.62	54.40
TiO2	0.05	0.05	0.07	0.00	0.12	0.11	0.11	0.07	0.12
Al2O3	0.10	0.12	0.07	0.08	0.14	0.37	0.24	0.21	0.18
Cr2O3	1.84	1.17	1.50	1.57	1.23	1.44	0.73	0.49	2.86
FeOT	2.58	2.55	2.31	2.19	3.69	4.74	2.82	2.13	2.20
MnO	0.07	0.10	0.09	0.09	0.10	0.14	0.11	0.05	0.09
MgO	16.31	16.66	16.47	16.60	16.25	15.70	17.71	18.13	16.42
CaO	22.15	22.52	22.26	22.45	21.29	21.09	21.75	19.69	20.52
Na2O	1.21	0.93	1.05	0.94	1.05	1.13	0.72	1.23	1.42
K2O	0.01	0.01	0.00	0.00	0.01	0.35	0.03	1.22	0.02
TOTAL	98.79	98.59	98.08	98.54	97.75	95.60	98.45	97.85	98.23
Fe2O3	0.63	0.37	0.21	0.00	0.48	5.27	0.92	2.37	0.00
FeO	2.02	2.22	2.12	2.47	3.26	0.00	1.99	0.00	2.85
Total novo	98.85	98.62	98.10	98.51	97.80	96.13	98.54	98.09	98.16
Number of ions on base of 6 oxygen									
TSi	2.032	2.024	2.031	2.037	2.025	1.947	2.005	2.007	2.055
TAl	0.000	0.000	0.000	0.000	0.000	0.017	0.000	0.000	0.000
TFe3	0.000	0.000	0.000	0.000	0.000	0.036	0.000	0.000	0.000
SOMA T	2.032	2.024	2.031	2.037	2.025	2.000	2.005	2.007	2.055
M1Al	0.004	0.005	0.003	0.004	0.006	0.000	0.010	0.009	0.008
M1Ti	0.001	0.001	0.002	0.000	0.003	0.003	0.003	0.002	0.003
M1Fe3	0.018	0.010	0.006	0.009	0.013	0.117	0.026	0.065	0.020
M1Zr	0.000	0.000	0.000	0.000	0.000	0.000	0.000	0.000	0.000

M1Mg	0.907	0.923	0.919	0.923	0.911	0.880	0.961	0.923	0.925
M1Fe2	0.063	0.060	0.066	0.077	0.066	0.000	0.000	0.000	0.084
M1Mn	0.002	0.000	0.003	0.003	0.000	0.000	0.000	0.000	0.000
SOMA M1	0.995	1.000	1.000	0.998	1.000	1.000	1.000	1.000	1.000
M2Mg	0.000	0.000	0.000	0.000	0.000	0.022	0.015	0.070	0.000
M2Fe2	0.000	0.009	0.000	0.000	0.037	0.000	0.062	0.000	0.006
M2Mn	0.000	0.003	0.000	0.000	0.003	0.005	0.003	0.002	0.003
M2Ca	0.885	0.897	0.893	0.897	0.858	0.871	0.862	0.775	0.831
M2Na	0.087	0.067	0.076	0.068	0.077	0.085	0.052	0.088	0.104
M2K	0.001	0.000	0.000	0.000	0.001	0.018	0.001	0.059	0.001
SOMA M2	0.973	0.976	0.969	0.966	0.975	1.000	0.995	0.993	0.944
Sum_cat	4.000	4.000	4.000	4.000	4.000	4.000	4.000	4.000	4.000
Jd	0.46	0.57	0.33	0.38	0.67	0.00	1.08	0.99	0.88
Ae	1.85	1.08	0.64	0.92	1.43	8.25	2.68	7.06	2.24
En	47.54	48.06	48.14	48.85	48.09	44.92	50.24	49.66	50.45
Fs	3.30	3.13	3.47	4.08	3.48	0.00	0.00	0.00	4.60
Mn	0.11	0.16	0.15	0.15	0.18	0.24	0.17	0.09	0.16
Wo	46.46	46.75	46.86	47.48	45.44	42.61	45.18	41.78	45.45
	99.72	99.74	99.58	101.84	99.28	96.01	99.36	99.56	103.78
Jd	0.46	0.57	0.33	0.38	0.66	0.00	1.04	0.95	0.88
Ae	1.85	1.08	0.64	0.92	1.40	9.79	2.58	6.81	2.24
Es	0.00	0.00	0.00	0.00	0.00	1.90	0.00	0.00	0.00
CaTiTs	0.00	0.00	0.00	0.00	0.00	0.08	0.00	0.13	0.00
CaTs	0.00	0.00	0.00	0.00	0.00	0.00	0.00	0.00	0.00
Wo	46.50	46.56	46.90	47.48	44.65	42.56	43.50	40.25	45.38
En	47.64	47.93	48.29	48.85	47.42	45.11	49.29	51.65	50.53
Fs	3.23	3.51	3.38	4.08	5.16	0.00	2.96	0.00	4.74
MnFs	0.04	0.09	0.04	0.15	0.00	0.12	0.01	0.04	0.00
Fe2+-NaT	0.28	0.26	0.42	0.00	0.70	0.46	0.62	0.16	0.70

Fe2-NaZ	0.00	0.00	0.00	0.00	0.00	0.00	0.00	0.00	0.00
	100.00	100.00	100.00	101.84	100.00	100.00	100.00	100.00	104.47
nomenc final morimoto (1990)	diopsídio	diopsídio	diopsídio	diopsídio	diopsídio	diopsídio com	augita	augita	diopsídio com
Jd	0.46	0.57	0.33	0.38	0.67	0.00	1.09	0.99	0.89
Ae	1.85	1.09	0.64	0.92	1.44	8.59	2.70	7.09	2.25
WEF	97.69	98.34	99.03	100.54	97.89	91.41	96.21	91.92	101.36
	100.00	100.00	100.00	101.84	100.00	100.00	100.00	100.00	104.51

Trace elements in pyroxene minerals of Indaiá Kimberlite

Concentrations in ppm (µg/g)

Li7	0.89	0.89	<0.59	2.98	6.66	<0.58
Be9	1.82	1.57	<0.33	0.96	0.68	1.65
B11	<4.46	<3.99	<3.61	<3.22	<4.95	<3.98
P31	23.93	16.18	<12.83	41.68	96.61	56.39
Sc45	88.80	94.04	98.90	88.96	58.36	99.15
Ti49	278.50	336.58	360.61	779.14	353.14	688.37
V51	297.73	285.16	348.38	388.58	206.14	384.57
Cr52	13224.83	11375.65	11074.93	7722.38	5167.97	18572.44
Mn55	752.92	756.34	765.72	931.67	630.31	707.83
Co59	17.23	17.97	15.37	25.16	17.71	19.39
Ni60	270.32	268.77	258.35	349.63	289.24	368.36
Cu65	<0.60	<0.57	<0.54	0.47	0.80	0.79
Zn66	21.24	16.89	11.23	27.35	12.25	14.88
Ga71	0.82	0.86	1.16	2.63	1.00	0.54
Rb85	3.35	1.04	<0.141	0.44	1.88	<0.145
Sr88	299.20	325.30	396.23	414.54	1187.43	454.20

Y89	6.33	6.02	10.01	7.50	12.20	6.40
Zr90	53.53	47.97	35.95	59.71	12.88	88.02
Nb93	0.34	0.21	<0.029	0.44	0.76	0.28
Mo95	0.16	<0.148	<0.178	<0.128	0.19	<0.161
Sn118	1.68	1.91	1.49	2.88	2.21	3.38
Sb121	<0.201	<0.189	<0.159	<0.145	<0.21	<0.171
Cs133	<0.046	<0.040	0.07	<0.032	<0.054	<0.033
Ba137	1.84	1.03	1.04	4.45	65.26	<0.126
La139	5.43	5.52	9.11	5.38	21.64	3.84
Ce140	23.33	23.62	42.42	23.44	76.26	18.27
Pr141	4.12	4.17	7.56	4.24	11.36	3.70
Nd143	21.74	20.96	36.94	21.91	49.84	20.52
Sm147	4.53	4.83	7.79	5.02	9.54	4.88
Eu151	1.52	1.49	2.44	1.65	3.01	1.50
Gd157	3.50	3.38	5.21	3.97	6.61	3.63
Tb159	0.47	0.45	0.71	0.49	0.77	0.48
Dy161	1.82	2.13	3.36	2.32	3.88	2.13
Ho165	0.31	0.32	0.47	0.33	0.55	0.32
Er166	0.64	0.61	0.84	0.74	1.00	0.63
Tm169	0.07	0.07	0.09	0.06	0.11	0.07
Yb172	0.37	0.37	0.48	0.30	0.61	0.28
Lu175	0.03	0.04	0.04	0.04	0.06	0.05
Hf179	3.16	2.65	2.62	2.90	0.73	3.74
Ta181	0.04	0.02	<0.0159	0.02	0.02	0.01
Pb206	0.59	0.58	1.14	0.57	1.99	0.41
Pb207	0.58	0.71	0.98	0.69	2.04	0.52
Pb208	0.60	0.62	1.10	0.76	2.08	0.42
Th232	0.07	0.05	0.02	0.07	0.31	0.01
U238	0.00	0.01	<0.0054	0.00	0.07	0.00

Table 21 (continuation)

	SP_ID 6_0020 PX.B	SP_ID 6_0021 PX.C	SP_ID 6_0021 PX.B	INDAIA _1_0001 PX.C	INDAIA _1_0001 PX.B	INDAIA _1_0005 PX.C	INDAIA _1_0005 PX.INT	INDAIA _2_0001 PX.C
SiO2	54.51	53.10	52.96	55.49	55.69	57.49	57.28	55.23
TiO2	0.11	0.06	0.04	0.04	0.24	0.00	0.06	0.04
Al2O3	0.16	3.45	3.70	0.02	0.07	1.90	1.84	1.05
Cr2O3	2.43	1.05	1.17	0.00	0.00	0.19	0.20	0.39
FeOT	2.20	1.92	1.89	2.39	1.07	5.46	5.46	1.17
MnO	0.08	0.07	0.08	0.13	0.04	0.15	0.14	0.06
MgO	16.48	15.74	15.32	16.37	17.84	35.27	35.57	17.91
CaO	21.11	22.31	22.12	24.59	24.99	0.09	0.13	23.99
Na2O	1.36	1.07	1.10	0.47	0.04	0.01	0.02	0.28
K2O	0.00	0.00	0.01	0.03	0.01	0.02	0.00	0.00
TOTAL	98.44	98.77	98.38	99.53	99.99	100.58	100.71	100.12
Fe2O3	0.00	0.06	0.00	0.00	0.00	0.00	0.80	0.00
FeO	2.47	1.87	2.51	3.29	2.74	5.49	4.74	2.06
Total novo	98.41	98.78	98.31	99.43	99.80	100.58	100.79	100.02
Number of ions on base of 6 oxygen								
TSi	2.047	1.961	1.967	2.030	2.019	1.963	1.952	2.000
TAl	0.000	0.039	0.033	0.000	0.000	0.037	0.048	0.000
TFe3	0.000	0.000	0.000	0.000	0.000	0.000	0.000	0.000
SOMA T	2.047	2.000	2.000	2.030	2.019	2.000	2.000	2.000
M1Al	0.007	0.111	0.129	0.001	0.003	0.039	0.026	0.045
M1Ti	0.003	0.002	0.001	0.001	0.007	0.000	0.002	0.001
M1Fe3	0.009	0.002	0.019	0.028	0.051	0.001	0.021	0.027
M1Zr	0.000	0.000	0.000	0.000	0.000	0.000	0.000	0.000

M1Mg	0.923	0.866	0.848	0.893	0.964	0.961	0.952	0.967
M1Fe2	0.076	0.019	0.040	0.101	0.077	0.000	0.000	0.015
M1Mn	0.000	0.000	0.000	0.004	0.000	0.000	0.000	0.000
SOMA M1	1.000	1.000	1.000	0.972	1.000	1.000	1.000	1.000
M2Mg	0.000	0.000	0.000	0.000	0.000	0.834	0.855	0.000
M2Fe2	0.002	0.038	0.038	0.000	0.006	0.157	0.135	0.048
M2Mn	0.002	0.002	0.002	0.000	0.001	0.004	0.004	0.002
M2Ca	0.849	0.883	0.880	0.964	0.971	0.003	0.005	0.931
M2Na	0.099	0.077	0.079	0.034	0.003	0.001	0.001	0.020
M2K	0.000	0.000	0.000	0.001	0.000	0.001	0.000	0.000
SOMA M2	0.953	1.000	1.000	0.999	0.981	1.000	1.000	1.000
Sum_cat	4.000	4.000	4.000	4.000	4.000	4.000	4.000	4.000
Jd	0.78	7.80	8.27	0.11	1.08	0.19	0.06	1.85
Ae	0.92	0.00	2.04	2.88	5.30	0.16	0.00	2.87
En	49.54	45.03	44.85	46.66	50.14	99.17	98.79	50.89
Fs	4.06	1.00	2.14	5.26	4.00	0.00	0.00	0.77
Mn	0.13	0.12	0.13	0.21	0.07	0.44	0.42	0.10
Wo	45.75	45.88	46.55	50.43	50.80	0.35	0.49	49.04
	101.19	99.83	103.97	105.55	111.39	100.32	99.77	105.52
Jd	0.78	7.67	8.04	0.11	0.31	0.16	0.14	1.98
Ae	0.92	0.32	1.95	2.89	5.22	0.08	0.33	2.76
Es	0.00	0.48	0.00	0.00	0.00	0.00	2.36	0.00
CaTiTs	0.00	0.00	0.00	0.00	0.00	0.00	0.00	0.00
CaTs	0.00	3.44	5.02	0.00	0.00	3.72	2.38	2.54
Wo	45.76	42.21	41.91	50.46	49.97	0.00	0.00	45.88
En	49.71	43.36	42.81	46.74	49.64	88.28	88.49	48.98
Fs	4.02	2.81	3.89	5.22	3.93	7.70	6.53	3.11
MnFs	0.00	0.03	0.07	0.15	0.00	0.21	0.11	0.04
Fe2+-NaT	0.66	0.32	0.21	0.22	1.36	0.00	0.33	0.23

Fe2-NaZ	0.00	0.00	0.00	0.00	0.00	0.00	0.00	0.00
	101.85	100.64	103.90	105.77	110.44	100.15	100.67	105.51
nomenc final morimoto (1990)	diopsídio	diopsídio	diopsídio	diopsídio	diopsídio	augita	augita	diopsídio
Jd	0.78	7.82	8.28	0.11	1.10	0.19	0.06	1.85
Ae	0.93	0.00	2.04	2.89	5.38	0.16	0.00	2.87
WEF	100.15	92.18	93.77	102.78	106.48	99.96	100.06	101.02
	101.86	100.00	104.09	105.78	112.96	100.32	100.12	105.75

Trace elements in pyroxene minerals of Indaiá Kimberlite

Concentrations in ppm (µg/g)

Li7	0.78	2.25	0.44
Be9	0.24	<0.44	<0.10
B11	<3.30	<4.07	<1.70
P31	16.15	38.91	7.17
Sc45	89.19	80.30	0.72
Ti49	279.55	271.66	4.27
V51	184.15	189.43	<0.83
Cr52	6692.08	7650.06	1.14
Mn55	551.28	628.09	348.92
Co59	16.34	17.84	50.20
Ni60	267.02	300.58	1097.81
Cu65	<0.45	<0.59	0.22
Zn66	7.75	8.94	12.15
Ga71	1.70	1.87	<0.037
Rb85	<0.124	0.48	<0.032
Sr88	181.15	211.44	0.03

Y89	3.72	3.81	<0.0043
Zr90	7.79	8.74	<0.0111
Nb93	1.82	3.44	0.01
Mo95	0.11	<0.159	<0.028
Sn118	0.92	0.76	0.32
Sb121	<0.125	<0.160	<0.044
Cs133	<0.034	<0.038	<0.0039
Ba137	0.60	26.17	0.14
La139	13.44	15.18	0.00
Ce140	29.37	31.90	0.00
Pr141	3.06	3.37	<0.00154
Nd143	10.71	12.13	<0.0251
Sm147	1.59	1.91	<0.0130
Eu151	0.46	0.56	<0.0044
Gd157	1.00	1.17	<0.0114
Tb159	0.16	0.11	<0.0046
Dy161	0.89	0.65	<0.0122
Ho165	0.12	0.14	<0.0029
Er166	0.39	0.43	<0.0076
Tm169	0.05	0.03	<0.00227
Yb172	0.60	0.55	<0.0089
Lu175	0.11	0.07	<0.0032
Hf179	<0.079	0.13	<0.0136
Ta181	0.26	0.30	<0.00
Pb206	0.79	0.75	<0.0186
Pb207	0.60	0.65	0.02
Pb208	0.54	0.73	<0.0127
Th232	0.58	0.75	0.00
U238	0.17	0.20	<0.00

Table 21 (continuation)

	INDAIA _2_0001 PX.B	INDAIA _2_0002 PX.C	INDAIA _2_0002 PX.B	INDAIA _2_0003 PX.C	INDAIA _2_0003 PX.B
SiO2	55.19	53.67	47.00	54.75	54.94
TiO2	0.00	0.38	0.00	0.22	0.16
Al2O3	0.89	0.58	0.94	0.02	0.00
Cr2O3	0.33	0.05	0.02	0.01	0.01
FeOT	1.18	1.82	4.67	1.69	1.83
MnO	0.07	0.09	0.10	0.23	0.44
MgO	17.79	15.81	24.90	17.46	17.43
CaO	24.08	26.17	10.93	25.34	25.21
Na2O	0.24	0.16	0.06	0.11	0.06
K2O	0.00	0.33	0.09	0.01	0.00
TOTAL	99.77	99.05	88.71	99.83	100.08
Fe2O3	0.00	0.99	5.19	0.42	0.10
FeO	2.25	0.93	0.00	1.32	1.74
Total novo	99.65	99.15	89.23	99.87	100.09
Number of ions on base of 6 oxygen					
TSi	2.006	1.977	1.858	1.992	1.996
TAl	0.000	0.023	0.044	0.001	0.000
TFe3	0.000	0.000	0.098	0.007	0.003
SOMA T	2.006	2.000	2.000	2.000	1.999
M1Al	0.038	0.002	0.000	0.000	0.000
M1Ti	0.000	0.010	0.000	0.006	0.004
M1Fe3	0.033	0.027	0.056	0.004	0.000
M1Zr	0.000	0.000	0.000	0.000	0.000

M1Mg	0.964	0.868	0.944	0.947	0.944
M1Fe2	0.031	0.029	0.000	0.040	0.051
M1Mn	0.000	0.003	0.000	0.003	0.000
SOMA M1	1.000	0.939	1.000	1.000	1.000
M2Mg	0.000	0.000	0.524	0.000	0.000
M2Fe2	0.038	0.000	0.000	0.000	0.001
M2Mn	0.002	0.000	0.003	0.004	0.014
M2Ca	0.938	1.033	0.463	0.988	0.982
M2Na	0.017	0.011	0.005	0.008	0.004
M2K	0.000	0.016	0.005	0.000	0.000
SOMA M2	0.994	1.060	1.000	1.000	1.001
Sum_cat	4.000	4.000	4.000	4.000	4.000
Jd	1.77	0.22	0.00	0.33	0.43
Ae	3.42	0.93	5.83	0.30	0.28
En	50.66	44.12	66.22	47.26	47.19
Fs	1.60	1.46	0.00	2.00	2.57
Mn	0.11	0.14	0.24	0.36	0.68
Wo	49.28	51.84	25.62	49.19	49.13
	106.85	98.71	97.91	99.44	100.28
Jd	1.73	0.22	0.00	0.00	0.00
Ae	3.32	0.48	0.94	0.38	0.43
Es	0.00	2.26	4.70	0.80	0.43
CaTiTs	0.00	0.00	0.00	0.00	0.00
CaTs	2.17	0.00	0.00	0.00	0.00
Wo	46.70	50.59	20.80	49.14	48.95
En	49.12	43.47	73.39	47.49	47.30
Fs	3.49	0.92	0.00	1.71	2.43
MnFs	0.10	0.00	0.17	0.06	0.46
Fe2+-NaT	0.00	2.06	0.00	1.18	0.87

Fe2-NaZ	0.00	0.00	0.00	0.00	0.00
	106.64	100.00	100.00	100.76	100.87

nomenc final morimoto (1990)	diopsídio	diopsídio	augita com Fe3+	diopsídio	diopsídio
Jd	1.77	0.22	0.00	0.33	0.44
Ae	3.42	0.94	6.76	0.31	0.28
WEF	101.65	98.84	106.76	100.64	100.72
	106.85	100.00	113.52	101.28	101.45

Trace elements in pyroxene minerals of Indaiá Kimberlite

Concentrations in ppm (µg/g)			
Li7	0.62	0.80	1.34
Be9	0.05	<0.139	<0.103
B11	<1.61	<2.34	<1.86
P31	5.00	<6.23	56.29
Sc45	0.86	1.25	1.87
Ti49	<2.25	<3.71	52.38
V51	1.39	<1.20	2.62
Cr52	7.10	10.69	218.05
Mn55	267.62	422.20	453.61
Co59	43.04	67.91	59.13
Ni60	927.18	1482.90	1024.73
Cu65	0.22	0.45	1.82
Zn66	14.45	22.81	39.98
Ga71	0.02	<0.043	<0.038
Rb85	<0.027	<0.045	<0.033
Sr88	0.04	0.32	0.05

Y89	<0.0052	0.00	0.02
Zr90	0.01	0.03	0.71
Nb93	0.25	0.46	0.05
Mo95	0.07	<0.053	0.03
Sn118	0.44	0.40	0.38
Sb121	<0.036	<0.064	<0.040
Cs133	<0.0041	<0.0056	<0.0034
Ba137	0.33	0.61	0.23
La139	<0.00141	<0.0045	0.01
Ce140	0.00	0.01	0.01
Pr141	0.00	<0.0027	<0.00116
Nd143	<0.0191	<0.033	<0.027
Sm147	<0.0095	<0.0185	0.02
Eu151	<0.0034	<0.0063	<0.0041
Gd157	<0.0156	<0.0163	<0.0070
Tb159	0.00	<0.00146	<0.00189
Dy161	0.01	<0.0110	<0.0058
Ho165	0.00	<0.0026	<0.00220
Er166	<0.0058	<0.0071	0.00
Tm169	<0.00145	<0.0030	<0.0017
Yb172	0.00	0.01	<0.0082
Lu175	<0.00172	0.00	<0.00102
Hf179	0.01	<0.023	0.04
Ta181	<0.00165	0.00	0.00
Pb206	0.02	0.04	0.05
Pb207	0.03	0.04	0.06
Pb208	0.03	0.04	0.05
Th232	<0.00	<0.00	<0.00
U238	<0.00082	<0.00130	<0.00095